The development of reliable chemical kinetic mechanisms to describe the oxidation of natural gas blends containing C_1– C_7 *n*-alkanes and the effects of NOx on natural gas oxidation at practical combustor relevant conditions

By

Ahmed Abd El-Sabor Mahmoud Mohamed

(M. Sc, B. Sc)

Supervisor: Prof. Henry J. Curran

Dissertation submitted in partial fulfillment of the requirements for the degree of

Doctor of Philosophy in the College of Science and Engineering

National University of Ireland Galway

Mechanical Engineering

National University of Ireland, Galway

Submitted October 2021

Abstract

The use of natural gas (NG) for transportation and heavy-duty power generation applications has led to an increase in demand for conventional and non-conventional NG sources. Moreover, techniques such as exhaust gas recirculation (EGR) are used to control NOx emissions from combustors such as internal combustion engines (ICEs) and gas turbines (GTs). Several studies have shown that the presence of higher hydrocarbon and/or NOx species in NG mixtures can significantly affect auto-ignition behavior, which is a critical parameter for gas turbines, spark-ignited (SI), and homogeneous charge compression ignition (HCCI) engines. Thus, it is critical to understand the oxidation of NG mixtures containing different fractions of higher alkanes and the impact of NOx species on the oxidation of their mixtures in order to mitigate emissions and increase engine efficiency. Therefore, this research study focuses on building a comprehensive database of experimental measurements of ignition delay times (IDTs) for NG mixtures contain C_1 – C_7 *n*-alkanes. Moreover, the effect of the addition of NOx on both methane and ethane oxidation, the primary components of NG mixtures, is studied. These data are critical in the development of a reliable chemical kinetic mechanism to describe the oxidation of these mixtures. In addition, the chemical kinetic mechanism is used to develop empirical equations which are helpful in quickly predicting the IDTs of different mixtures. The IDT experiments were carried out in two independent but complementary experimental facilities at NUI Galway, namely the (red) rapid compression machine (RCM) used for the low- to intermediate-temperature regimes and the high-pressure shock-tube (HPST) used to study the intermediate and high temperatures regimes depending on the fuel mixture's reactivity. The IDT measurements were performed over a wide range of operating conditions, including compressed temperatures (T_C) = 650 – 2000 K, compressed pressures (p_C) = 10 – 40 bar and at equivalence ratios (φ) = 0.5 – 2.0. These data provide a direct understanding of the auto-ignition characteristics of the mixtures studied and are used together with a wide range of available literature data including IDTs from RCMs and STs, speciation from a flow reactor (FR) and a jet-stirred reactor (JSR), as well as flame speed data to develop a reliable chemical kinetic mechanism.

This thesis is dedicated to those whom I love especially:

My parents, Abd Elsabor and Amaal

My dear wife, Noha, and my daughters Janna and Shams.

Acknowledgements

First and foremost, I thank ALLAH for all the blessings which are innumerable. ALLAH is the conciliator for all that is good and there is no power but from ALLAH Almighty.

I owe a deep sincerest gratitude to my supervisor Prof. Henry Curran not only for providing me with the precious opportunity to study at the Combustion Chemistry Centre (C^3), but also for the encouragement he has always given me during my PhD which gave me more confidence to finish my study on time and with good outcomes. It has been a great learning and a tremendously positive experience in my life that I will hold dear. Thank you, Henry.

I am obligated to Science Foundation Ireland and Siemens Energy Canada Ltd. for financially assisting my project via project number 16/SP/3829. I hope I have done justice to all of your expectations.

I must deeply thank Prof. Gilles Bourque for his support, management, and the good experience that he gave during the monthly meetings we had since I started working on the project.

I would also like to thank our administration/technical staff within the school of chemistry, particularly Mr. Dermot McGrath, Mr. Séamus Kellehan, Mr. Séamus Collier, and Mr. Gerard Reilly for their valuable technical support with regards to the experimental facilities and in ordering parts and consumables.

I must thank Dr. Mohammadreza Baigmohammadi, Dr. Kieran Somers, Dr. Ultan Burke, Dr. Snehasish Panigrahy, Dr. Amrit Sahu, and Dr. Shijun Dong who provided me with technical support. A big thanks to Dr. Patrick Meier who has provided immense technical support with the experimental facilities.

I have been fortunate to be surrounded by such amazing friends at C^3, I would like to thank my fellow PhD students, Dr. Jennifer, Dr. Yanjin, Sergio, Gavin, Vaibhav, Dr. Shashank, Dr. Nitin and all of the other visiting researchers for all of their technical support, fun, and making my time enjoyable.

Most importantly, I thank my parents (Abd Elsabor Mohamed and Amaal Saad) who worked and helped me to achieve our dream to be a good person who is useful for the human community.

My dear wife Noha, I could never have imagined pursuing a Doctoral degree without your belief in me and your encouragement over the last three and half years. As well as the very good achievements we have had since we started our life journey in August 2014 right now started by getting my master's degree and have two beautiful daughters Janna and Shams.

Declarations

This is to certify that:

1. This thesis consists of my original work towards the degree of Doctor of Philosophy except where indicated appropriately.
2. The work reported herein is as a result of my own investigation, except where acknowledged and referenced.

Ahmed Abd El-Sabor Mahmoud Mohamed (Ahmed Mohamed)

Peer reviewed journal articles

1. A.B. Sahu, **A. Abd El-Sabor Mohamed**, S. Panigrahy, G. Bourque, and H.J. Curran, "Ignition studies of $C_1 - C_7$ natural gas blends at gas-turbine relevant conditions." *J. Eng. Gas Turbines Power* 143(8) (2021) 081022. https://doi.org/10.1115/1.4050063. **(Chapter 2)**

2. **A. Abd El-Sabor Mohamed**, S. Panigrahy, A.B. Sahu, G. Bourque, H.J. Curran, "An experimental and modeling study of the auto-ignition of natural gas blends containing $C_1 - C_7$ *n*-alkanes", Proc. Combust. Inst. 38 (2021) 365–373. https://doi.org/10.1016/j.proci.2020.06.015. **(Chapter 3)**

3. **A. Abd El-Sabor Mohamed**, A.B. Sahu, S. Panigrahy, G. Bourque, H.J. Curran, "Ignition delay time correlation of $C_1 - C_5$ natural gas blends for intermediate and high temperature regime", *J. Eng. Gas Turbines Power* 143(12) (2021) 121025. https://doi.org/10.1115/1.4051908. **(Chapter 4)**

4. A.B. Sahu, **A. Abd El-Sabor Mohamed**, S. Panigrahy, G. Bourque, H.J. Curran, "An experimental and kinetic modeling study of NOx sensitization on methane autoignition and oxidation", Combust. Flame (available online 28th September 2021, 111746). https://doi.org/10.1016/j.combustflame.2021.111746. **(Chapter 5)**

5. M. Baigmohammadi, V. Patel, S. Nagaraja, A. Ramalingam, S. Martinez, S. Panigrahy, **A. Abd El-Sabor Mohamed**, K.P. Somers, U. Burke, K.A. Heufer, A. Pekalski, H.J. Curran, "Comprehensive Experimental and Simulation Study of the Ignition Delay Time Characteristics of Binary Blended Methane, Ethane, and Ethylene over a Wide Range of Temperature, Pressure, Equivalence Ratio, and Dilution", Energy Fuels. 34 (2020) 8808–8823. https://doi.org/10.1021/acs.energyfuels.0c00960. **(Chapter 7)**

6. S. Martinez, M. Baigmohammadi, V. Patel, S. Panigrahy, A.B. Sahu, S.S. Nagaraja, A. Ramalingam, **A. Abd El-Sabor Mohamed**, K.P. Somers, K.A. Heufer, A. Pekalski, H.J. Curran, "An experimental and kinetic modeling study of the ignition delay characteristics of binary blends of ethane/propane and ethylene/propane in multiple shock tubes and rapid compression machines over a wide range of temperature, pressure, equivalence ratio", Combust. Flame. 228 (2021) 401–414. https://doi.org/10.1016/j.combustflame.2021.02.009. **(Chapter 8)**

Articles in review

1. **A. Abd El-Sabor Mohamed**, A.B. Sahu, S. Panigrahy, G. Bourque, H.J. Curran, "The effect of the addition of nitrogen dioxides on the oxidation of ethane: an experimental and modeling study", Combust. Flame (2021) submitted. **(Chapter 6)**

Oral Presentations:

1. "An experimental and modeling study of the auto-ignition of natural gas blends containing C_1–C_7 *n*-alkanes", 38th International Symposium on Combustion, Adelaide, Australia, Virtual Conference, January 24, 2021 – January 29, 2021.
2. "Ignition delay time correlation of C_1–C_5 natural gas blends for intermediate and high temperature regime", ASME 2021 TURBO EXPO: Turbomachinery Technical Conference & Exposition, Virtual Conference and Exhibition: June 7 – 11, 2021.

Contents

Table of contents

Table of contents

List of Figures

Table of contents

Table of contents

Table of contents

List of Tables

Preface

This manuscript presents the scientific results I have obtained since I have started my PhD in July 2018. When I started my research at the Combustion Chemistry Centre (C^3), I was given a task to learn how to use the rapid composition machine (RCM) which was the first time for me to see such a piece of equipment. Once I was well trained and started to perform experiments, I have been asked to contribute to experiments on different projects and these experimental results have been included in two peer-reviewed scientific articles which are described in Chapters 7 and 8.

As part of my project to study the auto-ignition of NG mixtures comprising $C_1 - C_7$ *n*-alkanes, methane/NOx, and ethane/NOx, I acted as an experimental chemist and engineer. I was responsible for updating the inlet manifold system of the red RCM at C^3 by installing a new manifold with new connections which facilitated the connection of a mixing tank to prepare the seven components *n*-alkanes NG mixtures. Moreover, a 1 L tank was used to mix the NOx species with the studied fuels (methane and ethane), and a new pressure gauge with a small range of 20 mbar to accurately add NOx species at ppm concentrations.

Moreover, I have learned how to use the high-pressure shock tube. Once I was trained I started to perform experiments by myself to extend the experimental study of my project to higher temperatures than those accessible in the RCM.

Over the last three and half years I have been fortunate to be involved in many such projects, where my role as part of a collaboration has often been that of an experimental chemist, and engineer. In this way, I am proud to have a good role in my project team as well as with other project teams. In this way, my research has been an interdisciplinary journey. To showcase the complete work I performed, I have decided to write an article-based thesis. The published scientific articles are an effective way to communicate technical breakthroughs.

I have organized this manuscript into nine Chapters. Chapter 1 provides a background of the research questions addressed and gives a brief description of the lab-scale reactors used in the studies. Chapters 2 – 6 include the peer-reviewed publications from my main project. Chapters 7 and 8 provide the peer-reviewed publications of my experimental contribution to other projects. Chapter 9 reports general conclusions and recommended future work. Finally, appendices are included, which are a compilation of the supporting information from the publications and the experimental raw data.

CHAPTER 1

INTRODUCTION

Chapter 1: Introduction

This chapter presents the background and motivation of the work reported in this thesis and includes the importance of a chemical kinetic mechanism in understanding fuel characteristics and in developing an optimized combustor. Moreover, a brief description of the lab-scale reactors used to generate the experimental data is included and the simulation and analytical methods used are discussed.

1.1 Background and Motivation

Controlling energy production and consumption plays a vital role in improving living standards. Fossil fuels remain the primary source of energy production and consumption being responsible for about 80% of world energy supply as indicated in Fig. 1-1 [1].

Fossil fuels are a non-renewable source of energy that take millions of years to produce, and reserves are being depleted at a much faster rate than are being re-created. Fossil fuels are a unique blend in that they are an extraordinary energy source but also produce harmful emissions. The process of extracting energy from hydrocarbon fuels (fuel burn) ultimately produces carbon dioxide (CO_2), water vapor (H_2O), and many other harmful emissions such as nitrogen oxides (NOx), unburned hydrocarbons, sulfur dioxide (SO_2) and carbon monoxide (CO). Carbon dioxide comprises 74% of greenhouse gas (GHG) emissions, with the majority (89%) coming from the combustion of fossil fuels. Several combustion exhaust gases have been demonstrated as GHGs including CO_2, methane (CH_4), and N_2O [2].

Natural gas (NG) is the lowest CO_2 emitting fossil fuel when it burns [1], Table 1-1 compares the amount of CO_2 emitted per unit of energy output or heat content. Besides the low CO_2 emissions produced while burning NG compared to other fossil fuels it counts as an economical energy source. However, strict measures and precautions must be taken to prevent leakage when extracting, transporting, and using NG as it consists of mainly methane which is a strong GHG.

Chapter 1

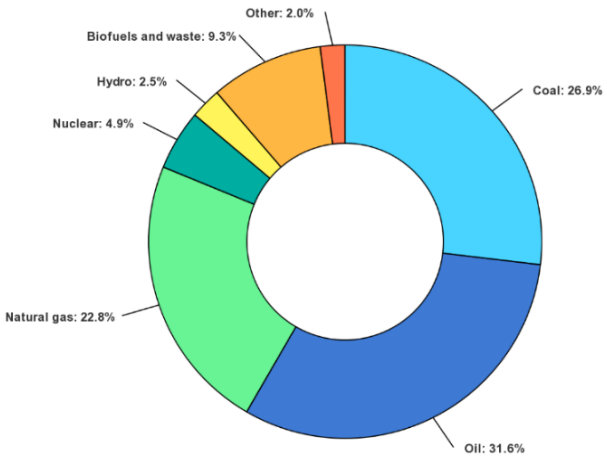

Figure 1-1. World total energy supply [1].

Table 1-1. Pounds of CO_2 emitted per million British thermal units (Btu) of energy [1].

Fossil fuels	Pounds of CO_2 emitted /10^6 KJ of energy
Coal (anthracite)	241.186
Coal (bituminous)	217.025
Coal (lignite)	227.259
Coal (subbituminous)	226.098
Diesel fuel and heating oil	170.181
Gasoline (without ethanol)	165.855
Propane	146.653
Natural gas	123.442

The potential of natural gas (NG) as an alternative fuel for transportation and heavy-duty power generation applications has led to an increase in demand for conventional and non-conventional NG sources. NG is primarily composed of methane with some heavier alkanes ranging from ethane to heptane [3,4]. The annual NG production, consumption, and gross exports report from the United States (U.S.) Energy Information Administration's (EIA) in 2019 [5] shows that dry natural gas production increased by 10%, reaching a record-high average of 2.636 billion cubic meter per day (Bm^3/d). Despite the increase in U.S. natural gas production, the consumption rate increased by 3%, led by greater use of natural gas in the electric power sector. Thus, the U.S. natural gas gross exports increased 29% to 12.8 Bcf/d.

The declining concentration of $>C_2$ species on a volume/mol basis is an observed trend in samples of NG found around the world. These are identified by Siemens Energy Canada Ltd. who wants to ensure that NG mixtures of varying composition can be used in its gas turbines and determine if there is any limitation in terms of pollutants, power range, or fuel supply systems. Thus, this study is motivated to achieve highly efficient and safe use of NG by performing both experimental and kinetic modeling studies for a wide range of NG mixtures to verify their varying combustion characteristics.

Combustion Engines (CEs) are devices that can convert the chemical energy stored in any kind of liquid fuel (e.g., petroleum), gaseous fuel (e.g., natural gas), and solid fuel (e.g., coal) through controlled combustion to produce thermal energy, ultimately producing useful mechanical energy. These devices are commonly classified into two types, internal combustion, and external combustion engines. The invention and development of CEs had a profound impact on human life. Currently, combustion engines are the most commonly used devices to generate power. These engines include gasoline engines, diesel engines, gas-turbine engines, and rocket-propulsion systems.

The ongoing development of combustion devices requires a better understanding of the characteristics of the fuel used over a wide range of conditions relevant to the conditions of its operation to finally achieve the highest possible efficiency of a combustor. One of the most effective techniques is exhaust gas recirculation (EGR) which plays a major role in reducing nitrogen oxides (NOx) emission levels by reducing the combustion temperature of internal combustion engines and gas turbines [6–8]. As the presence of NOx in the combustion products is unavoidable under such operating conditions, understanding the effect of NOx on fuel oxidation is necessary to achieve the highest possible efficiency of EGR applications. Thus, this study has been performed to achieve a better understanding of the effect of the presence of NOx species on the auto-ignition characteristic of methane and ethane which are the primary

components of NG mixtures. Therefore, this thesis includes both experimental and kinetic modeling studies of the auto-ignition of methane/NOx and ethane/NOx mixtures over a wide range of practical combustor relevant conditions.

1.2 Chemical kinetic models for fuel oxidation

As mentioned in the previous section to achieve highly efficient and safe use of wide range of NG mixtures and EGR technique it requires both experimental and kinetic modeling studies. The current experimental measurements along with the literature lead to accurately develop reliable kinetic mechanisms. These mechanisms then will be used to simulate the combustion processes in practical combustors for various fuels over a wide range of conditions at much lower cost relative to a direct experimental approach aiding to an efficient and optimized practical combustors. In their review [9] Westbrook and Dryer presented a hierarchical approach to mechanism development. Thus, this strategy has been used to develop reliable chemical kinetic mechanisms which can precisely describe in detail the pyrolysis, the thermal decomposition of the fuel, and/or oxidation processes of heavy and more complex hydrocarbons starting from the C_0 sub-mechanism, represented by the H_2/O_2 system, up to C_n species at elevated temperatures and pressures. Figure 1-2 shows a general schematic mechanism for ethane pyrolsis and methane oxidation. This strategy helps researchers to better understand the pyrolysis and oxidation processes of hydrocarbons by recognizing critical reaction pathways. In this way, it can easily recognize the foremost reactions which control these processes from relatively simple fuel combustion such as hydrogen or hydrogen/syngas mixtures to methane, and ethane up to very complex fuel combustion such as natural gas (NG), liquefied petroleum gas (LPG), gasoline, and diesel.

A fuel's combustion characteristics such as flame speed, speciation profiles, auto-ignition time, provide excellent validation data in the development of reliable chemical kinetic mechanisms

which can then be reduced and coupled with computational fluid dynamic (CFD) simulations to help in the design of efficient combustors. Laboratory scale combustion reactors such as combustion vessels, jet-stirred reactors, flow reactors (laminar and turbulent flow), rapid compression machines (RCMs), and shock tubes (STs) are used to measure combustion characteristics at conditions relevant to practical combustor operation.

Ignition delay time (IDT) is the time needed for a mixture of fuel and oxidizer to react and ignite at a certain temperature and pressure. The IDT measurements is one of the criteria that is extensively used to validate chemical kinetic mechanisms. Therefore, in this thesis, comprehensive IDTs measurements are reported using both a RCM and a high-pressure shock tube (HPST), reactors which have been used together with literature data to develop the NUIGMech versions which are reported upon in this thesis.

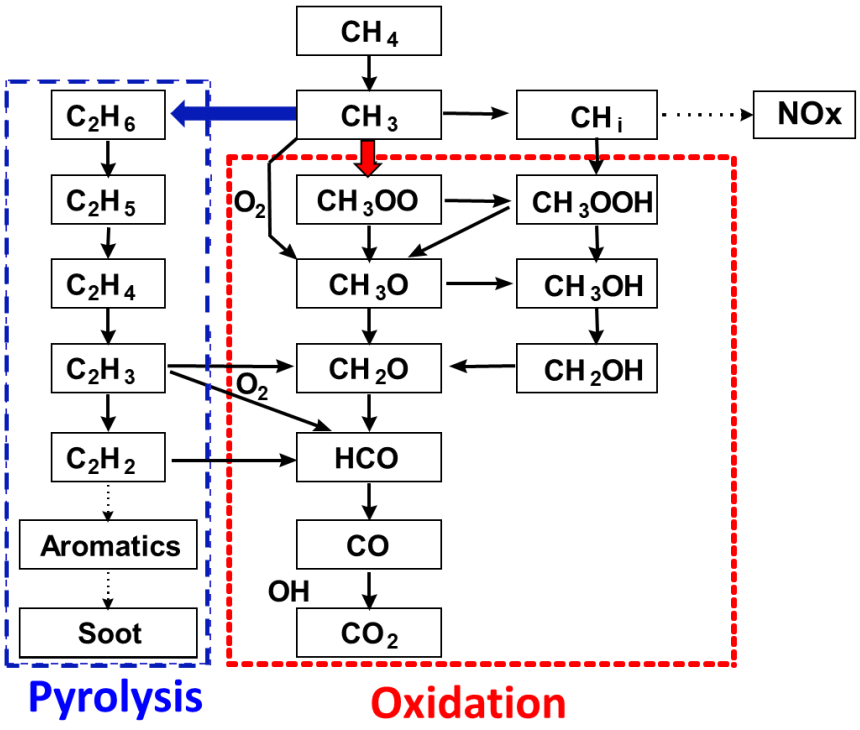

Figure 1-2. General schematic mechanism for ethane pyrolsis and methane oxidation.

1.3 Experimental facilities and mixture preparations

Fuel auto-ignition is an important fuel characteristic for combustor design. It is important to ensure that the time required to fully premix the fuel and air is shorter than the IDT required for the mixture at combustor operation conditions. Moreover, auto-ignition is the main process controlling combustion in homogeneous charge compression ignition (HCCI) engines.

RCMs and STs are two independent, but complementary lab-scale reactors used to investigate fuel auto-ignition characteristics at combustor relevant conditions. In this thesis, these two facilities were extensively used to study the autoignition of various fuels over a wide range of conditions. Associated non-idealities of both RCMs and STs during their normal operation can be found in refs. [10–15].

1.3.1 Rapid compression machine

The NUI Galway rapid compression machine is used to emulate the compression stroke of an internal combustion engine, but it is quite different in that it undergoes only one compression at a time and does not have the ability to perform multiple cycles. At the end of the compression process, the pistons are held in position using a hydraulic locking system so that the IDT characteristics of a mixture can be measured at a defined compressed temperature and pressure. RCMs have gained significant attention in the combustion community to study relatively low-temperature fuel oxidation chemistry at thermodynamic conditions relevant to IC engines and gas turbines.

At NUI Galway C^3 lab there are two RCMs and to differentiate between them it has refer been referred to them as red and blue which are the colors of the pneumatic cylinders. The general specifications of the NUI Galway (red) RCM are presented in Table 1-2**.** The RCM used to perform the IDTs measurements included in this thesis was originally designed by Affleck and Thomas [16]. In the 1960s the RCM was constructed at the Shell Thornton Research Centre and

re-commissioned at NUI Galway in the 1990s to perform chemical kinetic experiments [17]. Figure 1-3 shows a schematic diagram of the NUI Galway RCM facility and Figure 1-4 shows a digital photo of the red RCM, mixing tanks and the inlet manifold. The red-RCM has an opposed twin-piston design with creviced pistons to improve the homogeneity of the gas after compression [18]. The RCM comprises three main systems, the pneumatic system which controls piston movement in both the compression and retracting processes, the hydraulic system which is responsible for holding the pistons in place before and after compression, and finally the chemical reaction chamber which is responsible for holding the test mixture and the pressure sensor(s). Each system has its own components which are described briefly here and only the main components appear in the schematic diagram.

Table 1-2. Specifications of the NUI Galway (red) RCM.

Parameter	Value
Bore size of the reaction chamber (cm)	3.820
Volume of the reaction chamber (cm^3)	33.191
Piston's velocity (U_p) (cm/s)	934.0 ~ 1294.0
Pistons' stroke length (cm)	16.817
Piston's type	Flat head with the crevice
Type	Twin-counter pistons

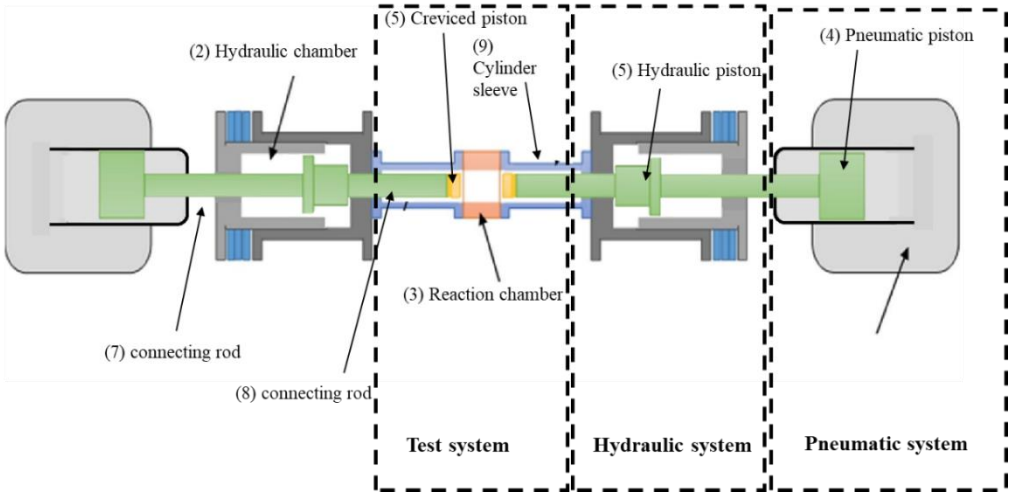

Figure 1-3. A schematic diagram of the NUIG RCM facility.

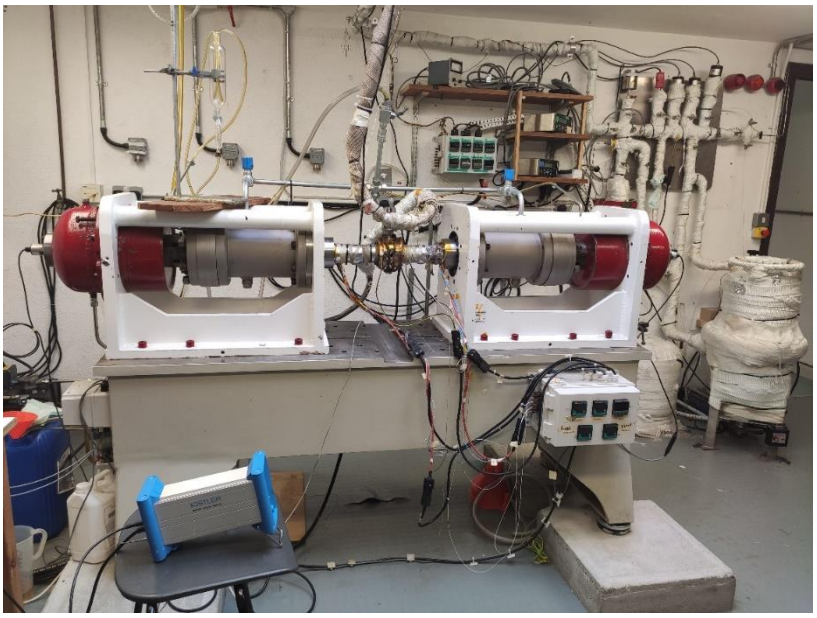

Figure 1-4. A photograph of the (red) RCM, including mixing tanks and the inlet manifold.

1.3.1.1 The pneumatic system components:

Two pneumatic chambers (1) are connected through a three-way valve to a compressed airline with a capacity of up to 10 bar pressure which can vent to the atmosphere and to a vacuum pump. The compressed airline supplies the pneumatic chambers with the appropriate amount of pressurized air needed for the compression process. These pistons are indirectly connected to the main pistons through two rods. The first rod (7) connects the pneumatic piston (4) to the hydraulic piston (5) and the second rod (8) connects the hydraulic piston (5) to the creviced piston. The vent is used to release the pressurized air to the atmosphere after performing an experiment, and the vacuum pump is responsible for retracting the pistons to their original positions.

1.3.1.2 The hydraulic system components:

Two hydraulic chambers (2) filled with hydraulic oil are connected to an oil pump which apply a locking pressure of 40 bar. The two chambers are connected to a valve in order to manually release the pressure allowing the two creviced pistons (5) to compress the test mixture in the reaction chamber (3).

1.3.1.3 The chemical reaction chamber components:

The reaction chamber consists of the reaction chamber (3), the two creviced pistons (5), and the two-cylinder sleeves (9). A Kistler 6045B pressure transducer, mounted flush with the reaction chamber wall, is connected to a Kistler charge amplifier in conjunction with an oscilloscope to record pressure/time (*p/t*) histories. As the geometric compression ratio (CR) of the RCM is fixed, in order to span a range of the compressed gas temperatures (T_C) and pressures (p_C), the initial temperature (T_i) and initial pressure (p_i) are varied following Equations 1-1 and 1-2. The variation in T_i is controlled using a heating system implemented on the walls of the cylinder and the reaction chamber together with five thermocouples installed on the outer body of two-cylinder sleeves (9) to accurately control T_i. The p_i is measured using pressure readings from the static pressure gauges connected to the inlet manifold. Gaseq [19] is used assuming an adiabatic compression/expansion, to calculate the compressed gas temperature according to Equation 1-3:

$$T_c = T_i \left(\frac{V_i}{V_c}\right)^{\gamma-1} \tag{1-1}$$

$$p_c = p_i \left(\frac{V_i}{V_c}\right)^{\gamma} \tag{1-2}$$

$$\ln\left(\frac{p_c}{p_i}\right) = \int_{T_i}^{T_c} \frac{\gamma}{\gamma - 1} \frac{dT}{T} \tag{1-3}$$

where V_i, V_c, are the initial volume (maximum volume) and the compressed volume (minimum volume) of the reaction chamber, respectively, and γ is specific heat ratio of the test mixture. The reactive (fuel/O_2/diluent) and non-reactive (fuel/diluent) test mixtures are transferred from the reactive and non-reactive tanks, respectively, to the reaction chamber through the inlet manifold. The reaction chamber is connected to a vacuum pump to flush the exhaust gases after completing an experiment.

For fuel/oxidizer mixtures which exhibit a strong peak pressure at ignition, the IDT is defined as the interval between the time of the first peak pressure at the end of compression (EOC) to the second global peak pressure due to the ignition event as shown in Figure 1-5. Due to the weak

pressure signal for the highly dilute ethane/NO_2 conditions, a photomultiplier (PMT) equipped with a CH* filter (CWL: 430 nm ± 10 FWHM; Thorlabs) is used together with the pressure trace to measure the IDT for dilute mixtures. The ignition event is reported at the maximum gradient pressure ($\frac{dp}{dt}$) or in CH^* ($\frac{dCH^*}{dt}$) after compression as shown in Figure 1-6.

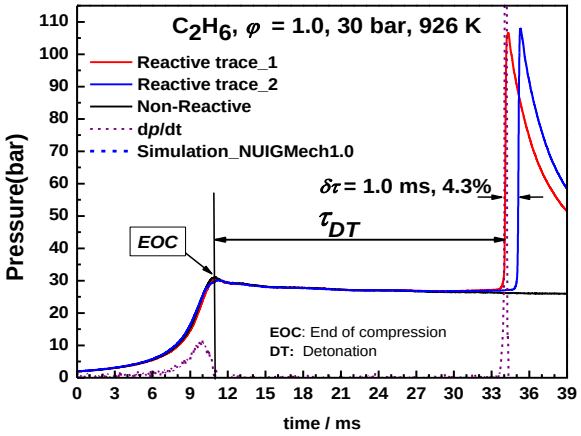

Figure 1-5. Typical RCM pressure-time histories for ethane oxidation at φ = 1.0 in 'air' and 30 bar.

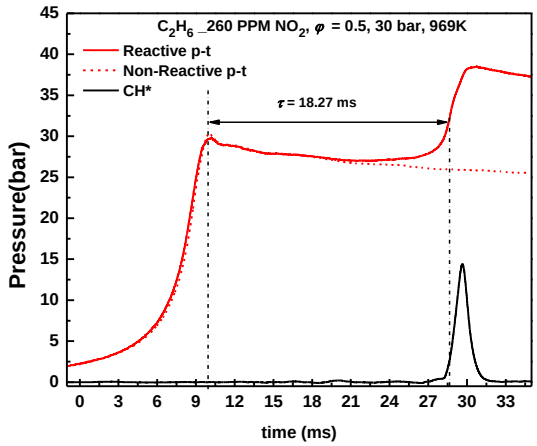

Figure 1-6. Typical RCM pressure versus time histories for ethane/NO_2 oxidation at φ = 0.5 and 91% dilution at p_C = 30 bar.

1.3.2 Mixture preparation and the used gases purity

The inlet manifold has been modified to prepare the mixtures presented in the thesis. Figure 1-7 shows the schematic diagram and the photograph of the red RCM Inlet manifold and mixing tanks.

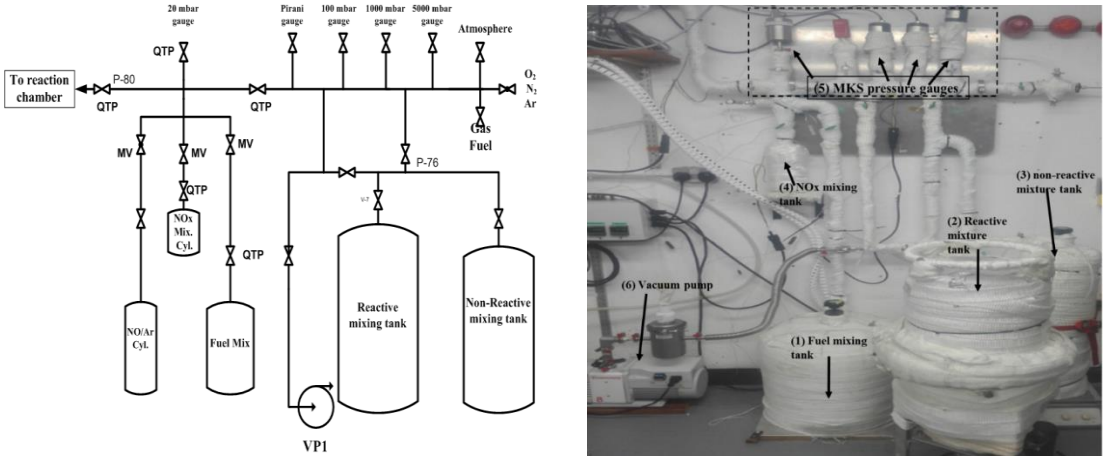

Figure 1-7. The schematic diagram and the photograph of the red RCM Inlet manifold and mixing tanks.

A fuel mixing tank (1) was used to prepare the seven component ($C_1 – C_7$) *n*-alkane fuel mixture in order to minimize any errors in mixture preparation. The mixture was allowed to homogenize via gaseous diffusion for at least 12 h before using it to prepare the final reactive fuel/O_2/(N_2/Ar) and non-reactive fuel/(N_2/Ar) mixtures in the reactive (2) and non-reactive (3) tanks respectively. The N_2/Ar fractions were varied to ensure a wide range of compressed gas temperatures. A separate 1.0 L NOx mixing tank (4) was connected to the line for NO_x (NO, NO_2 and N_2O) species addition where the desired NO_x species was allowed to mix with the fuel/O_2/(N_2/Ar) mixture for 5 – 10 min before filling the reaction chamber. In addition, a set of non-reactive experiments were performed at the same initial condition of the reactive experiments by replacing O_2 with N_2 in the reactive mixture, the pressure-time of which are converted to volume-time histories and are used as input files in Chemkin simulations in order to account for facility affects in simulating the RCM experiments.

The purities of the fuels used vary based on availability from the supplier and are as follows: methane (99.5%), ethane (99.5%), propane (99.5%), *n*-butane (99.9%), NO_2 diluted in Ar (99.99% purity) (2% NO_2/98% Ar), NO diluted in Ar (99.99% purity) (4% NO_2/96% Ar), and N_2O (99.5% purity) were supplied by Air Liquide company. The liquid fuels, *n*-pentane (99%), *n*-hexane (99%), and *n*-heptane (99%) were supplied by Sigma Aldrich and were used without

further purification. The diluent and oxidizer gases, nitrogen (> 99.96%), argon (> 99.98%), and oxygen (> 99.5%) were supplied by BOC Ireland.

1.3.3 Shock tube

A shock-tube is a laboratory device with no moving parts, extensively used in the fields of aerodynamics, physics and chemistry, to study fuel auto-ignition as well as elementary rate constant measurements usually at shorter times (≤ 2 ms) in the high temperature (≥ 1000 K) regime. In this study, the reflected shock technique was implemented to measure IDTs of various reactive fuel/air mixtures. As shown in Figure 1-8 the shock tube is a long tube with closed ends separated into two main sections, namely, the driver section (filled with high pressure driver gas—often helium or a helium/nitrogen mixture) usually separated by double diaphragm from the driven section (filled to a relatively low pressure of the test mixture).

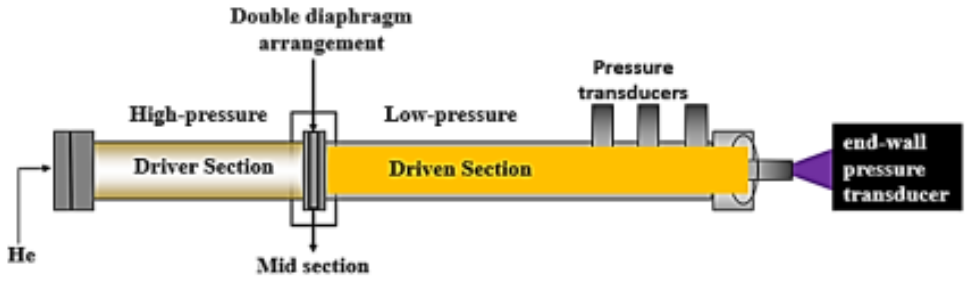

Figure 1-8. A schematic diagram of the NUIG HPST facility.

1.3.3.1 Principles of shock tube operation

In performing a ST experiment, both the driver, mid and driven sections were evacuated. Thereafter, the driven section is first filled with the low-pressure test gas mixture. Thereafter, the mid-section and the driver section are over-pressured to a high pressure of the driver gas, where normally the mid-section is filled to half the final desired driver pressure. Finally, the driver is filled to the final desired pressure and releasing the pressure of the mid-section allows the diaphragm to burst as a result of the pressure difference between the diver and driven sections.

Once the diaphragm bursts an incident shock wave propagates at supersonic speed toward the driven section, which causes an increase in the temperature and pressure of the test gas. The incident shock wave reaches the endwall and reflects back towards the driver section further compressing and heating the test gas to the desired test temperature and pressure. Steady test times of shock tubes are usually terminated by the arrival of rarefaction waves from the driven section or reflected waves from the shock-contact surface interaction, depending on the test condition and geometry of the shock tube. Figure 1-9 shows an idealized wave structure during shock wave experiments. It further illustrates a typical distance-time indicating the shock front position, plotted in an x-t diagram for successive longitudinal time-pressure distributions. Moreover, Figure 1-10 shows the shock tube pressure distribution before and after bursting the diaphragm. The test time used to study reflected shock experiments is considered as the time between the arrival of the shock wave at the endwall and the arrival of the contact surface, as shown in Figure 1-9. As a result of the effective step-change in shock conditions and the effective stagnation of the test gas mixture behind the reflected shock wave, the test gas mixture can potentially be treated as a 0-dimensional reactor and modeled assuming a constant volume. However, important deviations from the idealized constraints are often present such as pre-ignition pressure rise and a constant *dp/dt* that should be identified and reported upon when presenting experimental data. Figure 1-9 shows the five different gas regions present during shock tube experiments which are used to determine the gaseous conditions during an experiment. “Region 1” denotes the initial test gas conditions. “Region 2” refers to the conditions of the gas particles between the contact surface and the incident shock front. The condition of the gas between the contact surface and the rarefaction fan is denoted “region 3”. The initial driver gas conditions are denoted as “region 4” while the post reflected shock conditions are referred to as “region 5”.

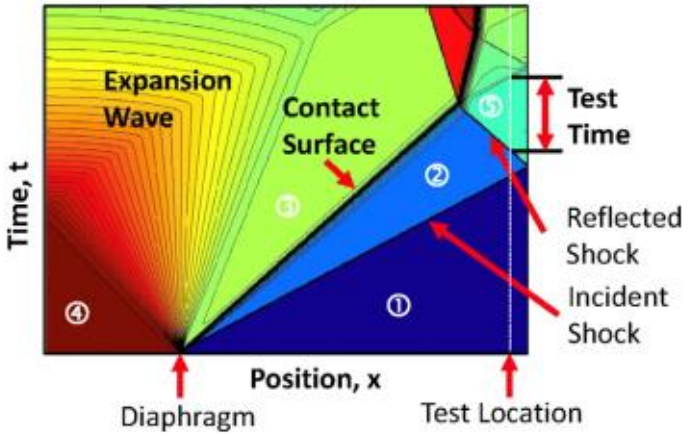

Figure 1-9. A representative x-t diagram of shock wave experiment. Brown, high-pressure driver gas (T_4, p_4); dark blue, low-pressure test gas mixture (T_1, p_1); blue, test gas mixture at incident shock conditions (T_2, p_2); green and yellow and red in expansion wave regime, expanded driver gas (T_3, p_3); turquoise triangle, test gas mixture at reflected shock conditions (T_5, p_5) , copied from [20].

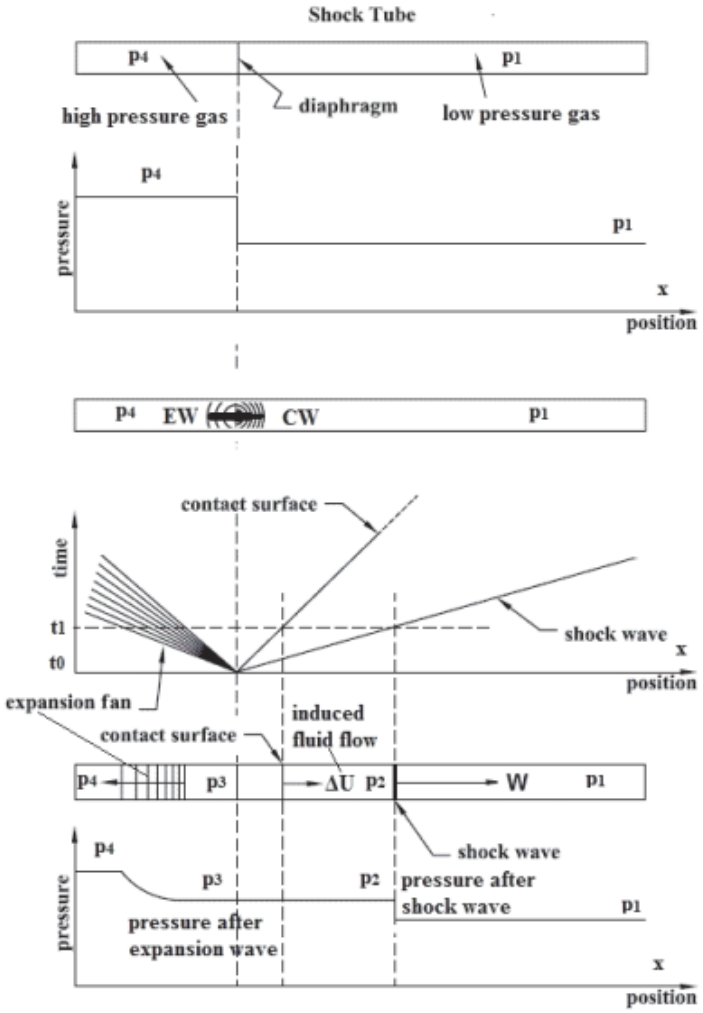

Figure 1-10. Shock tube pressure distribution before and after diaphragm burst, copied from [24].

1.3.3.2 Computation of flow behind shock waves

To understand the gas dynamics during a ST experiment, two frames of reference should be considered. These are (i) the shock-tube laboratory timeframe (t_l) and (ii) the gas-particle timeframe (tp). The time recorded on an external recording device is referred to as the laboratory fixed time and the time with respect to the movement of flowing gas particles through a static shock front is the gas-particle time or shock fixed time.

The theory behind the conditions across the shock front are governed by the equations of conservation of mass, momentum, and energy as described by Rankine-Hugoniot [21,22] and full analyses and associated equations are well documented and presented in the Chemkin manual [23].

1.3.3.2.1 Incident shock conditions

In considering the gas motion in relation to the shock front [23], one must consider two frames of reference, the gas enters the shock at a relative velocity u_1 and leaves with a relative velocity u_2. The shock is then considered to be at rest: u_2 is the incident shock velocity of the gas measured in shock-fixed coordinates while U_s is the measured in laboratory-fixed coordinates, the two frames of reference are related by:

$$u_1 = U_s \tag{1-4}$$

$$u_2 = U_s - U_2 \tag{1-5}$$

Figure 1-11 shows gas conditions associated with the incident shock in the two coordinate systems. The properties behind the incident, region 2, shock wave can be calculated using the three conservation equations of mass, linear momentum, and energy for gas phase reactive flow, Rankine-Hugoniot [21,22] relations:

$$\rho_1 u_1 = \rho_2 u_2 \tag{1-6}$$

$$p_1 + \rho_1 u_1^2 = p_2 + \rho_2 u_2^2 \tag{1-7}$$

$$h_1 + \frac{u_1^2}{2} = h_2 + \frac{u_2^2}{2} \tag{1-8}$$

where, ρ, h, and p are the density, enthalpy, and pressure of the gas, respectively.

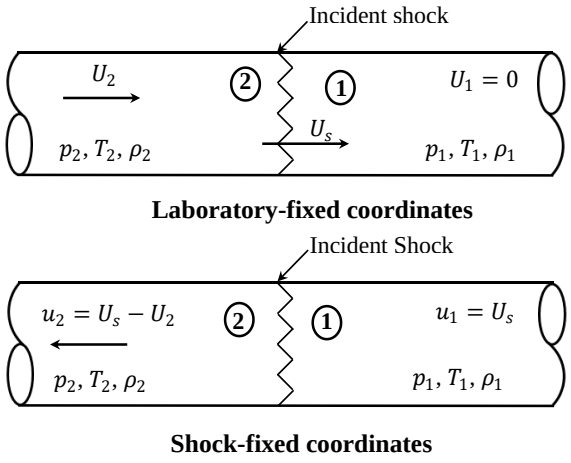

Figure 1-11. Laboratory-fixed and Incident-shock-fixed coordinate systems [23].

Utilizing the equation of state for the ideal Gas Law ($pV = nRT$) and Equation 1-6 to eliminate the velocity u_2 and from Equation 1-7 and Equation 1-8 results in the following expressions for the pressure and temperature ratios across the incident shock:

$$1 + \frac{\rho_1 {u_1}^2}{p_1}\left[1 - \left(\frac{T_2}{T_1}\right)\left(\frac{p_1}{p_2}\right)\right] - \frac{p_2}{p_1} = 0 \tag{1-9}$$

$$h_1 + \frac{{u_1}^2}{2}\left[1 - \left(\frac{T_2}{T_1}\right)^2\left(\frac{p_1}{p_2}\right)^2\right] - h_2 = 0 \tag{1-10}$$

As no change in gas composition across the shock assumed, and thus h is a function of temperature alone. Therefore, Equation 1-9 and Equation 1-10 represent a system of two equations with two unknowns. The solution gives ρ_2 and T_2 when conditions before the incident shock are specified. Knowing these, ρ_2 is determined from the equation of state and u_2 from Equation 1-6.

In this study, the incident shock speed (U_s), and the temperature (T_2) and pressure (p_2) behind the shock are reported. However, the gas velocity behind the shock must be calculated before the experiments can be modelled. Employing the equation of state in Equation 1-9 to eliminate ρ_1/p_1 results in:

$$1 + \frac{\rho_2 {u_1}^2}{p_2}\left(\frac{T_2}{T_1}\right)\left[1 - \left(\frac{T_2}{T_1}\right)\left(\frac{p_1}{p_2}\right)\right] - \frac{p_2}{p_1} = 0 \quad (1\text{-}11)$$

Equation 1-11 and Equation 1-10 again represent two equations with two unknowns. The solution gives T_1 and p_1 and from these the density in region 1 is determined from the equation of state. The velocity behind the shock (u_2) is determined from Equation 1-6.

The shock Mach number (M), Equation 1-12, also can be calculated. The upstream Mach number (M_1) is calculated based on, U_s, the incident shock speed reported during an experiment as shown in Equation 1-14, are also required for the calculation of the post-shock conditions.

$$M = \frac{u}{a} \quad (1\text{-}12)$$

$$a = \sqrt{\frac{\gamma p}{\rho}} \quad (1\text{-}13)$$

$$M_1 = U_s\left(\sqrt{\frac{\rho_1}{\gamma p_1}}\right) \quad (1\text{-}14)$$

where, $u, a,$ and γ are the gas local velocity, local speed of sound, and the ratio of specific heats, respectively.

1.3.3.2.2 Reflected shock conditions

Shock-fixed and laboratory-fixed coordinates are again employed for reflected shocks, but now shock-fixed coordinates refer to the reflected shock, which moves at velocity U_{rs} and Figure 1-12 shows gas conditions associated with the reflected shock in the two coordinate systems.

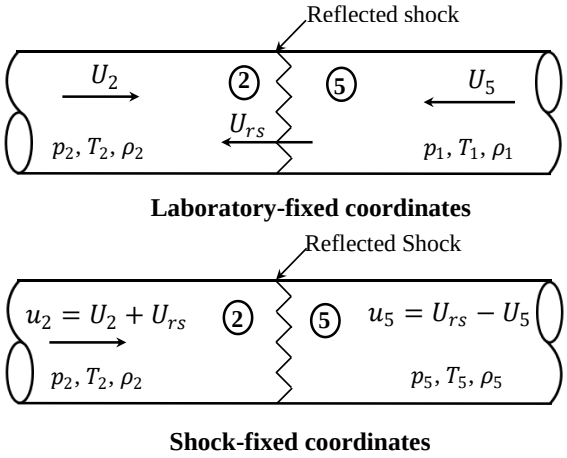

Figure 1-12. Laboratory-fixed and Reflected-shock-fixed coordinate systems [23].

As the reflected shock is considered to be at rest, gas at condition 2 flows into the shock front and gas at condition 5 flows out. The velocities in the two coordinate systems are as follows:

$$u_2' = U_{rs} + U_2 \tag{1-15}$$

$$u_5 = U_{rs} - U_5 \tag{1-16}$$

The Rankine-Hugoniot relations for properties across the reflected shock are:

$$\rho_2 u_2' = \rho_5 u_5 \tag{1-17}$$

$$p_2 + \rho_2 (u_2')^2 = p_5 + \rho_5 u_5^2 \tag{1-18}$$

$$h_2 + \frac{(u_2')^2}{2} = h_5 + \frac{u_5^2}{2} \tag{1-19}$$

Following the same analyses of the incident shock the solution for Equations 1-17, 1-18, and 1-19, is found by getting the values of T_5 and p_5 which satisfy:

$$1 + \frac{\rho_1 (u_2')^2}{p_1}\left[1 - \left(\frac{T_5}{T_2}\right)\left(\frac{p_2}{p_5}\right)\right] - \frac{p_2}{p_5} = 0 \tag{1-20}$$

$$h_2 + \frac{(u_2')^2}{2}\left[1 - \left(\frac{T_5}{T_2}\right)^2\left(\frac{p_2}{p_5}\right)^2\right] - h_5 = 0 \tag{1-21}$$

When the gas is assumed to be at rest behind the reflected shock, $U = 0$, then the reflected shock velocity, U_{rs}, is given by:

$$U_{rs} = \frac{\left(\frac{p_2}{p_5}\right)\left(\frac{T_5}{T_2}\right)(U_s - u_2)}{\left[1 - \left(\frac{T_5}{T_2}\right)\left(\frac{p_2}{p_5}\right)\right]} \tag{1-22}$$

1.3.3.3 NUI Galway high-pressure shock tube

The high-pressure shock tube (HPST) facility at NUI Galway were used to conduct the IDTs measurements reported in this thesis, a brief description for the facility and the experiment procedure are provided below. Figure 1-13 shows a photograph of the NUIG HPST facility, respectively.

Table 1-3 shows the general information of the NUI Galway HPST which comprises a 9.0 m long stainless-steel tube with a uniform cross-section of 63.5 mm inner diameter. It is divided into three sections; a driver section (3 m), a driven section (5.73 m), and a double-diaphragm chamber (0.27 m) which separates the driver and driven sections.

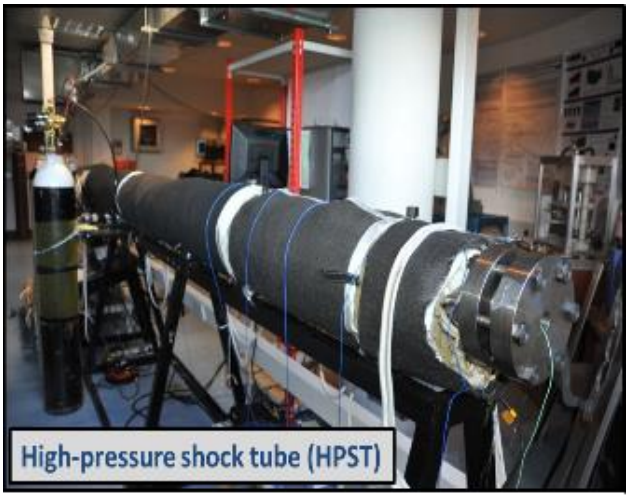

Figure 1-13. A photograph of the NUIG HPST.

Two pre-scored aluminium diaphragms are used, with the scoring depth varied depending on the target bursting pressure which enables improved control of the shock-wave. Helium is used as the driver gas and a fraction of nitrogen is used for tailoring. Six axially positioned PCB113B24 pressure transducers mounted in the walls of the tube at different location near to the endwall are used to measure the shock velocity (V_{Shock}). A Kistler 603B pressure transducer mounted in the endwall is used to measure the IDT. In the equilibrium program Gaseq [19] the "reflected shock" module, in conjunction with frozen chemistry, is used to calculate the reflected shock pressure (p_5) and temperature (T_5) using the initial pressure (p_1), the initial temperature (T_1), and V_{Shock}.

For the mixtures with 90% dilution, the IDTs were measured using a photodiode array detector (PDA) or photomultiplier (PMT) systems equipped with CH^* filter (CWL: 430 nm ± 10 FWHM; Thorlabs) installed on the sidewall of the shock tube's endcap due to very weak signals of the Kistler pressure transducer. The IDT of the HPST measurement is defined as the time interval between the pressure rise due to the shock-wave arrival at the endwall and the ignition event as shown in Figure 1-14 for fuel in 'air' mixture and Figure 1-15 for fuel in high dilution mixture.

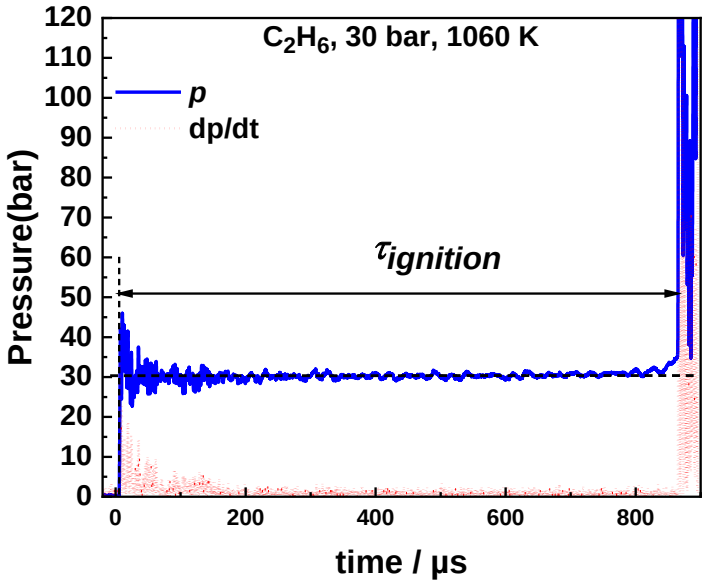

Figure 1-14. Typical HPST pressure-time histories for the ignition event at fuel in 'air' and 30 bar.

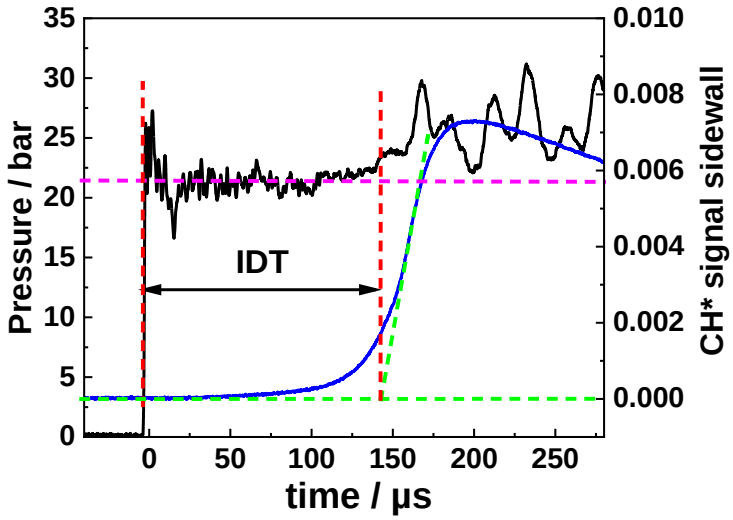

Figure 1-15. Typical HPST pressure-time histories for the ignition event at fuel in high dilution.

Table 1-3. Specifications of the NUI Galway high-pressure shock tube.

Total length	9.1 m	
Section	**Length (m)**	**Diameter (mm)**
Driver	3.0	63.5
Middle	0.04	63.5
Driven	5.7	63.5
Material	Stainless-steel (1.4571/316Ti and 1.4462/F51)	
Controlling system	Double-diaphragm type	
Diaphragm's material	Aluminium (1050 H14)	
Diaphragm's thickness	0.8~2 mm; according to target pressure	
Pre-scoring the diaphragms	0.2~1.1 mm; according to target pressure and the diaphragms' thickness	

1.4 Simulation and analytical methods

The experimental targets presented here were simulated using the appropriate modules available in Ansys Chemkin PRO [25] and a Python script based on the CANTERA [26] library for the ST simulations. A zero-dimensional constant volume reactor module was used and the reflected temperature and pressure conditions (T_C, p_C) were adopted as the initial conditions for the ST simulations. The RCM simulations are performed using the effective volume approach by imposing a heat loss boundary condition on the calculations due to facility effects, including heat losses, during compression and in the post-compression zone of the reaction chamber.

In order to better understand the fuel oxidation at wide range combustion relevant conditions, brute-force sensitivity analyses were performed to identify the reactions most influencing the IDT predictions at the experimental conditions studied. The sensitivity coefficient (S; [27]) is defined as Equation (1-23):

$$S = \frac{In(\tau_+/\tau_-)}{In(k_+/k_-)} = \frac{In(\tau_+/\tau_-)}{In(2.0/0.5)} \quad (1\text{-}23)$$

The sensitivity coefficient S is calculated using the brute force method and is based on the IDT (τ), with the pre-exponential factor in the Arrhenius equations for each reaction perturbed in the sensitivity analysis. The sensitivity coefficient can have either a positive or negative value, with a negative value indicating a reaction that promotes reactivity (decreasing the IDT), while a

positive value refers to a reaction that inhibits reactivity (increasing the IDT). Furthermore, flux and rate of production (ROP) analyses were carried out to track the most important reactions consuming the fuel and producing intermediate species.

1.5 Thesis layout

The focus of this thesis lies in building a comprehensive combustion kinetic data of IDT measurements from experiments in a RCM and in a HPST. A summary of the fuel compositions and corresponding experimental conditions studied as part of this thesis are shown in Tables (1-4) – (1-7).

Table 1-4. Natural gas blends studied.

Species	NG1	NG2	NG3	NG4	NG6	NG7	NG8	NG10
Methane (CH_4)	98.125	81.25	62.5	98.03125	60.625	72.635	45.27	35.601
Ethane (C_2H_6)	1	10	20	1	20	10	20	20
Propane (C_3H_8)	0.5	5	10	0.5	10	6.667	13.33	14.815
***n*-Butane(C_4H_{10})**	0.25	2.5	5.0	0.25	5.0	4.44	8.89	10.974
***n*-Pentane (*n*-C_5H_{12})**	0.125	1.25	2.5	0.125	2.5	2.965	5.93	8.129
***n*-Hexane (*n*-C_6H_{14})**	–	–	–	0.0625	1.25	1.976	3.95	6.021
***n*-Heptane (*n*-C_7H_{16})**	–	–	–	0.03125	0.625	1.317	2.63	4.460

Table 1-5. Experimental conditions of the natural gas blends studied.

Blend	φ	p_C / bar	T_C / K	Facilities
NG1	0.5, 1.5	20, 30	873 – 1037	RCM
NG2	0.5, 1.0, 2.0	10,18, 20, 30	711 – 1054	RCM
	1.0	20, 30	1037 – 1483	ST
NG3	1.0	20, 30	754 – 952	RCM
			1015 – 1426	ST
NG4	0.5, 1.5	20, 30	862 – 1031	RCM
NG6	1.0	20, 30	670 – 1032	RCM
NG7	0.5, 1.0, 1.5	10, 20, 30	688 – 952	RCM
NG8	1.0	20, 30	679 – 960	RCM
NG10	0.5, 1.0, 1.5	10, 20, 30	650 – 1052	RCM

The IDT data measured are vital in developing accurate chemical kinetic mechanisms and in improving the predictability of existing kinetic models to describe the highly complex combustion processes involved in practical combustors.

Table 1-6. Experimental conditions studied for NOx sensitization of methane auto-ignition.

Exp.	CH_4	O_2	N_2	Ar	NO_2(ppm)	N_2O (ppm)	Initial NO (ppm)	φ	p_C / MPa	T_C / K
Rapid compression machine experiments										
1	6.0	24.0	15.0	55.0	–	–	–	0.5	1.5, 3.0	923 – 1064
2	10	20	–	70.0	–	–	–	1.0	1.5, 3.0	926 – 1102
3	15.0	15.0	–	70.0	–	–	–	2.0	1.5, 3.0	888 – 1067
4	5.94	23.76	14.85	55.43	200	–	–	0.5	1.5, 3.0	912 – 1056
5	5.9	23.52	14.40	55.56	400	–	–	0.5	1.5, 3.0	919 – 1037
6	9.89	19.8	–	70.28	200	–	–	1.0	1.5, 3.0	935 – 1053
7	9.79	19.59	–	70.56	400	–	–	1.0	1.5, 3.0	937 – 1016
8	14.85	14.85	–	70.28	200	–	–	2.0	1.5, 3.0	901 – 1058
9	14.7	14.7	–	70.56	400	–	–	2.0	1.5, 3.0	904 – 1061
10	9.89	19.8	–	70.26	–	400	–	1.0	1.5, 3.0	926 – 1105
11	9.75	19.5	–	70.65	–	1000	–	1.0	3.0	939 – 1067
12	5.97	23.88	14.93	55.2	–	–	200	0.5	1.5, 3.0	926 – 1036
14	5.94	23.76	14.85	55.41	–	–	400	0.5	1.5, 3.0	912 – 1056
15	10	20	–	70.0	–	–	50 – 1000	1.0	3.0	900 – 1050
16	14.93	14.93	–	70.13	–	–	200	2.0	1.5, 3.0	920 – 1037
17	14.85	14.85	–	70.26	–	–	400	2.0	1.5, 3.0	891 – 1043
High-pressure shock tube experiments										
18	10	20	70.0	–	–	–	–	1.0	1.5, 3.0	1050 – 1650
19	9.89	19.8	69.3	0.98	200	–	–	1.0	1.5, 3.0	1050 – 1650

More specifically, Chapter 2 investigates the effect on IDT measurements of the addition of *n*-hexane and *n*-heptane to natural gas blends using the RCM and numerically using a detailed kinetic model. The experiments of NG mixtures containing alkanes from methane to *n*-pentane (NG1) and methane to *n*-heptane (NG4) were carried out over a wide range of temperature T_C = 840 – 1050 K, pressure p_C = 20 – 30 bar and equivalence ratio φ = 0.5 and 1.5. The effect on measured IDTs for NG3 with the addition of up to 50% by mole of *n*-hexane and *n*-heptane is

numerically studied by substituting CH_4 with different fractions of these higher hydrocarbons. The results show that the addition of even small amounts of *n*-hexane and *n*-heptane (1 – 2%) to the natural gas blends leads to a significant increase in reactivity.

Table 1-7. Experimental conditions studied for NOx sensitization on ethane auto-ignition.

Ethane/NO_2 at φ = 1.0 in 'air'								
Initial NO_2 (ppm)	**C_2H_6 %**	**NO_2 (ppm)**	**O_2 %**	**Diluent %**		**p_C / bar**	**T_C / K**	**Facility**
				N_2	**Ar**			
0	5.66	–	19.82	74.52	–	20, 30	1006 – 1382	ST
0	5.66	–	19.82	14.90	59.62	20, 30	885 – 970	RCM
200	5.61	200	19.62	73.77	0.98	20, 30	944 – 1351	ST
200	5.61	200	19.62	14.76	59.99	20, 30	873 – 988	RCM
1000	5.38	1000	18.83	70.79	4.90	20, 30	1004 – 1368	ST
1000	5.38	1000	18.83	14.16	61.53	20, 30	855 – 989	RCM
Ethane/NO at φ = 1.0 in 'air'								
Initial NO (ppm)	**C_2H_6**	**NO/NO_2**	**O_2**	**N_2**	**Ar**	**p_C (bar)**	**T_C (K)**	
200	5.64	135/65	19.72	14.83	59.80	30	869 – 973	RCM
1000	5.52	280/720	19.32	14.53	60.53	30	851 – 958	RCM
Ethane/N_2O at φ = 1.0 in 'air'								
Initial N_2O (ppm)	**C_2H_6**	**N_2O**	**O_2**	**N_2**	**Ar**	**p_C (bar)**	**T_C (K)**	
1000	5.66	1000	19.82	14.91	59.51	20, 30	900 – 995	RCM
Ethane/NO_2 at φ = 0.5 diluted								
Initial NO_2 (ppm)	**C_2H_6**	**NO_2**	**O_2**	**N_2**	**Ar**	**p_C (bar)**	**T_C (K)**	
260	1.01	260	7.05	54.38	37.53	20, 30	908 – 1038	RCM
2704	1.05	2704	7.31	78.12	13.25	20, 30	816 – 960	RCM
5163	1.00	5163	6.98	66.20	25.30	20, 30	805 – 961	RCM

Chapter 3 provides IDTs measurements for multi-component NG mixtures comprising $C_1 – C_7$ *n*-alkanes with methane as the major component (volume fraction: 0.35 – 0.98). These measurements were carried out using the rapid compression machine at conditions relevant to gas turbine operation, at equivalence ratios of 0.5 – 2.0 in 'air' in the temperature range 650 – 1050 K, at pressures of 10 – 30 bar. Significantly different IDTs are measured over a wide range of conditions along with the available literature data providing a strong validation target for the development of NUIGMech1.0. Replacing 1.875% methane with 1.25% *n*-hexane and 0.625%

n-heptane in a mixture containing $C_1 – C_5$ components leads to a significant increase in a mixture's reactivity.

Chapter 4 provides new HPST IDTs measurements for stoichiometric $C_1 – C_5$ NG blends with methane as the major component. The good agreement of the new IDTs experimental data with literature data shows the reliability of the new data at the conditions investigated. Empirical IDT correlation equations were developed by employing a traditional Arrhenius rate expression. The format includes dependencies on the individual fuel fraction, T_C, φ and p_C and are developed through multiple linear regression analyses for these $C_1 – C_5$ *n*-alkane/'air' mixtures using constant volume IDT simulations in the pressure range p_C = 10 – 50 bar, at T_C = 950 – 2000 K and at φ = 0.3 – 3.0.

Chapter 5 investigates the auto-ignition behavior of CH_4 and CH_4 doped with NO_x species (NO, NO_2, and N_2O) in the low- to intermediate temperature range of 900 – 1100 K at p_C = 15 and 30 bar using the RCM and CH_4 and CH_4 doped with 200 ppm NO_2 at high temperatures of 1050 – 1650 K at p_C = 15 and 30 bar using the HPST. These conditions are relevant to practical combustors (ICEs and GTs) and thus provide benchmark measurements for ignition behavior as a function of temperature, pressure, NO_x dilution levels and equivalence ratio. These experimental results together with available literature data were simulated using NUIGMech1.2 comprising an updated NO_x sub-mechanism.

Chapter 6 investigates the auto-ignition behavior of C_2H_6 and C_2H_6 doped with 0 – 1000 ppm NO_x species (NO, NO_2, and N_2O) in the low- to intermediate temperature range of 851 – 995 K at p_C = 20 and 30 bar using the RCM and C_2H_6 and C_2H_6 doped with 0 – 1000 ppm NO_2 in the high temperature range of 944 – 1382 K at p_C = 20 and 30 bar using the HPST. These experimental results along with the available literature data were simulated using NUIGMech1.2 comprising an updated NO_x sub-mechanism.

Chapters 7 and 8 provide a comprehensive database of IDT measurements for binary blends of $C_1 - C_2$ and $C_2 - C_3$ alkane/alkene gaseous fuels together with the literature data for single $C_1 - C_3$ alkane and alkene gaseous fuels that is used to develop and validate the core chemistry of NUIGMech1.0. Moreover, IDT correlation equations were also developed for these blends.

Chapter 7 reports a comprehensive database of IDT measurements for binary blended $C_1 - C_2$ alkane/alkene fuels including methane/ethylene, methane/ethane, and ethane/ethylene over a wide range of temperature, pressure, equivalence ratio, fuel/fuel volume fraction, and dilution. The experimental data provides a new insight into the oxidation of alkane/alkene blended fuel mixtures. These findings in terms of safety and the design of new low-emission and size-efficient combustion systems are very useful and informative.

Chapter 8 reports the IDT characteristics of $C_2 - C_3$ binary blends of gaseous hydrocarbons including ethylene/propane and ethane/propane studied over a wide range of temperatures (750 – 2000 K), pressures (1 – 135 bar), equivalence ratios ($\varphi = 0.5 - 2.0$) and dilutions (75 – 90%). The performance of NUIGMech1.1 and its corresponding derived correlations are evaluated against the experimental data collected.

References

[1] World Energy Outlook 2020 – Analysis – IEA.
[2] N.C. Report, https://climate.nasa.gov/causes/.
[3] L.J. Spadaccini, M.B. Colket, Ignition delay characteristics of methane fuels, Prog. Energy Combust. Sci., 20 (1994) 431–460.
[4] S. Faramawy, T. Zaki, A.A.E. Sakr, Natural gas origin, composition, and processing: A review, J. Nat. Gas Sci. Eng., 34 (2016) 34–54.
[5] E.I.A. (EIA), U.S. natural gas production, consumption, and exports set new records in 2019.
[6] K.K. Botros, G.R. Price, G. Kibrya, Thermodynamic, Environmental and Economic Assessment of Exhaust Gas Recirculation for NOx Reduction in Gas Turbine Based Compressor Station, (1999).
[7] M. Lapuerta, J.J. Hernandez, F. Gimenez, Evaluation of exhaust gas recirculation as a technique for reducing diesel engine NOx emissions, Proc. Inst. Mech. Eng. Part D J. Automob. Eng., 214 (2000) 85–93.
[8] C.N. Pratheeba, P. Aghalayam, Effect of Exhaust Gas Recirculation in NOx Control for Compression Ignition and Homogeneous Charge Compression Ignition Engines, Energy Procedia., 66 (2015) 25–28.
[9] C.K. Westbrook, F.L. Dryer, Chemical kinetic modeling of hydrocarbon combustion, Prog. Energy Combust. Sci., 10 (1984) 1–57.
[10] E.L. Petersen, R.K. Hanson, Nonideal effects behind reflected shock waves in a high-pressure shock tube, Shock Waves, 10 (2001) 405–420.
[11] E.L. Petersen, Interpreting Endwall and Sidewall Measurements in Shock-Tube Ignition Studies, Combust. Sci. Technol., 181 (2009) 1123–1144.
[12] C.-J. Sung, H.J. Curran, Using rapid compression machines for chemical kinetics studies, Prog. Energy Combust. Sci., 44 (2014) 1–18.
[13] R.K. Hanson, D.F. Davidson, Recent advances in laser absorption and shock tube methods for studies of combustion chemistry, Prog. Energy Combust. Sci., 44 (2014) 103–114.
[14] B.W. Weber, C.J. Sung, M.W. Renfro, On the uncertainty of temperature estimation in a rapid compression machine, Combust. Flame, 162(6) (2015) 2518–2528.
[15] S.S. Goldsborough, S. Hochgreb, G. Vanhove, M.S. Wooldridge, H.J. Curran, C.J. Sung, Advances in rapid compression machine studies of low- and intermediate-temperature autoignition phenomena, Prog. Energy Combust. Sci., 63 (2017) 1–78.
[16] W.S. Affleck, A. Thomas, An Opposed Piston Rapid Compression Machine for Preflame Reaction Studies, Proc. Inst. Mech. Eng., 183 (1968) 365–387.
[17] L. Brett, J. Macnamara, P. Musch, J.M. Simmie, Simulation of methane autoignition in a rapid compression machine with creviced pistons, Combust. Flame, 124 (2001) 326–329.
[18] J. Würmel, J.M. Simmie, CFD studies of a twin-piston rapid compression machine, Combust. Flame, 141 (2005) 417–430.
[19] C. Morley, Gaseq program, (n.d.). http://www.gaseq.co.uk (accessed September 29, 2017).
[20] S. Wang, D.F. Davidson, R.K. Hanson, Shock tube techniques for kinetic target data to improve reaction models, Comput. Aided Chem. Eng., 45 (2019) 169–202.
[21] W.J.M. Rankine, XV. On the thermodynamic theory of waves of finite longitudinal

disturbance, Philos. Trans. R. Soc. London, 160 (1870) 277–288.
[22] H. Hugoniot, Memoir on the propagation of movements in bodies, especially perfect gases (first part), J. l'Ecole Polytech., 57 (1887).
[23] R.J. Kee, F.M. Rupley, J.A. Miller, M. Coltrin, J. Grcar, E. Meeks, H. Moffat, A. Lutz, G. Dixon-Lewis, M. Smooke, CHEMKIN theory manual, USA React. Des. (2006).
[24] P.X. Huang, S. Yonkers, D. Hokey, D. Olenick, Screw pulsation generation and control: a shock tube mechanism, Inst. Mech. Eng. - 8th Int. Conf. Compressors Their Syst., (2013) 113–128.
[25] R. CHEMKIN-PRO, 15112, Reaction Design, Inc., San Diego, CA. (2011).
[26] D.G. Goodwin, R.L. Speth, H.K. Moffat, Cantera: an object-oriented software toolkit for chemical kinetics, thermodynamics, and transport processes. Version 2.2. 1, Version 2.4. 0 2018, (n.d.).
[27] V. Gururajan, F.N. Egolfopoulos, Direct sensitivity analysis for ignition delay times, Combust. Flame, 209 (2019) 478–480.

CHAPTER 2

IGNITION STUDIES OF C_1–C_7 NATURAL GAS BLENDS AT GAS-TURBINE RELEVANT CONDITIONS

Chapter 2: Ignition Studies of $C_1 - C_7$ Natural Gas Blends at Gas-Turbine Relevant Conditions

Published in: Journal of Engineering for Gas Turbines and Power, August 2021, 143(8): 081022.
DOI: https://doi.org/10.1115/1.4050063

Authors and Contributions

1) **Amrit Bikram Sahu** (National University of Ireland, Galway, Ireland)
Contribution: Chemical kinetic modelling and manuscript preparation.
2) **Ahmed Abd El-Sabor Mohamed** (National University of Ireland, Galway, Ireland)
Contribution: RCM experiments and manuscript preparation.
3) **Snehasish Panigrahy** (National University of Ireland, Galway, Ireland)
Contribution: Chemical kinetic modelling.
4) **Gilles Bourque** (Siemens Energy Canada Ltd, Montreal QC H9P 1A5, Canada)
Contribution: Project management and manuscript review.
5) **Henry J. Curran** (National University of Ireland, Galway, Ireland)
Contribution: Project management and manuscript review.

Abstract

New ignition delay time measurements of natural gas mixtures enriched with small amounts of *n*-hexane and *n*-heptane were performed in a rapid compression machine to interpret the sensitization effect of heavier hydrocarbons on auto-ignition at gas-turbine relevant conditions. The experimental data of natural gas mixtures containing alkanes from methane to *n*-heptane were carried out over a wide range of temperatures (840–1050 K), pressures (20–30 bar), and equivalence ratios (φ = 0.5 and 1.5). The experiments were complemented with numerical simulations using a detailed kinetic model developed to investigate the effect of *n*-hexane and *n*-heptane additions. Model predictions show that the addition of even small amounts (1–2%) of *n*-hexane and *n*-heptane can lead to increase in reactivity by ~40–60 ms at compressed temperature (T_C) = 700 K. The ignition delay time (IDT) of these mixtures decrease rapidly with an increase in concentration of up to 7.5% but becomes almost independent of the C_6/C_7 concentration beyond 10%. This sensitization effect of C_6 and C_7 is also found to be more pronounced in the

temperature range 700–900 K compared to that at higher temperatures (> 900 K). The reason is attributed to the dependence of IDT primarily on $H_2O_2(+M) \leftrightarrow \dot{O}H + \dot{O}H (+M)$ at higher temperatures while the fuel dependent reactions such as H-atom abstraction, $R\dot{O}_2$ dissociation or $\dot{Q}OOH + O_2$ reactions are less important compared to 700–900 K, where they are very important.

Keywords: Natural gas; RCM; kinetic modeling; *n*-hexane; *n*-heptane.

Abbreviations

IDT Ignition delay time
NG Natural gas
ST Shock tube
RCM Rapid compression machine
NTC Negative temperature coefficient
EOC End of compression

Nomenclature

T_C Compressed temperature
p Pressure
φ Equivalence ratio

2.1 Introduction

Due to increasing concerns about depleting petroleum fuel reserves, the combustion community have paid significant attention to fuel-flexible gas turbine engines for transportation and heavy-duty power generation applications. As a promising alternative fuel resource, natural gas (NG) is the most commonly used gaseous fuel for industrial gas turbine applications due to its high efficiency, low soot emissions and low greenhouse gas signature [1,2]. Although natural gas primarily contains methane (CH_4) [3,4], depending on the topographical origin and extraction process, it also comprises heavier hydrocarbons varying in composition from ethane (C_2H_6) to *n*-heptane (n-C_7H_{16}). In order to validate the combustion characteristics of NG with varying compositions, experimental and kinetic modeling investigations are necessary. One important combustion feature of any fuel is auto-ignition, which can be experimentally determined using a rapid compression machine (RCM) and/or a shock tube (ST) at gas turbine relevant conditions. Studying the ignition behavior of heavier hydrocarbon surrogates including *n*-hexane (n-C_6H_{14})

and *n*-heptane (*n*-C_7H_{16}) in NG blends can deliver a concrete understanding of NG oxidation, that can lead to more effective gas turbine engine design and operation.

As methane is the major component of NG mixtures, extensive studies of CH_4 auto-ignition and oxidation have been performed at conditions relevant to combustion devices, including gas turbines and internal combustion engines [5–10]. Several studies also developed chemical kinetic mechanisms to model various compositions of NG mixtures which included lighter weight alkanes *n*-C_1–C_5 [11–14]. After methane, ethane is typically the second most abundant component in NG mixtures. Thus, many studies have been devoted to investigating the effect of ethane addition on CH_4 auto-ignition over a wide range of conditions [11,15,16]. The ignition characteristics of CH_4/C_3H_8, CH_4/*n*-C_4H_{10}, and CH_4/*n*-C_5H_{12} [11,15,17–24] mixtures were investigated using RCMs and STs at various temperatures and pressures. These studies showed that replacing CH_4 with heavier hydrocarbons increases negative temperature coefficient (NTC) behavior as well as decreasing the ignition temperature. Low temperature chemistry plays a more significant role with the addition of higher hydrocarbons in NG mixtures.

Ignition delay times (IDTs) of ternary mixtures $CH_4/C_2H_6/C_3H_8$ with various fuel mole fractions have also been studied [12,15,24,25]. The combustion features of $CH_4/C_2H_6/C_3H_8$, CH_4/C_2H_6/*n*-C_4H_{10}, CH_4/C_2H_6/*n*-C_5H_{12}, CH_4/C_3H_8/*n*-C_4H_{10}, and CH_4/C_3H_8/*n*-C_5H_{12} mixtures were investigated by de Vries and Petersen [15] for mixtures at $\varphi = 0.5$ in air at 20 bar pressure. They showed that the activation energy for fuel ignition reduced with the addition of higher hydrocarbons. Moreover, the reactivity of all of the blends was faster compared to pure methane. An auto-ignition study of C_2H_6/C_3H_8/*n*-C_4H_{10} was also conducted by Eubank et al. [12] for highly dilute mixtures in a ST and they observed that adding 0.4% ethane, propane, and *n*-butane to a 1% methane mixture decreased the IDTs to a factor of thirteen compared to those measured for pure methane.

It is observed from the relevant literature that, although some efforts have been made towards studying the ignition behavior of C_1–C_5 alkanes [13,14,26], experimental measurements and kinetic modelling of NG mixture blends containing *n*-hexane and *n*-heptane have not yet been reported. The objective of the present work is to provide useful measurements of IDTs for these blends at low-temperature and high-pressure conditions, relevant to gas turbine operation. We also develop detailed chemical kinetic mechanisms to accurately predict the experimentally measured ignition data. In the present work new IDT experiments are carried out using an RCM at φ = 0.5 and 1.5 in air, at 20 and 30 bar pressure at temperature range of 860–1050 K and these measurements are utilized to validate a kinetic model.

2.2 Experimental procedure

A twin, creviced-piston RCM has been used at NUI Galway to conduct the IDT measurements for the current C_1–C_7 natural gas blends. The RCM has been described previously [27]. A 6045B model Kistler pressure transducer is installed in the chamber wall in conjunction with a Kistler charge amplifier. To record the pressure/time histories of the experiments, the charge amplifier is connected to a computer through an Oscilloscope. By changing the initial temperature and pressure, an extended range of compressed gas temperatures and pressures are achieved using a fixed geometric compression ratio. Therefore, a fully controlled heating system is installed on the RCM. The IDT is defined as the time to maximum *dp/dt* after the end of compression (EOC).

A separate mixing tank is connected to the manifold line to prepare the seven *n*-alkanes C_1–C_7 fuel components to achieve the seven-component fuel mixture and is allowed to mix for 12h via gaseous diffusion before use. The gaseous fuels were sourced from Air Liquide with the following purities; methane (99.5%), ethane (99.5%), propane (99.5%), and *n*-butane (99.9%). The liquid fuels were supplied by Sigma Aldrich with the following purities; *n*-pentane (99%), *n*-hexane (99%), and *n*-heptane (99%). The fuels were used without further purification. The

diluent and oxidizer gases, nitrogen (> 99.96%), argon (> 99.98%), and oxygen (> 99.5%), were supplied by BOC Ireland. Table 2-1 summarizes the composition of two natural gas blends containing C_1–C_5 *n*-alkanes which were studied previously [13,14] and the new NG4 mixture containing C_1–C_7 *n*-alkanes. The oxidizer mixture used for the current study comprises of O_2 and diluent gas in the volumetric ratio of 1:3.76, where the diluent varies from 100% N_2 to 45:55 N_2/Ar blends depending on the experimental conditions. The oxidizer gas is hereafter referred to as 'air' in this work, with the diluent composition specified when N_2:Ar blends are used. Table 2-2 provides the relative fuel/O_2/N_2/Ar concentrations for the cases studied. The input files for non-reactive pressure histories that are required for the model simulations are available on request to the corresponding author. A total uncertainty of ±15% is estimated in the RCM IDT measurements.

Table 2-1. Natural gas blends studied.

Natural Gas / **Species**	**NG1**	**NG3**	**NG4**
Methane (CH_4)	98.125	62.5	98.03125
Ethane (C_2H_6)	1	20	1
Propane (C_3H_8)	0.5	10	0.5
n-Butane (C_4H_{10})	0.25	5.0	0.25
n-Pentane (*n*-C_5H_{12})	0.125	2.5	0.125
n-Hexane (*n*-C_6H_{14})			0.0625
n-Heptane (*n*-C_7H_{16})			0.03125

Table 2-2. Mixture composition (in %) used in the current study.

	NG3			**NG1**		**NG4**	
φ	**0.5**	**1**	**2**	**0.5**	**1.5**	**0.5**	**1.5**
X_{CH4}	2.1300	4.1200	7.7300	4.7900	13.1000	4.7600	13.0000
X_{C2H6}	0.6820	1.3200	2.4700	0.0488	0.1330	0.0486	0.1330
X_{C3H8}	0.3410	0.6600	1.2400	0.0244	0.0667	0.0243	0.0664
X_{C4H10}	0.1700	0.3300	0.6190	0.0122	0.0333	0.0122	0.0332
X_{nC5H12}	0.0852	0.1650	0.3090	0.0061	0.0167	0.0061	0.0166
X_{nC6H14}	–	–	–	–	–	0.0030	0.0083
X_{nC7H16}	–	–	–	–	–	0.0015	0.0042
X_{O2}	20.3000	19.6000	18.4000	20.0000	18.2000	19.0000	18.2000
$X_{diluent}$	76.3000	73.8000	69.2000	74.5000	68.5000	76.1000	68.5000

2.3 Chemical kinetic model

The detailed chemical kinetic reaction mechanism used in the present work is based on the ongoing development of a C_1–C_7 mechanism. This model contains a H_2/O_2 sub-mechanism [28], along with an updated C_1–C_5 base mechanism [29]. The C_6 and C_7 sub-mechanisms adopted are based on the works by Zhang et al. [30,31]. The hierarchical nature of the model is constructed based on several prior mechanisms developed at NUIG and is validated against extensive experimentally measured data such as IDT, speciation profiles obtained using flow reactors and jet-stirred reactors, as well as laminar flame speed measurements. The detailed integrated model is provided in a recent work by Wu et al. [32]. The model will be referred to as NUIGMech1.1. Constant volume simulations were carried out using Chemkin19.0. Facility effects were accounted for the RCM cases by using the non-reactive pressure time histories.

2.4 Results and discussion

2.4.1 Model validation with existing measurements

2.4.1.1 *n*-hexane/*n*-heptane

Figure 2-1 shows comparisons of NUIGMech1.1 and Zhang et al. [31] model predictions of IDT measurements in a shock tube for pure *n*-hexane [30] and *n*-heptane [31] at pressures ranging from 15–38 bar. The NUIGMech1.1 model is able to reproduce the ignition behavior for these alkanes with satisfactory agreement.

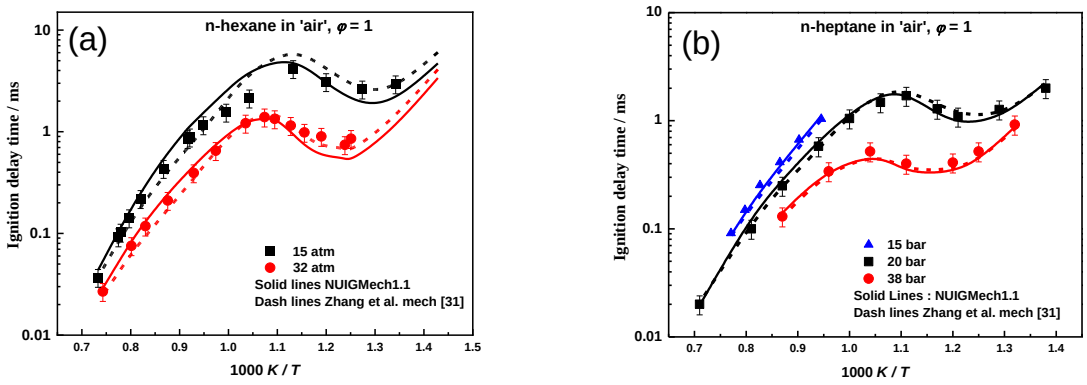

Figure 2-1. NUIGMech1.1 (solid lines) and Zhang et al. (dashed lines) simulation results for ignition delay times experiments (symbols) of pure fuel at stoichiometric condition (φ = 1.0) in air; (a) *n*-hexane [30]; and (b) *n*-heptane [31].

2.4.1.2 NG3 mixture

Figure 2-2 shows IDT measurements for the NG3 mixture at φ = 0.5–2.0 in air and pressures ranging from 8–30 bar which were reported previously [13,14]. NUIGMech1.1 reproduces these data with very good agreement over the range of conditions considered.

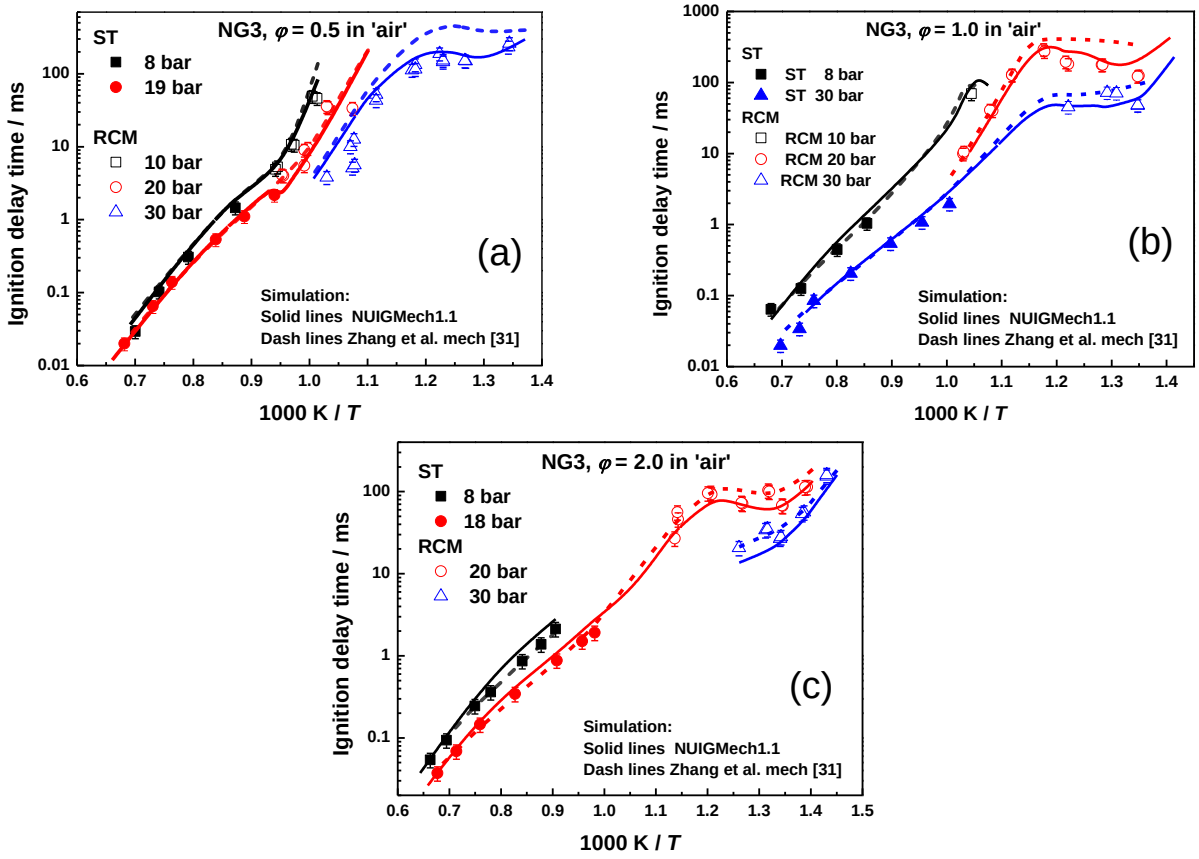

Figure 2-2. IDT predictions and measurements for NG3: symbols are experiments and lines are the simulations at different pressures; (a) fuel-lean mixtures (φ = 0.5); (b) stoichiometric mixture (φ = 1.0); and (c) fuel-rich mixtures (φ = 2.0) Simulations using NUIGMech1.1 and Zhang et al. [31] mechanisms.

2.4.2 Effect of addition of C_6 and C_7

2.4.2.1 Low level of C_6/C_7 addition (~ 0.1%)

Figure 2-3 illustrates the measured and computed IDTs for NG1 and NG4 mixtures at φ = 0.5 and 1.5, at compression pressures of 20 bar and 30 bar, in the temperature range 860–1050 K. NG4, which is similar to the NG1 mixture, with an additional ~0.1% *n*-C_6H_{14} and *n*-C_7H_{16}, shows a slight enhancement in reactivity for the fuel-rich cases especially at 30 bar, but there is no difference in measured IDTs for the fuel-lean cases. The model predictions using

NUIGMech1.1 capture these trends very well. In comparison, the Zhang et al. mechanism [31] tends to over-predict IDTs in the low–intermediate temperature regime for fuel-lean cases. For the fuel- rich conditions, as the fuel concentration is higher, any difference in the fuel compositions in the NG1 and NG4 mixtures becomes more significant when compared to the fuel-lean cases. As it is well known that low temperature chemistry relies on the fuel oxidation mechanism, and hence the difference in the reactivities between the two mixtures is more observable for the fuel-rich cases. However, at such low concentrations of *n*-C_6H_{14} and *n*-C_7H_{16}, the impact on the auto-ignition behavior is minimal.

2.4.2.1.1 Effect of pressure and equivalence ratio

The effect of pressure and equivalence ratio on the IDTs for the NG1 and NG4 mixtures are shown in Figures 2-4(a) and 2-4(b), respectively. A comparison of the experimental measurements with predictions shows that NUIGMech1.1 captures the reactivities almost perfectly at 20 bar for all cases. For both the NG1 and NG4 fuel-lean mixtures, the model over-predicts the IDTs by between 18–22% at 30 bar, which is within the uncertainty limits of the experimental measurements. Overall, NUIGMech1.1 shows a better agreement compared to the Zhang et al. mechanism [31].

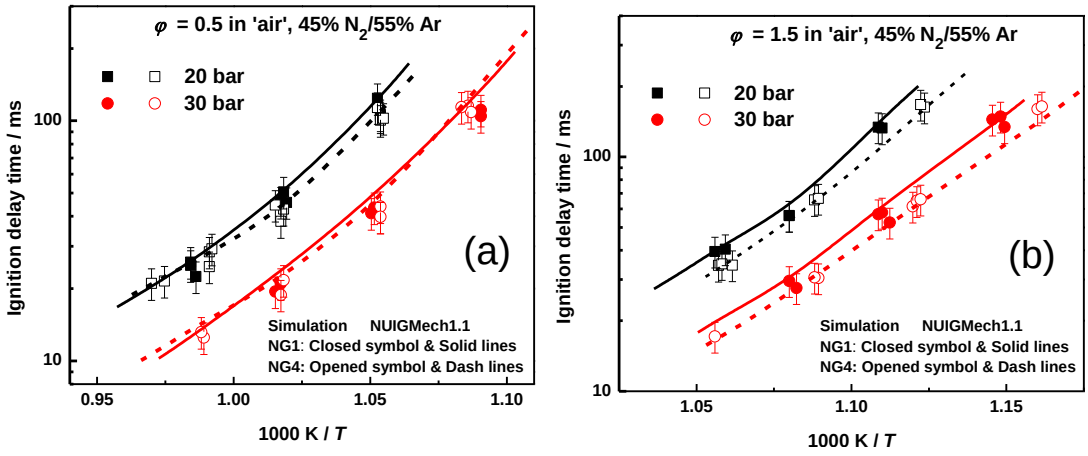

Figure 2-3. IDT predictions and measurements: symbols are experiments and lines are the simulations at fixed pressure 20 bar and 30 bar for NG1 and NG4; (a) fuel-lean mixtures (φ = 0.5); and (b) fuel-rich mixtures (φ = 1.5) from the current study.

The higher-pressure cases exhibit a faster ignition across the range of conditions studied. This is attributed to the increase in fuel concentration, thus resulting in a higher overall reaction rate and faster ignition. For the NG1 mixture, Figure 2-4(a), the IDT decreases from ~110 ms to 41 ms at T_C ~ 950 K and from 130 ms to 57 ms at T_C ~ 900 K for φ = 0.5 and 1.5, respectively as the pressure increased from 20 bar to 30 bar. Similarly, for the NG4 mixture, Figure 2-4(b), the IDT decreases from 106 ms to 40.5 ms at T_C = 950 K for φ = 0.5, and from 66 ms to 30.5 ms at T_C = 920 K for φ = 1.5. Note that increasing the pressure from 20 to 30 bar leads to a decrease in IDTs by an average factor of 2.2 for the lean and rich cases considered here.

Figure 2-4 also shows the effect of equivalence ratio on IDTs for two fuel-air mixtures at equivalence ratios of φ = 0.5 and 1.5. The experiments and simulations both show that fuel-rich mixtures ignite faster compared to the fuel-lean ones. For both NG1 and NG4, the IDT is shorter by a factor of three as the equivalence ratio increases from 0.5 to 1.5. This influence of equivalence ratio on IDT is attributed to the combined effect of fuel chemistry and the chain-branching reactions RH + $H\dot{O}_2$ ↔ R + H_2O_2 and H_2O_2(+M) ↔ 2$\dot{O}$H(+M). Increasing the equivalence ratio increases the fuel concentration, which leads to a higher reaction rate of these chain branching reactions, ultimately producing more $\dot{O}$H radicals. This reduces IDTs thus enhancing the reactivity of the fuel-air system.

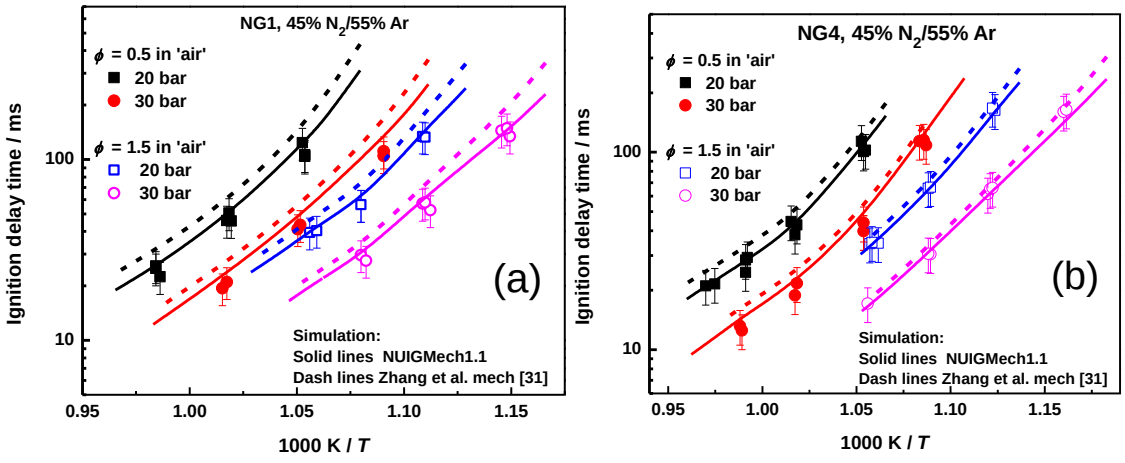

Figure 2-4. Ignition delay times: symbols are experiments and lines are the simulations at lean (φ = 0.5) and rich mixtures (φ = 1.5) and fixed pressure 20, and 30 bar; (a) NG1; and (b) NG4 from the current study.

2.4.2.2 Moderate to high levels of n-C_6 and n-C_7 addition

In this section, the effect of *n*-hexane and *n*-heptane addition of up 50% in the fuel mixture is numerically studied. Figures 2-5 and 2-6 show the effect of adding *n*-hexane and *n*-heptane to NG3. The composition of the new mixture is determined by substituting different fractions of these higher hydrocarbons with CH_4. Figure 2-6 compares IDTs as a function of *n*-hexane (solid lines) and *n*-heptane (dashed lines) concentration in the fuel mixture at T_C = 700 K, 800 K, 900 K and 1000 K. It can be seen in Figure 2-6 that the addition of even small amounts of *n*-hexane and *n*-heptane (~1–2%) significantly reduces IDTs. The plot highlights the impact of the addition of *n*-C_6/*n*-C_7 on IDT and shows that the addition of *n*-hexane and *n*-heptane in amounts of up to 7.5% significantly reduces the IDT by ~60–70 ms at T_C = 700 K and by ~40 ms at T_C = 800 K. Further addition of C_6/C_7 alkanes to the mixture has a much lower relative influence on the IDT in the mixture. At T_C = 900 K, the influence of C_6/C_7 addition is significantly reduced compared to lower temperatures, while at a T_C = 1000 K, IDTs for all of the blends are within 2–3 ms of each other. This behavior was also observed at high temperature conditions in previous studies [33,34]. A crossover in the IDT profiles can be seen between 800–900 K in Figure 2-6 and this is because both *n*-hexane and *n*-heptane exhibit strong NTC behavior in the temperature range studied. A discussion on the observed trends is provided in the next section using sensitivity analysis.

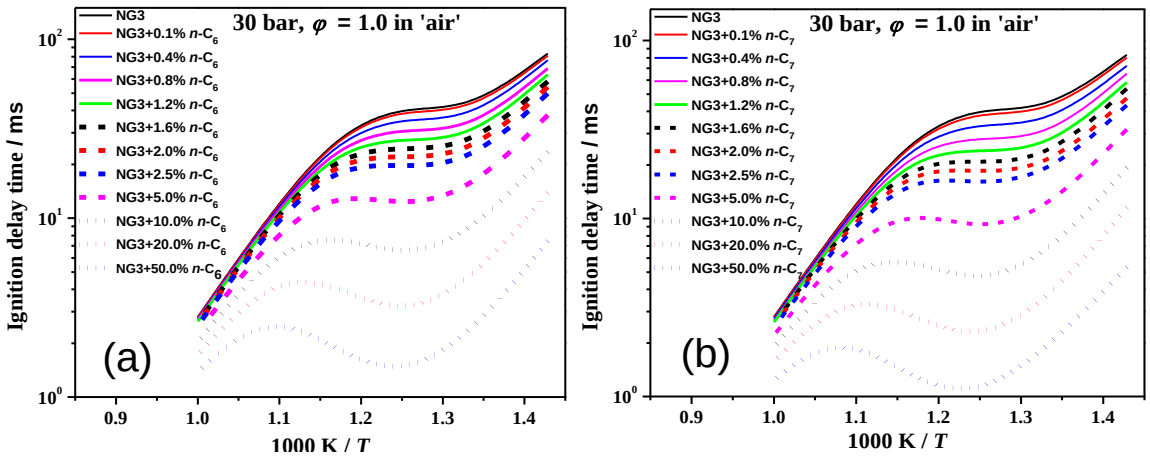

Figure 2-5. (a) Effect of adding *n*-hexane; and (b) *n*-heptane to NG3 on IDTs. Simulations using NUIGMech1.1.

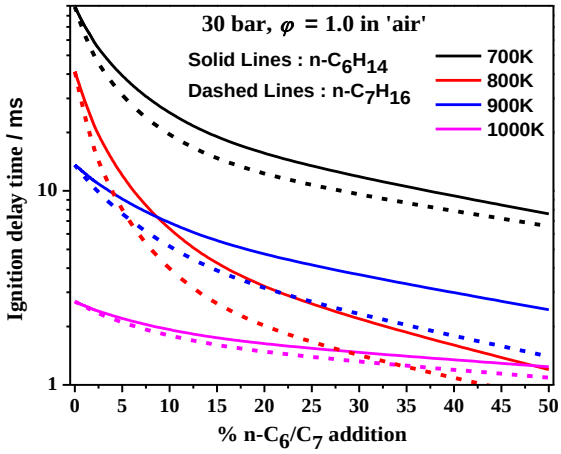

Figure 2-6. Effect of adding *n*-hexane (solid lines) *n*-heptane (dashed lines) to NG3 on IDTs. Simulations using NUIGMech1.1.

2.4.2.3 Sensitivity analysis

Figure 2-7 provides a sensitivity analysis to IDT for the NG3 mixture with 2.5%, 7.5% and 15% *n*-C_6H_{14}/*n*-C_7H_{16} addition at a T_C = 830 K. H-atom abstraction from the fuel, concerted elimination of an olefin and $H\dot{O}_2$ radical from various $R\dot{O}_2$ radicals and the addition of $\dot{Q}OOH$ radicals to O_2 are identified as the key reaction classes affecting IDT at 830 K. Even with 2.5% *n*-C_6H_{14} addition, the sensitivity coefficients of $C_3H_8 + \dot{O}H \leftrightarrow n\dot{C}_3H_7 + H_2O$ (R1) and $C_4H_{10} + \dot{O}H \leftrightarrow p\dot{C}_4H_9 + H_2O$ (R2) show similar orders of sensitivity as the $C_6H_{14} + \dot{O}H$ reaction producing $\dot{C}_6H_{13}$-1 (R3) or $\dot{C}_6H_{13}$-2 (R4) radicals.

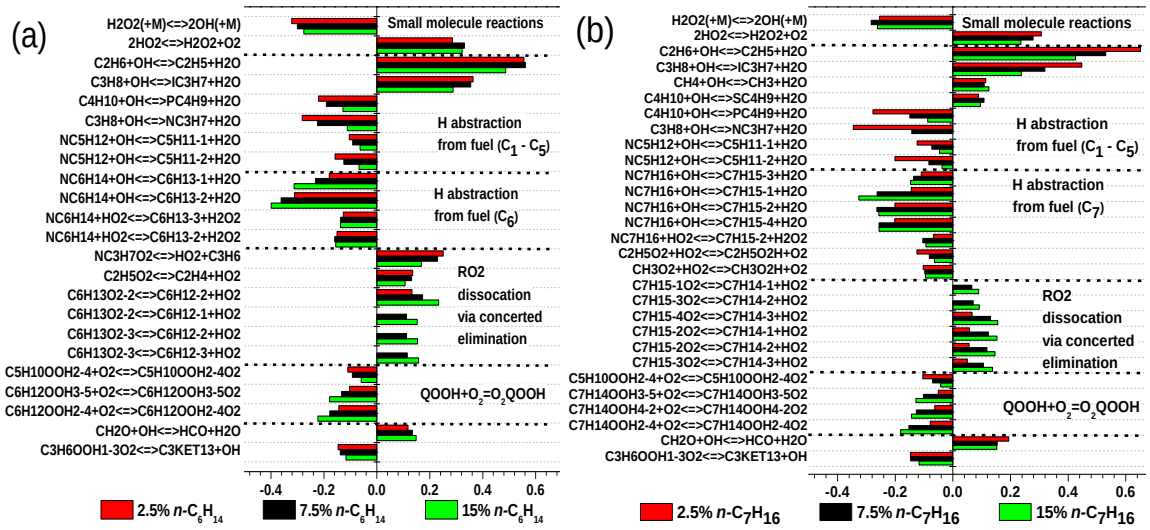

Figure 2-7. IDT sensitivity analysis for NG3 with 2.5%, 7.5% and 15%; (a) *n*-C_6H_{14}; and (b) *n*-C_7H_{16} addition at 830 K, and 30 bar.

The addition of $\dot{C}_6H_{12}OOH3\text{-}5$ (R5) and $\dot{C}_6H_{12}OOH2\text{-}4$ (R6) radicals to O_2 are also as sensitive as the addition of $\dot{C}_5H_{10}OOH2\text{-}4$ radicals (R7). This agrees with the previous observations made in Figure 2-7, that even at low levels (~2.5%) of *n*-hexane addition, IDTs are significantly decreased. With further addition of *n*-hexane, reactions R3 and R4 become the main fuel-based reactions promoting reactivity while the role of reactions R1 and R2 diminishes. Similar trends are observed for *n*-C_7H_{16} addition at T_C = 830 K, Figure 2-7(b). However, at T_C = 1000 K, the IDT of the mixture is highly sensitive only to H_2O_2 (+M) ↔ $\dot{O}H$ + $\dot{O}H$ (+M) (R8) and shows relatively very low sensitivity to other fuel-dependent reactions. The sensitivity coefficient of R8 remains largely un-altered for the different C_6/C_7 addition cases, while sensitivity coefficients for the other less important reactions show only small changes. Therefore, the IDT of the mixture exhibits a significantly low dependence on the amount of *n*- C_6H_{14}/*n*-C_7H_{16} addition at higher temperatures (T_C = 1000 K) as observed in Figure 2-8.

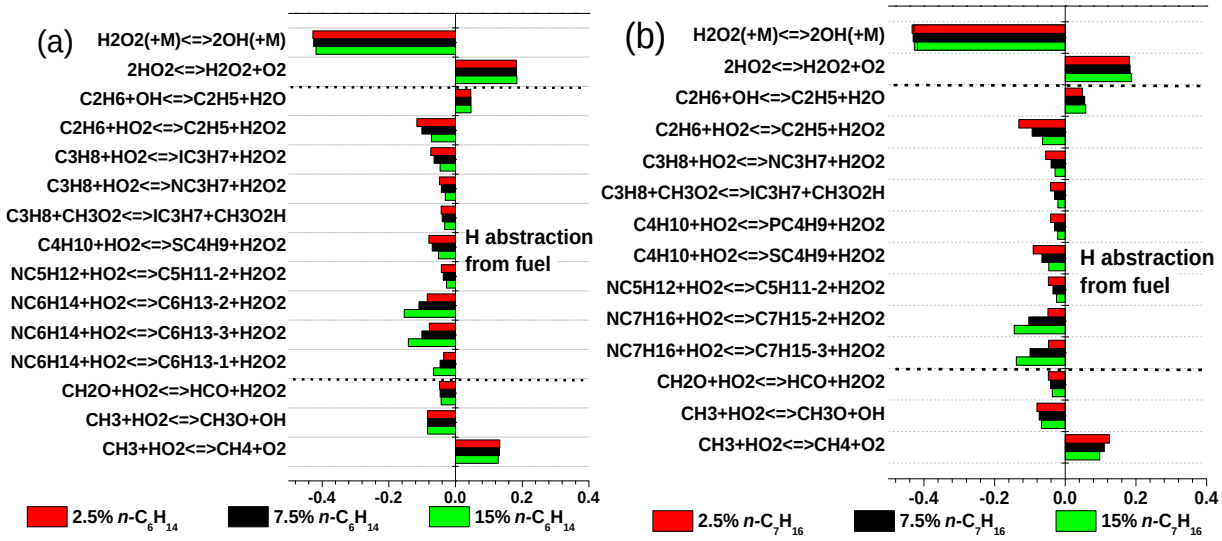

Figure 2-8. IDT sensitivity analysis for NG3 with 2.5%, 7.5% and 15%; (a) *n*-C_6H_{14}; and (b) *n*-C_7H_{16} addition at 1000 K, and 30 bar.

2.5 Conclusions

In this study IDT measurements for multi-component (C_1–C_7) NG blends are reported using a rapid compression machine at conditions relevant to gas turbine operation, at φ = 0.5 and 1.5, at p = 20 bar and 30 bar over the temperature range 860–1050 K. Simulations using NUIGMech1.1

are found to be in good agreement with the new measurements as well as with previous measurements of pure *n*-hexane, *n*-heptane and with data for NG3 available in the literature. This study also shows that the addition of even small amounts of *n*-hexane and *n*-heptane (1–2%) to natural gas blends leads to a significant increase in reactivity. At lower temperatures (T_C < 900 K), the addition of C_6/C_7 *n*-alkanes in concentrations of up to 7.5% rapidly reduces the IDT of the mixture while the influence decreases for concentrations greater than 7.5%. At temperatures > 900 K, the impact on the auto-ignition behavior of the NG mixtures is low. Sensitivity analyses for the 2.5% C_6/C_7 addition cases show that the role of H-atom abstraction reactions and addition of C_6/C_7 $\dot{Q}OOH$ radical species to molecular oxygen are as important as the reactions pertaining to lower alkane species at T_C = 830 K. Whereas, at 1000 K, the IDT of the mixture shows significant sensitivity only to the decomposition of hydrogen peroxide $H_2O_2(+M) \leftrightarrow 2\dot{O}H(+M)$ with a very low sensitivity observed for fuel-based reactions, irrespective of the C_6/C_7 concentration. Therefore, the effect on IDT of *n*-C_6H_{14}/*n*-C_7H_{16} addition to the NG3 mixture is limited at higher temperatures but is significant at low- to intermediate temperatures, 600–1000 K.

Acknowledgements

The authors would like to acknowledge Science Foundation Ireland for funding via project numbers 15/IA/3177 and 16/SP/3829. We also acknowledge funding from Siemens Canada Ltd.

Permission for use

References

[1] Burnes D., Camou A. Impact of fuel composition on gas turbine engine performance, J. Eng. Gas Turbines Power, 141 (2019) 101006-1–10.
[2] Role of Gas in Today's Energy Transitions, International Energy Agency report, 2019
[3] Faramawy, S., Zaki, T., Sakr, A.A.E. Natural gas origin, composition, and processing: A review, J. Nat. Gas Sci. Eng., 34 (2016) 34–54.
[4] Spadaccini, L.J., Colket, M.B. Ignition delay characteristics of methane fuels, Prog. Energy Combust. Sci., 20 (1994) 431–460.
[5] Melvin, A. Spontaneous ignition of methane-air mixtures at high pressure I-the ignition delay preceding explosion, Combust. Flame, 10 (1966) 120–128.
[6] Dagaut, P., Boettner, J.C., Cathonnet, M. Methane oxidation: Experimental and kinetic modeling study, Combust. Sci. Technol., 77 (1991) 127–148.
[7] Zhukov, V.P., Sechenov, V.A., Starikovskii, A.Y. Spontaneous Ignition of Methane–Air Mixtures in a Wide Range of Pressures, Combust. Explos. Shock Waves, 39 (2003) 487–495.
[8] Huang, J., Hill, P.G., Bushe, W.K., Munshi, S.R. Shock-tube study of methane ignition under engine-relevant conditions: experiments and modeling, Combust. Flame, 136 (2004) 25–42.
[9] Levy, Y., Olchanski, E., Sherbaum, V., Erenburg, V., Burcat A., Shock-tube ignition study of methane in air and recirculating gases mixtures, J. Propuls. Power, 22 (2006) 669–676.
[10] El Merhubi, H., Kéromnès A., Catalano G., Lefort B., Le Moyne, L., A high pressure experimental and numerical study of methane ignition, Fuel, 177 (2016) 164–172.
[11] Lamoureux, N., Paillard, C.E. Natural gas ignition delay times behind reflected shock waves: Application to modelling and safety, Shock Waves, 13 (2003) 57–68.
[12] Eubank, C.S., Rabinowitz, M.J., Gardiner, W.C., Zellner, R.E. Shock-initiated ignition of natural gas-Air mixtures, 18th Intl. Symp. Combust., (1981) 1767–1774.
[13] Bourque, G., Healy, D., Curran, H., Zinner, C., Kalitan, D., De Vries, J., Aul, C., Petersen, E. Ignition and flame speed kinetics of two natural gas blends with high levels of heavier hydrocarbons, Proc. ASME Turbo Expo., 3 (2008) 1051–1066.
[14] Healy, D., Kalitan, D.M., Aul, C.J., Petersen, E.L., Bourque, G., Curran, H.J. Oxidation of C_1−C_5 Alkane Quinternary Natural Gas Mixtures at High Pressures, Energy Fuels, 24 (2010) 1521–1528.
[15] De Vries, J., Petersen, E.L. Autoignition of methane-based fuel blends under gas turbine conditions, Proc. Combust. Inst., 31(2) (2007) 3163–3171.
[16] Ramalingam, A., Zhang, K., Dhongde, A., Virnich, L., Sankhla, H., Curran, H., Heufer, A. An RCM experimental and modeling study on CH_4 and CH_4/C_2H_6 oxidation at pressures up to 160bar, Fuel, 206 (2017) 325–333.
[17] Spadaccini, L.J., Colket, M.B. Ignition delay characteristics of methane fuels, Prog. Energy Combust. Sci., 20 (1994) 431–460.
[18] Zellner, R., Niemitz, K., Warnatz, J., Gardiner, W., Eubank, C., Simmie, J. Hydrocarbon Induced Acceleration of Ignition of Methane-Air Ignition, in: Flames, Lasers React. Syst., American Institute of Aeronautics and Astronautics, (1983) 252–272.
[19] Crossley, R.W., Dorko, E.A., Scheller, K., Burcat, A. The effect of higher alkanes on the ignition of methane-oxygen-argon mixtures in shock waves, Combust. Flame, 19 (1972) 373–378.
[20] Higgin, R.M.R., Williams, A. A shock-tube investigation of the ignition of lean methane and n-butane mixtures with oxygen, 12th Intl. Symp. Combust., (1969) 579–590.
[21] Huang, J., Bushe, W.K. Experimental and kinetic study of autoignition in methane/ethane/air and methane/propane/air mixtures under engine-relevant conditions, Combust. Flame, 144 (2006) 74–88.

[22] Petersen, E.L., Hall, J.M., Smith, S.D., de Vries, A.R. Amadio, J., Crofton, M.W. Ignition of lean methane-based fuel blends at gas turbine pressures, J. Eng. Gas Turbines Power, 129 (2007) 937–944.
[23] Healy, D., Kopp, M.M., Polley, N.L., Petersen, E.L., Bourque, G., Curran, H.J. Methane/n-Butane Ignition Delay Measurements at High Pressure and Detailed Chemical Kinetic Simulations, Energy Fuels, 24 (2010) 1617–1627.
[24] Beerer, D.J., McDonell, V.G. An experimental and kinetic study of alkane autoignition at high pressures and intermediate temperatures, Proc. Combust. Inst., 33 (2011) 301–307.
[25] Healy, D., Curran, H.J., Simmie, J.M., Kalitan, D.M., Zinner, C.M., Barrett, A.B., Petersen, E.L., Bourque, G. Methane/ethane/propane mixture oxidation at high pressures and at high, intermediate and low temperatures, Combust. Flame, 155 (2008) 441–448.
[26] Vallabhuni, S.K., Lele, A.D., Patel, V., Lucassen, A., Moshammer, K., AlAbbad, M., Farooq, A., Fernandes, R.X. Autoignition studies of Liquefied Natural Gas (LNG) in a shock tube and a rapid compression machine, Fuel, 232 (2018) 423–430.
[27] Affleck, W.S., Thomas, A. An Opposed Piston Rapid Compression Machine for Preflame Reaction Studies, Proc. Inst. Mech. Eng., 183 (1968) 365–387.
[28] Zhang, Y., Mathieu, O., Petersen, E.L., Bourque, G., Curran, H.J. Assessing the predictions of a NOx kinetic mechanism using recent hydrogen and syngas experimental data. Combust. Flame, 182 (2017) 122–141.
[29] Mohamed A.A.E., Panigrahy, S., Sahu, A.B., Bourque, G., Curran, H. An Experimental and Modeling Study of the Auto-ignition of Natural Gas Blends Containing C_1–C_7 n-Alkanes, Proc. Combust. Inst., 38 (2021) 365–373.
[30] Zhang, K., Banyon, C., Togbé, C., Dagaut, P., Bugler, J., Curran, H.J. An experimental and kinetic modeling study of n-hexane oxidation, Combust. Flame. 162 (2015) 4194–4207.
[31] Zhang, K., Banyon, C., Bugler, J., Curran, H.J., Rodriguez, A., Herbinet, O., Battin-Leclerc, F., B'Chir, C., Heufer, K.A. An updated experimental and kinetic modeling study of n-heptane oxidation, Combust. Flame, 172 (2016) 116–135.
[32] Wu, Y., Panigrahy, S., Sahu, A.B., Bariki, C., Beeckmann, J., Liang, J., Mohamed A.A.E., Dong, S., Tang, C., Pitsch, H., Huang, Z., Curran, H.J. Understanding the antagonistic effect of methanol as a component in surrogate fuel models: A case study of methanol/n-heptane mixtures, Combustion and Flame, 226 (2021) 229–242.
[33] He, Y., Wang, Y., Grégoire, C., Niedzielska, U., Mével, R., Shepherd, J.E. Ignition characteristics of dual-fuel methane-n-hexane-oxygen-diluent mixtures in a rapid compression machine and a shock tube, Fuel, 249 (2019) 379–391.
[34] Liang, J., Zhang, Z., Li, G., Wan, Q., Xu, L., Fan, S. Experimental and kinetic studies of ignition processes of the methane–n-heptane mixtures, Fuel, 235 (2019) 522–529.

CHAPTER 3

AN EXPERIMENTAL AND KINETIC MODELING STUDY OF THE AUTO-IGNITION OF NATURAL GAS BLENDS CONTAINING C_1–C_7 ALKANES

Chapter 3: An Experimental and Kinetic Modeling Study of the Auto-Ignition of Natural Gas Blends Containing C_1–C_7 Alkanes

Published in: Proceedings of the Combustion Institute, Volume 38, Issue 1, 2021, Pages 365-373.
DOI: https://doi.org/10.1016/j.proci.2020.06.015

Authors and Contributions

1) **Ahmed Abd El-Sabor Mohamed** (National University of Ireland, Galway, Ireland)
Contribution: RCM experiments and manuscript preparation.
2) **Snehasish Panigrahy** (National University of Ireland, Galway, Ireland)
Contribution: Chemical kinetic modelling and manuscript review.
3) **Amrit Bikram Sahu** (National University of Ireland, Galway, Ireland)
Contribution: Chemical kinetic modelling and manuscript review.
4) **Gilles Bourque** (Siemens Energy Canada Ltd, Montreal QC H9P 1A5, Canada)
Contribution: Project management and manuscript review.
5) **Henry J. Curran** (National University of Ireland, Galway, Ireland)
Contribution: Project management and manuscript review.

Abstract

Ignition delay time measurements for multi-component natural gas mixtures were carried out using a rapid compression machine at conditions relevant to gas turbine operation, at equivalence ratios of 0.5–2.0 in ‘air’ in the temperature range 650–1050 K, at pressures of 10–30 bar. Natural gas mixtures comprising C_1–C_7 *n*-alkanes with methane as the major component (volume fraction: 0.35–0.98) were considered. A design of experiments was employed to minimize the number of experiments needed to cover the wide range of pressures, temperatures and equivalence ratios. The new experimental data, together with available literature data, were used to develop and assess a comprehensive chemical kinetic model. Replacing 1.875% methane with 1.25% *n*-hexane and 0.625% *n*-heptane in a mixture containing C_1–C_5 components leads to a significant increase in a mixture’s reactivity. The mixtures containing heavier hydrocarbons

also tend to show a strong negative temperature coefficient and two-stage ignition behavior. Sensitivity analyses of the C_1–C_7 blends have been performed to highlight the key reactions controlling their ignition behavior.

Keywords: Natural gas; ignition delay time; rapid compression machine; kinetic modeling.

3.1 Introduction

The potential of natural gas (NG) as an alternative fuel for transportation and heavy-duty power generation applications has led to an increase in demand for conventional and non-conventional NG sources. NG is primarily composed of methane with some heavier alkanes ranging from ethane to heptane [1], [2]. Thus, to achieve highly efficient and safe use of NG, experimental and kinetic modeling studies are needed for a wide range of NG mixtures to verify their varying combustion characteristics. One of the fundamental combustion characteristics of a fuel is auto-ignition which can be measured experimentally at relevant reaction times using both rapid compression machines (RCMs) and shock tubes (STs). Methane, being a major component of NG, has been studied extensively in the literature [3]–[8] and there are many available mechanisms describing its oxidation at conditions relevant to combustion devices [9]–[13]. Studying blends of alkanes with compositions similar to available sources of NG can provide tangible targets in predicting the combustion characteristics of these alternate NG mixtures to test their suitability for use in practical combustors.

A summary of experimental studies of methane with larger hydrocarbons was presented previously [1], [7], [14] and a summary is updated and added in appendix A. Ignition delay times (IDTs) of binary NG blends of methane/ethane up to methane/*n*-heptane were studied experimentally using RCMs and STs over a wide range of combustion conditions [15],[16],[17][24–30]. The results showed an increase in negative temperature coefficient (NTC) behavior and a decrease in the onset of ignition temperature with increasing concentrations of

higher order hydrocarbons in the mixtures. A recent study of CH_4/*n*-C_6H_{14} mixtures by He et al. [22] showed a significant decrease in IDTs with increasing *n*-hexane content at low temperature. A kinetic analysis showed that a strong effect stems from the decomposition of H_2O_2 which induces the production of ȮH radicals. Liang et al. [21] studied a different CH_4/*n*-C_7H_{16} mixtures in a ST. The results showed that the fuel composition with methane concentrations of less than 75% had IDTs close to pure *n*-heptane. Kinetic analyses showed that dominant reactions occurred between *n*-heptane and the radicals, particularly ȮH and HO_2 and methane consumption occurred close to the ignition event. Similar behavior was also observed for CH_4/*n*-C_6H_{14} ST experiments [22].

IDT measurements of ternary blends, including CH_4/C_2H_6/C_3H_8 as well as higher alkanes with volume percentages of up to 50% of the entire fuel composition have also been studied [18], [23], [27], [29], [31], [32]. De Vries and Petersen [29] observed that adding higher hydrocarbons up to *n*-pentane strongly reduces the activation energy at high pressures and low temperatures with an observed faster and stronger ignition behavior for all of the blends compared to pure methane. C_1–C_4 ST experiments were also studied [33] for highly dilute mixtures containing 14.29% ethane, 7.14% propane, 7.14% *n*-butane, and 71.43% methane. It was found that IDTs were shortened by up to a factor of 13 compared to pure methane. Recently, C_1–C_5 alkanes blends were studied in both an RCM and in a ST with higher hydrocarbons up to 37.5% by volume of the fuel composition [14], [34], [35]. Beerer and McDonell [18] used a turbulent flow reactor to measure IDTs for a lean (φ = 0.6) mixture containing C_1–C_6 species at p = 9 atm, in the temperature range 845–895 K. They showed that the inclusion of higher alkanes can help reduce NOx emissions by decreasing the onset of ignition temperatures for NG mixtures.

The declining concentration of >C_2 species on a volume/mol basis is an observed trend in samples of NG found around the world. These are supplied to Siemens by potential customers

who are interested in ensuring their feasibility as fuels for engine applications and understanding the limitations in terms of pollutants, power range, or fuel supply systems. Although several studies have explored C_1–C_5 *n*-alkanes mixtures with limited work performed on C_1–C_6 alkane blends [18].

However, to our knowledge no IDT measurements are available for C_1–C_7 alkane blends. The aim of the present work is to provide useful measurements of IDTs for C_1–C_7 *n*-alkanes blends at conditions relevant to gas turbine (GT) operation and to develop an accurate chemical kinetic mechanism to understand the underlying kinetics of NG mixture combustion at the specified conditions.

3.2 Experiments

Experiments were conducted using the RCM at NUI Galway, which was described previously [36]. A brief description of the machine and the experimental procedure are provided in appendix A. Table 3-1 shows the C_1–C_7 *n*-alkanes blends by volume percentage, reported as NG1 to NG10.

Initially the NG1–NG3 blends were selected, where NG1 and NG2 compositions are very similar to North American and European natural gases, respectively. NG3 is an extension of the compositions along the NG mixture trends in order to capture the increasing content of > C_2 species. The new natural gas mixtures NG4–NG10 are intended to consider both the impact of C_6 and C_7 *n*-alkane addition and higher amounts of > C_2 species. The motive in the increased content of > C_2 is to ensure that future natural gas compositions can be included. Constant volume simulations were performed for all of the NG blends in Table 3-1 as shown in Figure AS1 to help select the final experimental conditions. NG2 experiments which had been studied previously in our laboratory [14], [34] helped in validating the new experiment targets and confirm the reliability of the old data. The NG3 and NG6 experiments were performed to study

the effect of replacing 1.875% methane in the NG3 blend with *n*-hexane and *n*-heptane at the same conditions of pressure and dilution concentrations. Finally, NG7, NG8, and NG10 were chosen so that different levels of higher hydrocarbon in the blends with different conditions can be tested. Developing a chemical kinetic mechanism that can reproduce well the experiments in the different conditions will be useful in predicting other NG blends that have not been studied experimentally. Concerning the DOE approach, we have not applied the methodology in a strict manner implied by the terminology but rather a sensitivity analysis was performed to identify the experiments that would be the most informative to develop/validate/calibrate the mechanism within the large parameter space of pressure, equivalence, temperature, and natural gas compositions considered. Table 3-2 shows the experimental conditions with the NG blends which were chosen in the current study. The measured IDT is quantified from the reactive pressure-time trace as shown in Figure AS2. Each experimental point is repeated at least three times and the IDTs measurement uncertainty in the current study is estimated to be ±15%.

Table 3-1. Natural gas blends.

Species	NG1	NG2	NG3	NG4	NG5	NG6	NG7	NG8	NG9	NG10
Methane (CH_4)	98.125	81.25	62.5	98.03125	80.3125	60.625	72.635	45.27	63.107	35.601
Ethane (C_2H_6)	1	10	20	1	10	20	10	20	10	20
Propane (C_3H_8)	0.5	5	10	0.5	5	10	6.667	13.33	8.0	14.815
***n*-Butane(C_4H_{10})**	0.25	2.5	5.0	0.25	2.5	5.0	4.44	8.89	6.40	10.974
***n*-Pentane (*n*-C_5H_{12})**	0.125	1.25	2.5	0.125	1.25	2.5	2.965	5.93	5.12	8.129
***n*-Hexane (*n*-C_6H_{14})**	–	–	–	0.0625	0.625	1.25	1.976	3.95	4.097	6.021
***n*-Heptane (*n*-C_7H_{16})**	–	–	–	0.03125	0.3125	0.625	1.317	2.63	3.276	4.460

Table 3-2. Experimental conditions studied in the RCM.

Blend	φ	p_C / bar	T_C / K	
NG2	0.5, 1.0, 2.0	10,18, 20, 30	711 – 1054	[14],[34], current study
NG3	1.0	20, 30	754 – 952	[14],[34], current study
NG6	1.0	20, 30	670 – 1032	current study
NG7	0.5, 1.0, 1.5	10, 20, 30	688 – 952	current study
NG8	1.0	20, 30	679 – 960	current study
NG10	0.5, 1.0, 1.5	10, 20, 30	650 – 1052	current study

3.3 Kinetic modelling

The detailed chemical kinetic mechanism employed here, NUIGMech1.0, is built in a hierarchical way and has been derived by merging our C_0–C_5 base chemistry [37]–[40] with the hexane isomer mechanisms from Zhang et al. [41]. Rate constants for the *n*-heptane sub-mechanism are incorporated from a previously published model by Zhang et al. [42]. This mechanism has been validated against the experimentally measured IDTs from the present work across a wide range of temperature (T_C = 650–1500 K), equivalence ratio (φ = 0.4–2.0), and pressure (p_C = 10–100 bar) as well as a variety of natural gas mixture compositions [31], [35], [22], [32] as shown in Figures AS10–AS16. A detailed description of the important reactions for the conditions studied here identified in sensitivity analyses are provided in the following sections. In addition, the performance of NUIGMech1.0 is compared with that published by Zhang et al. [42] and Mehl et al. [43].

3.4 Results and Discussion

The results of the IDTs for the tested NG blends listed in Table 3-1 are provided in this section. The term “in air” in the figures refers to the oxidizer mixture containing O_2/diluent in the ratio of 1:3.76. The diluent was either 100% N_2 or 45:55 N_2: Ar. The fuel compositions, initial conditions, IDT data, and pressure/time histories for the simulations are all provided as in Appendix A and with the online version of the paper.

3.4.1 Experimental validation

Figure 3-1 and Figure AS3 show that the current IDT measurements for NG2 at different compressed gas temperatures and NG3 at stoichiometric conditions are comparable with our previously published data [14], [34]. Moreover, simulations of the new IDTs using three kinetic models, C5_49 which was previously used to simulate the NG2 and NG3 data [14], that from Zhang et al. [42], and NUIGMech1.0. The three models show good agreement with the

experiments, with NUIGMech1.0 showing particularly good agreement, especially at low temperatures. Overall, there is good agreement among the old and new data and the difference which appears clearly in the fuel-lean and stoichiometric conditions at temperature above 900 K stems from the use of 100% Ar as the diluent gas in the old data. Using only Argon as a diluent makes the IDTs longer as reported by Würmel et al. [44] whereas in the new data 45% N_2/55% Ar is used. At fuel-rich conditions for NG2 the same diluent was used for both studies and they show very good agreement, Figure AS3(c).

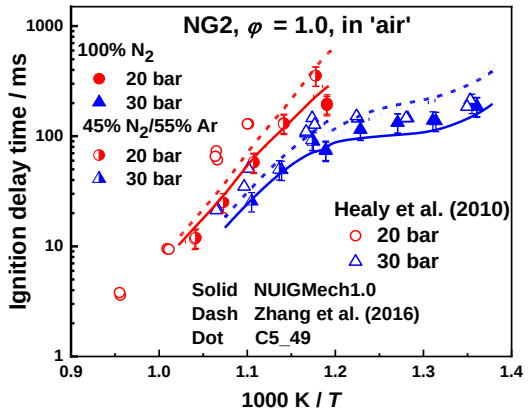

Figure 3-1. Comparison of current study IDTs measurements for NG2 verse NG2 previous study [34] and the simulations, NUIGMech1.0 (solid line, Zhang et al [42] (dash lines), and C5_49 [14] (Dotted line).

3.4.2 Effect of fuel composition

Comparisons of the IDTs of the different NG mixtures, NG2, NG3, NG6, NG7, NG8, and NG10, studied here are presented in Figure 3-2 for stoichiometric mixtures at 20 bar and 30 bar and 675–1000 K. It is observed that NG2 and NG3 mixtures containing highest percentage of smaller alkanes (C_1–C_3) amongst all fuels exhibit the lowest reactivity, with reactivity increasing with the increasing percentage of higher order hydrocarbons present. Mixture NG10, which has a total of almost 10% *n*C_6H_{14} and *n*C_7H_{16}, exhibits the highest reactivity. The effect of composition on the IDTs is seen to be the largest in the temperature range 700–900 K. For NG3 at 770 K, 20 bar, the IDT is ~150 ms while for NG10 the IDT is ~6 ms, showing that there is more than an order of magnitude reduction in reactivity with changing fuel compositions. Figure

3-2 also shows that NUIGMech1.0 can predict the IDTs with very good agreement for the range of NG mixtures at both 20 and 30 bar and also accurately reproduces the NTC behavior. The Zhang et al. [42] model under-estimates the reactivity of the mixtures by a factor of two for the NG3 and NG6 mixtures. The agreement becomes better for NG mixtures with higher alkanes but still over-predicts the IDT by factor of 1.5 compared to the experiments in the NTC region. Moreover, the Mehl et al. [43] model over-estimates the reactivity of NG2 and NG3 and begins to under-estimate the reactivity of the mixtures with increasing higher order hydrocarbons in NG6–NG10 and by increasing the pressure from 20 bar to 30 bar. A detailed sensitivity analysis is presented in the chemical kinetics analysis section to gain insights on the underlying kinetics at different conditions. Figure AS6 shows reactive *p*/*t* histories for the conditions similar to Figure 3-2(b) for NG7, NG8, and NG10 at T_C 770 K along with simulated *p*/*t* histories using the experimental non-reactive *p*/*t* trace to include the effect of heat loss. It is obvious that the mechanism can also capture the first stage and total ignition very well.

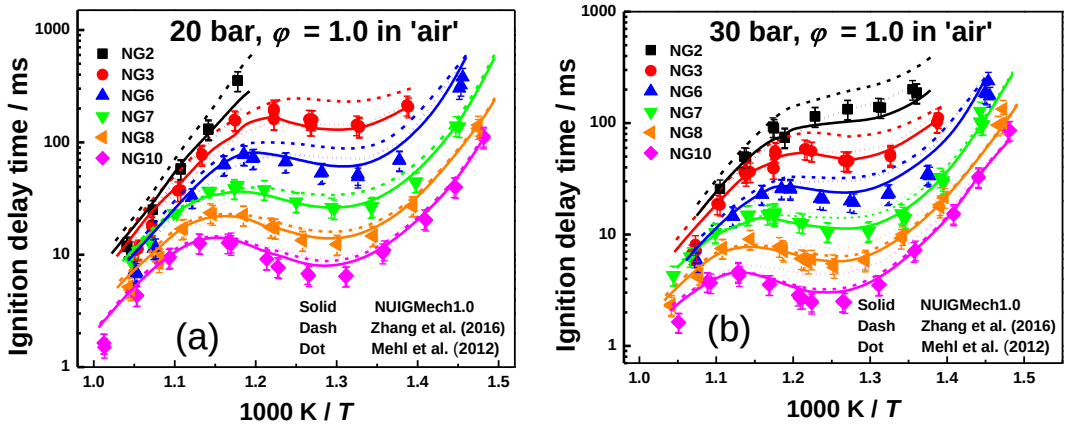

Figure 3-2. Comparison of experimental (symbols) and model predicted (lines) IDTs of various NG mixtures at φ = 1.0; (a) p_C = 20 bar; and (b) p_C = 30 bar, measured in an RCM.

3.4.3 Effect of pressure and equivalence ratio

Figure 3-3 shows a comparison of model predictions with IDT measurements for fuel-lean and fuel-rich NG mixtures at 10–30 bar. A similar comparison for the stoichiometric mixtures is provided in Figure AS7. The IDTs for all mixtures decrease with increasing pressure, thus

showing an increase in reactivity. This is primarily due to the increasing concentration of the reactant molecules with pressure. The sensitivity of IDT with pressure shows a non-linear trend with respect to temperature. For stoichiometric NG6–NG10 mixtures, the IDT shortens by a factor of 1.5 at T_C < 700 K as the pressure increases from 20 to 30 bar, while it reduces by a factor of 2 at T_C > 700 K until the end of NTC region. The dependence on pressure again decreases with a further increase in temperature. For fuel-lean and fuel-rich mixtures, an increase in pressure from 10 bar to 30 bar leads to a reduction in IDT of almost a factor of nine in the NTC region, as shown in Figure 3-3. Comparisons of model predictions with measurements (Figures. 3-3 and AS7), show that NUIGMech1.0 is able to successfully predict the IDTs with very good agreement for a wide range of pressures (10–30 bar) and equivalence ratios (φ = 0.5–2.0).

3.4.4 Chemical kinetics analysis

Figure 3-4 shows the brute-force sensitivity analysis for NG3, NG6 and NG10 mixture blends at φ = 1.0, p_C = 30 bar, and T_C = 830 K. Modifications have been made to some of these important reactions and the choice of the updated rate constants are discussed here.

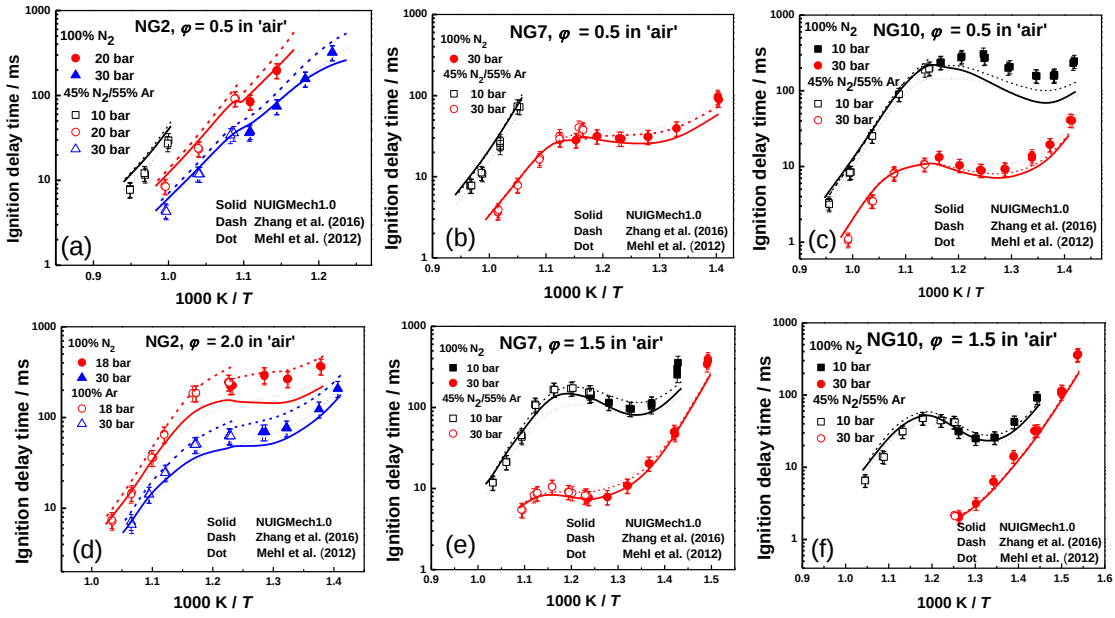

Figure 3-3. Ignition delay times at different p_C (a) NG2, φ = 0.5; (b) NG7, φ = 0.5; (c) NG10, φ = 0.5; (d) NG2, φ = 2.0; (e) NG7, φ = 1.5; and (f) NG10, φ = 1.5.

The reactivity of the NG mixtures (NG3, NG6 and NG10) is highly sensitive to ȮH radical reactions with propane producing *n*-propyl and *iso*-propyl radicals, via $C_3H_8 + ȮH \leftrightarrow nĊ_3H_7 + H_2O$ and $C_3H_8 + ȮH \leftrightarrow iĊ_3H_7 + H_2O$, respectively. The previous model [42] utilised the rate constant measured by Droege and Tully [45] at temperatures below 900 K. More recently, Sivaramakrishnan et al. [46] directly measured site-specific rate constants for the C_3H_8 + ȮH system at high temperatures (927–1146 K). Their measurements showed a slightly higher branching fraction to $iĊ_3H_7$ than measured by Droege and Tully [45]. The current model applies a fit which takes account of the direct measurement for $C_3H_8 + ȮH \leftrightarrow iĊ_3H_7 + H_2O$ by Sivaramakrishnan et al. [46]. It is evident from Figure 3-4 that for all NG mixtures direct hydrogen-abstraction from C_2H_6 by ȮH radical has the largest inhibiting effect on the NG ignition. In the present model, the rate constant for $C_2H_6 + ȮH \leftrightarrow Ċ_2H_5 + H_2O$ is adopted from the fit recommended by Krasnoperov and Michael [47]. A sensitivity analysis also shows that the low temperature reactions pertaining to C_3H_8 chemistry influence the overall reactivity of NG mixtures. The formation of carbonyl hydroperoxide species via the isomerization reactions of $C_3H_6OOH1\text{-}3Ȯ_2$ promotes the overall reactivity of the NG mixtures containing higher concentration of *n*-hexane and *n*-heptane fuels (NG6 and NG10). Whereas the concerted elimination reaction, producing $C_3H_6 + HȮ_2$, inhibits NG oxidation at low temperatures. For the reaction $nC_3H_7O_2 \leftrightarrow C_3H_6 + HȮ_2$, the rate constant used in the previous model was based on the calculation by Villano et al. [48] while for ($C_3H_6OOH1\text{-}3O_2 \leftrightarrow C_3KET13 + ȮH$), the rate parameters were taken from the study of Sharma et al. [49]. In the current model, the rate constant for these reactions are adopted from the high-level quantum chemical calculation by Goldsmith et al. [50], and these updates improved the model predictions as shown in Figure 3-2.

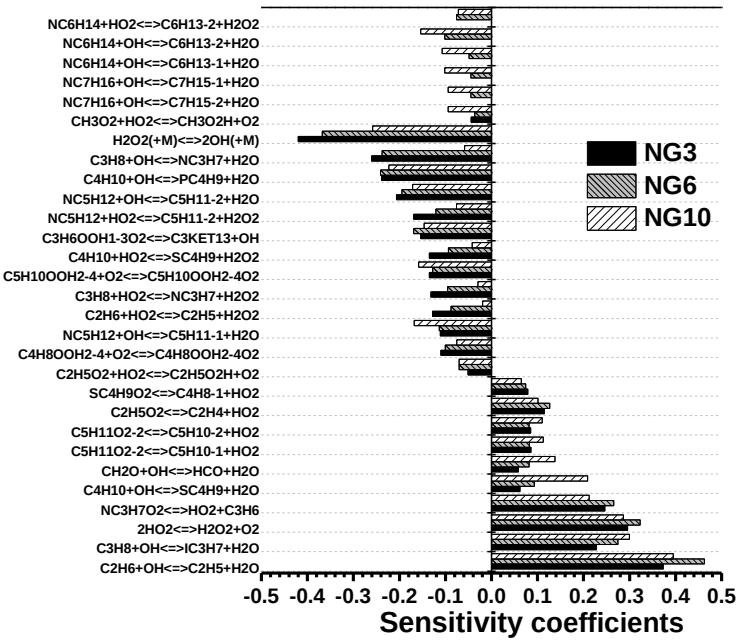

Figure 3-4. Brute-force sensitivity analysis of various NG mixtures (NG3, NG6, NG10) IDTs at φ = 1.0, 30 bar, and 830 K.

The chain terminating reaction between $H\dot{O}_2$ radicals ($H\dot{O}_2 + H\dot{O}_2 \leftrightarrow H_2O_2 + O_2$) is an important reaction that inhibits reactivity under these conditions, while the decomposition of H_2O_2 is the most important reaction enhancing reactivity of NG mixtures for all conditions. For the reaction $H\dot{O}_2 + H\dot{O}_2 \leftrightarrow H_2O_2 + O_2$, we use the rate constant from the recent high-level ab-initio theoretical study by Klippenstein et al. [51]. Notably, this value is slightly lower than the rate constant assigned in our previous model [42], in which the rate parameters were taken from the experimental work of Hong et al. [52]. Interestingly, in NG6 and NG10 mixtures, the sensitivities of the important promoting reactions from the C_2H_6 to *n*-C_5H_{12} sub-mechanism are reduced significantly as compared to the NG3 mixture. However, the *n*-C_6H_{14} and *n*-C_7H_{16} chemistries begin to control the reactivity for NG6 and NG10. The H-atom abstraction from the *n*-C_6H_{14} and *n*-C_7H_{16} by $\dot{O}H$ radicals become more important for NG10.

Figure 3-5 depicts brute-force sensitivity analyses performed for the NG10 mixture at p_C = 10 and 30 bar, and at an intermediate temperature of 830 K. Figure AS9 shows the sensitivity analyses comparisons for different equivalence ratios (φ = 0.5, 1.0 and 1.5) for the NG10 mixture at 30 bar pressure and at an intermediate temperature of 830 K. The most important

reactions are governed by the hydrogen abstraction reactions by ȮH and HȮ$_2$ radicals that initiate the fuel consumption. The low-temperature chemistries such as the addition of Ċ$_5$H$_{10}$OOH2-4 and Ċ$_6$H$_{12}$OOH2-4 radicals to O$_2$ are also sensitive reactions that promote the reactivity. The concerted elimination reactions, producing an olefin + HȮ$_2$, inhibits NG ignition. Meanwhile HȮ$_2$ + HȮ$_2$ ↔ H$_2$O$_2$ + O$_2$ is the most inhibiting reaction. The resultant H$_2$O$_2$ generates two ȮH radicals through H$_2$O$_2$ (+M) ↔ ȮH + ȮH (+M). Figure AS9 shows that, for fuel-lean conditions, the chain branching reaction H$_2$O$_2$ (+M) ↔ ȮH + ȮH (+M) dominates the reactivity and exhibits higher sensitivity than at stoichiometric and fuel-rich conditions. A similar trend in sensitivity coefficients at 10 bar and 30 bar (Figure 3-5) indicates that the chemistry is not responsible for the increase in reactivity at 30 bar, but rather the higher fuel concentration causes the observed reduction in IDTs.

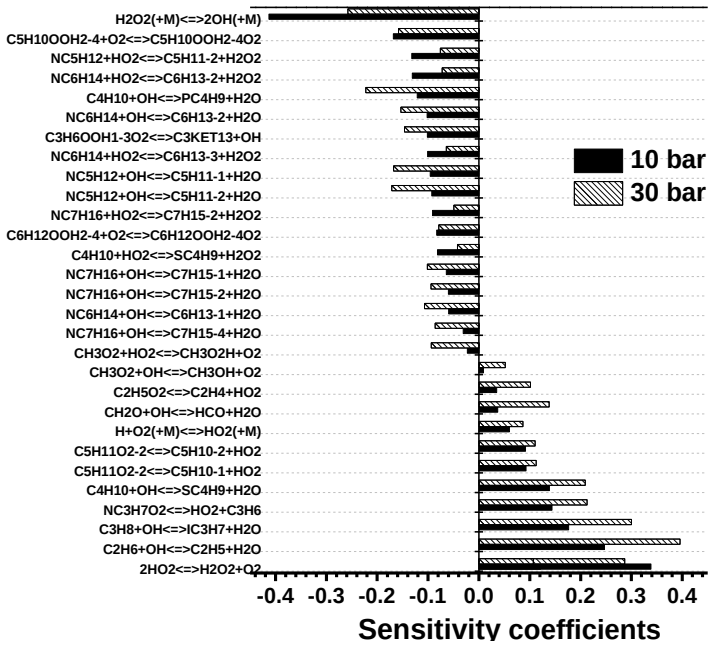

Figure 3-5. Brute-force sensitivity analysis of NG10 mixtures at φ = 1.0, 830 K, for both 10 bar and 30 bar.

3.5 Conclusions

In the current study, ignition delay time measurements for C$_1$–C$_7$ n-alkanes blends were performed by using NUI Galway RCM at conditions relevant to GT operating conditions. Six compositions of natural gas mixtures with methane being the major component were chosen for

the study. The measurements were carried out for mixtures in 'air' in the temperature range of 650–1050 K at equivalence ratios 0.5, 1.0, 1.5 and 2.0 and pressures varying from 10–30 bar. The wide range of conditions provides a comprehensive overview of the reactivity of the natural gas mixtures. The experimental results showed that for the range of fuel-compositions considered in this study, the IDTs of the mixture shortened by an order of magnitude at the same pressure and temperature conditions. For NG3 mixture, the IDT measured was approximately 150 ms while for NG10 the IDT was as low as 6 ms at T_C = 770 K and p_C ~20 bar. Significantly different IDTs measured over a wide range of conditions provide a strong validation target for developing accurate and robust chemical kinetic mechanisms. The new detailed kinetic mechanism NUIGMech1.0, with update reaction rates based on recent theoretical and experimental studies together with the heptane mechanism developed by Zhang et al. were chosen to simulate the experimental conditions in this study. The NUIGMech1.0 model showed excellent agreement with the IDT measurements for mixtures with compositions ranging from quinternary mixtures (C_1–C_5) to seven-component mixtures (C_1–C_7) represented by NG6–NG10. The Zhang et al. model showed reasonable agreement with mixtures containing *n*-heptane but overestimated the IDTs by more than 50% in the NTC region for mixtures containing large amounts lower hydrocarbons (NG2–NG6). The agreement of NUIGMech1.0 with measurements recorded in this study along existing literature data highlights its robustness.

Acknowledgements

The authors would like to acknowledge Science Foundation Ireland for funding via project number16/SP/3829. We also acknowledge funding from Siemens Canada Ltd.

References

[1] L. J. Spadaccini, M. B. Colket, "Ignition delay characteristics of methane fuels," Prog. Energy Combust. Sci., 20(5) (1994) 431–460.

[2] S. Faramawy, T. Zaki, A. A. E. Sakr, "Natural gas origin, composition, and processing: A review," J. Nat. Gas Sci. Eng., 34 (2016) 34–54.

[3] A. Melvin, "Spontaneous ignition of methane-air mixtures at high pressure I-the ignition delay preceding explosion," Combust. Flame, 10(2) (1966) 120–128.

[4] Y. Levy, E. Olchanski, V. Sherbaum, V. Erenburg, A. Burcat, "Shock-tube ignition study of methane in air and recirculating gases mixtures," J. Prop. Power, 22(3) (2006) 669–676.

[5] P. Dagaut, J. C. Boettner, M. Cathonnet, "Methane oxidation: Experimental and kinetic modeling study," Combust. Sci. Technol., 77(1–3) (1991) 127–148.

[6] J. Huang, P. G. Hill, W. K. Bushe, S. R. Munshi, "Shock-tube study of methane ignition under engine-relevant conditions: experiments and modeling," Combust. Flame, 136(1) (2004) 25–42.

[7] H. El Merhubi, A. Kéromnès, G. Catalano, B. Lefort, L. Le Moyne, "A high pressure experimental and numerical study of methane ignition," Fuel, 177 (2016) 164–172.

[8] V. P. Zhukov, V. A. Sechenov, A. Y. Starikovskii, "Spontaneous Ignition of Methane–Air Mixtures in a Wide Range of Pressures," Combust. Explos. Shock Waves, 39(5) (2003) 487–495.

[9] E. L. Petersen, D. M. Kalitan, S. Simmons, G. Bourque, H. J. Curran, J. M. Simmie, "Methane/propane oxidation at high pressures: Experimental and detailed chemical kinetic modeling," Proc. Combust. Inst., 31(1) (2007) 447–454.

[10] H. Hashemi, J. M. Christensen, S. Gersen, H. Levinsky, S. J. Klippenstein, P. Glarborg, "High-pressure oxidation of methane," Combust. Flame, 172 (2016) 349–364.

[11] H. Jin et al., "Experimental and kinetic modeling study of PAH formation in methane coflow diffusion flames doped with n-butanol," Combust. Flame, 161(3) (2014) 657–670.

[12] F. H. V. Coppens, J. De Ruyck, A. A. Konnov, "The effects of composition on burning velocity and nitric oxide formation in laminar premixed flames of $CH_4 + H_2 + O_2 + N_2$," Combust. Flame, 149(4) (2007) 409–417.

[13] C. L. Rasmussen, J. G. Jakobsen, P. Glarborg, "Experimental measurements and kinetic modeling of CH_4/O_2 and $CH_4/C_2H_6/O_2$ conversion at high pressure," Int. J. Chem. Kinet., 40(12) (2008) 778–807.

[14] D. Healy, D. M. Kalitan, C. J. Aul, E. L. Petersen, G. Bourque, H. J. Curran, "Oxidation of C_1−C_5 Alkane Quinternary Natural Gas Mixtures at High Pressures," Energy Fuels, 24(3) (2010) 1521–1528.

[15] R. M. R. Higgin A. Williams, "A shock-tube investigation of the ignition of lean methane and n-butane mixtures with oxygen," 12th Intl. Symp. Combust., (1969) 579–590.

[16] R. W. Crossley, E. A. Dorko, K. Scheller, and A. Burcat, "The effect of higher alkanes on the ignition of methane-oxygen-argon mixtures in shock waves," Combust. Flame, 19(3) (1972) 373–378.

[17] D. Healy, M. M. Kopp, N. L. Polley, E. L. Petersen, G. Bourque, H. J. Curran, "Methane/n-Butane Ignition Delay Measurements at High Pressure and Detailed Chemical Kinetic Simulations," Energy Fuels, 24(3) (2010) 1617–1627.

[18] D. J. Beerer, V. G. McDonell, "An experimental and kinetic study of alkane autoignition at high pressures and intermediate temperatures," Proc. Combust. Inst., 33(1) (2011) 301–307.

[19] C. J. Aul, W. K. Metcalfe, S. M. Burke, H. J. Curran, E. L. Petersen, "Ignition and kinetic modeling of methane and ethane fuel blends with oxygen: A design of experiments approach," Combust. Flame, 160(7) (2013) 1153–1167.

[20] A. Ramalingam et al., "An RCM experimental and modeling study on CH_4 and CH_4/C_2H_6

oxidation at pressures up to 160 bar," Fuel, 206 (2017) 325–333.
[21] J. Liang, Z. Zhang, G. Li, Q. Wan, L. Xu, S. Fan, "Experimental and kinetic studies of ignition processes of the methane–n-heptane mixtures," Fuel, 235 (2019) 522–529.
[22] Y. He, Y. Wang, C. Grégoire, U. Niedzielska, R. Mével, J. E. Shepherd, "Ignition characteristics of dual-fuel methane-n-hexane-oxygen-diluent mixtures in a rapid compression machine and a shock tube," Fuel, 249 (2019) 379–391.
[23] C. S. Eubank, M. J. Rabinowitz, W. C. Gardiner, and R. E. Zellner, "Shock-initiated ignition of natural gas-Air mixtures," 18th Intl. Symp. Combust., 1 (1981) 1767–1774.
[24] R. Zellner, K. Niemitz, J. Warnatz, W. Gardiner, C. Eubank, J. Simmie, "Hydrocarbon Induced Acceleration of Ignition of Methane-Air Ignition," in Flames, Lasers and Reactive Systems, American Institute of Aeronautics and Astronautics, (1983) 252–272.
[25] M. Frenklach, D. E. Bornside, "Shock-initiated ignition in methane-propane mixtures," Combust. Flame, 56(1) (1984) 1–27.
[26] L. J. Spadaccini, M. B. Colket, "Ignition delay characteristics of methane fuels," Prog. Energy Combust. Sci., 20(5) (1994) 431–460.
[27] N. Lamoureux, C. E. Paillard, "Natural gas ignition delay times behind reflected shock waves: Application to modelling and safety," Shock Waves, 13(1) (2003) 57–68.
[28] J. Huang, W. K. Bushe, "Experimental and kinetic study of autoignition in methane/ethane/air and methane/propane/air mixtures under engine-relevant conditions," Combust. Flame, 144(1) (2006) 74–88.
[29] J. De Vries and E. L. Petersen, "Autoignition of methane-based fuel blends under gas turbine conditions," Proc. Combust. Inst., 31(2) (2007) 3163–3171.
[30] E. L. Petersen, J. M. Hall, S. D. Smith, J. de Vries, A. R. Amadio, M. W. Crofton, "Ignition of lean methane-based fuel blends at gas turbine pressures," J. Eng. Gas Turbines Power, 129(4) (2007) 937–944.
[31] D. Healy et al., "Methane/ethane/propane mixture oxidation at high pressures and at high, intermediate and low temperatures," Combust. Flame, 155(3) (2008) 441–448.
[32] S. Schuh, A. K. Ramalingam, H. Minwegen, K. A. Heufer, and F. Winter, "Experimental Investigation and Benchmark Study of Oxidation of Methane-Propane-n-Heptane Mixtures at Pressures up to 100 bar," Energies, 12(18) (2019) 3410.
[33] C. S. Eubank, M. J. Rabinowitz, W. C. Gardiner, R. E. Zellner, "Shock-initiated ignition of natural gas-Air mixtures," 18th Intl. Symp. Combust., 1 (1081) 1767–1774.
[34] G. Bourque et al., "Ignition and flame speed kinetics of two natural gas blends with high levels of heavier hydrocarbons," Proc. ASME Turbo Expo, 3(B) (2008) 1051–1066.
[35] S. K. Vallabhuni et al., "Autoignition studies of Liquefied Natural Gas (LNG) in a shock tube and a rapid compression machine," Fuel, 232 (2018) 423–430.
[36] W. S. Affleck, A. Thomas, "An Opposed Piston Rapid Compression Machine for Preflame Reaction Studies," Proc. Inst. Mech. Eng., 183(1) (1968) 365–387.
[37] J. Bugler, K.P. Somers, E.J. Silke, H.J. Curran, "Revisiting the Kinetics and Thermodynamics of the Low-Temperature Oxidation Pathways of Alkanes: A Case Study of the Three Pentane Isomers," J. Phys. Chem. A, 119(28) (2015) 7510–7527.
[38] J. Bugler et al., "An ignition delay time and chemical kinetic modeling study of the pentane isomers," Combust. Flame, 163 (2016) 138–156.
[39] J. Bugler et al., "An experimental and modelling study of n-pentane oxidation in two jet-stirred reactors: The importance of pressure-dependent kinetics and new reaction pathways," Proc. Combust. Inst., 36(1) (2017) 441–448.
[40] C.-W. Zhou et al., "An experimental and chemical kinetic modeling study of 1,3-butadiene combustion: Ignition delay time and laminar flame speed measurements," Combust. Flame, 197 (2018) 423–438.
[41] K. Zhang et al., "An experimental and kinetic modeling study of the oxidation of hexane

isomers: Developing consistent reaction rate rules for alkanes," Combust. Flame, 206 (2019) 123–137.
[42] K. Zhang et al., "An updated experimental and kinetic modeling study of n-heptane oxidation," Combust. Flame, 172 (2016) 116–135.
[43] M. Mehl, W. J. Pitz, C. K. Westbrook, H. J. Curran, "Kinetic modeling of gasoline surrogate components and mixtures under engine conditions," Proc. Combust. Inst., 33(1) (2011) 193–200.
[44] J. Würmel, E. J. Silke, H. J. Curran, M. S. Ó Conaire, J. M. Simmie, "The effect of diluent gases on ignition delay times in the shock tube and in the rapid compression machine," Combust. Flame, 151(1–2) (2007) 289–302.
[45] A. T. Droege, F. P. Tully, "Hydrogen-atom abstraction from alkanes by hydroxyl. 3. Propane," J. Phys. Chem., 90(9) (1986) 1949–1954.
[46] R. Sivaramakrishnan, C. F. Goldsmith, S. Peukert, J. V Michael, "Direct measurements of channel specific rate constants in $OH + C_3H_8$ illuminates prompt dissociations of propyl radicals," Proc. Combust. Inst., 37(1) (2019) 231–238.
[47] L. N. Krasnoperov, J. V Michael, "Shock Tube Studies Using a Novel Multipass Absorption Cell: Rate Constant Results For OH + H_2 and OH + C_2H_6," J. Phys. Chem. A, 108(26) (2004) 5643–5648.
[48] S. M. Villano, H.-H. Carstensen, A. M. Dean, "Rate Rules, Branching Ratios, and Pressure Dependence of the HO_2 + Olefin Addition Channels," J. Phys. Chem. A, 117(30) (2013) 6458–6473.
[49] S. Sharma, S. Raman, W. H. Green, "Intramolecular Hydrogen Migration in Alkylperoxy and Hydroperoxyalkylperoxy Radicals: Accurate Treatment of Hindered Rotors," J. Phys. Chem. A, 114(18) (2010) 5689–5701.
[50] C. F. Goldsmith, W. H. Green, S. J. Klippenstein, "Role of O_2 + QOOH in Low-Temperature Ignition of Propane. 1. Temperature and Pressure Dependent Rate Coefficients," J. Phys. Chem. A, 116(13) (2012) 3325–3346.
[51] S. Klippenstein et al., "HO_2 + HO_2: High level theory and the role of singlet channels," in 11th US National Combustion Meeting, 2019.
[52] Z. Hong, K.-Y. Lam, R. Sur, S. Wang, D. F. Davidson, R. K. Hanson, "On the rate constants of OH+HO_2 and HO_2+HO_2: A comprehensive study of H_2O_2 thermal decomposition using multi-species laser absorption," Proc. Combust. Inst., 34(1) (2013) 565–571.

CHAPTER 4

IGNITION DELAY TIME CORRELATION OF $C_1 – C_5$ NATURAL GAS BLENDS FOR INTERMEDIATE AND HIGH TEMPERATURE REGIME

Chapter 4: Ignition Delay Time Correlation of $C_1 - C_5$ Natural Gas Blends for Intermediate and High Temperature Regime

Published in: Journal of Engineering for Gas Turbines and Power, Dec 2021, 143(12): 121025.
DOI: https://doi.org/10.1115/1.4051908

Authors and Contributions

1) **Ahmed Abd El-Sabor Mohamed** (National University of Ireland, Galway, Ireland)
Contribution: High pressure shock-tube experiments (HPST), Correlation development and manuscript preparation.
2) **Amrit Bikram Sahu** (National University of Ireland, Galway, Ireland)
Contribution: Chemical kinetic modelling and manuscript review.
3) **Snehasish Panigrahy** (National University of Ireland, Galway, Ireland)
Contribution: Chemical kinetic modelling and manuscript review.
4) **Gilles Bourque** (Siemens Canada Ltd, Montreal QC H9P 1A5, Canada)
Contribution: Project management and manuscript review.
5) **Henry J. Curran** (National University of Ireland, Galway, Ireland)
Contribution: Project management and manuscript review.

Abstract

New ignition delay time (IDT) data for stoichiometric natural gas (NG) blends composed of $C_1 - C_5$ n-alkanes with methane as the major component were recorded using a high-pressure shock tube (HPST) at reflected shock pressures (p_5) and temperatures (T_5) in the range 20 – 30 bar and 1000 – 1500 K, respectively. The good agreement of the new IDT experimental data with literature data shows the reliability of the new data at the conditions investigated. Comparisons of simulations using the NUI Galway mechanism (NUIGMech1.0) show very good agreement with the new experimental results and with the existing data available in the literature. Empirical IDT correlation equations have been developed through multiple linear regression analyses for these $C_1 - C_5$ n-alkane/air mixtures using constant volume IDT simulations in the pressure range $p_C = 10 - 50$ bar, at temperatures $T_C = 950 - 2000$ K and in the equivalence ratio (φ) range 0.3 – 3.0. Moreover, a global correlation equation is developed using NUIGMech1.0, to predict the

IDTs for these NG mixtures and other relevant data available in the literature. The correlation expression utilized in this study employs a traditional Arrhenius rate form including dependencies on the individual fuel fraction, T_C, φ and p_C.

Keywords: Chemical kinetics; Gas turbines; Internal Combustion Engines; Oxidation; Natural gas; ST; IDT correlation.

Nomenclature

T_C Compressed temperature, K
p_C Compressed pressure, bar
φ Equivalence ratio
E_{ac} Activation energy, Kcal/mol
R Universal gas constant, Kcal/K/mol

4.1 Introduction

Due to stringent emissions legislation natural gas (NG) is becoming a potential fuel for internal combustion engines (ICEs) to reduce pollutant emissions and is used as a main fuel for gas turbines (GTs) [1–5]. The current work is motivated by numerous concerns, including the need to understand the suitability of using fuels from non-conventional NG sources in combustion devices such as GTs and ICEs. Furthermore, a chemical kinetic mechanism has been developed to describe NG oxidation. This mechanism has been used to develop a tool to predict IDTs that will save time and cost of designing combustion devices. Auto-ignition is an important fuel characteristic for combustor design. It is important to ensure that the time required to fully premix the fuel and air is shorter than the ignition time required for the mixture at the conditions of combustor operation. Moreover, auto-ignition is the main process controlling combustion in homogeneous charge compression ignition (HCCI) engines. Recently, the development of these engines using NG has attracted more attention due to its high efficacy in decreasing harmful emissions (nitrogen oxides and particulate matter) while increasing fuel economy [6–11]. The chemical kinetics of a fuel controls auto-ignition in a combustion device, which depends not only on the fuel/air ratio and exhaust-gas recirculation rate but also on the thermodynamic conditions (pressure and temperature) inside the engine cylinder [12]. Therefore, to achieve

reliable results an accurate chemical kinetic mechanism describing a fuel's oxidation needs to be developed which can ultimately lead to the development and optimization of more effective engine combustion technologies [13–15]. NG mixtures consist largely of methane with larger hydrocarbons, sometimes including up to *n*-heptane [16]. Therefore, a detailed chemical kinetic mechanism describing NG oxidation should include the sub-chemistry of each fuel component from C_1 – C_7 hydrocarbons. However, such a mechanism comprises 2746 species and 11270 reactions [17–22], which results in a prohibitive cost for high-fidelity simulations of a full combustor system.

Lab-scale reactors such as rapid compression machines (RCMs) and shock tubes (STs) are used to measure IDTs at combustor relevant conditions, which are then commonly used to validate a detailed chemical kinetic mechanism over a wide range of conditions. Once a mechanism that yields good agreement with the experimental data is validated, it can be used to create a test dataset to develop a correlation equation for IDT data to reduce both experimental and computational cost. This equation should include functions for key parameters such as pressure, equivalence ratio and fuel concentration.

Several regression analyses of IDTs producing correlations (Eq. (4-1)– (4-6)) based on the Arrhenius equation form were published previously [23–28]. These expressions include the fuel dependence, either through fuel concentration, fuel mole fraction, fuel component percentage (volume %), or number of carbon atoms in the fuel, and also include a dependence on pressure, equivalence ratio, dilution, and oxygen concentration.

$$\tau = A\,[\mathrm{Fuel}]^a[\mathrm{O2}]^b[\mathrm{Dilute}]^c e^{(\frac{E_{ac}}{RT})} \quad (4\text{-}1)$$

$$\tau = A\,p^a\,\varphi^{\,b} e^{(\frac{E_{ac}}{RT})} \quad (4\text{-}2)$$

$$\tau = A\,p^a {X_{\mathrm{O2}}}^b e^{(\frac{E_{ac}}{RT})} \quad (4\text{-}3)$$

$$\tau = A\,p^a {X_{\mathrm{O2}}}^b\,\varphi^{\,c}\,e^{(\frac{E_{ac}}{RT})} \quad (4\text{-}4)$$

$$\tau = A\,p^a {X_{\mathrm{O2}}}^b \mathrm{C}^{\,c}\,e^{(\frac{E_{ac}}{RT})} \quad (4\text{-}5)$$

$$\tau = A\,p^a {X_{\mathrm{O2}}}^b \varphi^{\,c-\frac{d}{T}}\,e^{(\frac{E_{ac}}{RT})} \quad (4\text{-}6)$$

where τ, A, p, φ, X_{O2}, C, R, T, [Fuel] represent the IDT, frequency factor, compressed pressure, equivalence ratio, oxygen mole fraction, number of carbon atoms, universal gas constant, compressed temperature, and fuel concentration [mole m^{-3}], respectively. The exponents $a, b, and\ c$ represent the exponential coefficients of the dependence parameter.

The current study focuses on the challenges of acquiring one global correlation equation for IDTs as a function of individual parameters such as fuel fraction, p_C, T_C and φ, as well as an investigation of the sensitivity of these parameters to IDT predictions over the temperature range studied. The correlation equations are developed to accurately express the IDT behavior of a series of C_1 – C_5 *n*-alkane mixtures at intermediate and high temperatures. For the training dataset the range of each fuel component in the mixture is varied from the minimum to the maximum values of their concentrations in the NG1 to NG3 mixtures as shown in Table 4-1 [18, 29, 30]. The presented correlation equations have been tested over a wider range of experimental shock tube IDT measurements. In the following Sections experimental details, the chemical kinetic model, and the correlation development procedure are provided followed by a discussion of the results.

4.2 Experiment

The NUI Galway (NUIG) high-pressure shock tube (HPST) was used to perform the IDT experiments presented here. A brief description of the facility is provided here as greater detail has been provided previously [17], [31]. The driver gases used are helium for non-tailored and helium/nitrogen mixtures for tailored experiments. To measure the shock velocity there are six PCB113B24 pressure transducers mounted axially positioned to the tube wall in the driven section at different location near the endwall. An endwall mounted Kistler 603B pressure transducer is used to record the pressure-trace used to measure the IDTs. The initial pressure (p_1), the initial temperature (T_1), and the shock velocity (V_{shock}) of the tested mixture are

implemented in the "Gaseq" software [32] using the problem type 'reflected shock' in conjunction with frozen chemistry assumption with the thermodynamic data file (NUIGMech1.0.dat) [17–22] to calculate the compressed gas temperature (T_5) and pressure (p_5) behind the reflected shock which listed in Table 4-3. The ignition event in the current experiment is identified as the time of maximum pressure gradient. Figure 4-1 shows the time histories of pressure and the *dp/dt* profiles for NG2 at stoichiometric conditions (φ = 1.0), 1248 K, and 20 bar. At time zero the initial pressure oscillations in the pressure time history in Figure 4-1 are due to the shock wave hitting the pressure transducer which is fixed at the endwall and these oscillations are minimal for the sidewall pressure time history [33–37].

The IDTs measurements in which the pressure/time histories exhibit a clear pre-ignition (PI) pressure rise before the major main ignition event are reported as pre-ignition events in Table 4-3 and are plotted as open symbols with crosses through them in Figure 4-6. The estimated uncertainty limits of the current measurement are ± 20 K in T_5, ± 0.5% in mixture composition, and ± 20% in measured IDT.

To prepare the mixture, the liquid fuel (*n*-pentane) is first injected into the mixing tank via an injection port until the desired partial pressure is attained. Subsequently, the other gases (O_2/N_2) are filled in ascending order based on their increasing partial pressures. The mixture is allowed to homogenize via gaseous diffusion for at least 12h before performing experiments.

The purity of the fuels used are as follows; methane (99.5%), ethane (99.5%), propane (99.5%), and *n*-butane (99.9%) were supplied by Air Liquide and the liquid fuels, *n*-pentane (99%) was supplied by Sigma Aldrich and was used without further purification. The oxidizer gases nitrogen (> 99.96%) and oxygen (> 99.5%) were supplied by BOC Ireland.

Table 4-2 shows the experimental conditions for NG2 and NG3 which have been carried out in the HPST and the twin-piston RCM at NUIG in the current and previous studies [18, 29, 30]. The error bars in the figures below represent ± 20% of the measured IDT.

4.3 Numerical model

In the present work, the newly published detailed chemical kinetic model NUIGMech1.0 [17–22] is used to simulate the experimentally measured IDTs. NUIGMech1.0 is hierarchically developed for important hydrocarbon and oxygenated fuels ranging from hydrogen/syngas to C_7 chemistry and includes 2746 species and 11270 reactions. In our simulations, the IDT is defined as the maximum gradient of pressure with respect to time.

4.4 Results and discussion

Results of the new HPST IDTs for NG2 and NG3 along with the HPST and RCM IDTs for NG2 and NG3 from previous studies [18, 29, 30] at the conditions listed in Table 4-2. are provided here. The results of multiple regression analyses for the correlation equations are also provided. The simulations of the ST IDTs as a constant volume simulation are performed using the reflected shock pressure and temperature as the initial pressure and temperature, respectively.

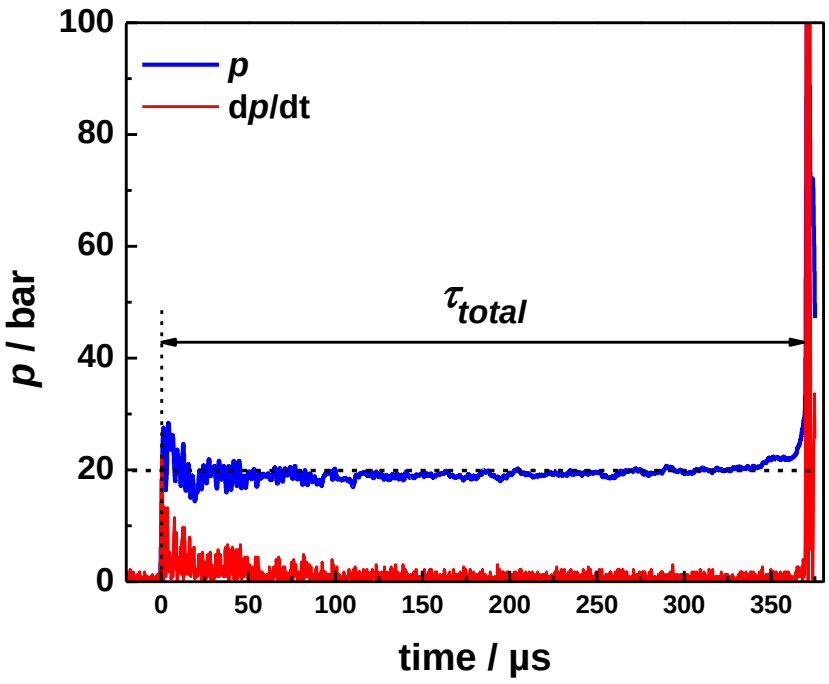

Figure 4-1. Sock tube pressure/time history for NG2 at φ = 1.0, p_5 = 20 bar, and T_5 = 1248 K.

Table 4-1. NG blends.

Species	NG1	NG2	NG3
Methane (CH_4)	98.125	81.25	62.5
Ethane (C_2H_6)	1	10	20
Propane (C_3H_8)	0.5	5	10
***n*-Butane(C_4H_{10})**	0.25	2.5	5.0
***n*-Pentane (nC_5H_{12})**	0.125	1.25	2.5

Table 4-2. HPST and RCM experiments conditions for NG1 – NG3 current and previous studies.

Blend	*T* (K)	*p* (bar)	φ	*Facility*	*Ref.*
NG2	1106 – 1427	30	0.3	HPST	[29, 30]
	821 – 1054	20 – 30	0.5	RCM	[18, 29, 30]
	1121 – 1444	18		HPST	[29, 30]
	738 – 960	20, 30	1.0	RCM	[18, 29, 30]
	1051 – 1518	30		HPST	[29, 30]
	1037 – 1483	20, 30		HPST	Current study
	711 – 968	18, 30	2.0	RCM	[18, 29, 30]
	1099 – 1549	18		HPST	[29, 30]
NG3	1084 – 1472	30	0.3	HPST	[29, 30]
	745 –1062	10 – 30	0.5	RCM	[29, 30]
	1064 – 1467	20		HPST	[29, 30]
	754 – 952	20, 30	1.0	RCM	[18, 29, 30]
	995 – 1470	30		HPST	[29, 30]
	1015 – 1426	20, 30		HPST	Current study
	699 – 886	20, 30	2.0	RCM	[29, 30]
	1019 – 1508	20		HPST	[29, 30]

4.4.1 Validation of IDT experiments

Figure 4-2 shows a comparison of the current HPST IDT experiments with previous measurements for stoichiometric NG2 (Figure 4-2(a)) and NG3 (Figure 4-2(b)) mixtures at p_C = 30 bar. The red and black lines represent the NUIGMech1.0 predictions using the p_5 and T_5 from the previous study [29, 30] and the current study, respectively. The current measurements are within the uncertainty of previous work ensuring the validity of the facility and experimental procedure. Figure 4-2(b) shows some discrepancy in the IDTs at high temperature for NG3 at 30 bar between the current and previous measurements. This may be because the short IDTs (~20 μs) are affected by pressure oscillation at time zero due to the shock wave arrival at the endwall, as evident in Figure 4-1. The IDTs predictions using NUIGMech1.0 also show very good agreement with the experiments data.

Table 4-3. ST IDTs data for NG2 and NG3 at φ =1.0 and p_5 =20 and 30 bar from the current study.

p_1 (bar)	T_1 (K)	V_{Shock} (m/s)	p_5 (bar)	T_5(K)	IDT (μs)
NG2					
0.474	308.15	938.04	17.683	1040.4	2107 (PI)
0.474	308.15	941.16	17.867	1045.2	1774 (PI)
0.474	308.15	968.86	19.500	1087.7	1216 (PI)
0.430	308.15	1010.51	20.110	1153.1	848.2
0.361	308.15	1069.44	19.953	1248.7	369.8
0.308	308.15	1123.0	19.660	1338.8	140
0.271	308.15	1180.1	19.940	1438.0	59.3
0.250	308.15	1205.4	19.555	1483.0	38.39
0.879	308.15	911.27	30.002	1000.1	2107 (PI)
0.788	308.15	936.2	29.213	1037.6	1649 (PI)
0.711	308.15	983.34	30.603	1110.2	945.8
0.590	308.15	1049.0	30.795	1215.2	343.3
0.499	308.15	1102.2	30.155	1303.5	149.6
0.430	308.15	1155.7	29.787	1395.2	66.8
0.380	308.15	1204.2	29.845	1486.3	32.64
NG3					
0.524	308.15	914.39	18.628	1007.7	2080 (PI)
0.524	308.15	919.47	18.950	1015.3	2062 (PI)
0.524	308.15	939.29	20.237	1045.4	1434
0.463	308.15	977.68	20.175	1104.5	887.6
0.421	308.15	1012.8	20.370	1160.1	546.8
0.353	308.15	1066.56	19.915	1247.6	232
0.301	308.15	1112.8	19.259	1325.3	113.1
0.270	308.15	1171	20.032	1426.3	43.8
0.859	308.15	903.98	29.460	992.5	1931 (PI)
0.859	308.15	919.27	31.026	1015.0	1382 (PI)
0.770	308.15	945.43	30.680	1056.3	1132
0.695	308.15	976.88	30.188	1103.3	653.8
0.576	308.15	1048.6	30.947	1218.0	206
0.488	308.15	1106	30.645	1313.0	90.6
0.420	308.15	1156.4	30.021	1400.7	39

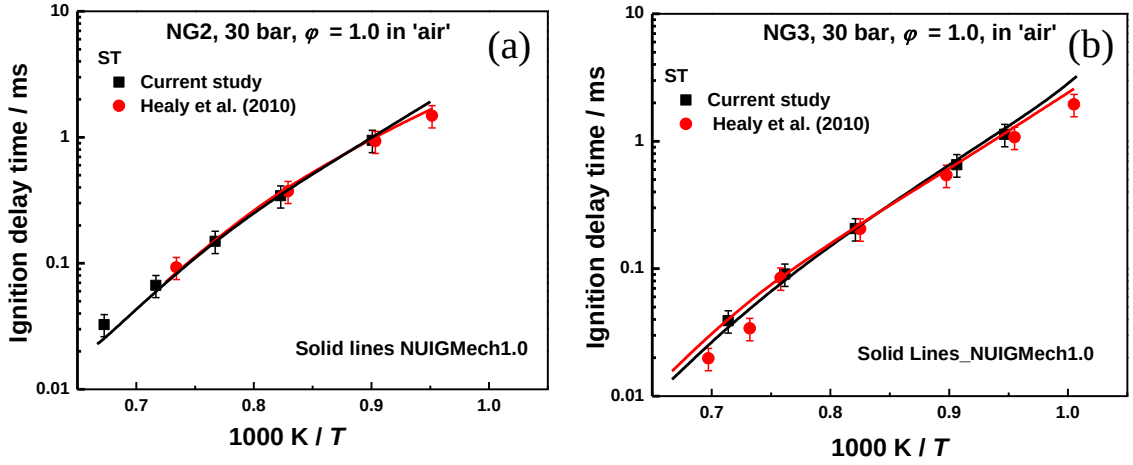

Figure 4-2. HPST IDTs experiments (symbols) and simulation (lines) at φ = 1.0 and p_5 = 30 bar for; (a) NG2; and (b) NG3.

4.4.2 Correlation development

4.4.2.1 IDT trends for $C_1 – C_5$ *n*-alkanes

Figure 4-3 shows constant volume simulations for fuel/air mixtures including *n*-alkanes from methane (CH_4) up to *n*-pentane (nC_5H_{12}) at temperatures ranging from 900 – 2000 K at 30 bar pressure. On addition of longer-chained alkanes the mixture reactivity increases from methane (CH_4) to *n*-pentane for temperatures from 900 K to 1100 K. But this trend changes at higher temperatures where C_2H_6 exhibits the fastest ignition followed by nC_5H_{12}, nC_4H_{10}, C_3H_8 and CH_4. At low temperatures, secondary alkyl radicals are formed in greater abundance for the heavier alkanes which lead to low-temperature chain branching pathways via multiple additions to O_2 generating ȮH radicals and consequently increase the reactivity for the larger hydrocarbons. At high temperatures, the reactivity of all fuels is controlled by the chain branching reaction Ḣ + O_2 ↔ Ö + ȮH. The production of significant amount of Ḣ atoms is responsible for the faster ignition of C_2H_6/air mixtures at higher temperatures. Ethyl radicals decompose quickly to produce C_2H_4 and Ḣ atoms. Thereafter, C_2H_4 undergoes H-atom abstraction to form vinyl radicals which react with O_2 generating vinoxy radicals and Ö atoms in a chain branching process. Moreover, vinoxy radicals and Ö atoms further proceed through dissociation and bimolecular reactions with C_2H_4, producing more Ḣ atoms. In the case of higher *n*-alkanes, Ḣ atom production is primarily governed by unimolecular decomposition of the fuel. The higher rate constant of unimolecular decomposition for heavier alkanes causes the faster ignition of nC_5H_{12} and nC_4H_{10} compared to C_3H_8. Whereas, for CH_4 and C_3H_8, the formation of large amount of $\dot{C}H_3$ radicals inhibits their reactivity through the chain terminating reaction $\dot{C}H_3$ + $H\dot{O}_2$ ↔ CH_4 + O_2 and $\dot{C}H_3$ + $\dot{C}H_3$ (+M) ↔ C_2H_6 (+M).

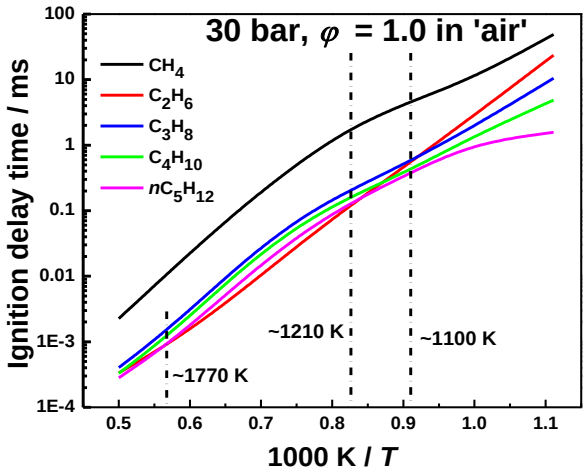

Figure 4-3. Constant volume IDT simulation by using NUIGMech1.0 at φ = 1.0 and 30 bar for C_1 – C_5 *n*-alkanes.

4.4.2.2 Impact of equivalence ratio

Figure 4-4 shows the effect of increasing the equivalence ratio from for φ = 0.3 – 3.0 for the NG1 (Figure 4-4(a)), NG2 (Figure 4-4(b)), and NG3 (Figure 4-4(c)) mixtures at 30 bar in the temperature range 900 – 2000 K. It is observed in Figure 4-4 that the fuel-rich mixtures ignite faster for temperature from 900 K up to 1150 K but at temperatures above ~1300 K the fuel-lean mixtures clearly show a faster reactivity. Figure 4-4 also shows that the crossover temperature between the equivalence ratios starts at ~1170 K for φ = 3.0 and 2.0 and ends at ~1270 K for φ = 3.0 with φ = 0.3 for NG1 mixture (98% CH_4). This crossover range changes for different NG mixtures comprising higher amounts of larger hydrocarbons as shown in Figure 4-4(b) and Figure 4-4(c) for the NG2 and NG3 mixtures, respectively.

4.4.2.3 Impact of pressure

Figure 4-5 shows constant volume simulations at φ = 1.0 in the temperature range 900 – 2000 K at pressures of 10 – 50 bar for the NG1 (Figure 4-5(a)), NG2 (Figure 4-5(b)), and NG3 (Figure 4-5(c)) mixtures. The reactivity of the mixture increases consistently with pressure over the entire temperature range. This is primarily attributed to higher concentrations of fuel and oxidizer in the reaction mixture with increasing pressures.

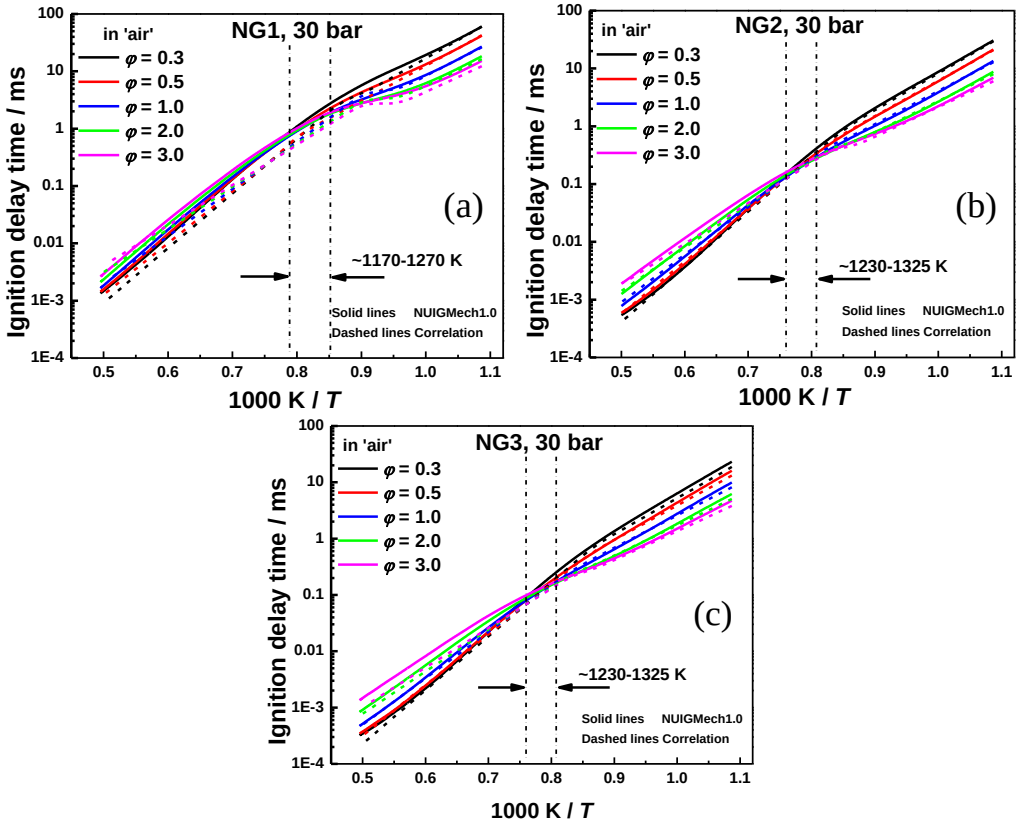

Figure 4-4. Constant volume IDT simulation by using NUIGMech1.0 at φ = 0.3 – 3.0 and 30 bar for; (a) NG1; (b) NG2; and (c) NG3.

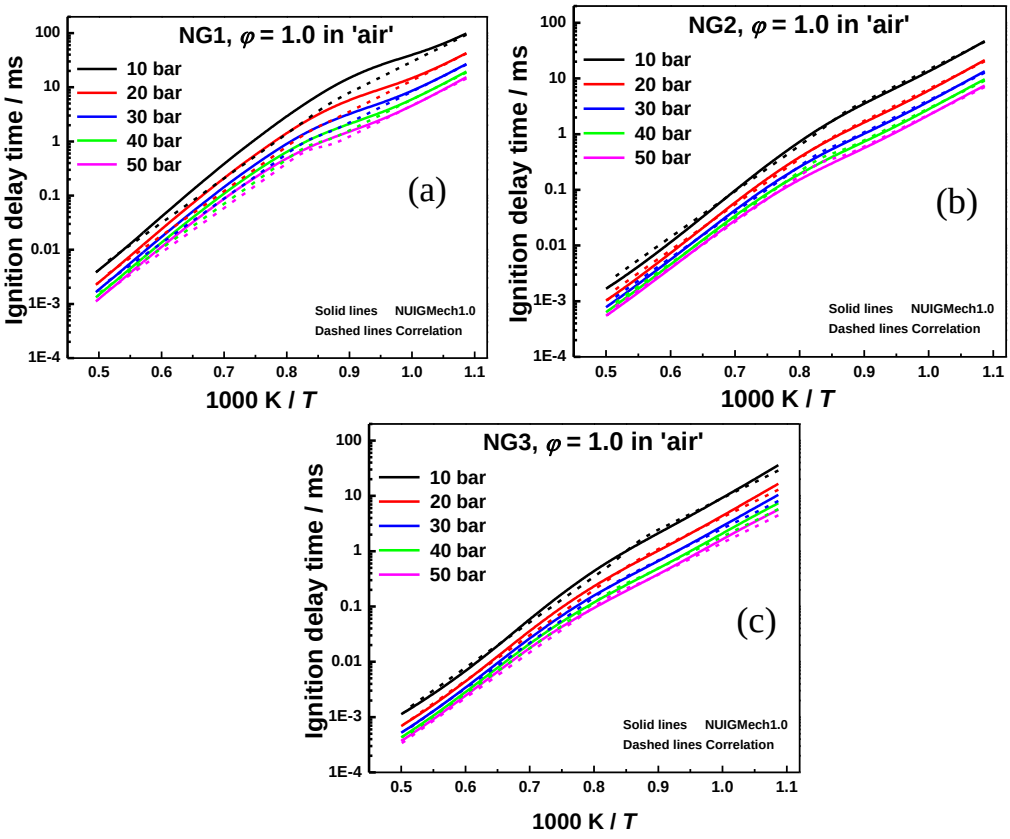

Figure 4-5. Constant volume IDT simulation by using NUIGMech1.0 at φ = 1.0 and p = 10 – 50 bar for; a) NG1; (b) NG2; and (c) NG3.

The non-monotonous dependencies on *n*-alkanes, pressure, and equivalence ratio across the range of temperature make it very difficult to find one correlation coefficient for each fuel component which can describe the IDT of $C_1 – C_5$ mixtures, while capturing all the trends successfully. Therefore, the temperature range has been divided into two sections to simplify the correlation development: one from 950 – 1150 K and the other from 1200 – 2000 K. To ensure a smooth transition between these two regions we include the 1150 K simulation from both of the correlation equations.

4.4.2.4 Multiple linear regression

The applicability of the linearization of the Arrhenius equation through logarithmic transformation has been tested before by Klicka and Kubacek [38] and the results showed that the statistical properties of the Arrhenius equation transformation can be affected by biased estimates. However, these are strongly overlapped by the standard deviations therefore, they can be completely neglected. In the current study, we have confirmed this by using the un-weighted nonlinear curve fitting method with multiple linear regression of the log-transformed Arrhenius equation, an approach shown by Sundberg [39] to be reliable. In the following section, the results obtained for $C_1 – C_5$ *n*-alkane IDT correlations are provided. The IDT is correlated as a function of the key parameters including fuel fraction, equivalence ratio, pressure, temperature, and activation energy.

Equation (4-7) shows the general form of the IDT correlation equation which is analogous to the Arrhenius equation and is a function of fuel fraction (C_nH_{2n+2}), equivalence ratio (φ), pressure (p) and temperature (T). A pre-exponential factor (A) and an activation energy term ($\frac{E_{ac}}{RT}$) are also included. Equation (4-8) is the linearized form of equation (4-7) produced by log-transformation as shown below. Table 4 summarizes the values of the coefficients obtained from the multiple linear regression analysis with R-square values of 98.4% and 99.0% using over 48000 and 81000 IDTs constant volume simulation points for the intermediate and high

temperature regimes, respectively. The absolute average error over these IDTs target points are ± 15.33%, and ± 21.89% for intermediate and high temperature regime, respectively.

$$\tau = A\ \mathrm{CH_4}^{a}\ \mathrm{C_2H_6}^{b}\ \mathrm{C_3H_8}^{c}\ \mathrm{C_4H_{10}}^{d}\ n\mathrm{C_5H_{12}}^{e}\ (\varphi)^{f+\frac{g}{T}}\ p^{h}\ e^{(\frac{E_{ac}}{RT})} \quad (4\text{-}7)$$

$$\ln(\tau) = \ln A + a\ln(\mathrm{CH_4}) + b\ln(\mathrm{C_2H_6}) + c\ln(\mathrm{C_3H_8}) + d\ln(\mathrm{C_4H_{10}}) + e\ln(n\mathrm{C_5H_{12}}) + (f + \frac{g}{T})\ \ln(\varphi) + h\ \ln(p) + \frac{E_{ac}}{RT} \quad (4\text{-}8)$$

It should be noted that in Table 4-4 methane has a positive coefficient (*a*) while all of the other *n*-alkanes has negative coefficients (*b* – *e*). A positive coefficient signifies that adding methane to a mixture would result in longer IDTs (inhibit reactivity) while increasing the concentration of any other alkane would shorten IDTs (promote reactivity). For the intermediate temperature range (950 – 1150 K), the coefficients' value increases from ethane to *n*-pentane indicating that adding larger hydrocarbons would have a greater impact on increasing the mixtures' reactivity. Furthermore, for the high-temperature regime (*T* > 1200 K) the value of ethane's coefficient becomes the most negative compared to the other larger hydrocarbons (C_3 – C_5) showing that adding ethane would have the highest impact in increasing reactivity at these temperatures. These trends are consistent with the IDT predictions shown previously in Figure 4-3 as ethane is seen to be the most reactive at high temperatures.

Table 4-4. Summary of correlation equation coefficients for intermediate and high temperature.

***T*, K**	**950 – 1150**		**1200 – 2000**	
Coefficients	**Evaluated value**	**Standard Error**	**Evaluated value**	**Standard Error**
ln A	–8.45	0.018	–14.16	0.016
a	1.17	0.019	1.74	0.020
b	–0.021	0.002	–0.058	0.002
c	–0.051	0.001	–0.029	0.001
d	–0.06	0.001	–0.045	0.001
e	–0.086	0.001	–0.072	0.001
f	0.642	0.011	1.91	0.006
g	–1226.12	11.647	–2520	8.167
h	–1.16	0.001	–0.782	0.001
E_{ac}	26.3	0.019	37.65	0.014

To address the change of the impact of equivalence ratio on IDT with temperature, the equivalence ratio coefficient was used with a temperature dependence defined as: $(f + \frac{g}{T})$. In the

intermediate temperature range, the value of (*f)* is positive and (*g*) is negative, which makes the final value of the total coefficient negative, but it decreases with increasing temperature in this temperature range. This keeps the reactivity of the fuel-rich mixtures higher than that of the fuel-lean ones. However, the difference in the reactivity decreases with increasing temperature, which is in line with the mechanism predictions shown in Figure 4-4. For the high temperature range the values of (*f)* and (*g*) increase by a factor of ~ 3 and 2, respectively, which makes the final value of the total coefficient decrease faster compared to intermediate temperatures and they become positive with increasing temperature. This leads to a crossover in reactivity for the fuel-lean and fuel-rich mixtures in the temperature range of ~1170 – 1325 K. Therefore, increasing the equivalence ratio at these temperatures lowers the reactivity and increases IDTs. The correlations predict this behavior within ≤ 15% for mixtures with ($C_2 – C_5$) volume fractions larger than 15% (for NG2 and NG3) as shown in Figure 4-4(b) and Figure 4-4(c), but over-predicts the reactivity for mixtures with high concentrations of methane (in NG1) at high temperatures as shown in Figure 4-4(a).

Moreover, the negative value of the pressure coefficients for the two regimes ensures that increasing the pressure leads to lower IDT values and faster reactivity. These trends agree with the underlying chemical kinetics. The correlations predict the reactivity at different pressures within 10% error for mixtures with ($C_2 – C_5$) volume fraction greater than 15% but they over-predict the reactivity by 35% for the NG1 mixture at 10 bar. This decreases to 20% as the pressure increases to 50 bar, Figure 4-5.

4.4.2.5 Performance of correlations for natural gas mixtures

This section shows the performance of the correlation equations compared to the experimental IDTs for the NG mixtures and to the NUIGMech1.0 predictions at different pressures and equivalence ratios. The IDT measurements, simulation and correlation are represented by symbols, solid lines, and dashed lines, respectively in Figures (4-6) – (4-9).

Figures 4-6 shows the IDTs measurements for stoichiometric NG2 and NG3 mixtures at 20 bar and 30 bar, Figure 4-6(a) and Figure 4-6(b), respectively. NUIGMech1.0 captures the IDT values with excellent quantitative agreement, being within 20% of the measurements for both the low- and high-temperature regimes. The calculations using the correlation equations are also observed to agree well within 20% with the model and experiments over the entire temperature range apart from the slightly faster estimations at ~950 K. The impact of pressure is also observed to be accurately captured by the correlation equations in Figure 4-6.

Figures 4-7 and 4-8 show comparisons of the model and correlation predictions compared to the experimental data for NG2 and NG3 mixtures at fuel-lean, stoichiometric, and fuel-rich conditions. The correlations are observed to successfully predict the IDT values within 20% of the experimental values for all equivalence ratios. Moreover, they also tend to both qualitatively and quantitatively capture the experimentally measured trends in IDT crossover behavior for the fuel-rich to fuel-lean mixtures. The crossover temperatures from fuel-lean (φ = 0.5) to stoichiometric (φ = 1.0) and from stoichiometric (φ = 1.0) to fuel-rich (φ = 2.0) mixtures are observed to be ~1330 K and 1175 K, respectively for both NG2 and NG3 experiments as shown in Figures 4-7 and 4-8. NUIGMech1.0 captures these crossover trends with excellent quantitative agreement, while the estimates using the correlation equations are delayed by ~30 K but remain in reasonable agreement with the measurements.

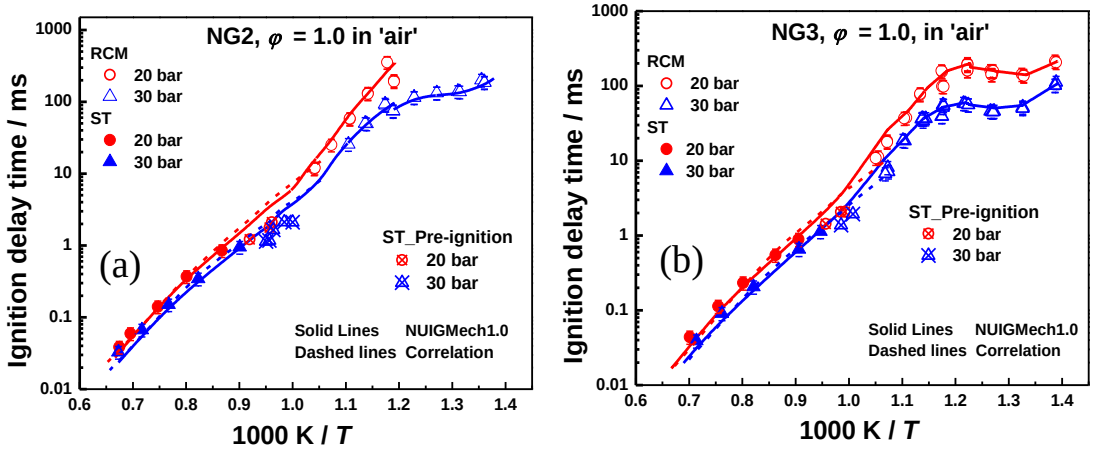

Figure 4-6. Effect of pressure on IDT at φ = 1.0 and both 20 bar and 30 bar for; (a) NG2; and (b) NG3, ST IDTs (current study), RCM IDTs [18].

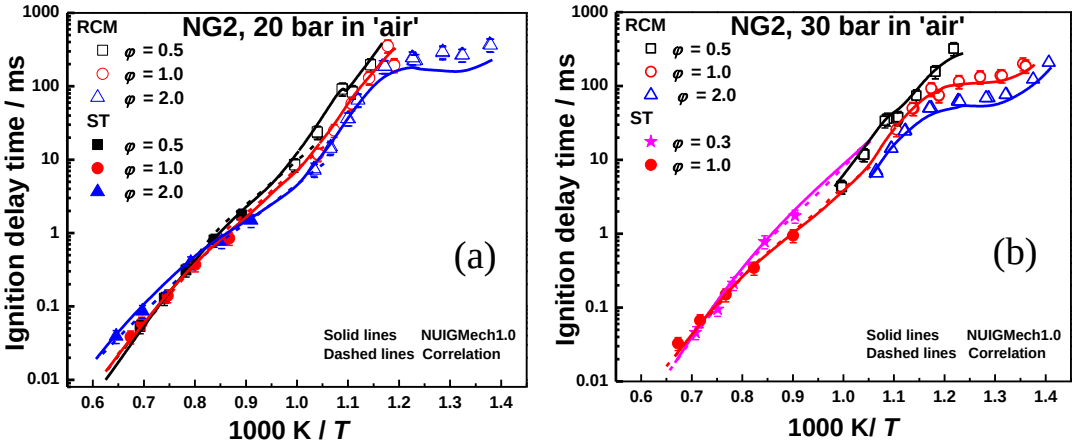

Figure 4-7. Effect of equivalence ratio on IDT for NG2 at; (a) 20 bar; and (b) 30 bar.

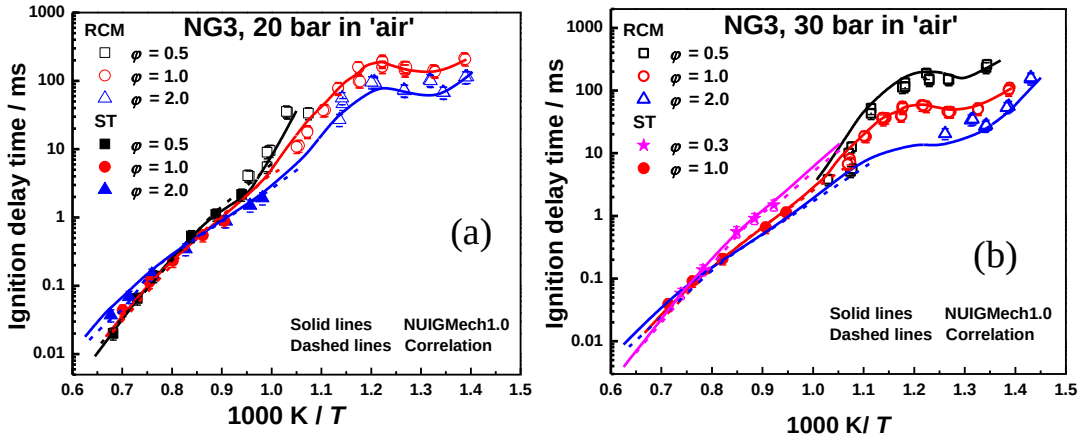

Figure 4-8. Effect of equivalence ratio on IDT for NG3 at; (a) 20 bar; and (b) 30 bar.

Figures 4-9 (a–d) compare the correlation estimations with the model predictions and experimental measurements from the literature [40] for two LNG mixtures at two equivalence ratios (φ = 0.4 and 1.2) and p_5 = 20, and 40 bar. Satisfactorily agreement (within 25%) is observed with the experimental data for variations in temperature, pressure, and equivalence ratio.

4.4.3 Chemical kinetic analysis

The crossover of IDT trends for fuel-rich and fuel-lean natural gas mixtures was observed in both the experimental measurements and in the model predictions as the temperature gradually increases from ~ 1175 – 1325 K. In order to understand the kinetics behind this crossover, sensitivity analyses were performed for the three NG mixtures. Figures 4-10(a) and 4-10(b) compare the most sensitive reactions to IDT for the 1050 K and 1850 K cases, respectively. At

1050 K, the two most sensitive reactions are the competing reactions $\dot{C}H_3 + H\dot{O}_2 \leftrightarrow CH_3\dot{O} + \dot{O}H$ and $\dot{C}H_3 + H\dot{O}_2 \leftrightarrow CH_4 + O_2$. While the former reaction is a chain propagation, it leads to the production of highly reactive $\dot{O}H$ radicals and it thus promotes reactivity, while the latter is a chain termination reaction producing stable molecules.

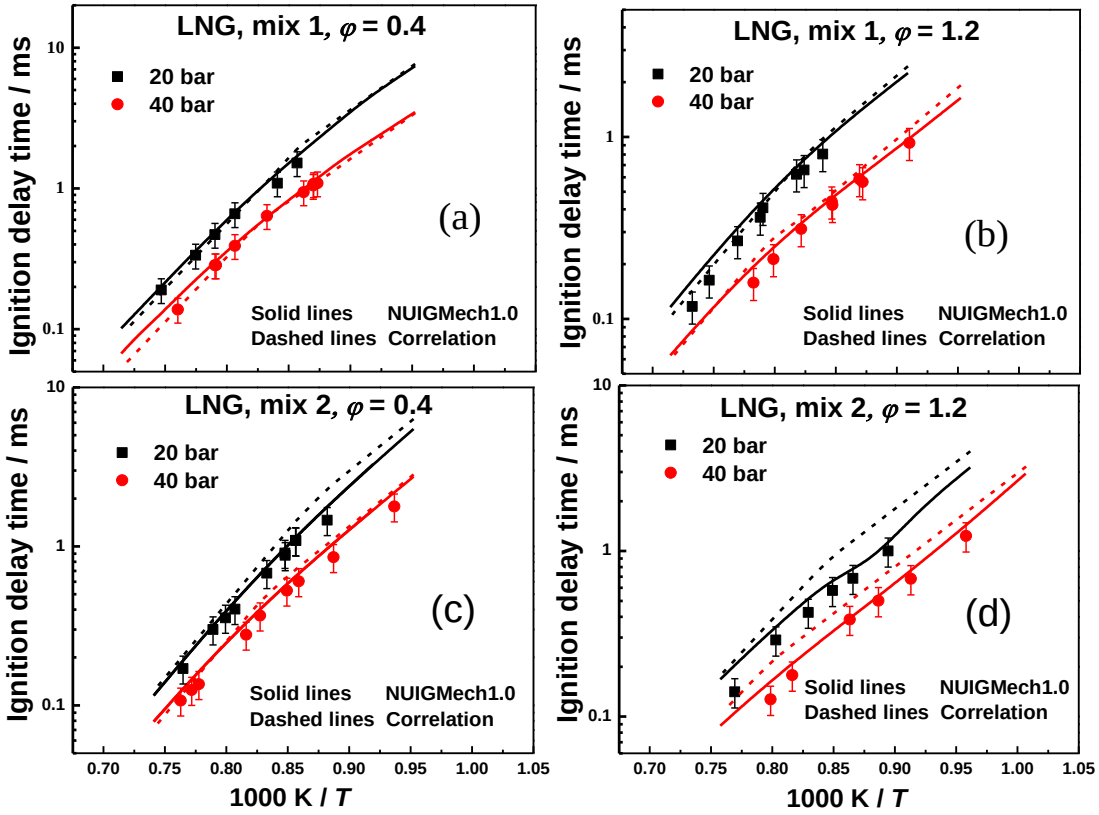

Figure 4-9. Correlation prediction performance verses ST IDT experiments at 20 bar and 40 bar for two mixtures of LNG; mix-1 (a) φ =0.4; (b) φ = 1.2 and mix-2 (c) φ = 0.4; and (d) φ = 1.2 [40].

Since enhancing the reaction rate of $\dot{C}H_3 + H\dot{O}_2 \leftrightarrow CH_4 + O_2$ would inhibit the production of $\dot{O}H$ radicals, a large positive sensitivity towards IDT is seen in Figure 4-10(a). The methyl recombination reaction also shows a large positive coefficient owing to its chain terminating nature and depleting the concentration of $\dot{C}H_3$ radicals. Other methane based reactions such as $CH_3\dot{O}_2 + \dot{C}H_3 \leftrightarrow CH_3\dot{O} + CH_3\dot{O}$, $CH_4 + H\dot{O}_2 \leftrightarrow \dot{C}H_3 + H_2O_2$ and $CH_2O + H\dot{O}_2 \leftrightarrow H\dot{C}O + H_2O_2$ also exhibit negative sensitivity coefficients thereby promoting reactivity. For the NG1 mixture, the kinetics is seen to be governed by CH_4 based reactions, compared to the other alkanes, owing to its large concentration in the fuel. For the NG2 and NG3 mixtures, the sensitivity coefficient of the reaction $C_2H_6 + H\dot{O}_2 \leftrightarrow \dot{C}_2H_5 + H_2O_2$ is seen to increase and eventually becoming

comparable to the CH_4 based reactions owing to the increase in C_2H_6 concentrations and therefore, its importance. The significance of H-atom abstraction reactions from other alkanes also exhibit increasing sensitivities for the NG2 and NG3 mixtures.

The unimolecular dissociation reaction, H_2O_2 (+M) ↔ ȮH + ȮH (+M) also shows an increasing sensitivity in the NG2 and NG3 mixtures as it leads to the production of two highly reactive ȮH radicals from a relatively stable H_2O_2 molecule. This increased sensitivity coefficients towards IDT for NG2 and NG3 mixtures is primarily attributed to the increasing rate of H-atom abstraction from fuel molecules by $HȮ_2$ radicals producing H_2O_2 and the corresponding alkyl radicals. Overall, it is observed that the key reactions governing the ignition kinetics at 1050 K are primarily fuel-based. Therefore, higher equivalence ratio mixtures (higher fuel mole fractions), exhibit faster ignition behavior. At higher temperatures (T = 1850 K), the chain branching reaction, Ḣ + O_2 ↔ Ö + ȮH is the single most important reaction promoting reactivity for all of the NG mixtures, irrespective of fuel composition. The fuel-based reactions are seen to have negligible sensitivities towards IDT, indicating that the kinetics is primarily governed by O_2 based reactions. Thus, leaner mixtures tend to show higher reactivity at higher temperatures. This behavior of the crossover of reactivities with equivalence ratio is also successfully shown by the correlations proposed in this study.

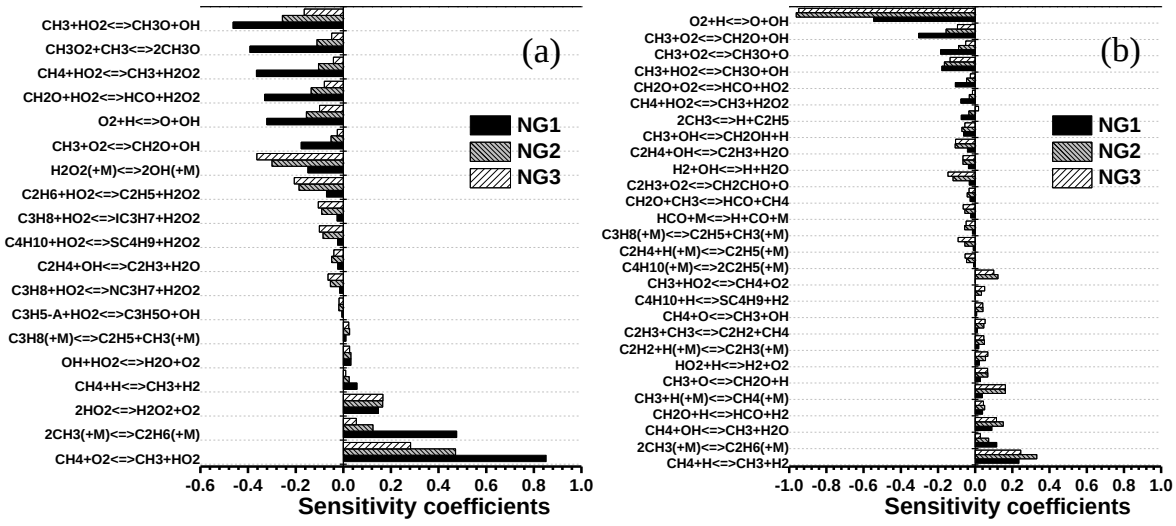

Figure 4-10. IDT sensitivity analysis for NG1, NG2, and NG3 at φ = 1.0 and 30 bar for; (a) 1050 K; and (b) 1850 K.

4.5 Conclusions

In this study new IDT measurements for NG2 and NG3 blends are reported using a HPST at reflected shock pressures (p_5) and temperatures (T_5) in the range 20 – 30 bar and 1000 – 1500 K, respectively. The IDT measurements for different NG mixtures showed that reactivity increases with increasing equivalence ratio, from fuel-lean to fuel-rich mixtures, at low and intermediate temperatures ($T \leq 1250$ K). On the contrary, at high temperatures ($T \geq 1250$ K), fuel-lean mixtures become more reactive than fuel-rich mixtures. The crossover temperature in reactivity depends on mixture composition as well as pressure. Model predictions using NUIGMech1.0 for the new IDTs measurements show excellent agreement with the current data as well as with other available data in the literature. Multiple linear regression analyses were used to develop IDT correlation equations for both the intermediate and high temperature regime for NG blends composed of $C_1 – C_5$ *n*-alkanes with methane as the major component. Dividing the correlations analysis into two temperature regimes allowed us to capture the impact of different *n*-alkanes as well as the pressure and equivalence ratio successfully. The coefficients' values derived from the multiple regression analyses reflect well the chemical effects of each parameter on the IDT. The correlation equations provided reproduce the IDT measurements with very good agreement (within 20%) in the temperature range 950 – 1500 K for different equivalence ratios. Therefore, the correlations proposed in this study should be a valuable tool to estimate the ignition characteristics of NG mixtures quickly and accurately.

Acknowledgements

The authors would like to acknowledge Science Foundation Ireland for funding via project numbers 15/IA/3177 and 16/SP/3829. We also acknowledge funding from Siemens Energy Canada Ltd.

References

[1] H. M. Cho, B.-Q. He, "Spark ignition natural gas engines—A review," Energy Convers. Manag., 48(2) (2007) 608–618.

[2] T. Korakianitis, A. M. Namasivayam, R. J. Crookes, "Natural-gas fueled spark-ignition (SI) and compression-ignition (CI) engine performance and emissions," Prog. Energy Combust. Sci., 37(1) (2011) 89–112.

[3] L. Wei, P. Geng, "A review on natural gas/diesel dual fuel combustion, emissions and performance," Fuel Process. Technol., 142 (2016) 264–278.

[4] Y. Koç, H. Yağlı, A. Görgülü, A. Koç, "Analysing the performance, fuel cost and emission parameters of the 50 MW simple and recuperative gas turbine cycles using natural gas and hydrogen as fuel," Int. J. Hydrogen Energy, 45(41) (2020) 22138–22147.

[5] W. Zeng, L. Pang, W. Zheng, E. Hu, "Study on combustion and emission characteristics of a heavy-duty gas turbine combustor fueled with natural gas," Fuel, 275 (2020) 117988.

[6] H. M. Cho and B.-Q. He, "Combustion and Emission Characteristics of a Natural Gas Engine under Different Operating Conditions," Environ. Eng. Res., 14(2) (2009) 95–101.

[7] K. Kobayashi et al., "Development of HCCI natural gas engines," J. Nat. Gas Sci. Eng., 3(5) (2011) 651–656.

[8] M. Djermouni, A. Ouadha, "Thermodynamic analysis of an HCCI engine based system running on natural gas," Energy Convers. Manag., 88 (2014) 723–731.

[9] G. Du, Z. Wang, D. Wang, X. Wang, X. Fu, "Study on the effect of water addition on combustion characteristics of a HCCI engine fueled with natural gas," Fuel, 270 (2020) 117547.

[10] M. Djermouni, A. Ouadha, "Comparative assessment of LNG and LPG in HCCI engines," Energy Procedia, 139 (2017) 254–259.

[11] P. Zhu et al., "High-efficiency conversion of natural gas fuel to power by an integrated system of SOFC, HCCI engine, and waste heat recovery: Thermodynamic and thermo-economic analyses," Fuel, 275 (2020) 117883.

[12] C. Jin, Z. Zheng, "A Review on Homogeneous Charge Compression Ignition and Low Temperature Combustion by Optical Diagnostics," J. Chem., 2015 (2015) 910348.

[13] M. Li, H. Wu, T. Zhang, B. Shen, Q. Zhang, Z. Li, "A comprehensive review of pilot ignited high pressure direct injection natural gas engines: Factors affecting combustion, emissions and performance," Renew. Sustain. Energy Rev., 119 (2020) 109653.

[14] J. You, Z. Liu, Z. Wang, D. Wang, Y. Xu, "Impact of natural gas injection strategies on combustion and emissions of a dual fuel natural gas engine ignited with diesel at low loads," Fuel, 260 (2020) 116414.

[15] Z. Chen, J. He, H. Chen, L. Wang, and L. Geng, "Experimental study of the effects of spark timing and water injection on combustion and emissions of a heavy-duty natural gas engine," Fuel, 276 (2020) 118025.

[16] S. Faramawy, T. Zaki, A. A. E. Sakr, "Natural gas origin, composition, and processing: A review," J. Nat. Gas Sci. Eng., 34 (2016) 34–54.

[17] M. Baigmohammadi et al., "A Comprehensive Experimental and Simulation Study of Ignition Delay Time Characteristics of Single Fuel C_1–C_2 Hydrocarbons over a Wide Range of Temperatures, Pressures, Equivalence Ratios, and Dilutions," Energy Fuels, 34(3) (2020)

3755–3771.

[18] A. A. E.-S. Mohamed, S. Panigrahy, A. B. Sahu, G. Bourque, and H. Curran, "An experimental and kinetic modeling study of the auto-ignition of natural gas blends containing C_1–C_7 alkanes," Proc. Combust. Inst., 38 (2021) 365–373.

[19] S. Dong et al., "A comparative reactivity study of 1-alkene fuels from ethylene to 1-heptene," Proc. Combust. Inst., 38 (2021) 611–619.

[20] M. Baigmohammadi et al., "Comprehensive Experimental and Simulation Study of the Ignition Delay Time Characteristics of Binary Blended Methane, Ethane, and Ethylene over a Wide Range of Temperature, Pressure, Equivalence Ratio, and Dilution," Energy Fuels, 34(7) (2020) 8808–8823.

[21] S. S. Nagaraja et al., "A single pulse shock tube study of pentene isomer pyrolysis," Proc. Combust. Inst., 38 (2021) 881–889.

[22] S. Panigrahy et al., "A comprehensive experimental and improved kinetic modeling study on the pyrolysis and oxidation of propyne," Proc. Combust. Inst., 38 (2021) 479–488.

[23] A. Lifshitz, K. Scheller, A. Burcat, G. B. Skinner, "Shock-tube investigation of ignition in methane-oxygen-argon mixtures," Combust. Flame, 16(3) (1971) 311–321.

[24] L. J. Spadaccini, "Autoignition Characteristics of Hydrocarbon Fuels at Elevated Temperatures and Pressures," J. Eng. Power, 99(1) (1977) 83–87.

[25] M. B. Colket, L. J. Spadaccini, "Scramjet Fuels Autoignition Study," J. Propuls. Power, 17(2) (2001) 315–323.

[26] D. C. Horning, D. F. Davidson, R. K. Hanson, "Study of the High-Temperature Autoignition of n-Alkane/O/Ar Mixtures," J. Propuls. Power, 18(2) (2002) 363–371.

[27] D. N. Assanis, Z. S. Filipi, S. B. Fiveland, M. Syrimis, "A Predictive Ignition Delay Correlation Under Steady-State and Transient Operation of a Direct Injection Diesel Engine ," J. Eng. Gas Turbines Power, 125(2) (2003) 450–457.

[28] F. Khaled, A. Farooq, "On the universality of ignition delay times of distillate fuels at high temperatures: A statistical approach," Combust. Flame, 210 (2019) 145–158.

[29] G. Bourque et al., "Ignition and Flame Speed Kinetics of Two Natural Gas Blends With High Levels of Heavier Hydrocarbons," J. Eng. Gas Turbines Power, 132(2) (2009) 21504–21511.

[30] D. Healy, D. M. Kalitan, C. J. Aul, E. L. Petersen, G. Bourque, and H. J. Curran, "Oxidation of C_1−C_5 Alkane Quinternary Natural Gas Mixtures at High Pressures," Energy Fuels, 24(3) (2010) 1521–1528.

[31] H. Nakamura et al., "An experimental and modeling study of shock tube and rapid compression machine ignition of n-butylbenzene/air mixtures," Combust. Flame, 161(1) (2014) 49–64.

[32] C. Morley, "Gaseq program." [Online]. Available: http://www.gaseq.co.uk. [Accessed: 29-Sep-2017].

[33] C. J. Brown, G. O. Thomas, "Experimental studies of shock-induced ignition and transition to detonation in ethylene and propane mixtures," Combust. Flame, 117(4) (1999) 861–870.

[34] E. L. Petersen, "Interpreting Endwall and Sidewall Measurements in Shock-Tube Ignition Studies," Combust. Sci. Technol., 181(9) (2009) 1123–1144.

[35] L. Wei, C. Tang, X. Man, X. Jiang, Z. Huang, "High-Temperature Ignition Delay Times and Kinetic Study of Furan," Energy Fuels, 26(4) (2012) 2075–2081.

[36] J. W. Hargis, E. L. Petersen, "Methane Ignition in a Shock Tube with High Levels of CO_2 Dilution: Consideration of the Reflected-Shock Bifurcation," Energy Fuels, 29(11) (2015) 7712–7726.

[37] S. Downes, A. Knott, I. Robinson, "Towards a shock tube method for the dynamic calibration of pressure sensors," Philos. Trans. A. Math. Phys. Eng. Sci., 372(2023) (2014) 20130299.

[38] R. Klicka, L. Kubácek, "Statistical properties of linearization of the Arrhenius equation via the logarithmic transformation," Chemom. Intell. Lab. Syst., 39(1) (1997) 69–75.

[39] R. Sundberg, "Statistical aspects on fitting the Arrhenius equation," Chemom. Intell. Lab. Syst., 41(2) (1998) 249–252.

[40] S. K. Vallabhuni et al., "Autoignition studies of Liquefied Natural Gas (LNG) in a shock tube and a rapid compression machine," Fuel, 232 (2018) 423–430.

CHAPTER 5

AN EXPERIMENTAL AND KINETIC MODELING STUDY OF NO_X SENSITIZATION ON METHANE AUTOIGNITION AND OXIDATION

Chapter 5: An Experimental and Kinetic Modeling Study of NO_x Sensitization on Methane Auto-ignition and Oxidation

Published in: Combustion and flame, available online 28 September 2021, 111746.
DOI: https://doi.org/10.1016/j.combustflame.2021.111746

Authors and Contributions

1) **Amrit Bikram Sahu** (National University of Ireland, Galway, Ireland)
Contribution: Chemical kinetic modelling and manuscript preparation.
2) **Ahmed Abd El-Sabor Mohamed** (National University of Ireland, Galway, Ireland)
Contribution: RCM and HPST experiments and manuscript preparation.
3) **Snehasish Panigrahy** (National University of Ireland, Galway, Ireland)
Contribution: Chemical kinetic modelling.
4) **Gilles Bourque** (Siemens Energy Canada Ltd, Montreal QC H9P 1A5, Canada)
Contribution: Project management and manuscript review.
5) **Henry J. Curran** (National University of Ireland, Galway, Ireland)
Contribution: Project management and manuscript review.

Abstract

An experimental and kinetic modeling study of the influence of NO_x (i.e. NO_2, NO and N_2O) addition on the ignition behavior of methane/'air' mixtures is performed in this work. Ignition delay time measurements are taken in a rapid compression machine (RCM) and in a shock tube (ST) at temperatures and pressures ranging from 900 – 1500 K and 1.5 – 3.0 MPa, respectively for equivalence ratios of 0.5 – 2.0 in 'air'. The conditions chosen are relevant to spark ignition and homogeneous charge compression ignition engine operating conditions where exhaust gas recirculation can potentially add NO_x to the premixed charge. The RCM measurements show that the addition of 200 ppm NO_2 to the stoichiometric CH_4/oxidizer mixture results in a factor of three increase in reactivity compared to the baseline case without NO_x for temperatures in the range 600 – 1000 K. However, adding up to 1000 ppm N_2O does not show any appreciable effect on the measurements. The promoting effect of NO_2 was found to increase with temperature in the range 950 – 1150 K, while the sensitization effect decreases at higher pressures. The

experimental results measured are simulated using NUIGMech1.2 comprising an updated NO_x sub-chemistry in this work. A kinetic analysis indicates that the competition between the reactions $\dot{C}H_3 + NO_2 \leftrightarrow CH_3\dot{O} + NO$ and $\dot{C}H_3 + NO_2 (+M) \leftrightarrow CH_3NO_2 (+M)$, the former being a propagation and the latter being a termination reaction governs NO_x sensitization on CH_4 ignition. Recent calculations by Matsugi and Shiina (A. Matsugi, H. Shiina, J. Phys. Chem. A. 121 (2017) 4218–4224) for the nitromethane formation reaction $CH_3 + NO_2 (+M) \leftrightarrow CH_3NO_2$ (+M), together with the recently calculated rate constants for $HONO/HNO_2$ reactions significantly improve ignition delay time predictions in the temperature range 600 – 1000 K. Furthermore, the experiments with NO addition reveal a non-monotonous sensitization impact on CH_4 ignition at lower temperatures with NO initially acting as an inhibitor at low NO concentrations and then as a promoter as NO concentrations increase in the mixture. This non-monotonous trend is attributed to the role of the chain-termination reaction $\dot{C}H_3 + NO_2 (+M) \leftrightarrow CH_3NO_2 (+M)$ and the impact of NO on the transition to the chain-branching steps $CH_2O + H\dot{O}_2 \leftrightarrow H\dot{C}O + H_2O_2$, $H_2O_2 (+M) \leftrightarrow \dot{O}H + \dot{O}H (+M)$, $H\dot{C}O \leftrightarrow CO + \dot{H}$ followed by $CO + O_2 \leftrightarrow CO_2 + \ddot{O}$ and $\dot{H} + O_2 \leftrightarrow \ddot{O} + \dot{O}H$. NUIGMech1.2 is systematically validated against the new ignition delay measurements taken here together with species measurements and high temperature ignition delay time data available in the literature for CH_4/oxidizer mixtures diluted with $NO_2/N_2O/NO$ and is observed to accurately capture the sensitization trends.

Keywords: Methane/NO_x; ignition delay time; rapid compression machine; chemical kinetic modelling.

5.1 Introduction

It is important to understand the interaction of a hydrocarbon and its related species with NO_x species during combustion at conditions relevant to practical combustors in order to develop cleaner, more efficient combustors. Exhaust gas recirculation (EGR) is an effective strategy to reduce thermal NO_x emissions by lowering the peak flame temperatures [1]. However, EGR

implicitly leads to mixing of various NO_x species (NO, NO_2 and N_2O) with the fuel/air premixed charge along with the major diluents namely, N_2, CO_2 and H_2O. Several studies have shown that the presence of NO_x can significantly affect auto-ignition behaviour which is a critical parameter for the efficient operation of spark-ignited and homogeneous charge compression ignition (HCCI) engines [2,3]. Additionally, several solid-state propellants and energetic materials are nitrate based compounds which potentially produce N_2O as a key intermediate during the combustion process [4,5]. Therefore, the study of the influence of NO_x on combustion kinetics is important to the research community.

Natural gas is one of the potential fuels used in SI engines as well as in stationary gas-turbines, and thus the sensitisation effect of NO_x on methane and other alkanes has garnered wide interest. Several studies investigating the effect of NO_x on CH_4 oxidation have been carried out using laminar flow reactors [6,7] and jet-stirred reactors (JSRs) [8,9]. The primary routes of NO/NO_2 reactions with CH_4 oxidation have been identified as: $\dot{C}H_3 + NO_2 \leftrightarrow CH_3\dot{O} + NO$ and $CH_3\dot{O}_2 + NO \leftrightarrow CH_3\dot{O} + NO_2$. In addition, the reaction $NO + H\dot{O}_2 \leftrightarrow NO_2 + \dot{O}H$ serves as a chain propagation reaction promoting the conversion of less-reactive $H\dot{O}_2$ radicals into reactive $\dot{O}H$ radicals and is also a key step in the NO/NO_2 inter-conversion process, especially at low to intermediate temperatures (600 – 1000 K). Recently, Song et al. [9] conducted an atmospheric pressure JSR experimental and kinetic modeling study of CH_4 oxidation doped with NO and NO_2. The model showed overall good agreement with several key intermediate species such as HCN and HONO but over-estimated the formation of nitromethane (CH_3NO_2).

While many studies have been conducted on the oxidation process, most of them have been limited to pressures below 1.0 MPa. Apart from the work of Gersen et al. [10] we believe no other studies of direct measurements of the auto-ignition for NO_x doped methane/oxidizer mixtures exist at high pressures ($\geq$ 1.0 MPa) and low to intermediate temperatures (600 – 1000 K).

Herein we attempt to systematically investigate the effect of NO, NO_2 and N_2O addition on the auto-ignition behaviour of $CH_4/O_2/N_2/Ar$ mixtures in an RCM at pressures (p_C) of 1.5 MPa and 3.0 MPa, at temperatures (T_C) ranging from 890 – 1100 K, at equivalence ratios (φ) of 0.5, 1.0 and 2.0 in 'air'. Typical NO_x emissions from natural gas fired engines have been reported to range from 500 – 3500 ppm depending on the load and operating conditions [11–14]. EGR may result in an effective NO_x composition in the range of 50 – 200 ppm in the premixed charge [11–14], whereas gas-turbine combustors equipped with EGR typically target NO_x (@ 15% O_2) emissions of ≤ 50 ppm [15]. The dilution levels considered in this study not only cover NO_x concentrations comparable to those of practical combustors but also extends the higher levels of NO_x concentration (~1000 ppm) to aid our experimental investigation and model development. The study also provides comparisons of experimental and model predictions obtained here together with other RCM and shock tube measurements available in the literature. In addition, simulations have also been carried out to compare with measured speciation data for $CH_4/O_2/N_2/NO_x$ mixtures [9], thus providing a comprehensive overview of the model performance.

5.2 Experimental procedure

5.2.1 Rapid compression machine

The red RCM facility at NUI Galway is used to measure the ignition delay times (IDTs) presented here. A complete description of the RCM was published previously [16]. Briefly, it has twin-opposed creviced pistons assembly which permits fast compression (~16 – 17 ms), and helps prevent roll-up vortices, that improves the temperature homogeneity of the compressed gas [17]. A range of compressed gas temperatures is achieved by varying the initial temperature of the test gas via an electrical heating system installed on the outer body of the reaction chamber. The dynamic pressure of the tests was monitored using a Kistler 6045B pressure transducer flush-mounted with the chamber wall and connected to a Kistler charge amplifier in conjunction

with an oscilloscope to record the pressure/time histories. The measured IDT is calculated from the reactive pressure-time trace as the time from the first peak pressure at the EOC to the second global peak at the total ignition event. The compressed gas temperature (T_C) of each test was calculated using Gaseq [18] using the adiabatic compression/expansion assumption with the initial temperature (T_i), initial pressure (p_i), and the measured compressed pressure (p_C) as known parameters.

5.2.2 High-pressure shock tube

IDTs for neat methane/O_2/Ar and NO_2 diluted mixtures were measured in the NUI Galway high-pressure shock tube (HPST) at high temperatures (1050 – 1650 K) and pressures of 1.5 and 3.0 MPa, as the IDTs are typically less than 3 ms at these conditions. Details of this shock tube and the methodology used to measure the IDTs were published previously [19,20]. The IDT is defined as the time interval between the arrival of reflected shock wave at the end-wall and the maximum rate of pressure rise due to heat release during ignition. Prior to ignition, the rate of pressure rise behind the reflected shock wave was less than 2%/ms, therefore confirming the limited non-ideal effects of the HPST facility on the IDT measurements. For all of the IDT measurements an uncertainty of ± 20% is assigned according to a previous study [19] using the same facility.

5.2.3 Mixture preparation

The gases used in the current work are CH_4 (99.5% purity), NO_2 diluted in Ar (99.99% purity) (2% NO_2/98% Ar), NO diluted in Ar (99.99% purity) (4% NO_2/96% Ar), and N_2O (99.5% purity) which were supplied by Air Liquide. The dilution gases, N_2 (> 99.96% purity), Ar (> 99.98% purity), and O_2 (> 99.5% purity) were supplied by BOC Ireland. The CH_4/O_2/N_2/Ar mixtures were prepared following Dalton's law of partial pressure, with the pressures monitored using four MKS pressure transducers (2, 10, 100, and 500 kPa). A non-reactive mixture was

prepared in another tank by replacing O_2 with N_2 so that these pressure/time histories could be used in our simulations to account for facility effects, including heat losses. Table 5-1 shows the experimental conditions considered in this study. A separate 1.0 L mixing tank was connected to the line for NO_x addition where the desired NO_x (NO, NO_2 and N_2O) species was allowed to mix with the $CH_4/O_2/(N_2/Ar)$ mixture for 5 – 10 min before filling the reaction chamber.

Table 5-1. Experimental conditions studied for NOx sensitization on methane auto-ignition.

Exp.	CH_4	O_2	N_2	Ar	NO_2(ppm)	N_2O (ppm)	Initial NO (ppm)	φ	p_C / MPa	T_C / K
Rapid compression machine experiments										
1	6.0	24.0	15.0	55.0	–	–	–	0.5	1.5, 3.0	923 – 1064
2	10	20	–	70.0	–	–	–	1.0	1.5, 3.0	926 – 1102
3	15.0	15.0	–	70.0	–	–	–	2.0	1.5, 3.0	888 – 1067
4	5.94	23.76	14.85	55.43	200	–	–	0.5	1.5, 3.0	912 – 1056
5	5.9	23.52	14.40	55.56	400	–	–	0.5	1.5, 3.0	919 – 1037
6	9.89	19.8	–	70.28	200	–	–	1.0	1.5, 3.0	935 – 1053
7	9.79	19.59	–	70.56	400	–	–	1.0	1.5, 3.0	937 – 1016
8	14.85	14.85	–	70.28	200	–	–	2.0	1.5, 3.0	901 – 1058
9	14.7	14.7	–	70.56	400	–	–	2.0	1.5, 3.0	904 – 1061
10	9.89	19.8	–	70.26	–	400	–	1.0	1.5, 3.0	926 – 1105
11	9.75	19.5	–	70.65	–	1000	–	1.0	3.0	939 – 1067
12	5.97	23.88	14.93	55.2	–	–	200	0.5	1.5, 3.0	926 – 1036
14	5.94	23.76	14.85	55.41	–	–	400	0.5	1.5, 3.0	912 – 1056
15	10	20	–	70.0	–	–	50 – 1000	1.0	3.0	900 – 1050
16	14.93	14.93	–	70.13	–	–	200	2.0	1.5, 3.0	920 – 1037
17	14.85	14.85	–	70.26	–	–	400	2.0	1.5, 3.0	891 – 1043
High-pressure shock tube experiments										
18	10	20	70.0	–	–	–	–	1.0	1.5, 3.0	1050 – 1650
19	9.89	19.8	69.3	0.98	200	–	–	1.0	1.5, 3.0	1050 – 1650

Separate tests with different mixing times ranging from 5 – 25 min for the same mixture showed that IDTs are within the experimental uncertainties to ensure homogeneous mixing. Figure BS6 of appendix B provides a comparison of IDT measurements for 6 min and 12 h mixing time for a stoichiometric $CH_4/O_2/N_2/Ar$ mixture with 200 ppm NO_2 added. The IDTs are within 20% of

each other, therefore confirming homogeneous mixing within 6 min. However, for NO addition, a mixing time of 5 – 10 min in the presence of O_2 can lead to the conversion of a considerable fraction of NO to NO_2, thus affecting the degree of sensitization. Several literature studies investigated the conversion of NO to NO_2 in the presence of oxygen or the reverse process via the termolecular reaction $2NO + O_2 \leftrightarrow 2NO_2$ [21–24]. In addition, a study by Herzler and Naumann [25] also reported the challenge of using NO for shock-tube/RCM experiments due to the rapid oxidation of NO. Therefore, the final NO/NO_2 mixture compositions for the NO dilution cases were obtained through 0-d simulations of possible reaction in the mixing tank over the period of time that NO was allowed to mix with the test fuel/'air' mixture. The final NO/NO_2 composition used for our calculations have been provided in Table 5-2. Further details of the calculations are provided in appendix B.

Table 5-2. Final NO/NO_2 mixture composition used in our NO sensitized methane calculations.

Initial NO (ppm)	Final NO_2 (ppm)	Final NO (ppm)	φ
50	15	35	1.0
100	31	69	1.0
200	97	103	1.0
400	265	135	1.0
1000	846	154	1.0
200	115	85	0.5
400	299	101	0.5
200	91	109	2.0
400	253	147	2.0

5.3 Chemical kinetic modelling

NUIGMech1.2 is used to simulate the data measured in this study. This model has been hierarchically developed and validated for a comprehensive array of fuels ranging from $C_0 – C_7$ hydrocarbons [26–30] including binary/ternary blends [31,32] and natural gas mixtures [33,34], comprising an extensive series of work for these fuels. The hydrocarbon model has been integrated with an updated NO_x sub-mechanism which is based on the recently published mechanism by Glarborg et al. [35] and the hydrogen/syngas–NO_X chemistry adopted from

Zhang et al. [36]. Further updates to the NO_x sub-mechanism have been made based on critical assessment of recent measurements or high-level calculations of rate parameters available in the literature. Ab-initio calculations for gas-phase thermochemistry performed by Bugler et al. [37] for over 60 nitrogenous compounds are included in the current mechanism owing to their accuracy and internal consistency. A collision limit violation check was also performed in the temperature range 600 – 2500 K using a web-based application https://combustiontools.llnl.gov, developed by Killingsworth et al. [38], and the report, showing that no reactions involved in CH_4/NO_X kinetics seriously violate the collision limits, is provided as supplementary material (NUIGMech1.2_REPORT.txt) of the online version of the paper. The reverse reaction of $C_3H_6OOH \rightleftharpoons C_3H_6 + HO_2$ exceeds the unimolecular rate constant limit (1×10^{14}) by a factor of 1.6 but only at temperatures about above ~2400K, which is outside of typical combustion temperatures of interest. The reverse rates of 4 bimolecular reactions exceeded the bimolecular collision rate limit by a factor of 1.3 to 2.2. However, this is a very clean report for a reaction mechanism where literature mechanisms often report many violations, and the limits are violated by a larger amount.

Recently, Chen et al. [39] studied the unimolecular reaction of the HONO/HNO_2 system and provided rates for the $HONO \rightleftharpoons HNO_2$ isomerization and HONO decomposition reactions. Their calculated values of temperature- and pressure-dependent rate constants for the $HONO \rightleftharpoons HNO_2$ reaction are found to be approximately four orders of magnitude lower than the values recommended by Glarborg et al. [35]. Chen et al. [39] also calculated pressure-dependent rate constants for $HNO_2 \leftrightarrow NO + \dot{O}H$, a key channel for HNO_2 consumption, which was not present in any of the previous mechanisms [9,35]. A chemically consistent rate constant recommended by Li et al. [40] for $NO_2 + \ddot{O} \leftrightarrow NO + O_2$ was adopted in the current mechanism. Furthermore, nitromethane (CH_3NO_2) is identified as one of the key intermediates in the CH_4/NO_x system, therefore choices of rate parameters for CH_3NO_2 relevant reactions and their impact on NO_x

sensitization are discussed below. In addition, the enthalpy of formation ($\Delta H_{f,298K}$) for CH_3NO_2 was updated to –17.80 kcal mol^{-1} which is within 0.8 kcal mol^{-1} of the Bugler et al. calculation (–18.61 kcal mol^{-1}) [37] and within 0.06 kcal mol^{-1} of value recommended in the ATcT database (–17.86 kcal mol^{-1}) [41]. The merged mechanism, including the updated NO_x chemistry is referred to as NUIGMech1.2 and is provided as supplementary material of the online version of the paper.

Two hydrocarbon/NO_x mechanisms recently developed at DTU by Glarborg et al. [35] and by the POLIMI group [42,43] are also considered here. We have merged the DTU mechanism describing $C_0 – C_3$ chemistry [44] with their NO_x sub-mechanism [35] which we refer to as DTU_Mech. The second mechanism, Song_Mech, is derived from a CH_4/NO_x model published by Song et al. [9] in their investigation of the NO/NO_2 sensitization effects on methane oxidation at atmospheric pressure. This detailed mechanism, is primarily based on the POLIMI model [42,43]. The RCM IDT simulations were performed using CHEMKIN-Pro [45] including volume/time histories to account for facility effects, see Section 5.2.1. The shock-tube simulations were performed using the "Homogeneous Closed Volume Reactor" module. The logarithmic sensitivity coefficient (S) is defined as in Equation (5-1), where IDT and A represent ignition delay time and pre-exponential factor, respectively. The subscripts + and – represent values corresponding to positive and negative perturbations of A, respectively. The sensitivity coefficients were calculated using the direct sensitivity analysis approach developed by Gururajan and Egolfopoulos [46].

$$S = \ln(IDT_+ / IDT_-) \Big/ \ln(A_+ / A_-) \tag{5-1}$$

5.4 Results and discussion

The test conditions for the RCM/ST studies were chosen to provide benchmark IDT measurements for $NO_2/N_2O/NO$ doped methane/oxidizer mixtures highlighting the sensitization effects as a function of temperature, pressure, NO_x dilution levels and equivalence ratio. In this

section, results on the effect of NO_2 addition on methane IDTs have been provided followed by the studies with N_2O and NO dilution.

5.4.1 Effect of NO_2 on ignition delay time

5.4.1.1 Low to intermediate temperatures (600 – 1000 K)

IDT measurements for neat $CH_4/O_2/Ar$ mixtures were performed at 1.5 and 3.0 MPa for φ = 0.5, 1.0 and 2.0 mixtures in 'air' which serve as the baseline cases. The neat methane experiments were followed by similar mixtures but diluted with 200 and 400 ppm NO_2. Figures 5-1(a) – (c) show that the presence of small amounts of NO_2 in the mixture (~200 ppm) greatly enhances its reactivity for all equivalence ratios. At φ = 1.0, T_C = 1000 K and p_C = 1.5 MPa, an addition of 200 ppm NO_2 leads to a decrease in IDT from ~ 60 ms to 17 ms (> factor of 3).

Increasing the NO_2 dilution level to 400 ppm only reduces the IDT by an additional ~ 6 – 9 ms, showing that the effect of NO_2 is not linear. This dependence of sensitization on the level of NO_2 dilution is observed for all equivalence ratios as shown in Figures. 5-1(a) – (c). Furthermore, it should be noted that, within the temperature range considered, the effect of NO_2 dilution on the percentage change in IDT becomes stronger with increasing T_C. At p_C = 3.0 MPa, the addition of NO_2 has almost no effect on predicted IDTs at low temperatures (T_C < 950 K), Figure 5-2. Calculations using only NUIGMech1.2 are shown for the neat methane cases for clarity. Comparison of predictions using the other models [5,47] are provided in appendix B and are found to be within the experimental uncertainty (< 20%) of the measurements for neat methane cases but show discrepancies for the NO_2 sensitized cases. As the pressure increases, the reactivity enhancing effect of NO_2 on IDT is noticeable, but it is significantly lower than that observed at 1.5 MPa. For example, for the φ = 1.0 case at T_C = 1000 K, an addition of 400 ppm NO_2 reduces the IDT by ~ 60 ms (a factor of five) relative to the neat methane case at 1.5 MPa, but it only reduces it by 11 ms (a factor of 2.5) at 3.0 MPa. This reduced impact of NO_2 on IDT at higher pressures is analyzed using output from NUIGMech1.2 simulations as discussed below.

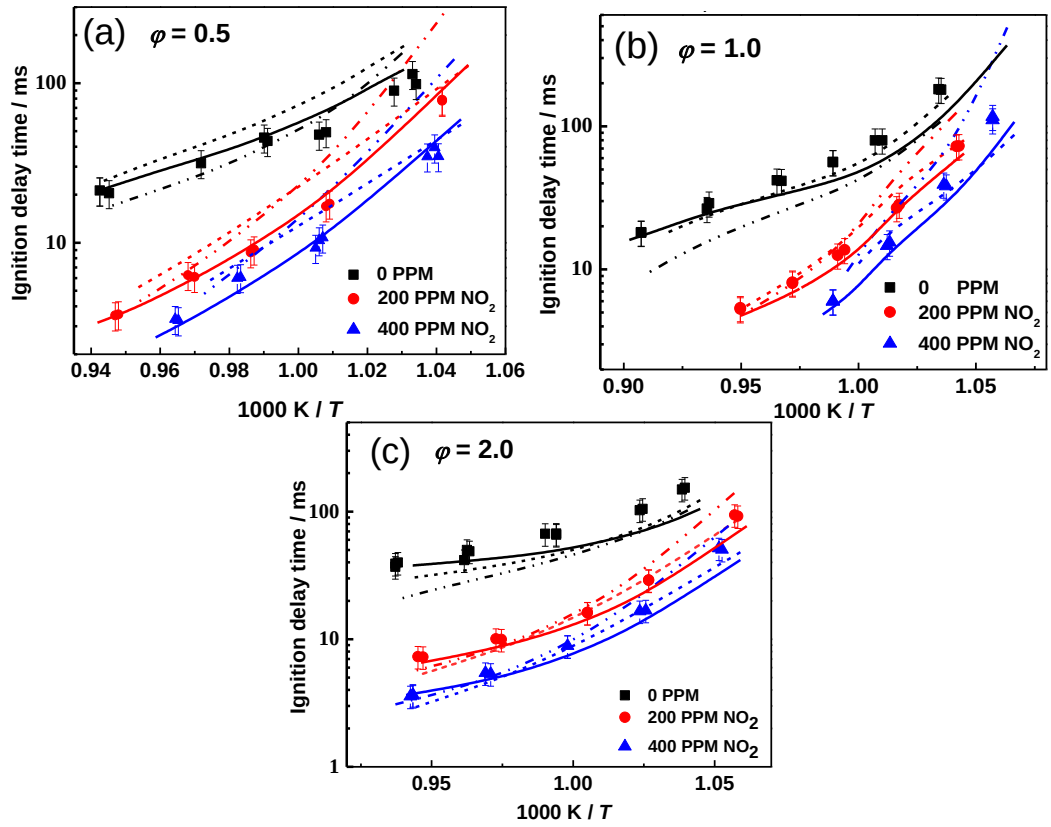

Figure 5-1. Effect of NO_2 addition on methane IDT (symbols: experiments, solid line: NUIGMech1.2, dashed lines: Song_mech, dash-dotted lines: DTU_mech) at 1.5 MPa for; (a) φ = 0.5; (b) φ = 1.0; and (c) φ = 2.0.

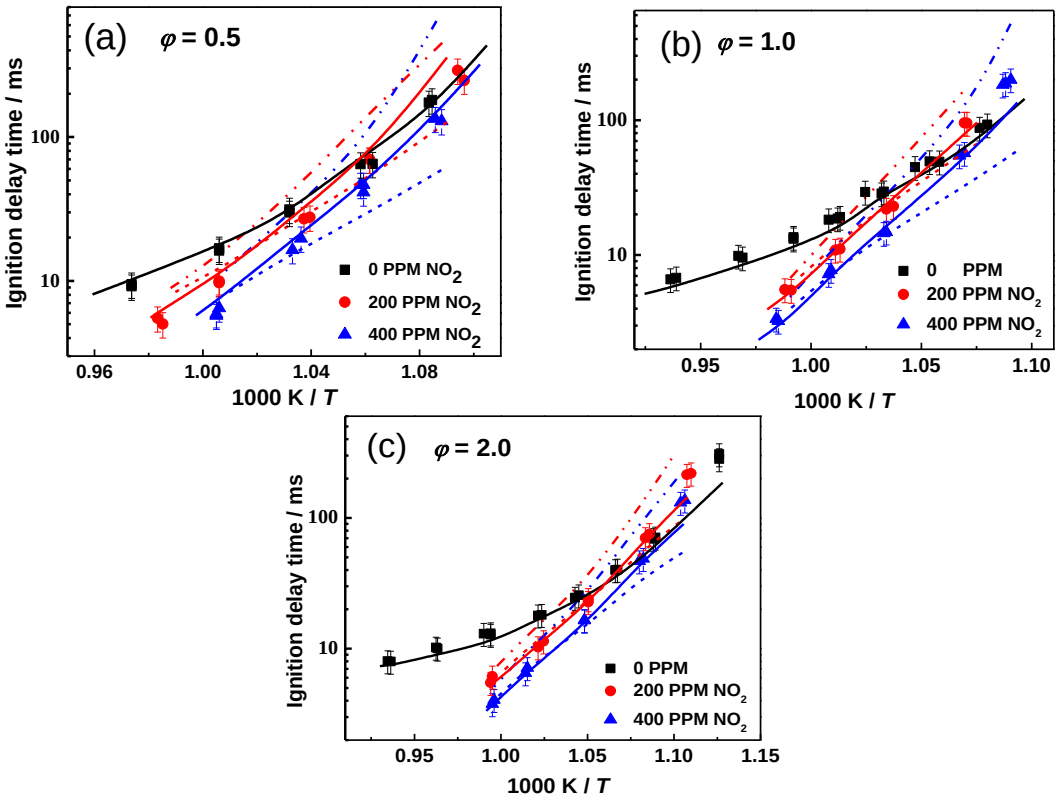

Figure 5-2. Effect of NO_2 addition on methane IDT (symbols: experiments, solid line: NUIGMech1.2, dashed lines: Song_mech, dash-dotted lines: DTU_mech) at 3.0 MPa for; (a) φ = 0.5; (b) φ = 1.0; and (c) φ = 2.0.

Numerical simulations using NUIGMech1.2 (solid lines) show the predictions to be in very good agreement with the measurements for the NO_2 diluted cases for all equivalence ratios (Figures.5-1 and 5-2). Both DTU_mech and Song_mech capture the impact of NO_2 dilution on ignition successfully for the intermediate temperatures ($T_C \geq 1000$ K); however, they show a high level of discrepancy with the measurements at lower temperatures ($T_C < 960$ K). The former mechanism over-predicts the IDTs by more than a factor of two for most equivalence ratios at 1.5 and 3.0 MPa. On the contrary, Song_Mech is observed to under-predict the IDTs especially at higher pressures. Overall, NUIGMech1.2 is observed to show the best agreement with the experimental measurements across the entire temperature range. A comparison of the mean deviations of predictions from IDT measurements of various mechanisms is provided in Section 5.4.4.

Figure 5-3 shows a sensitivity analysis to IDT for a $CH_4/O_2/N_2/NO_2$ mixture at 1000 K and pressures 1.5 and 3.0 MPa. The reaction $\dot{C}H_3 + NO_2 \leftrightarrow CH_3\dot{O} + NO$ (R1) has the highest negative sensitivity in promoting reactivity, followed by the ever-important chain-branching reaction $\dot{H} + O_2 \leftrightarrow \ddot{O} + \dot{O}H$ (R2). The reaction $CH_3N\dot{O}_2\,(+M) \leftrightarrow \dot{C}H_3 + NO_2\,(+M)$ (R3) shows a strong positive sensitivity towards IDT as it leads to the formation of nitromethane and competes with R1 hindering the formation of reactive $CH_3\dot{O}$ and NO species.

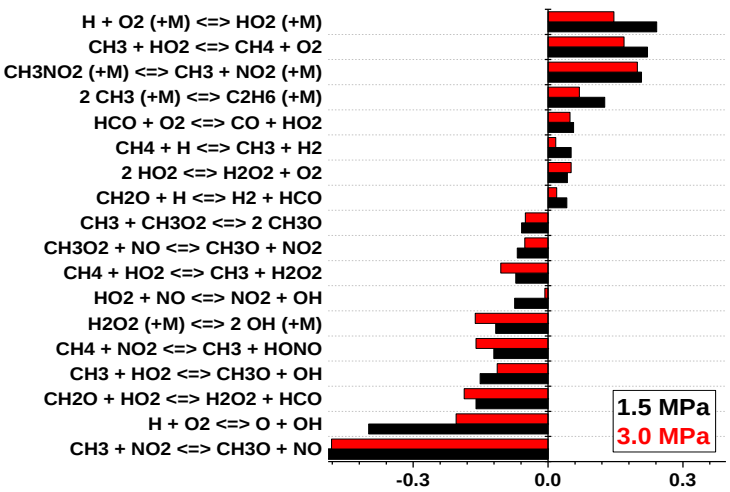

Figure 5-3. IDT sensitivity analysis for $CH_4/O_2/Ar$ mixture with 200 ppm NO_2 at φ = 1.0, and 1000 K between 1.5 MPa and 3.0 MPa.

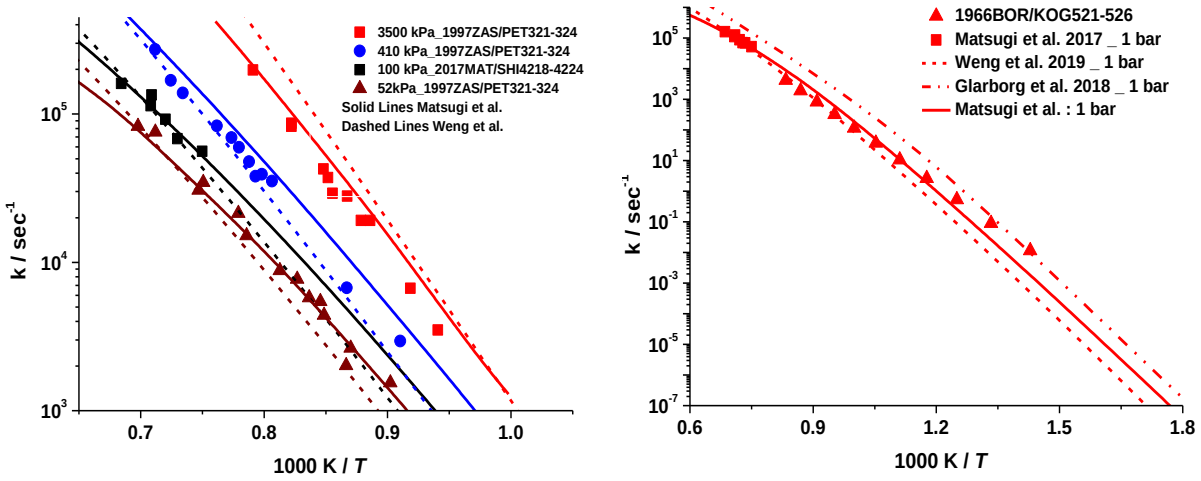

Figure 5-4. Pressure dependent rate constants for CH_3NO_2 (+M) ↔ $\dot{C}H_3$ + NO_2 (+M).

Matsugi and Shiina [48] performed ab-initio calculations of the CH_3NO_2 (+M) ↔ $\dot{C}H_3$ + NO_2 (+M) reaction, providing pressure-dependent rate constants which are found to be in good agreement with the measurements by Zaslonko et al. [49] and Matsugi and Shiina [48] at T > 1000 K and accurately captures the pressure dependence as shown in Figure 5-4(a). Moreover, at lower temperatures the calculations by Matsugi and Shiina [48] agree with experimental measurements better than the rates used in the Glarborg et al. mechanism [35] and in a recent mechanism published by Weng et al. [50] (see Figure 5-4(b)). The relatively higher rates constants for reaction R3 in the DTU_mech at T > 850 K contributes to the under-prediction in the reactivity of the methane/NO_2 systems at 1000 K as observed in Figures. 5-2 and 5-3. Therefore, in the current model, the calculations by Matsugi and Shiina [48] have been adopted for R3. For $\dot{C}H_3$ + NO_2 ↔ $CH_3\dot{O}$ + NO, the rate constants from Glarborg et al. [35] have been adopted and are within the uncertainty limits of experimental measurements available in the literature at both high and low temperatures (Figure 5-5).

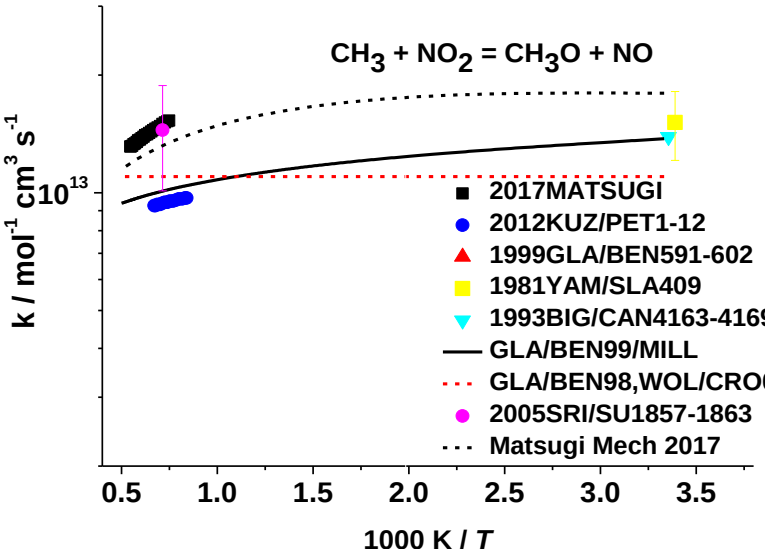

Figure 5-5. Rate constants for $\dot{C}H_3 + NO_2 \leftrightarrow CH_3\dot{O} + NO$.

The improvement in mechanism predictions with the implementation of updates have been illustrated in appendix B. As discussed earlier, for all the mechanisms considered in this study, the influence of NO_2 dilution on IDT decreases at higher pressures in the low- to intermediate-temperature range. Since the reaction $\dot{C}H_3 + NO_2 \leftrightarrow CH_3\dot{O} + NO$ (R1) is the primary channel promoting ignition for mixtures with NO_2 addition, we have compared the normalized flux for $\dot{C}H_3$ radicals with other competing channels at pressures ranging from 0.5 – 5.0 MPa, Figure 5-6. It is observed that, at lower pressures, R1 is one of the major channels consuming $\dot{C}H_3$ radicals. However, as the pressure increases from 0.5 to 5.0 MPa, there is an increased importance of $\dot{C}H_3$ radicals reacting with molecular oxygen ($\dot{C}H_3 + O_2$ (+M) $\leftrightarrow CH_3\dot{O}_2$ (+M)) leading to a corresponding decrease in $\dot{C}H_3$ radicals reacting with NO_2 in R1. We consider this to be the reason for the reduced impact of NO_2 addition in promoting reactivity at higher pressures. Additional validations of the mechanism against speciation measurements and ignition data available in the literature [9,10] are provided in appendix B.

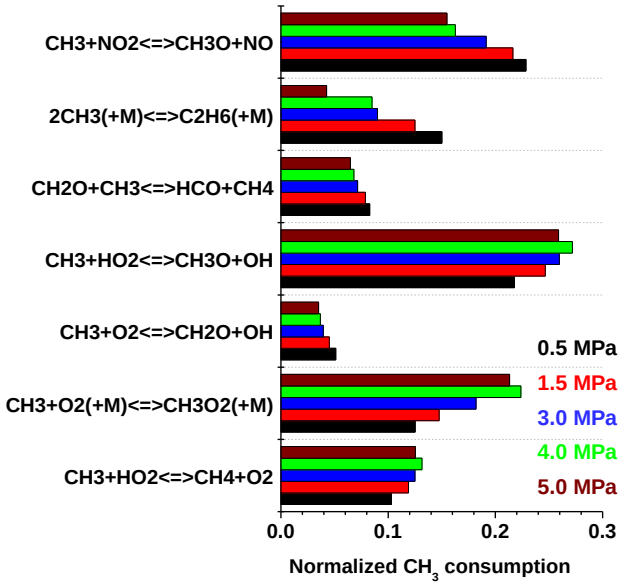

Figure 5-6. Normalized contribution towards $\dot{C}H_3$ consumption for CH_4/O_2/Ar mixture (φ = 0.5) with 200 ppm NO_2 addition at 950 K and20% fuel consumption for 0.5, 1.5, 3.0 and 4.0 MPa.

5.4.1.2 Chemistry validation at high temperatures

Figure 5-7 compares NUIGMech1.2 predictions with the shock-tube measurements taken here (Figures. 5-7(a) and (b)) together with those by Mathieu et al. [47] (Figures. 5-7(c) and (d)) recorded at higher temperatures (1250 K $\leq T_C \leq$ 1750 K) for fuel-lean and stoichiometric methane/air mixtures diluted with NO_2. The model shows good agreement with the measurements. Additional model validations with the high-temperature IDT measurements by Mathieu et al. [47] and Zhang et al. [51] are provided in appendix B. The IDT measurements at $T \approx$ 1250 K are reported in Figures. 5-7(a) and (b) with cross marks as they show pre-ignition pressure rise. In shock tube IDT measurements, there are three common behaviors of ignition observed in the recorded pressure/time traces that can explain the pre-ignition phenomena. The first ignition behavior is a strong pressure rise observed due to the ignition of the fuel/air mixture, also known as normal ignition, and found to exhibit constant pressure throughout the ignition event as shown in Figure BS1(b).

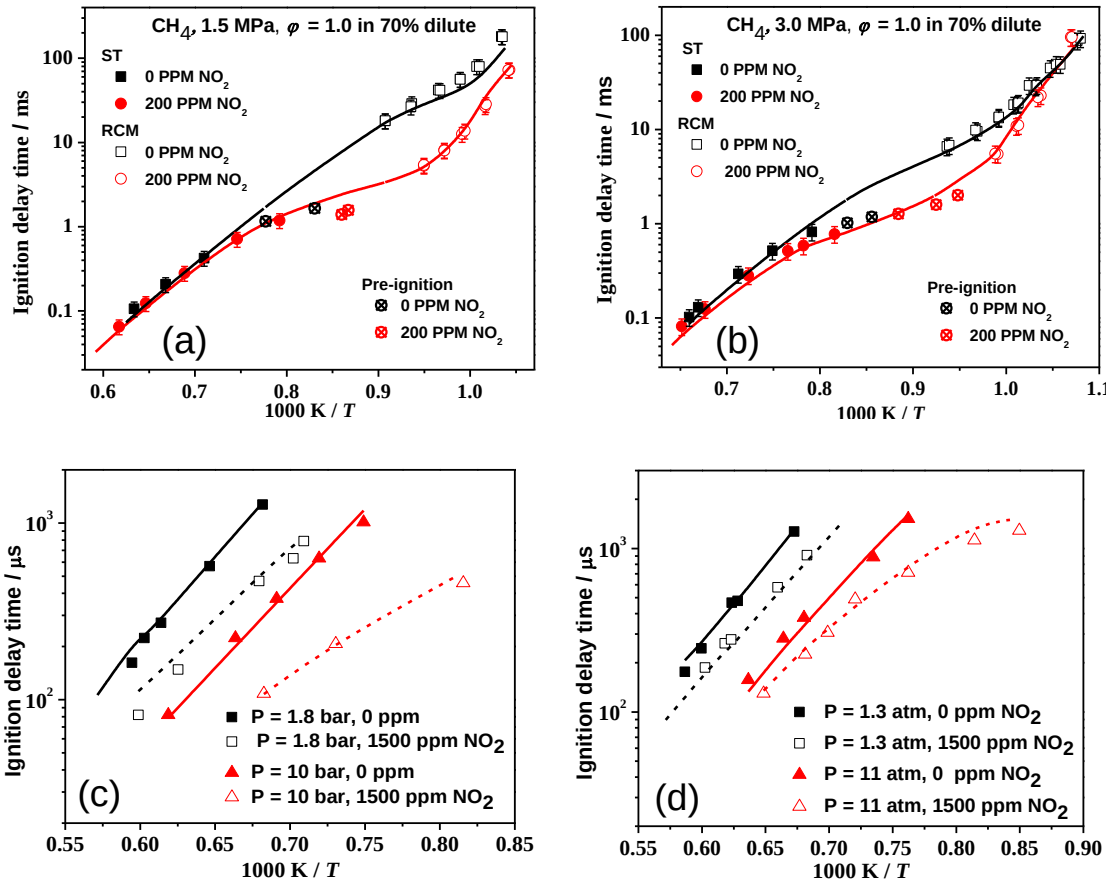

Figure 5-7. Comparison of model predicted IDTs (lines) with experiments (symbols) for CH_4 in air mixtures with and without NO_2 addition; (a) 1.5 MPa, φ = 1.0 (this work); and (b) 3.0 MPa, φ = 1.0 (this work) and for; (c) φ = 0.5 [47]; and (d) φ = 1.0 [47].

The second ignition behavior represents a pre-ignition which is defined as a gradual increase in pressure before the main ignition, shortening the overall IDT as showed in Figure BS1(c). The behavior of pre-ignition and normal ignition with a strong pressure rise has also been observed and reported in our previous published work [52–54] as well as in this study.

The third ignition behavior is characterized by a constant rate of pressure rise (*dp/dt*) starting from the first pressure-peak due to the reflected shock until ignition occurs, and this can be accounted for in simulations by implementing the known *dp/dt* of the particular measurement as documented in Figure 3 of Zhang et al. [52] using the same facility as that employed in *this work*. Discussions of shock tube IDT measurements and their pre-ignition behavior have been reported previously [55–58] and these studies explain how IDT acquisition methods can lead to misleading evaluations and validations of chemical kinetic mechanisms. It is important that the

pressure/time traces be scrutinized for each experiment to distinguish normal ignition from pre-ignition events.

5.4.2 Effect of N_2O on ignition delay times

5.4.2.1 Low to intermediate temperature regime

The effect of N_2O on IDTs was investigated for $CH_4/Ar/O_2$ mixtures at φ = 1.0 with 0 and 400 ppm N_2O added. The measurements without and with N_2O indicate that it does not have any noticeable impact on the IDTs in the low- to intermediate temperature range, Figure 5-8. Additional tests with 1000 ppm N_2O dilution conducted at p_C = 3.0 MPa also showed a negligible effect on IDTs. Simulations using NUIGMech1.2 also show a similar effect of N_2O dilution on the predictions as seen in the experiments. The predictions are in good agreement with experimental measurements (Figure 5-8).

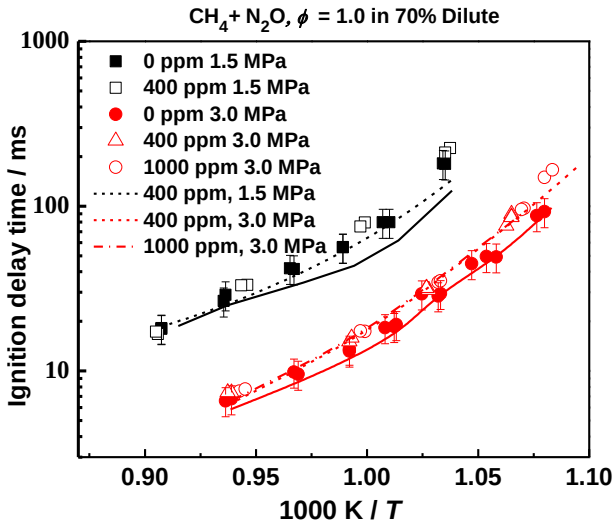

Figure 5-8. Comparison of measured IDTs (symbols) and predictions (lines) for $CH_4/Ar/O_2$ mixtures doped with 0 ppm, 400 ppm and 1000 ppm N_2O at φ = 1.0, p_C = 1.5 and 3.0 MPa.

5.4.2.2 High temperature regime

Figures 5-9(a) and (b) compare model predictions to the ST IDT measurements reported by Mathieu et al. [47] for N_2O diluted methane IDT measurements at higher temperatures ($1250 \leq T_C \leq 2100$ K). NUIGMech1.2 mechanism is able to capture the impact of N_2O successfully at low to intermediate pressures (0.1 – 1.1 MPa), even for mixtures with high levels of N_2O dilution

(~3500 ppm) at higher pressures (~2.6 MPa). Note that both the model predictions and measurements show that N_2O addition on IDT is negligible at low- to intermediate-temperatures, but at higher temperatures N_2O promotes reactivity. This is primarily due to the high energy barrier for the dissociation of the N_2O molecule, producing N_2 and ignition-promoting Ö atoms.

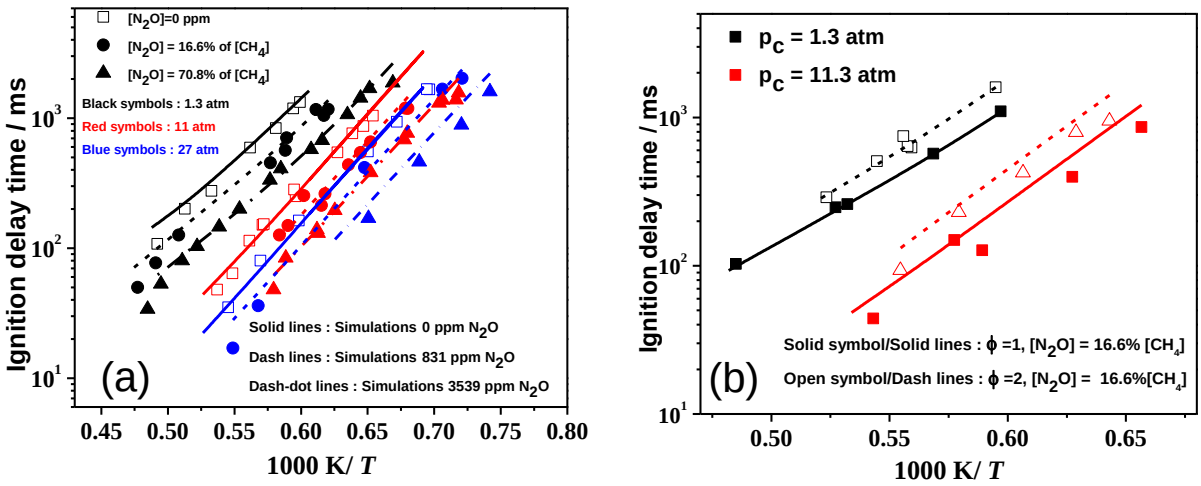

Figure 5-9. Comparison of IDT measurements (symbols) [51] and model predictions (lines) for CH_4/O_2/Ar mixtures with N_2O addition at; (a) φ = 0.5; and (b) φ = 1.0 and 2.0.

Since, at low- to intermediate-temperatures, the N_2O dissociation reaction is slower than the base hydrocarbon chemistry and the effect of N_2O on IDTs is very limited. Comparisons of model predictions with other ST IDT measurements for $CH_4/N_2O/O_2$ mixtures at ~2.8 atm reported by Mevel et al. [5] also show very good agreement and are provided in appendix B.

5.4.3 Effect of NO on ignition delay time

Figure 5-10 shows the impact of NO addition on IDT measurements for a stoichiometric CH_4/O_2/Ar mixture at p_C = 3.0 MPa and T_C = 900 – 1025 K with NO dilution levels ranging from 0 – 1000 ppm. The simulations were performed by estimating the composition of the mixture by performing a simulation to determine how much NO is oxidized to NO_2 during the time of mixing of the (CH_4/O_2/Ar)/NO blend at the specific T and p conditions, as discussed in Section 5.2.3. Figure 5-11 shows the impact of NO on fuel-lean (φ = 0.5), Figure 5-11(a), and fuel-rich (φ = 2.0), Figure 5-11(b), $CH_4/O_2/N_2$/Ar mixtures. It is observed that similar to the NO_2 cases,

mixture reactivity increases with higher NO levels. NUIGMech1.2 is able to capture the trends very well across the range of temperature and pressure studied.

It is interesting to note in Figure 5-10 that an addition of 50 ppm NO tends to inhibit reactivity at 930 K, but promotes reactivity at $T > 950$ K, thus, exhibiting a cross-over point at 950 K. A similar trend is observed for the 200 ppm NO dilution case, with the cross-over temperature at ~930 K. To understand this non-monotonous behaviour, reaction flux and sensitivity analyses were performed for the $CH_4/Ar/O_2$ mixtures with 0, 50, 400 ppm NO addition at 3.0 MPa and T_C = 800 K.

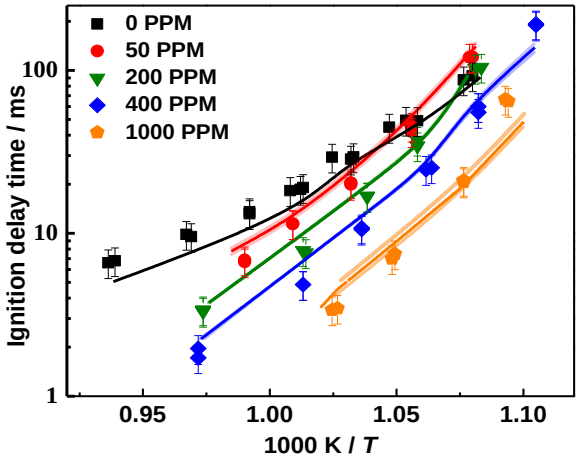

Figure 5-10. Comparison of IDT measurements (symbols) and NUIGMech1.2 model predictions (solid lines) for $CH_4/O_2/Ar$ mixtures with different levels of NO addition (0 – 1000 ppm) at φ = 1.0 and p_C = 3.0 MPa. The legends refer to initial mole fraction of NO added to the mixture. Light bands represent the uncertainty in predictions due to uncertainty in NO/NO_2 composition.

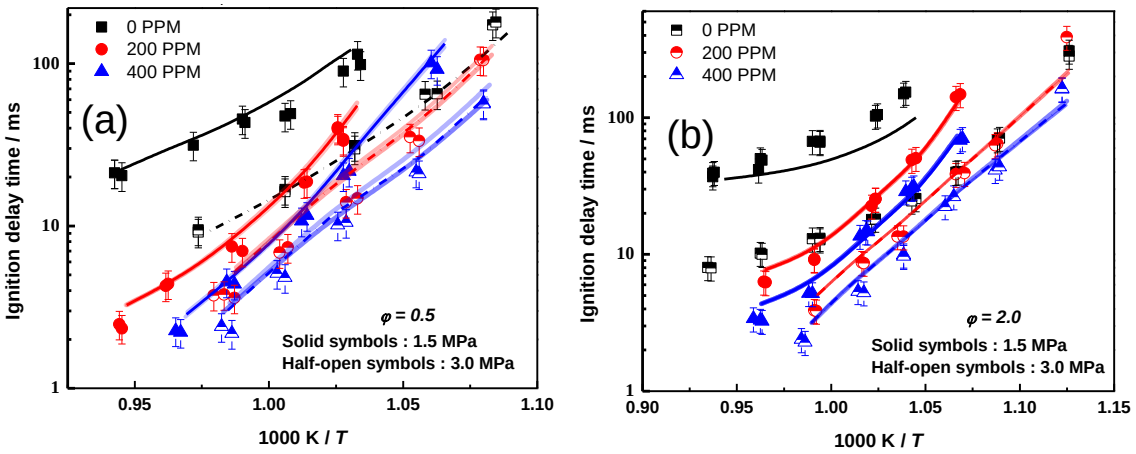

Figure 5-11. Comparison of IDT measurements (symbols) and NUIGMech1.2 model predictions (lines) for $CH_4/O_2/Ar$ mixtures with different levels of NO addition (0 – 400 ppm) at; (a) φ = 0.5; and (b) φ = 2.0 and p_C = 1.5 MPa (solid lines), 3.0 MPa (dash-dot lines). The legends refer to the initial mole fraction of NO added to the mixture. Light bands represent the uncertainty in predictions due to uncertainty in NO/NO_2 composition.

Figure 5-12(a) compares the reaction flux channels for 0 ppm (black), 50 ppm (red) and 400 ppm (blue) NO addition at 20% fuel consumption. It is observed that more than 90% of the fuel is consumed via H-atom abstraction by ȮH producing $\dot{C}H_3$ radicals and the remainder by Ḣ and Ö atoms and $H\dot{O}_2$ radicals. Approximately 35% of the $\dot{C}H_3$ radials produced react with $H\dot{O}_2$ producing $CH_3\dot{O} + H_2O$ while ~27% react with O_2 producing $CH_3\dot{O}_2$ radicals. Approximately 16% of $\dot{C}H_3$ radicals produce CH_4 via the reaction $\dot{C}H_3 + H\dot{O}_2 \leftrightarrow CH_4 + O_2$, and 16% of them re-combine to produce C_2H_6. A large fraction of $CH_3\dot{O}_2$ radicals is converted to $CH_3\dot{O}$ either through the $CH_3\dot{O}_2 + \dot{C}H_3 \leftrightarrow CH_3\dot{O} + CH_3\dot{O}$ or via the $CH_3\dot{O}_2 + H\dot{O}_2 \rightarrow CH_3O_2H \rightarrow CH_3\dot{O} + \dot{O}H$ reaction channels. The subsequent thermal dissociation reaction $CH_3\dot{O}\ (+M) \leftrightarrow CH_2O + \dot{H}\ (+M)$ is the major source of Ḣ atoms which then react with O_2 producing $H\dot{O}_2$ radicals at these relatively high-pressure (3.0 MPa) conditions. The reaction flux diagram shows that the presence of 400 ppm NO_X (265 ppm NO_2/135 ppm NO) in the mixture leads to an additional 13% of the flux for $\dot{C}H_3 \rightarrow CH_3\dot{O}$ conversion proceeding through the reaction $\dot{C}H_3 + NO_2 \leftrightarrow CH_3\dot{O} + NO$ while the flux via the $\dot{C}H_3$ self-recombination reaction reduces to 13% from 16%. Approximately 89% of the NO produced in the system rapidly reacts with HO_2 radicals to regenerate NO_2 and an ȮH radical, which then to react with more $\dot{C}H_3$ radicals. On the other hand, the addition of 50 ppm NO shows a very limited flux (~1.9%) of $\dot{C}H_3$ radicals via the $\dot{C}H_3 + NO_2 \leftrightarrow CH_3\dot{O} + NO$ reaction due to the relatively low concentration of NO_x species in the mixture.

Figure 5-12(b) compares the concentration profiles of key intermediate species as a function of time for the three cases. We observe that almost all of the NO is oxidized to NO_2 through the reaction $NO + H\dot{O}_2 \leftrightarrow NO_2 + \dot{O}H$ within the first 20% of the total reaction time (i.e. < 70 ms), as also seen in the ROP plot, please see lower part of Figure 5-12(b). Once the NO_2 concentration reaches a threshold, the $\dot{C}H_3 + NO_2\ (+M) \leftrightarrow CH_3NO_2\ (+M)$ reaction becomes competitive leading

to the conversion of > 95% of the NO_x species to the relatively stable CH_3NO_2 molecule prior to ignition.

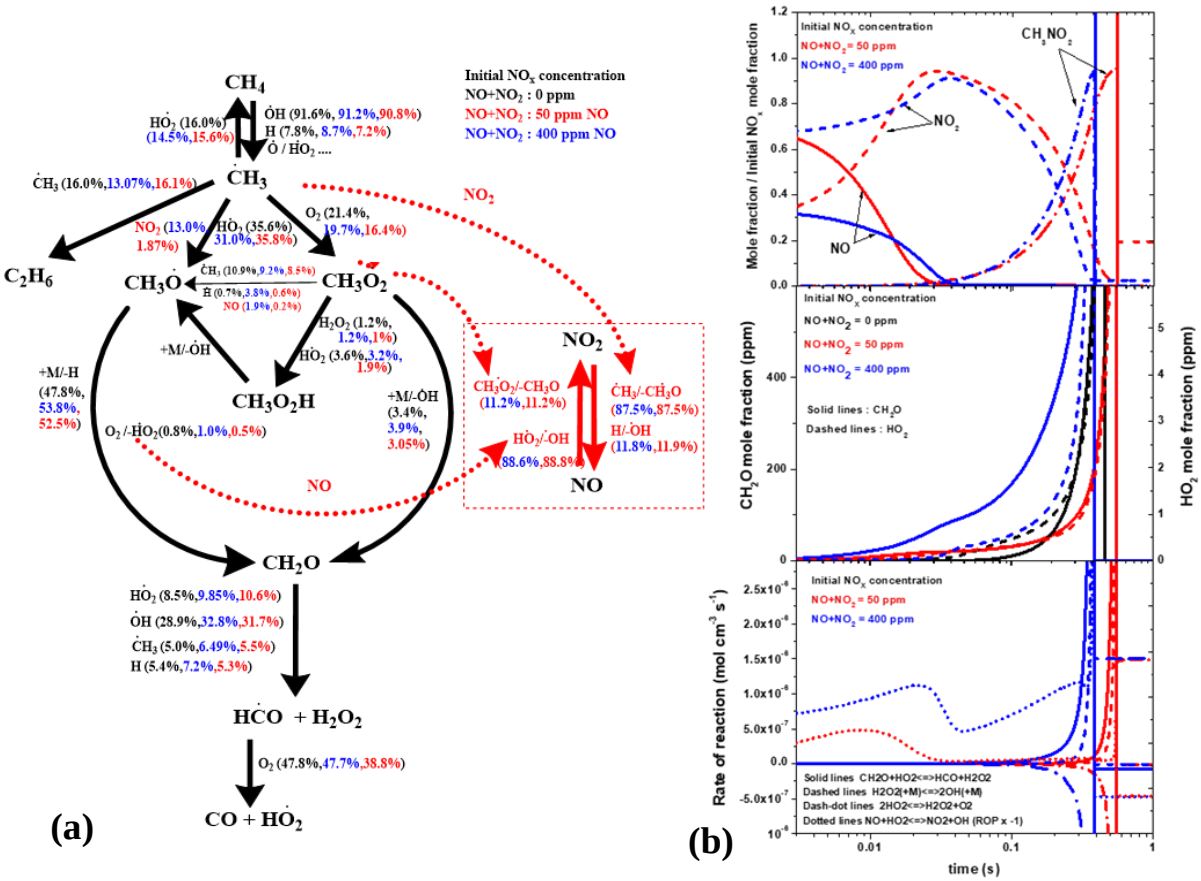

Figure 5-12. (a) Flux analysis; and (b) temporal species concentrations and ROP plots for stoichiometric $CH_4/O_2/Ar$ mixtures ignition with 0 ppm (black), 50 ppm (red) and 400 ppm (blue) NO_X addition at 3.0 MPa and 800 K. The flux analysis is performed at 20% fuel consumption.

This chain-termination reaction acts as a rate-limiting step since it inhibits the conversion of $\dot{C}H_3$ radicals to $CH_3\dot{O}$ radicals by scavenging NO_2 and $\dot{C}H_3$ radicals, thereby decreasing the rate of the $\dot{C}H_3 + NO_2 \leftrightarrow CH_3\dot{O} + NO$ reaction. It is also interesting to note that for the 400 ppm NO addition case a distinct sudden increment in the CH_2O and $H\dot{O}_2$ concentration profiles at ~60 ms is observed which is then followed by a rapid increase in reactivity leading to ignition. By contrast, the 50 ppm NO addition case does not show this behavior and moreover, it demonstrates an even slower rise in the concentrations of CH_2O and $H\dot{O}_2$ radicals compared to the neat CH_4 case. In the initial phase (< 70 ms), the addition of 400 ppm NO leads to a higher rate of $H\dot{O}_2$ radical conversion to $\dot{O}H$ radicals, thereby resulting in a higher rate of fuel consumption via H-atom abstraction by $\dot{O}H$ followed by the subsequent $\dot{C}H_3 \rightarrow CH_3\dot{O} \rightarrow CH_2O$

conversion either via $\dot{C}H_3 + NO_2/H\dot{O}_2/CH_3\dot{O}_2 \leftrightarrow CH_3\dot{O} + NO/\dot{O}H/CH_3O$ and $CH_3\dot{O}$ (+M) ↔ $CH_2O + \dot{H}$ (+M) or via the $\dot{C}H_3 + O_2$ (+M) ↔ $CH_3\dot{O}_2$ (+M) ↔ $CH_2O + \dot{O}H$ reaction channels. Therefore, a larger accumulation of CH_2O is observed for the 400 ppm NO case compared to the 50 ppm NO addition case in the initial stage. As the NO concentrations decrease with time, the rate of $H\dot{O}_2$ consumption drops leading to a rise in the HO_2 concentrations as seen in Figure 5-12(b). These $H\dot{O}_2$ radicals abstract hydrogen atoms from CH_2O producing H_2O_2 which then dissociates producing *two* $\dot{O}H$ radicals per $H\dot{O}_2$ radical, as opposed to the $NO + H\dot{O}_2 \leftrightarrow NO_2 + \dot{O}H$ and $H\dot{O}_2 + H\dot{O}_2 \rightarrow O_2 + H_2O_2 \rightarrow \dot{O}H + \dot{O}H$ reactions which produce *one* $\dot{O}H$ radical per $H\dot{O}_2$ radical. This transition to chain-branching leads to a significant rise in reactivity and overcomes the inhibiting effects of $\dot{C}H_3 + NO_2$ (+M) ↔ CH_3NO_2 (+M) leading to a faster ignition for 400 ppm NO addition. For the 50 ppm NO case, since the rate of production of CH_2O and $H\dot{O}_2$ are low in the initial phase owing to the low concentration of NO, the rate of the chain-branching process ($CH_2O + H\dot{O}_2 = H\dot{C}O + H_2O_2$, followed by $H\dot{C}O + M = \dot{H} + CO + M$ and then $\dot{H} + O_2 = \ddot{O} + \dot{O}H$, $CO + O_2 = CO_2 + \ddot{O}$ and H_2O_2 (+M) → $\dot{O}H + \dot{O}H$ (+M)) is not sufficient to overcome the inhibiting effects of NO addition, Figure 5-12(b), thereby resulting in a slower ignition compared to the neat methane case.

Sensitivity analyses performed for the three mixtures, Figure 5-13, also identify the reaction CH_3NO_2 (+M) ↔ $\dot{C}H_3 + NO_2$ (+M) as being the key rate-limiting step for both 50 ppm and 400 ppm NO addition cases. It also shows that the reaction $CH_2O + H\dot{O}_2 \leftrightarrow H\dot{C}O + H_2O_2$ is a sensitive ignition-promoting reaction for all mixtures, supporting our discussion above. The $\dot{C}H_3 + NO_2 \leftrightarrow CH_3\dot{O} + NO$ reaction has a large sensitivity only for the addition of higher concentrations of NO, since it significantly contributes to the conversion of $\dot{C}H_3 \rightarrow CH_3\dot{O}$ for the 400 ppm case compared to the 50 ppm case, Figure 5-12(a).

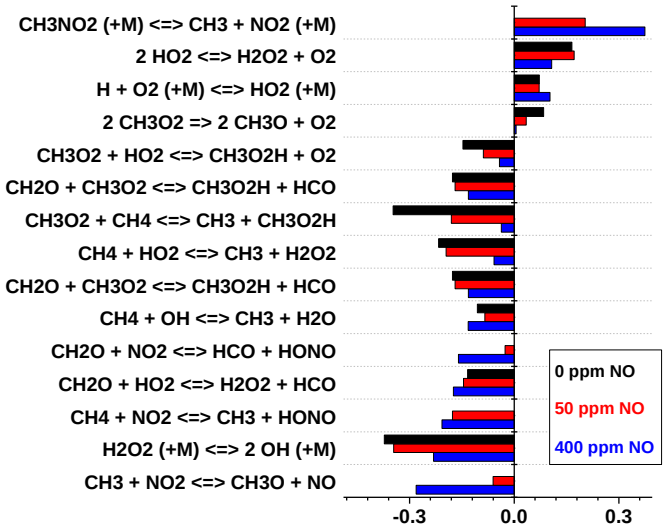

Figure 5-13. IDT sensitivity analysis for $CH_4/O_2/Ar$ mixtures with 0 (black), 50 (red) and 400 ppm (blue) NO addition at 3.0 MPa, 800 K and φ = 1.0.

It is interesting to note that in Figure 5-2, the 200 ppm NO_2 addition case also exhibits a small inhibition effect at lower temperatures at 3.0 MPa, while the 400 ppm NO_2 case tends to promote ignition. Figure 5-14(a) compares constant volume IDT calculations at p = 3.0 MPa and T_C = 850 K for stoichiometric CH_4/air mixture with and without NO_2. It shows that an addition of 50 ppm NO_2 leads to slowest ignition with 27% longer IDT, whereas 400 ppm NO_2 addition case exhibits a 14% faster IDT relative to the 0 ppm case. This trend is qualitatively similar to the trends observed for NO addition cases. Figures 5-14 (b, and c) compare the concentration profiles of key species and rate of reactions as a function of time to understand this trend. The 0 ppm case shows a delayed rise in HO_2 concentration compared to the NO_2 doped cases, which leads to the formation of H_2O_2 either by the self-recombination reaction, $H\dot{O}_2 + H\dot{O}_2 \leftrightarrow H_2O_2 + O_2$ or via $CH_2O + H\dot{O}_2 \leftrightarrow HCO + H_2O_2$, and then dissociates to produce two $\dot{O}H$ radicals. The latter pathway effectively produces two $\dot{O}H$ radicals per $H\dot{O}_2$ radical which is chain branching in nature ultimately leading to ignition, as discussed earlier. In the NO_2 addition cases, the $H\dot{O}_2$ formation occurs earlier because the reaction $CH_3 + NO_2 \leftrightarrow CH_3\dot{O} + NO$ advances the production of $CH_3\dot{O}$ and the subsequent dissociation reaction, $CH_3\dot{O}$ (+M) $\leftrightarrow CH_2O + H$ (+M). The H atoms produced then rapidly react with O_2 forming $H\dot{O}_2$ radicals. Once enough NO and $H\dot{O}_2$ concentration is available in the radical pool, $NO+H\dot{O}_2 \leftrightarrow NO_2+\dot{O}H$ reaction promptly converts

the $H\dot{O}_2$ into $\dot{O}H$ radicals while regenerating NO_2. The competition for $H\dot{O}_2$ tends to delay the transition to self-recombination reaction and the $CH_2O+H\dot{O}_2=HCO+H_2O_2$ reaction in the initial reaction period.

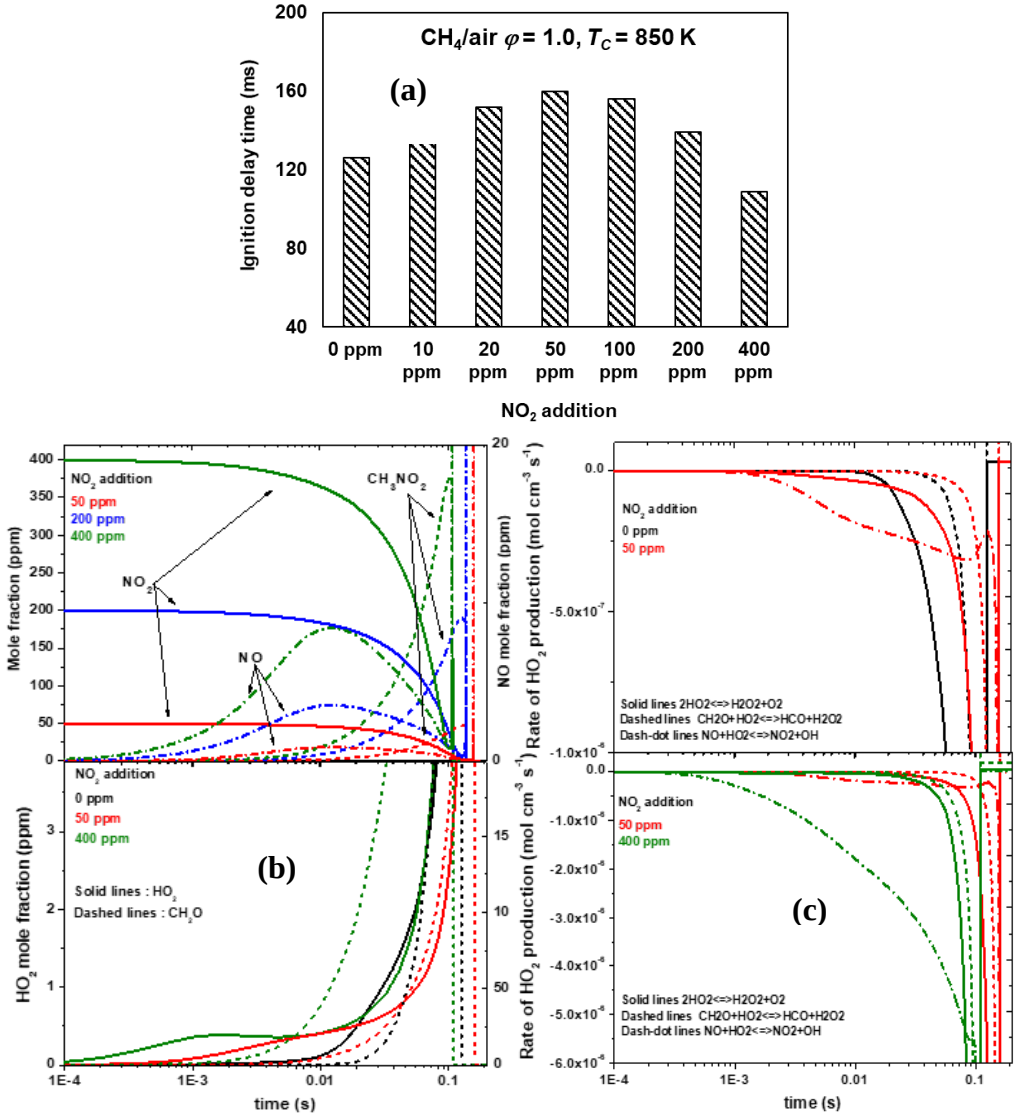

Figure 5-14. (a) Effect of NO_2 addition on methane IDT calculations using NUIGMech1.2 at φ =1.0, and 3.0 MPa; (b) temporal concentration profiles of NO_X, $H\dot{O}_2$ and CH_2O; and (c) ROP of $H\dot{O}_2$ radicals via key reactions for 0 (black), 50 (red), 200 (blue) and 400 (green) ppm NO_2 addition cases.

As time progresses, the chain terminating reaction $\dot{C}H_3 + NO_2 (+M) \leftrightarrow CH_3NO_2 (+M)$ consumes NO_2 and $\dot{C}H_3$ radicals forming a stable CH_3NO_2. With the depletion of NO/NO_2, the $NO + H\dot{O}_2 \leftrightarrow NO_2 + \dot{O}H$ reaction slows down and the transition to $H\dot{O}_2 + H\dot{O}_2 \leftrightarrow H_2O_2 + O_2$ and $CH_2O + H\dot{O}_2 \leftrightarrow HCO + H_2O_2$ reactions takes place, ultimately leading to ignition. At lower levels of NO_2 addition, since the production of $\dot{O}H$ is not high enough via $NO + H\dot{O}_2 \leftrightarrow NO_2 + \dot{O}H$ and H_2O_2

(+M) ↔ ȮH + ȮH (+M) to overcome the inhibiting impact of CH_3NO_2, it leads to overall longer IDTs. Whereas at higher levels of NO_2 addition, although the inhibiting effect of $\dot{C}H_3 + NO_2$ (+M) ↔ CH_3NO_2 (+M) is still significant, the rate of ȮH production via $NO + H\dot{O}_2 \leftrightarrow NO_2 + \dot{O}H$ is significantly high in the initial stage, to rapidly consume fuel via H-atom abstraction by ȮH producing sufficient amount of CH_2O and $H\dot{O}_2$ radicals in the pool, which ultimately leads to a quicker transition to the chain branching process $CH_2O + H\dot{O}_2 \rightarrow HCO + H_2O_2 \rightarrow \dot{O}H + \dot{O}H$, thus promoting ignition.

Figure BS8 of appendix B shows a comparison of the effect of NO and NO_2 addition on methane IDTs, which show their similarity, with the results being within the uncertainty error of the experiments (~20%). This has also been investigated by performing constant volume simulations of five NO/NO_2 fractions, ranging from 100% NO, through 75/25, 50/50, 25/75 and 100% NO_2 concentrations for 200, 400, 1000 ppm NO_x dilutions presented in Figure BS9, which shows that all of the predicted IDTs for all mixtures with varying NO/NO_2 concentrations lie within 15% of one another.

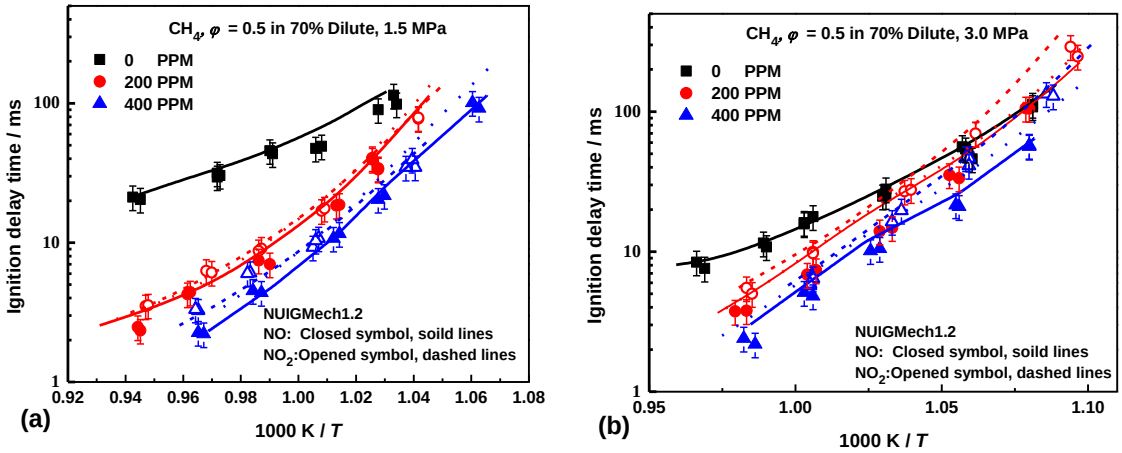

Figure 5-15. Comparison of NO and NO_2 addition on methane IDT (symbols: experiments, lines: NUIGMech1.2, at; (a) φ =0.5, p_C = 1.5 MPa; and (b) φ =0.5, p_C = 3.0 MPa.

To distinguish the influence of the RCM facility effect on the reactivity of the mixtures with NO/NO_2, Figure 5-15 show comparisons of the addition of 200 ppm and 400 ppm of NO and NO_2 on methane IDTs at 1.5 and 3.0 MPa at φ = 0.5. The closed symbols and opened symbols represent the experimental data for NO and NO_2 blended mixtures, respectively. The solid lines

represent the current model predictions for the NO blended methane mixtures calculated using the equilibrium concentrations of the NO and NO_2 reactants at their respective input operating conditions. The dotted lines are obtained by utilizing the same non-reactive volume profiles of methane/NO mixtures and considering the conversion of all NO into NO_2 in the IDTs simulations. Finally, the dashed lines represent the model predictions of IDTs for the methane/NO_2 mixtures. It can be seen that the differences in the reactivities between the methane/NO and methane/NO_2 blends are due to the combined outcomes of the facility effects and their corresponding NOx chemistry. Moreover, the simulations show that all results are within the uncertainty error of their respective experiments (20%).

5.4.4 Mean error analysis

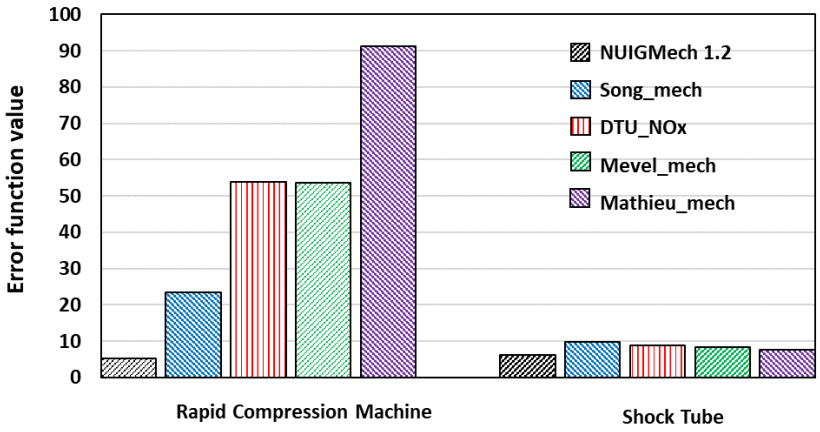

Figure 5-16. Comparison of average deviations of different mechanisms from experimental measurements for $CH_4/O_2/N_2/Ar$ mixtures with and without $NO/NO_2/N_2O$ addition.

In Figure 5-16 a quantitative comparison of the model performance against the RCM (150 datapoints/30 datasets) and ST IDT measurements (783 datapoints/96 datasets) performed in this study in addition to those in the literature is conducted following the approach of Olm et al. [59] where an overall error function value is calculated using equations (5-2) and (5-3) below.

$$E_i = \frac{1}{N_i}\sum_{j=1}^{N_i}\left(\frac{\left(Y_{ij}^{sim} - Y_{ij}^{expt}\right)}{\sigma(Y_{ij}^{expt})}\right)^2 \quad (5\text{-}2)$$

$$E = \frac{1}{N}\sum_{i=1}^{N} E_i \quad (5\text{-}3)$$

where, $Y_{ij} = \ln(y_{ij})$. N and N_i represent the total number of datasets and the number of data points in a particular dataset, respectively. y_{ij} represents the j^{th} IDT measurement of i^{th} dataset, and $\sigma(Y_{ij}^{expt})$ represents its standard deviation that includes experimental uncertainty and statistical error. Further details of the approach are discussed by Olm et al. [59]. The comparisons in Figure 16 show that the NUIGMech1.2 tends to perform better against the IDT measurements especially in the RCM range of conditions. For shock tube experiments which typically comprise of high temperature ignition data, the performance of the mechanisms is quite similar.

5.5 Conclusions

In this work, the auto-ignition behavior of CH_4 and CH_4-doped with NO_2, N_2O and NO has been investigated in the low- to intermediate temperature range of 900 – 1100 K at p_C = 1.5 and 3.0 MPa using a rapid compression machine facility. The tests conditions are particularly relevant to practical combustors and thus provide benchmark measurements for ignition behavior as a function of temperature, pressure, NO_x dilution levels and equivalence ratio. Experimental measurements were simulated using an updated hydrocarbon mechanism merged with a NO_x sub-mechanism, NUIGMech1.2 together with two recently published mechanisms developed at DTU [37, 45] (DTU_Mech) and Milano [9] (Song_Mech). Experiments showed that the addition of 200 ppm NO_2 reduces IDTs by a factor of three at T_C ~ 1000 K and p_C = 1.5 MPa. The impact of NO_2 on the change in IDT becomes stronger with increasing temperature. Further addition of NO_2 to the mixture does not result in a significant increase in reactivity, indicating that its effect is non-linear. At higher pressures, the addition of NO_2 shows an increase in reactivity, however the impact was much lower compared to the 1.5 MPa cases. This is attributed to the increase in importance of methyl radical recombination and its competition for $\dot{C}H_3$ radicals with the reaction $\dot{C}H_3 + NO_2 \leftrightarrow CH_3\dot{O} + NO$ at higher pressures. The predictions using DTU_Mech under-

estimate the effect of NO_2 sensitization on IDT in the low- to intermediate temperature range, while Song_Mech is in closer agreement with the measurements but is consistently faster than the experimental data at lower temperatures. The adoption of the recent calculations by Matsugi and Shiina [48] for the $\dot{C}H_3 + NO_2 (+M) \leftrightarrow CH_3NO_2 (+M)$ reaction together with newly calculated rates for $HONO/HNO_2$ chemistry by Chen et al. [40], adopted in NUIGMech1.2 and thermodynamic properties of CH_3NO_2 according to ATcT database, show a significant improvement in the predictions of the experimental measurements in the low- to intermediate temperature range. The performance of this mechanism was further validated using other available literature data including ST IDT and JSR speciation measurements with satisfactory agreement observed.

Experimental and modeling studies of CH_4/'air' diluted with N_2O in concentrations up to 1000 ppm show that N_2O sensitization has no noticeable impact on IDTs in the low- to intermediate temperature range (600 – 1000 K). However, at high temperatures (≥ 1000 K), NUIGMech1.2 is able to successfully capture the enhancement by N_2O and is also consistent with other literature measurements.

Experimental and modeling studies show non-monotonous trends in NO sensitization effects at lower levels of NO addition. This is primarily attributed to competition between the rate limiting effects of $\dot{C}H_3 + NO (+M) \leftrightarrow CH_3NO_2 (+M)$ and the impact of NO addition on the transition to the chain branching process of $CH_2O + H\dot{O}_2 \rightarrow H\dot{C}O + H_2O_2 \rightarrow \dot{O}H + \dot{O}H$ leading to ignition. NUIGMech1.2 satisfactorily captures the $NO_2/N_2O/NO$ sensitization effects on auto-ignition in the low- to high temperature regimes over a wide range of pressures.

Acknowledgements

The authors would like to acknowledge Science Foundation Ireland for funding via project numbers 15/IA/3177 and 16/SP/3829. We also acknowledge funding from Siemens Energy Canada Ltd.

Chapter 5

References

[1] B. Yu, S.M. Kum, C.E. Lee, S. Lee, Study on the combustion characteristics of a premixed combustion system with exhaust gas recirculation, Energy, 61 (2013) 345–353.

[2] P.A. Glaude, N. Marinov, Y. Koshiishi, N. Matsunaga, M. Hori, Kinetic Modeling of the Mutual Oxidation of NO and Larger Alkanes at Low Temperature, Energy Fuels, 19 (2005) 1839–1849.

[3] G. Moréac, P. Dagaut, J.F. Roesler, M. Cathonnet, Nitric oxide interactions with hydrocarbon oxidation in a jet-stirred reactor at 10 atm, Combust. Flame, 145 (2006) 512–520.

[4] S. Javoy, R. Mevel, C.E. Paillard, A study of N_2O decomposition rate constant at high temperature: Application to the reduction of nitrous oxide by hydrogen, Int. J. Chem. Kinet., 41 (2009) 357–375.

[5] R. Mével, J.E. Shepherd, Ignition delay-time behind reflected shock waves of small hydrocarbons–nitrous oxide(–oxygen) mixtures, Shock Waves, 25 (2015) 217–229.

[6] A.B. Bendtsen, P. Glarborg, K.I.M. Dam-Johansen, Low temperature oxidation of methane: the influence of nitrogen oxides, Combust. Sci. Technol., 151 (2000) 31–71.

[7] Y.L. Chan, F.J. Barnes, J.H. Bromly, A.A. Konnov, D.K. Zhang, The differentiated effect of NO and NO2 in promoting methane oxidation, Proc. Combust. Inst., 33 (2011) 441–447.

[8] P. Dagaut, A. Nicolle, Experimental study and detailed kinetic modeling of the effect of exhaust gas on fuel combustion: mutual sensitization of the oxidation of nitric oxide and methane over extended temperature and pressure ranges, Combust. Flame, 140 (2005) 161–171.

[9] Y. Song, L. Marrodán, N. Vin, O. Herbinet, E. Assaf, C. Fittschen, A. Stagni, T. Faravelli, M.U. Alzueta, F. Battin-Leclerc, The sensitizing effects of NO_2 and NO on methane low temperature oxidation in a jet stirred reactor, Proc. Combust. Inst., 37(1) (2019) 667–675.

[10] S. Gersen, A. V Mokhov, J.H. Darmeveil, H.B. Levinsky, P. Glarborg, Ignition-promoting effect of NO_2 on methane, ethane and methane/ethane mixtures in a rapid compression machine, Proc. Combust. Inst., 33 (2011) 433–440.

[11] R.G. Papagiannakis, D.T. Hountalas, Combustion and exhaust emission characteristics of a dual fuel compression ignition engine operated with pilot Diesel fuel and natural gas, Energy Convers. Manag., 45 (2004) 2971–2987.

[12] T. Korakianitis, A.M. Namasivayam, R.J. Crookes, Natural-gas fueled spark-ignition (SI) and compression-ignition (CI) engine performance and emissions, Prog. Energy Combust. Sci., 37 (2011) 89–112.

[13] S. Szwaja, E. Ansari, S. Rao, M. Szwaja, K. Grab-Rogalinski, J.D. Naber, M. Pyrc, Influence of exhaust residuals on combustion phases, exhaust toxic emission and fuel consumption from a natural gas fueled spark-ignition engine, Energy Convers. Manag., 165 (2018) 440–446.

[14] M. Li, X. Zheng, Q. Zhang, Z. Li, B. Shen, X. Liu, The effects of partially premixed combustion mode on the performance and emissions of a direct injection natural gas engine, Fuel, 250 (2019) 218–234.

[15] Y. Tanaka, M. Nose, M. Nakao, K. Saitoh, E. Ito, Development of low nox combustion system with EGR for 1700 C-class gas turbine, in: 2013.

[16] W.S. Affleck, A. Thomas, An opposed piston rapid compression machine for preflame reaction studies, Proc. Inst. Mech. Eng., 183 (1968) 365–387.
[17] J. Würmel, J.M. Simmie, CFD studies of a twin-piston rapid compression machine, Combust. Flame, 141 (2005) 417–430.
[18] C. Morley, Gaseq program, (n.d.). http://www.gaseq.co.uk (accessed September 29, 2017).
[19] Y. Li, C.W. Zhou, H.J. Curran, An extensive experimental and modeling study of 1-butene oxidation, Combust. Flame, 181 (2017) 198–213.
[20] Y. Wu, S. Panigrahy, A.B. Sahu, C. Bariki, J. Beeckmann, J. Liang, A.A.E. Mohamed, S. Dong, C. Tang, H. Pitsch, Z. Huang, H.J. Curran, Understanding the antagonistic effect of methanol as a component in surrogate fuel models: A case study of methanol/n-heptane mixtures, Combust. Flame, 226 (2021) 229–242.
[21] P.G. Ashmore, M.G. Burnett, Concurrent molecular and free radical mechanisms in the thermal decomposition of nitrogen dioxide, Trans. Faraday Soc., 58 (1962) 253–261.
[22] W.A. Glasson, C.S. Tuesday, The atmospheric thermal oxidation of nitric oxide, J. Am. Chem. Soc., 85 (1963) 2901–2904.
[23] M. Röhrig, E.L. Petersen, D.F. Davidson, R.K. Hanson, The pressure dependence of the thermal decomposition of N_2O, Int. J. Chem. Kinet., 28 (1996) 599–608.
[24] J. Park, N.D. Giles, J. Moore, M.C. Lin, A comprehensive kinetic study of thermal reduction of NO_2 by H_2, J. Phys. Chem. A, 102 (1998) 10099–10105.
[25] J. Herzler, C. Naumann, Shock tube study of the influence of nox on the ignition delay times of natural gas at high pressure, Combust. Sci. Technol., 184 (2012) 1635–1650.
[26] M. Baigmohammadi, V. Patel, S. Martinez, S. Panigrahy, A. Ramalingam, U. Burke, K.P. Somers, K.A. Heufer, A. Pekalski, H.J. Curran, A comprehensive experimental and simulation study of ignition delay time characteristics of single fuel C_1–C_2 hydrocarbons over a wide range of temperatures, pressures, equivalence ratios, and dilutions, Energy Fuels, 34 (2020) 3755–3771.
[27] S. Panigrahy, J. Liang, S.S. Nagaraja, Z. Zuo, G. Kim, S. Dong, G. Kukkadapu, W.J. Pitz, S.S. Vasu, H.J. Curran, A comprehensive experimental and improved kinetic modeling study on the pyrolysis and oxidation of propyne, Proc. Combust. Inst., 38(1) (2021) 479–488.
[28] S.S. Nagaraja, J. Power, G. Kukkadapu, S. Dong, S.W. Wagnon, W.J. Pitz, H.J. Curran, A single pulse shock tube study of pentene isomer pyrolysis, Proc. Combust. Inst., 38(1) (2021) 881–889.
[29] S. Dong, K. Zhang, P.K. Senecal, G. Kukkadapu, S.W. Wagnon, S. Barrett, N. Lokachari, S. Panigaphy, W.J. Pitz, H.J. Curran, A comparative reactivity study of 1-alkene fuels from ethylene to 1-heptene, Proc. Combust. Inst., 38(1) (2021) 611–619.
[30] S.S. Nagaraja, J. Liang, S. Dong, S. Panigrahy, A. Sahu, G. Kukkadapu, S.W. Wagnon, W.J. Pitz, H.J. Curran, A hierarchical single-pulse shock tube pyrolysis study of C_2–C_6 1-alkenes, Combust. Flame, 219 (2020) 456–466.
[31] M. Baigmohammadi, V. Patel, S. Nagaraja, A. Ramalingam, S. Martinez, S. Panigrahy, A.A.E.-S. Mohamed, K.P. Somers, U. Burke, K.A. Heufer, A. Pekalski, H.J. Curran, Comprehensive Experimental and Simulation Study of the Ignition Delay Time Characteristics of Binary Blended Methane, Ethane, and Ethylene over a Wide Range of Temperature, Pressure, Equivalence Ratio, and Dilution, Energy Fuels, 34 (2020) 8808–

8823.

[32] S. Martinez, M. Baigmohammadi, V. Patel, S. Panigrahy, A.B. Sahu, S.S. Nagaraja, A. Ramalingam, A.A.E.S. Mohamed, K.P. Somers, K.A. Heufer, A. Pekalski, H.J. Curran, An experimental and kinetic modeling study of the ignition delay characteristics of binary blends of ethane/propane and ethylene/propane in multiple shock tubes and rapid compression machines over a wide range of temperature, pressure, equivalence ratio, , Combust. Flame, 228 (2021) 401–414.

[33] A.A.E.-S. Mohamed, S. Panigrahy, A.B. Sahu, G. Bourque, H. Curran, An experimental and kinetic modeling study of the auto-ignition of natural gas blends containing C_1–C_7 alkanes, Proc. Combust. Inst., 38(1) (2021) 365-373.

[34] A.B. Sahu, A.A.E.-S. Mohamed, S. Panigrahy, G. Bourque, H. Curran, Ignition studies of C_1–C_7 natural gas blends at gas-turbine-relevant conditions, J. Eng. Gas Turbines Power, 143 (2021) 081022 (7 pages).

[35] P. Glarborg, J.A. Miller, B. Ruscic, S.J. Klippenstein, Modeling nitrogen chemistry in combustion, Prog. Energy Combust. Sci., 67 (2018) 31–68.

[36] Y. Zhang, O. Mathieu, E.L. Petersen, G. Bourque, H.J. Curran, Assessing the predictions of a NOx kinetic mechanism on recent hydrogen and syngas experimental data, Combust. Flame, 182 (2017) 122–141.

[37] J. Bugler, K.P. Somers, J.M. Simmie, F. Güthe, H.J. Curran, Modeling nitrogen species as pollutants: thermochemical influences, J. Phys. Chem. A, 120 (2016) 7192–7197.

[38] N.J. Killingsworth, M.J. McNenly, R.A. Whitesides, S.W. Wagnon, Cloud based tool for analysis of chemical kinetic mechanisms, Combust. Flame, 221 (2020) 170–179.

[39] X. Chen, M.E. Fuller, C. Franklin Goldsmith, Decomposition kinetics for HONO and HNO2, React. Chem. Eng., 4 (2019) 323–333.

[40] Y. Li, S. Javoy, R. Mevel, X. Xu, A chemically consistent rate constant for the reaction of nitrogen dioxide with the oxygen atom, Phys. Chem. Chem. Phys., 23 (2021) 585–596.

[41] D.H.B. B. Ruscic, Active Thermochemical Tables (ATcT) values based on ver. 1.122p of the Thermochemical Network, Available at ATcT.anl.gov. (2020).

[42] A. Frassoldati, T. Faravelli, E. Ranzi, Kinetic modeling of the interactions between NO and hydrocarbons at high temperature, Combust. Flame, 135 (2003) 97–112.

[43] T. Faravelli, A. Frassoldati, E. Ranzi, Kinetic modeling of the interactions between NO and hydrocarbons in the oxidation of hydrocarbons at low temperatures, Combust. Flame, 132 (2003) 188–207.

[44] H. Hashemi, J.M. Christensen, L.B. Harding, S.J. Klippenstein, P. Glarborg, High-pressure oxidation of propane, Proc. Combust. Inst., 37 (2019) 461–468.

[45] R. CHEMKIN-PRO, 15112, Reaction Design, Inc., San Diego, CA. (2011).

[46] V. Gururajan, F.N. Egolfopoulos, Direct sensitivity analysis for ignition delay times, Combust. Flame, 209 (2019) 478–480.

[47] O. Mathieu, J.M. Pemelton, G. Bourque, E.L. Petersen, Shock-induced ignition of methane sensitized by NO_2 and N_2O, Combust. Flame, 162 (2015) 3053–3070.

[48] A. Matsugi, H. Shiina, Thermal decomposition of nitromethane and reaction between CH3 and NO2, J. Phys. Chem. A, 121 (2017) 4218–4224.

[49] I. Zaslonko, Y. Petrov, V. Smirnov, Thermal decomposition of nitromethane in shock waves : The effect of pressure and collision partners, Kinet. Catal., 38 (1997) 321–324.

[50] J.J. Weng, Z.Y. Tian, K.W. Zhang, L.L. Ye, Y.X. Liu, L.N. Wu, D. Yu, J.Z. Yang, C.C. Cao, J.B. Zou, Experimental and kinetic investigation of pyrolysis and oxidation of nitromethane, Combust. Flame, 203 (2019) 247–254.

[51] X. Zhang, W. Ye, J.C. Shi, X.J. Wu, R.T. Zhang, S.N. Luo, Shock-Induced ignition of methane, ethane, and methane/ethane mixtures sensitized by NO_2, Energy Fuels, 31 (2017) 12780–12790.

[52] K. Zhang, C. Banyon, C. Togbé, P. Dagaut, J. Bugler, H.J. Curran, An experimental and kinetic modeling study of n-hexane oxidation, Combust. Flame, 162 (2015) 4194–4207.

[53] K. Zhang, C. Banyon, U. Burke, G. Kukkadapu, S.W. Wagnon, M. Mehl, H.J. Curran, C.K. Westbrook, W.J. Pitz, An experimental and kinetic modeling study of the oxidation of hexane isomers: Developing consistent reaction rate rules for alkanes, Combust. Flame, 206 (2019) 123–137.

[54] A. Ahmed, W.J. Pitz, C. Cavallotti, M. Mehl, N. Lokachari, E.J.K. Nilsson, J.Y. Wang, A.A. Konnov, S.W. Wagnon, B. Chen, Z. Wang, S. Kim, H.J. Curran, S.J. Klippenstein, W.L. Roberts, S.M. Sarathy, Small ester combustion chemistry: Computational kinetics and experimental study of methyl acetate and ethyl acetate, Proc. Combust. Inst., 37 (2019) 419–428.

[55] S.M. Gallagher, H.J. Curran, W.K. Metcalfe, D. Healy, J.M. Simmie, G. Bourque, A rapid compression machine study of the oxidation of propane in the negative temperature coefficient regime, Combust. Flame, 153 (2008) 316–333.

[56] E.L. Petersen, M. Lamnaouer, J. de Vries, H. Curran, J. Simmie, M. Fikri, C. Schulz, G. Bourque, Discrepancies between shock tube and rapid compression machine ignition at low temperatures and high pressures BT - Shock Waves, in: K. Hannemann, F. Seiler (Eds.), Springer Berlin Heidelberg, Berlin, Heidelberg, (2009) 739–744.

[57] D.F. Davidson, R.K. Hanson, Recent advances in shock tube/laser diagnostic methods for improved chemical kinetics measurements, Shock Waves, 19 (2009) 271–283.

[58] M. Chaos, F.L. Dryer, Chemical-kinetic modeling of ignition delay: Considerations in interpreting shock tube data, Int. J. Chem. Kinet., 42 (2010) 143–150.

[59] C. Olm, I.G. Zsély, R. Pálvölgyi, T. Varga, T. Nagy, H.J. Curran, T. Turányi, Comparison of the performance of several recent hydrogen combustion mechanisms, Combust. Flame, 161 (2014) 2219–2234.

CHAPTER 6

THE EFFECT OF THE ADDITION OF NITROGEN OXIDES ON THE OXIDATION OF ETHANE: AN EXPERIMENTAL AND MODELLING STUDY

Chapter 6: The Effect of the Addition of Nitrogen Oxides on the Oxidation of Ethane: an Experimental and Modelling Study

Paper under review: submitted to Combustion and flame

Authors and Contributions

1) **Ahmed Abd El-Sabor Mohamed** (National University of Ireland, Galway, Ireland)
Contribution: RCM and HPST experiments, Chemical kinetic modelling and manuscript preparation.
2) **Snehasish Panigrahy** (National University of Ireland, Galway, Ireland)
Contribution: Chemical kinetic modelling and manuscript review.
3) **Amrit Bikram Sahu** (National University of Ireland, Galway, Ireland)
Contribution: Chemical kinetic modelling and manuscript review.
4) **Gilles Bourque** (Siemens Energy Canada Ltd, Montreal QC H9P 1A5, Canada)
Contribution: Project management and manuscript review.
5) **Henry J. Curran** (National University of Ireland, Galway, Ireland)
Contribution: Project management and manuscript review.

Abstract

This study reports new ignition delay time (IDT) measurements of ethane (C_2H_6)/air mixtures with NOx (nitric oxide (NO), nitrogen dioxide (NO_2), and nitrous oxide (N_2O)) addition in the range 0 – 1000 ppm at stoichiometric fuel to air (φ) ratios, at compressed temperatures (T_C) of 851 – 1390 K, and at compressed pressures (p_C) of 20 – 30 bar. In addition, new IDT measurements of three highly diluted C_2H_6/NO_2 mixtures at φ = 0.5, T_C = 805 – 1038 K, and p_C = 20 – 30 bar are also studied. These new experimental data, together with data already available in the literature are used to validate NUIGMech1.2 with an updated NOx sub-mechanism. Although the addition of 200 ppm of NO or NO_2 to ethane shows a minimal promoting effect, the addition of 1000 ppm significantly promotes the reactivity of ethane. The similarity of the effect of the addition of both NO and NO_2 addition is due to the fast conversion of NO into NO_2 in the presence of molecular oxygen. However, the 1000 ppm NO doped ethane mixtures exhibit

~20% faster reactivity compared to the NO_2 blended mixtures. The addition of 1000 ppm of N_2O exhibits no effect on ethane oxidation at the conditions studied. The NUIGMech1.2 predictions can reproduce the sensitisation effect of NOx on ethane with good agreement over a wide range of pressure, temperature, equivalence ratio, and percentage dilution. Sensitivity and flux analyses of C_2H_6/NOx are performed to highlight the key reactions controlling ignition over the different temperature regimes studied. The analyses show that there is a competition between the reactions $\dot{R} + NO_2 \leftrightarrow R\dot{O} + NO$ and $\dot{R} + NO_2 (+M) \leftrightarrow RNO_2 (+M)$. This governs NOx sensitization on C_2H_6 ignition.

Keywords: Ethane/NOx; Nitrogen oxides; Ignition delay times; Rapid compression machine; Shock tube; Chemical kinetics mechanism.

6.1 Introduction

Exhaust gas recirculation (EGR) plays a major role in reducing nitrogen oxides (NOx) emission levels by reducing the combustion temperature of internal combustion engines and gas turbines [1–3]. As the presence of NOx in the combustion product is unavoidable under such operating conditions, therefore understanding the effect of NOx on fuel oxidation is necessary to achieve the highest possible efficiency of EGR applications in the design and operation of advanced combustors.

A fuel's combustion characteristics such as flame speed, speciation profiles, auto-ignition etc. play a vital role in the design of optimized combustors. Laboratory scale combustion reactors such as combustion vessels, jet-stirred reactors, flow reactors (laminar and turbulent flow), rapid compression machines (RCMs), and shock tubes (STs) are used to measure combustion characteristics at conditions relevant to practical combustor operation. Thereafter, the data measured in the laboratory is commonly used to validate detailed chemical mechanisms over a wide range of conditions.

Chapter 6

Ethane is not only an important component in natural gas (NG) [4,5] but it is also a pivotal intermediate formed in the combustion of higher hydrocarbon fuels. Therefore, numerous studies have investigated the combustion characteristics of ethane at combustor relevant conditions [6–10]. As NOx species are present in EGR, numerous studies explored hydrocarbon (HC)/NOx interactions [11–16] which show prompting [17–26] and inhibiting [27–30] effects on HC reactivity depending on the concentration of NOx present and the relevant temperature regime studied. Therefore, understanding NOx interactions with ethane in the low-, intermediate-, and high-temperature regimes will help in the development of hierarchical chemical mechanisms of hydrocarbon/NOx systems.

In respect of the C_2H_6/NOx interaction chemistry, most literature studies have reported experiments with highly diluted mixtures which show a significant promoting effect on ethane auto-ignition even with 200 ppm NO_2 added [23,25,26,31–34]. The study by Gersen et al. [19] is the only one that reported the interactions between NO_2 and ethane for fuel/'air' mixtures. They showed that there is a minimal reduction on ethane IDTs by adding 270 ppm NO_2. However, they did not perform non-reactive experiments, so that facility effects cannot be well accounted for in simulating their experiments.

The main goal of the current study is to investigate the impact of NOx (NO, NO_2, and N_2O) on the auto-ignition of ethane at combustors relevant conditions. Therefore, new IDTs measurements are reported using an RCM and a HPST for stoichiometric C_2H_6/NOx (NO, NO_2, and N_2O) mixtures diluted in 'air' at different levels of NO_x addition varying from 0 – 1000 ppm at p_C = 20 – 30 bar and T_C = 851 – 1390 K. In addition to these new IDT measurements which are carried out using 'air' as the oxidizer, three highly diluted C_2H_6/NO_2 mixtures at φ = 0.5, T_C = 805 – 1038 K, and p_C = 20 – 30 bar were also studied. A chemical kinetic model is developed and validated against the current experimental data along with available literature data. Sensitivity

and reaction pathway analyses are performed to highlight the most important reaction and pathway for ethane oxidation with NOx addition.

6.2 Experiments

IDTs experiments were conducted using both red RCM and high-pressure shock tube (HPST) facilities at NUI Galway, a brief description for both facilities and the experiment procedure are provided below.

6.2.1 Rapid compression machine

The RCM has a twin- creviced piston design [35] to ensure the gas temperature after compression is more homogeneous [36]. As the geometric compression ratio of the RCM is fixed, in order to span a range of compressed gas temperatures, the initial temperature (T_i) is varied from 303 – 403 K. This variation in T_i is controlled using a heating system implemented on the walls of the cylinder and reaction chamber together with five thermocouples installed on the outer body of the cylinder to accurately control T_i. A Kistler 6045B pressure transducer, installed in the reaction chamber wall, is connected to a Kistler charge amplifier in conjunction with an oscilloscope to record pressure/time histories as shown in Fig. 1. The IDT is defined as the interval between the time between the first peak pressure at the end of compression (EOC) to the second global peak pressure due to the ignition event as shown in Fig. 6-1(a). Due to the weak pressure signal for the highly dilute ethane/NO_2 conditions, a photomultiplier (PMT) equipped with a CH* filter (CWL: 430 nm ± 10 FWHM; Thorlabs) is used together with the pressure trace to measure the IDT for the dilute mixtures. The ignition event is reported at the maximum gradient pressure ($\frac{dp}{dt}$) or in CH^* ($\frac{dCH^*}{dt}$) after compression as shown in Fig. 6-1(b). The equilibrium program Gaseq [37], is used to calculate T_C by providing the mixture composition, T_i, initial pressure (p_i), and the measured p_C as inputs, assuming an adiabatic compression/expansion. These data are available in appendix C. Each experimental point is

repeated at least once (sometimes twice) to confirm the reproducibility of the measured IDT within ≤ 10%.

6.2.2 High pressure shock tube

The HPST comprises a 9.0 m long stainless-steel tube with a uniform cross-section of 63.5 mm inner diameter. It is divided into three sections; a driver section (3 m), a driven section (5.73 m), and a double-diaphragm chamber (0.27 m) which separates the driver and driven sections. Two pre-scored aluminium diaphragms are used, with the scoring depth varied depending on the target bursting pressure which enables improved control of the shock-wave. Helium is used as the driver gas and a fraction of nitrogen is used for tailoring. Six axially positioned PCB113B24 pressure transducers mounted in the walls of the tube at different location near to the endwall are used to measure the shock velocity (V_{Shock}). A Kistler 603B pressure transducer mounted in the endwall is used to measure the IDT, defined as the time interval between the pressure rise due to the shock-wave arrival at the endwall and the ignition event as shown in Fig. 6-2. In the equilibrium program Gaseq [37] the "reflected shock" module, in conjunction with frozen chemistry, is used to calculate the reflected shock pressure (p_5) and temperature (T_5) using the initial pressure (p_1), the initial temperature (T_1), and V_{Shock} and are all appendix C.

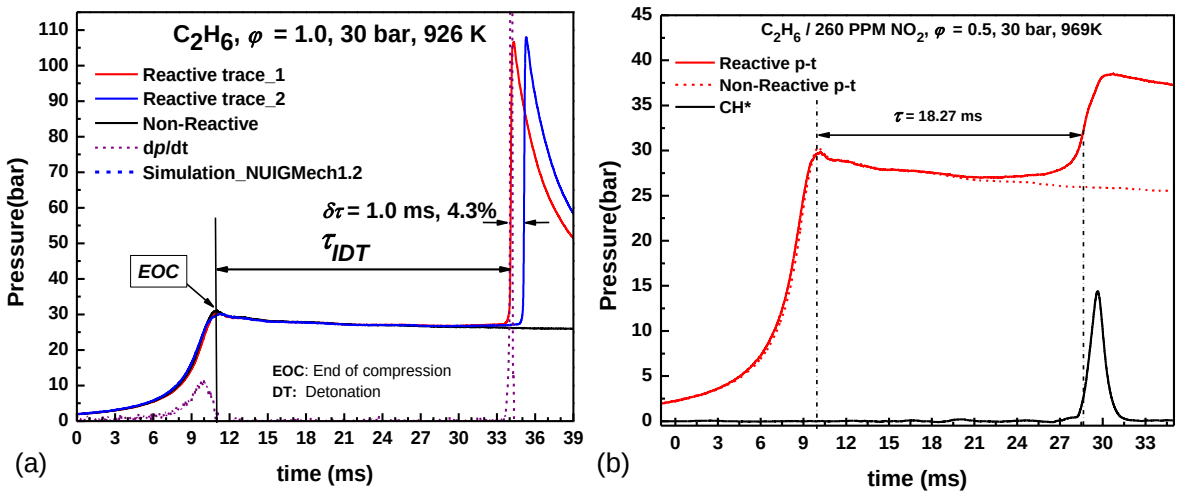

Figure 6-1. RCM pressure-time histories for ethane oxidation at 30 bar; (a) φ = 1.0 in 'air'; and (b) φ = 0.5 at 91% dilution.

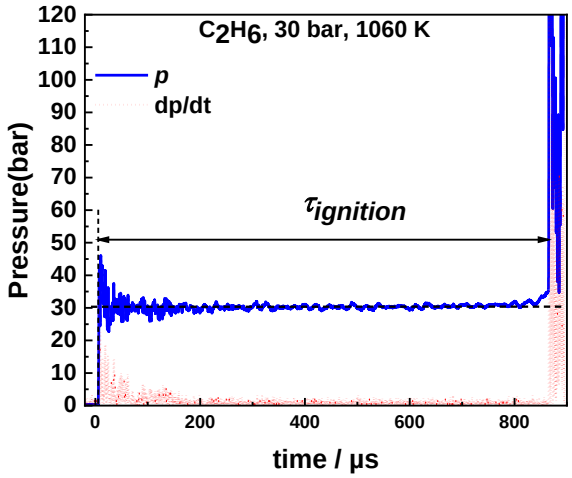

Figure 6-2. HPST pressure-time histories for ethane oxidation shows the ignition event.

6.2.3 Mixture preparation

The purity of the fuels used is based on the supplier and are as follows: ethane (99.5%), 4% NO diluted in argon, 2% NO_2 diluted in argon, and 99% N_2O were supplied by Air Liquide and were used without further purification. Nitrogen (> 99.96%), argon (> 99.98%), and oxygen (> 99.5%) gases were supplied by BOC Ireland.

The ethane/O_2/NO_2/(N_2/Ar) mixtures were prepared based on the partial pressure of each component starting from the lowest partial pressure using four MKS pressure transducers (20, 100, 1000, and 5000 mbar) with accuracies of ± 0.5% of the reading installed in the manifold lines. Thereafter, each mixture was allowed to homogenise via gaseous diffusion for at least 12 h. Different fractions of N_2 and Ar were used as the diluent in order to cover the wide range of compressed temperatures. For the experiments with NO added to ethane, due to the fast conversion of NO to NO_2 in the presence of O_2 [38], the C_2H_6/O_2/N_2/Ar mixture was prepared separately and a 1.0 L mixing tank was connected to the manifold in order to prepare the final C_2H_6/O_2/N_2/Ar/NO mixture. This method was used to minimise the mixing time of NO with O_2 to be within 5 min before performing the IDT experiments so as to limit the conversion of NO into NO_2. 0-D simulations were carried out for the C_2H_6/O_2/N_2/Ar/NO mixtures to obtain the final NO/NO_2 mixture composition used in simulating our C_2H_6/NO experiments as summarized

in Table 6-1. Also, a set of non-reactive experiments were performed where O_2 was replaced with N_2 in the non-reactive mixture to account for facility effects (heat losses, etc.) in the RCM experiments. Table 6-1 shows the mixture composition and the experiment conditions of the current study. The high diluted ethane/NO_2 mixtures were studied previously by Deng et al. [25] at 30 bar and are repeated here together with new results at 20 bar.

Table 6-1. Experimental conditions and mixtures compositions.

Ethane/NO_2 at φ = 1.0 in 'air'									
Initial NO_2 (ppm)	**C_2H_6 %**	**NO_2 (ppm)**	**O_2 %**	**Diluent %**		***p* (bar)**	***T* (K)**	**Facility**	**Ref.**
				N_2	**Ar**				
0	5.60	–	19.4	75.00	–	20	947 – 1390	ST	[10]
0	5.60	–	19.4	22.50	52.50	20	891 – 954	RCM	[10]
0	5.66	–	19.82	74.52	–	20, 30	1006 – 1382	ST	pw*
0	5.66	–	19.82	14.90	59.62	20, 30	885 – 970	RCM	pw
200	5.61	200	19.62	73.77	0.98	20, 30	944 – 1351	ST	pw
200	5.61	200	19.62	14.76	59.99	20, 30	873 – 988	RCM	pw
1000	5.38	1000	18.83	70.79	4.90	20, 30	1004 – 1368	ST	pw
1000	5.38	1000	18.83	14.16	61.53	20, 30	855 – 989	RCM	pw
Ethane/NO at φ = 1.0 in 'air'									
Initial NO (ppm)	**C_2H_6**	**NO/NO_2**	**O_2**	**N_2**	**Ar**	***p*$_C$ (bar)**	***T*$_C$ (K)**	**Facility**	**Ref.**
200	5.64	135/65	19.72	14.83	59.80	30	869 – 973	RCM	pw
1000	5.52	280/720	19.32	14.53	60.53	30	851 – 958	RCM	pw
Ethane/N_2O at φ = 1.0 in 'air'									
Initial N_2O (ppm)	**C_2H_6**	**N_2O**	**O_2**	**N_2**	**Ar**	***p*$_C$ (bar)**	***T*$_C$ (K)**	**Facility**	**Ref.**
1000	5.66	1000	19.82	14.91	59.51	20, 30	900 – 995	RCM	pw
Ethane/NO_2 at φ = 0.5 diluted									
Initial NO_2 (ppm)	**C_2H_6**	**NO_2**	**O_2**	**N_2**	**Ar**	***p*$_C$ (bar)**	***T*$_C$ (K)**	**Facility**	**Ref.**
260	1.01	260	7.05	54.38	37.53	20, 30	908 – 1038	RCM	pw
2704	1.05	2704	7.31	78.12	13.25	20, 30	816 – 960	RCM	pw
5163	1.00	5163	6.98	66.20	25.30	20, 30	805 – 961	RCM	pw
pw*: present work									

6.3 Chemical kinetic model

NUIGMech1.2 is used to simulate the current data together with the available literature data. This detailed mechanism has been hierarchically developed and validated for a comprehensive array of fuels ranging from C_0 – C_7 hydrocarbons [10,39–42] including binary/ternary blends [43,44] and natural gas mixtures [45,46], comprising an extensive series of studies on these fuels. The hydrocarbon model has been integrated with an updated NO_x sub-mechanism which is based on the recently published mechanism by Glarborg et al. [47] and the hydrogen/syngas–

NO_X chemistry adopted from Zhang et al. [48]. The CH_4/NO_x sub-mechanism is adopted based on a recent study on NO_x sensitization of CH_4 ignition and oxidation [49]. Further updates to the C_2/NO_x sub-mechanism are based on a critical assessment of recent measurements or high-level calculations of rate parameters available in the literature and are discussed in the following sections. Ab-initio calculations for gas-phase thermochemistry performed by Bugler et al. [50] for over 60 nitrogenous compounds are included in the current mechanism owing to their relatively high accuracy and internal consistency.

6.4 Results and discussion

The results of the IDTs for the mixtures listed in Table 6-1 are provided here. The term “in air” in the figures refers to the oxidizer mixture containing O_2/diluent in the ratio of 1:3.76 and the equivalence ratio is calculated based on the fuel/O_2 ratio, neglecting the oxygen present in the NOx species. The initial conditions and the IDT data are provided in appendix C and the pressure/time histories for use in the simulations are provided as supplementary material of the online version of the paper. In this section, the results of the effect of adding NO_2, NO and N_2O to ethane oxidizer mixtures on IDT measurements are provided. The RCM and HPST IDT simulations are performed using CHEMKIN-Pro [62]. To account for facility effects (the compression process and heat loss after compression) within the RCM, simulations are performed using volume/time histories recorded for non-reactive mixtures. The homogeneous closed volume reactor module is used to simulate the ST IDTs using the experimental conditions listed in appendix C (T_5, p_5, and mixtures compositions).

6.4.1 Effect of NO_2 on Ethane IDT

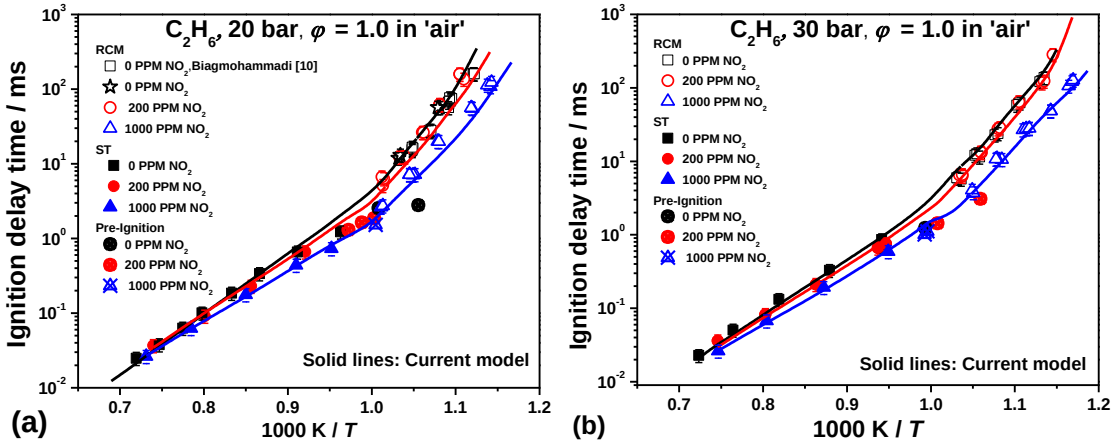

Figure 6-3. Ignition delay times measurements of C_2H_6/NO_2 (symbols) and NUIGMech1.2 model prediction (lines) at φ = 1.0 at; (a) 20 bar; and (b) 30 bar.

Figure 6-3 shows the current RCM and HPST IDTs measurements for a stoichiometric C_2H_6/air mixtures at 20 bar, Fig. 6-3(a), and 30 bar, Fig. 6-3(b), in the temperature range of 855 – 1390 K at three levels of NO_2 addition (0, 200, 1000 ppm). Moreover, the lines represent the IDTs predictions calculated using NUIGMech1.2. Figure 6-3 shows that the onset ignition temperature decreases with increasing NO_2 concentration. For the 200 ppm NO_2 blended C_2H_6/air mixture IDTs are within 20% of the pure ethane IDTs which is within the uncertainty limit of our measurements. However, with the addition of 1000 ppm NO_2 the IDTs data become significantly more reactive by factor of ~2.5 at low temperatures (830 – 1000 K) compared to the pure C_2H_6/air mixture. This factor gradually decreases with increasing temperature, reaching ~1.23 at high temperatures (1430 K) showing the non-linearity of NO_2 effect in different temperature regimes. The simulations using NUIGMech1.2 show very good agreement with the experimental measurements across the temperature range at the two pressures and the three levels of NO_2 addition examined in this study.

To explore the controlling chemistry responsible for the increase in reactivity of the NO_2 blended C_2H_6/air mixtures, the rate of destruction of C_2H_6 as function of time is shown in Fig. 6-4(c) for pure C_2H_6/air mixtures and C_2H_6/NO_2/air blend mixtures at T_C = 950 K and p_C = 30 bar

condition. Moreover, Figs. 6-4(a) and 6-4(b) present the sensitivity and ROP analyses of C_2H_6/air mixtures blended with 0, 200, and 1000 ppm NO_2 at T_C = 950 K and p_C = 30 bar. As shown in Fig. 6-4(c), for the pure C_2H_6/air mixtures and the C_2H_6/NO_2/air mixtures fuel reactivity is governed by the H-atom abstraction by $H\dot{O}_2$ radicals producing ethyl radicals ($\dot{C}_2H_5$) and hydrogen peroxide (H_2O_2). H_2O_2 further dissociates into hydroxyl radicals, via H_2O_2 (+M) ↔ ȮH + ȮH (+M) which significantly promotes the reactivity of the fuels. Figure 6-4(c) shows that in the case of C_2H_6/NO_2 mixtures, in the early stage of ignition, C_2H_6 is primarily consumed by H-atom abstraction by NO_2 forming HONO and $\dot{C}_2H_5$ radicals, which becomes important for enhancing the reactivity of the NO_2 blended mixtures, Fig. 6-4(a). In NUIGMech1.2 we have adopted the rate coefficients for the C_2H_6 + NO_2 reaction from the high-level theoretical study of Chai and Goldsmith [63] using the compound method with CCSD(T)-F12a/cc-pVTZ-f12//B2PLYPD3/cc-pVTZ level of theory. The HONO so produced subsequently decomposes generating NO and ȮH radicals that also has a large promoting effect on the ethane oxidation as seen in the sensitivity analysis, Fig. 6-4(a), by initiating the H-atom abstraction reaction, through C_2H_6 + ȮH ↔ $\dot{C}_2H_5$+ H_2O. The ROP analysis shows that at 950 K C_2H_6 is mostly consumed by H-atom abstraction by ȮH and $H\dot{O}_2$ radicals forming ethyl radicals for all of the C_2H_6/NO_2/air mixtures. When NO_2 is added to the C_2H_6/air mixtures, a greater fraction of C_2H_6 is consumed by ȮH radicals relative to that consumed by $H\dot{O}_2$ radicals. The formation of large amount of ȮH radicals in the early stage of ignition through C_2H_6 + NO_2 ↔ $\dot{C}_2H_5$ + HONO and subsequently via HONO ↔ ȮH + NO is responsible for the increase in C_2H_6 consumption by ȮH radicals for the C_2H_6/NO_2 blend mixtures. From Fig 6-4(b) it can be seen that 76% and 19.7% of the fuel undergoes H-atom abstraction by ȮH and $H\dot{O}_2$ radicals producing $\dot{C}_2H_5$ radicals, whereas, for the 1000 ppm NO_2 doped C_2H_6/air mixtures the percentage contribution to C_2H_6 consumption by ȮH radicals increases to 79.1% and the flux through H-atom abstraction by $H\dot{O}_2$ radicals decreases to 13%.

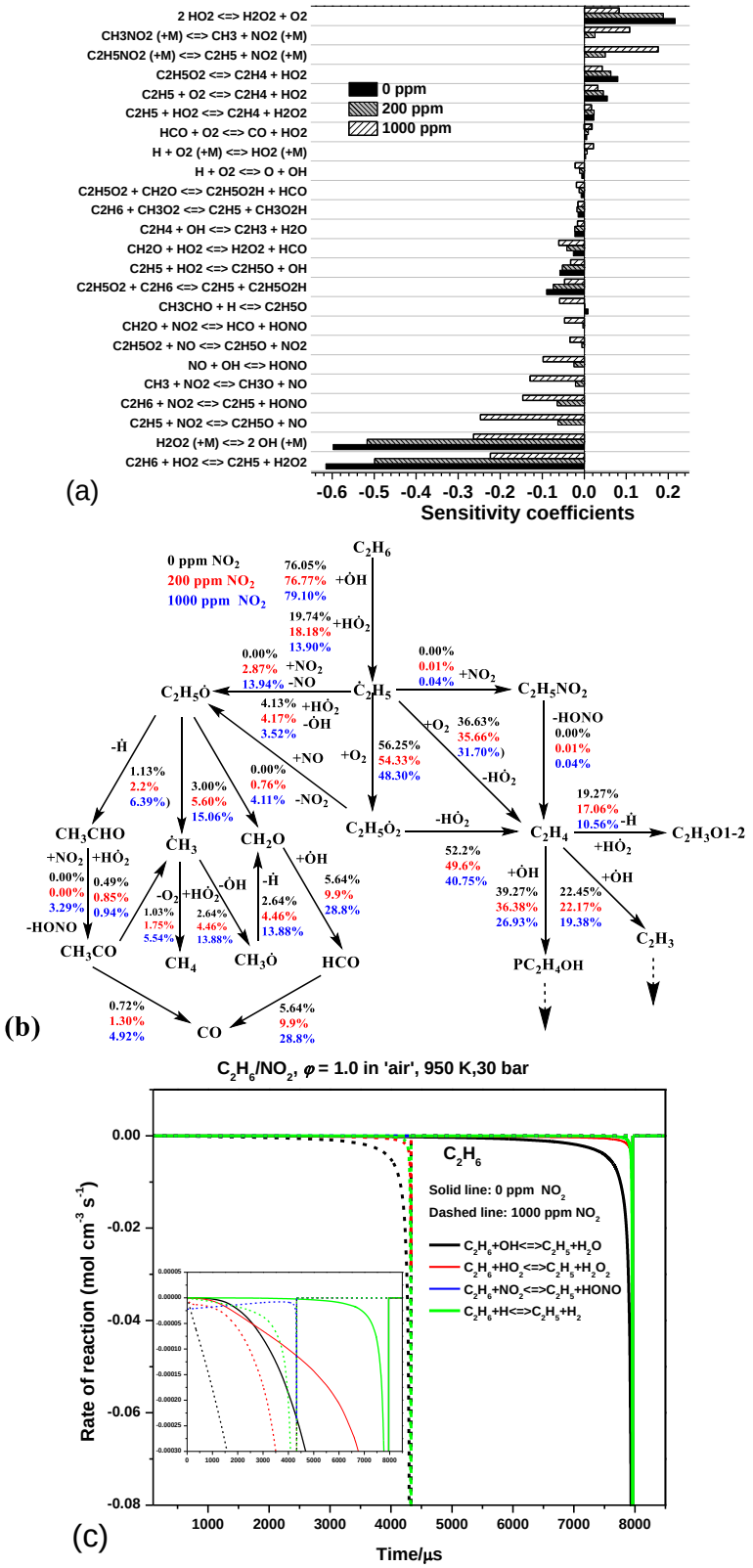

Figure 6-4. (a) Brute-force sensitivity (b) flux analyses at 10% of fuel consumption of C_2H_6/NO_2 mixtures, and (c) Rate of consumption of C_2H_6 at early stage of ignition for pure C_2H_6 and C_2H_6/NO_2blends at φ = 1.0, 950 K, and 30 bar.

Most of the $\dot{C}_2H_5$ radicals add to O_2 forming ethylperoxy ($C_2H_5\dot{O}_2$) radicals, which subsequently undergoes a concerted elimination reaction, $C_2H_5\dot{O}_2 \leftrightarrow C_2H_4 + H\dot{O}_2$. In the case of the NO_2 blended C_2H_6/air mixtures new reaction channels consuming $\dot{C}_2H_5$ become available. A relatively high concentration of ethoxy ($C_2H_5\dot{O}$) radicals is formed through the reaction $\dot{C}_2H_5 + NO_2 \leftrightarrow C_2H_5\dot{O} + NO$, promoting ignition of the NO_2 blended mixtures. A relatively small concentration of nitroethane ($C_2H_5NO_2$) is also produced by the addition of NO_2 to $\dot{C}_2H_5$, via $\dot{C}_2H_5 + NO_2 (+M) \leftrightarrow C_2H_5NO_2 (+M)$ which exhibits a positive sensitivity towards IDT due to its competition with $\dot{C}_2H_5 + NO_2 \leftrightarrow C_2H_5\dot{O} + NO$, inhibiting reactivity, Fig. 6-4(b). In the current mechanism the rate constants for $\dot{C}_2H_5 + NO_2 (+M) \leftrightarrow C_2H_5NO_2 (+M)$ is adopted by analogy with the $\dot{C}H_3 + NO_2 (+M) \leftrightarrow CH_3NO_2 (+M)$ reaction calculated by Matsugi and Shiina [66]. It should be noted that the rate constant of $\dot{C}H_3 + NO_2 (+M) \leftrightarrow CH_3NO_2 (+M)$ has been increased by 100% compared with that calculated by Matsugi and Shiina [66] to obtain better prediction accuracy with the measured IDTs data. The rate constant for its competing reaction $\dot{C}_2H_5 + NO_2 \leftrightarrow C_2H_5\dot{O} + NO$ is adopted by analogy to $\dot{C}H_3 + NO_2 (+M) \leftrightarrow CH_3\dot{O} + N\dot{O}_2$ from Glarborg et al. [49].

In Fig. 6-4(b) it is observed that when NO_2 is added to the C_2H_6/air mixtures relatively large concentrations of $C_2H_5\dot{O}$ radicals are produced during the ignition process. The $C_2H_5\dot{O}$ radicals produced can either decompose to form acetaldehyde and a $\dot{H}$ atom or formaldehyde and $\dot{C}H_3$ radicals. The acetaldehyde so produced is consumed by NO_2, via H-atom abstraction reaction yielding HONO and acetyl radicals ($CH_3\dot{C}O$) which decompose forming $\dot{C}H_3$ radicals and carbon monoxide (CO), through $CH_3\dot{C}O (+M) \leftrightarrow \dot{C}H_3 + CO (+M)$. Figure 6-4(b) shows that the NO_2 blended C_2H_6/air mixtures generate a significant amount of $\dot{C}H_3$ radicals in the oxidation process. These $\dot{C}H_3$ radicals are mainly consumed by reaction with $H\dot{O}_2$ radicals, via $\dot{C}H_3 + H\dot{O}_2 \leftrightarrow \dot{C}H_3O + \dot{O}H$ and $\dot{C}H_3 + H\dot{O}_2 \leftrightarrow CH_4 + O_2$. When NO_2 is present in the reactant mixtures some of the $\dot{C}H_3$ radicals also react with NO_2 to produce methoxy radicals ($CH_3\dot{O}$) by $\dot{C}H_3 +$

$NO_2 \leftrightarrow CH_3\dot{O} + NO$ which promotes reactivity. Moreover, a small fraction of $\dot{C}H_3$ radicals are consumed via the reaction $\dot{C}H_3 + NO_2 (+M) \leftrightarrow CH_3NO_2 (+M)$ which competes with the chain branching reaction $\dot{C}H_3 + NO_2 \leftrightarrow CH_3\dot{O} + NO$, inhibiting reactivity as shown in the sensitivity analysis, Fig. 6-4(a). The methoxy radicals produced decompose to form $\dot{H}$ atoms and formaldehyde, via $CH_3\dot{O} (+M) \leftrightarrow CH_2O + \dot{H} (+M)$. The NO_2 blended C_2H_6/air mixtures produce large amounts of $\dot{H}$ atoms compared to the pure C_2H_6/air mixtures. According to Fig. 6-4(b), the formation of $\dot{H}$ atoms accounts for ~2.65% of the total flux for the pure C_2H_6/air mixtures, while 1000 ppm of NO_2 blended C_2H_6/air mixtures contribute ~13.9% of the total flux to produce $\dot{H}$ atoms via $CH_3\dot{O} (+M) \leftrightarrow CH_2O + \dot{H}$. A large fraction of $\dot{H}$ atoms add to O_2 forming $H\dot{O}_2$ radicals which can self-react to generate H_2O_2 or abstract a hydrogen atom from the parent fuel C_2H_6 producing $\dot{C}_2H_5$ radicals.

Figure 6-5(a) presents comparisons of NUIGMech1.2 predictions with the IDT measurements of Deng et al. [25] for seven C_2H_6/NO_2/air mixtures at $\varphi = 0.5$ and $p_C = 30$ bar at 91% dilution. The model can reproduce most of the experimental data within a 20% limit except for the 2700 ppm and 5160 ppm NO_2 blended mixtures, where the mechanism under-predicts the reactivity by more than 40%.

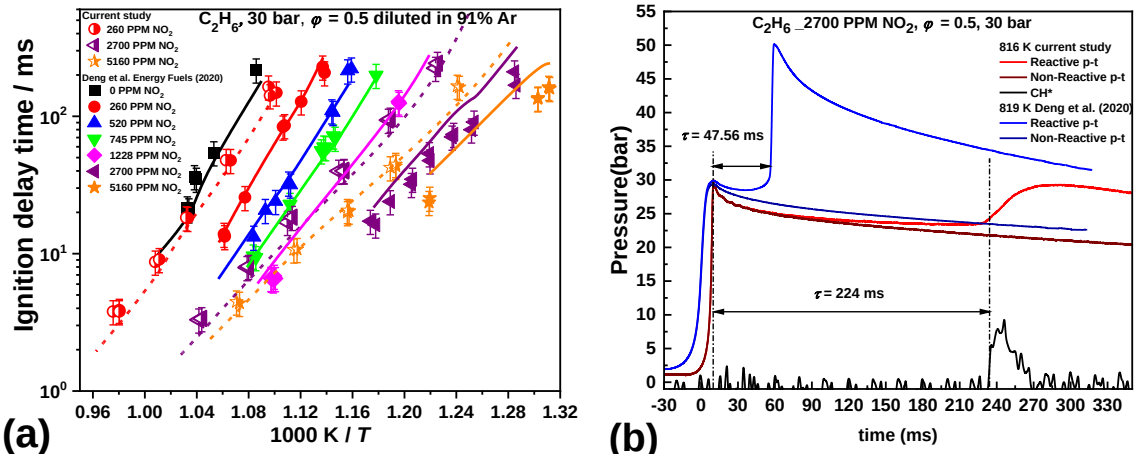

Figure 6-5. (a) Comparison of experimental measurements (symbols) and NUIGMech1.2 predictions (lines) from both the current study and Deng et al. [25] (symbols) at $\varphi = 0.5$, $p_C = 30$ bar, and 0 – 5163 ppm NO_2; and (b) Comparison of pressure-time histories from current study and Deng et al. [25] at 91% dilution conditions.

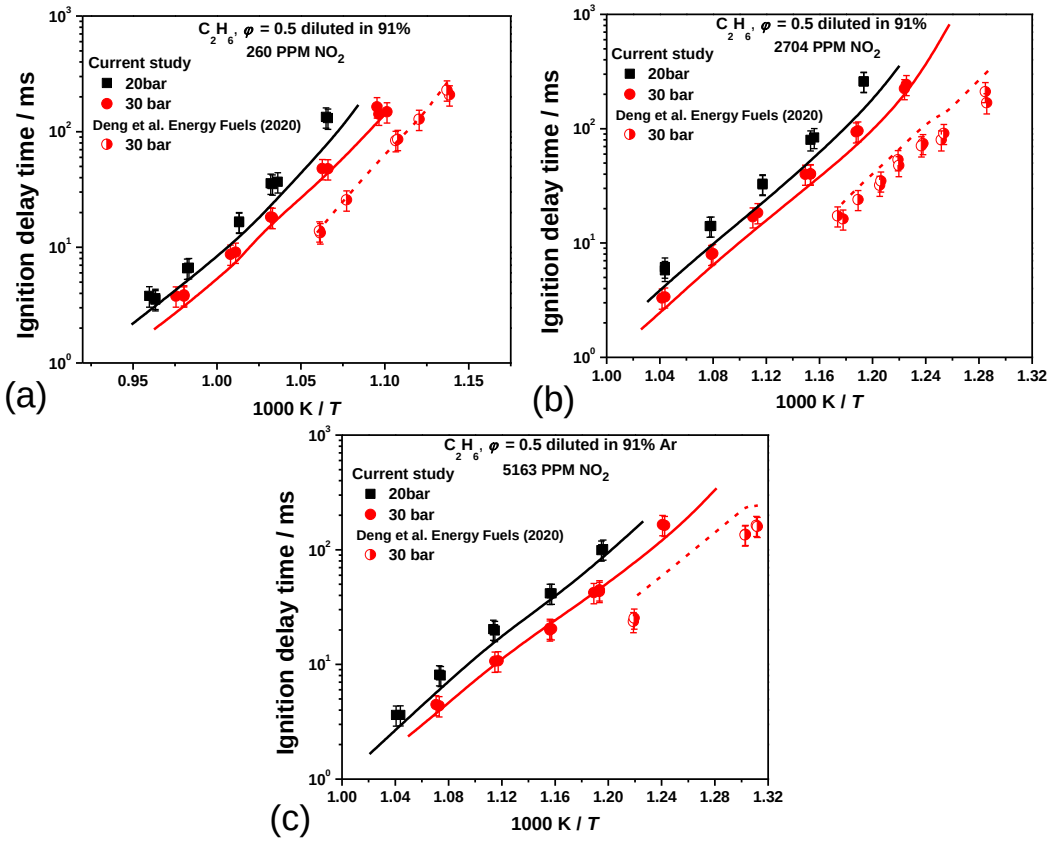

Figure 6-6. Comparison of experimental measurements (symbols) and NUIGMech1.2 predictions (lines) from both the current study and Deng et al. [25] (symbols) at φ = 0.5, p_C = 30 bar; (a) 260 ppm NO_2; (b) 2704 ppm NO_2; and (c) 5163 ppm NO_2, all at 91% dilution conditions.

Therefore, to confirm the repeatability of the measurements the experiments under the two extreme data conditions are reproduced for the 2700 ppm and 5160 ppm NO_2 blended mixtures where the mechanism is not able to capture the reported measurements from Deng et al. [25]. Furthermore, to compare the measurements, the experiments were also repeated for the 260 ppm NO_2 blended C_2H_6/NO_2/air mixture case at the same condition studied by Deng et al. [25]. Figure 6-6 shows comparisons of the current IDT measurements at the three NO_2 addition levels (260, 2700, and 5160 ppm) with the Deng et al. [25] data at 30 bar and with the new 20 bar data. Although the new IDTs are longer than those measured by Deng et al., the mechanism is able to predict the new data at the two compressed pressures. Figure 6-5(b) illustrates the comparison of pressure/time histories recorded from two RCMs which were used at NUIG and by Deng et al. [25]. It indicates that the facility effects in the RCM at NUIG are larger than those in the Deng et al. [25] RCM facility, making our IDT longer than those recorded by Deng et al. [25]. Figures

CS10 to CS15 show the performance of NUIGMech1.2 for the available RCM and ST IDT data available in the literature for C_2/NO_2 mixtures at different equivalence ratio, pressure and temperatures [25,26,33,34,51]. The comparisons show good agreement, with the predictions being within an uncertainty limit of ~22% for the RCM and ~18% for the ST experiments. As both the NUIGMech1.2 and Deng et al. [26] models are able to predict the IDTs measurements for 0–1228 ppm NO_2 addition experiments from Deng et al. [25] and compare well with the experiments we repeated the 260, 2700, and 5163 ppm NO_2 addition data, suggesting that the previous 2700 ppm and 5163 ppm NO_2 addition data reported by Deng et al. [25] may not be entirely reliable.

6.4.2 Effect of NO on ethane IDT

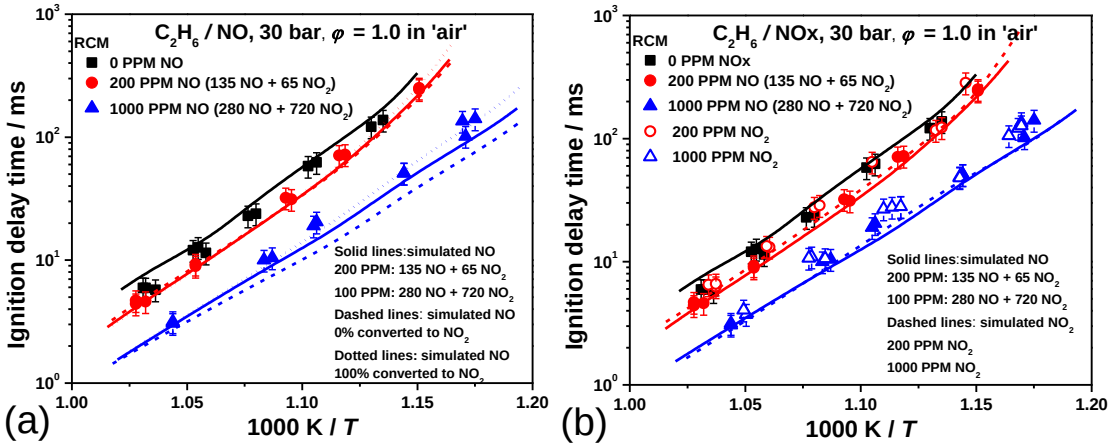

Figure 6-7. Comparison of experimental measurements (symbols) and NUIGMech1.2 model predictions (solid lines) for various $C_2H_6/NO/NO_2$ mixtures at φ = 1.0 and p_C = 30 bar.

Figure 6-7(a) shows the current RCM IDTs measurements for stoichiometric C_2H_6/air mixtures with the addition of 0, 200 and 1000 ppm NO at 30 bar pressure and in the temperature range of 851 – 973 K. The results show that the addition of 200 and 1000 ppm NO to C_2H_6/air mixtures increases the reactivity by approximately 26% and 65%, respectively. In Fig. 6-7(a) the lines represent the model predictions using NUIGMech1.2 with the solid lines are simulated considering the equilibrium concentration of NO to NO_2 conversion as the reactant mixtures; the dashed lines are simulations considering 100% NO blended with the C_2H_6/air mixtures (no

conversion of NO to NO_2), and the dotted lines are simulations considering 100% NO_2 blended to the C_2H_6/air mixtures (complete conversion of NO to NO_2). All of the simulations are performed using the same input files which were formulated using the measured C_2H_6/NO non-reactive pressure time histories. The model predictions, considering the final NO/NO_2 reactant mixtures obtained from the 0-D simulations as reported in Table 6-1, are in good agreement with the experimental data. The model predictions in Fig. 6-7(a) for the 100% NO and 100% NO_2 blend cases indicate that the prompting effect of NO on C_2H_6/air mixtures is approximately 20% larger than that with NO_2, indicating that the reactivity of the NO doped mixtures is higher than for the NO_2 doped ones. Figure 6-7(b) confirms that the NO doped mixtures exhibit approximately 20% higher reactivities compared to mixtures with the same NO_2 blending level.

To identify the dominant reactions controlling the oxidation of $C_2H_6/NO/NO_2$/air mixtures, Fig. 6-8 compares brute-force sensitivity analyses of C_2H_6/1000 ppm NOx mixtures at φ = 1.0 in air at p_C = 30 bar and T_C = 850 K. Furthermore, to examine the higher promoting effect of the NO blended mixtures compared to the NO_2 blended ones, the ROP analyses of important species as a function of time in Fig. 6-9 is illustrated for the addition of 1000 ppm each of NO and NO_2 to C_2H_6/air mixtures at p_C = 30 bar and T_C = 850 K.

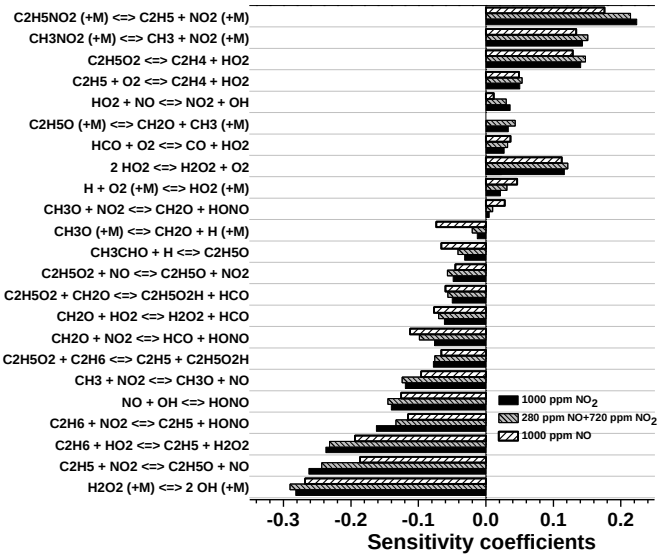

Figure 6-8. Brute-force sensitivity of C2H6/1000 ppm NOx mixtures at φ = 1.0 in air, 30 bar and 850 K.

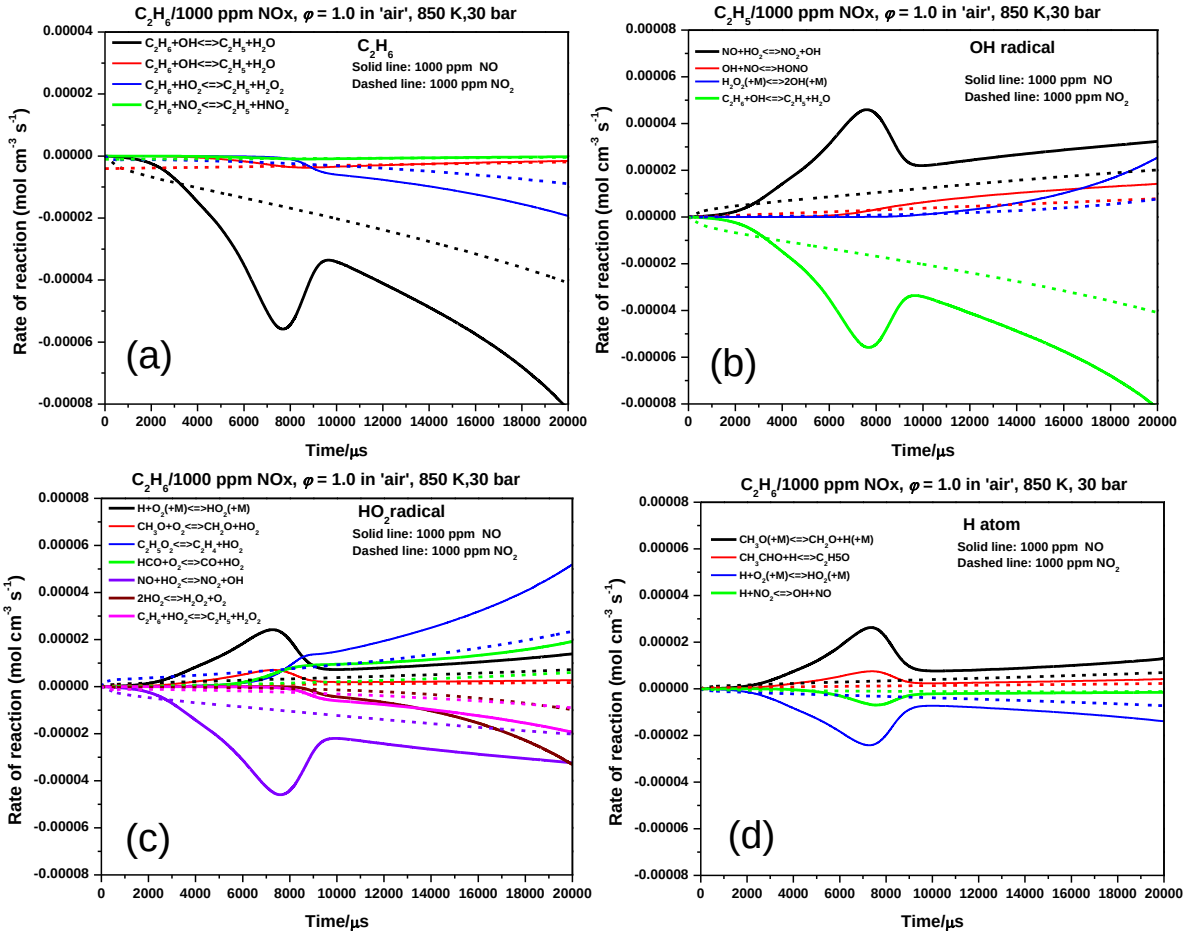

Figure 6-9. ROP analysis comparing the effect of 1000 ppm NO and 1000 ppm NO_2 addition on the oxidation of C_2H_6/air mixtures at φ = 1.0 in air, 30 bar and 850 K.

Figure 6-9 shows that both the rate of production and rate of destruction of the primary reactions responsible for the formation of important species are increased when NO is present compared to NO_2. Figure 6-9(a) provides the ROC of C_2H_6 with respect to time for the 1000 ppm NO and 1000 ppm NO_2 addition cases. At the early stage of ignition, H-atom abstraction by ȮH radicals, C_2H_6 + ȮH ↔ $\dot{C}_2H_5$+ H_2O is the dominant consumption pathway for C_2H_6 and the rate of progress of this reaction is higher for the NO blended mixtures leading to the faster ignition of the fuel compared to the NO_2 blended mixtures. This is primarily due to the availability of larger concentration of ȮH radicals in the case of the NO blended mixtures. The important reactions responsible for the formation of ȮH radicals are shown in Fig. 6-9(b). It is observed that for the 1000 ppm NO blended mixtures since large amount of NO is present in the system, it increases ȮH radical formation via the reaction NO + $H\dot{O}_2$ ↔ NO_2 + ȮH in the early stage of reaction.

The major reactions related to the formation of $H\dot{O}_2$ radicals are shown in Fig. 6-9(c). It can be observed that $\dot{H} + O_2 (+M) \leftrightarrow H\dot{O}_2 (+M)$ is responsible for the significant rise in $H\dot{O}_2$ radicals for the 1000 ppm NO blended mixtures compared to the NO_2 blended ones.

Finally, Fig. 6-9(d) shows that with the addition of NO instead of NO_2 to the C_2H_6/air mixtures, the rate of formation of the dissociation reaction $CH_3\dot{O} (+M) \leftrightarrow CH_2O + \dot{H} (+M)$ increases significantly producing larger concentrations of $\dot{H}$ atoms which subsequently generates larger concentrations of $H\dot{O}_2$ radicals via $\dot{H} + O_2 (+M) \leftrightarrow H\dot{O}_2 (+M)$, and hence generating higher concentrations of $\dot{O}H$ radicals via $NO + H\dot{O}_2 \leftrightarrow NO_2 + \dot{O}H$ which ultimately enhances the reactivity for the NO blended C_2H_6/air mixtures by promptly initiating the H-atom abstraction reaction $C_2H_6 + \dot{O}H \leftrightarrow \dot{C}_2H_5 + H_2O$. This can be confirmed by the increase in sensitivity coefficient of the $CH_3\dot{O} (+M) \leftrightarrow CH_2O + \dot{H} (+M)$ for the 1000 ppm NO blended mixtures compared to 1000 ppm NO_2 blended mixtures, Fig. 6-8.

6.4.3 Effect of N_2O on Ethane IDT

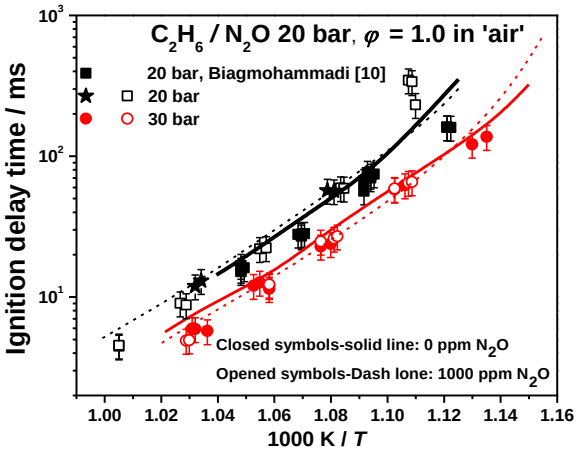

Figure 6-10. Comparison of RCM IDT measurements for C_2H_6/1000 ppm N_2O (symbols) and NUIGMech1.2 IDT predictions (solid lines) at φ = 1.0, and p_C = 20 and 30 bar condition.

Figure 6-10 shows the IDT measurements for stoichiometric C_2H_6/air mixtures in the temperature range 900 – 1000 K and 20 – 30 bar pressure conditions with and without addition of 1000 ppm N_2O. It indicates that N_2O addition has no effect on C_2H_6/air oxidation at the conditions studied. NUIGMech1.2 also predicts that there is no effect of addition of N_2O to the

C_2H_6/air mixtures. This is due to the high energy barrier for the decomposition reaction N_2O (+M) ↔ N_2 + Ö (+M) at the low temperature conditions. Figure 6-10 shows that the predictions are in satisfactory agreement with the experimental measurements.

6.5 Mean error analysis

Figures CS2–CS9 of appendix C show a comparison of the current RCM and ST IDTs measurements compared to available C_2/NOx literature models, including Deng et al. [26], DTU_NOx [47], Mevel et al. [23], Song et al. [61], and Zhang et al. [48]. Although Figures S2(a)–S7(a) show that the Deng et al. [26] model can predict the current C_2H_6/NOx data reasonably well, it is not able to capture the recently published CH_4/NOx [51] IDT data. Figures 6-11 and 6-12 present the comparisons of CH_4/NO_2 and CH_4/NO IDTs measurements compared to the current model predictions using NUIGMech1.2 together with the model published by Deng et al. [26]. The results show that Deng et al. model [26] over-predicts the IDTs for the CH_4/NO_2 and CH_4/NO mixtures.

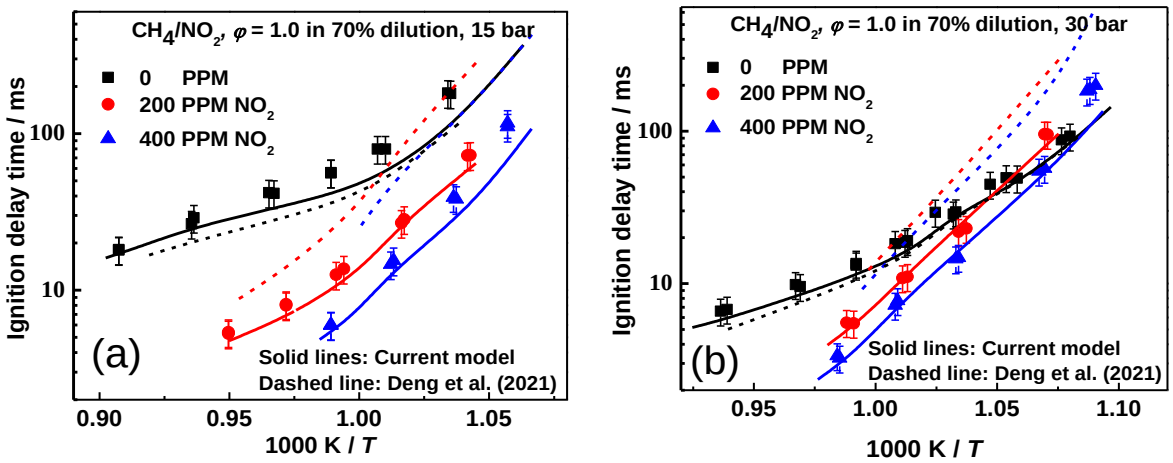

Figure 6-11. Comparison of RCM IDT measurements for CH_4/NO_2 mixtures [49] with the model predictions using NUIGMech1.2 and Deng et al. [26] at φ = 1.0, and; (a) p_C = 15; and (b) p_C = 30 bar.

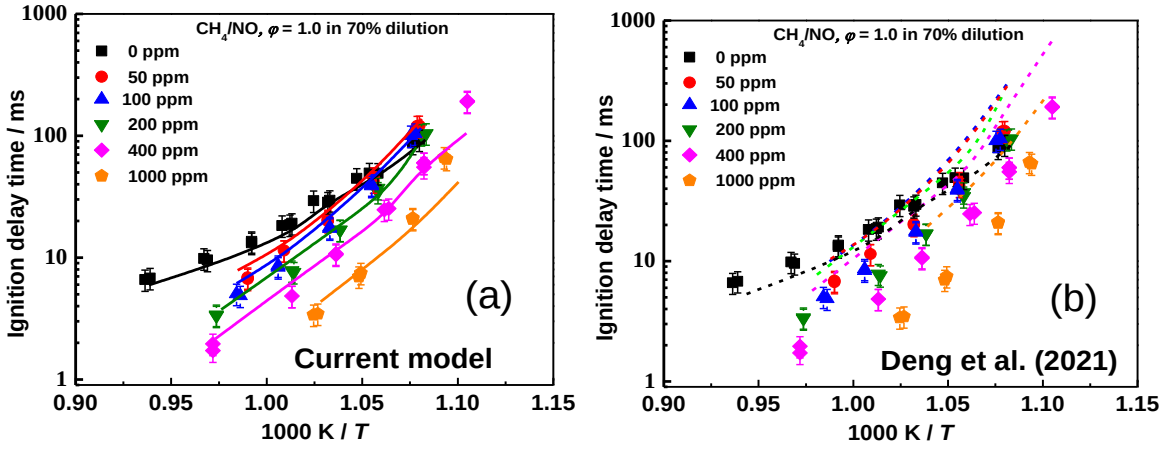

Figure 6-12. Comparison of RCM IDT measurements for CH_4/NO mixtures at φ = 1.0, and p_C = 30 bar [49], with; (a) NUIGMech1.2 IDT prediction; and (b) Deng et al. [26] model prediction.

Figures CS2(b)–CS7(b) in appendix C show that DTU_NOx [47] model over-predicts the IDTs for the RCM experiments especially for high ppm NOx addition levels. Furthermore, Figs. CS2(c)–CS7(c) indicate that the Mevel et al. [23] model under-predicts the IDTs for the fuel/'air' conditions by a factor of 2.5 and over-predicts the IDT data at the 90% dilution conditions by a factor of 4.0 for the 5163 ppm level of NO_2 addition. From Figs. CS2(d)–CS7(d) it is observed that Song et al. [61] model under-predicts the RCM IDT measurements by more than an order of magnitude at low temperatures. Moreover, Figs. CS2(e)–CS7(e) show that Zhang et al. [48] model consistently over-predicts the IDTs measured at low temperatures by a factor of ~2.7.

Figure 6-13 shows a quantitative comparison of the performances of the current model against the five available C_2/NOx models in the literature [23,26,47,48,61] are illustrated following the approach of the recently published CH_4/NOx paper [49]. The comparison was performed using the IDTs measured in the current study together with those from the literature, both from RCM (322 datapoints/31 datasets) and ST (572 datapoints/72 datasets) facilities. The error analysis has been conducted following the method described by Olm et al. [65] and the overall error function value is calculated using equations (6-1) and (6-2) below,

$$E_i = \frac{1}{N_i}\sum_{j=1}^{N_i}\left(\frac{\left(Y_{ij}^{sim} - Y_{ij}^{expt}\right)}{\sigma(Y_{ij}^{expt})}\right)^2 \quad (6\text{-}1)$$

$$E = \frac{1}{N}\sum_{i=1}^{N} E_i \quad (6\text{-}2)$$

where, $Y_{ij} = \ln(y_{ij})$. N and N_i represent the total number of datasets and the number of data points in a particular dataset, respectively. y_{ij} represents the j^{th} IDT measurement of i^{th} dataset, and $\sigma(Y_{ij}^{expt})$ represents its standard deviation that includes experimental uncertainty and statistical error.

Figure 6-13 shows a comparison of the average deviations of the different models from the current and various literature ST (solid bars) and RCM (dashed bars) IDT measurements for C_2H_6/NOx mixtures. It is observed that all models predict high temperature IDTs within a 10% error in the ST measurement regime with the lowest errors using NUIGMech1.2 and the Deng et al. [26] model. Moreover, both the current model and the model published by Deng et al. [26] perform better than the models from Mevel et al. [23], Zhang et al. [48], DTU_NOx [47], and Song et al. [61] for the low and intermediate temperature RCM IDT predictions.

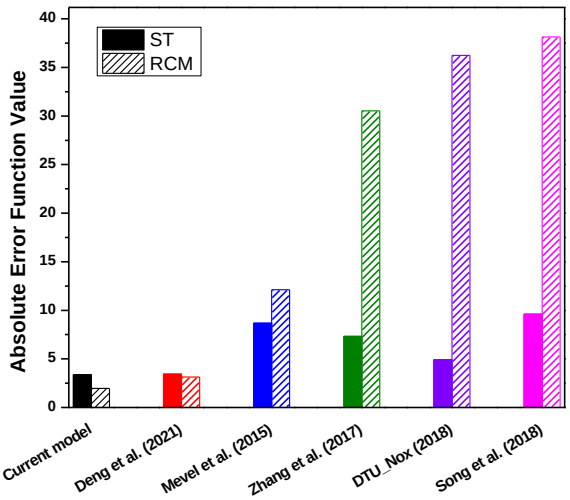

Figure 6-13. Comparison of average deviations of different models from current and literature ST and RCM IDTs experimental measurements for C_2H_6/NOx mixtures.

6.6 Effect of NOx on ethylene and acetylene oxidation

In our effort to develop a comprehensive hydrocarbon/NOx mechanism, NUIGMech1.2 has been developed hierarchically by integrating the $C_1 – C_2$ hydrocarbon and the NOx interaction chemistries. In addition to ethane, NUIGMech1.2 is also assessed against ethylene and acetylene oxidation data available in the literature. Dagaut et al. [56,58] investigated the effect of NO addition to C_2H_4 at atmospheric pressure in a jet-stirred reactor in the temperature range 700 – 1300 K. It was found that the addition of NO promoted C_2H_4 oxidation due to the formation of a large concentration of ȮH radicals via $NO + H\dot{O}_2 \leftrightarrow NO_2 + \dot{O}H$. Figure 6-14 compares the current model predictions with the speciation measurements by Dagaut et al. [56,58] for C_2H_4/NO mixtures at φ = 0.1, 1.0 and 1.5 in the temperature range of 700 – 1300 K at 1 atm pressure. The results show reasonable agreement between the present model and experimentally measured species mole fraction profiles.

Deng et al. [53] recently reported IDT measurements of $C_2H_4/O_2/NO_2$/Ar mixtures with varying levels of NO_2 concentrations relative to the fuel. The experiments showed that the impact of NO_2 is significant at lower temperatures and gradually decreases with increasing temperature. The inclusion of the pressure dependent reaction $\dot{C}_2H_3 + NO_2 (+M) \leftrightarrow C_2H_3NO_2 (+M)$ by analogy with $\dot{C}H_3 + NO_2 (+M) \leftrightarrow CH_3NO_2 (+M)$ and $HOC_2H_4NO_2$ dissociation reactions based on the calculations by Deng et al. [53] are responsible for the ability of NUIGMech1.2 to capture the NO_x sensitization trends on C_2H_4 oxidation as shown in Fig. CS15 of appendix C. The rate constant for $\dot{C}_2H_3 + NO_2 (+M) \leftrightarrow C_2H_3NO_2 (+M)$ used in NUIGmech1.2 has been decreased by 15% compared to that for $\dot{C}H_3 + NO_2 (+M) \leftrightarrow CH_3NO_2 (+M)$ to attain better agreement with the jet-stirred reactor data from Dagaut et al. [56,58]. While the performance of NUIGMech1.2 has improved, it and the Deng et al. mechanism still over-predict the reactivity of the fuel rich C_2H_4/NOx/air mixtures at higher temperatures (Fig. CS15).

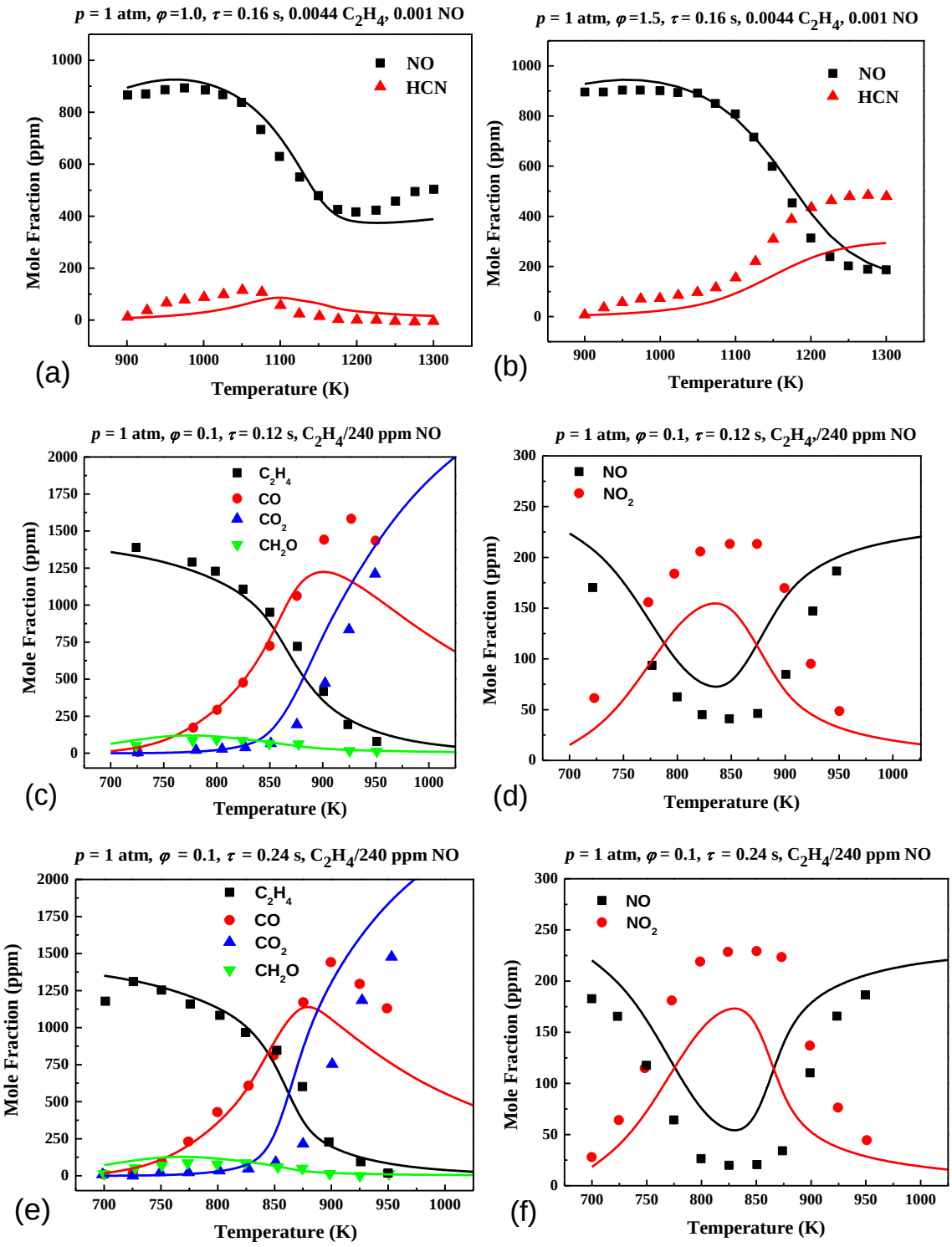

Figure 6-14. Comparisons of NUIGMech1.2 model predictions verses JSR measurements [56,58] of C_2H_4/NO mixtures for; (a) φ = 1.0 and τ = 0.16 s; (b) φ = 1.5 and τ = 0.16 s; (c, and d) φ = 0.1 and τ = 0.12 s; and (e, and f) φ = 1.0 and τ = 0.24 s at 1.0 atm.

There have been very few studies on the interaction of C_2H_2 with NOx added. Only one study by Marshall et al. [54] reported the interaction of C_2H_2/O_2 and NOx in a flow reactor in the intermediate temperature range of 600 – 900 K at 60 bar pressure. Figure 6-15 shows a

comparisons of NUIGMech1.2 predictions of the flow reactor speciation data from Marshall et al. [54] for the oxidation of C_2H_2/500 ppm NO_2 mixtures. Although, NUIGMech1.2 capture the NO_2 sensitization trends on C_2H_2 oxidation it shows faster consumption of C_2H_2 compared to the measurements when 500 ppm of NO_2 is present in the mixture at all equivalence ratio conditions. Comparison of NUIGMech1.2 predictions of C_2H_2 oxidation are provided in Fig. S24 in appendix C and it show reasonable agreement the measurements.

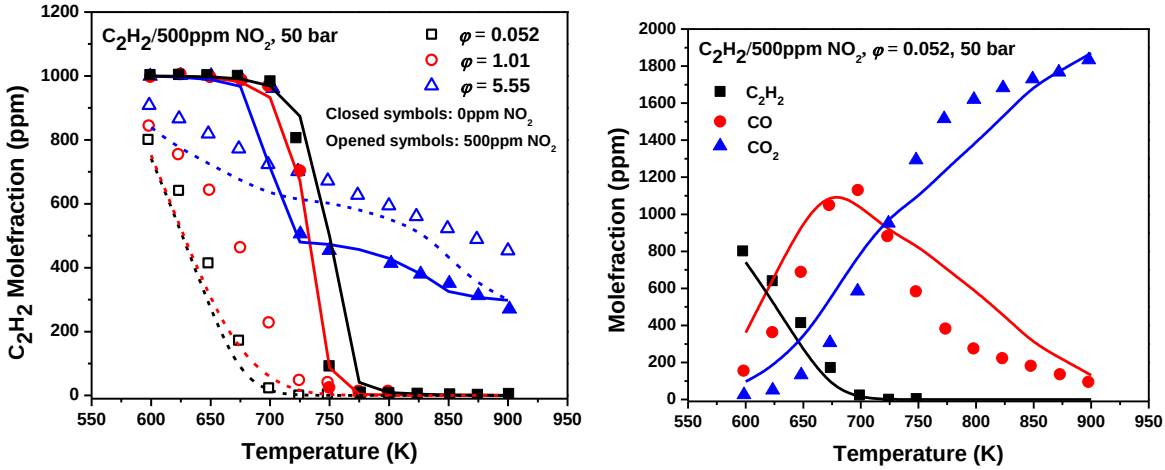

Figure 6-15. Comparisons of NUIGMech1.2 model predictions verses FR measurements [54][56,58] for C_2H_2/ 500 ppm NO_2 mixtures at 50 bar.

While the NOx sensitization impact on C_2H_6 oxidation is well captured by NUIGMech1.2 across a wide range of temperature and pressures conditions, there is still scope to improve the NO_x/C_2H_4 and NO_x/C_2H_2 interaction reactions such as $\dot{R} + NO_2 \leftrightarrow R\dot{O} + NO$ and $\dot{R} + NO_2$ (+M) $\leftrightarrow RNO_2$ (+M). Future studies targeting more experimental measurements and ab-initio calculations focused on NO_x/unsaturated hydrocarbons (C_2H_4 and C_2H_2) interactions is necessary in this regard.

6.7 Conclusions

This study reports new IDTs measurements for C_2H_6/NOx mixtures at combustor relevant conditions. These measurements were performed using the NUI Galway RCM and HPST facilities. The IDTs measurements include C_2H_6/NO, C_2H_6/NO_2, and C_2H_6/N_2O at stoichiometric

air mixtures with NOx blends varying from 0 to 1000 ppm for T_C = 851 – 1390 K and p_C = 20 – 30 bar. Moreover, new IDT measurements for highly diluted C_2H_6/NO_2/air mixtures with 260, 2700, and 5160 ppm blends of NO_2 at φ = 0.5, T_C = 805 – 1038 K, and p_C = 20 – 30 bar conditions were also investigated. NUIGMech1.2 was validated using these IDT data together with available literature data, using an updated NOx sub-chemistry model. The results indicate a minimal promoting effect with the addition of 200 ppm NO or NO_2 to ethane/air mixtures. However, the addition of 1000 ppm of either NO or NO_2 significantly promotes the reactivity of ethane/air mixtures. Moreover, there is no significant change in reactivity observed when N_2O is present in the reactant mixtures. NUIGMech1.2 predicts the sensitisation effect of NOx addition to ethane and methane and is in better agreement with experimental measurements compared to other available literature models over a wide range of pressures, temperatures, equivalence ratios, and dilutions. Sensitivity and flux analyses of C_2H_6/NOx were performed to highlight the key reactions controlling ignition over the different temperature regimes studied. Further experimental measurements and ab-initio calculations studies are necessary to investigate the NO_x/unsaturated hydrocarbons interaction reactions over a wide range of temperature and pressure conditions.

Acknowledgements

The authors would like to acknowledge Science Foundation Ireland for funding via project numbers 15/IA/3177 and 16/SP/3829. We also acknowledge funding from Siemens Energy Canada Ltd.

References

[1] K.K. Botros, G.R. Price, G. Kibrya, Thermodynamic, Environmental and Economic Assessment of Exhaust Gas Recirculation for NOx Reduction in Gas Turbine Based Compressor Station, (1999).

[2] C.N. Pratheeba, P. Aghalayam, Effect of Exhaust Gas Recirculation in NOx Control for Compression Ignition and Homogeneous Charge Compression Ignition Engines, Energy Procedia, 66 (2015) 25–28.

[3] M. Lapuerta, J.J. Hernandez, F. Gimenez, Evaluation of exhaust gas recirculation as a technique for reducing diesel engine NOx emissions, Proc. Inst. Mech. Eng. Part D J. Automob. Eng., 214 (2000) 85–93.

[4] S. Faramawy, T. Zaki, A.A.E. Sakr, Natural gas origin, composition, and processing: A review, J. Nat. Gas Sci. Eng., 34 (2016) 34–54.

[5] L.J. Spadaccini, M.B. Colket, Ignition delay characteristics of methane fuels, Prog. Energy Combust. Sci., 20 (1994) 431–460.

[6] P. Dagaut, M. Cathonnet, J. Boettner, Kinetics of ethane oxidation, Int. J. Chem. Kinet., 23 (1991) 437–455.

[7] T.B. Hunter, T.A. Litzinger, H. Wang, M. Frenklach, Ethane oxidation at elevated pressures in the intermediate temperature regime: Experiments and modeling, Combust. Flame, 104 (1996) 505–523.

[8] C.J. Aul, W.K. Metcalfe, S.M. Burke, H.J. Curran, E.L. Petersen, Ignition and kinetic modeling of methane and ethane fuel blends with oxygen: A design of experiments approach, Combust. Flame, 160 (2013) 1153–1167.

[9] H. Hashemi, J.G. Jacobsen, C.T. Rasmussen, J.M. Christensen, P. Glarborg, S. Gersen, M. van Essen, H.B. Levinsky, S.J. Klippenstein, High-pressure oxidation of ethane, Combust. Flame, 182 (2017) 150–166.

[10] M. Baigmohammadi, V. Patel, S. Martinez, S. Panigrahy, A. Ramalingam, U. Burke, K.P. Somers, K.A. Heufer, A. Pekalski, H.J. Curran, A Comprehensive Experimental and Simulation Study of Ignition Delay Time Characteristics of Single Fuel C_1–C_2 Hydrocarbons over a Wide Range of Temperatures, Pressures, Equivalence Ratios, and Dilutions, Energy Fuels, 34 (2020) 3755–3771.

[11] P. Dagaut, M. Cathonnet, J.-C. Boettner, A Kinetic Modeling Study of Propene Oxidation in JSR and Flame, Combust. Sci. Technol., 83 (1992) 167–185.

[12] P.F. Nelson, B.S. Haynes, Hydrocarbon-NOx interactions at low temperatures—1.Conversion of NO to NO_2 promoted by propane and the formation of HNCO, 25th Intl. Symp. Combust., (1994) 1003–1010.

[13] P. Dagaut, J. Luche, M. Cathonnet, Experimental and kinetic modeling of the reduction of NO by propene at 1 atm, Combust. Flame, 121 (2000) 651–661.

[14] P. Dagaut, J. Luche, M. Cathonnet, Reduction of NO by propane in a JSR at 1atm: experimental and kinetic modeling, Fuel, 80 (2001) 979–986.

[15] M. Hori, Y. Koshiishi, N. Matsunaga, P. Glaude, N. Marinov, Temperature dependence of NO to NO_2 conversion by n-butane and n-pentane oxidation, Proc. Combust. Inst., 29 (2002) 2219–2226.

[16] P.A. Glaude, N. Marinov, Y. Koshiishi, N. Matsunaga, M. Hori, Kinetic Modeling of the

Mutual Oxidation of NO and Larger Alkanes at Low Temperature, Energy Fuels, 19 (2005) 1839–1849.

[17] P. Dagaut, F. Lecomte, J. Mieritz, P. Glarborg, Experimental and kinetic modeling study of the effect of NO and SO_2 on the oxidation of CO-H_2 mixtures, Int. J. Chem. Kinet., 35 (2003) 564–575.

[18] D.A. Knyazkov, A.G. Shmakov, I. V Dyakov, O.P. Korobeinichev, J. De Ruyck, A.A. Konnov, Formation and destruction of nitric oxide in methane flames doped with NO at atmospheric pressure, Proc. Combust. Inst., 32 (2009) 327–334.

[19] S. Gersen, A. V Mokhov, J.H. Darmeveil, H.B. Levinsky, P. Glarborg, Ignition-promoting effect of NO2 on methane, ethane and methane/ethane mixtures in a rapid compression machine, Proc. Combust. Inst., 33 (2011) 433–440.

[20] J. Herzler, C. Naumann, Shock Tube Study of the Influence of NOx on the Ignition Delay Times of Natural Gas at High Pressure, Combust. Sci. Technol., 184 (2012) 1635–1650.

[21] O. Mathieu, A. Levacque, E.L. Petersen, Effects of NO_2 addition on hydrogen ignition behind reflected shock waves, Proc. Combust. Inst., 34 (2013) 633–640.

[22] O. Mathieu, J.M. Pemelton, G. Bourque, E.L. Petersen, Shock-induced ignition of methane sensitized by NO_2 and N_2O, Combust. Flame, 162 (2015) 3053–3070.

[23] R. Mével, J.E. Shepherd, Ignition delay-time behind reflected shock waves of small hydrocarbons–nitrous oxide(–oxygen) mixtures, Shock Waves, 25 (2015) 217–229.

[24] F.E. Alam, F.M. Haas, T.I. Farouk, F.L. Dryer, Influence of Trace Nitrogen Oxides on Natural Gas Oxidation: Flow Reactor Measurements and Kinetic Modeling, Energy Fuels, 31 (2017) 2360–2369.

[25] D. Fuquan, Z. Ningbo, W. Yingtao, Y. Jialong, T. Chenglong, L. Zhiming, Z. Hongtao, H. Zuohua, Experimental and Kinetic Study of the Promoting Effect of Nitrogen Dioxide on Ethane Autoignition in a Rapid Compression Machine, Energy Fuels, 34 (2020) 7509–7521.

[26] F. Deng, H. Xu, X. Liu, Y. Wu, H. Zheng, Z. Li, Effect of nitrogen dioxide addition on ethane auto-ignition at different pressures and equivalence ratios: Experiments and chemical kinetic modeling, Fuel, 285 (2021) 119042.

[27] M.D. Johnson, S. Korcek, Effects of NOx on liquid phase oxidation and inhibition at elevated temperatures, Lubr. Sci., 3 (1991) 95–118.

[28] J.C.G. Andrae, Kinetic Modeling of the Influence of NO on the Combustion Phasing of Gasoline Surrogate Fuels in an HCCI Engine, Energy Fuels, 27 (2013) 7098–7107.

[29] H. Zhao, A.G. Dana, Z. Zhang, W.H. Green, Y. Ju, Experimental and modeling study of the mutual oxidation of N-pentane and nitrogen dioxide at low and high temperatures in a jet stirred reactor, Energy, 165 (2018) 727–738.

[30] H. Zhao, L. Wu, C. Patrick, Z. Zhang, Y. Rezgui, X. Yang, G. Wysocki, Y. Ju, Studies of low temperature oxidation of n-pentane with nitric oxide addition in a jet stirred reactor, Combust. Flame, 197 (2018) 78–87.

[31] P. Dagaut, F. Lecomte, S. Chevailler, M. Cathonnet, Experimental and Detailed Kinetic Modeling of Nitric Oxide Reduction by a Natural Gas Blend in Simulated Reburning Conditions, Combust. Sci. Technol., 139 (1998) 329–363.

[32] A.A. Konnov, F.J. Barnes, J.H. Bromly, J.N. Zhu, D. Zhang, The pseudo-catalytic promotion of nitric oxide oxidation by ethane at low temperatures, Combust. Flame, 141

(2005) 191–199.
[33] X. Zhang, W. Ye, J.C. Shi, X.J. Wu, R.T. Zhang, S.N. Luo, Shock-Induced Ignition of Methane, Ethane, and Methane/Ethane Mixtures Sensitized by NO_2, Energy Fuels, 31 (2017) 12780–12790.
[34] D. Fuquan, P. Youshun, S. Wuchuan, Y. Feiyu, Z. Yingjia, H. Zuohua, An ignition delay time and chemical kinetic study of ethane sensitized by nitrogen dioxide, Fuel, 207 (2017) 389–401.
[35] W.S. Affleck, A. Thomas, An Opposed Piston Rapid Compression Machine for Preflame Reaction Studies, Proc. Inst. Mech. Eng., 183 (1968) 365–387.
[36] J. Würmel, J.M. Simmie, CFD studies of a twin-piston rapid compression machine, Combust. Flame, 141 (2005) 417–430.
[37] C. Morley, Gaseq program, (n.d.). http://www.gaseq.co.uk (accessed September 29, 2017).
[38] W.A. Glasson, C.S. Tuesday, The Atmospheric Thermal Oxidation of Nitric Oxide, J. Am. Chem. Soc., 85 (1963) 2901–2904.
[39] S. Panigrahy, J. Liang, S.S. Nagaraja, Z. Zuo, G. Kim, S. Dong, G. Kukkadapu, W.J. Pitz, S.S. Vasu, H.J. Curran, A comprehensive experimental and improved kinetic modeling study on the pyrolysis and oxidation of propyne, Proc. Combust. Inst., 38 (2021) 479–488.
[40] S.S. Nagaraja, J. Power, G. Kukkadapu, S. Dong, S.W. Wagnon, W.J. Pitz, H.J. Curran, A single pulse shock tube study of pentene isomer pyrolysis, Proc. Combust. Inst., 38 (2021) 881–889.
[41] S. Dong, K. Zhang, P.K. Senecal, G. Kukkadapu, S.W. Wagnon, S. Barrett, N. Lokachari, S. Panigaphy, W.J. Pitz, H.J. Curran, A comparative reactivity study of 1-alkene fuels from ethylene to 1-heptene, Proc. Combust. Inst., 38 (2021) 611–619.
[42] S.S. Nagaraja, J. Liang, S. Dong, S. Panigrahy, A. Sahu, G. Kukkadapu, S.W. Wagnon, W.J. Pitz, H.J. Curran, A hierarchical single-pulse shock tube pyrolysis study of C_2–C_6 1-alkenes, Combust. Flame, 219 (2020) 456–466.
[43] M. Baigmohammadi, V. Patel, S. Nagaraja, A. Ramalingam, S. Martinez, S. Panigrahy, A.A.E.-S. Mohamed, K.P. Somers, U. Burke, K.A. Heufer, A. Pekalski, H.J. Curran, Comprehensive Experimental and Simulation Study of the Ignition Delay Time Characteristics of Binary Blended Methane, Ethane, and Ethylene over a Wide Range of Temperature, Pressure, Equivalence Ratio, and Dilution, Energy Fuels, 34 (2020) 8808–8823.
[44] S. Martinez, M. Baigmohammadi, V. Patel, S. Panigrahy, A.B. Sahu, S.S. Nagaraja, A. Ramalingam, A.A.E.S. Mohamed, K.P. Somers, K.A. Heufer, A. Pekalski, H.J. Curran, An experimental and kinetic modeling study of the ignition delay characteristics of binary blends of ethane/propane and ethylene/propane in multiple shock tubes and rapid compression machines over a wide range of temperature, pressure, equivalence ratio, , Combust. Flame, 228 (2021) 401–414.
[45] A.A.E.-S. Mohamed, S. Panigrahy, A.B. Sahu, G. Bourque, H. Curran, An experimental and kinetic modeling study of the auto-ignition of natural gas blends containing C_1–C_7 alkanes, Proc. Combust. Inst. 38 (2021) 365–373.
[46] A.B. Sahu, A.A.E.-S. Mohamed, S. Panigrahy, G. Bourque, H. Curran, Ignition Studies of C_1–C_7 Natural Gas Blends at Gas-Turbine-Relevant Conditions, J. Eng. Gas Turbines

Power, 143(8) (2021) 081022 (7 pages).
[47] P. Glarborg, J.A. Miller, B. Ruscic, S.J. Klippenstein, Modeling nitrogen chemistry in combustion, Prog. Energy Combust. Sci., 67 (2018) 31–68.
[48] Y. Zhang, O. Mathieu, E.L. Petersen, G. Bourque, H.J. Curran, Assessing the predictions of a NOx kinetic mechanism on recent hydrogen and syngas experimental data, Combust. Flame, 182 (2017) 122–141.
[49] A.B. Sahu, A.A.E.-S. Mohamed, S. Panigrahy, C. Saggese, V. Patel, G. Bourque, W.J. Pitz, H.J. Curran, An experimental and kinetic modeling study of NOx sensitization on methane autoignition and oxidation, Combust. Flame, (2021) 111746.
[50] J. Bugler, K.P. Somers, J.M. Simmie, F. Güthe, H.J. Curran, Modeling Nitrogen Species as Pollutants: Thermochemical Influences, J. Phys. Chem. A, 120 (2016) 7192–7197.
[51] E. Hu, Y. Chen, Z. Zhang, X. Li, Y. Cheng, Z. Huang, Experimental Study on Ethane Ignition Delay Times and Evaluation of Chemical Kinetic Models, Energy Fuels, 29 (2015) 4557–4566.
[52] J. Gimenez-Lopez, C.T. Rasmussen, H. Hashemi, M.U. Alzueta, Y. Gao, P. Marshall, C.F. Goldsmith, P. Glarborg, Experimental and Kinetic Modeling Study of C_2H_2 Oxidation at High Pressure, Int. J. Chem. Kinet., 48 (2016) 724–738.
[53] F. Deng, Y. Zhang, W. Sun, W. Huang, Q. Zhao, X. Qin, F. Yang, Z. Huang, Towards a kinetic understanding of the NOx sensitization effect on unsaturation hydrocarbons: A case study of ethylene/nitrogen dioxide mixtures, Proc. Combust. Inst. 37(1) (2019) 719–726.
[54] P. Marshall, C. Leung, J. Gimenez-Lopez, C.T. Rasmussen, H. Hashemi, P. Glarborg, M. Abian, M.U. Alzueta, The C_2H_2 + NO_2 reaction: Implications for high pressure oxidation of C2H2/NOx mixtures, Proc. Combust. Inst., 37(1) (2019) 469–476.
[55] P. Glarborg, M.U. Alzueta, K. Dam-Johansen, J.A. Miller, Kinetic Modeling of Hydrocarbon/Nitric Oxide Interactions in a Flow Reactor, Combust. Flame, 115 (1998) 1–27.
[56] P. Dagaut, F. Lecomte, S. Chevailler, M. Cathonnet, The reduction of NO by ethylene in a jet-stirred reactor at 1 atm: experimental and kinetic modelling, Combust. Flame, 119 (1999) 494–504.
[57] F. Lecomte, P. Dagaut, S. Chevailler, M. Cathonnet, NO-Reduction by Ethane in a JSR at Atmospheric Pressure: Experimental and Kinetic Modeling, Combust. Sci. Technol., 150 (2000) 181–203.
[58] P. Dagaut, O. Mathieu, A. Nicolle, G. Dayma, Experimental study and detailed kinetic modeling of the mutual sensitization of the oxidation of nitric oxide, ethylene, and ethane, Combust. Sci. Technol., 177 (2005) 1767–1791.
[59] J. Giménez-López, M.U. Alzueta, C.T. Rasmussen, P. Marshall, P. Glarborg, High pressure oxidation of C_2H_4/NO mixtures, Proc. Combust. Inst., 33 (2011) 449–457.
[60] J. Giménez-López, A. Millera, R. Bilbao, M.U. Alzueta, Experimental and kinetic modeling study of the oxy-fuel oxidation of natural gas, CH_4 and C_2H_6, Fuel, 160 (2015) 404–412.
[61] Y. Song, L. Marrodán, N. Vin, O. Herbinet, E. Assaf, C. Fittschen, A. Stagni, T. Faravelli, M.U. Alzueta, F. Battin-Leclerc, The sensitizing effects of NO_2 and NO on methane low temperature oxidation in a jet stirred reactor, Proc. Combust. Inst. 37(1) (2019) 667–675.
[62] R. CHEMKIN-PRO, 15112, Reaction Design, Inc., San Diego, CA. (2011).

[63] J. Chai, C.F. Goldsmith, Rate coefficients for fuel+NO_2: Predictive kinetics for HONO and HNO_2 formation, Proc. Combust. Inst., 36 (2017) 617–626.

[64] A. Matsugi, H. Shiina, Thermal Decomposition of Nitromethane and Reaction between CH_3 and NO_2, J. Phys. Chem. A, 121 (2017) 4218–4224.

[65] C. Olm, I.G. Zsély, R. Pálvölgyi, T. Varga, T. Nagy, H.J. Curran, T. Turányi, Comparison of the performance of several recent hydrogen combustion mechanisms, Combust. Flame, 161 (2014) 2219–2234.

CHAPTER 7

COMPREHENSIVE EXPERIMENTAL AND SIMULATION STUDY OF THE IGNITION DELAY TIME CHARACTERISTICS OF BINARY BLENDED METHANE, ETHANE, AND ETHYLENE OVER A WIDE RANGE OF TEMPERATURE, PRESSURE, EQUIVALENCE RATIO, AND DILUTION

Chapter 7: Comprehensive Experimental and Simulation Study of the Ignition Delay Time Characteristics of Binary Blended Methane, Ethane, and Ethylene over a Wide Range of Temperature, Pressure, Equivalence Ratio, and Dilution

Published in: Energy and Fuels, Volume 34, Issue 7, July 2020, Pages 8808–8823.
DOI: https://doi.org/10.1021/acs.energyfuels.0c00960

Authors and Contributions

1) **Mohammadreza Baigmohammadi** (National University of Ireland, Galway, Ireland)
Contribution: High pressure shock tube experiments and manuscript preparation.
2) **Vaibhav Patel** (National University of Ireland, Galway, Ireland)
Contribution: RCM experiments
3) **Shashank S. Nagaraja** (National University of Ireland, Galway, Ireland)
Contribution: Low pressure shock tube experiments.
4) **Ajoy Ramalingam** (PCFC, RWTH Aachen, Germany)
Contribution: RCM experiments.
5) **Sergio Martinez** (National University of Ireland, Galway, Ireland)
Contribution: Chemical kinetic modelling.
6) **Snehasish Panigrahy** (National University of Ireland, Galway, Ireland)
Contribution: Chemical kinetic modelling.
7) **Ahmed Abd El-Sabor Mohamed** (National University of Ireland, Galway, Ireland)
Contribution: RCM experiments.
8) **Kieran P. Somers** (National University of Ireland, Galway, Ireland)
Contribution: Chemical kinetic modelling.
9) **Ultan Burke** (National University of Ireland, Galway, Ireland)
Contribution: Chemical kinetic modelling.
10) **Karl A. Heufer** (PCFC, RWTH Aachen, Germany)
Contribution: Project management and manuscript review.
11) **Andrzej Pekalski** (Shell research limited, Shell Centre London)
Contribution: Project management and manuscript review.
12) **Henry J. Curran** (National University of Ireland, Galway, Ireland)
Contribution: Project management and manuscript review.

Abstract

A comprehensive experimental and kinetic modelling study of the ignition delay time (IDT) characteristics of some binary–blends of C_1–C_2 gaseous hydrocarbons such as methane/ethylene, methane/ethane, and ethane/ethylene were performed over a wide range of composition (90%/10%, 70%/30%, 50%/50%), temperature (~800–2000 K), pressure (~1–40 bar), equivalence ratio (~0.5–2.0), and dilution (~75–90%). An extensive literature review was conducted, and available data were extracted to create a comprehensive database for our simulations. Based on existing literature data, an experimental matrix was designed using the Taguchi approach (L_9) in order to identify and complete the experimental matrix required to generate a comprehensive experimental IDT set necessary for the validation of a chemical kinetic model. The required high- and low-temperature IDTs were collected using low/high-pressure shock tubes and rapid compression machines, respectively. The predictions of NUIGMech1.0 are examined versus all of the available experimental data, including those taken in the current study using the IDT simulations and a correlation technique. Moreover, the individual effect of the studied parameters, including mixture composition, pressure, equivalence ratio, and dilution on IDT is investigated over the studied temperature range. Correlations that were developed based on NUIGMech1.0 are presented for each specific blended fuel over the conditions studied. These correlations show an acceptable performance versus the experimental data.

Keywords: methane, ethane, ethylene, shock tube, RCM, ignition delay time.

7.1 Introduction

Explaining the pyrolysis and/or oxidation processes of heavy and complex hydrocarbon fuels depends on the development of high-fidelity chemical mechanisms. In this regard, understanding the pyrolysis and/or oxidation processes of small (C_1–C_2) hydrocarbons are important because of

their crucial role in kinetic behavior at the end chain of the pyrolysis and/or oxidation processes of larger hydrocarbons. Therefore, developing a high-fidelity chemical mechanism that can precisely explain the pyrolysis and/or oxidation processes of small hydrocarbons is very desirable in terms of explaining conditions relevant to industrial burners, gas turbines, and internal combustion engines. Ignition delay time (IDT) is a criterion extensively used to validate chemical mechanisms, and it is often used for comparing various chemical mechanisms and developing new ones. To do so, a comprehensive IDT database is required as a prerequisite so that mechanisms can be tested and validated. Therefore, an extensive literature review was performed, and available IDTs for binary-fuel mixtures of methane/ethylene [1], methane/ethane [2–11], and ethane/ethylene were extracted and stored, as shown in Figure 7-1. It can be seen that, although there is sufficient IDT data in the literature for methane/ethane (alkane–alkane) mixtures, there is no comprehensive data for alkane/alkene mixtures including methane/ethylene and ethane/ethylene over a wide range of pressures, temperatures, equivalence ratios, and dilution (squares in Figure 7-1). Therefore, new experimental tests were defined for targeted binary-fuel mixtures (alkane/alkene) + O_2 + N_2 + Ar (spheres in Figure 7-1) to encapsulate a wide range of temperature, pressure, equivalence ratio, alkane ratio, and dilution.

It is believed that conducting the required experiments under the compressed pressure range of ~1–40 bar and also the compressed temperature range of ~800–2000 K from fuel-lean to fuel-rich conditions and at different levels of dilution, and with different alkene concentrations may disclose data which could not be interpreted from the available literature. Thus, we aim to present a comprehensive chemical mechanism that can precisely reproduce the experimental IDTs of various binary-fuel C_1–C_2 mixtures over a wide range of operating conditions. In the present study, the Taguchi (Design of Experiments) method was applied to optimize the number of required experiments.

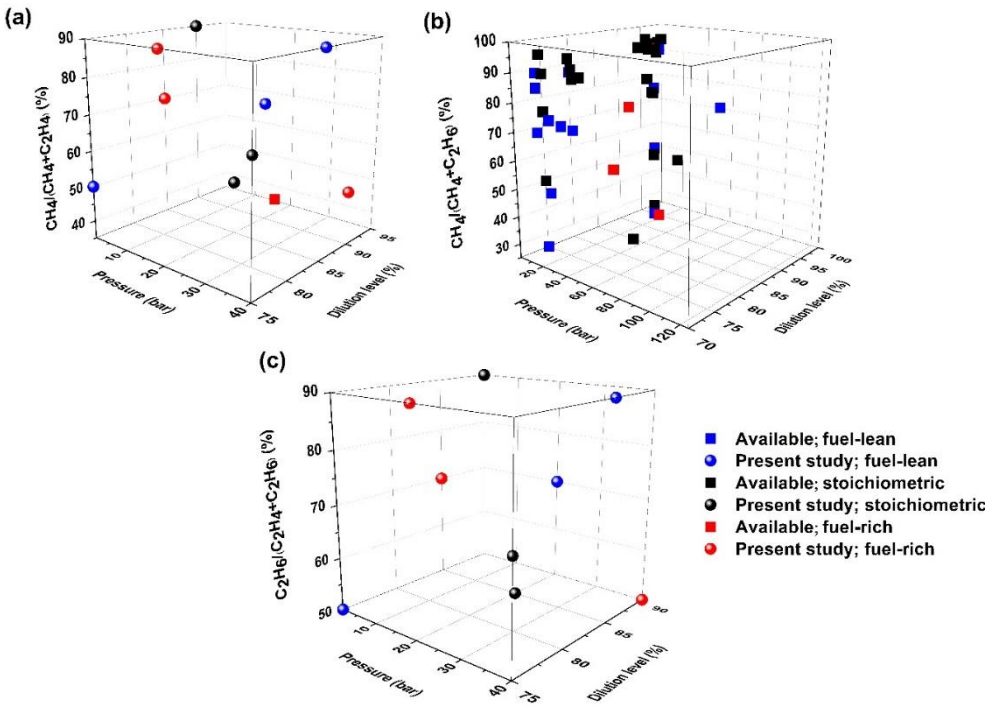

Figure 7-1. Extracted data from the studied literature (squares); new experimental tests defined in the current study (spheres); Blue-spheres/squares: fuel-lean mixtures; Black-spheres/squares: stoichiometric mixtures; Red-spheres/squares: fuel-rich mixtures.

7.2 Design of experiments and experimental approach

The experiments were designed using an L_9 Taguchi matrix [12] for four parameters of ethylene concentration, pressure, equivalence ratio, and dilution. This approach is analogous to previous work by Baigmohammadi et al. [13], and details can be found there. In this current study, alkanes (methane and ethane) are the abundant components, so that the presence of the alkene (ethylene) in a mixture is defined as: $\left[1-\left(\frac{mole\ fraction|_{Alkane}}{mole\ fraction|_{Fuel}}\right)\right]\times 100\%$, which is varied from 10–50%. Also, the diluents (N_2 and Ar) concentrations are varied from 75% to 90% of the reactive mixtures. Three equivalence ratios, 0.5, 1.0, and 2.0, and three compressed mixture pressures (p_5, p_C), namely 1, 20, and 40 were selected to cover the proposed cubes presented in Figures 7-1(a) and (c). Besides, the compressed temperature (T_5, T_C) range was varied from ~800–2000 K based on the defined cases and the viability of the applied instruments in measuring IDTs with acceptable accuracy.

Mixture IDTs of the defined mixtures and conditions presented in Table 7-1 were measured using low/high-pressure shock tubes (L/HPST) and rapid compression machines (RCMs) all at NUI Galway in the low- and high-temperature regimes, respectively. However, some low-temperature IDTs (RCM; P8C3,4,8 in Table 7-1) were measured in collaboration with the Physico-Chemical Fundamentals of Combustion (PCFC) group of RWTH Aachen University to increase the fidelity of the database and to ensure that they are facility independent. The physical performance of the facilities are well known and have been extensively discussed previously [10,11,14–19]. However, a summary of the facility characteristics and exemplary pressure traces are provided in appendix D (Sections 2–6).

As seen in Figure 7-1(b), sufficient available IDT data exists in the literature for methane/ethane mixtures precluding the need for more experiments. As presented in Table 7-1, a unique code has been assigned to each experiment. It should be noted that the presented data in this paper is a part of a larger project (3 of 12; phases (P): 5, 6, and 8) so that, for better handling of the data, we have been using a common description for the applied mixtures and conditions throughout the papers. In this regard, “Px” refers to the fuel blends, which is “P5: methane/ethylene”, “P6: methane/ethane”, and “P8: ethane/ethylene”, respectively. Also, the “C” notation refers to the studied conditions, which change from 1 to 9 in accordance with changes in fuel composition, pressure, equivalence ratio, and dilution.

7.2.1 Set-up and procedure

The current study is categorized into six different stages; 1: an extensive literature review; 2: database development; 3: simulating the available literature data using NUIGMech1.0; 4: defining new experimental tests using an L9 Taguchi matrix; 5: conducting the RCM and L/HPST experiments; 6: modelling the new experimental results with NUIGMech1.0. To make the study more concise, comprehensive Supplementary material files are provided in support of

the data presented in the main manuscript. The supplementary files include non-reactive RCM traces, the original spreadsheets of the experimental tests, L/HPST oscilloscope traces are presented on the online version of the paper, and the combined figures of reactive, non-reactive, and simulation pressure traces are shown in appendix D. Furthermore, all of the general information related to the applied gases (fuel/oxygen/argon/nitrogen), the applied facilities are presented in appendix D, and data acquisition systems to collect the IDTs are provided as supplementary material of the online version of the paper.

Table 7-1. Test conditions defined in the current study.

No	Code	Mixture composition (mole fraction)					φ	T (K)	p (bar)	*Ref.*
		CH_4	C_2H_4	C_2H_6	O_2	N_2+Ar				
1	P5C1	0.02083	0.02083	0	0.2083	0.75+0.0	0.5	1167–2024	1	*This study:* NUIG ST and RCM
2	P5C2	0.02143	0.02143	0	0.1071	0.85	1.0	923–1546	20	
3	P5C3	0.0222	0.0222	0	0.0555	0.90	2.0	869–1745	40	
4	P5C4	0.05303	0.02273	0	0.17424	0.75	1.0	845–1465	40	
5	P5C5	0.0488	0.0209	0	0.0802	0.75+0.10	2.0	1471–2022	1	
6	P5C6	0.0125	0.0054	0	0.082	0.90	0.5	995–1783	20	
7	P5C7	0.10976	0.0122	0	0.12805	0.75	2.0	947–1840	20	
8	P5C8	0.02596	0.00288	0	0.12115	0.85	0.5	921–1738	40	
9	P5C9	0.029	0.0032	0	0.0677	0.75+0.15	1.0	1570–2082	1	
10	P6C1	0.0015	0	0.0015	0.0017	0.0+0.98	0.5	1248–1571	1.46	Aul et al. [9]
11	P6C2	0.0067	0	0.0067	0.0367	0.0+0.95	1.0	1190–1377	32.02	
12	P6C3	0.0316	0	0.0316	0.0868	0.0+0.85	2.0	1094–1366	15.44	
13	P6C4	0.0091	0	0.0273	0.1136	0.0+0.85	1.0	1166–1266	31.42	
14	P6C5	0.0514	0	0.0171	0.0814	0.0+0.85	2.0	1143–1513	29.03	
15	P6C6	0.0228	0	0.0123	0.2015	0.7574+0.0	0.5	1091–1437	22.26	Petersen et al. [5]
							0.6	848–883	9.62	Beerer and McDonell [8]
16	P6C7	0.0419	0	0.0047	0.2003	0.7531+0.0	0.5	1155–1532	22.71	Petersen et al. [5]
17	P6C8	0.0801	0	0.0089	0.1913	0.7197+0.0	1.0	911–1221	40	Huang and Bushe [3]
		0.0766	0	0.0085	0.1830	0.3+0.432		909–1038		Gersen et al.[7]
18	P6C9	0.0012	0	0.0036	0.0152	0.0+0.98	1.0	1324–1700	1.36	Aul et al. [9]
19	P8C1	0	0.0167	0.0167	0.2167	0.75+0.0	0.5	1153–1862	1	*This study:* NUIG ST and RCM
20	P8C2	0	0.01765	0.01765	0.11471	0.85	1.0	901–1452	20	
21	P8C3	0	0.0190	0.0190	0.0619	0.90	2.0	892–1540	40	*This study:* NUIG (ST) & RWTH Aachen (RCM)
22	P8C4	0	0.01724	0.04023	0.19253	0.75	1.0	1106–1411	40	*This study:* NUIG (ST)
								902–971	30	*This study:* RWTH Aachen (RCM)
23	P8C5	0	0.0168	0.0392	0.0939	0.75+0.10	2.0	1252–1870	1	*This study:* NUIG ST and RCM
24	P8C6	0	0.0039	0.0091	0.087	0.90	0.5	958–1503	20	
25	P8C7	0	0.0092	0.0826	0.1583	0.75	2.0	892–1520	20	
26	P8C8	0	0.0019	0.0171	0.1310	0.85	0.5	933–1446	40	*This study:* NUIG (ST) & RWTH Aachen (RCM)
27	P8C9	0	0.0022	0.0202	0.0775	0.75+0.15	1.0	1250–1930	1	*This study:* NUIG (ST)

7.2.2 Uncertainty analysis

To increase the fidelity of the results, a comprehensive uncertainty analysis was conducted using the data taken in both our L/HPST and RCM and is briefly discussed here. The uncertainty analysis was developed based on studies conducted by Petersen et al. [20] and Weber et al. [21]. In this regard, the average uncertainties in the compressed mixture temperatures (T_C or T_5) and measured IDTs in STs and RCM are summarized in Table 7-2. Details of this analysis are provided in appendix D (Section 7).

Table 7-2. Average uncertainties for compressed mixture temperature (T_C or T_5) and measured IDTs.

Facility	$\sigma_{T_{C,5}}$ (K)	σ_{IDT} (%)
NUIG–L/HPST	± 30/20	± 25
NUIG–RCM	± 10	± 20
PCFC–RCM [11]	± 5	

According to the literature, [20,22,23] and also the conditions studied here, values of ± 30/20 K (L/HPST), ± 5–15 K (RCM), and ± 25% (L/HPST) and 20% (RCM) are estimated as the average uncertainties for both the end of compression temperature (T_C) and the measured IDTs, respectively.

7.3 Computational modelling

Simulations were conducted using NUIGMech1.0 to simulate the experimental targets. This is a modified version of NUIGMech0.9 [13] for higher hydrocarbons up to C_8 and aromatics. In this regard, the experimental data were simulated using a Python script based on the CANTERA [24] library (ST simulations) and also CHEMKIN-Pro 18.2 [25] software (RCM simulations). As already comprehensively discussed in the literature [22,23], although the simulations in the ST operating regimes are performed using the constant volume reactor model, the RCM simulations are performed using the effective volume approach by imposing a heat loss boundary condition

on the calculations due to facility effects, including heat losses, during compression and in the post-compression zone of the reaction chamber [11,14,26].

7.4 Results and discussions

All experimental results related to the studied conditions in Table 7-1, whether taken from the literature or from the present study, are presented in the following figures in accordance to the applied fuels (methane/ethylene, methane/ethane, and ethane/ethylene) and the wide range of operating conditions examined.

7.4.1 General performance of the NUIG mechanism and the correlations versus experimental data

The performance of NUIGMech1.0 versus all experimental available IDT data is shown in Figures (7-2) – (7-4). The symbols refer to the experimental data; however, the square symbols with a cross through them demonstrate experimental data affected by pre-ignition or facility effects. The solid black line refers to NUIGMech1.0 predictions and the dashed lines refers to the correlation predictions which will be discussed in detail in Section 7.4.3.

Figures (7-2) – (7-4) show that NUIGMech1.0 predicts the methane/ethylene, methane/ethane, and ethane/ethylene binary-fuel blend IDT measurements very well over the wide range of conditions studied (φ: 0.5–2.0, T: ~830–2100 K, p: 1–40 bar, 9 different compositions, and dilution: 75–90%). However, there is a deviation between the simulations and experimental data in Figures 7-3(h) and 7-4(d). Figure 7-4(d) illustrates that the experimental data are affected by the facility's boundary conditions in the temperature range 900–1050 K at p = 40 bar. These data suffer from pre–ignition events that occur behind the reflected shock in the NUIG–HPST. This pre-ignition was observed even on cleaning the shock tube after each experiment. The same phenomenon occurred for the same mixture at 40 bar in the low-temperature regime in the PCFC–RCM. In both cases, pre-ignition appeared as a gradual increase in pressure before the

main ignition, shortening the overall IDT. In the case of the RCM, some deposits have been observed on the reactor endwall, which may induce the pre-ignition. However, these deposits were only present for the 40 bar experiments so that they and related pre-ignitions were suppressed by reducing the compressed pressure to 30 bar. Similarly, it might be inferred that the experimental data presented in Figure 7-3(h) (Figure DS34) may suffer from a kind of pre–ignition (specifically in [7] due to the very short reported IDTs of < 3 ms) in the intermediate-to-low temperature regime in [3] and at 1000–1050 K in [7]. Comparing the conditions presented in Figures 7-3(h) and 7-4(d), it is interesting to note that ethane is the common fuel component in the mixtures, and the common conditions are 40 bar and 75% dilution. Therefore, it may be concluded that this undesirable effect stems from the presence of ethane in the blends at 40 bar and at fuel/air conditions (~71–75% dilution). Although it is known that ethylene and ethane are more reactive fuels compared to methane, the individual effect and portion of each studied parameter on the reactivity of the mixtures cannot be understood directly from Figures (7-2) – (7-4) as too many parameters, e.g. binary fuel combination, pressure, equivalence ratio, and dilution, are all changing at once. Thus, the individual and combined effects of the studied parameters on IDTs of the studied methane/ethylene and ethane/ethylene mixtures are considered below.

Furthermore, comprehensive comparisons of IDT, laminar burning velocities (LBVs), and speciation plots shown in appendix D (Figures DS26–38 in Section 9) demonstrate that NUIGMech1.0 can not only accurately predict the experimental IDTs studied, but it can also reasonably anticipate experimental LBVs and speciation data taken from the literature in comparison to the available chemical mechanisms (Table DS11).

7.4.2 Individual effect of the studied parameters on IDT

The general performance of NUIGMech1.0 and its fidelity in predicting the IDTs of the various C_1–C_2 binary fuel mixtures over the wide range of conditions studied has been demonstrated. In this section, the effects on IDTs of the studied parameters on the mixtures are discussed in detail, whereas the focus will be on the description of the individual parameters. To investigate the effect of each individual parameter on IDT, the P5C1 and P8C1 (φ = 0.5, p_C = 1 bar, dilution = 75%) conditions are chosen as the base cases for each binary-fuel combination (methane/ethylene and ethane/ethylene). For example, in studying the effect of equivalence ratio on ethylene IDT, we only perturb the equivalence ratio to 1.0 and 2.0 in the P5/8C1 cases, so that the other parameters remain unchanged. Namely, by perturbing the equivalence ratio from 1.0 to 2.0, the new cases are defined as (φ = 1.0, p_C = 1 bar, dilution = 75%) and (φ = 2.0, p_C = 1 bar, dilution = 75%), respectively. The same procedure is followed for the other parameters. Therefore, the effect of each parameter on IDT in the temperature range (800–2100 K) is calculated as follows:

$$\text{IDT } ratio = \frac{\text{IDT}|_{\varphi,p_C,dilution,PxCy}}{\text{IDT }|_{PxC1}} \tag{7-1}$$

Where “x”, and “y” are “5, 8” and “2–9”, respectively. In the above equation, values larger than unity indicate a decrease in reactivity, while values smaller than unity show an increase in reactivity in comparison to the base cases. The individual effect of each parameter on methane/ethylene and ethane/ethylene IDTs are presented in Figure 7-5. For better visualization, the y-axis in Figure 7-5 is scaled in “$\log_2$” so that 2^{-1}, 2^0, and 2^1 refers to a factor of two decrease, no change, and a factor of two increase in IDT ratio, respectively. It is seen that the individual effect of each parameter on IDT changes qualitatively and quantitatively over the temperature range studied. In this regard, the individual effect of the studied parameters such as the binary blend composition, pressure, equivalence ratio, and dilution on IDT predictions of methane/ethylene and ethane/ethylene mixtures are discussed in detail.

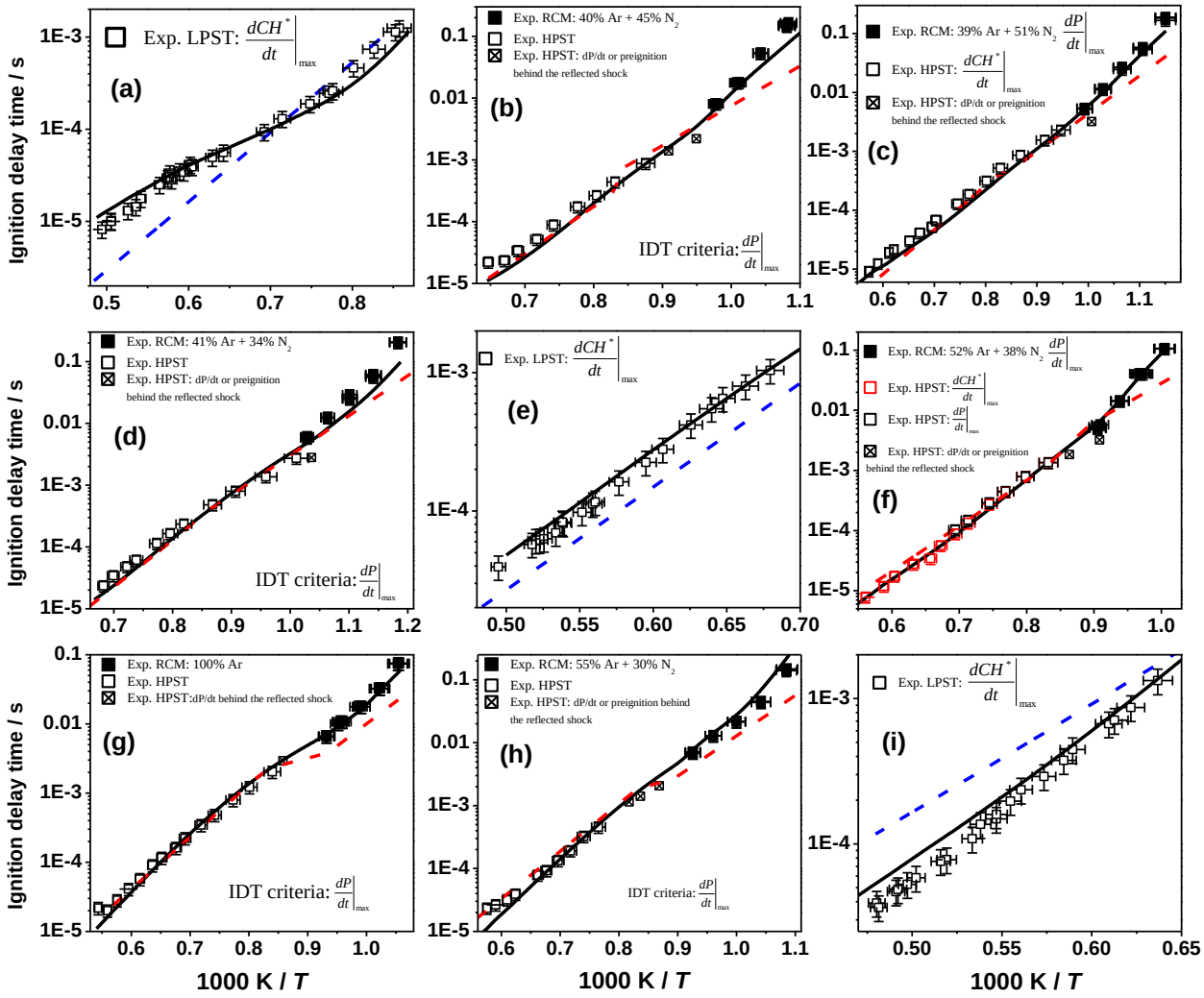

Figure 7-2. Experimental and simulation data of methane/ethylene's IDT values: (a) 2.08% CH_4, 2.08% C_2H_4, 20.83% O_2, (φ = 0.5) in 75% N_2 at p_C = 1 bar, P5C1; (b) 2.143% CH_4, 2.143% C_2H_4, 10.71% O_2, (φ = 1.0) in 75% N_2, 10% Ar, p_C = 20 bar, P5C2; (c) 2.22% CH_4, 2.22% C_2H_4, 5.55% O_2, (φ = 2.0) in 75% N_2, 15% Ar, p_C = 40 bar, P5C3; (d) 5.303% CH_4, 2.273% C_2H_4, 17.424% O_2, (φ = 1.0) in 75% N_2, p_C = 40 bar, P5C4; (e) 4.88% CH_4, 2.09% C_2H_4, 8.02% O_2, (φ = 2.0) in 75% N_2, 10% Ar, p_C = 1 bar, P5C5; (f) 1.25% CH_4, 0.54% C_2H_4, 8.2% O_2 (φ = 0.5) in 75% N_2, 15% Ar at p_C = 20 bar, P5C6; (g) 10.976% CH_4, 1.22% C_2H_4, 12.805% O_2, (φ = 2.0) in 75% N_2, p_C = 20 bar, P5C7; (h) 2.596% CH_4, 0.288% C_2H_4, 12.115% O_2 (φ = 0.5) in 75% N_2, 10% Ar at p_C = 40 bar, P5C8; (i) 2.9% CH_4, 0.32% C_2H_4, 6.77% O_2, (φ = 2.0) in 75% N_2, 15% Ar, p_C =1 bar, P5C9. (solid–line: NUIGMech1.0, dashed–line: derived correlations (Section 7.4.3)).

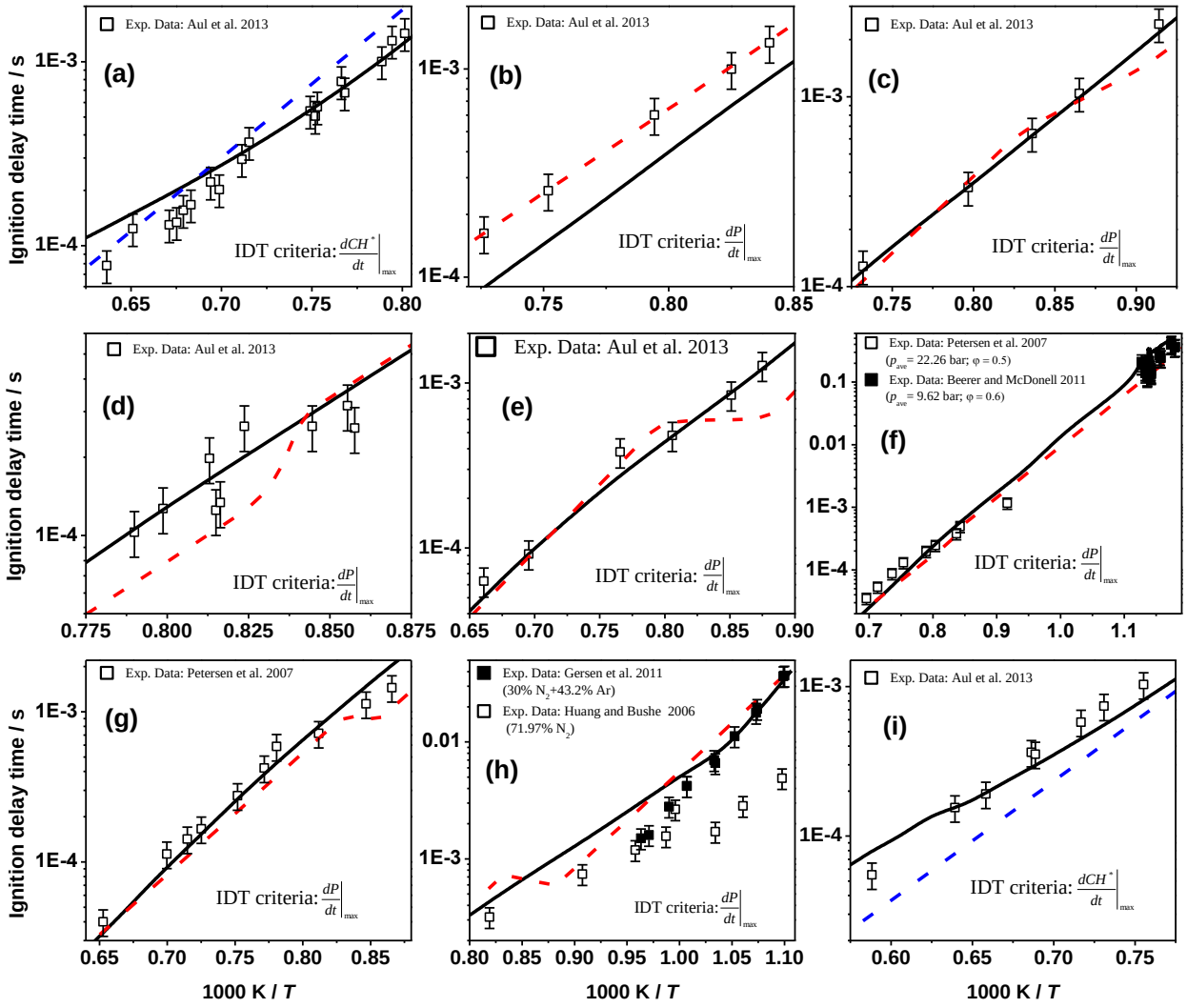

Figure 7-3. Available experimental and simulated data of methane/ethane's IDT values at: (a) 0.15% CH_4, 0.15% C_2H_6, 1.7% O_2, (φ = 0.5) in 98% Ar, p_C = 1.46 bar, P6C1; (b) 0.67% CH_4, 0.67% C_2H_6, 3.67% O_2, (φ = 1.0) in 95% Ar, p_C = 32.02 bar, P6C2; (c) 3.16% CH_4, 3.16% C_2H_6, 8.68% O_2, (φ = 2.0) in 85% Ar, p_C = 15.44 bar, P6C3; (d) 0.91% CH_4, 2.73% C_2H_6, 11.36% O_2 , (φ = 1.0) and 85% Ar, p_C = 31.42 bar, P6C4; (e) 5.14% CH_4, 1.71% C_2H_6, 8.14% O_2, (φ = 2.0) in 85% Ar, p_C = 29.03 bar, P6C5; (f) 2.28% CH_4, 1.23% C_2H_6, 20.15% O_2, (φ = 0.5 [5] and 0.6 [8]) in 75.74% N_2, p_C = 22.26 bar [5] and 9.62 bar [8], P5C6; (g) 4.19% CH_4, 0.47% C_2H_6, 20.03% O_2, (φ = 0.5) in 75.31% N_2, p_C = 22.71 bar, P5C7; (h) 8.01% [3]/7.66% [7] CH_4, 0.89% [3]/ 0.85% [7] C_2H_6, 19.13% [3]/18.3% [7] O_2, (φ = 1.0) in 71.97% N_2 [3]/30% N_2+43.2% Ar [7], p_C = 40 bar; P6C8; (i) 0.12% CH_4, 0.36% C_2H_6, 1.52% O_2, (φ = 1.0) and 98% Ar, p_C = 1.36 bar, P6C9. (solid–line: NUIGMech1.0, dash–line: derived correlations (Section 7.4.3)).

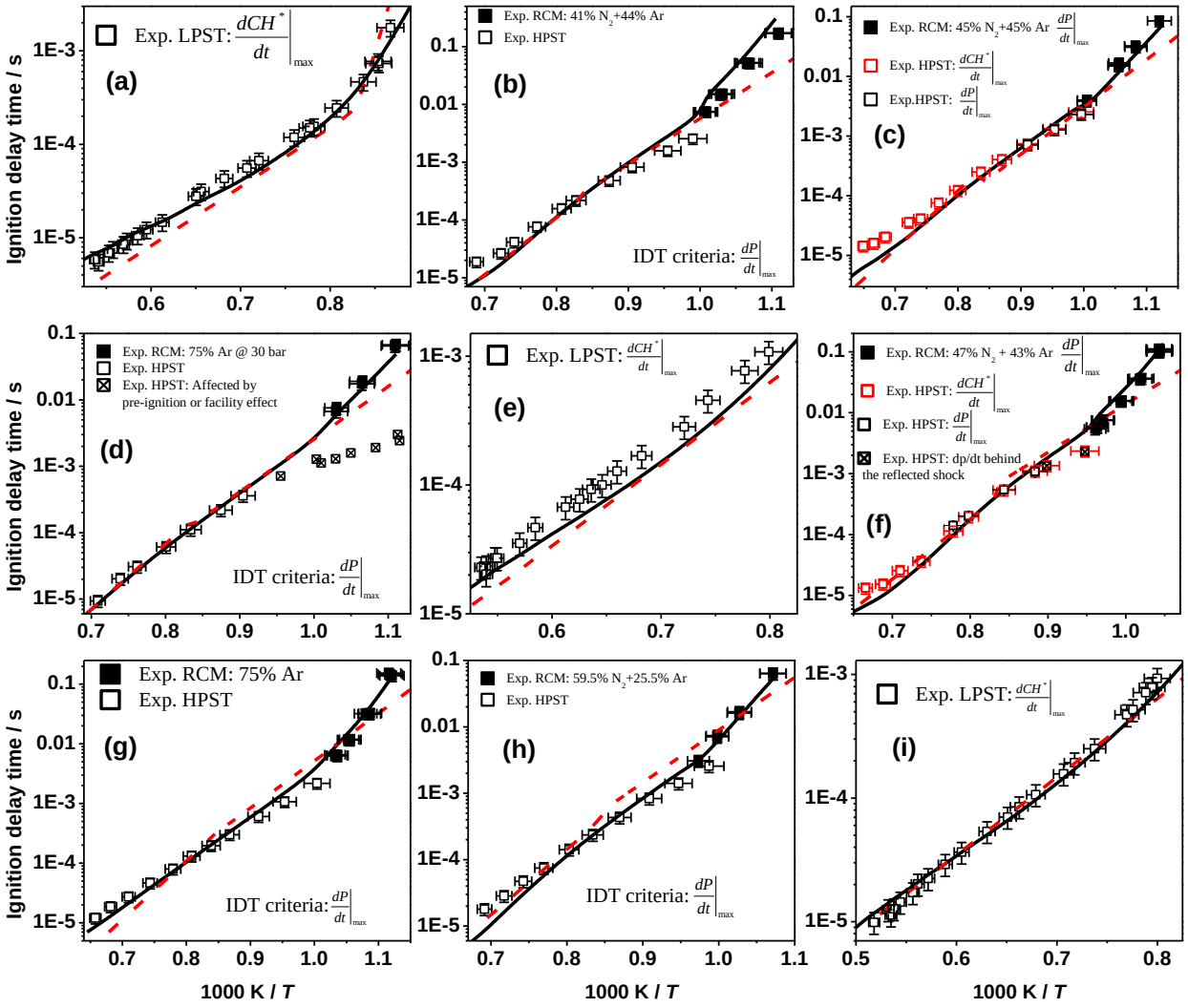

Figure 7-4. Experimental and simulation data for ethane/ethylene oxidation at: (a) 1.67% C_2H_6, 1.67% C_2H_4, 21.67% O_2 (φ = 0.5), 75% N_2, p_C = 1 bar, P8C1; (b) 1.765% C_2H_6, 1.765% C_2H_4, 11.471% O_2 (φ = 1.0), 75% N_2, 10% Ar, p_C = 20 bar, P8C2; (c) 1.9% C_2H_6, 1.9% C_2H_4, 6.19% O_2 (φ = 2.0), 75% N_2, 15% Ar, p_C = 40 bar, P8C3; (d) 4.023% C_2H_6, 1.724% C_2H_4, 19.253% O_2 (φ = 1.0), 75% N_2, p_C = 40 bar, P8C4; (e) 3.92% C_2H_6, 1.68% C_2H_4, 9.39% O_2 (φ = 2.0), 75% N_2, 10% Ar, p_C = 1 bar, P8C5; (f) 0.91% C_2H_6, 0.39% C_2H_4, 8.7% O_2 (φ = 0.5), 75% N_2, 15% Ar, p_C = 20 bar, P8C6; (g) 8.26% C_2H_6, 0.92% C_2H_4, 15.83% O_2 (φ = 2.0), 75% N_2, p_C = 20 bar, P8C7; (h) 1.71% C_2H_6, 0.19% C_2H_4, 13.10% O_2 (φ = 0.5), 75% N_2, 10% Ar, p_C = 40 bar, P8C8; (i) 2.02% C_2H_6, 0.22% C_2H_4, 7.75% O_2 (φ = 1.0), 75% N_2, 15% Ar, p_C = 1 bar, P8C9. (solid–line: NUIGMech1.0, dash–line: derived correlations (Section 7.4.3)).

7.4.2.1.1 Effect of binary blend compositions

As seen in Figure 7-5(a), decreasing the ethylene concentration in the methane and the ethane blends have a significant semi-Gaussian distribution on decreasing reactivity, especially in the intermediate temperature regime (~1200 K). Specifically, decreasing the ethylene concentration in the methane/ethylene blend progressively from 50% to 30% and finally to 10% suppresses the

average mixture reactivity by approximately 120% and 990%, respectively, while decreasing the ethylene concentration in the ethane/ethylene blend only suppresses the reactivity by approximately 11% and 22%, respectively. This clearly shows that methane is much more sensitive to ethylene blending than ethane. Moreover, Figure 7-5(a) shows that, although the reduction in ethylene concentration has a less negative effect on the reactivity of the methane/ethylene mixtures at high (≥ 1670 K) and low temperatures (≤ 900 K), the effect of ethylene concentration on the reactivity of the ethane/ethylene mixture is minor over the entire temperature range. In this way, one can see in Figure 7-5(a) that decreasing ethylene concentration has no significant effect on the reactivity of ethane/ethylene mixtures at temperatures higher than 1670 K (1000/T = 0.6). To understand this more fully, sensitivity analyses to IDT, including both brute-force and direct sensitivity analyses [27] (Figure 7-6) followed by flux analyses (not shown here for brevity) were conducted at 1200 K (0.833) where the effect of ethylene addition is most prominent. In the brute-force and the direct sensitivity analyses, the sensitivity coefficient (S) is calculated as:

$$S = \frac{ln\left(\frac{\tau^+}{\tau^-}\right)}{ln\left(\frac{2}{0.5}\right)} \tag{7-2}$$

As shown above, the rate constant for each reaction is increased/decreased by a factor of two, and IDTs are calculated as τ^+ (increased) and τ^- (decreased), respectively. A positive sensitivity coefficient indicates inhibition of reactivity, while a negative coefficient indicates a promotion in reactivity. Figure 7-6 indicates that adding ethylene to methane makes the chemistry more complex in terms of the number of important reactions involved (sensitivity coefficient ≥ 0.1) in IDT in comparison to addition to ethane.

Figure 7-6 shows that increasing methane concentration in the methane/ethylene blend promotes the chain-termination reactions: $\dot{C}H_3 + \dot{C}H_3$ (+M) ↔ C_2H_6 (+M) and $\dot{C}H_3 + H\dot{O}_2$ ↔ $CH_4 + O_2$. Simultaneously, increasing the methane concentration promotes the reactions: $CH_4 + \dot{O}H$ ↔

$\dot{C}H_3 + H_2O$, $CH_4 + \ddot{O} \leftrightarrow \dot{C}H_3 + \dot{O}H$, $\dot{C}H_3 + H\dot{O}_2 \leftrightarrow CH_3\dot{O} + \dot{O}H$, $\dot{C}H_3 + O_2 \leftrightarrow CH_2O + \dot{O}H$ in competition with the reactions: $C_2H_4 + \dot{O}H \leftrightarrow \dot{C}_2H_3 + H_2O$, $C_2H_4 + \ddot{O} \leftrightarrow \dot{C}H_2CHO + \dot{H}$, $\dot{C}_2H_3 + O_2 \leftrightarrow \dot{C}H_2CHO + \ddot{O}$, which all dramatically suppress the blends reactivity at 1200 K. Thus, increasing ethylene concentration in the fuel blend promotes reactivity by inhibiting methyl radical ($\dot{C}H_3$) reactions but instead promotes reactions of vinyl radicals, which are more reactive than methyl radicals. As seen in Figure 7-6, increasing the ethane concentration (50%→90%) in the ethane/ethylene blend at 1200 K has no significant effect on the ten most prominent reactions, so that this increment promotes $\dot{H} + O_2$ (+M) $\leftrightarrow H\dot{O}_2$ (+M), $\dot{H} + H\dot{O}_2 \leftrightarrow \dot{O}H + \dot{O}H$, and $\dot{C}H_3 + H\dot{O}_2 \leftrightarrow CH_3\dot{O} + \dot{O}H$ against the suppression of the important reaction: $\dot{C}_2H_3 + O_2 \leftrightarrow \dot{C}H_2CHO + \ddot{O}$. Thus, the decrease in reactivity of the ethane/ethylene fuel blend with increasing ethane concentration (Figure 7-5(a)), mainly stems from competition among the chain propagating reactions: $\dot{C}_2H_5 + O_2 \leftrightarrow C_2H_4 + H\dot{O}_2$ and $C_2H_4 + \dot{H}$ (+M) $\leftrightarrow \dot{C}_2H_5$ (+M) and the chain branching reaction: $\dot{C}_2H_3 + O_2 \leftrightarrow \dot{C}H_2CHO + \ddot{O}$ by scavenging $\dot{C}_2H_5$ radical and O_2 molecules from the radical pool.

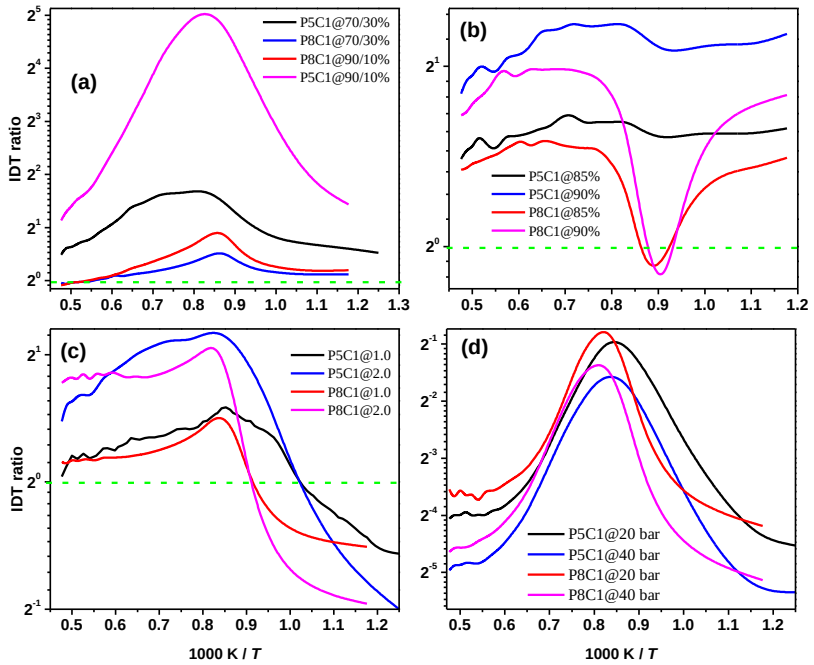

Figure 7-5. Individual effects of the studied parameters on methane/ethylene and ethane/ethylene IDTs: (a) effect of blending composition; (b) effect of dilution level; (c) effect of equivalence ratio; and (d) effect of pressure.

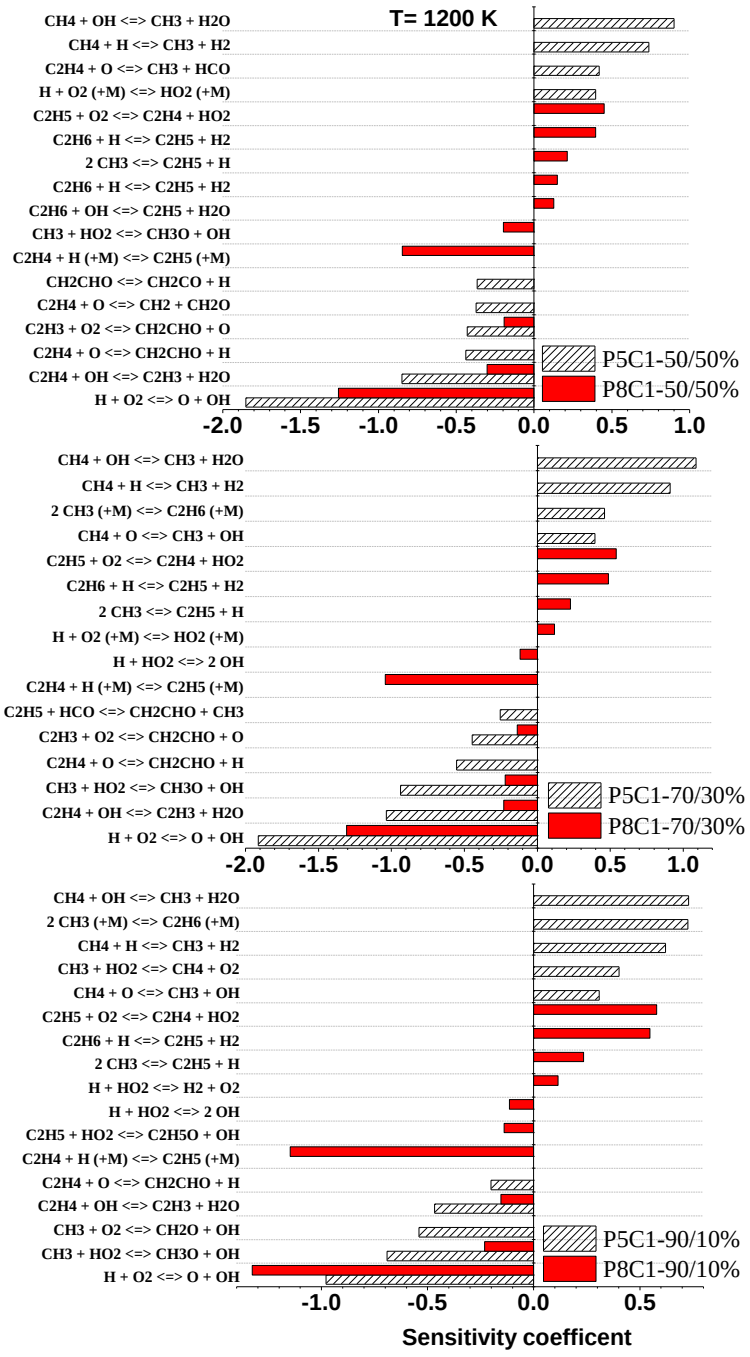

Figure 7-6. Sensitivity analysis of IDT corresponding to the temperature of 1200 K (0.833) in Figure 7-5(a).

7.4.2.1.2 Effect of dilution

The effect on the reactivity of increasing dilution on the methane/ethylene and ethane/ethylene mixtures is demonstrated in Figure 7-5(b). It is seen that increasing dilution from 75% to 85% and then 90% in the methane/ethylene mixtures decreases reactivity by approximately 55% and 115%, respectively. However, this effect on the ethane/ethylene mixture is not monotonic.

Surprisingly, it is seen in Figure 7-5(b) that increasing the dilution level in the ethane/ethylene mixture, not only suppresses the negative effect of dilution on reactivity within the temperature range of 1000–1250 K but enhances reactivity by ~10% at 1100 K (0.909). In this regard, three new experimental datasets within the target temperature range (1000–1200 K), under 1 bar, 50% C_2H_6 + 50% C_2H_4, φ = 0.5, and dilution levels (Ar) of 75%, 85%, and 90% conditions were performed. However, some of the measured IDTs (> 4–5 ms) are located at the upper working limit of NUIG-LPST. As mentioned, although some of the IDTs are relatively long for available LPST in C^3-NUIG, most of them have been taken under tailoring conditions with almost plateau pressure profiles behind the reflected shock (*dp/dt* ~ 0) during the induction time before ignition. However, those data with significant *dp/dt* behind the reflected shock had already been removed from the graph for increasing the data reliability demonstrated in Figure 7-7. As seen in Figure 7-7, although NUIGMech1.0 could somehow capture the behaviour and the IDT trends by increasing the dilution level from 75% to 90%, it fails to reproduce the experimental IDTs beyond the dilution level of 75% so that the predictions of NUIGMech1.0 are consistently shorter than the experimental measurements over the temperature range studied. By comparing the effect of dilution on the reactivities of the methane/ethylene and ethane/ethylene blends shown in Figure 7-8, it is inferred that this behaviour stems from the effect of dilution (third body) and the competition between $\dot{C}_2H_4 + \dot{H}$ (+M) ↔ $\dot{C}_2H_5$ (+M) and $\dot{C}_2H_5 + O_2 \leftrightarrow C_2H_4 + H\dot{O}_2$ in consuming $\dot{C}_2H_5$ radicals. On the one hand, increasing the dilution level intensifies the reverse reaction of $\dot{C}_2H_4 + \dot{H}$ (+M) ↔ $\dot{C}_2H_5$ (+M) which produces more reactive $\dot{H}$ atoms. On the other hand, increasing the dilution level decreases the oxygen concentration in the radical pool, which suppresses the reaction $\dot{C}_2H_5 + O_2 \leftrightarrow C_2H_4 + H\dot{O}_2$. Also, Figure 7-8 shows that increasing the dilution level inhibits the reaction of H_2O_2 (+M) ↔ $\dot{O}H + \dot{O}H$ (+M) and simultaneously promotes $\dot{C}H_3 + H\dot{O}_2 \leftrightarrow CH_3\dot{O} + \dot{O}H$, $\dot{H} + O_2$ (+M) ↔ $H\dot{O}_2$ (+M), and $\dot{H} + H\dot{O}_2 \leftrightarrow \dot{O}H + \dot{O}H$. Apart from the intermediate temperature regime, it is seen in Figure 7-5(b) that the

effect on the reactivity of increasing the dilution level is much less pronounced in the ethane/ethylene mixtures compared to the methane/ethylene mixtures.

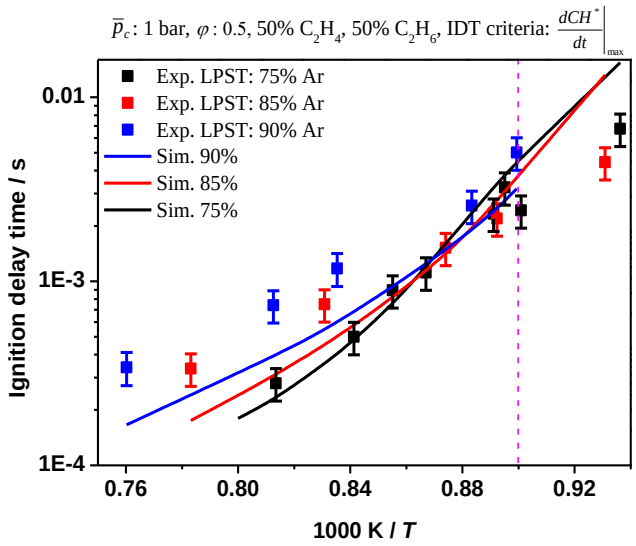

Figure 7-7. Experimental and simulation data for ethane/ethylene oxidation concerning Figure 7-5(b). The magenta dash–line refers to the turning point temperature (0.909) in Figure 7-5(b).

7.4.2.1.3 Effect of equivalence ratio

The effect of increasing equivalence ratio from 0.5 to 1.0 and 2.0 on the reactivity of the methane/ethylene and ethane/ethylene mixtures is depicted in Figure 7-5(c). Increasing the equivalence ratio has a complex effect on the reactivity of the mixtures over the temperatures studied. Increasing the equivalence ratio has a drastic effect on decreasing the mixtures' reactivity in the temperature range 800–1200 K, which is followed by a mild effect in increasing mixture reactivity at temperatures ≥ 1200 K. It is seen in Figure 7-5(c) that, although the reactivity of ethane/ethylene blends is less sensitive to an increasing equivalence ratio with temperature compared to methane/ethylene mixtures, it shows a higher sensitivity in the temperature range 1050–1200 K. The maximum gradient in decreasing the reactivity of the ethane/ethylene mixtures $\left(\left.\frac{\partial IDT\ ratio}{\partial T}\right|_{max}\right)$ is about 0.73 and 1.36 %/K (at 1100 K) at equivalence ratios of 1.0 and 2.0 respectively, in the temperature range 800–1200 K, while the values for the methane/ethylene mixtures are about 0.4 and 0.82 % K^{-1} (at 1000 K) at equivalence ratios of 1.0 and 2.0, respectively.

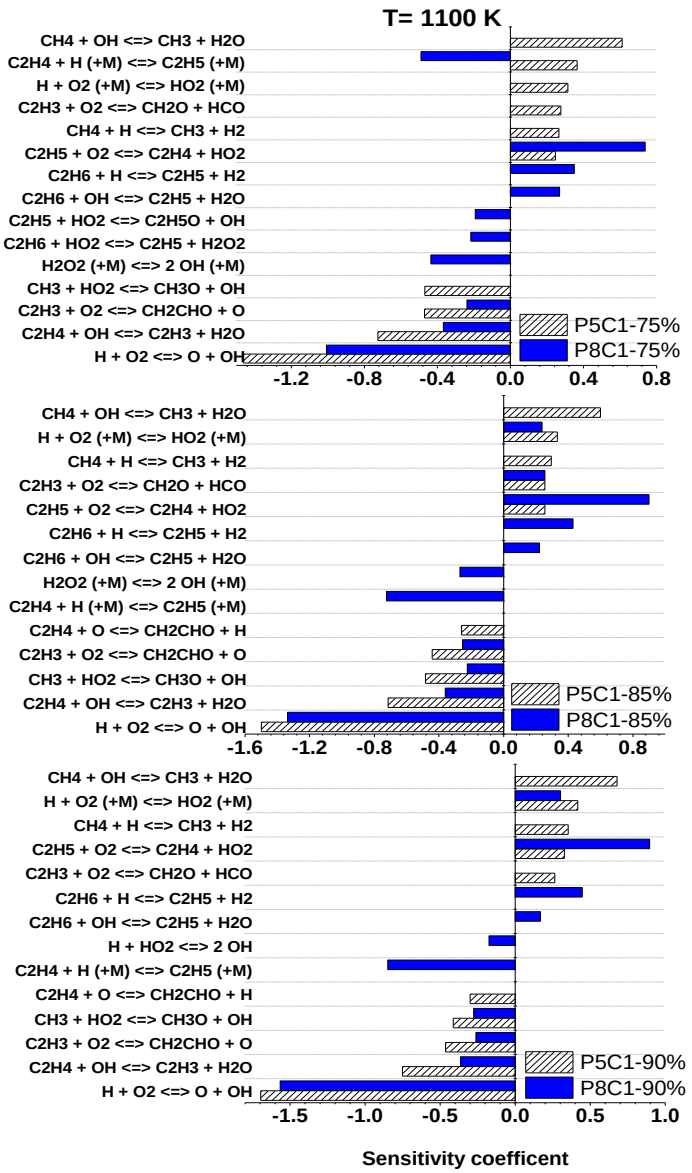

Figure 7-8. Sensitivity analysis of IDT corresponding to the temperature 1100 K (0.91) in Figure 7-5(b).

The reactivity of the fuel-rich mixtures is much more affected by changes in temperature, especially in the 800–1200 K temperature range. In this regard, Figures 7-9 and DS40 show that increasing the equivalence ratio in the methane/ethylene blends at 1200 K intensifies H-atom abstraction from CH_4 and C_2H_4 by Ḣ atoms instead of ȮH radicals. This effect makes the system less reactive (Figure DS41). However, increasing the equivalence ratio promotes the chain branching reaction of $\dot{C}_2H_3 + O_2 \leftrightarrow \dot{C}H_2CHO + \ddot{O}$ compared to the more reactive chain branching reaction $C_2H_4 + \ddot{O} \leftrightarrow \dot{C}H_2CHO + \dot{H}$, so that as seen in Figure DS41 this promotion reduces the blend reactivity. Also, Figure 7-9 shows that increasing the equivalence ratio to 2.0

promotes the reverse reaction of $C_3H_6 + \dot{H} \leftrightarrow C_2H_4 + \dot{C}H_3$ in competition with $C_2H_4 + \ddot{O} \leftrightarrow \ddot{C}H + CH_2O$ and $\dot{C}H_2CHO \leftrightarrow CH_2CO + \dot{H}$.

Similar to the methane/ethylene blend, it is shown in Figures 7-9 and DS42 that increasing the equivalence ratio of the ethane/ethylene blend from 0.5 to 2.0 at 1200 K changes the H-atom abstraction pattern from $\dot{O}H$ radicals to $\dot{H}$ atoms so that this shift makes the blend less reactive at 1200 K. In fact, decreasing oxygen concentration by increasing equivalence ratio and also competition between C_2H_6 and C_2H_4 in consuming $\dot{H}$ atoms and $\dot{O}H$ radicals and producing $\dot{C}_2H_5$ and $\dot{C}_2H_4$ radicals affect blend reactivity due to the higher reactivity of vinyl radicals compared to ethyl radicals in the blends studied.

7.4.2.1.4 Effect of pressure

The effect of pressure on the reactivity of the methane/ethylene and ethane/ethylene blends is demonstrated in Figure 7-5(d). One can see that increasing pressure increases the reactivity of all mixtures. In this regard, it can be seen in Figure 7-5(d) that increasing the pressure from 1 to 40 bar has a Gaussian distribution effect on reactivity with temperature, in that it decreases reactivity in the temperature range 1050–1550 K, while its effect on the reactivity is almost constant at $T \geq 1540$ K and $T \leq 1050$ K for the ethane/ethylene blends and at $T \leq 920$ K for the methane/ethylene blends. Moreover, Figure 7-5(d) shows that although the positive effect of increasing pressure for the methane/ethylene blends at $T \geq 1200$ K is higher than for the ethane/ethylene mixtures, this trend is reversed at $T \leq 1200$ K. At 1200 K, the minimum effect of the Gaussian distribution on increasing the reactivity of the methane/ethylene mixtures is about 48% at 20 bar and 66% at 40 bar, while the values for the ethane/ethylene mixtures at 20 and 40 bar are 42% and 62%, respectively.

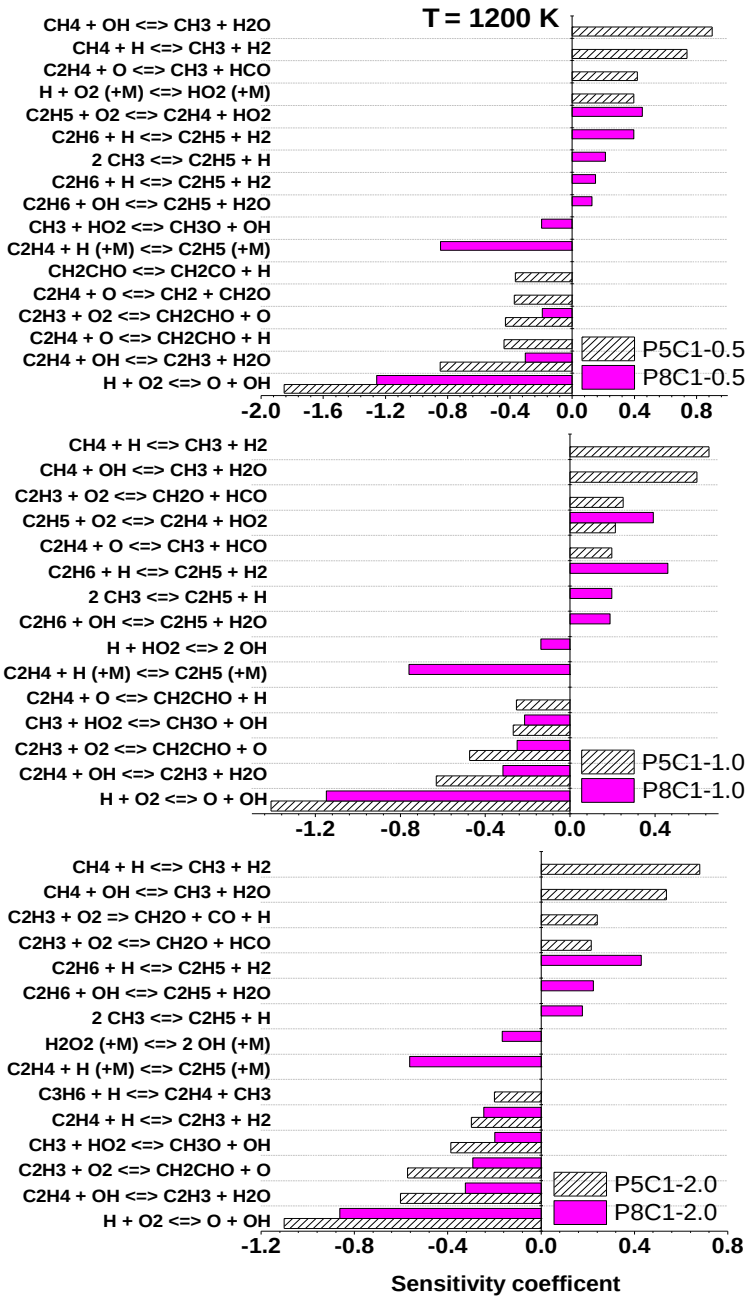

Figure 7-9. Sensitivity analysis of IDT corresponding to the temperature 1200 K (0.833) in Figure 7-5(c).

In addition, Figure 7-5(d) shows that although the effect of pressure on the reactivity of the methane/ethylene mixtures is more sensitive to temperature in comparison to the ethane/ethylene mixtures, this effect shows a very high sensitivity to temperature for the ethane/ethylene mixtures in the temperature range 1050–1500 K. Increasing the temperature of the ethane/ethylene mixture from 1050 K to 1220 K decreases the reactivity by approximately 48%, while further increasing the temperature to 1500 K retrieves the mixture's reactivity.

Furthermore, it is demonstrated in Figure 7-5(d) that the reactivity of ethane/ethylene mixtures is more sensitive to pressure rise compared to the methane/ethylene mixtures. However, they show almost the same sensitivity and dependency at high-temperatures (≥ 1666 K) and low-temperatures (≤ 900 K). Figure 7-5(d) also shows that for both the methane/ethylene and ethane/ethylene mixtures, increasing pressure has the most prominent effect on reactivity in the temperature range 1100–1330 K.

Sensitivity and flux analyses (Figures 7-10, DS43 and DS44) reveal that increasing the pressure of the methane/ethylene and the ethane/ethylene blends from 1 to 40 bar at 1200 K, intensifies H-atom abstraction from CH_4, C_2H_6, and C_2H_4 by $\dot{O}H$ and $H\dot{O}_2$ radicals and simultaneously inhibits abstraction by $\dot{H}$ atoms. These may stem from the promotions in importance of the reactions: $\dot{H} + O_2 (+M) \leftrightarrow H\dot{O}_2 (+M)$ and $H_2O_2 (+M) \leftrightarrow \dot{O}H + \dot{O}H (+M)$ with increasing pressure. One can see in Figures 7-10 and ES44 that these effects are more pronounced in the ethane/ethylene blend, and thus the blend shows a higher sensitivity to the effects at 1200 K. As seen in Figure 7-10, increasing the pressure at 1200 K suppresses the $C_2H_4 + \ddot{O} \leftrightarrow \ddot{C}H + CH_2O/\dot{C}H_3 + H\dot{C}O$ reactions, and in particular the important chain branching reaction $C_2H_4 + \ddot{O} \leftrightarrow \dot{C}H_2CHO + \dot{H}$. Moreover, Figures 7-10 and DS44 demonstrate that increasing the pressure of the ethane/ethylene blend at 1200 K suppresses the reverse chain branching reaction $\dot{C}_2H_4 + \dot{H} (+M) \leftrightarrow \dot{C}_2H_5 (+M)$ and simultaneously promotes the chain propagating reactions $C_2H_6 + H\dot{O}_2 \leftrightarrow \dot{C}_2H_5 + H_2O_2$ and $C_2H_4 + H\dot{O}_2 \leftrightarrow \dot{C}_2H_3 + H_2O_2$. All of these effects make the methane/ethylene, and the ethane/ethylene blends less reactive compared to the base cases (P5C1 and P8C1).

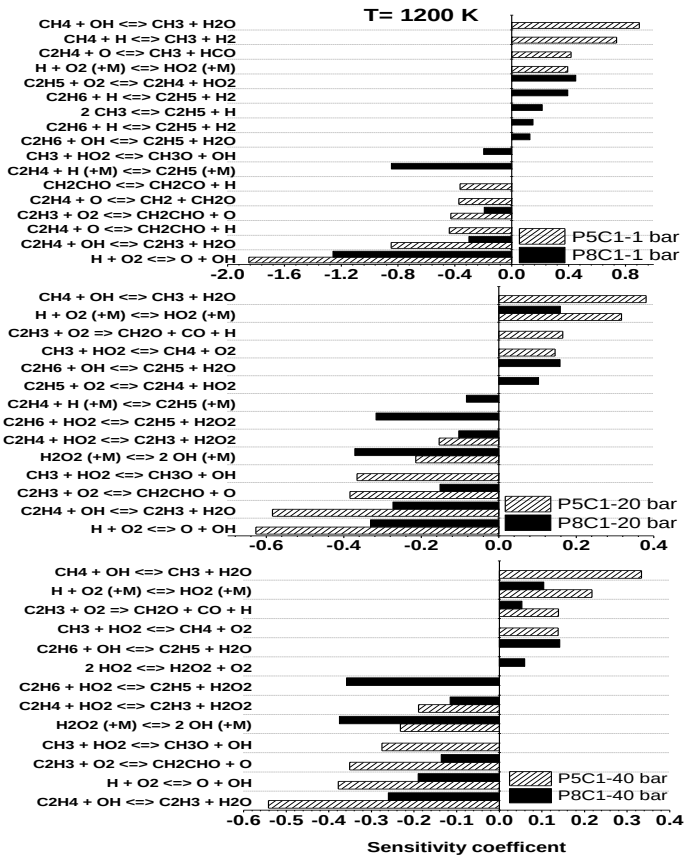

Figure 7-10. Sensitivity analysis of IDT corresponding to the temperature 1200 K (0.833) in Figure 7-5(d).

7.4.3 Correlations and their performances

Having reliable global expressions that can properly explain the reactivity of different mixtures under different physio-chemical conditions is demanding. Global correlations can significantly decrease the computational time of real-time/scale combustion systems and CFD simulations. Hence, in this section, several correlations are derived based on the constant volume simulations of NUIGMech1.0 [13], which we have shown can reasonably predict IDTs for methane/ethylene, methane/ethane, and ethane/ethylene mixtures over a wide range of binary blended fuel conditions. The applied procedure for deriving the correlations has already been discussed by the authors [13]. The validity ranges of the correlations are: $1 \leq p \leq 50$ atm, $800 \leq T \leq 2000$ K, $0.25 \leq \varphi \leq 3.0$, 75% ≤ dilution ≤ 95%, and Fuel_1/Fuel_2: 30/70%, 50/50%, and 70/30% which stems from the targets of the current study. Thus, the following simple correlation style is used to mathematically explain the relationship for the conditions studied:

$$\tau_{\mathrm{idt,corr}} = 10^{\mathrm{A}} \exp\left(\frac{\mathrm{B}}{T}\right)[\mathrm{Fuel\_1}]^{\mathrm{C}}[\mathrm{Fuel\_2}]^{\mathrm{D}}[\mathrm{Oxygen}]^{\mathrm{E}}[\mathrm{Diluent}]^{\mathrm{F}} \qquad (7\text{-}3)$$

where the concentrations (mol m^{-3}) of fuels, oxygen, and diluent are calculated based on the ideal gas law in accordance with the partial pressure of each species in the mixture at a specific temperature. Tables (7-3) – (7-5) show that the correlations are evaluated by sub-dividing the numerically studied conditions into two regimes; a) low, intermediate, and high temperatures; and b) high- and low-pressure, corresponding to the different chemistry controlling ignition over these conditions. However, based on our correlation procedure (constant-volume adiabatic simulations), the derived correlations for the low-temperature regime are not able to capture the experimental IDTs where non-ideal effects (mostly heat loss effects) are prominent. Therefore, the performance of the correlations is evaluated only in the intermediate-to-high temperature regime. In this regard, Origin 8.5 software [28] is used to derive the correlation parameters included in Eq. (7-3). The coefficients of the extracted correlations for methane/ethylene, methane/ethane, and ethane/ethylene, including standard errors and validity ranges over the studied conditions, are presented in Tables (7-3) – (7-5).

The performance of the derived correlations versus the available experimental IDT data in the literature (methane/ethane) and the newly-taken data of the present study (methane/ethylene and ethane/ethylene) was already shown in Figures (7-2) – (7-4). In these figures, the red dashed lines refer to the derived correlations. However, the red dashed line is replaced by a blue line if one parameter (e.g., pressure or dilution) is outside the range of correlation. It is seen in Figure 7-2 that the correlation formula can duplicate the experimental IDT data trend of the methane/ethylene mixtures over a wide range of conditions. The correlation coefficients for the methane/ethylene mixtures are presented in Table 7-3. Although, as seen in Figures 7-2(a), (e), and (i), correlating the simulation results using the format presented in Eq. (7-3) is inaccurate with significant uncertainties due to the highly non-linear behavior of the methane/ethylene mixtures at pressures in the range 1–15 atm. As already shown in the sensitivity analysis plots,

the highly non-linearity of IDTs within 1–15 bar range almost stems from high sensitivity of the IDTs to $\dot{H} + O_2 (+M) \leftrightarrow H\dot{O}_2 (+M)$ and $\dot{H} + O_2 \leftrightarrow \ddot{O} + \dot{O}H$ which change significantly with pressure over the range investigated. In this regard, the average ($\bar{\delta}_{corr-exp}$) and standard ($\bar{\sigma}_{corr-exp}$) deviation of the methane/ethylene correlations from the experimental data (only shock–tube data) over the studied temperature range is presented in Table 7-6.

Here, it should be noted that highly non-linear behavior of the oxidation chemistry of the studied binary blended fuels over certain ranges of the studied conditions may cause that the simple form of the correlation presented in Eq. (7-3) fails to accurately predict experimental IDTs, especially in the range 1–20 atm. In fact, high sensitivity of IDT to some non–linear dependency of vital reactions and also changing the vital reactions over certain ranges of fuel concentration, temperature, and pressure make the chemically predicted IDTs more scattered in terms of the defined parameters in Eq. (7-3), so that the derived regressions would be less accurate depending on the scattering level of the calculated IDTs by the parent high fidelity chemical mechanism. Such deviations could be somehow understood by looking at R^2, χ^2, and importantly high standard errors of the derived coefficients for the parameters in Eq. (7-3). Therefore, as seen in the relevant table for methane + ethylene blends, it was not possible to derive a proper simple shape correlation for IDTs in the pressure range of 1–15 atm. For compensating the issue, the authors tried to divide the correlation zones into several regions in accordance with temperature, pressure, and equivalence ratios and bundle the same pose regions into one category to get more accurate correlations. Moreover, as mentioned above, in some regions related to low temperatures in which the experimental IDTs measured using RCM, again, some discrepancies between the correlation and the model predictions could be seen. These discrepancies stem from the fact that the correlations are derived based on constant volume adiabatic calculations, while the experiments suffer from non-idealities such as heat loss, which substantially can affect the measured IDT. However, these non-idealities can be robustly treated in the RCM simulations of

the parent chemical model by imposing a volume history profile. Thus, the red dashed lines for IDTs above 10 ms often show under prediction, which can be explained by the heat loss effect that occurs in the RCM experiments, which are not taken into account in the correlations. Furthermore, the IDT criterion is another parameter that may affect the performance of the correlations versus the parent chemical mechanism. The correlations have been derived based on IDTs calculated by the maximum gradient in pressure history, while some experimental IDTs and their respective simulation data (specially < 10 bar) were determined using different definitions such as the maximum gradient in CH^* or OH^* history.

Figure 7-3 shows that the simple derived correlations which are reported in Table 7-4 for the methane/ethane mixtures can reasonably reproduce the experimental IDTs and their trends, even for those outside of the range of the correlation (Figures 7-3(a) and (i); dilution level > 95%). Thus, the average and standard deviation of the methane/ethane correlations from the experimental data (only shock tube data) over the temperature range studied are provided in Table 7-7. It is seen that the average deviation between the correlations and the experimental data over the studied conditions in the high-temperature regime is approximately 35%.

The performance of the derived correlations in predicting the IDTs of the ethane/ethylene mixtures is shown in Figure 7-4. The coefficients of the correlations are presented in Table 7-5 at both low and high temperatures. By comparing the experimental data and the correlations in Figure 7-4, it is apparent that the derived correlations can acceptably predict the measured IDTs with an accuracy comparable to NUIGMech1.0. In this regard, it is observed in Table 7-8 that the average deviation between the correlations and the experimental data over the studied conditions in the high-temperature regime is approximately 40%.

Furthermore, by increasing the compressed pressure to 20 and 40 bar, it is seen in Figures (7-2 – (7-4) that all of the correlations can acceptably predict experimental IDTs even in the intermediate-to-low temperature regime. This stems from the fact that the high-pressure

chemistry does not significantly change within the 15–50 bar (3.33 times) window in deriving the correlations, while this effect is dramatically sensitive to changes in pressure in the range 1–15 bar (15 times). This fact is somehow demonstrated in Figure 7-11. Although the correlations were derived over 1–50 atm, according to the pressure effect discussed above, the correlation could satisfactorily predict the experimental IDTs (within ±40%) over 125 bar, low temperature, and relatively short IDT regimes in where the heat loss effect would be minor in RCM facilities. This finding could be interesting in terms of mimicking gas engine operating pressure, which is almost above 40 bar. Furthermore, it is interesting to note that the performance of the simple correlations in reproducing the experimental IDTs is better than NUIGMech1.0 at some conditions (e.g., high-temperature regime > 1400 K) such as in Figures 7-2(h), 7-3(b), 7-4(f) and 7-4(h).

Table 7-3. Evaluated coefficients for correlation of the simulated IDTs for methane + ethylene mixtures.

$0.25 \leq \varphi \leq 2.0$ $75 \leq$ Dilution $\leq 95\%$	$20 \leq p_{5,c} \leq 50$ /atm	
	$800 \leq T_{5,c} < 1200$ /K	$1200 \leq T_{5,c} \leq 2000$ /K
A	-8.335 ± 0.021	-9.901 ± 0.0236
B	15676.25 ± 36.39	18356.2 ± 63.216
C [methane]	-0.214 ± 0.0018	1.047 ± 0.0053
D [ethylene]	-0.598 ± 0.0019	-1.1196 ± 0.0054
E	-0.1362 ± 0.0023	-1.2955 ± 0.0046
F	0.0746 ± 0.004	0.684 ± 0.0069
R^2	0.991	0.976
χ^2	2.54E-04	3.05E-10

Table 7-4. Evaluated coefficients for correlation of the simulated IDTs for methane + ethane mixtures.

$0.25 \leq \varphi \leq 2.0$ $75 \leq$ Dilution $\leq 95\%$	$20 \leq p_{5,c} \leq 50$ /atm	$1 \leq p_{5,c} \leq 15$ /atm	$15 < p_{5,c} \leq 50$ /atm
	$800 \leq T_{5,c} < 1200$ /K	$1200 \leq T_{5,c} < 2000$ /K	
A	-9.783 ± 0.0151	-9.101 ± 0.033	-9.949 ± 0.0264
B	19718.499 ± 26.840	19258.657 ± 97.04	19458.945 ± 72.877
C [methane]	-0.1653 ± 9.26E-04	1.439 ± 0.008	0.7469 ± 0.0042
D [ethane]	-0.4759 ± 0.001	-0.2413 ± 0.009	-0.717 ± 0.0045
E	-0.067 ± 0.0012	-2.111 ± 0.0107	-1.129 ± 0.0044
F	-0.1378 ± 0.002	0.3386 ± 0.0054	0.4771 ± 0.007
R^2	0.998	0.974	0.973
χ^2	3.74E-04	4.32E-09	2.34E-10

Table 7-5. Evaluated coefficients for correlation of the simulated IDTs for ethane + ethylene mixtures.

$0.25 \leq \varphi \leq 2.0$ $75 \leq$ Dilution $\leq 95\%$	$20 \leq p_{5,c} \leq 50$ /atm $800 \leq T_{5,c} < 1200$ /K	$1 \leq p_{5,c} \leq 15$ /atm $1200 \leq T_{5,c} < 2000$ /K	$15 < p_{5,c} \leq 50$ /atm
A	-9.827 ± 0.0261	-8.6581 ± 0.0209	-12.118 ± 0.0298
B	19125.037 ± 46.261	15455.624 ± 62.281	23088.771 ± 86.772
C [ethylene]	-0.466 ± 0.0017	-0.0348 ± 0.004	-0.2374 ± 0.0027
D [ethane]	-0.2555 ± 0.0018	0.4395 ± 0.0044	0.0316 ± 0.0029
E	-0.0496 ± 0.0021	-1.2105 ± 0.0057	-0.4924 ± 0.0034
F	-0.08497 ± 0.0037	0.2072 ± 0.0045	0.41 ± 0.0056
R^2	0.992	0.977	0.976
χ^2	5.19E-04	1.12E-10	1.19E-11

Table 7-6. Performance of the methane/ethylene correlations versus the experimental data shown in Figure 2.

Experimental data set	$\overline{\delta}_{corr-exp}$ (%)	$\overline{\sigma}_{corr-exp}$ (%)
P5C1	47.5	22.1
P5C2	28.3	7.5
P5C3	29.0	15.0
P5C4	33.8	22.8
P5C5	38.4	5.9
P5C6	26.0	17.0
P5C7	9.9	9.6
P5C8	19.8	9.1
P5C9	131.0	56.4

Table 7-7. Performance of the methane/ethane correlations versus the experimental data shown in Figure 3.

Experimental data set	$\overline{\delta}_{corr-exp}$ (%)	$\overline{\sigma}_{corr-exp}$ (%)
P6C1	34.1	15.5
P6C2	2.1	0.8
P6C3	18.5	7.1
P6C4	49.1	47.2
P6C5	40.8	36.3
P6C6	30.7	10.1
P6C7	68.1	8.3
P6C8	24.5	26.0
P6C9	45.3	3.8

Table 7-8. Performance of the ethane/ethylene correlations versus the experimental data shown in Figure 4.

Experimental data set	$\overline{\delta}_{corr-exp}$ (%)	$\overline{\sigma}_{corr-exp}$ (%)
P8C1	39.5	11.8
P8C2	28.8	3.4
P8C3	80.6	92.9
P8C4	36.5	37.3
P8C5	36.8	4.0
P8C6	24.9	33.9
P8C7	24.7	11.9
P8C8	74.6	92.5
P8C9	9.9	11.8

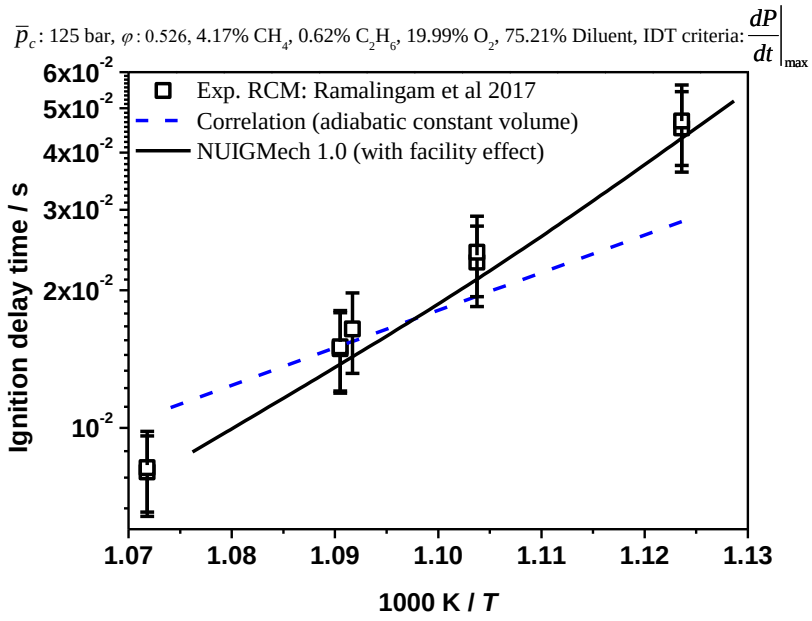

Figure 7-11. Performance of the derived correlation under an overpressure (> 50 bar) condition [11].

7.5 Conclusions

To create a comprehensive IDT database, a detail experimental and simulation study of the IDT characteristics of binary blended C_1–C_2 alkane/alkene fuels including methane/ethylene, methane/ethane, and ethane/ethylene combinations over a wide range of temperature, pressure, equivalence ratio, binary combination, and dilution was performed. An extensive literature review was conducted, and available data, especially for methane/ethane blends were extracted to be used in the simulations. The experimental tests were designed using the Taguchi matrix (L_9). Nine data sets including 160 data points for methane + ethylene (p_C: 1, 20 and 40 bar; φ: 0.5, 1.0, and 2.0; dilution: 75, 85, and 90%) and nine data sets including 140 data points for ethane + ethylene (p_C: 1, 20, and 40 bar; φ: 0.5, 1.0, and 2.0; dilution: 75, 85, and 90%) were recorded using L/HPST and RCM facilities at C^3-NUIG and PCFC-RWTH Aachen University. The experimental data presented here provides a new insight into the oxidation of alkane/alkene blended fuel mixtures. These findings are technologically important in terms of safety and the design of new low-emission and size-efficient combustion systems.

The individual effects of the studied parameters (alkane ratio, dilution, equivalence ratio, and dilution) on the IDTs have been considered in detail. The results showed that most parameters do not have a monotonic effect on mixture reactivity over the entire temperature range (800–2100 K), in that the reactivity of mixtures in certain temperature ranges can be very sensitive to the studied parameters, while this sensitivity can be low over other temperature ranges. Interestingly, it was shown that increasing the alkanes concentration in the alkane + alkene blends at 1 bar, φ: 0.5 and dilution of 75% has a Gaussian distribution with temperature around 1200 K. However, increasing the pressure or dilution percent has a minimum effect on the blends reactivity at 1200 K and 1100 K, respectively.

Furthermore, the performances of NUIGMech1.0, in addition to several derived correlations for the blended fuels, were evaluated using all of the available and measured experimental IDT data. The results showed that NUIGMech1.0 could acceptably predict the measured IDTs. Moreover, the results showed that the derived correlations based on NUIGMech1.0 for the studied blended fuel mixtures could satisfactorily reproduce the experimental IDT data within the studied range. This can be a very versatile rule-of-thumb tool to use in predicting the IDT characteristics of the fuel blends studied.

Acknowledgements

The authors would like to express their gratitude to Shell Research Ltd. and Science Foundation Ireland (SFI) for funding via project numbers 15/IA/3177 and 16/SP/3829. The authors from PCFC, RWTH Aachen University, would like to recognize the funding support from the German Research Foundation (Deutsche Forschungsgemeinschaft, DFG) through the project number – 322460823 (HE7599/2-1).

References

[1] J. Shao, D.F. Davidson, R.K. Hanson, A shock tube study of ignition delay times in diluted methane, ethylene, propene and their blends at elevated pressures, Fuel, 225 (2018) 370–380.

[2] N. Lamoureux, C.-E. Paillard, Natural gas ignition delay times behind reflected shock waves: Application to modelling and safety, Shock Waves, 13 (2003) 57–68.

[3] J. Huang, W.K. Bushe, Experimental and kinetic study of autoignition in methane/ethane/air and methane/propane/air mixtures under engine-relevant conditions, Combust. Flame, 144 (2006) 74–88.

[4] J. De Vries, E.L. Petersen, Autoignition of methane-based fuel blends under gas turbine conditions, Proc. Combust. Inst, 31(2) (2007) 3163–3171.

[5] E.L. Petersen, J.M. Hall, S.D. Smith, J. de Vries, A.R. Amadio, M.W. Crofton, Ignition of lean methane-based fuel blends at gas turbine pressures, J. Eng. Gas Turbines Power, 129 (2007) 937–944.

[6] J. Herzler, C. Naumann, Shock-tube study of the ignition of methane/ethane/hydrogen mixtures with hydrogen contents from 0% to 100% at different pressures, Proc. Combust. Inst, 32(1) (2009) 213–220.

[7] S. Gersen, A. V Mokhov, J.H. Darmeveil, H.B. Levinsky, P. Glarborg, Ignition-promoting effect of NO2 on methane, ethane and methane/ethane mixtures in a rapid compression machine, Proc. Combust. Inst., 33(1) (2011) 433–440.

[8] D.J. Beerer, V.G. McDonell, An experimental and kinetic study of alkane autoignition at high pressures and intermediate temperatures, Proc. Combust. Inst., 33(1) (2011) 301–307.

[9] C.J. Aul, W.K. Metcalfe, S.M. Burke, H.J. Curran, E.L. Petersen, Ignition and kinetic modeling of methane and ethane fuel blends with oxygen: A design of experiments approach, Combust. Flame, 160 (2013) 1153–1167.

[10] S.M. Burke, W. Metcalfe, O. Herbinet, F. Battin-Leclerc, F.M. Haas, J. Santner, F.L. Dryer, H.J. Curran, An experimental and modeling study of propene oxidation. Part 1: Speciation measurements in jet-stirred and flow reactors, Combust. Flame, 161 (2014) 2765–2784.

[11] A. Ramalingam, K. Zhang, A. Dhongde, L. Virnich, H. Sankhla, H. Curran, A. Heufer, An RCM experimental and modeling study on CH4 and CH_4/C_2H_6 oxidation at pressures up to 160 bar, Fuel, 206 (2017) 325–333.

[12] P.J. Ross, T. Techniques, Taguchi Techniques for Quality Engineering, (1988).

[13] M. Baigmohammadi, V. Patel, S. Martinez, S. Panigrahy, A. Ramalingam, U. Burke, K.P. Somers, K.A. Heufer, A. Pekalski, H.J. Curran, A Comprehensive Experimental and Simulation Study of Ignition Delay Time Characteristics of Single Fuel C_1–C_2 Hydrocarbons over a Wide Range of Temperatures, Pressures, Equivalence Ratios, and Dilutions, Energy Fuels, 34 (2020) 3755–3771.

[14] U. Burke, K.P. Somers, P. O'Toole, C.M. Zinner, N. Marquet, G. Bourque, E.L. Petersen, W.K. Metcalfe, Z. Serinyel, H.J. Curran, An ignition delay and kinetic modeling study of methane, dimethyl ether, and their mixtures at high pressures, Combust. Flame, 162 (2015) 315–330.

[15] D. Healy, H.J. Curran, J.M. Simmie, D.M. Kalitan, C.M. Zinner, A.B. Barrett, E.L. Petersen, G. Bourque, Methane/ethane/propane mixture oxidation at high pressures and at

high, intermediate and low temperatures, Combust. Flame, 155 (2008) 441–448.
[16] S.M. Gallagher, H.J. Curran, W.K. Metcalfe, D. Healy, J.M. Simmie, G. Bourque, A rapid compression machine study of the oxidation of propane in the negative temperature coefficient regime, Combust. Flame, 153 (2008) 316–333.
[17] N. Donohoe, K.A. Heufer, C.J. Aul, E.L. Petersen, G. Bourque, R. Gordon, H.J. Curran, Influence of steam dilution on the ignition of hydrogen, syngas and natural gas blends at elevated pressures, Combust. Flame, 162 (2015) 1126–1135.
[18] D. Healy, D.M. Kalitan, C.J. Aul, E.L. Petersen, G. Bourque, H.J. Curran, Oxidation of C1−C5 Alkane Quinternary Natural Gas Mixtures at High Pressures, Energy Fuels, 24 (2010) 1521–1528.
[19] D. Healy, H.J. Curran, S. Dooley, J.M. Simmie, D.M. Kalitan, D.K. Petersen, G. Bourque, Methane/propane mixture oxidation at high pressures and at high, intermediate and low temperatures, Combust. Flame, 155 (2008) 451–461.
[20] E.L. Petersen, M.J.A. Rickard, M.W. Crofton, E.D. Abbey, M.J. Traum, D.M. Kalitan, A facility for gas- and condensed-phase measurements behind shock waves, Meas. Sci. Technol., 16 (2005) 1716–1729.
[21] B.W. Weber, C.J. Sung, M.W. Renfro, On the uncertainty of temperature estimation in a rapid compression machine, Combust. Flame. 162(6) (2015) 2518–2528.
[22] C.-J. Sung, H.J. Curran, Using rapid compression machines for chemical kinetics studies, Prog. Energy Combust. Sci., 44 (2014) 1–18.
[23] S.S. Goldsborough, S. Hochgreb, G. Vanhove, M.S. Wooldridge, H.J. Curran, C.J. Sung, Advances in rapid compression machine studies of low- and intermediate-temperature autoignition phenomena, Prog. Energy Combust. Sci., 63 (2017) 1–78.
[24] D.G. Goodwin, R.L. Speth, H.K. Moffat, Cantera: an object-oriented software toolkit for chemical kinetics, thermodynamics, and transport processes. Version 2.2. 1, Version 2.4. 0 2018, (n.d.).
[25] R. CHEMKIN-PRO, 15112, Reaction Design, Inc., San Diego, CA. (2011).
[26] E.E. Dames, A.S. Rosen, B.W. Weber, C.W. Gao, C.J. Sung, W.H. Green, A detailed combined experimental and theoretical study on dimethyl ether/propane blended oxidation, Combust. Flame, 168 (2016) 310–330.
[27] V. Gururajan, F.N. Egolfopoulos, Direct sensitivity analysis for ignition delay times, Combust. Flame, 209 (2019) 478–480.
[28] O. Pro, 8.5. 0, Orig. Corp. One Roundhouse Plaza Northampton, MA, USA. (2010).

CHAPTER 8

AN EXPERIMENTAL AND KINETIC MODELING STUDY OF THE IGNITION DELAY CHARACTERISTICS OF BINARY BLENDS OF ETHANE/PROPANE AND ETHYLENE/PROPANE IN MULTIPLE SHOCK TUBES AND RAPID COMPRESSION MACHINES OVER A WIDE RANGE OF TEMPERATURE, PRESSURE, EQUIVALENCE RATIO, AND DILUTION

Chapter 8: An Experimental and Kinetic Modeling Study of the Ignition Delay Characteristics of Binary Blends of Ethane/Propane and Ethylene/Propane in Multiple Shock Tubes and Rapid Compression Machines over a Wide Range of Temperature, Pressure, Equivalence Ratio, and Dilution

Published in: Energy and Fuels, Volume 34, Issue 7, July 2020, Pages 8808–8823.
DOI: https://doi.org/10.1021/acs.energyfuels.0c00960

Authors and Contributions

1) **Sergio Martinez** (National University of Ireland, Galway, Ireland)
Contribution: Chemical kinetic modelling and manuscript preparation.
2) **Mohammadreza Baigmohammadi** (National University of Ireland, Galway, Ireland)
Contribution: High pressure shock tube experiments.
3) **Vaibhav Patel** (National University of Ireland, Galway, Ireland)
Contribution: RCM experiments
4) **Snehasish Panigrahy** (National University of Ireland, Galway, Ireland)
Contribution: Chemical kinetic modelling.
5) **Amrit B. Sahu** (National University of Ireland, Galway, Ireland)
Contribution: Chemical kinetic modelling.
6) **Shashank S. Nagaraja** (National University of Ireland, Galway, Ireland)
Contribution: Low pressure shock tube experiments.
7) **Ajoy Ramalingam** (PCFC, RWTH Aachen, Germany)
Contribution: RCM experiments.
8) **Ahmed Abd El-Sabor Mohamed** (National University of Ireland, Galway, Ireland)
Contribution: RCM experiments.
9) **Kieran P. Somers** (National University of Ireland, Galway, Ireland)
Contribution: Chemical kinetic modelling.
10) **Karl A. Heufer** (PCFC, RWTH Aachen, Germany)
Contribution: Project management and manuscript review.
11) **Andrzej Pekalski** (Shell research limited, Shell Centre London)
Contribution: Project management and manuscript review.

12) **Henry J. Curran** (National University of Ireland, Galway, Ireland)
Contribution: Project management and manuscript review.

Abstract

In this work, the ignition delay time characteristics of C_2 – C_3 binary blends of gaseous hydrocarbons including ethylene/propane and ethane/propane are studied over a wide range of temperatures (750 – 2000 K), pressures (1 – 135 bar), equivalence ratios (φ = 0.5 – 2.0) and dilutions (75 – 90%). A matrix of experimental conditions is generated using the Taguchi (L9) approach to cover the range of conditions for the validation of a chemical kinetic model. The experimental ignition delay time data are recorded using low- and high-pressure shock tubes and two rapid compression machines (RCM) to include all the designed conditions. These novel experiments provide a direct validation of the chemical kinetic model, NUIGMech1.1, and its performance is characterized via statistical analysis, with the agreement between experiments and model being within ~ 26.4% over all of the conditions studied, which is comparable with a general absolute uncertainty of the applied facilities (~ 20%). Sensitivity and flux analyses allow for the key reactions controlling the ignition behavior of the blends to be identified. Subsequent analyses are performed to identify those reactions which are important for the pure fuel components and for the blended fuels, and synergistic/antagonistic blending effects are therefore identified over the wide range of conditions. The overall performance of NUIGMech1.1 and the correlations generated are in good agreement with the experimental data.

Keywords: Ethane, ethylene, propane, shock-tube, rapid compression machine, ignition delay time, detailed kinetic model

8.1 Introduction

According to the U.S. Energy Information Administration (EIA) report 2019 [1], it is projected that global energy consumption will increase by approximately 28% in 2050 compared to 2018 levels, with fossil fuels providing around 77% of the total energy demand. Liquid fuels, natural gas, and coal are the most important sources amongst all fossil fuels. Liquid fuels, such as gasoline, diesel, etc. are predicted to represent around 33% of energy consumption, with natural gas at close to 30%, coal near 18%, with the remaining 19% corresponding to nuclear, hydropower, and renewable sources [2].

The combustion of fossil fuels is the main sources of CO_2, SO_x, and NO_x emissions, among other pollutants. In this regard, natural gas is considered preferable to other fossil fuels including liquid fuels and coal as it is a cleaner energy source, having the highest hydrogen/carbon among them. Widely used in the domestic, transportation, and industrial sectors, liquefied natural gas (LNG) is typically composed of methane (82 – 100%) but can contain substantial amounts of ethane, propane and butane, while liquified petroleum gas (LPG) includes mainly propane, and butane. To reduce emissions, it is necessary to improve the efficiency of the combustion systems for which a detailed understanding of the combustion chemistry is essential. The oxidation kinetics of small hydrocarbons play an important role as the base of any mechanism for alternative fuels. For these reasons, the combustion community is interested in enhancing our understanding of the chemistry controlling the oxidation of hydrocarbons to increase the efficiency of engines and to reduce the emission of pollutants such as soot, NOx, UHCs (unburned hydrocarbons), and greenhouse gases in general. Thus, the generation of reliable chemical kinetic mechanisms is essential in achieving this. A hierarchical [3-6] (bottom-up) strategy has proven to be a good way to develop reliable chemical kinetic mechanisms and improve our understanding of the chemistry controlling pyrolysis and oxidation.

Chapter 8

Combustion properties of fuels such as ignition delay time (IDT), speciation profiles, flame speed, and others become invaluable for the optimization of combustors. Relevant experiments and modeling studies for mono-fuels and some blends, such as ethylene, ethane, and propane, have been carried out with different methods and are available in the literature [7-14].

Dagaut et al. [15-17] studied species profiles consumed and produced during the oxidation ethylene, ethane, and propane in a jet-stirred reactor (JSR) using fuel mixtures diluted with nitrogen, at equivalence ratios (φ) of 0.1 – 4.0, at pressures ranging from 1 – 10 atm in the temperature range 800 – 1250 K. Their conclusions showed the importance of small molecule sub-mechanisms including CO_2, CH_2O, CH_4, C_2H_2, C_2H_4, and C_3H_6 on the combustion of higher hydrocarbons.

Lowry et al. [18] measured laminar premixed flame speeds of pure methane, ethane, propane, and their binary blends with methane, at $\varphi = 0.7 – 1.3$, in a constant-volume cylindrical vessel, in the pressure range 1 – 10 atm, at room temperature (298 K). It was highlighted the need to extensively the synergistic effect of blends in comparison to pure fuels.

Baigmohammadi et al. [5, 6] measured IDTs for pure ethylene, ethane, and propane, and binary alkane/alkene blends in a shock tube (ST) and a rapid compression machine (RCM) at $\varphi = 0.5 – 2.0$, at pressures ranging from 20 – 40 atm in the temperature range of 800 – 2000 K. Their conclusions showed that the synergistic effect on the reactivity of the mixture is important not only based on the fuel blends but in each variable considered during the combustion phenomena such as pressure, temperature, dilution, etc. These previous studies [5, 6, 15-17] also used chemical kinetic mechanisms to predict the experimental data presented and identify the most relevant chemical reactions controlling the oxidation of these fuels.

Despite the large amount of data for pure ethylene, ethane, and propane fuels, there are comparatively fewer studies of their blends, Table 8-1.

Table 8-1. IDTs for C_2H_4, C_2H_6, C_3H_8, and binary blends from the literature.

Facility	Fuel	p_C / atm	T_C / K	Year	Reference
ST/RCM	C_2H_4	1 – 40	773 – 2200	1999 – 2020	[5, 8, 19-22]
ST/RCM	C_2H_6	1 – 40	830 – 1862	1971 – 2020	[5, 9, 23-25]
ST/RCM	C_3H_8	1 – 40	689 – 2615	1977 – 2013	[26-31]
ST/RCM	C_2H_4/C_2H_6	1 – 40	800 – 2000	2020	[6]

Firstly, the current study aims to address this by providing IDT data for binary C_2H_4/C_3H_8 and C_2H_6/C_3H_8 blends over a wide range of temperatures, pressures, equivalence ratios, and dilutions relevant to engine and gas turbine conditions. Secondly, it aims to validate a detailed chemical kinetic model using novel experiments and literature data. Provided first is a summary of the experimental condition details and approaches taken for this study, followed by details of the modeling work. The results and discussion section encompasses all the comparisons of the model performance with the experimental data. Additionally, a comparison of the most important reactions for the pure fuels and their binary blends are presented to determine the kinetics controlling the reactivity of the blends.

8.2 Design of experiments and experimental approaches

All of the measured IDTs collected and presented in this study were obtained using two different shock tubes (ST) and two rapid compression machines (RCMs). For those experiments carried out at NUI Galway at pressures ranging from 1 – 40 bar and intermediate-to-high-temperatures (> 1000 K), low- (LPST) (p_C = 1 bar) and high-pressure ($p_C \geq 20$ bar) shock tubes (HPSTs) were applied. The IDT experiments corresponding to the relatively high-pressure ($20 \leq p_C \leq 40$ bar) and low-temperature (< 1000 K) regimes were taken using a twin-piston RCM. Some experiments at working pressures of 40 bar and greater were measured using a single-piston RCM at the Physico-Chemical Fundamentals of Combustion (PCFC)-RWTH [32, 33] Aachen University to enhance the fidelity of the experimental IDTs. Details of these facilities and their operating characteristics are available in the literature [6, 34, 35].

For the IDT experiments performed at NUIG, ethane, ethylene, and propane gases with a purity of 99.95% were supplied by Air liquid UK. BOC Ireland provided all other gases with purities of 99.99% for oxygen, nitrogen, argon, and 99.96% for helium. At the PCFC-RWTH Aachen University, the alkane/alkene gases were supplied by Westfalen AG with a 99.95% purity. All other gases were supplied by Westfalen AG and Praxair with purities of oxygen ≥ 99.995%, nitrogen ≥ 99.95%, and argon ≥ 99.996%.

To stochastically distribute the experimental IDTs, the experimental conditions for this study were generated using the Taguchi [36] approach by applying an L_9 matrix based on four parameters of propane concentration, pressure, equivalence ratio, and dilution and also three different levels for each parameter studied. This approach has already been described by Baigmohammadi et al. [5, 6].

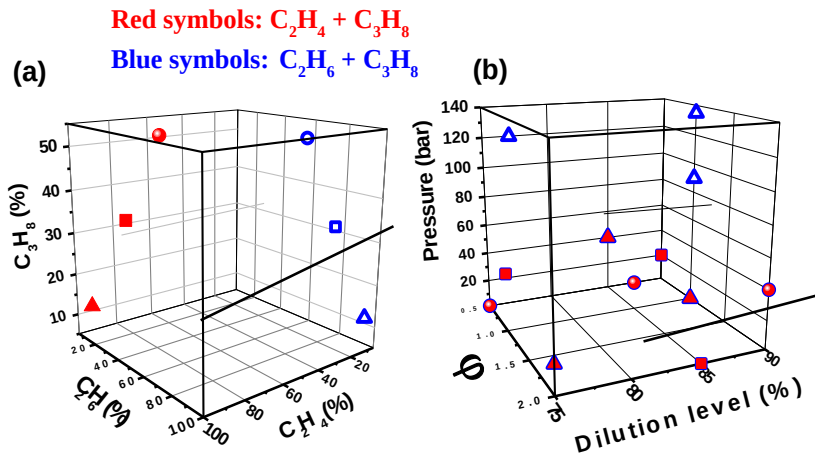

Figure 8-1. Experimental Taguchi [36] L9 matrix of conditions. For 90%/10%, 70%/30%, and 50%/50% ratios (a) red: binary C_2H_4/C_3H_8 blends, blue: binary C_2H_6/C_3H_8 blends; and (b) pressure, equivalence ratio, and dilution parameters.

For the mixture conditions studied, the propane concentration in the fuel blends varies from 10 – 50%, at pressures ranging from 10 – 135 bar, for φ of 0.5 – 2.0 and at dilutions of 75 – 90% (75% N_2 + 0–15% Ar). However, the ratio between the diluents were changed at low–temperature regime (RCM) depending on the desired compressed gas temperature. A synopsis of the designed conditions is presented Figure 8-1 in Table 8-2.

In the current study, most of the measured IDTs in the HPST and RCMs [10, 33, 37-42] are defined as the time between compression and the maximum gradient in pressure ($\frac{dp}{dt}$) behind the reflected shock. However, we define the ignition event as the maximum gradient in CH*($\frac{dCH^*}{dt}$) behind the reflected shock in the LPST measured by a photomultiplier and also when the test mixture is highly diluted in the HPST.

Table 8-2. C_2H_4/C_3H_8 and C_2H_6/C_3H_8 mixture compositions in % mole volume in the current study. Where keywords NUIG refers to ST/RCM facilities at C^3-NUIGalway, and PCFC refers to RCM facility at PCFC-RWTH Aachen University, respectively.

	No.	% C_2H_6	% C_2H_4	% C_3H_8	% O_2	Dilution	φ	p_C / bar	Facility
C_2H_4/C_3H_8 50%/50%	1	0.000	1.40	1.400	22.20	75% N_2	0.5	1	NUIG
	2	0.000	1.50	1.500	12.00	75% N_2+10% Ar	1.0	20	NUIG
	3	0.000	1.70	1.700	6.60	75% N_2+15% Ar	2.0	40	NUIG/ PCFC
C_2H_4/C_3H_8 70%/30%	4	0.000	3.75	1.610	9.64	75% N_2+10% Ar	2.0	1	NUIG
	5	0.000	0.85	0.360	8.790	75% N_2+15% Ar	0.5	20	NUIG
	6	0.000	3.80	1.600	19.60	75% N_2	1.0	40	NUIG
C_2H_4/C_3H_8 90%/10%	7	0.000	2.10	0.200	7.70	75% N_2+15% Ar	1.0	1	NUIG
	8	0.000	8.60	1.000	15.40	75% N_2	2.0	20	NUIG
	9	0.000	1.80	0.200	13.00	75% N_2+10% Ar	0.5	40	NUIG/ PCFC
C_2H_6/C_3H_8 50%/50%	10	1.300	0.00	1.300	22.40	75% N_2	0.5	1	NUIG
	11	1.430	0.00	1.430	12.14	75% N_2+10% Ar	1.0	20	NUIG
	12	1.600	0.00	1.600	6.80	75% N_2+15% Ar	2.0	40	NUIG/ PCFC
C_2H_6/C_3H_8 70%/30%	13	3.530	0.00	1.510	9.96	75% N_2+10% Ar	2.0	1	NUIG
	14	0.790	0.00	0.340	8.87	75% N_2+15% Ar	0.5	20	NUIG
	15	3.535	0.00	1.515	19.95	75% N_2	1.0	40	NUIG
C_2H_6/C_3H_8 90%/10%	16	1.940	0.00	0.220	7.84	75% N_2+15% Ar	1.0	1	NUIG
	17	8.000	0.00	0.900	16.10	75% N_2	2.0	20	NUIG
	18	1.600	0.00	0.200	13.20	75% N_2+10% Ar	0.5	40	NUIG/ PCFC
	19	1.860	0.00	0.210	7.53	45.2% N_2+45.2% Ar	1.0	90	PCFC
	20	2.520	0.00	0.280	20.40	76.8% N_2	0.5	120	PCFC
	21	1.860	0.00	0.210	7.53	65.4% N_2+25% Ar	1.0	135	PCFC

The corresponding uncertainties involved in the measured IDTs are discussed by Baigmohammadi et al. [5, 6]. Based on the analysis, the uncertainties in compressed mixture temperatures ($\sigma_{Tc,5}$) and measured IDTs change for every individual experimental point depending on the initial temperature, pressure, and/or mixture composition. In this regard, the average uncertainties of the compressed temperatures and the measured IDTs in NUIG-L/HPSTs are estimated to be approximately ± 10/20 K and ± 25%, respectively. However, the compressed

temperature uncertainty and the measured IDT variation in the NUIG and PCFC RCMs are evaluated to be about ± 5 – 15 K and ± 20% over the entire range of conditions.

8.3 Computational modeling

In the current study, NUIGMech1.1 is used to simulate the experimental targets. This mechanism comprises 2746 species and 11270 reactions, which is developed based on series of recent experimental [4-6, 43-47] and theoretical studies [48-50]. These works are outcome of continuous evolution of the detailed NUIGMech1.1 model which is extensively validated in the prior studies for oxidation of C_1–C_2 hydrocarbons [5, 6], natural gas mixtures [44], propane/propene blends [47], propyne [45], iso-butene [51], as well as auto-ignition and pyrolysis of C_2 – C_6 alkenes [4, 46]. The current work is a part of simultaneous development of the overall NUIGMecah1.1 mechanism. For the purpose of comparison, AramcoMech3.0 [52] is also utilized to perform simulations against the IDT experimental data from this study. Modifications of the most important reactions explicit to ethane, ethylene and propane chemistry in NUIGMech1.1 haven't been mentioned in detail in the previous publications [5, 6, 43, 50], and thus are discussed in this study.

The experimental results were simulated using Python scripts based on the Cantera 2.4 [53] library and the CHEMKIN-Pro 18.2 [54] software, Cantera is suitable for automatization making data manipulation faster; however, Chemkin-Pro is faster for simulations involving large mechanisms and thus is more suitable for simulations when a full mechanism is required. As mentioned above, the definition of IDT is taken as the maximum gradient of pressure or radical concentration with respect to time for the ST simulations. In the RCM simulations, facility effects are included using the volume-time profiles derived from non-reactive experimental pressure-time traces in which O_2 is replaced by N_2 in the mixture [55, 56].

The global model uncertainties, ϵ_{MAD} and ϵ_{MAPE}, are calculated based on the differences between experimental data and mechanism simulated data using the Mean Absolute Deviations (MAD), and the Mean Absolute Percentage Error (MAPE), equations 8-1 and 8-2 respectively. However, to analyze the data with an individual error, the Relative Percentage Error (RPE), ε_{RPE}, was used (equation 8-3) to generate the histograms presented in this work. The mathematical expressions used are the following:

$$\epsilon_{\mathrm{MAD}} = \frac{1}{n}\sum |IDT_{\mathrm{mod}} - IDT_{\mathrm{exp}}| \tag{8-1}$$

$$\epsilon_{\mathrm{MAPE}} = \frac{1}{n}\sum \left(\left|\frac{IDT_{\mathrm{mod}} - IDT_{\mathrm{exp}}}{IDT_{\mathrm{exp}}}\right|\right) * 100 \tag{8-2}$$

$$\varepsilon_{\mathrm{RPE}} = \left(\frac{IDT_{\mathrm{mod}} - IDT_{\mathrm{exp}}}{IDT_{\mathrm{exp}}}\right) * 100 \tag{8-3}$$

where *n* is the total number of experimental measurements. Further details about the statistical analysis are provided appendix E.

To identify the reactions controlling IDTs, brute-force sensitivity analyses were performed at the experimental conditions presented in this study. The sensitivity coefficient (S; [57]) is defined as:

$$S = \frac{In(\tau_{+}/\tau_{-})}{In(k_{+}/k_{-})} = \frac{In(\tau_{+}/\tau_{-})}{In(2.0/0.5)}$$

The sensitivity coefficient *S* calculated using the brute force method is based on the IDT (τ), with the pre-exponential factor in the Arrhenius equations for each reaction perturbed in the sensitivity analysis. The sensitivity coefficient can be negative or positive, where a negative value refers to a reaction promoting reactivity (decreasing IDT), while a positive value refers to a reaction inhibiting reactivity (increasing IDT). Furthermore, rate of production (ROP) analyses was carried out to track the consumption of the blends and the production of intermediate species.

The global correlation discussion based on constant volume (CV) IDT simulations using NUIGMech1.1 is presented in the "Regression analysis" section (Section 8.4.5), together with general equations sorted by various temperature and pressure conditions. The aim of these correlations is to provide an easy and quick way to determine the IDT behavior of the binary fuels. It does not require any kind of software pre-set up, and the coefficients of interest can be directly substituted in the equations provided in the respective section. A complete table of coefficient values and further details is provided in appendix E.

8.4 Results and discussions

All of the experimental results for the ethane/propane (C_2H_6/C_3H_8) and ethylene/propane (C_2H_4/C_3H_8) blends are presented in Section 8.4.1 together with simulations using NUIGMech1.1 and AramcoMech3.0 [52]. Henceforth, in all figures, the open symbols represent experimental LPST and/or HPST data, and the solid symbols represent the experimental low-temperature RCM data. Sections 8.4.2 – 8.4.4 present results for the effects of blend composition, pressure, and equivalence ratio using NUIGMech1.1 and their corresponding correlations. Finally, Section 8.4.5 discuss the correlation performance.

8.4.1 Ethylene/propane and ethane/propane blends

Figures 8-2 and 8-3 present experimental data and model predictions of IDTs over the range of conditions studied for the binary C_2H_4/C_3H_8 and C_2H_6/C_3H_8 blends.

Figures 8-2 and 8-3 show that NUIGMech1.1 is in better agreement than AramcoMech3.0 with the experimental data. Statistical analyses were conducted using the IDTs from the experiments, and those calculated using both NUIGMech1.1 and AramcoMech3.0. A total sample of 328 IDTs was used to determine the mean, standard deviation (σ), mean absolute deviation (MAD), relative percentage error (RPE), and mean absolute percentage error (MAPE). Figures. ES10(a) and ES10(b), with "ES" notation referring to the Supplementary material in appendix E, provide

the RPE frequency distribution for NUIGMech1.1 and AramcoMech3.0 relative to the IDT experiments. It can be inferred that the differences between NUIGMech1.1 and AramcoMech3.0 are a consequence of the poor predictions of AramcoMech3.0 in the low-temperature regime for the C_2H_4/C_3H_8 blends. Furthermore, the absolute values of MAPE calculated over the entire dataset using NUIGMech1.1 were 26.4%, while that for AramcoMech3.0 is 31.9%, indicating the greater accuracy of NUIGMech1.1. As it can accurately predict the IDT data measured over a wide range of temperatures, pressures and equivalence ratios, CV simulations are performed using NUIGMech1.1 to understand the effects of these operating conditions on the IDTs of pure fuels and their binary blends.

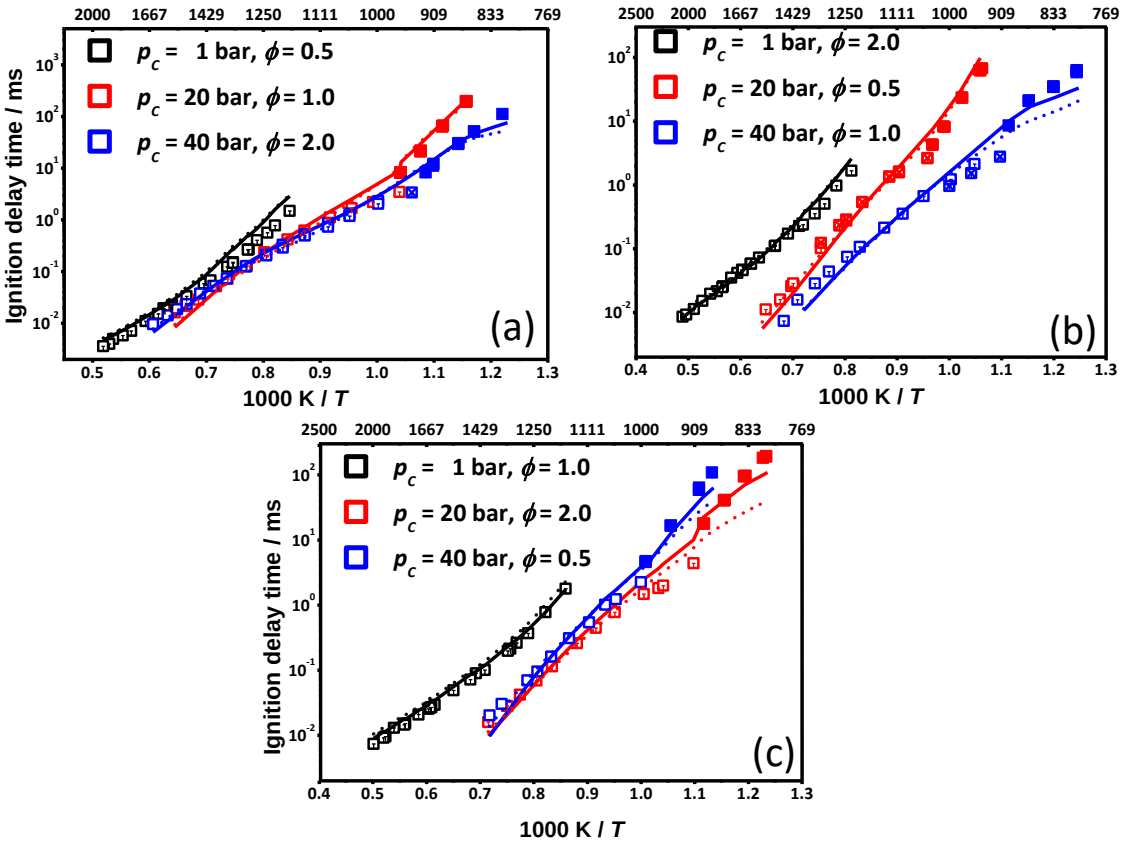

Figure 8-2. Comparisons of experimental ST (□) and RCM (■) data against model predictions using NUIGMech1.1 (solid lines) and AramcoMech3.0 (dashed lines) for; (a) a 50% C_2H_4/50% C_3H_8 blend at 75% N_2 (black symbols/lines), 75% N_2 + 10% Ar (red symbols/lines), and 75% N_2 + 15% Ar (blue symbols/lines); (b) a 70% C_2H_4/30% C_3H_8 blend at 75% N_2 + 10% Ar (black symbols/lines), 75% N_2 + 15% Ar (red symbols/lines), and 75% N_2 (blue symbols/lines); and (c) a 90% C_2H_4/10% C_3H_8 blend at 75% N_2 + 15% Ar (black symbols/lines), 75% N_2 (red symbols/lines), and 75% N_2 + 10% Ar (blue symbols/lines).

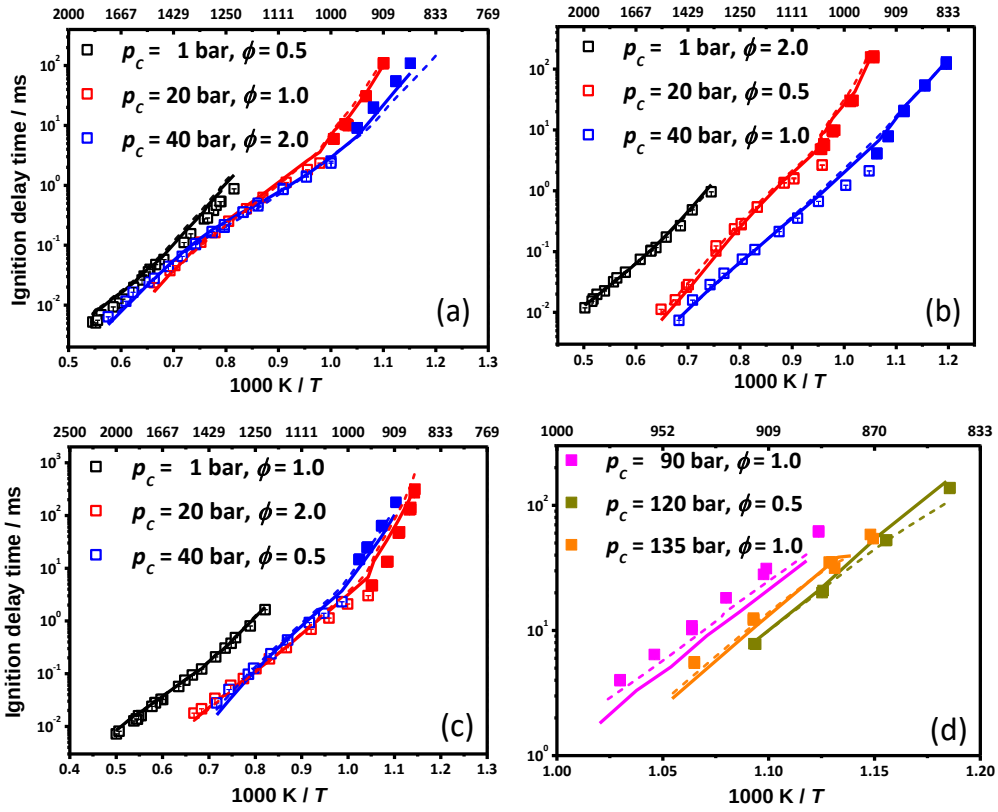

Figure 8-3. Comparisons of experimental ST (□) and RCM (■) data against model predictions using NUIGMech1.1 (solid lines) and AramcoMech3.0 (dashed lines), for; (a) a 50% C2H6/50% C3H8 blend at 75% N2 (black symbols/lines), 75% N2 + 10% Ar (red symbols/lines), and 75% N2 + 15% Ar (blue symbols/lines); (b) a 70% C2H6/30% C3H8 blend at 75% N2 + 10% Ar (black symbols/lines), 75% N2 + 15% Ar (red symbols/lines), and 75% N2 (blue symbols/lines); (c) a 90% C2H6/10% C3H8 blend at 75% N2 + 15% Ar (black symbols/lines), 75% N2 (red symbols/lines), and 75% N2 + 10% Ar (blue symbols/lines); and (d) a 90% C2H6/10% C3H8 blend at 45.2% N2 + 45.2% Ar (magenta symbols/lines), 76.8% N2 (green symbols/lines), and 65.4% N2 + 25% Ar (orange symbols/lines).

8.4.2 Synergistic/antagonistic effect of blends

First, the ignition behavior of pure fuels is analyzed to determine the important reactivity controlling reactions. In Figure 8-4, the IDT predictions for C_2H_4/air, C_2H_6/air, and C_3H_8/air mixtures at fuel-lean conditions, at p_C = 40 bar and T_C in the range 740 − 1660 K are shown. At lower temperatures (T_C < 1050 K), C_3H_8 is the fastest fuel to ignite, however, the trend tends to reverse at higher temperatures, and it exhibits the slowest reactivity compared to both the C_2H_4 and C_2H_6 mixtures. The reactivity of C_2H_4 is observed to be higher than C_2H_6 at all temperatures studied here.

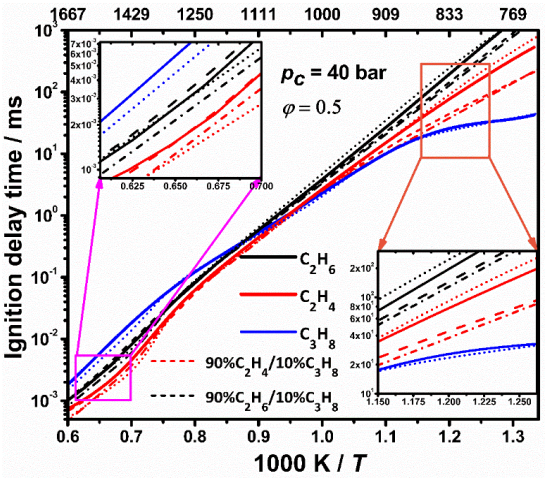

Figure 8-4. IDT predictions of pure fuels, 90% C_2H_4/10% C_3H_8 and 90% C_2H_6/10% C_3H_8 binary blend in air. The corresponding derived correlation predictions are marked as dotted lines for pure fuels and dotted-dashed for binary blends.

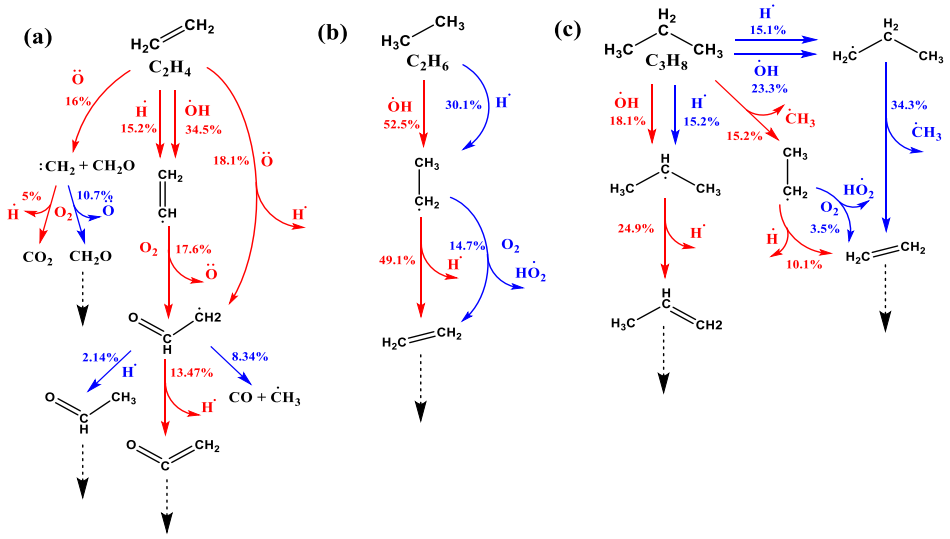

Figure 8-5. Flux analyses of pure (a) C_2H_4, (b) C_2H_6, and (c) C_3H_8 fuel ignition for T_C = 1430 K, p = 40 bar and φ = 0.5, at the time of 15% fuel consumption.

To explore the controlling chemistry at high-temperature conditions, ROP analyses for C_2H_4/air, C_2H_6/air, and C_3H_8/air mixtures are illustrated in Figure 8-5 at T_C = 1430 K and p_C = 40 bar. The ROP analyses are performed following an elemental carbon (C) balance. The percentage value above the arrow refers to the percentage of the fuel proceeding through that pathway. The reaction paths represent the promoting (red color) and inhibiting (blue color) channels of the corresponding fuels. At high temperatures, the reactivity of all fuels is governed by the dominating chain branching reaction $\dot{H} + O_2 \leftrightarrow \ddot{O} + \dot{O}H$, which depends on the concentrations of $\dot{H}$ atoms and O_2. In the case of C_2H_4/air ignition, at 1430 K, the fuel mainly undergoes H-atom

abstraction by ȮH and Ḣ producing vinyl ($\dot{C}_2H_3$) radicals. This radical reacts with O_2 to generate vinoxy radical ($\dot{C}H_2CHO$) through the chain branching reaction $\dot{C}_2H_3 + O_2 \leftrightarrow \dot{C}H_2CHO + Ö$. Oxygen atoms further react with ethylene greatly promoting reactivity by generating Ḣ atoms through two different channels, $C_2H_4 + Ö \leftrightarrow \dot{C}H_2CHO + Ḣ$ (18.1%) and $C_2H_4 + Ö \leftrightarrow \dot{C}H_2 + CH_2O$ (16%) followed by $\dot{C}H_2 + O_2 \leftrightarrow CO_2 + Ḣ + Ḣ$. For the reaction of oxygen atoms with ethylene the total rate constant and the branching fractions through the various product channels ($\dot{C}H_3 + H\dot{C}O$, $\dot{C}H_2CHO + Ḣ$, $\dot{C}H_2 + CH_2O$, $CH_2CO + H_2$) are taken from the calculations by Li et al. [58]. These are in good agreement available experimental data, as shown in Figure 8-6(a). Figure 8-6(b) compares the rate constants for the individual pathways associated with the $C_2H_4 + Ö$ system. AramcoMech3.0 used the rate constants for $C_2H_4 + Ö$ producing $\dot{C}H_3 + H\dot{C}O$ and $\dot{C}H_2CHO + Ḣ$ based on the Baulch et al. [59] recommendation. The pathway producing $\dot{C}H_2 + CH_2O$ was not included in AramcoMech3.0, and its inclusion in NUIGMech1.1 significantly increases the predicted reactivity. The effect on IDT predictions of updating the rate constant for $C_2H_4 + Ö \rightarrow$ products for C_2H_4/air mixtures is shown in Figure ES19 of appendicx E. The $\dot{C}H_2CHO$ radical formed here further decomposes to produce ketene and Ḣ atom, Figure 8-5(a). The formation of substantial concentrations of Ḣ atoms is responsible for the faster ignition of C_2H_4/air mixtures at higher temperatures.

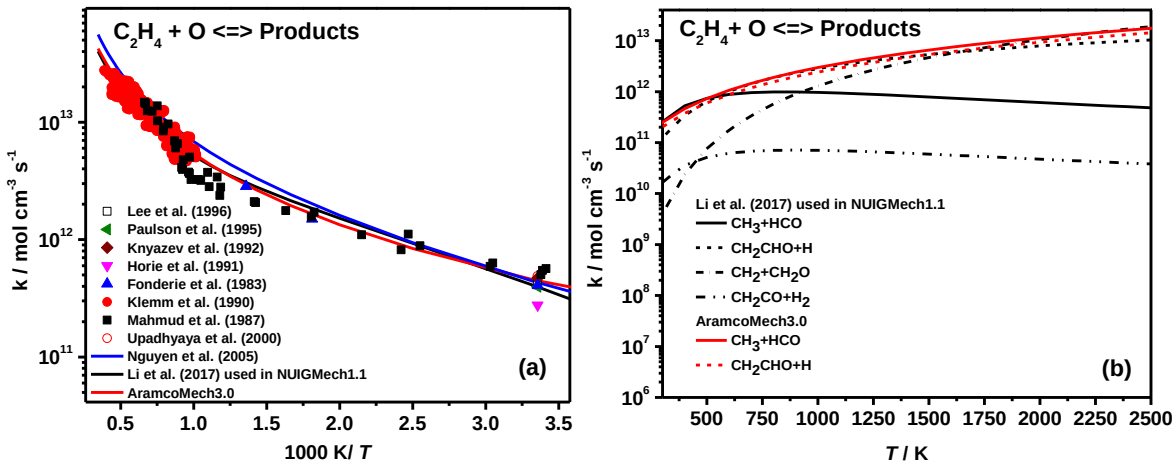

Figure 8-6. Comparisons for experimental and theoretical determinations for (a) the total reaction rate constant of $C_2H_4 + Ö$ [58, 60-68] and (b) product pathways for the reaction $C_2H_4 + Ö$.

Ethylene is an important intermediate in C_2H_6 oxidation. At 1430 K, C_2H_6 consumption is initiated by H-atom abstraction primarily by ȮH and Ḣ forming ethyl ($\dot{C}_2H_5$) radicals. There has been a wide variety of experimental investigations for these rate constants, as shown in Figure ES13. NUIGMech1.1 has an updated rate constant for H-atom abstraction by ȮH based on the fit recommended by Krasnoperov et al. [69]. For H-atom abstraction by Ḣ, we have adopted the theoretical calculations from Sivaramakrishnan et al. [70]. $\dot{C}_2H_5$ radicals decompose promptly to C_2H_4 and Ḣ atoms, which undergo chain branching by reacting with O_2 via Ḣ + O_2 ↔ Ö + ȮH, promoting reactivity. However, at 1430 K, approximately 15% of $\dot{C}_2H_5$ radicals react with O_2 to form C_2H_4 through the H-atom abstraction reaction that competes with $\dot{C}_2H_5$ radical decomposition. The subsequent reaction pathways associated with the C_2H_6 consumption flux are governed by the high-temperature chemistry of C_2H_4, as discussed in the previous paragraph. At higher temperature conditions, $\dot{C}_2H_5$ + O_2 ↔ C_2H_4 + $H\dot{O}_2$, as well as the H-atom abstraction by Ḣ from the fuel which competes with the major chain branching reaction Ḣ + O_2 ↔ Ö + ȮH, are responsible for the lower reactivity of C_2H_6 compared to C_2H_4.

Similar to ethane and ethylene, propane oxidation is mainly driven by H-atom abstraction by Ȯ-radicals and Ḣ atoms, generating primary ($n\dot{C}_3H_7$) and secondary propyl ($i\dot{C}_3H_7$) radicals. Due to the importance of H-atom abstraction by ȮH from propane, there have been a large number of measurements performed, Figure ES14. The rate constant adopted in this work is the best fit from the more recent direct measurements by Sivaramakrishnan et al. [71], who investigated the branching fraction for the abstraction of the secondary C–H bond in the temperature range 927 – 1146 K, together with the measurement by Droege et al. [72] over the temperature range 298 – 900 K (Figure ES14). At 1430 K, approximately 15% of the C_3H_8 is consumed by unimolecular decomposition producing $\dot{C}_2H_5$ and methyl radicals ($\dot{C}H_3$), Figure 8-5(c). Substantial concentrations of $\dot{C}H_3$ radicals are also formed from the β-scission of $n\dot{C}_3H_7$ radicals. Methyl radicals are consumed by reaction with $H\dot{O}_2$ to produce methoxy radicals through the chain

branching reaction $\dot{C}H_3 + H\dot{O}_2 \leftrightarrow \dot{C}H_3O + \dot{O}H$, which promotes reactivity. The route through the chain-terminating reaction $\dot{C}H_3 + H\dot{O}_2 \leftrightarrow CH_4 + O_2$ inhibits reactivity. This competition between chain branching and termination significantly influences IDT predictions for C_3H_8. The rate constants for these reactions are taken from the theoretical calculations of Jasper et al. [73] and Zhu et al. [74] respectively. The rate constants and the branching ratio of the two $\dot{C}H_3 + H\dot{O}_2$ channels agree well with the most recent experimental measurements by Hong et al. [75] (Figure ES15). The self-recombination of $\dot{C}H_3$ radicals producing C_2H_6 further contributes to a reduction in the reactivity of propane. The presence of high concentrations of $\dot{C}H_3$ radicals ultimately decreases the reactivity of C_3H_8 compared to C_2H_6 at high-temperature conditions.

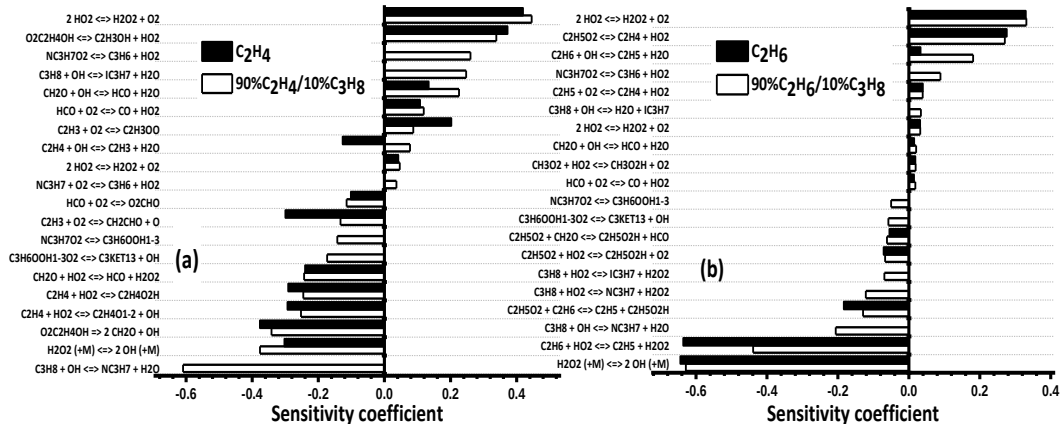

Figure 8-7. Sensitivity analyses to IDT at 790 K, 40 atm, and φ = 0.5, for; (a) C_2H_4 and 90% C_2H_4/10% C_3H_8, in air; and (b) C_2H_6 and 90% C_2H_6/10% C_3H_8 in air.

The effects on IDTs of the addition of C_3H_8 to C_2H_4/air and C_2H_6/air mixtures are presented in Figure 8-4. The reactivities of the mixtures increase significantly for the 90% C_2H_4/10% C_3H_8 and 90% C_2H_6/10% C_3H_8 binary blends at lower temperatures in the range 740 – 1000 K. The addition of only 10% C_3H_8 to the C_2H_4/air and C_2H_6/air mixtures shortens IDTs by a factor of 2.8 and 2.0 respectively, at 790 K. To interpret the influence of C_3H_8 addition on the ignition of the C_2H_4/air and C_2H_6/air mixtures, sensitivity analyses were performed at 790 K, Figure 8-7. Moreover, Figure 8-8 illustrates the flux analyses performed for these mixtures in the same condition. The black color represents the flux for the pure C_2H_4/air or C_2H_6/air mixtures, and the

red color represents the flux for the C_3H_8 blended binary mixtures. The flux analysis presented in Figure 8-8 shows that adding propane in the mixture does not alter the reaction pathways of ethylene and ethane chemistry and it also makes insignificant changes to their flux values.

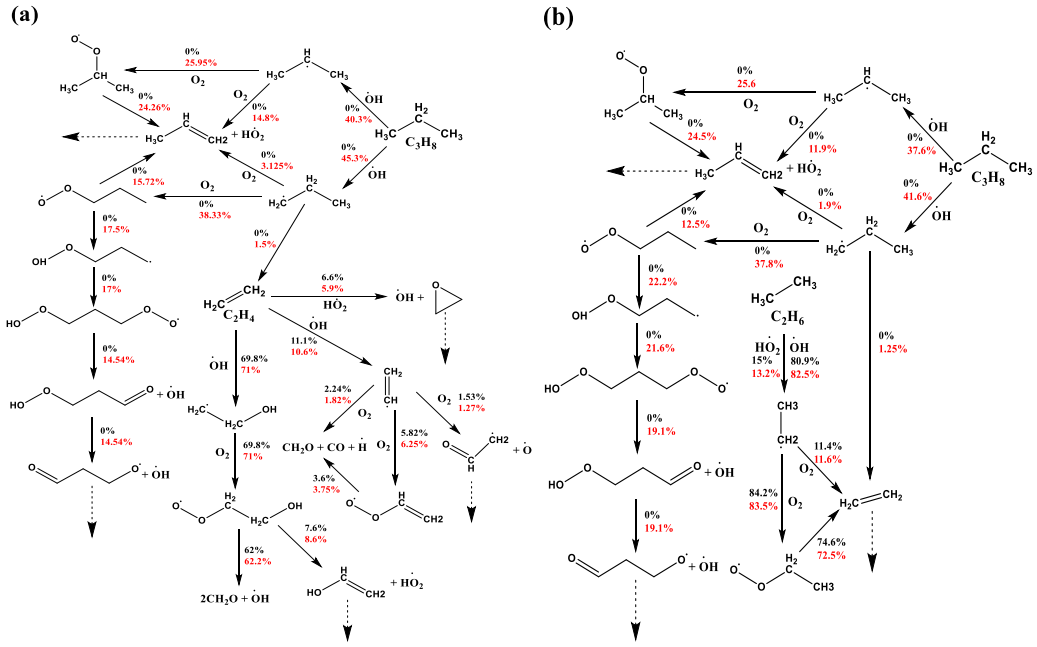

Figure 8-8. Flux analyses for; (a) pure C_2H_4 (black) and 90% C_2H_4/10% C_3H_8 (red); and (b) pure C_2H_6 (black) and 90% C_2H_6/10% C_3H_8 (red) mixtures ignition for 790 K and at 40 atm, and φ = 0.5.

At 790 K, for both pure C_2H_4 and 90% C_2H_4/10% C_3H_8 blend, ethylene is primarily consumed by the addition of ȮH radical to the double bond forming hydroxyethyl radicals, which accounts for around 70% of the overall C_2H_4 consumption. These add to molecular oxygen producing hydroxyethyl-peroxy radicals ($\dot{O}_2C_2H_4OH$), which subsequently decompose, producing two formaldehyde molecules and an ȮH radical or form vinyl alcohol and $H\dot{O}_2$ radicals, the former being the most favorable product channel promoting reactivity for the C_2H_4/air mixture, Figure 8-8(a). Besides ȮH addition, $H\dot{O}_2$ addition to ethylene producing oxirane (C_2H_4O1-2) and ȮH radical also has a large promoting effect on the reactivity of ethylene at low temperatures, especially for fuel-rich conditions.

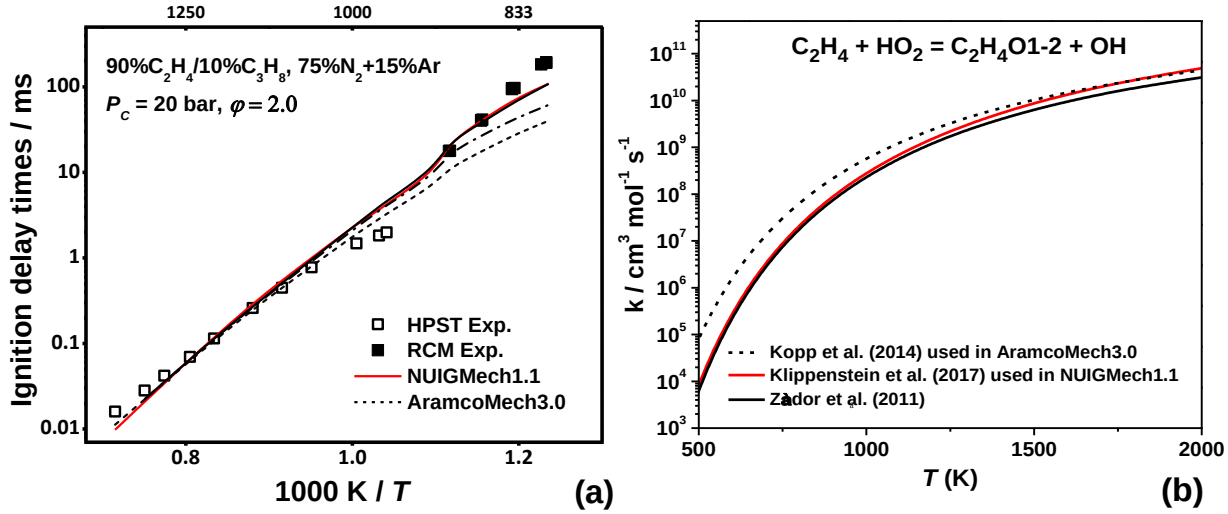

Figure 8-9. (a) Effect of changing the rate constant for C_2H_4 + $H\dot{O}_2$ ↔ C_2H_4O1-2 + $\dot{O}H$ and $\dot{O}_2C_2H_4OH$ → products on IDT predictions for 90% C_2H_4/10% C_3H_8 mixtures, — NUIGMech1.1, ------ AramcoMech3.0, —·—· AramcoMech3.0 plus updated rate constant [76] for C_2H_4 + $H\dot{O}_2$ ↔ C_2H_4O1-2 + $\dot{O}H$, ── AramcoMech3.0 plus updated rate constant for C_2H_4 + $H\dot{O}_2$ ↔ C_2H_4O1-2 + $\dot{O}H$ and $\dot{O}_2C_2H_4OH$ → products [77]; and (b) Comparison of current rate constant [75] for C_2H_4 + $H\dot{O}_2$ ↔ C_2H_4O1-2 + $\dot{O}H$ against the study by Kopp et al. [11] and Zádor et al. [78].

The importance of the C_2H_4 + $H\dot{O}_2$ ↔ C_2H_4O1-2 + $\dot{O}H$ and $\dot{O}_2C_2H_4OH$ → products reaction systems on C_2H_4 oxidation is shown in Figure 8-9(a), which also presents the performance of the current mechanism and AramcoMech3.0 as can be seen by red solid line and black dashed line, respectively for 90% C_2H_6/10% C_3H_8 mixtures at p_C = 20 atm, and φ = 2.0. AramcoMech3.0 severely underpredict the IDT, particularly in the low temperature region in the range of 800 – 900 K. AramcoMech3.0 implemented a reaction rate for C_2H_4 + $H\dot{O}_2$ ↔ C_2H_4O1-2 + $\dot{O}H$ based on the recommendation by Kopp et al. [11]. Recently Zádor et al. [77] and Klippenstein et al. [76] studied the potential energy surfaces of the $C_2H_5\dot{O}_2$ system using high-level quantum chemistry calculations. NUIGMech1.1 has adopted the rate constant for C_2H_4 + $H\dot{O}_2$ from Klippenstein et al. [76], which is approximately a factor of three lower than the rate constant recommended by Kopp et al [11] at 800 K, Figure 8-9(b), and updating this rate constant in AramocMech3.0 leads to a significant improvement in IDT predictions as depicted by the dashed-dotted line in Figure 8-9(a). Another important reaction pathway controlling ethylene IDT is the consumption of $\dot{O}_2C_2H_4OH$ radicals through the Waddington [79] mechanism $\dot{O}_2C_2H_4OH$ → $2CH_2O$ + $\dot{O}H$ and the $H\dot{O}_2$ elimination channel producing C_2H_3OH which inhibits

reactivity. In NUIGMech1.1 the rate constant for the dissociation of $\dot{O}_2C_2H_4OH$ radicals is adopted from Zádor et al. [78]. AramcoMech3.0 utilized an estimated rate constant for the Waddington pathway that is an order of magnitude higher than the rate determined by Zádor et al. [78], while surprisingly, the $H\dot{O}_2$ elimination channel was not included in the mechanism. The last agreement represented by black solid line in Figure 8-9a is attained by updating both $C_2H_4+H\dot{O}_2$ and dissociations of $\dot{O}_2C_2H_4OH$ reactions in AramcoMech3.0 that leads to significant improvement in the agreement of the simulations compared to experimental measurements.

As seen in Figure 8-8(a), $\dot{O}H$ radicals can abstract a hydrogen atom from ethylene producing $\dot{C}_2H_3$ radicals. These add to O_2 generating vinyl-peroxy radicals, which subsequently dissociate to formaldehyde, CO, and $\dot{H}$ atoms. Some $\dot{C}_2H_3$ radicals also produce $\dot{C}H_2CHO$ and $\ddot{O}$ atoms increasing the reactivity of ethylene ignition, as shown in Figure 8-8(a). For the C_2H_6/air mixture, the fuel is mainly consumed by H-atom abstraction reaction by $\dot{O}H$ and $H\dot{O}_2$ radicals forming $\dot{C}_2H_5$ radicals. These react with O_2 to produce ethylperoxy ($C_2H_5\dot{O}_2$) radicals, which subsequently decompose to C_2H_4 and $H\dot{O}_2$ radicals. Figure 8-7(b) shows that the concerted elimination reaction $C_2H_5\dot{O}_2 \leftrightarrow C_2H_4 + H\dot{O}_2$ is important in inhibiting the autoignition of C_2H_6.

Figures 8-7(a) and 8-7(b) show that C_3H_8 specific reactions become important when propane is added to the C_2H_4/air and C_2H_6/air mixtures. At 790 K, H-atom abstraction from C_3H_8 by $\dot{O}H$ producing $n\dot{C}_3H_7$ and H_2O is the most sensitive reaction promoting reactivity, while abstraction leading to $i\dot{C}_3H_7$ radicals inhibits reactivity. At 790 K, ~14.8% (C_2H_4/C_3H_8 blend) and ~11.9% (C_2H_6/C_3H_8 blend) of $i\dot{C}_3H_7$ radicals react with O_2 to form C_3H_6 and $H\dot{O}_2$ radicals, which reduces reactivity. However, ~38.3% (C_2H_4/C_3H_8 blend) and ~37.8% (C_2H_6/C_3H_8 blend) of $n\dot{C}_3H_7$ radicals add to O_2 forming n-propyl-peroxy ($n\dot{C}_3H_7O_2$) radicals which undergo isomerization generating hydroper4oxyl-propyl ($\dot{C}_3H_6OOH1\text{-}3$) radicals. These then further add to O_2 producing hydroperoxyl-propyl peroxy radical ($\dot{C}_3H_6OOH1\text{-}3O_2$), which isomerizes to produce a carbonylhydroperoxide and an $\dot{O}H$ radical. The carbonylhydroperoxide further dissociates,

producing a carbonyl-alkoxy radical and a second ȮH radical, which is a chain branching pathway, resulting in higher reactivity of the C_3H_8 blended mixtures compared to the pure C_2H_4/air or C_2H_6/air mixtures.

8.4.3 Effect of pressure on ignition

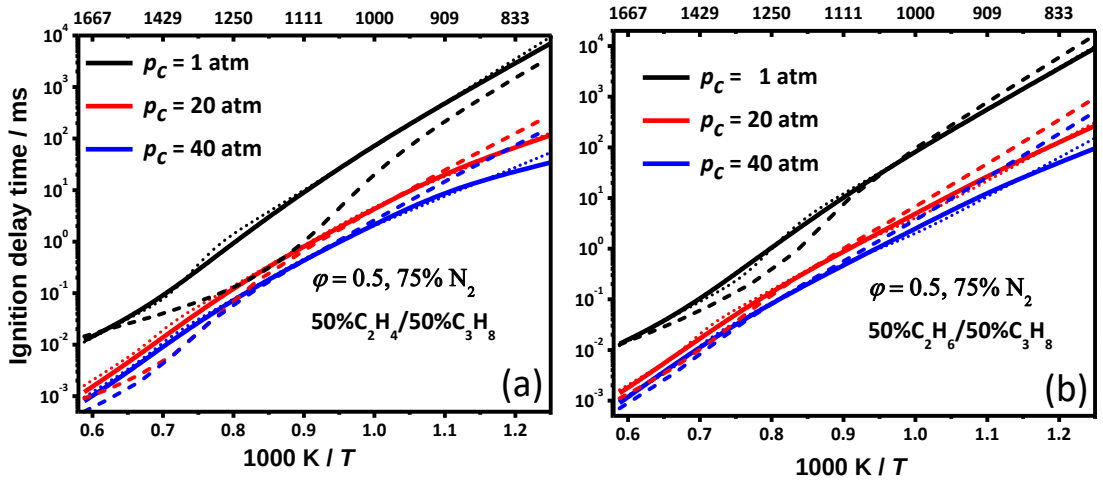

Figure 8-10. Effect of pressure for; (a) 50% C_2H_4/50% C_3H_8 (solid lines) binary blend and pure ethylene (dashed lines); and (b) 50% C_2H_6/50% C_3H_8 (solid lines) binary blend and pure ethane (dashed lines). The derived correlation predictions for binary blends are represented by dotted lines.

Figure 8-10 presents the influence of pressure on the IDTs for the 50% C_2H_4/50% C_3H_8 and 50% C_2H_6/50% C_3H_8 binary mixtures as well as for the pure C_2H_4 and C_2H_6 at φ = 0.5 and 75% N_2 dilution. The model predicts that the reduction in reactivity due to the addition of C_3H_8 with C_2H_4 at 1 atm is more than its corresponding 20 atm and 40 atm cases at intermediate and higher temperature conditions. The self-recombination of methyl radicals is responsible for the lower reactivity of the propane blended mixtures as discussed in Section 8.4.2. In the case of the C_2H_4/C_3H_8 blend at 1250 K, as the pressure decreases to 1 atm the $\dot{C}H_3$ + $\dot{C}H_3$ (+M) ↔ C_2H_6 (+M) reaction more strongly inhibits reactivity, accounting for 35% of the total flux through methyl radicals, while at 40 bar this reaction contributes only 12% to $\dot{C}H_3$ consumption. Furthermore, from Figure 8-10 it is observed that the overall reactivity of the system increases with pressure due to the corresponding increase in the concentration of the reactants. At 800 K, upon increasing the pressure from 1 to 20 atm, there is an order of magnitude increase in

reactivity observed for both the C_2H_4/C_3H_8 and C_2H_6/C_3H_8 mixtures. There is approximately a four-fold increase in reactivity by increasing the pressure from 20 to 40 atm. To determine the reactions controlling IDT predictions at these conditions, sensitivity analyses are presented in Figure 8-11 and Figure ES16 for the binary mixtures at p_C = 1, 20, and 40 atm.

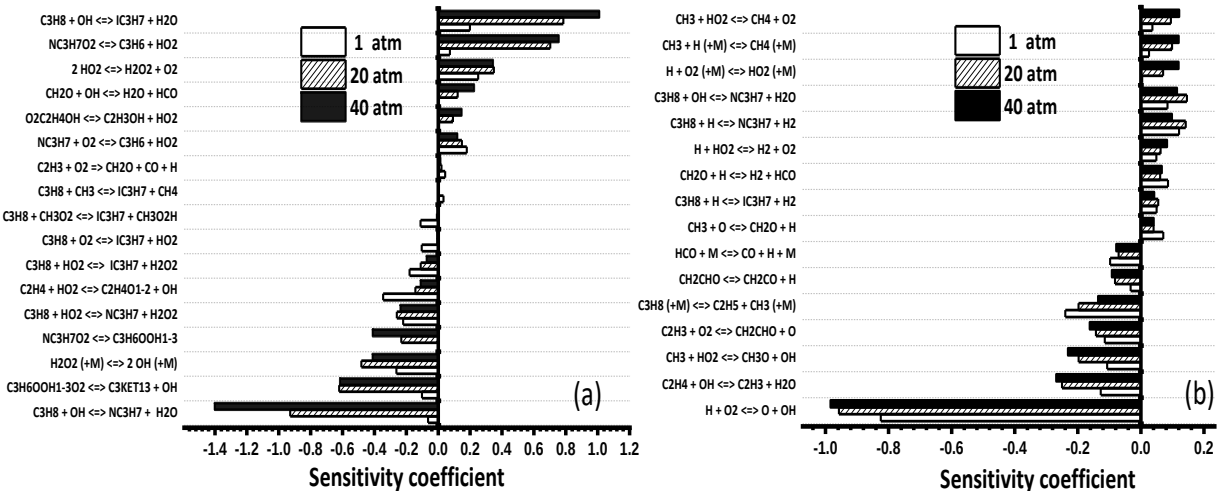

Figure 8-11. Sensitivity analyses to IDT predictions as function of pressure at φ = 0.5, 50% C_2H_4/50% C_3H_8; (a) 800 K; and (b) 1600 K.

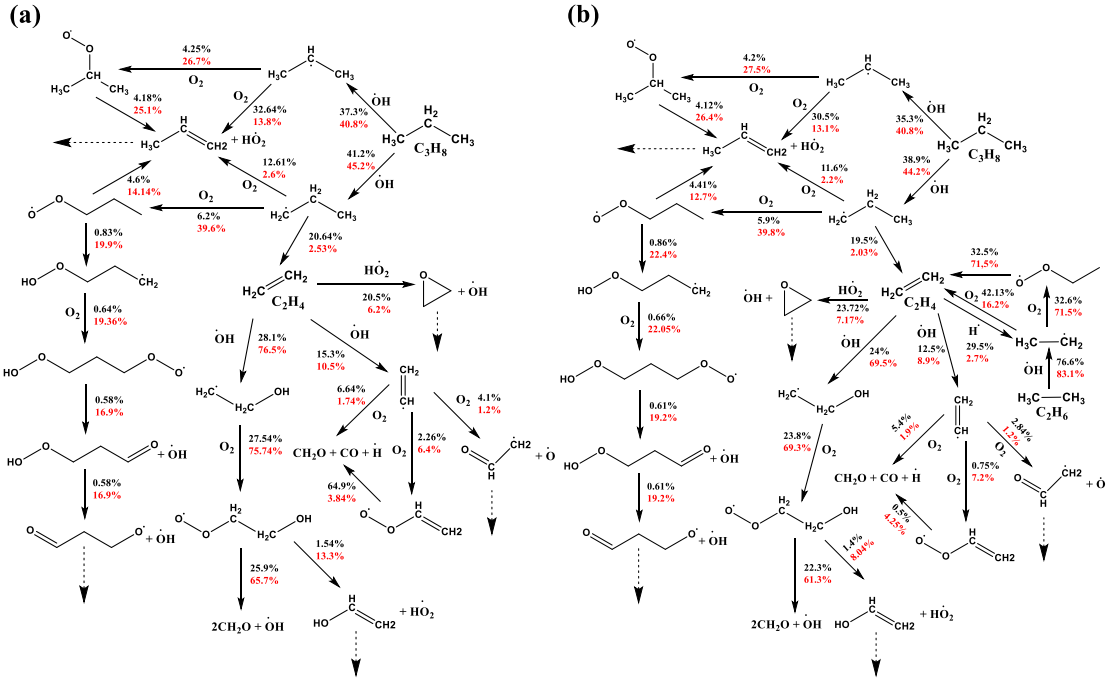

Figure 8-12. Flux analyses at 800 K, φ = 0.5, p = 1 (black), and 40 atm (red), with 75% N_2 as diluent for; (a) 50% C_2H_4/50% C_3H_8; and (b) 50% C_2H_6/50% C_3H_8.

Figure 8-11 shows that at low temperature (800 K) and high-pressure conditions (20 and 40 atm), the reactivity of the binary blends is mainly controlled by H-atom abstraction from C_3H_8

by ȮH radicals, with the formation of nĊ$_3$H$_7$ radicals promoting reactivity and iĊ$_3$H$_7$ radicals inhibiting reactivity. However, at 800 K and 1 atm, H-atom abstraction from C_3H_8 no longer influences IDT predictions, but rather the competition between the reactions generating and consuming hydrogen peroxide, via HȮ$_2$ + HȮ$_2$ ↔ H_2O_2 + O_2 and H_2O_2 (+M) ↔ ȮH + ȮH (+M), respectively control the reactivity of the binary blends. The flux analyses presented in Figure 8-12 show that, at 40 atm pressure, the percentage contribution of nĊ$_3$H$_7$ radical β-scission forming C_2H_4 and ĊH$_3$ reduces, while the importance of nĊ$_3$H$_7$ radical addition to O_2 increases compared to the 1 atm case. Since the addition of nĊ$_3$H$_7$ radicals to O_2 and the subsequent chain branching channels produces two reactive ȮH radicals and thus increases reactivity, the formation of nĊ$_3$H$_7$ radicals, and other low-temperature reactions those are not favorable at low pressures become significant at higher pressures in controlling the overall reactivity of binary mixtures. At the higher temperature of 1600 K, the reactivity is only controlled by the chain branching reaction, Ḣ + O_2 ↔ Ö + ȮH irrespective of pressure, as seen in Figures. 8-11(b) and ES16. The reactions that consume Ḣ atoms such as, C_3H_8 + Ḣ ↔ nĊ$_3$H$_7$ +H_2, C_3H_8 + Ḣ ↔ iĊ$_3$H$_7$ +H_2, C_2H_6 + Ḣ ↔ Ċ$_2$H$_5$ +H_2, CH_2O + Ḣ ↔ HĊO + H_2 and Ḣ + O_2 (+M) ↔ HȮ$_2$ (+M) compete with Ḣ + O_2 ↔ Ö + ȮH and thus inhibit the reactivity of the binary mixtures.

8.4.4 Effect of equivalence ratio on ignition

Figure 8-13 presents the effect of equivalence ratio on IDTs for the pure fuels, 50% C_2H_4/50% C_3H_8 and 50% C_2H_6/50% C_3H_8 binary mixtures at p_C = 20 atm, 75% N_2, and at φ = 0.5, 1.0, and 2.0. It is observed that at temperatures above 1250 K, the reactivities of both pure fuels and binary mixtures are fastest for the fuel-lean mixtures and slowest for the fuel-rich mixtures.

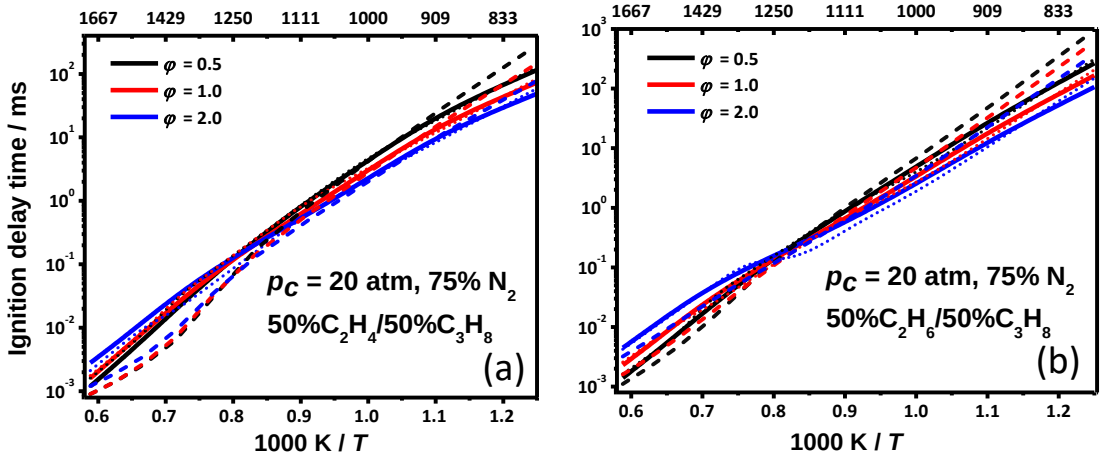

Figure 8-13. Effect of equivalence ratio in (a) 50% C_2H_4/50% C_3H_8 (solid lines) binary blend and pure ethylene (dashed lines); and (b) 50% C_2H_6/50% C_3H_8 (solid lines) binary blend and pure ethane (dashed lines). The derived correlation predictions for binary blends are represented by dotted lines.

However, at a temperature below 1250 K, fuel-rich mixtures are fastest to ignite, and the fuel-lean mixtures are slowest. To determine the governing chemistry under these conditions, sensitivity analyses were performed, the results of which are presented as a function of equivalence ratio in Figures. ES17 and ES18 at 800 K and 1600 K. At high temperatures (> 1250 K), IDTs are mainly controlled by the concentration of O_2 in the binary blends through the main chain branching reaction Ḣ + O_2 ↔ Ö + ȮH, and its influence increases as the mixture become leaner. Thus, fuel-lean mixtures are fastest to ignite at high temperatures. However, at low temperatures (< 1250 K), the reactivity is mainly governed by the addition of the fuel derived alkyl radicals to O_2 and the following low-temperature chemistry leading to chain branching, which is limited by the fuel concentration through H-atom abstraction from propane by ȮH radicals. Thus, at a lower temperature, the dependence on the equivalence ratio is reversed, with fuel-rich mixtures being the most reactive.

8.4.5 Regression analysis

Global regression equations have been developed using NUIGMech1.1 with approximately 17280 CV simulations for each blend mixture spanning over five parameters: p_C (1 – 40 atm), T_C (800 – 2000 K), φ (0.2 – 2.0), dilution (75% – 90%) and fuel ratio composition (50% C_2H_4 or

C_2H_6/50% C_3H_8, and 70% C_2H_4 or C_2H_6/30% C_3H_8). The regression equations developed using the predictions are compared with the ST experimental data in Figure ES20 and ES21 of the appendix E. The expression (τ_{corr}) used is analogous to the Arrhenius rate expression and is defined as shown in equation 8-4 below:

$$\tau_{corr} = 10^{A} e^{\frac{B}{T_C}} [C_2H_4]^{C} [C_2H_6]^{D} [C_3H_8]^{E} [\text{oxidizer}]^{F} [\text{diluent}]^{G} \quad (8\text{-}4)$$

where A represents the pre-exponential factor coefficient, B represents the activation energy, and C – G represent concentrations of ethylene, ethane, propane, oxidizer, and dilution, respectively. A synopsis of the derived correlations for the binary fuels studied in the pressure range $20 \leq p_C \leq 40$ atm over three regimes of temperature is presented below. However, details of the coefficients of the derived correlations along with their corresponding χ^2 and R^2 for the C_2H_4/C_3H_8 and C_2H_6/C_3H_8 mixtures are presented in Table ES6 and ES7, respectively.

For $1500 \leq T_C \leq 2000$ K:

$$\tau_{corr} = 10^{-10.34} e^{\frac{21386.6}{T_C}} [C_2H_4]^{-0.502} [C_3H_8]^{0.463} [\text{oxidizer}]^{-1.080} [\text{diluent}]^{0.354} \quad (8\text{-}5)$$

$$\tau_{corr} = 10^{-9.402} e^{\frac{20465}{T_C}} [C_2H_6]^{0.113} [C_3H_8]^{0.413} [\text{oxidizer}]^{-1.344} [\text{diluent}]^{0.131} \quad (8\text{-}6)$$

For $1100 \leq T_C \leq 1500$ K:

$$\tau_{corr} = 10^{-9.89} e^{\frac{19220.37}{T_C}} [C_2H_4]^{-0.491} [C_3H_8]^{-0.056} [\text{oxidizer}]^{-0.447} [\text{diluent}]^{0.149} \quad (8\text{-}7)$$

$$\tau_{corr} = 10^{-9.79} e^{\frac{19065.65}{T_C}} [C_2H_6]^{-0.408} [C_3H_8]^{-0.169} [\text{oxidizer}]^{-0.330} [\text{diluent}]^{0.062} \quad (8\text{-}8)$$

For $800 \leq T_C \leq 1100$ K:

$$\tau_{corr} = 10^{-7.217} e^{\frac{14136.9}{T_C}} [C_2H_4]^{-0.44} [C_3H_8]^{-0.392} [\text{oxidizer}]^{-0.427} [\text{diluent}]^{-0.017} \quad (8\text{-}9)$$

$$\tau_{corr} = 10^{-9.52} e^{\frac{18630.7}{T_C}} [C_2H_6]^{-0.145} [C_3H_8]^{-0.555} [\text{oxidizer}]^{-0.186} [\text{diluent}]^{-0.145} \quad (8\text{-}10)$$

At high temperatures (1500 – 2000 K), the coefficient for ethylene is strongly negative, while those for ethane and propane are positive. This is because at high temperatures increasing the ethylene concentration increases the concentration of vinyl radicals, which react with O_2 ($\dot{C}_2H_3$ +

$O_2 \leftrightarrow \dot{C}H_2CHO + \ddot{O}$) in a reaction which is chain branching. On the other hand, both ethane and propane compete with O_2 for $\dot{H}$ atoms, and if their concentrations increase, the rate of $\dot{H} + O_2 \leftrightarrow \ddot{O} + \dot{O}H$ will decrease, reducing reactivity. For ethane/propane mixtures, both coefficients are positive, but it is less positive for ethane than propane, as the oxidation of ethane leads to higher concentrations of ethylene. Thus, increasing the concentration of ethane relative to propane will increase reactivity and vice versa.

At low temperatures (800 – 1100 K), the coefficients associated with ethylene, ethane, and propane become negative, with ethane being less negative than propane. At low temperatures, propane promotes reactivity through the addition of propyl radicals to O_2 that proceeds to chain branching through the low-temperature reaction sequence that generates two highly active $\dot{O}H$ radicals. Thus, for the ethane/propane mixtures, increasing the propane concentration will increase mixture reactivity. However, for ethylene/propane mixtures, the coefficient of ethylene is comparable to that of propane, as ethylene and propane exhibit similar reactivity in the temperature range between 900 – 1100 K, as seen in Figure 8-4.

It is interesting to note that, at high temperatures (Eqns. 8-5 and 8-6), the magnitude of the oxidizer coefficients (–1.08 and –1.344 for C_2H_4/C_3H_8 and C_2H_6/C_3H_8 blends, respectively) are significantly larger, by a factor of two or more, than for the corresponding fuel coefficients, thus showing a higher sensitivity towards oxidizer concentrations at these conditions. As we approach the lower temperature regimes (Eqns. 8-9 and 8-10), the coefficients associated with each fuel become higher and are even larger than the corresponding oxidizer coefficients, thus representing the increasing importance of fuel-based kinetics. These characteristics observed in the correlations corroborate the underlying kinetics understanding discussed in Section 8.4 above and enable the correlations to capture the IDT trends effectively.

8.5 Conclusions

An experimental and kinetic modeling study of the IDT characteristics of $C_2 - C_3$ binary blends of C_2H_4/C_3H_8 and C_2H_6/C_3H_8 mixtures over a wide range of experimental conditions, pressures (1 – 135 atm), temperatures (~750 – 2000 K), equivalence ratios ($0.5 \leq \varphi \leq 2.0$) and 75 – 90% of dilution percentage were presented. The performance of NUIGMech1.1 and its corresponding derived correlations have been evaluated against the experimental data collected. Results show that NUIGMech1.1 is in good agreement within ~26.4% of model uncertainty to the measured IDTs over the studied conditions, compared to ~35% for AramcoMech3.0. Moreover, the correlations can predict the experimental IDTs appropriately under specific regimes, becoming a useful tool for predicting the behavior of $C_2 - C_3$ binary blends at specific conditions.

Finally, the effects of blend composition, pressure and equivalence ratio on the IDTs were investigated for various mixtures containing C_2H_4, C_2H_6, and C_3H_8 as reactants. It was observed that for all mixtures, as the temperature and pressure increase, IDTs decrease. For the equivalence ratio, an expected crossover point was observed at T_C ~ 1250 K, wherein the controlling chemistry switches such that the trends invert their behavior. The reactivity of C_2H_4 - was found to be higher than for C_2H_6 throughout the temperature range examined in this study. At higher temperatures, vinoxy radicals and oxygen atoms formed from vinyl radical's reaction with O_2, proceed via dissociation and bimolecular reactions with C_2H_4, to produce a substantial amount of Ḣ atoms resulting in faster ignition of C_2H_4/air mixtures. The concerted elimination reaction between $\dot{C}_2H_5$ and O_2 is responsible for the reduction in ethane reactivity. It was observed that C_3H_8 blended fuels were the fastest to ignite at lower temperatures (< 1250 K), however, the trend is reversed at higher temperatures, and C_3H_8 exhibited the slowest reactivity compared to both C_2H_4 and C_2H_6 at T > 1250 K. In the case of C_3H_8, at low temperatures n-propyl radical formation, followed the classical low-temperature chain branching pathways via

its addition to O_2 generate $\dot{O}H$ radicals promoting reactivity, while methyl radical recombination and its consumption by $H\dot{O}_2$ leading to CH_4 and O_2 reduce reactivity at higher temperatures.

Acknowledgements

The authors would like to express their gratitude to Science Foundation Ireland (SFI) via their Research Centre Program through project numbers 15/IA/3177 and 16/SP/3829, KAY-ICHEC via the project ngche079c, and to Shell Research Ltd. The authors from PCFC RWTH Aachen University would like to recognize the funding support from the German Research Foundation (Deutsche Forschungsgemeinschaft, DFG) through the project number –322460823 (HE7599/2-1).

References

[1] U.S.E.I. Administration, International Energy Outlook 2019 with projections to 2050, IEO2019, 2019.

[2] S. Bilgen, Structure and environmental impact of global energy consumption, Renew. Sust. Energ. Rev., 38 (2014) 890–902.

[3] W.K. Metcalfe, S.M. Burke, S.S. Ahmed, H.J. Curran, A hierarchical and comparative kinetic modeling study of C_1−C_2 hydrocarbon and oxygenated fuels, Int. J. Chem. Kinet., 45 (2013) 638–675.

[4] S.S. Nagaraja, J. Liang, S. Dong, S. Panigrahy, A. Sahu, G. Kukkadapu, S.W. Wagnon, W.J. Pitz, H.J. Curran, A hierarchical single-pulse shock tube pyrolysis study of C_2–C_6 1-alkenes, Combust. Flame, 219 (2020) 456–466.

[5] M. Baigmohammadi, V. Patel, S. Martinez, S. Panigrahy, A. Ramalingam, U. Burke, K. P. Somers, K. A. Heufer, A. Pekalski, H.J. Curran, A comprehensive experimental and simulation study of ignition delay time characteristics of single fuel C_1−C_2 hydrocarbons over a wide range of temperatures, pressures, equivalence ratios, and dilutions, Energy Fuels, 34 (3) (2020) 3755–3771.

[6] M. Baigmohammadi, V. Patel, S. Nagaraja, A. Ramalingam, S. Martinez, S. Panigrahy, A. A. E. Mohamed, K. P. Somers, U. Burke, K. A. Heufer, A. Pekalski, H.J. Curran, Comprehensive experimental and simulation study of the ignition delay time characteristics of binary blended methane, ethane, and ethylene over a wide range of temperature, pressure, equivalence ratio, and dilution, Energy Fuels, 34 (7) (2020) 8808–8823.

[7] M.M. Kopp, N.S. Donato, E.L. Petersen, W.K. Metcalfe, S.M. Burke, H.J. Curran, Oxidation of ethylene–air mixtures at elevated pressures, part 1: Experimental results, J. Propuls. Power, 30 (2014) 790–798.

[8] M.M. Kopp, E.L. Petersen, W.K. Metcalfe, S.M. Burke, H.J. Curran, Oxidation of ethylene-air mixtures at elevated pressures, part 2: Chemical kinetics, J. Propuls. Power, 30 (2014) 799–811.

[9] C.J. Aul, W.K. Metcalfe, S.M. Burke, H.J. Curran, E.L. Petersen, Ignition and kinetic modeling of methane and ethane fuel blends with oxygen: A design of experiments approach, Combust. Flame, 160 (2013) 1153–1167.

[10] S.M. Gallagher, H.J. Curran, W.K. Metcalfe, D. Healy, J.M. Simmie, G. Bourque, A rapid compression machine study of the oxidation of propane in the negative temperature coefficient regime, Combust. Flame, 153 (2008) 316–333.

[11] I.G. Zsély, T. Nagy, J.M. Simmie, H.J. Curran, Reduction of a detailed kinetic model for the ignition of methane/propane mixtures at gas turbine conditions using simulation error minimization methods, Combust. Flame, 158 (2011) 1469–1479.

[12] A. Burcat, R. W. Crossley, K. Scheller, Shock tube investigation of ignition in ethane-oxygen-argon mixtures, Combust. Flame, 18 (1972) 115–123.

[13] H. Hashemi, J. G. Jacobsen, C. T. Rasmussen, J. M. Christensen, P. Glarborg, S. Gersen, M. van Essen, H.B. Levinsky, S.J. Klippenstein, High-pressure oxidation of ethane, Combust. Flame, 182 (2017) 150–166.

[14] S. Gersen, A.V. Mokhov, J.H. Darmeveil, H.B. Levinsky, P. Glarborg, Ignition-promoting effect of NO_2 on methane, ethane and methane/ethane mixtures in a rapid compression

machine, Proc. Combust. Inst., 33 (2011) 433–440.
[15] P. Dagaut, J.C.C. Boettner, M. Cathonnet, Ethylene pyrolysis and oxidation: A kinetic modeling study, Int. J. Chem. Kinet., 22 (1990) 641–664.
[16] P. Dagaut, M. Cathonnet, J.C. Boettner, F. Gaillard, Kinetic modeling of propane oxidation, Combust. Sci. Technol., 56 (1987) 23–63.
[17] P. Dagaut, M. Cathonnet, J.c.c. Boettner, Kinetics of ethane oxidation, Int. J. Chem. Kinet., 23 (1991) 437–455.
[18] W Lowry, J de Vries, M Krejci, E Petersen, Z Serinyel, W Metcalfe, H Curran, G. Bourque, Laminar flame speed measurements and modeling of pure alkanes and alkane blends at elevated pressures, Proceedings of ASME Turbo Expo 2010: Power for Land, Sea and Air, (2010).
[19] C.J. Brown, G.O. Thomas, Experimental studies of shock-induced ignition and transition to detonation in ethylene and propane mixtures, Combust. Flame, 117 (1999) 861–870.
[20] D. Davidson, W. Ren, R. Hanson, Experimental database for development of a HiFiRE JP-7 Surrogate Fuel Mechanism, 50th AIAA Aerospace Sciences Meeting including the New Horizons Forum and Aerospace Exposition, 2012.
[21] O.G. Penyazkov, K.L. Sevrouk, V. Tangirala, N. Joshi, High-pressure ethylene oxidation behind reflected shock waves, Proc. Combust. Inst., 32 (2009) 2421–2428.
[22] S. Saxena, M.S.P. Kahandawala, S.S. Sidhu, A shock tube study of ignition delay in the combustion of ethylene, Combust. Flame, 158 (2011) 1019–1031.
[23] K.S. Alexander Burcat, and Assa Lifshitz, Shock-tube investigation of comparative ignition delay times for C_1-C_5 alkanes, Combust. Flame, 16 (1971) 29–33.
[24] J. de Vries, J.M. Hall, S.L. Simmons, M.J.A. Rickard, D.M. Kalitan, E.L. Petersen, Ethane ignition and oxidation behind reflected shock waves, Combust. Flame, 150 (2007) 137–150.
[25] Y Hidaka, K Sato, H Hoshikawa, T Nishimori, R Takahashi, H Tanaka, K Inami, N. Ito, Shock-tube and modeling study of ethane pyrolysis and oxidation, Combust. Flame, 120 (2000) 245–264.
[26] A.G. McLain, C.J. Jachimowski, Chemical kinetic modeling of propane oxidation behind shock waves, National Aeronautics and Space Administration, (1977).
[27] P. Cadman, G.O. Thomas, P. Butler, The auto-ignition of propane at intermediate temperatures and high pressures, Phys. Chem. Chem. Phys., 2 (2000) 5411–5419.
[28] Z Qin, V V. Lissianski, H Yang, W C. Gardiner, S G. Davis, H. Wang, Combustion chemistry of propane: a case study of detailed reaction mechanism optimization, Proc. Combust. Inst. 28 (2000) 1663–1669.
[29] K.G. Yeong, S.G. Su, Shock tube and modeling study of the ignition of propane, Bull. Korean Chem. Soc., 22 (2001) No. 2003.
[30] J. Herzler, L. Jerig, P. Roth, Shock-tube study of the ignition of propane at intermediate temperatures and high pressures, Combust. Sci. Technol., 176 (2004) 1627–1637.
[31] E. Hu, Z. Zhang, L. Pan, J. Zhang, Z. Huang, Experimental and modeling study on ignition delay times of dimethyl ether/propane/oxygen/argon mixtures at 20 bar, Energy Fuels, 27 (2013) 4007–4013.
[32] C. Lee, S. Vranckx, K.A. Heufer, S.V. Khomik, Y. Uygun, H. Olivier, On the chemical kinetics of ethanol oxidation: shock tube, rapid compression machine and detailed modeling

study, Z Phys Chem, 226(1) (2012) 1–28.
[33] A. Ramalingam, K. Zhang, A. Dhongde, L. Virnich, H. Sankhla, H. Curran, A. Heufer, An RCM experimental and modeling study on CH_4 and CH_4/C_2H_6 oxidation at pressures up to 160 bar, Fuel, 206 (2017) 325–333.
[34] L. Brett, J. Macnamara, P. Musch, J.M. Simmie, Brief Communication: Simulation of methane autoignition in a rapid compression machine with creviced pistons, Combust. Flame, 124 (2001) 326–329.
[35] E.L. Petersen, M. Röhrig, D.F. Davidson, R.K. Hanson, C.T. Bowman, High-pressure methane oxidation behind reflected shock waves, 26th Intl. Symp. Combust., (1996) 799–806.
[36] P.J. Ross, Taguchi Techniques for Quality Engineering, New York, (1988).
[37] S.M. Burke, U. Burke, R. Mc Donagh, O. Mathieu, I. Osorio, C. Keesee, A. Morones, E.L. Petersen, W. Wang, T.A. DeVerter, M.A. Oehlschlaeger, B. Rhodes, R.K. Hanson, D.F. Davidson, B.W. Weber, C.J. Sung, J. Santner, Y. Ju, F.M. Haas, F.L. Dryer, E.N. Volkov, E.J.K. Nilsson, A.A. Konnov, M. Alrefae, F. Khaled, A. Farooq, P. Dirrenberger, P.A. Glaude, F. Battin-Leclerc, H.J. Curran, An experimental and modeling study of propene oxidation. Part 2: Ignition delay time and flame speed measurements, Combust. Flame, 162 (2015) 296–314.
[38] S.M. Burke, W. Metcalfe, O. Herbinet, F. Battin-Leclerc, F.M. Haas, J. Santner, F.L. Dryer, H.J. Curran, An experimental and modeling study of propene oxidation. Part 1: Speciation measurements in jet-stirred and flow reactors, Combust. Flame, 161 (2014) 2765–2784.
[39] U. Burke, K.P. Somers, P. O'Toole, C.M. Zinner, N. Marquet, G. Bourque, E.L. Petersen, W.K. Metcalfe, Z. Serinyel, H.J. Curran, An ignition delay and kinetic modeling study of methane, dimethyl ether, and their mixtures at high pressures, Combust. Flame, 162 (2015) 315–330.
[40] D. Healy, H.J. Curran, S. Dooley, J.M. Simmie, D.M. Kalitan, E.L. Petersen, G. Bourque, Methane/propane mixture oxidation at high pressures and at high, intermediate and low temperatures, Combust. Flame, 155 (2008) 451–461.
[41] D. Healy, H.J. Curran, J.M. Simmie, D.M. Kalitan, C.M. Zinner, A.B. Barrett, E.L. Petersen, G. Bourque, Methane/ethane/propane mixture oxidation at high pressures and at high, intermediate and low temperatures, Combust. Flame, 155 (2008) 441–448.
[42] D. Healy, D.M. Kalitan, C.J. Aul, E.L. Petersen, G. Bourque, H.J. Curran, Oxidation of C_1−C_5 alkane quinternary natural gas mixtures at high pressures, Energy Fuels, 24 (2010) 1521–1528.
[43] A. Mohamed, S. Panigrahy, A. Sahu, G. Bourque, H.J. Curran, An experimental and modeling study of the auto-ignition of Natural Gas blends containing C_1–C_7 n-alkanes, Proc. Combust. Inst., 38 (2021) 365–373.
[44] S. Nagaraja, J. Power, G. Kukkadapu, S. Dong, S. .W. Wangon, W. J. Pitz, H.J. Curran, A single pulse shock tube study of pentene isomer pyrolysis, Proc. Combust. Inst. 38 (2021).
[45] S. Panigrahy, J. Liang, S. Nagaraja, Z. Zuo, G. Kim, T. MacDougall, S.S. Vasu, H.J. Curran, A comprehensive experimental and improved kinetic modeling study on the pyrolysis and oxidation of propyne, Proc. Combust. Inst., 38 (2021) 881–889.
[46] S. Dong, K. Zhang, P.K. Senecal, G. Kukkadapu, S.W. Wagnon, S. Barrett, N. Lokachari,

S. Panigrahy, W.J. Pitz, H.J. Curran, A comparative reactivity study of 1-alkene fuels from ethylene to 1-heptene, Proc. Combust. Inst., 38 (2021) 611–619.

[47] A. Ramalingam, S. Panigrahy, Y. Fenard, H. Curran, K.A. Heufer, A chemical kinetic perspective on the low-temperature oxidation of propane/propene mixtures through experiments and kinetic analyses, Combust. Flame, 223 (2021) 361–375.

[48] Y. Sun, C.-W. Zhou, K. P. Somers, H.J. Curran, An ab initio/transition state theory study of the reactions of C_5H_9 species of relevance to 1,3-pentadiene, Part I: Potential energy surfaces, thermochemistry and high-pressure limiting rate constants, J. Phys. Chem. A, 123 (2019) 9019–9052.

[49] Y. Sun, C.-W. Zhou, K. P. Somers, H.J. Curran, An ab initio/transition state theory study of the reactions of C_5H_9 species of relevance to 1,3-pentadiene, Part II: Pressure dependent rate constants and implications for combustion modelling, J. Phys. Chem. A, 124 (2020) 4605–4631.

[50] J. Power, K. P. Somers, C.-W. Zhou, S. Peukert, H.J. Curran, A theoretical, experimental and modeling study of the reaction of hydrogen atoms with 1- and 2-Pentene, J. Phys. Chem. A, 123 (2019) 8506–8526.

[51] N. Lokachari, S. Panigrahy, G. Kukkadapu, G. Kim, S. S. Vasu, W. J. Pitz, H.J. Curran, The influence of iso-butene kinetics on the reactivity of di-isobutylene and iso-octane, Combust. Flame, 222 (2020) 186–195.

[52] C.W. Zhou, Y. Li, U. Burke, C. Banyon, K.P. Somers, S. Ding, S. Khan, J.W. Hargis, T. Sikes, O. Mathieu, E.L. Petersen, M. AlAbbad, A. Farooq, Y. Pan, Y. Zhang, Z. Huang, J. Lopez, Z. Loparo, S.S. Vasu, H.J. Curran, An experimental and chemical kinetic modeling study of 1,3-butadiene combustion: Ignition delay time and laminar flame speed measurements, Combust. Flame, 197 (2018) 423–438.

[53] D.G. Goodwin, R.L. Speth, H.K. Moffat, B.W. Weber, Cantera: An object-oriented software toolkit for chemical kinetics, thermodynamics, and transport processes. https://www.cantera.org, doi:10.5281/zenodo.170284. doi: 10.5281/zenodo.170284.

[54] Reaction-Design, CHEMKIN-PRO 18.2, San Diego, (2013).

[55] S. Chih-Jen, H.J. Curran, Using rapid compression machines for chemical kinetics studies, Prog. Energy Combust. Sci., 44 (2014) 1–18.

[56] S. S. Goldsborough, S. Hochgreb, G. Vanhove, M.S. Wooldridge, H.J. Curran, C-J. Sung, Advances in rapid compression machine studies of low- and intermediate-temperature autoignition phenomena, Prog. Energy Combust. Sci., 63 (2017) 1–78.

[57] V. Gururajan, F.N. Egolfopoulos, Direct sensitivity analysis for ignition delay times, Combust. Flame, 209 (2019) 478–480.

[58] X. Li, A.W. Jasper, J. Zádor, J.A. Miller, S.J. Klippenstein, Theoretical kinetics of O + C_2H_4, Proc. Combust. Inst., 36 (2017) 219–227.

[59] D. L. Baulch, C. T. Bowman, C. J. Cobos, R. A. Cox, Th. Just, J. A. Kerr, M. J. Pilling, D. Stocker, J. Troe, W. Tsang, R. W. Walker, J. Warnatz, Evaluated Kinetic Data for Combustion Modeling: Supplement II, J. Phys. Chem. 34 (2005).

[60] H.P. Upadhyaya, A. Kumar, P.D. Naik, A.V. Sapre, Discharge flow reaction kinetic studies of O (^{3}P) with chloroethylenes CH_2CCl_2 , $CHClCCl_2$, CCl_2CCl_2, Chem. Phys. Lett., 321 (2000) 411–418.

[61] S.Y. Lee, H.S. Yoo, W.K. Kang, K.H. Jung, Reaction of O(^{3}P) atoms with CF 2 = CXY (X, Y = H, F, C1, Br). Discharge flow-chemiluminescence imaging technique, Chem. Phys. Lett., 257 (1996) 415–420.

[62] S.E. Paulson, J.J. Orlando, G.S. Tyndall, J.G. Calvert, Rate coefficients for the reactions of O(^{3}P) with selected biogenic hydrocarbons, Int. J. Chem. Kinet., 27 (1995) 997–1008.

[63] V.D. Knyazev, V.S. Arutyunov, V.I. Vedeneev, The mechanism of O(^{3}P) atom reaction with ethylene and other simple olefins, Int. J. Chem. Kinet., 24 (1992) 545–561.

[64] O. Horie, R. Taege, B. Reimann, N.L. Arthur, P. Potzinger, Kinetics and mechanism of the reactions of O (3P) with SiH_4, CH_3SiH_3,(CH_3) $2SiH_2$, and (CH_3) 3SiH, J. Phys. Chem., 95(11) (1991) 4393–4400.

[65] D.M. V. Fonderie, & J. Peeters, The kinetic coefficient of the C_2H_4+O reaction over extended pressure and temperature ranges, In Physico-Chemical Behaviour of Atmospheric Pollutants Springer, Dordrecht (1984) 274–282.

[66] R.B. Klemm, J.W. Sutherland, M.A. Wickramaaratchi, G. Yarwood, Flash photolysis-shock tube kinetic study of the reaction of atomic oxygen (^{3}P) with ethylene: 1052K. ltoreq. T. ltoreq. 2284K, J. Phys. Chem., 94(8) (1990) 3354–3357.

[67] K. Mahmud, P. Marshall, A. Fontijn, A high-temperature photochemistry kinetics study of the reaction of oxygen (^{3}P) atoms with ethylene from 290 to 1510 K, J. Phys. Chem., 91(6) (1987) 1568–1573.

[68] T.L. Nguyen, L. Vereecken, X.J. Hou, M.T. Nguyen, J. Peeters, Potential energy surfaces, product distributions and thermal rate coefficients of the reaction of O (^{3}P) with C_2H_4 (XAg): a comprehensive theoretical study, J. Phys. Chem. A, 109(33) (2005) 7489–7499.

[69] L.N. Krasnoperov, J.V. Michael, Shock tube studies using a novel multipass absorption Cell: Rate constant results for OH + H_2 and OH + C_2H_6, J. Phys. Chem. A, 108 (2004) 5643–5648.

[70] R. Sivaramakrishnan, J.V. Michael, B. Ruscic, High-temperature rate constants for H/D+ C_2H_6 and C_3H_8, Int. J. Chem. Kinet., 44(3) (2012) 194–205.

[71] R. Sivaramakrishnan, C.F. Goldsmith, S. Peukert, J.V. Michael, Direct measurements of channel specific rate constants in OH + C_3H_8 illuminates prompt dissociations of propyl radicals, Proc. Combust. Inst., 37 (2019) 231–238.

[72] A.T. Droege, F.P. Tully, Hydrogen-atom abstraction from alkanes by hydroxyl. 3. Propane, J. Phys. Chem., 90 (1986) 1949–1954.

[73] A.W. Jasper, S.J. Klippenstein, L.B. Harding, Theoretical rate coefficients for the reaction of methyl radical with hydroperoxyl radical and for methylhydroperoxide decomposition, Proc. Combust. Inst., 32 (2009) 279–286.

[74] R. Zhu, C. Lin, The CH_3 + HO_2 Reaction: First-principles prediction of its rate constant and product branching probabilities, J. Phys. Chem. A, 105 (2001) 6243–6248.

[75] Z. Hong, D.F. Davidson, K.-Y. Lam, R.K. Hanson, A shock tube study of the rate constants of HO_2 and CH_3 reactions, Combust. Flame, 159(10) (2012) 3007–3013.

[76] S.J. Klippenstein, From Theoretical reaction dynamics to chemical modeling of combustion, Proc. Combust. Inst. 36 (2017) 77–111.

[77] J. Zádor, R.X. Fernandes, Y. Georgievskii, G. Meloni, C.A. Taatjes, J.A. Miller, The Reaction of Hydroxyethyl Radicals with O_2: A theoretical analysis and experimental

product study, Proc. Combust. Inst., 32 (2009) 271–277.
[78] J. Zador, S.J. Klippenstein, J.A. Miller, Pressure-dependent OH yields in alkene+HO_2 reactions: A theoretical study, J. Phys. Chem. A, 115 (2011) 10218–10225.
[79] M.S. Stark, D.J. Waddington, Oxidation of propene in the gas phase, Int. J. Chem. Kinet., 27(2) (1995) 123–151.

CHAPTER 9

CONCLUSIONS AND FUTURE WORKS

Chapter 9: Conclusions and Future Works

This chapter concludes the research studies which have been included in this thesis. The research conclusions are briefly described and highlighted within the research aim and objectives. Finally, future studies are recommended.

9.1 General conclusions

The focus of this work was to investigate the auto-ignition characteristics of multi-component natural gas mixtures comprising C_1 – C_7 *n*-alkanes with methane as the major component. Moreover, NOx addition effects to methane and ethane auto-ignition were also studied with the development of a comprehensive IDT database for alkane/alkene binary mixtures of $C_1 - C_2$, and C_2 – C_3 blends. These comprehensive IDTs measurements along with literature IDTs, flame speed and speciation measurements have been used to assess and develop reliable chemical kinetic mechanisms, NUIGMech1.0, 1.1 and 1.2. These mechanisms are able to reasonably describe the fuel mixtures oxidation included in this study.

The IDT measurements included in this thesis were performed using the red RCM and HPST at C^3. The measurements cover a wide range of combustion conditions relevant to ICEs and GTs at φ = 0.5 – 2.0, T = 650 – 2000 K, p = 10 – 40 bar, and at different fuel compositions (binary alkane/alkene blends of $C_1 - C_2$, and $C_2 - C_3$ blends, as well as NG blends of $C_1 - C_5$ and $C_1 - C_7$ *n*-alkanes, methane/NOx, and ethane/NOx.

NUIGMech1.0 and NUIGMech1.1 were used after validation to generate a dataset of constant volume simulations of IDTs that have been used to develop correlation equations that are valuable tools to estimate fuel ignition characteristics quickly and accurately. These equations include functions for key parameters such as pressure, equivalence ratio, and fuel concentration which represent both thermodynamic and chemical effects.

The general conclusions of the research study can be summarized as follows:

- The sensitization effects of both *n*-hexane and *n*-heptane on the NG blends are found to be more noticeable in the temperature range 700 – 900 K compared to those at higher temperatures (> 900 K). This is attributed to the dependence of IDT on H_2O_2 (+M) ↔ ȮH + ȮH (+M) at high temperatures while the fuel-dependent reactions such as H-atom abstraction, RȮ$_2$ dissociation or ȮOOH + O_2 reactions are less important compared to the temperature range 700 – 900 K, where they are very important.
- Both the experimental measurements and the model predictions show that the addition of even small amounts of *n*-hexane and *n*-heptane (1 – 2%) to natural gas blends leads to a significant increase in mixture reactivity at low temperatures, and mixtures containing high concentrations of larger ($C_3 – C_7$) hydrocarbons tend to have a strong NTC behavior and a lower onset ignition temperature.
- The IDT measurements for the NG blends studied showed that the reactivity of the blends increase with increasing concentrations of higher hydrocarbons, equivalence ratio, and temperatures and pressures. Moreover, the reactivity increases from fuel-lean to fuel-rich mixtures, at low to intermediate temperatures ($T \leq 1250$ K). On the contrary, fuel-lean mixtures become more reactive compared to stoichiometric and fuel-rich mixtures at high temperatures ($T \geq 1250$ K).
- The wide range of conditions studied provides a comprehensive overview of the reactivity of the natural gas mixtures which will reflect on its efficient use in the combustion devices and investigate its limitation in terms of pollutants, power range, or fuel supply systems.
- The derived coefficients' values from the multiple regression analyses reflect well both the chemical and thermodynamic effects of each parameter on IDT. The IDT correlation equations show reasonable agreement with both the measurements and model predictions in the intermediate- and high-temperature regimes – IDTs range ≤ 10 ms-, however the correlations under-predict the IDT measurements in the intermediate-temperature regime -

IDTs range > 10 ms- due mostly to the significant heat losses associated with the RCM experiments.

- The addition of 200 ppm NO_2 to methane leads to a significant increase in mixture reactivity compared to the baseline case without NO_2 in the temperature range 950 – 1100 K. However, this increase in reactivity decreases with increasing pressure. A kinetic analysis indicates that the competition between the reactions $\dot{C}H_3 + NO_2 \leftrightarrow CH_3\dot{O} + NO$ and $\dot{C}H_3 + NO_2 (+M) \leftrightarrow CH_3NO_2 (+M)$, the former being a propagation and the latter being a termination reaction governs NO_x sensitization during CH_4 ignition. Moreover, IDT experiments with NO addition detect a non-monotonous sensitization impact on CH_4 ignition; at lower temperatures NO initially acts as an inhibitor at low NO concentrations and then as a promoter as NO concentrations increase in the mixture. NO and NO_2 showed a similar impact on methane auto-ignition.
- Although the addition of 200 ppm NO_2 significantly increases the reactivity of methane/air mixtures it showed a minimal promoting effect on ethane/air mixtures. However, the addition of 1000 ppm significantly promotes the reactivity of the ethane/air mixtures. The similarity of the effect of the addition of both NO and NO_2 addition is due to the fast conversion of NO into NO_2 in the presence of molecular oxygen. However, the 1000 ppm NO doped ethane mixtures exhibit ~20% faster reactivity compared to the NO_2 doped ones.
- The addition of up to 1000 ppm N_2O exhibits no effect on both methane and ethane oxidation at the conditions studied. This is due to the high energy barrier for the decomposition reaction $N_2O (+M) \leftrightarrow N_2 + \ddot{O} (+M)$ at these temperature conditions.
- The new comprehensive experimental data of the binary alkane/alkene $C_1 – C_2$, and $C_2 – C_3$ blends gave a new insight into the oxidation of alkane/alkene blended fuel mixtures as well as their importance in validating the chemical kinetic mechanism. These mixtures along

with accurate predictions of their combustion characteristics provide new recommendations that are technologically important in terms of the safety and design of new low-emission and size-efficient combustion systems.

9.2 Recommended future works

- As correlation equations proved to be a useful and a quick tool in predicting ignition characteristics, further studies in developing correlation equations for the low-temperature regime will be useful for the NG mixtures with higher hydrocarbons.
- Furthermore, comprehensive IDT experiments are needed for NG mixtures comprising *n*- and *iso*-alkenes to investigate their effect on NG oxidation. This will also help in developing a detailed chemical kinetic mechanism that can accurately predict the ignition characteristics of different NG mixtures that can exist.
- The sensitivity and flux analyses of both methane/NOx and ethane/NOx mixtures show that there is a competition between the reactions $\dot{R} + NO_2 \leftrightarrow R\dot{O} + NO$ and $\dot{R} + NO_2 (+M) \leftrightarrow RNO_2 (+M)$ which governs NOx sensitization on methane and ethane ignition. Therefore, more measurements or high-level calculations of these reactions are needed to accurately simulate these reaction classes for higher hydrocarbons.
- Comprehensive IDT experiments are needed to investigate the effect of NOx addition to higher *n*-alkane ($> C_2$) as well as NG blends. These measurements can have a great impact in developing detailed chemical kinetic mechanisms that can accurately predict mixture oxidation that leads to efficient use of EGR techniques in ICEs and GTs.

Appendices

Appendix A

(Supplementary information of chapter 3)

An Experimental and Modeling study of the Auto-ignition of Natural Gas Blends containing C_1–C_7 Alkanes

1. Verifying the experimental target with help of CV simulations

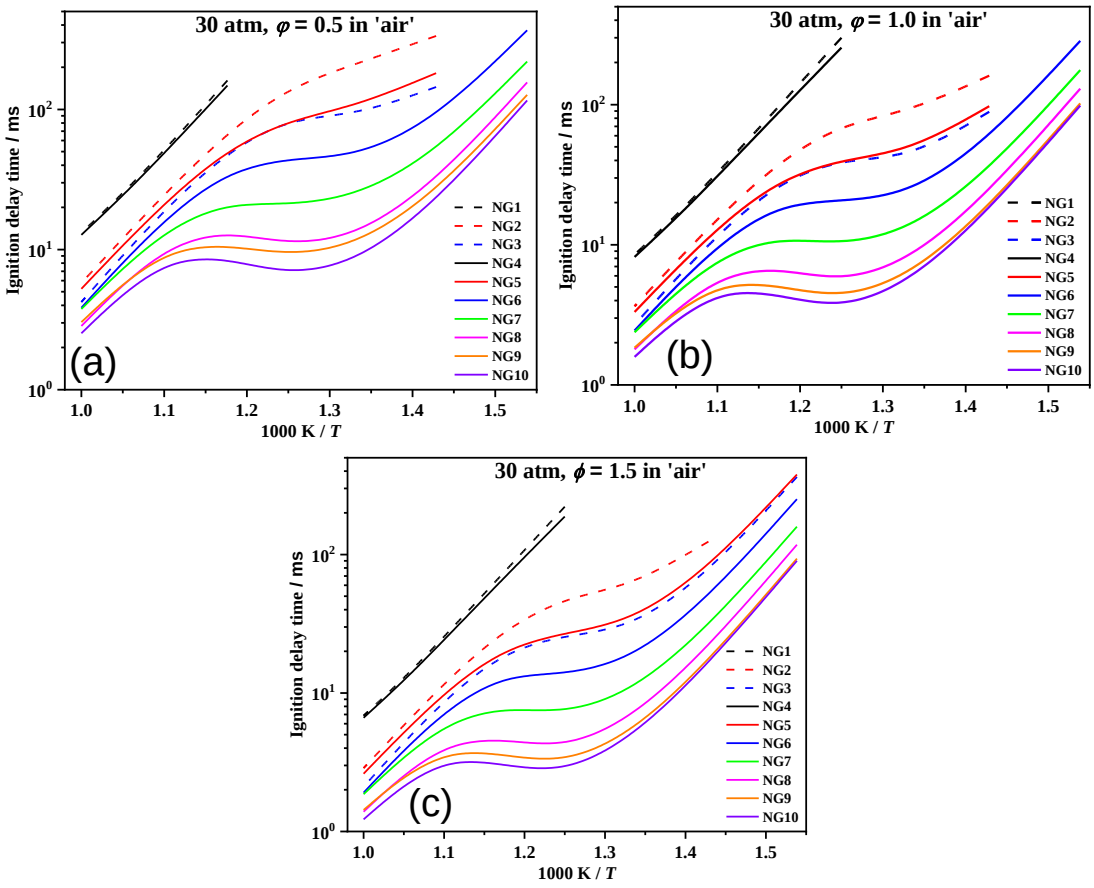

Figure AS1 Constant volume IDT simulations with NUIGMech1.0 for different NG blends in Table 3-1 at p_C = 30 bar for φ = (a) 0.5, (b) 1.0 and, (c) 1.5.

Figure AS1 shows the constant volume simulations of the IDTs for the NG blends in Table 3-1 at constant compressed pressure 30 bar and at the three equivalence ratios (φ = 0.5, 1.0, and 1.5). It is obvious, increasing the amount of the heavier hydrocarbon in the NG blend makes the IDTs shorter and that appears in the three equivalence ratios. And These simulations help in minimizing the number of the experiments which cover a wide range of C_1–C_7 mixtures and combustion conditions. Reproducing NG2 RCM experiments which had been studied previously in our lab [1], [2] helps in validating the new experiment target and confirm the reliability of the old data. NG3 RCM experiments at stoichiometric condition and compressed pressures 20, and

30 bar were done to study the effect of replacing 1.875% of the methane concentration in NG3 blend by *n*-hexane and *n*-heptane at the same condition of pressure and dilution concentrations. Finally, NG7, NG8, and NG10 from the new NG blends had chosen for the current study for the conditions shown in Table 3-2 as different levels of higher of hydrocarbon in the blends and different test conditions can be seen. Developing chemical kinetic mechanism which can reach good level of agreement with the experiments in the different conditions will be useful in prediction the rest of NG blends which did not study.

2. Experiments

2.1. RCM description

Experiments have been conducted using the RCM at NUI Galway [3]. It has twin, creviced pistons to improve the homogeneity of the gas temperature after compression [4]. A heating system permits variations in initial temperatures for a fixed geometric compression ratio to span a range of compressed gas temperatures. A Kistler 6045B pressure transducer, flush with the chamber wall, is connected to a Kistler charge amplifier in conjunction with an oscilloscope to record pressure/time (p/t) histories. The measured IDT is quantified from the reactive pressure-time trace as shown in Figure AS2-a as the time from the first peak pressure at the end of compression (EOC) to the second global peak at the total ignition event. Figure AS2-b shows a two-stage ignition event. Gaseq [5] is used with the adiabatic compression/expansion assumption, to calculate the compressed gas temperature according to the following equation:

$$\ln\left(\frac{p_c}{p_i}\right) = \int_{T_i}^{T_c} \frac{\gamma}{\gamma - 1}\frac{dT}{T} \qquad \text{(AS-1)}$$

where T_C and p_C are the compressed gas temperature, and pressure respectively, and T_i and p_i are the initial gas temperature, and pressure and γ is the specific heat ratio of the mixture. The IDTs measurements uncertainty in the current study estimated ±15%.

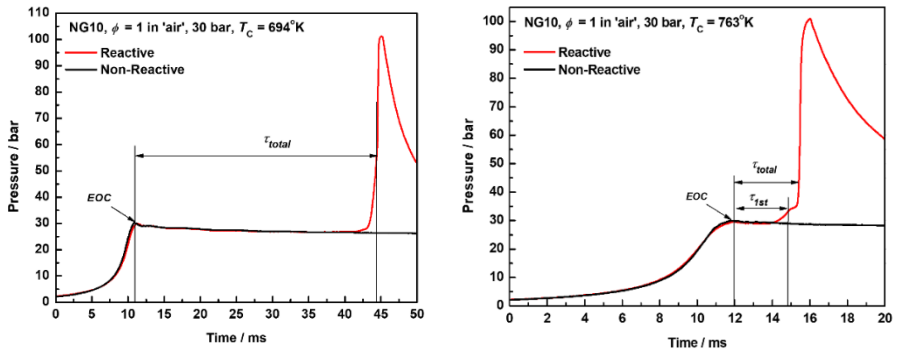

(a) (b)

Figure AS2. Reactive and non-reactive pressure histories for NG10 for φ = 1.0 at p_C = 30 bar; (a) total ignition time; (b) two-stage ignition.

2.2. Mixture preparation and the used gases purity

A fuel mixing tank had been used to prepare the seven-fuel component of the *n*-alkanes C_1–C_7 to minimize the error in the mixture preparation. Then mixture allowed to mix via gaseous diffusion for at least 12h before using it to prepare the final reactive fuel/O_2/(N_2/Ar) and non-reactive fuel/(N_2/Ar) mixtures in the reactive and non-reactive tanks respectively. 100% N_2 and 45% N_2/55% Ar fraction were used as diluent for all the data obtained in the current study to cover wide range of compressed temperature. Also, a set of non-reactive experiments performed with the same initial condition of the reactive experiments by replacing O_2 with N_2 in the reactive mixture which are useful to consider the heat losses for the simulations of the RCM experiments. These non-reactive pressure histories were used to build the input file which were used for the simulation. The purity of the used fuels based on the supplier are as follows; methane (99.5%), ethane (99.5%), propane (99.5%), and *n*-butane (99.9%) which supplied from Air Liquide company and for the liquid fuels, *n*-pentane (99%), *n*-hexane (99%), and *n*-heptane (99%) were supplied by Sigma Aldrich and were used without further purification. And for dilute and oxidizer gases, nitrogen (> 99.96%), argon (> 99.98%), and oxygen (> 99.5%), gases were supplied by BOC Ireland.

2.3. Experiment validation with NG2 and NG3 new and previous IDTs data

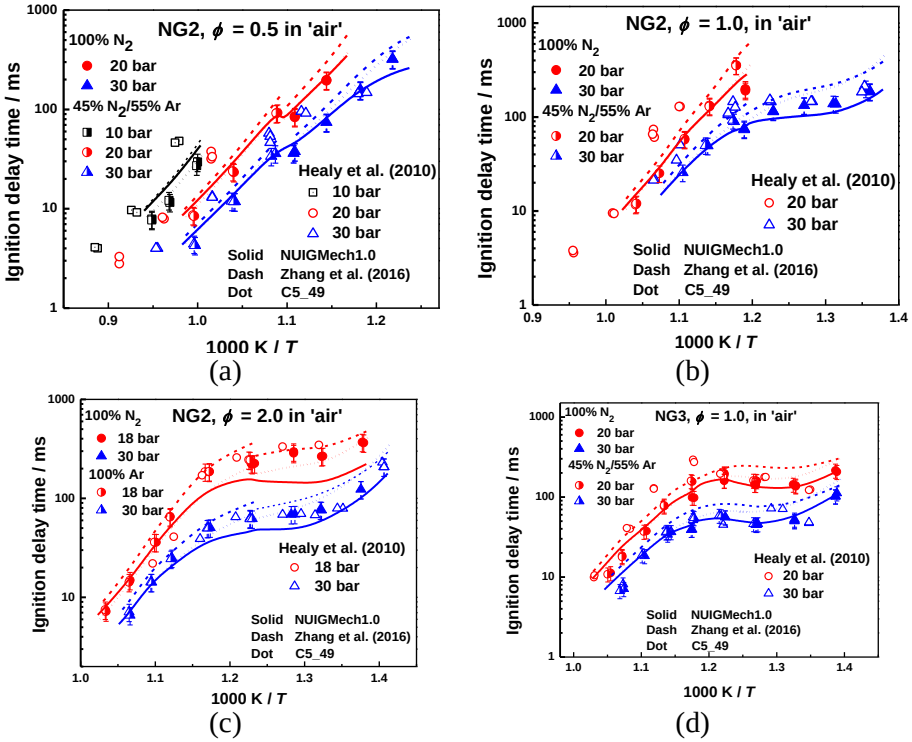

Figure AS3. Reproduced IDTs for NG2 and NG3 current study verse NG2 and NG3 IDTs previous study[2,6] and solid line for NUIGMech1.0 kinetics model, dash lines Zhang et al [7]and Dot line C5_49 [2].

3. Effect *n*-Hexane and *n*-Heptane addition to the natural gas

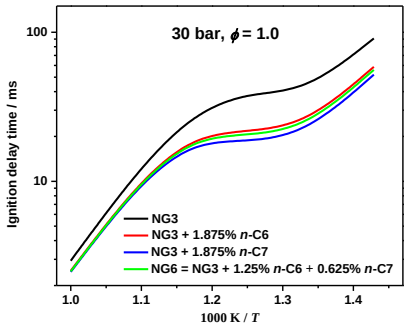

Figure AS4 Constant volume simulation with NUIGMech1.0 results show effect of adding 1.875% n-C_6, 1.875% n-C_7 and 1.875% (n-C_6 +n-C_7) to NG3 on the ignition delay times at *p* =30 bar and stoichiometric mixtures (φ = 1.0).

Figure AS3 shows the comparison of effect of n-C_6H_{14} and n-C_7H_{16} addition to the natural gas mixture on IDT. An addition of 1.875% of n-C_6 reduces the IDT by factor of 1.9 while, same amount of n-C_7 reduces it by factor of 2.3, indicating n-C_7 to have a stronger impact. Simulation with NG6, which as 2:1 ratio n-C_6: n-C7 (Xn-C_6+Xn-C_7 = 1.875%) shows decrease in IDT by

factor 2.05 which the cumulative impact between the pure n-C_6 and n-C_7 addition cases but slightly near to pure n-C_6.

4. Sample of pressure/time histories

Figure AS5 shows the reactive *p*/*t* histories for two compressed temperatures 765 K and 825 ± 10 K at the conditions of figure 3-4(b). It is obvious that, these blends show two stage ignition which appears clearly for NG3 up to NG10 at 765 K and only for NG7, NG8 and NG10 for 825 K. a slight increase in the post ignition pressure observed at 765 K between NG2 and the other NGs in figure AS5(a) but this increase becomes clear at 825K in figure AS5(b). This increases due to the increase volume percentage of the higher hydrocarbon compared to methane from NG2 to NG6 and decreased again in NG7 which has methane amount larger than NG3 and NG6. And noticeable increase from NG7 to NG10 due to the drop of the methane percentage.

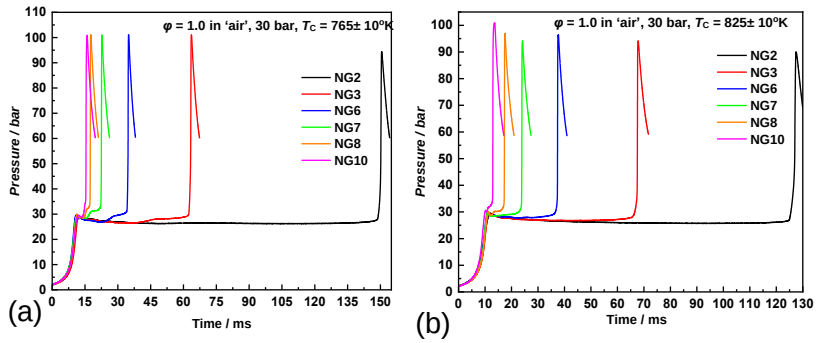

Figure AS5 Pressure/time histories for stoichiometric NG2, NG3, NG6, NG7, NG8, and NG10/air mixtures at p_C = 30 bar and T_C = (a) 765 ± 10 K; (b) 825 ± 10 K.

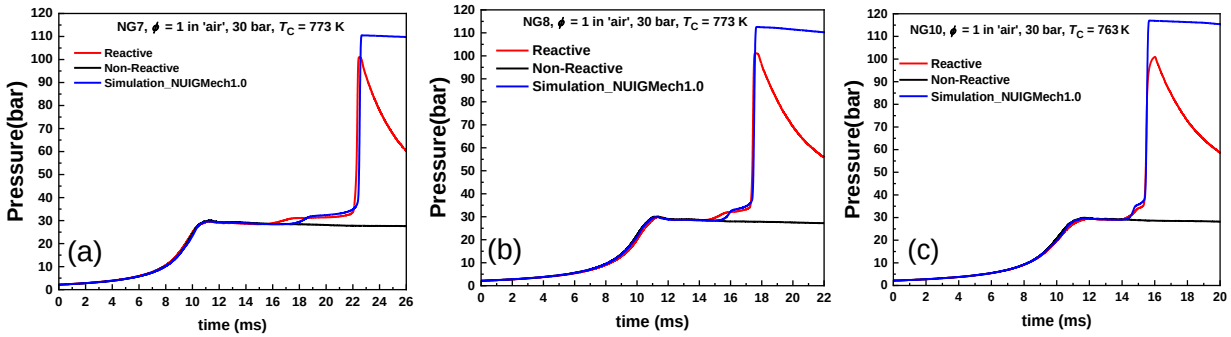

Figure AS6 Samples of pressure/time histories at stoichiometric mixture (φ = 1.0) and p_C = 30 bar show strong first stage ignition with comparison of NUIGMech1.0 simulation (a) NG7; (b) NG8; (c) NG10.

5. Effect of pressure for NG6, NG7, NG8, and NG10

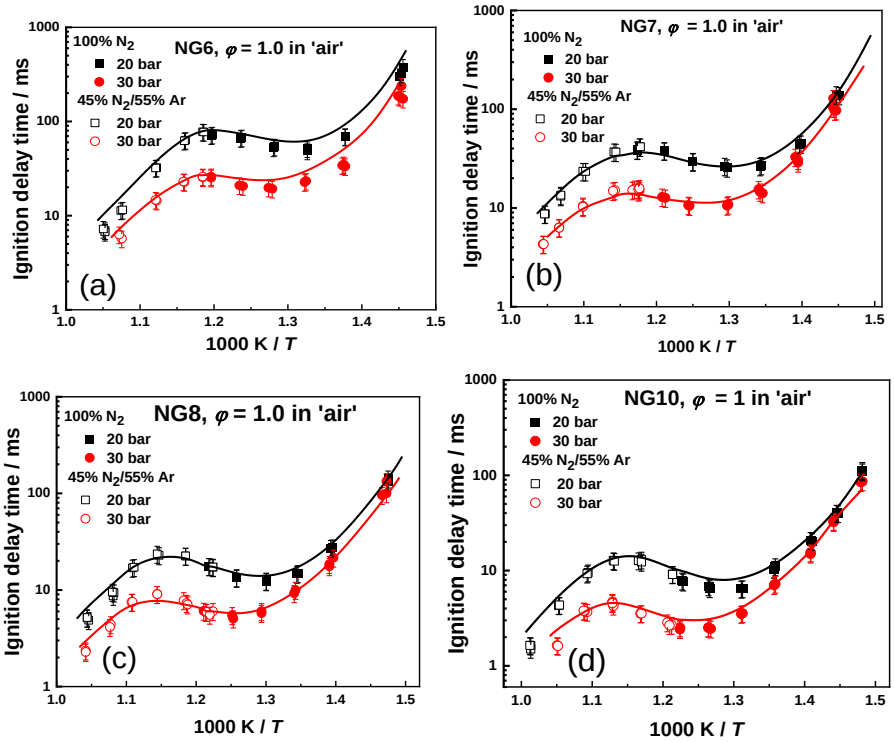

Figure AS7. Effect of pressure on ignition delay times at stoichiometric condition; (a) NG6; (b) NG7; (c) NG8; (d) NG10 simulated with NUIGMech1.0.

6. Effect of equivalence ratio for NG7 and NG10 blends

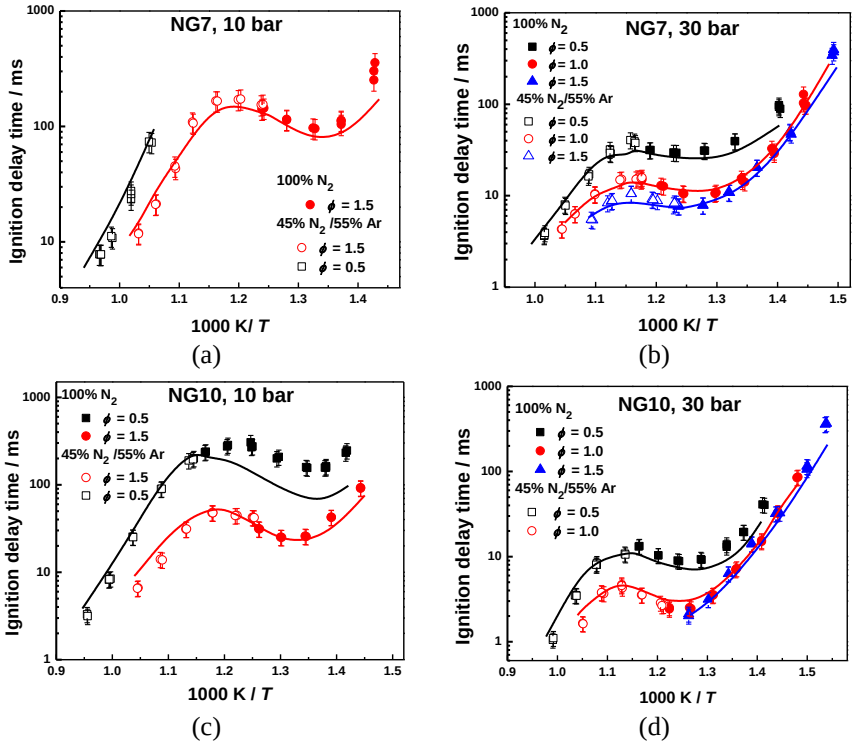

Figure AS8. Effect of equivalence ratio on Ignition delay times at different p_C (a) NG7, 10 bar; (b) NG7, 30bar; (c) NG10, 10 bar; (d) NG10, 30 bar simulated with NUIGMech1.0.

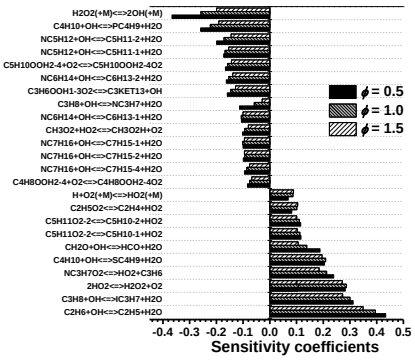

Figure AS9 Brute-force sensitivity analysis of NG10 mixtures at 830 K, and 30 bar for equivalence ratios (φ = 0.5, 1.0 and 1.5).

7. Model validation with literature data

7.1. *n*-hexane and *n*-heptane

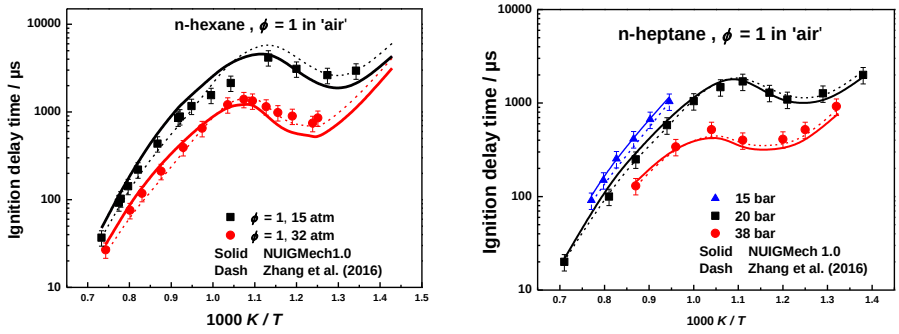

Figure AS10 Ignition delay times experiments (symbols) of pure fuel at stoichiometric condition (φ = 1.0) in air and simulations (lines) of (a) *n*-hexane [8], (b) *n*-heptane [7].

7.2. Methane/Ethane/Propane mixtures [9]

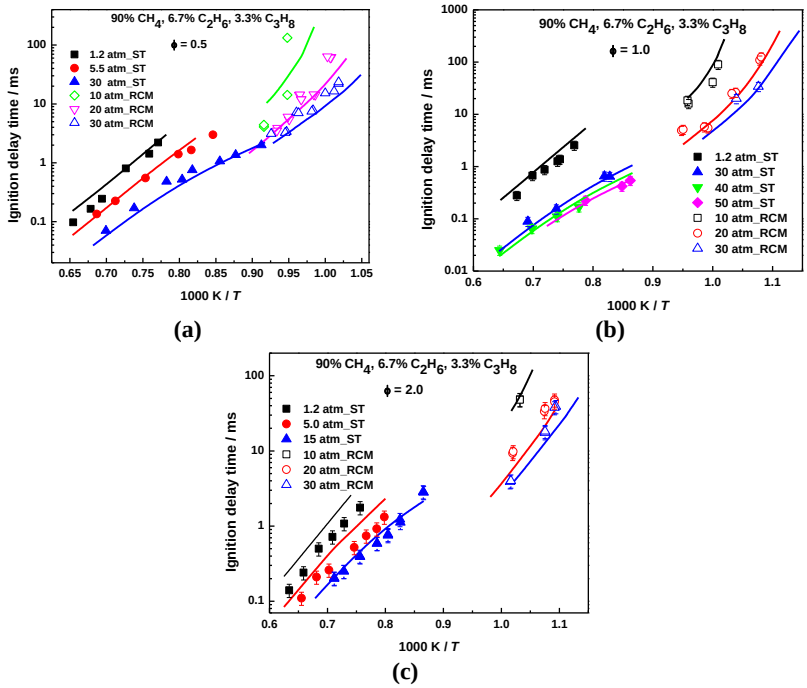

Figure AS11 Ignition delay times for methane/ethane/propane mixtures (90/6.7/3.3): experiments (symbols) [9] and simulation (lines) with NUIGMech1.0, (a) (φ = 0.5); (b) (φ = 1.0); (c) (φ = 2.0).

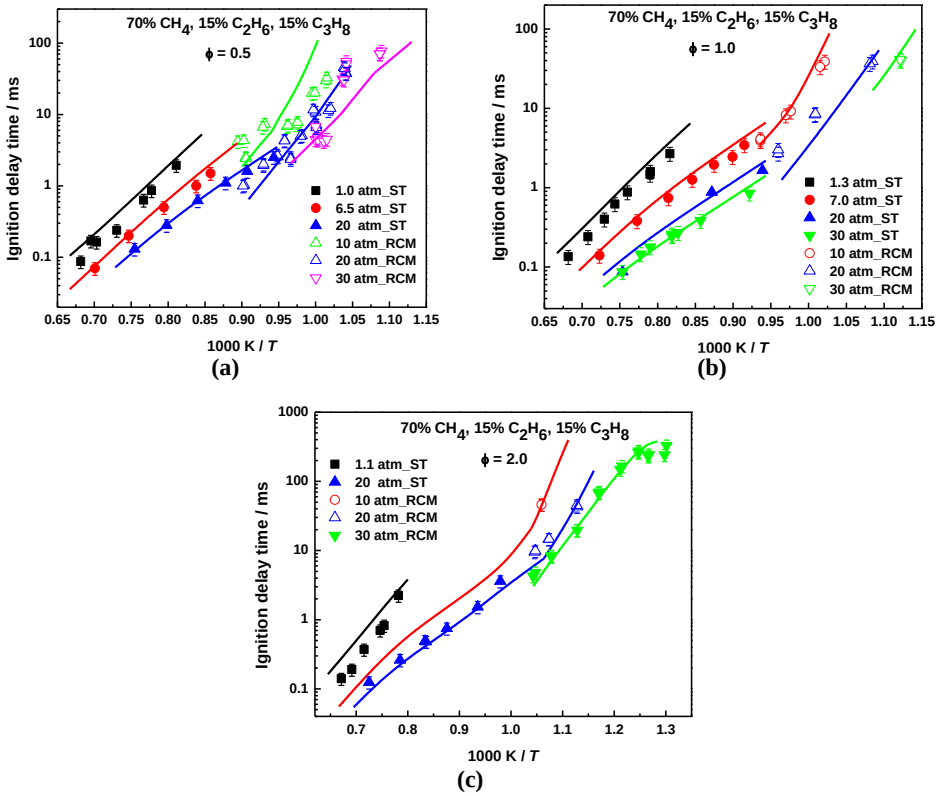

Figure AS12 Ignition delay times for methane/ethane/propane mixtures (70/15/15): experiments (symbols) [9] and simulation (lines) with NUIGMech1.0, (a) (φ = 0.5); (b) (φ = 1.0); (c) (φ = 2.0).

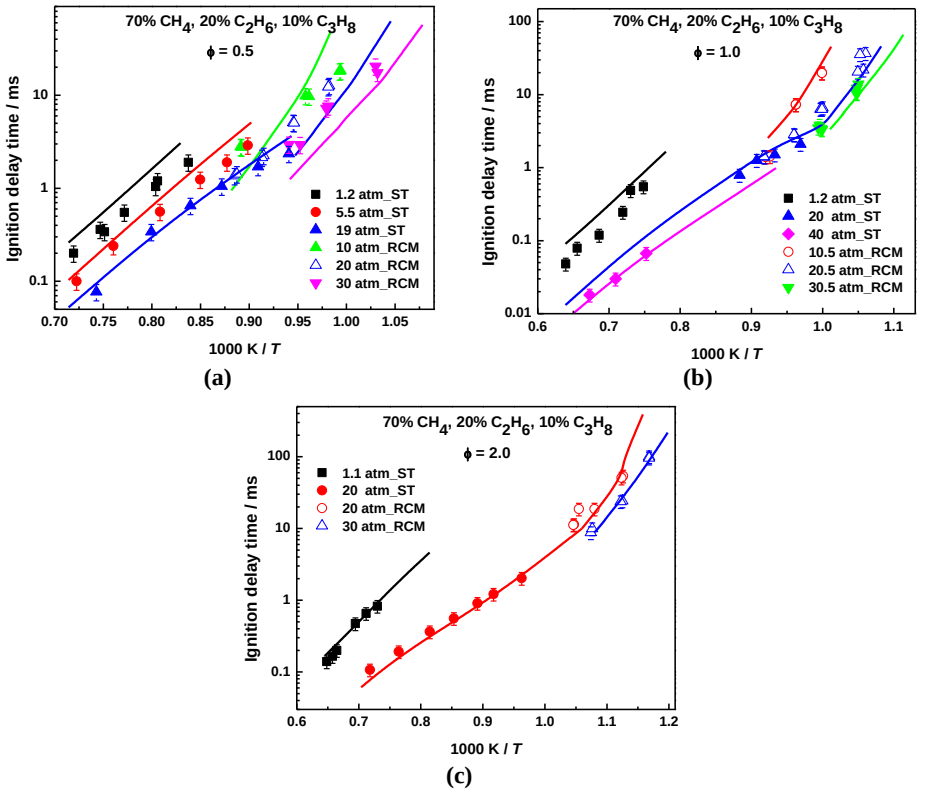

Figure AS13 Ignition delay times for methane/ethane/propane mixtures (70/20/10): experiments (symbols) [9] and simulation (lines) with NUIGMech1.0, (a) (φ = 0.5); (b) (φ = 1.0); (c) (φ = 2.0).

7.3. LNG C_1–C_5 mixtures [10]

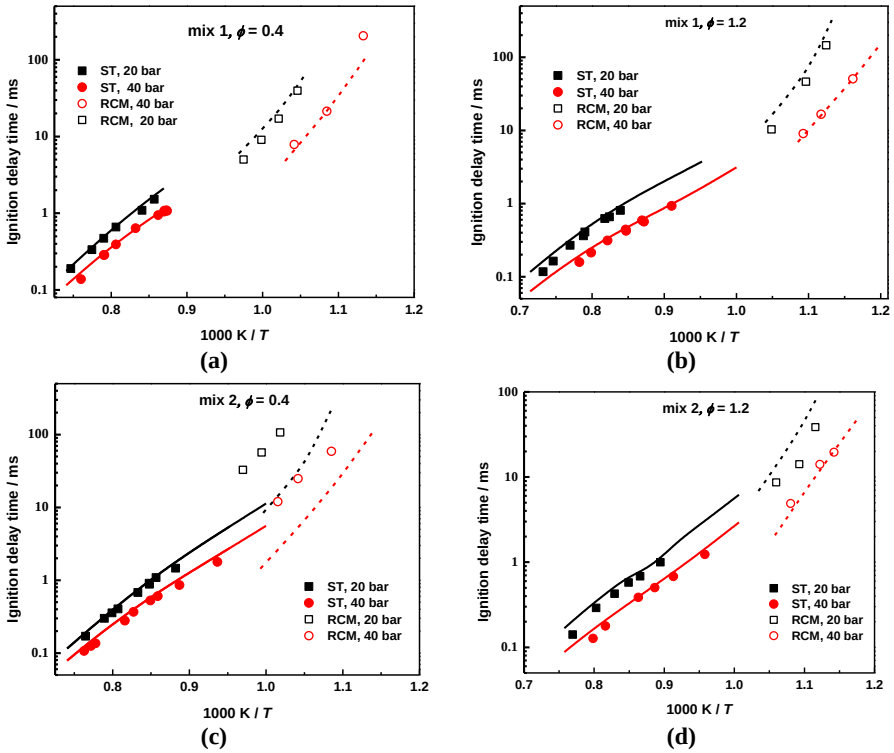

Figure AS14 Ignition delay times for LNG (C_1–C_5) mixtures: experiments (symbols) [10], and ST simulations (solid line), RCM simulations (dash line) with NUIGMech1.0 , (a) Mix-1 (φ = 0.4); (b) Mix-1 (φ = 1. 2); (c) Mix-2 (φ = 0.4); (d) Mix-2 (φ = 1. 2).

7.4. Methane/n-Hexane mixtures [11]

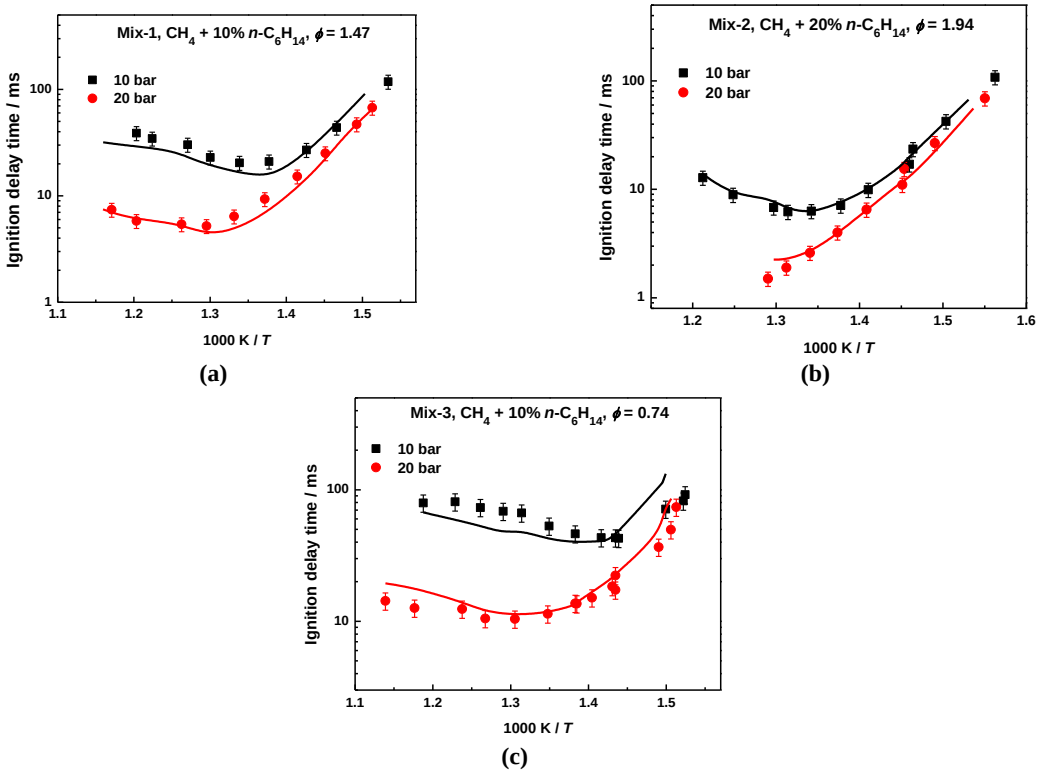

Figure AS15 Ignition delay times for Methane/n-Hexane mixtures: experiments (symbols) [11] and simulation (lines) with NUIGMech1.0, (a) Mix-1; (b) Mix-2; (c) Mix-3.

7.5. Methane/propane/*n*-heptane mixtures [12]

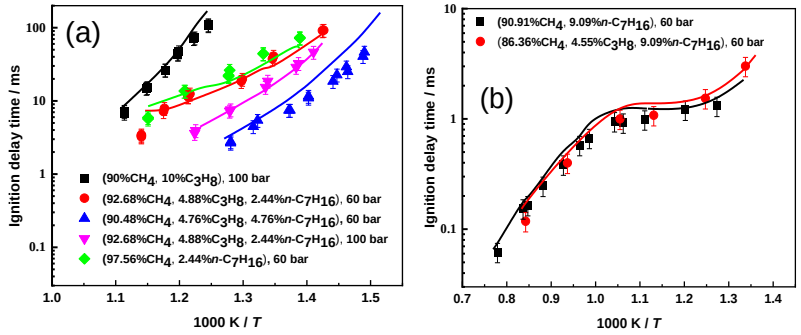

Figure AS16 Ignition delay times for methane/propane/*n*-heptane mixtures: experiments (symbols) [12] and simulation (lines) with NUIGMech1.0, (a) RCM; (b) ST.

References

[1] G. Bourque, D. Healy, H. Curran, C. Zinner, D. Kalitan, J. de Vries, C. Aul, E. Petersen, Ignition and Flame Speed Kinetics of Two Natural Gas Blends With High Levels of Heavier Hydrocarbons, J. Eng. Gas Turbines Power, 132 (2009) 21504–21511.

[2] D. Healy, D.M. Kalitan, C.J. Aul, E.L. Petersen, G. Bourque, H.J. Curran, Oxidation of C_1−C_5 Alkane Quinternary Natural Gas Mixtures at High Pressures, Energy Fuels, 24 (2010) 1521–1528.

[3] W.S. Affleck, A. Thomas, An Opposed Piston Rapid Compression Machine for Preflame Reaction Studies, Proc. Inst. Mech. Eng., 183 (1968) 365–387.

[4] J. Würmel, J.M. Simmie, CFD studies of a twin-piston rapid compression machine, Combust. Flame, 141 (2005) 417–430.

[5] C. Morley, No Title, (n.d.). http://www.gaseq.co.uk (accessed September 29, 2017).

[6] G. Bourque, D. Healy, H. Curran, C. Zinner, D. Kalitan, J. De Vries, C. Aul, E. Petersen, Ignition and flame speed kinetics of two natural gas blends with high levels of heavier hydrocarbons, Proc. ASME Turbo Expo., 3 (2008) 1051–1066.

[7] K. Zhang, C. Banyon, J. Bugler, H.J. Curran, A. Rodriguez, O. Herbinet, F. Battin-Leclerc, C. B'Chir, K.A. Heufer, An updated experimental and kinetic modeling study of n-heptane oxidation, Combust. Flame, 172 (2016) 116–135.

[8] K. Zhang, C. Banyon, C. Togbé, P. Dagaut, J. Bugler, H.J. Curran, An experimental and kinetic modeling study of n-hexane oxidation, Combust. Flame, 162 (2015) 4194–4207.

[9] D. Healy, H.J. Curran, J.M. Simmie, D.M. Kalitan, C.M. Zinner, A.B. Barrett, E.L. Petersen, G. Bourque, Methane/ethane/propane mixture oxidation at high pressures and at high, intermediate and low temperatures, Combust. Flame, 155 (2008) 441–448.

[10] S.K. Vallabhuni, A.D. Lele, V. Patel, A. Lucassen, K. Moshammer, M. AlAbbad, A. Farooq, R.X. Fernandes, Autoignition studies of Liquefied Natural Gas (LNG) in a shock tube and a rapid compression machine, Fuel, 232 (2018) 423–430.

[11] Y. He, Y. Wang, C. Grégoire, U. Niedzielska, R. Mével, J.E. Shepherd, Ignition characteristics of dual-fuel methane-n-hexane-oxygen-diluent mixtures in a rapid compression machine and a shock tube, Fuel, 249 (2019) 379–391.

[12] S. Schuh, K.A. Ramalingam, H. Minwegen, A.K. Heufer, F. Winter, Experimental Investigation and Benchmark Study of Oxidation of Methane–Propane–n-Heptane Mixtures at Pressures up to 100 bar, Energies, 12(18) (2019) 3410.

Appendix A

NG IDTs and Experiments conditions

Table AS1. IDTs and Experiments conditions for NG2, φ = 0.5 in 'air'.

T_i_K	p_i_bar	T_C_K	p_C_bar	IDT_STG1_ms	IDT_STG2_ms	N2/Ar
383.19	0.383	1000	10	0	29.55	45/55
383.15	0.383	1001	10.05	0	27.14	45/55
398.09	0.39	1032	10.13	0	11.6	45/55
398.15	0.39	1033	10.17	0	12.14	45/55
408.55	0.396	1054	10.26	0	7.88	45/55
408.65	0.396	1054	10.26	0	7.69	45/55
383.05	0.832	874	19.7	0	198	100/0
383.19	0.832	874	19.67	0	195	100/0
397.95	0.841	902	19.82	0	85.11	100/0
398.07	0.841	902	19.81	0	83.24	100/0
343.13	0.716	918	19.56	0	92.44	44/55
343.15	0.716	919	19.65	0	91.26	44/55
363.21	0.733	961	19.65	0	20.01	44/55
363.19	0.733	961	19.66	0	23.3	44/55
363.09	0.733	962	19.78	0	23.85	44/55
383.17	0.743	1005	19.8	0	8.6	44/55
383.25	0.743	1004	19.76	0	8.43	44/55
353.05	1.235	821	30.41	0	322	100/0
353.15	1.235	821	30.33	0	320	100/0
368.13	1.229	846	29.43	0	157	100/0
368.13	1.229	846	29.39	0	156	100/0
383.19	1.236	874	29.33	0	74.24	100/0
383.19	1.236	874	29.36	0	74.05	100/0
398.11	1.256	903	29.63	0	36.14	100/0
398.09	1.256	902	29.55	0	37.66	100/0
343.13	1.069	920	29.38	0	35.95	44/55
343.19	1.069	924	29.87	0	33.76	44/55
363.23	1.086	963	29.43	0	11.95	44/55
363.15	1.086	960	29.13	0	11.81	44/55
363.19	1.086	961	29.15	0	11.8	44/55
383.27	1.105	1004	29.34	0	4.42	44/55
383.17	1.105	1003	29.28	0	4.28	44/55

Table AS2. IDTs and Experiments conditions for NG2, φ = 1.0 in 'air'.

T_i_K	p_i_bar	T_C_K	p_C_bar	IDT_STG1_ms	IDT_STG2_ms	N2/Ar
383.21	0.885	840	20.02	0	198.1	100/0
383.19	0.885	840	19.97	0	191.1	100/0
333.41	0.751	849	19.61	0	354.6	44/55
333.47	0.751	849	19.55	0	353.5	44/55
348.17	0.77	876	19.65	0	132	44/55
348.29	0.77	876	19.62	0	129.3	44/55
363.23	0.78	903	19.51	0	57.3	44/55

363.29	0.78	903	19.51	0	58.4	44/55
378.23	0.8	932	19.79	0	25.11	44/55
393.29	0.816	961	19.99	0	11.69	44/55
393.25	0.816	960	19.91	0	11.98	44/55
323.21	1.255	738	30.47	99.53	200.5	100/0
323.15	1.255	735	30.1	92.29	187.7	100/0
323.25	1.255	735	29.94	91.16	185.2	100/0
338.17	1.26	763	29.87	45.98	138.9	100/0
338.27	1.26	761	29.6	45.49	137.4	100/0
353.07	1.28	787	29.59	0	133.2	100/0
353.15	1.28	787	29.61	0	132.8	100/0
368.09	1.295	814	29.71	0	114.3	100/0
368.13	1.295	814	29.64	0	115.2	100/0
383.11	1.307	841	29.64	0	73.55	100/0
383.27	1.307	841	29.58	0	75.23	100/0
333.43	1.119	851	29.4	0	89.5	44/55
333.31	1.119	852	29.61	0	92.8	44/55
348.31	1.136	878	29.19	0	49.43	44/55
348.21	1.136	880	29.47	0	49.99	44/55
363.21	1.164	905	29.3	0	25.64	44/55

Table AS3. IDTs and Experiments conditions for NG2, φ = 2.0 in 'air'.

T_i_K	p_i_bar	T_C_K	p_C_bar	IDT_STG1_ms	IDT_STG2_ms	N2/Ar
338.11	0.816	726	18.59	0	370	100/0
338.09	0.816	725	18.55	0	410	100/0
338.15	0.816	725	18.56	0	364.1	100/0
355.15	0.823	756	18.8	101.4	265.5	100/0
355.15	0.823	755	18.62	100.5	267.1	100/0
368.09	0.822	778	18.63	0	286.2	100/0
368.15	0.822	778	18.6	0	296	100/0
390.15	0.836	814	18.73	0	224.5	100/0
390.13	0.836	811	18.42	0	225	100/0
390.17	0.836	813	18.59	0	220.8	100/0
308.17	0.702	816	19.01	0	245.1	0/100
308.03	0.702	815	18.92	0	243.3	0/100
327.27	0.698	857	18.95	0	185.4	0/100
327.33	0.698	853	18.58	0	184.6	0/100
327.35	0.698	853	18.58	0	187.1	0/100
345.15	0.698	893	18.85	0	65.8	0/100
345.17	0.698	893	18.83	0	64.48	0/100
356.15	0.704	908	18.41	0	35.95	0/100
356.11	0.704	910	18.59	0	36.04	0/100
373.15	0.729	938	18.68	0	14.87	0/100
373.13	0.729	939	18.77	0	14.2	0/100
388.17	0.735	967	18.8	0	7.17	0/100
388.15	0.735	968	18.88	0	7.48	0/100

328.23	1.312	711	30.43	0	207.8	100/0
328.25	1.312	711	30.43	0	208.7	100/0
338.15	1.319	727	30.31	108.3	123.3	100/0
338.17	1.319	727	30.35	107.1	123.1	100/0
355.19	1.319	756	29.96	44.82	76.07	100/0
355.17	1.319	757	30.15	44.15	76.4	100/0
368.15	1.332	777	30.09	31.14	69.05	100/0
368.13	1.332	780	30.47	30.86	68.77	100/0
390.25	1.332	815	29.86	0	63.13	100/0
390.23	1.332	815	29.97	0	62.53	100/0
308.29	1.091	815	29.38	0	61.97	0/100
308.37	1.091	813	29.18	0	62.12	0/100
327.23	1.111	852	29.51	0	50.49	0/100
327.19	1.111	855	29.84	0	49.87	0/100
327.21	1.111	854	29.81	0	50.09	0/100
345.15	1.13	891	30.19	0	24.99	0/100
345.11	1.13	892	30.42	0	24.41	0/100
356.15	1.132	914	30.3	0	14.22	0/100
356.15	1.132	913	30.15	0	14.21	0/100
373.17	1.142	939	29.4	0	7.1	0/100
373.15	1.142	938	29.28	0	6.58	0/100

Table AS4. IDTs and Experiments conditions for NG3, φ = 1.0 in 'air'.

T_i_K	p_i_bar	T_C_K	p_C_bar	IDT_STG1_ms	IDT_STG2_ms	N2/Ar
338.15	0.822	755	19.35	57.93	143.1	100/0
338.09	0.822	753	19.19	53.96	139.2	100/0
338.09	0.822	753	19.15	52.41	136.1	100/0
357.11	0.874	788	20.2	0	141.8	100/0
357.09	0.874	789	20.27	0	142.8	100/0
374.01	0.88	818	20.08	0	159.8	100/0
374.05	0.88	818	20.11	0	161.3	100/0
393.09	0.885	851	19.94	0	98.7	100/0
393.17	0.885	849	19.74	0	97.93	100/0
323.49	0.858	721	19.49	161.1	214.7	100/0
323.37	0.858	720	19.41	151.8	206.5	100/0
307.97	0.748	790	19.94	0	160.4	45/55
308.13	0.748	788	19.74	0	159.8	45/55
308.01	0.748	787	19.64	0	158.3	45/55
323.17	0.758	818	19.73	0	198.6	45/55
323.23	0.758	818	19.7	0	188.9	45/55
323.27	0.758	818	19.65	0	194.4	45/55
338.15	0.769	851	20.05	0	155.2	45/55
338.19	0.769	852	20.1	0	158.8	45/55
353.07	0.782	882	20.29	0	76.62	45/55
353.15	0.782	882	20.28	0	78.58	45/55
368.09	0.79	903	19.6	0	37.48	45/55
368.15	0.79	906	19.84	0	36.97	45/55

383.11	0.796	933	19.65	0	18.4	45/55
383.07	0.796	933	19.67	0	17.79	45/55
393.09	0.813	948	19.61	0	11.23	45/55
393.09	0.813	952	19.93	0	10.83	45/55
338.11	1.259	754	29.46	30.91	50.87	100/0
338.15	1.259	754	29.53	31.97	52.38	100/0
338.15	1.259	754	29.52	28.14	49.92	100/0
357.15	1.293	786	29.44	0	45.88	100/0
357.17	1.293	787	29.63	0	44.94	100/0
374.07	1.313	817	29.86	0	55.95	100/0
374.11	1.313	817	29.81	0	55.87	100/0
393.11	1.347	852	30.46	0	38.95	100/0
393.11	1.347	851	30.39	0	39.22	100/0
323.39	1.327	721	30.22	87	102.7	100/0
323.45	1.327	721	30.19	85	101.3	100/0
308.15	1.113	790	29.51	0	46.02	45/55
308.25	1.113	788	29.24	0	45.02	45/55
323.43	1.131	823	30.11	0	58.53	45/55
323.59	1.131	821	29.79	0	57.76	45/55
338.15	1.155	850	30.04	0	51.58	45/55
338.19	1.155	850	29.94	0	55.85	45/55
338.09	1.155	849	29.87	0	54.71	45/55
353.11	1.16	878	29.58	0	33.95	45/55
353.15	1.16	880	29.83	0	36.12	45/55
353.15	1.16	874	29.01	0	36.52	45/55
353.15	1.16	877	29.38	0	36.33	45/55
353.15	1.16	879	29.65	0	36.86	45/55
368.17	1.181	905	29.5	0	18.34	45/55
368.09	1.181	908	29.88	0	18.77	45/55
383.13	1.197	932	29.43	0	8.12	45/55
383.15	1.197	931	29.26	0	7.11	45/55
383.13	1.197	936	29.88	0	6.7	45/55

Table AS5. IDTs and Experiments conditions for NG6, φ = 1.0 in 'air'.

T_i_K	p_i_bar	T_C_K	p_C_bar	IDT_STG1_ms	IDT_STG2_ms	N2/Ar
303.57	0.818	689	19.61	0	301.8	100/0
303.53	0.818	688	19.53	0	322.4	100/0
303.53	0.818	687	19.48	0	379.3	100/0
323.09	0.828	726	19.68	53.4	68.72	100/0
323.17	0.828	726	19.68	51.3	69.63	100/0
338.11	0.835	754	19.67	24.13	51.72	100/0
338.15	0.835	754	19.7	22.1	49.09	100/0
353.09	0.836	780	19.43	16	53.95	100/0
353.07	0.836	781	19.61	14.4	52.84	100/0
368.11	0.858	809	19.99	0	66.6	100/0
368.09	0.858	808	19.87	0	67.28	100/0
383.11	0.858	835	19.78	0	72.2	100/0
383.11	0.858	836	19.87	0	71.32	100/0

338.15	0.772	844	19.71	0	77.7	45/55
338.19	0.772	843	19.57	0	77.24	45/55
348.21	0.781	861	19.51	0	63.38	45/55
348.15	0.781	862	19.64	0	62.38	45/55
363.15	0.79	891	19.62	0	32.3	45/55
363.15	0.79	892	19.73	0	32.06	45/55
383.11	0.799	931	19.77	0	11.79	45/55
383.11	0.799	929	19.59	0	12	45/55
393.29	0.81	950	19.82	0	7.3	45/55
393.29	0.81	950	19.87	0	6.96	45/55
393.15	0.81	952	20.05	0	7.5	45/55
303.27	1.236	688	29.62	0	238.1	100/0
303.33	1.236	689	29.69	0	181.9	100/0
303.45	1.236	687	29.45	0	174.1	100/0
303.45	1.236	690	29.94	0	186.6	100/0
323.21	1.257	726	29.91	29	33.4	100/0
323.09	1.257	727	30.17	28	34.85	100/0
323.23	1.257	728	30.29	30	34.16	100/0
338.11	1.243	755	29.55	14.6	23.31	100/0
338.19	1.243	756	29.7	14.2	22.7	100/0
353.09	1.268	782	29.84	7.84	19.28	100/0
353.11	1.268	785	30.3	8.2	19.78	100/0
368.09	1.304	807	30.05	6.63	20.58	100/0
368.11	1.304	810	30.5	6.5	20.93	100/0
383.05	1.303	836	30.26	0	26	100/0
383.13	1.303	836	30.16	0	25.28	100/0
338.09	1.168	844	29.77	0	25.53	45/55
338.15	1.168	844	29.74	0	25.96	45/55
348.13	1.179	862	29.68	0	22.74	45/55
348.11	1.179	863	29.75	0	23.02	45/55
363.15	1.19	891	29.57	0	14.84	45/55
363.07	1.19	892	29.72	0	15.12	45/55
383.13	1.206	930	29.67	0	6.1	45/55
383.15	1.206	933	29.97	0	6.69	45/55

Table AS6. IDTs and Experiments conditions for NG7, φ = 0.5 in 'air'.

T_i_K	p_i_bar	T_C_K	p_C_bar	IDT_STG1_ms	IDT_STG2_ms	N2/Ar
363.11	0.38	949	9.97	0	72.33	45/55
363.15	0.38	953	10.11	0	73.86	45/55
378.13	0.38	981	9.89	0	23.37	45/55
378.13	0.38	981	9.89	0	25.95	45/55
378.15	0.38	981	9.89	0	27.5	45/55
393.13	0.383	1012	9.85	0	10.83	45/55
393.15	0.383	1014	9.94	0	11.2	45/55
403.13	0.385	1035	9.92	0	7.8	45/55
403.15	0.385	1033	9.87	0	7.75	45/55

403.15	0.385	1032	9.83	0	7.79	45/55
303.17	1.218	713	30	54.9	93.43	100/0
303.27	1.218	712	29.78	51.36	89.27	100/0
323.21	1.219	752	29.52	12.87	39.45	100/0
323.29	1.219	752	29.48	12.63	39.52	100/0
338.13	1.237	781	29.59	6.32	31.01	100/0
338.15	1.237	782	29.83	6.72	31.15	100/0
353.15	1.244	811	29.78	5.01	29.48	100/0
353.11	1.244	814	30.24	5.09	29.66	100/0
368.15	1.247	840	29.59	0	31.6	100/0
368.13	1.247	841	29.75	0	31.45	100/0
383.13	1.253	868	29.56	0	28.12	100/0
383.09	1.253	867	29.42	0	28.59	100/0
320.27	1.069	864	29.81	0	40.55	45/55
320.11	1.069	859	29.17	0	39.28	45/55
320.07	1.069	858	29.15	0	37.8	45/55
333.26	1.074	890	29.35	0	31.99	45/55
333.29	1.074	889	29.28	0	28.74	45/55
333.31	1.074	890	29.31	0	29.38	45/55
348.09	1.099	918	29.29	0	17.06	45/55
348.17	1.099	919	29.31	0	16.2	45/55
363.17	1.099	953	29.27	0	8.02	45/55
363.13	1.099	952	29.19	0	7.78	45/55
378.11	1.119	985	29.56	0	3.64	45/55
378.09	1.119	985	29.59	0	3.71	45/55
378.09	1.119	984	29.42	0	3.912	45/55

Table AS7. IDTs and Experiments conditions for NG7, φ = 1.0 in 'air'.

T_i_K	p_i_bar	T_C_K	p_C_bar	IDT_STG1_ms	IDT_STG2_ms	N2/Ar
303.35	0.82	689	19.63	114.7	138.2	100/0
303.35	0.82	691	19.91	117.9	140.8	100/0
318.17	0.829	715	19.5	29.8	44.7	100/0
318.13	0.829	716	19.64	29.22	44.36	100/0
333.31	0.842	745	19.78	12.23	26.43	100/0
333.21	0.842	744	19.69	12.78	26.99	100/0
348.13	0.848	773	19.88	8.1	26.51	100/0
348.17	0.848	771	19.66	7.39	25.61	100/0
363.13	0.864	800	20.08	6.2	29.44	100/0
363.13	0.864	800	20.08	6.4	29.73	100/0
378.13	0.864	826	19.87	0	37.97	100/0
378.11	0.864	826	19.86	0	38.14	100/0
393.13	0.872	852	19.77	0	38.97	100/0
393.17	0.872	852	19.79	0	38.66	100/0
341.15	0.791	850	20.04	0	41.71	45/55
341.13	0.791	849	19.93	0	41.6	45/55
353.11	0.793	876	20.13	0	37.02	45/55
353.13	0.793	874	19.98	0	36.81	45/55
368.15	0.794	910	20.33	0	23.52	45/55

368.15	0.794	907	20.1	0	23.47	45/55
383.13	0.794	936	19.89	0	13.18	45/55
383.15	0.794	936	19.93	0	13.49	45/55
393.15	0.8	955	19.93	0	8.73	45/55
393.13	0.8	956	20.03	0	8.69	45/55
303.23	1.218	693	29.91	91.4	103.1	100/0
303.27	1.218	691	29.56	86.16	97.41	100/0
303.29	1.218	692	29.71	85	96.6	100/0
318.19	1.229	719	29.61	27	32.79	100/0
318.27	1.229	717	29.18	23	28.84	100/0
318.41	1.229	717	29.17	24.7	30.59	100/0
333.15	1.272	746	30.1	10.65	15.45	100/0
333.17	1.272	743	29.64	9.254	14.09	100/0
333.23	1.272	745	29.95	9.621	14.58	100/0
348.17	1.28	770	29.57	5.14	10.84	100/0
348.13	1.28	771	29.7	4.98	10.58	100/0
363.17	1.293	804	30.63	3.43	10.68	100/0
363.15	1.293	803	30.45	3.04	10.51	100/0
378.13	1.295	828	30.06	0	12.93	100/0
378.13	1.295	825	29.6	0	12.66	100/0
393.19	1.306	850	29.3	0	15.03	100/0
393.13	1.306	851	29.47	0	14.68	100/0
341.15	1.158	857	30.2	0	15.14	45/55
341.11	1.158	851	29.43	0	15.46	45/55
341.13	1.158	850	29.3	0	15.81	45/55
353.09	1.18	875	29.9	0	15.11	45/55
353.13	1.18	877	30.08	0	14.89	45/55
368.09	1.187	910	30.5	0	10.48	45/55
368.15	1.187	910	30.5	0	10.28	45/55
383.15	1.187	938	30.03	0	6.35	45/55
383.13	1.187	938	30.05	0	6.31	45/55
393.11	1.188	958	29.93	0	4.3	45/55
393.11	1.188	957	29.85	0	4.31	45/55

Table AS8. IDTs and Experiments conditions for NG7, φ = 1.5 in 'air'.

T_i_K	p_i_bar	T_C_K	p_C_bar	IDT_STG1_ms	IDT_STG2_ms	N2/Ar
323.47	0.436	701	9.82	0	302.2	100/0
323.53	0.436	701	9.79	0	252.1	100/0
338.19	0.437	729	9.89	57.3	104	100/0
338.21	0.437	729	9.91	59.25	112.9	100/0
338.27	0.437	729	9.87	59.52	110.9	100/0
353.11	0.439	753	9.76	28.25	95.55	100/0
353.13	0.439	755	9.84	28.47	96.86	100/0
368.17	0.445	781	9.96	19.78	113.8	100/0
368.11	0.445	781	9.94	19.85	115.2	100/0
383.11	0.451	805	9.93	0	143.7	100/0
383.17	0.451	807	10.03	0	141.2	100/0
383.13	0.451	807	10.01	0	140.7	100/0
339.09	0.401	808	9.83	0	153.8	45/55
339.09	0.401	806	9.72	0	155.6	45/55
353.11	0.41	834	9.94	0	170.6	45/55

353.13	0.41	831	9.82	0	172.7	45/55
368.13	0.416	861	9.98	0	166.2	45/55
368.15	0.416	859	9.92	0	165.9	45/55
383.15	0.419	891	10.11	0	109.1	45/55
383.15	0.419	890	10.03	0	106.4	45/55
398.13	0.423	914	9.92	0	43.2	45/55
398.17	0.423	915	9.97	0	45.3	45/55
413.17	0.426	942	9.98	0	21.31	45/55
413.15	0.426	943	9.99	0	21.1	45/55
428.19	0.429	969	9.97	0	11.93	45/55
428.25	0.429	969	9.96	0	11.74	45/55
303.23	1.268	670	29.94	0	395.6	100/0
303.31	1.268	670	29.91	0	372	100/0
323.17	1.279	704	29.43	0	50.27	100/0
323.31	1.279	703	29.31	0	46.91	100/0
323.35	1.279	704	29.41	0	49.45	100/0
338.13	1.311	732	30.28	17.68	20.4	100/0
338.15	1.311	732	30.18	17.05	20.28	100/0
353.15	1.325	758	30.33	7.62	10.92	100/0
353.15	1.325	757	30.14	7.33	10.8	100/0
368.15	1.333	783	30.05	4.33	7.89	100/0
368.17	1.333	783	30.03	4.3	7.83	100/0
383.11	1.343	809	30.18	2.52	7.65	100/0
383.09	1.343	808	30.09	2.8	7.69	100/0
339.07	1.193	811	29.68	3.43	8.22	45/55
339.09	1.193	813	29.88	3.44	8.29	45/55
353.17	1.225	832	29.49	0	8.78	45/55
353.11	1.225	838	30.27	0	9.15	45/55
353.15	1.225	837	30.11	0	9.02	45/55
368.15	1.231	863	29.88	0	10.59	45/55
368.13	1.231	863	29.84	0	10.51	45/55
383.11	1.241	893	30.25	0	8.325	45/55
383.15	1.241	888	29.5	0	8.673	45/55
383.13	1.241	887	29.33	0	8.814	45/55
398.15	1.26	913	29.48	0	5.4	45/55
398.15	1.26	915	29.7	0	5.5	45/55

Table AS9. IDTs and Experiments conditions for NG8, φ = 1.0 in 'air'.

T_i_K	p_i_bar	T_C_K	p_C_bar	IDT_STG1_ms	IDT_STG2_ms	N2/Ar
303.21	0.83	678	19.57	0	133.1	100/0
303.25	0.83	678	19.48	0	142	100/0
323.65	0.848	717	19.87	21.8	27.44	100/0
323.63	0.848	718	19.9	21	27.11	100/0
338.13	0.855	743	19.75	9.71	14.88	100/0
338.11	0.855	744	19.87	9.73	14.67	100/0
353.13	0.857	769	19.57	4.96	12.28	100/0
353.15	0.857	769	19.5	5.07	12.42	100/0
368.11	0.877	795	19.71	3.25	13.34	100/0
368.19	0.877	795	19.76	3.5	13.49	100/0
383.17	0.888	820	19.69	4.51	17.62	100/0
383.15	0.888	821	19.8	4.72	17.59	100/0

331.23	0.783	817	19.71	3.31	17.16	45/55
331.25	0.783	817	19.76	3.23	17.31	45/55
343.13	0.784	844	19.85	0	22.49	45/55
343.13	0.784	844	19.86	0	22.54	45/55
358.15	0.786	872	19.66	0	22.83	45/55
358.13	0.786	874	19.79	0	23.6	45/55
373.15	0.788	902	19.56	0	16.93	45/55
373.13	0.788	900	19.42	0	17.19	45/55
388.15	0.809	925	19.42	0	8.68	45/55
388.13	0.809	924	19.32	0	9.38	45/55
388.15	0.809	926	19.54	0	9.54	45/55
403.17	0.82	956	19.76	0	4.86	45/55
403.15	0.82	958	19.94	0	5.14	45/55
403.15	0.82	958	19.96	0	5.18	45/55
303.11	1.259	679	29.81	0	100	100/0
303.13	1.259	682	30.36	0	95.9	100/0
323.39	1.289	716	30.04	0	21.56	100/0
323.45	1.289	719	30.51	0	18.48	100/0
323.57	1.289	719	30.45	0	17.58	100/0
338.17	1.29	745	30.16	7.87	9.99	100/0
338.13	1.29	746	30.33	7.55	9.24	100/0
353.13	1.292	773	30.06	3.38	6.02	100/0
353.15	1.292	773	30.09	3.05	5.77	100/0
368.15	1.297	799	29.8	1.9	5.47	100/0
368.13	1.297	798	29.75	1.69	5.06	100/0
383.17	1.316	826	30.18	1.5	6.07	100/0
383.13	1.316	824	29.8	1.41	5.93	100/0
331.19	1.16	823	30.08	1.44	5.92	45/55
331.23	1.16	820	29.6	1.22	5.53	45/55
343.11	1.163	846	29.73	1.28	7.81	45/55
343.19	1.163	843	29.29	1.11	7.31	45/55
343.15	1.163	842	29.18	1.04	7.075	45/55
358.09	1.178	874	29.68	0	9.07	45/55
358.11	1.178	874	29.72	0	9.04	45/55
373.15	1.188	903	29.69	0	7.47	45/55
373.13	1.188	902	29.57	0	7.54	45/55
388.15	1.22	928	29.76	0	4.4	45/55
388.15	1.22	929	29.81	0	4.13	45/55
403.25	1.225	960	29.97	0	2.36	45/55
403.15	1.225	960	30.02	0	2.28	45/55

Table AS10. IDTs and Experiments conditions for NG10, φ= 0.5 in 'air'.

T_i_K	p_i_bar	T_C_K	p_C_bar	IDT_STG1_ms	IDT_STG2_ms	N2/Ar
302.99	0.405	704	9.82	105.2	315.2	100/0
303.03	0.405	706	9.95	90.7	286.4	100/0
313.75	0.408	724	9.8	34.26	157.3	100/0
313.69	0.408	724	9.79	32.8	162.4	100/0
313.67	0.408	725	9.81	31.77	156.9	100/0
323.01	0.415	742	9.9	19.92	156.1	100/0
323.05	0.415	743	9.92	20.84	158.8	100/0
338.15	0.42	773	9.99	13.57	199.7	100/0

338.17	0.42	771	9.92	14.4	208	100/0
353.15	0.425	802	10.02	13.46	306	100/0
353.15	0.425	800	9.92	14.49	274	100/0
353.13	0.425	801	9.97	14.38	268.9	100/0
368.15	0.428	830	10	0	274	100/0
368.13	0.428	829	9.97	0	285	100/0
383.17	0.436	858	10.11	0	234.8	100/0
383.17	0.436	857	10.08	0	238.8	100/0
333.21	0.381	880	10.38	0	189.2	45/55
333.15	0.381	873	10.08	0	200.9	45/55
333.21	0.381	874	10.1	0	194.9	45/55
353.11	0.375	922	10.02	0	95.76	45/55
353.15	0.375	920	9.94	0	89.26	45/55
353.17	0.375	919	9.91	0	90.01	45/55
373.15	0.38	968	10.2	0	25.86	45/55
373.15	0.38	965	10.06	0	25.41	45/55
373.17	0.38	964	10.03	0	25.18	45/55
393.13	0.385	1006	10.03	0	8.22	45/55
393.17	0.385	1003	9.94	0	8.44	45/55
393.19	0.385	1005	10	0	8.3	45/55
413.21	0.394	1052	10.3	0	3.42	45/55
413.25	0.394	1047	10.14	0	3.302	45/55
413.23	0.394	1046	10.08	0	3.15	45/55
303.05	1.182	707	29.17	31.39	40.37	100/0
303.03	1.182	709	29.52	31.43	41.02	100/0
313.29	1.19	729	29.47	15.12	21.65	100/0
313.53	1.19	728	29.22	12.99	19.44	100/0
313.65	1.19	729	29.37	13.02	19.44	100/0
322.71	1.222	747	30.01	7.85	13.88	100/0
322.85	1.222	747	29.93	7.12	13.03	100/0
338.15	1.227	777	29.77	3.66	9.34	100/0
338.15	1.227	776	29.62	3.47	9.16	100/0
353.13	1.234	806	29.81	1.85	8.98	100/0
353.15	1.234	804	29.5	1.75	8.84	100/0
368.15	1.245	832	29.39	1.1	10.33	100/0
368.15	1.245	832	29.35	1.06	10.36	100/0
383.17	1.251	860	29.26	0	13.1	100/0
383.15	1.251	859	29.24	0	13.27	100/0
333.19	1.115	881	30.47	0	10.81	45/55
333.27	1.115	880	30.26	0	10.54	45/55
353.13	1.069	927	29.22	0	7.98	45/55
353.15	1.069	927	29.22	0	8.34	45/55
353.11	1.069	928	29.25	0	8	45/55
373.15	1.123	966	29.86	0	3.5	45/55
373.13	1.123	964	29.59	0	3.52	45/55
373.15	1.123	963	29.54	0	3.47	45/55
393.15	1.125	1009	29.68	0	1.05	45/55
393.15	1.125	1008	29.54	0	1.1	45/55

Table AS11. IDTs and Experiments conditions for NG10, φ= 1.0 in 'air'.

T_i_K	p_i_bar	T_C_K	p_C_bar	IDT_STG1_ms	IDT_STG2_ms	N2/Ar

303.27	0.84	674	19.59	0	103.1	100/0
303.23	0.84	675	19.8	0	109.5	100/0
303.27	0.84	675	19.73	0	113.4	100/0
313.49	0.845	692	19.57	0	40.29	100/0
313.53	0.845	691	19.41	0	39.84	100/0
323.25	0.858	709	19.53	16.74	20.3	100/0
323.29	0.858	710	19.65	17.4	20.9	100/0
338.09	0.876	736	19.9	8.07	11.05	100/0
338.15	0.876	737	19.93	7.73	10.38	100/0
353.11	0.885	763	19.85	3.52	6.44	100/0
353.15	0.885	762	19.8	3.7	6.48	100/0
368.23	0.89	791	19.92	2.27	6.8	100/0
368.15	0.89	790	19.93	2.16	6.51	100/0
383.15	0.901	815	19.85	1.21	7.82	100/0
383.13	0.901	814	19.76	1.28	7.64	100/0
338.15	0.796	824	19.69	1.64	9.17	45/55
338.17	0.796	824	19.72	1.58	9.104	45/55
353.19	0.802	855	19.85	5.19	12.98	45/55
353.11	0.802	858	20.06	5.1	12.75	45/55
353.15	0.802	855	19.85	5.46	12.33	45/55
368.15	0.809	885	19.87	0	12.76	45/55
368.11	0.809	884	19.81	0	12.58	45/55
383.15	0.817	914	19.97	0	9.51	45/55
383.13	0.817	915	20.02	0	9.27	45/55
403.19	0.822	950	19.72	0	4.31	45/55
403.19	0.822	949	19.64	0	4.34	45/55
423.15	0.844	987	19.97	0	1.63	45/55
423.21	0.844	987	19.98	0	1.5	45/55
423.21	0.844	988	20.06	0	1.64	45/55
303.47	1.267	675	29.73	0	86.15	100/0
303.19	1.267	676	29.93	0	84.71	100/0
313.37	1.272	694	29.71	0	33.05	100/0
313.41	1.272	694	29.67	0	32.27	100/0
323.21	1.281	710	29.46	13.52	15.46	100/0
323.21	1.281	710	29.47	13.2	15	100/0
338.13	1.303	736	29.57	5.8	7.25	100/0
338.15	1.303	737	29.62	5.71	7.03	100/0
353.17	1.323	763	29.66	2.28	3.5	100/0
353.09	1.323	762	29.62	2.42	3.55	100/0
368.15	1.335	789	29.72	1.11	2.45	100/0
368.07	1.335	791	30	1.22	2.52	100/0
368.15	1.335	791	30.04	1.18	2.51	100/0
383.15	1.343	817	29.83	0.31	2.52	100/0
383.15	1.343	817	29.87	0.27	2.42	100/0
338.13	1.223	825	30.36	0.56	2.68	45/55
338.15	1.223	829	31.02	0.71	2.85	45/55
338.13	1.223	827	30.7	0.58	2.66	45/55
353.11	1.223	856	30.4	0.36	3.54	45/55
353.09	1.223	855	30.23	0.28	3.55	45/55
368.17	1.224	885	30.11	0	4.27	45/55
368.17	1.224	886	30.27	0	4.68	45/55
368.15	1.224	886	30.23	0	4.55	45/55

383.13	1.225	915	30.13	0	3.68	45/55
383.13	1.225	918	30.51	0	3.74	45/55
383.15	1.225	919	30.53	0	3.79	45/55
403.19	1.233	952	29.73	0	1.64	45/55
403.17	1.233	951	29.68	0	1.62	45/55

Table AS12. IDTs and Experiments conditions for NG10, φ= 1.5 in 'air'.

***T*i_K**	***p*$_i$_bar**	***T*$_C$_K**	***p*$_C$_bar**	**IDT_STG1_ms**	**IDT_STG2_ms**	**N2/Ar**
328.09	0.449	693	10.06	0	91.33	100/0
328.21	0.449	693	10.01	0	92.6	100/0
343.15	0.455	719	10.11	37.93	42.68	100/0
343.15	0.455	719	10.12	36.77	42.35	100/0
358.15	0.46	744	10.11	16.72	25.85	100/0
358.13	0.46	743	10.02	16.36	25.61	100/0
373.11	0.468	768	10.12	9.66	25.03	100/0
373.15	0.468	769	10.16	9.25	25.11	100/0
388.17	0.478	792	10.2	6.77	31.15	100/0
388.15	0.478	793	10.3	6.93	31.46	100/0
345.11	0.412	800	10.06	14.5	42.35	45/55
345.11	0.412	799	10	14.53	42.15	45/55
345.13	0.412	798	9.95	14.57	42	45/55
358.15	0.425	818	9.98	14.75	44.66	45/55
358.17	0.425	820	10.11	14.77	44.41	45/55
373.13	0.43	849	10.24	0	47.94	45/55
373.15	0.43	848	10.19	0	47.8	45/55
373.17	0.43	848	10.19	0	47.62	45/55
393.19	0.435	884	10.2	0	31.03	45/55
393.17	0.435	883	10.19	0	31.21	45/55
413.21	0.438	921	10.29	0	14.08	45/55
413.21	0.438	918	10.14	0	13.8	45/55
433.15	0.441	956	10.26	0	6.62	45/55
433.19	0.441	957	10.28	0	6.53	45/55
303.17	1.31	650	29.88	0	367	100/0
303.25	1.31	651	29.96	0	358	100/0
303.23	1.31	651	29.91	0	357.2	100/0
313.25	1.323	667	29.72	0	114.9	100/0
313.35	1.323	666	29.5	0	113.3	100/0
313.45	1.323	667	29.78	0	105.6	100/0
328.05	1.324	696	30.25	0	31.89	100/0
328.09	1.324	695	29.98	0	32.06	100/0
328.07	1.324	692	29.48	0	32.48	100/0
343.11	1.334	720	29.77	12.46	14	100/0
343.09	1.334	720	29.86	12.8	14.27	100/0
358.19	1.36	745	30	5.16	6.3	100/0
358.13	1.36	745	30.08	4.98	6.31	100/0
373.09	1.368	768	29.63	2.55	3.15	100/0
373.15	1.368	768	29.56	2.38	3.148	100/0
388.13	1.382	792	29.58	1.21	2.12	100/0
388.15	1.382	792	29.57	1.11	2.01	100/0

Appendix A

Natural gas ignition delay times previous studies of *n*–alkane blends

1. Binary blends

Methane (CH_4)/ Ethane (C_2H_6)

Exp. Dev.	Ethane %	p_C atm	T_C K	φ	Dilute %	Paper	Year
ST	1.4, 9	0.2	1400–2000	1	89.5% Ar	[1]	1972
ST	16.6	4	1200–1850	0.135	78% Ar	[2]	1981
ST	10	3.3	1250–1600	1	78% Ar	[3]	1983
ST	1, 3, 6, 10	3–15	1300–2000	0.45–1.25	89.5% Ar	[4]	1994
ST	4.4, 6, 8.4, 10, 20	3–13	1485–1900	0.5–2	95–99% Ar	[5]	2003
ST	3.7, 7, 10	16–40	900–1400	1	72% N_2	[6]	2006
ST	10, 30	0.54–30.0	1090–2000	0.5	75% N_2	[7]	2007
ST	25, 50	20	800	0.5	75% Ar	[8]	2007
TFR	10, 15, 30	9, 12	785–935	0.4, 0.6	N2 in Air	[9]	2011
ST	25, 50, 75	1, 11–16, 25–31	1154–2248	0.5, 1, 2	75, 85, 95 %	[10]	2013
RCM	13	105, 125, 150, 160	885–940	0.526	75.2 % N_2	[11]	2017

Methane (CH_4)/ Propane (C_3H_8)

Exp. Dev.	Propane %	p_C atm	T_C K	φ	Dilute %	Paper	Year
ST	4.5, 39	0.2	1400–2000	1	89.5% Ar	[1]	1972
ST	10	3.3	1250–1600	1	78% Ar	[3]	1983
ST	2, 5, 10, 20		1300–1600	1	71.5% Ar	[12]	1984
ST	3, 6	3–15	1300–2000	0.45–1.25	89.5% Ar	[4]	1994
ST	1.25, 5	16–40	900–1400	1	72% N_2	[6]	2006
ST	20	0.54–30.0	1090–2000	0.5	75% N_2	[7]	2007
ST	25	20	800	0.5	75% Ar	[8]	2007
TFR	5, 10, 30	9	785–935	0.6	N2 in Air	[9]	2011

Methane (CH_4)/ butane (C_4H_{10})

Exp. Dev.	Butane %	p_C atm	T_C K	φ	Dilute %	Paper	Year
ST	*n*– Butane (1, 5, 10)	0.263– 0.395	1800–2500	0.5	90% Ar	[13]	1969
ST	*n*– Butane (1.4)	0.2	1400–2000	1	89.5% Ar	[1]	1972
ST	*i*– Butane (10)	3.3	1250–1600	1	78% Ar	[3]	1983
ST	*n*&*i*–(3, 6)	3–15	1300–2000	0.45–1.25	89.5% Ar	4]	1994
ST	*n*–Butane (25, 50)	20	800	0.5	75% Ar	[8]	2007
ST, RCM	*n*–Butane (10, 30)	10–30	660–1330	0.3–2.3	67–77% Ar, N2	[14]	2010

Methane (CH_4)/ Pentane (n–C_5H_{12})

Exp. Dev.	Pentane %	p_C atm	T_C K	φ	Dilute %	Paper	Year
ST	4.3, 10	0.2	1400–2000	1	89.5% Ar	[1]	1972
ST	25, 50	20	800	0.5	75% Ar	[8]	2007

Methane (CH_4)/ n–Hexane (n–C_6H_{14})

Exp. Dev.	*n*–Hexane %	p_C atm	T_C K	φ	Dilute %	Paper	Year
ST, RCM	0, 10, 20	10, 20 for RCM 1.97–4.11 for ST	640–2286	0.67–2.06	N2/Ar in air for RCM 96% Ar for ST	[15]	2019

Appendix A

Methane (CH_4)/ n–Heptane (n–C_7H_{16})

Exp. Dev.	n–Heptane %	p_C atm	T_C K	φ	Dilute %	Paper	Year
ST	0–100	10	1250–1750	1.0	95% Ar	[16]	2019
ST, RCM	0.025, 0.1	60	720–1284	0.5	N2/Ar in air	[18]	2019

2. Ternary blends

Methane (CH_4)/ Ethane (C_2H_6)/ Propane (C_3H_8)

Exp. Dev.	Ethane/ Propane %	p_C atm	T_C K	φ	Dilute %	Paper	Year
ST	15.4/7.7	4	1200–1850	0.16	78% Ar	[2]	1981
ST	8.5/1.6, 15.8/1.9, 8.4/1.6	3–13	1485–1900	0.5–2	95–99% Ar	[5]	2003
ST	3.74/1.21	16–40	900–1400	1	72% N_2	[6]	2006
ST	25/25	20	800	0.5	75% Ar	[8]	2007
ST, RCM	6.6/3.3, 15/15, 20/10	10–50	770–1580	0.5, 1, 2	75% Ar, N_2	[17]	2008
TFR	15/15	7, 9, 15	785–935	0.5, 0.6	N_2 in Air	[9]	2011

Methane (CH_4)/ Ethane (C_2H_6)/ Propane (C_3H_8)

Methane (CH_4)/ Ethane (C_2H_6)/ Butane (C_4H_{10})

Methane (CH_4)/ Ethane (C_2H_6)/ Pentane (n–C_5H_{12})

Methane (CH_4)/Propane (C_3H_8)/ Butane (C_4H_{10})

Methane (CH_4)/Propane (C_3H_8)/ Pentane (n–C_5H_{12})

Exp. Dev.	%	p_C atm	T_C K	φ	Dilute %	Paper	Year
ST	25/25	20	800	0.5	75% Ar	[8]	2007

Methane (CH_4)/ Propane (C_3H_8)/ n–Heptane (n–C_7H_{16})

Exp. Dev.	%	p_C atm	T_C K	φ	Dilute %	Paper	Year
ST, RCM	5/0.025, 5/0.05, 5/0.1	60, 100	671–1187	0.5	N2/Ar in air	[18]	2019

3. Quaternary blends

Methane (CH_4)/ Ethane (C_2H_6)/ Propane (C_3H_8) /butane (C_4H_{10})

Exp. Dev.	Ethane/ Propane/butane %	p_C atm	T_C K	φ	Dilute %	Paper	Year
ST	14/7.1/7.1	4	1200–1850	0.19	78% Ar	[2]	1981

Appendix A

4. Quinternary blends

Methane (CH_4)/ Ethane (C_2H_6)/ Propane (C_3H_8) /butanes (C_4H_{10})/ Pentanes (C_5H_{12})

Exp. Dev.	$C_2/C_3/C_4/C_5$ %	p_C atm	T_C K	φ	Dilute %	Paper	Year
ST, RCM	10/5/2.5/1.25, 20/10/5/2.5	1–34	740–1660	0.3–2	69–76% Ar, N_2	[19]	2009
ST, RCM	10/5/2.5/1.25, 20/10/5/2.5	10–30	630–1550	0.5–2	69–76% Ar, N_2	[20]	2010
ST, RCM	*n* & *i*–Butane, *n* & *i*–Pentane 7.27/2.92/1.36/0.21, 14/3.4/2/0.3, 12.9/1.5/0.41/0.05, 5.7/1.3/0.32/0.08, 2/1/0.6/0.047/	20, 40	850–1450	0.4, 1.2	N_2 in Air	[21]	2018

5. Hexarnary mixture

Methane (CH_4)/ Ethane (C_2H_6)/ Propane (C_3H_8) /butane (C_4H_{10})/ Pentane (C_5H_{12})/ n-Hexane (n-C_6H_{14})

Exp. Dev.	%	p_C atm	T_C K	φ	Dilute %	Paper	Year
TFR	5/1/0.6/0.3/0.03	9	785–935	0.6	N_2 in Air	[9]	2011

References

[1] R. W. Crossley, E. A. Dorko, K. Scheller, and A. Burcat, "The effect of higher alkanes on the ignition of methane–oxygen–argon mixtures in shock waves," Combust. Flame, 19(3) (1972) 373–378.

[2] C. S. Eubank, M. J. Rabinowitz, W. C. Gardiner, and R. E. Zellner, "Shock–initiated ignition of natural gas—Air mixtures," 18th Intl. Symp. Combust., 1 (1981) 1767–1774.

[3] R. Zellner, K. Niemitz, J. Warnatz, W. Gardiner, C. Eubank, and J. Simmie, "Hydrocarbon Induced Acceleration of Ignition of Methane–Air Ignition," in Flames, Lasers and Reactive Systems, American Institute of Aeronautics and Astronautics, (1983) 252–272.

[4] L. J. Spadaccini and M. B. Colket, "Ignition delay characteristics of methane fuels," Prog. Energy Combust. Sci., 20(5) (1994) 431–460.

[5] N. Lamoureux and C.–E. Paillard, "Natural gas ignition delay times behind reflected shock waves: Application to modelling and safety," Shock Waves, 13(1) (2003) 57–68.

[6] J. Huang and W. K. Bushe, "Experimental and kinetic study of autoignition in methane/ethane/air and methane/propane/air mixtures under engine–relevant conditions," Combust. Flame, 144(1) (2006) 74–88.

[7] E. L. Petersen, J. M. Hall, S. D. Smith, J. de Vries, A. R. Amadio, and M. W. Crofton, "Ignition of Lean Methane–Based Fuel Blends at Gas Turbine Pressures," J. Eng. Gas Turbines Power, 129(4) (2007) 937–944.

[8] J. de Vries and E. L. Petersen, "Autoignition of methane–based fuel blends under gas turbine conditions," Proc. Combust. Inst., 31(2) (2007) 3163–3171.

[9] D. J. Beerer and V. G. McDonell, "An experimental and kinetic study of alkane autoignition at high pressures and intermediate temperatures," Proc. Combust. Inst., 33(1) (2011) 301–307.

[10] C. J. Aul, W. K. Metcalfe, S. M. Burke, H. J. Curran, and E. L. Petersen, "Ignition and kinetic modeling of methane and ethane fuel blends with oxygen: A design of experiments approach," Combust. Flame, 160(7) (2013) 1153–1167.

[11] A. Ramalingam et al., "An RCM experimental and modeling study on CH_4 and CH_4/C_2H_6 oxidation at pressures up to 160 bar," Fuel, 206 (2017) 325–333.

[12] M. Frenklach and D. E. Bornside, "Shock–initiated ignition in methane–propane mixtures," Combust. Flame, 56(1) (1984) 1–27.

[13] R. M. R. Higgin and A. Williams, "A shock–tube investigation of the ignition of lean methane and n–butane mixtures with oxygen," 12th Intl. Symp. Combust., 1 (1969) 579–590.

[14] D. Healy, M. M. Kopp, N. L. Polley, E. L. Petersen, G. Bourque, and H. J. Curran, "Methane/n–Butane Ignition Delay Measurements at High Pressure and Detailed Chemical Kinetic Simulations," Energy Fuels, 24(3) (2010) 1617–1627.

[15] Y. He, Y. Wang, C. Grégoire, U. Niedzielska, R. Mével, and J. E. Shepherd, "Ignition characteristics of dual–fuel methane–n–hexane–oxygen–diluent mixtures in a rapid compression machine and a shock tube," Fuel, 249 (2019) 379–391.

[16] J. Liang, Z. Zhang, G. Li, Q. Wan, L. Xu, and S. Fan, "Experimental and kinetic studies of ignition processes of the methane–n–heptane mixtures," Fuel, 235 (2019) 522–529.

[17] D. Healy et al., "Methane/ethane/propane mixture oxidation at high pressures and at high, intermediate and low temperatures," Combust. Flame, 155(3) (2008) 441–448.

[18] S. Schuh, K. A. Ramalingam, H. Minwegen, A. K. Heufer, and F. Winter, "Experimental Investigation and Benchmark Study of Oxidation of Methane–Propane–n–Heptane Mixtures at Pressures up to 100 bar," Energies, 12(18) (2019) 3410.

[19] G. Bourque et al., "Ignition and Flame Speed Kinetics of Two Natural Gas Blends With High Levels of Heavier Hydrocarbons," J. Eng. Gas Turbines Power, 132(2) (2009) 21504–21511.

[20] D. Healy, D. M. Kalitan, C. J. Aul, E. L. Petersen, G. Bourque, and H. J. Curran, "Oxidation of C_1−C_5 Alkane Quinternary Natural Gas Mixtures at High Pressures," Energy Fuels, 24(3) (2010) 1521–1528.

[21] S. K. Vallabhuni et al., "Autoignition studies of Liquefied Natural Gas (LNG) in a shock tube and a rapid compression machine," Fuel, 232 (2018) 423–430.

Appendix B

(Supplementary material for Chapter 5)

An experimental and kinetic modeling study of NO_x sensitization on methane autoignition and oxidation

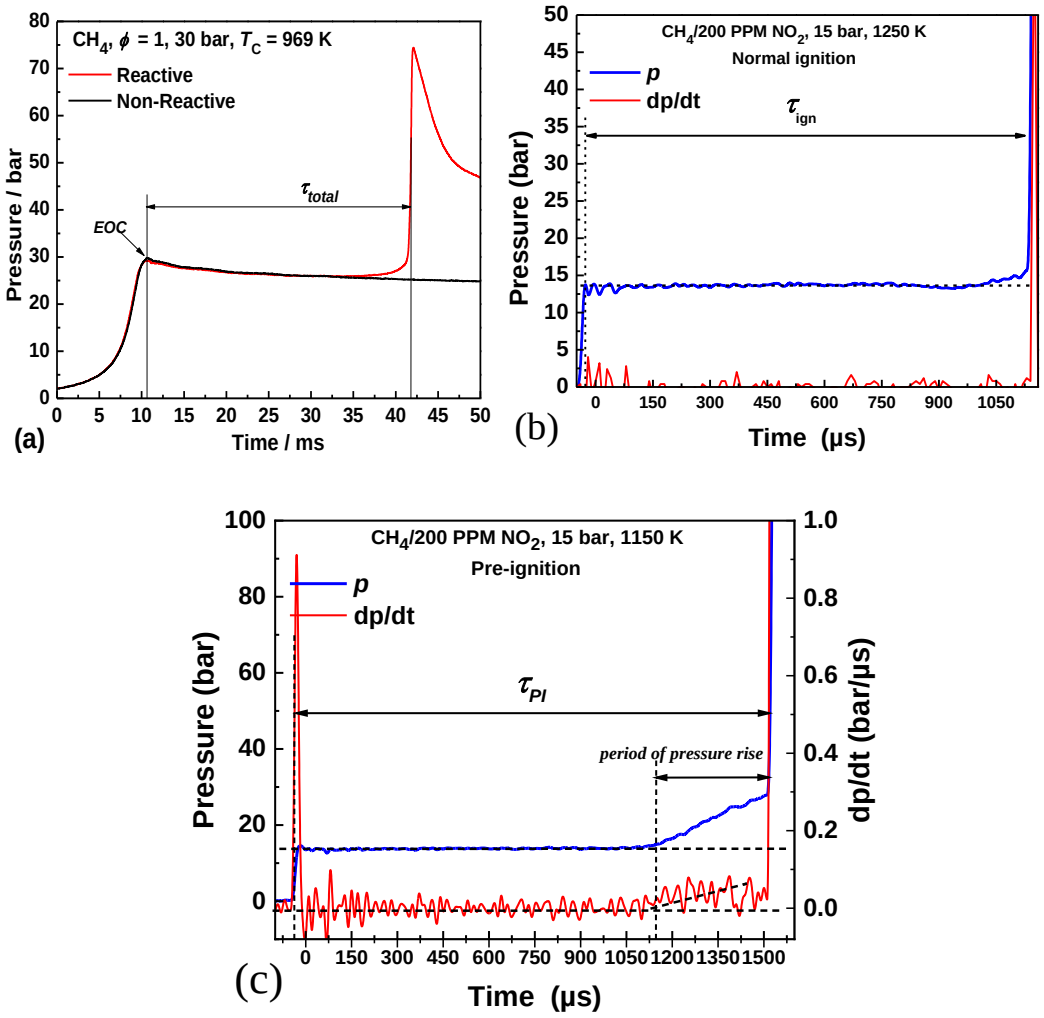

Figure BS1. Typical pressure-time histories for (a) CH_4 ignition in Rapid compression machine for φ = 1.0. T_C = 769 K, (b) CH_4/NO_2 ignition in ST at φ = 1.0 and 15 bar showing normal ignition, at T_5 = 1250 K; and (c) pre-ignition (pressure rise before ignition) at T_5 = 1150 K.

Appendix B

$NO \rightarrow NO_2$ conversion during mixture preparation

($CH_4/O_2/N_2$ + 400 ppm NO)

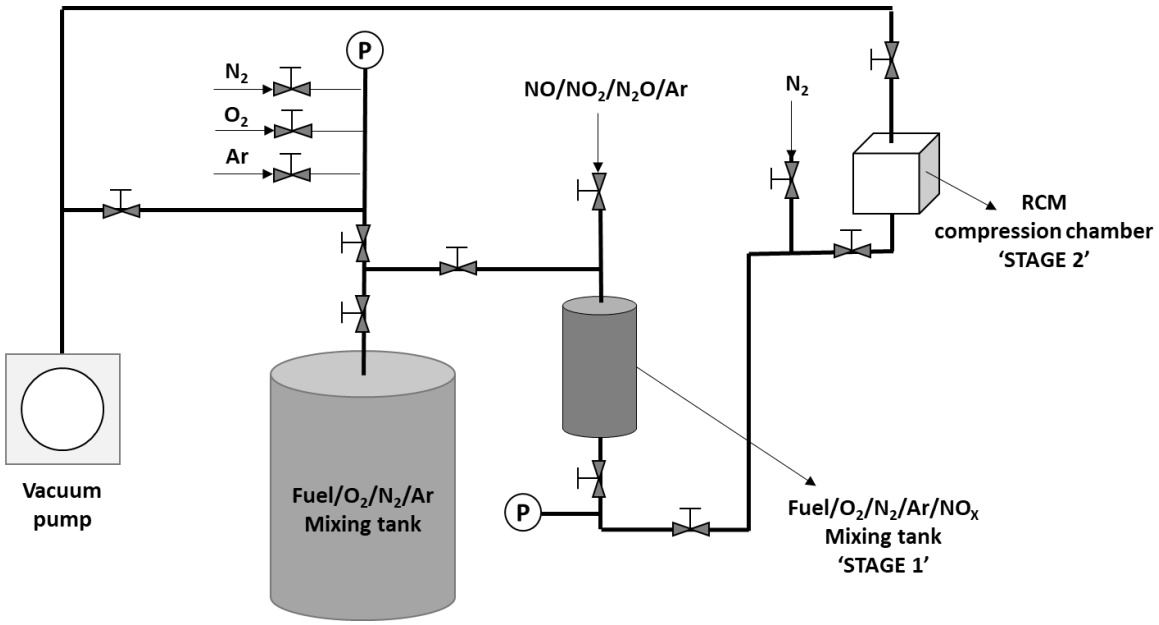

Figure BS2. Schematic of the mixture preparation setup.

Description of the mixing process

STAGE 1: Fuel/O_2/N_2/Ar is mixed with NO_x and then allowed to homogenize for ~6 mins in a small mixing tank.

STAGE 2: The homogeneous mixture is then transferred to the preheated reaction chamber where the mixture resides for approximately 2 – 3 mins before the experiment is conducted. This is the typical time required for locking pistons and filling up the pneumatic section.

Uncertainty in NO concentration while mixing

The NO and NO_2 diluted in Ar mixture (99.99% purity) comprises of 4% NO/96% Ar, and 2% NO_2/98% Ar, respectively. A 1 litre tank with a total filling pressure of 300 kPa was used for preparing the final $CH_4/O_2/(N_2/Ar)/NOx$ before filling the reaction chamber. So, filling 1.0 kPa of the 300 kPa with NO/Ar leads to an NO mole fraction of 0.04*1/300 = 0.0001333 or 133.3 ppm. The fraction of the filling pressure from NO/Ar cylinder was varied from 0.38 to 7.7 kPa for obtaining 50 to 1000 ppm levels, respectively. And there are four MKS pressure transducers (2, 10, 100, and 500 kPa) connected to the line with two decimals point with 0.5% accuracy

reading. For example, in case of 50 ppm, a filling pressure of 0.39 or 0.37 instead of 0.38 would lead to 51.9 or 49.27 ppm with maximum error of 1.9 ppm. The impact of 2 ppm variation is minimal on the IDTs.

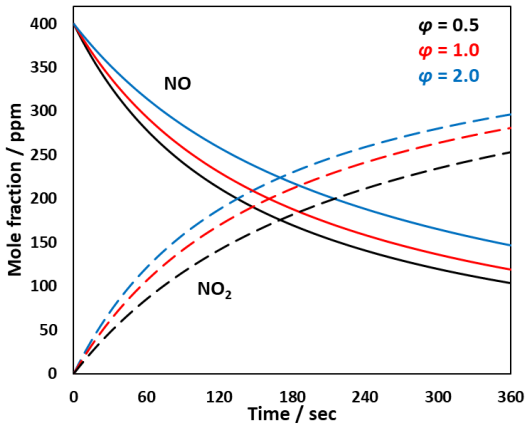

Figure BS3. Time-history of NO/NO2 mole fraction during Stage 1 mixing at *T* = 300 K, *p* = 0.3 MPa, *φ* = 1.0, NO = 400 ppm.

Constant volume simulations for $CH_4/O_2/N_2$ mixed with 400 ppm of NO were carried out at *T* = 300 K, and *p* = 0.3 MPa representing the conditions for 'Stage 1' mixing process. Figure BS3 shows that over a span of 6 minutes, more than 65% of NO oxidizes to NO_2 for lean, rich and stoichiometric mixtures through the reaction $2NO + O_2 \leftrightarrow 2NO_2$. Lean mixtures exhibit the fastest rate of oxidation owing to larger oxygen concentrations. Thus, the mixture transferred to RCM reaction chamber effectively comprises of both NO and NO_2.

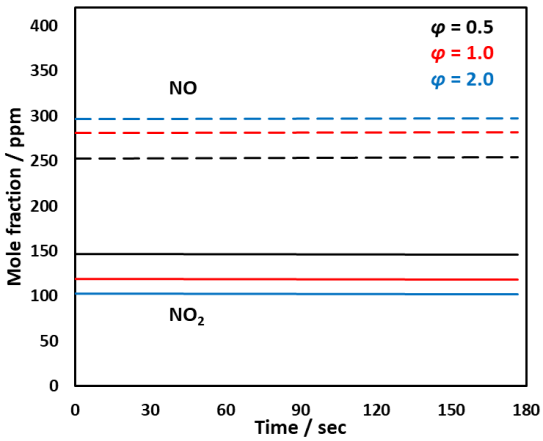

Figure BS4. Time-history of NO mole fraction in RCM reaction chamber (heating fuel/oxidizer/NOx mixture) Stage 2 mixing at *T* = 300 K, *p* = 0.3 MPa, *φ* = 1.0. (NO/NO2 composition same as Stage-1 end-point).

Appendix B

Premixed charge with the NO_x compositions calculated at the end-time of 'Stage 1' were used for constant volume simulations at p = 0.05 MPa and T =390 K representing 'Stage 2'. The composition remains fairly constant over the span of time with only < 1% decrease in NO mole fraction (Figure BS4). Overall, the rate of oxidation of NO into NO_2 is much slower in Stage 2 compared to the Stage 1.

The oxidation of NO to NO_2 or the reverse process via the termolecular reaction NO + NO + O_2 ↔ 2 NO_2 has been studied extensively in the literature [1–6] and the rate constants provided by these works are consistent with each other [1]. Therefore, we have adopted the rate constant by Park et al. [1] in our mechanism. In addition, Herzier and Nauman [7] have also reported the challenge of using NO for shock-tube/RCM experiments due to the rapid oxidation of NO. Therefore, in our work we carried out calculations to obtain the final NO/NO_2 composition in the mixture.

A flux analysis of NO conducted for the mixture at condition of the mixing chamber clearly shows that the termolecular reaction NO + NO + O_2 ↔ 2 NO_2 is responsible for the NO to NO_2 conversion (Figure BS5).

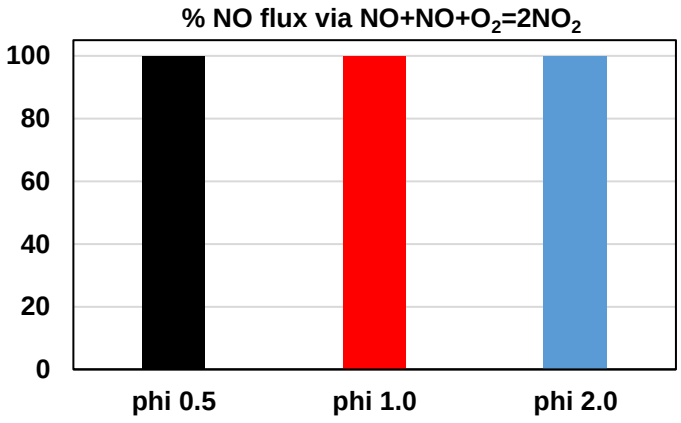

Figure BS5. NO flux comparison for $CH_4/O_2/N_2$/NO mixtures with 400 ppm NO addition for φ = 0.5, 1.0, 2.0.

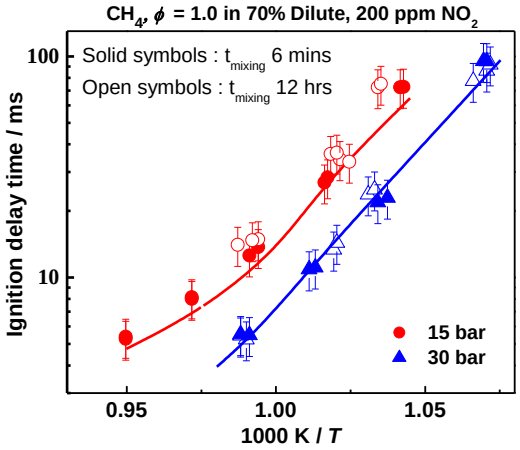

Figure BS6. Effect of mixing time on NO_2 sensitization of methane IDTs (symbols: experiments, line: NUIGMech1.2) at 1.5 and 3.0 MPa for φ = 1.0, and NO_2 = 400 ppm.

References

[1] J. Park, N.D. Giles, J. Moore, M.C. Lin, A comprehensive kinetic study of thermal reduction of NO_2 by H_2, J. Phys. Chem. A, 102 (1998) 10099–10105.

[2] M. Rohrig, E.L. Petersen, D.F. Davidson, R. K. Hanson, The pressure dependence of the thermal decomposition of N2O, Int. J. Chem. Kinet., 28 (1996) 599–608.

[3] W. Tsang, J.T. Herron, Chemical kinetic data base for propellant combustion I. Reactions involving NO, NO_2, HNO, HNO_2, HCN and N_2O. Journal of physical and chemical reference data, 20(4) (1991) 609–663.

[4] P.G. Ashmore, M.G. Burnett, Concurrent molecular and free radical mechanisms in the thermal decomposition of nitrogen dioxide. Transactions of the Faraday Society, 58 (1962) 253–261.

[5] E. Zimet, Thermal decomposition of N_2O_4 and NO_2 by shock waves. The Journal of Chemical Physics, 53(2) (1970) 515–518.

[6] W.A. Glasson, A.S. Tuesday, The Atmospheric Thermal Oxidation of Nitric Oxide, Journal of the American Chemical Society, 85(19) (1963) 2901–2904.

[7] J. Herzler, C. Naumann, Shock tube study of the influence of NOx on the ignition delay times of natural gas at high pressure, Combust. Sci. Technol., 184 (2012) 1635–1650.

Appendix B

Effect of fuel impurities

The maximum impurities associated with the methane cylinder are nitrogen (N_2), oxygen (O_2), carbon dioxide (CO_2), and water (H_2O) with reported maximum concentration being 3000, 100, 100, and 20 ppm, respectively.

Figure BS7 below shows constant volume simulations performed to evaluate the effect of these impurities on methane IDT prediction with and without 200 PPM NO_2 addition. The IDT predictions for both 0% and 0.5% impurities overlap on each other for the corresponding cases, while the addition of 200 PPM NO_2 leads to significant decrease on IDT. This confirm that at these levels of impurities using pure methane for simulations is acceptable.

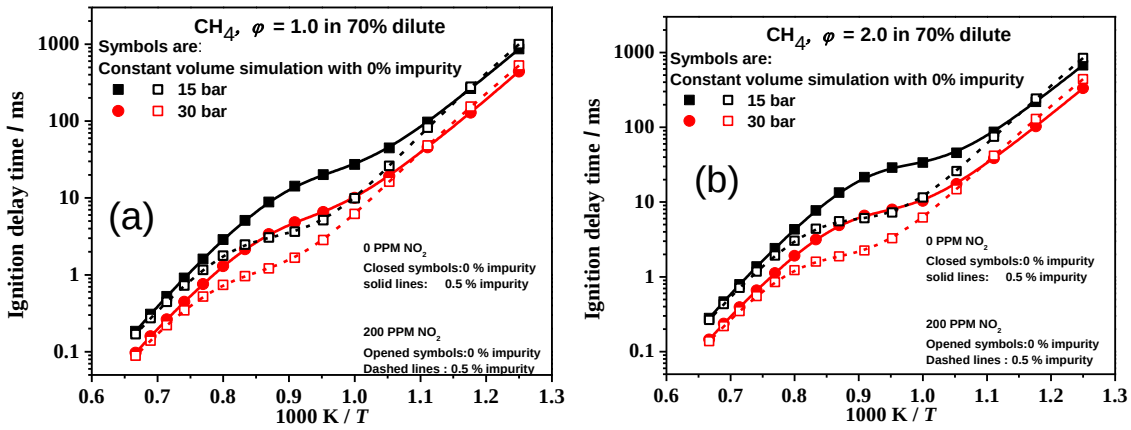

Figure BS7. The maximum impurities associated with the methane cylinder are nitrogen (N_2), oxygen (O_2), carbon dioxide (CO_2), and water (H_2O) with reported maximum concentration being 3000, 100, 100, and 20 ppm, respectively.

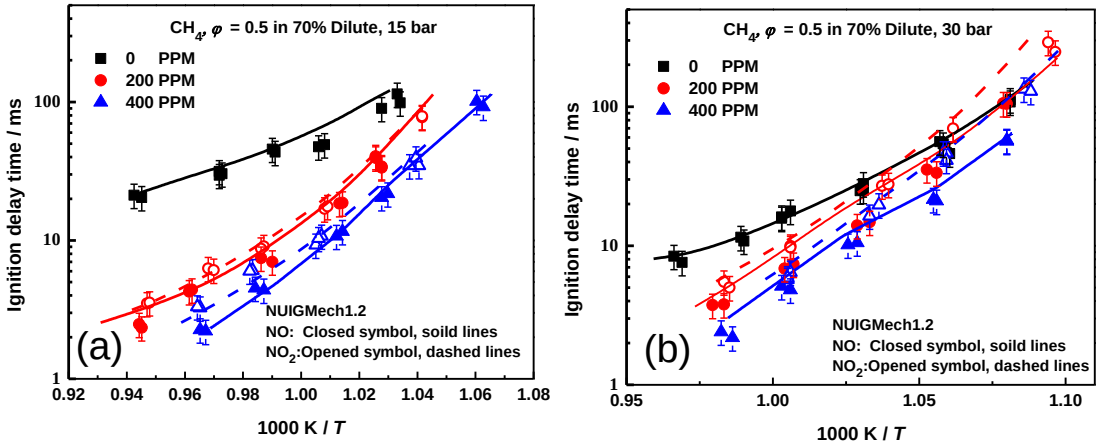

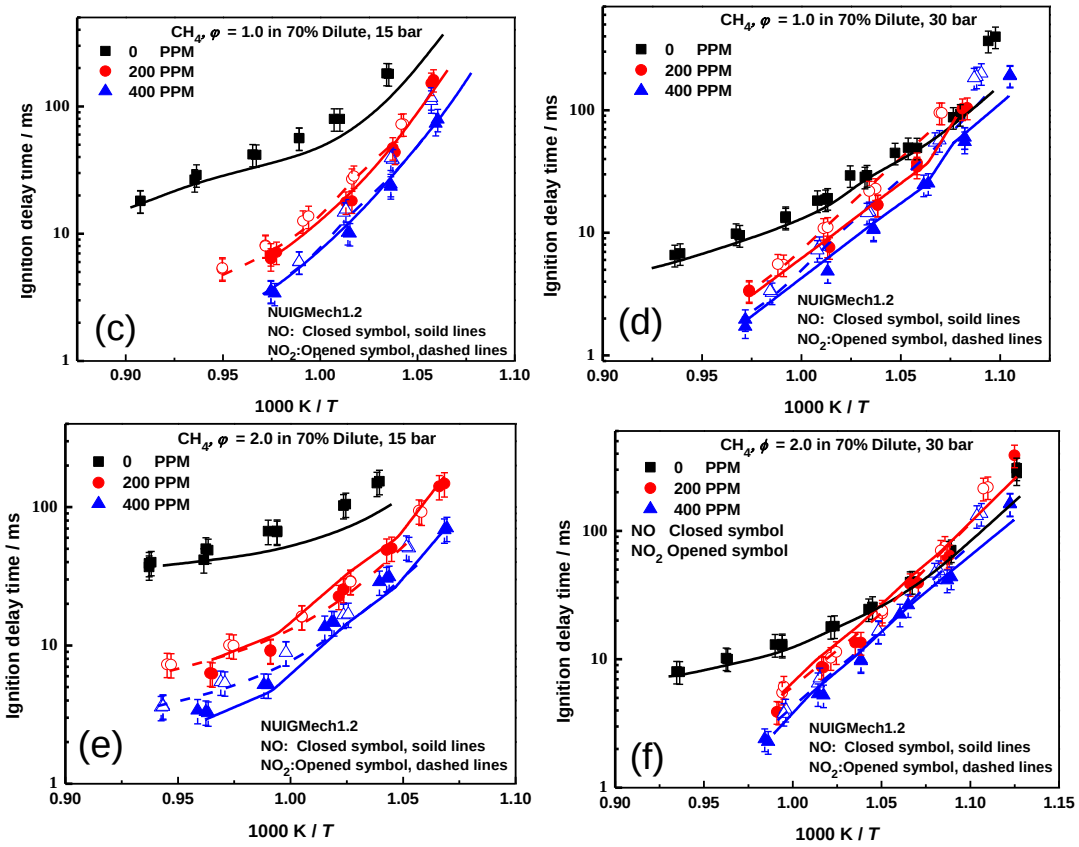

Figure BS8. Comparison of NO and NO_2 addition on methane IDT (symbols: experiments, solid line: NUIGMech1.2, at (a) φ =0.5, 1.5 MPa, (b) φ =0.5, 3.0 MPa, (c) φ =1.0, 1.5 MPa, (d) φ =1.0, 3.0 MPa, (e) φ =2.0, 1.5 MPa, (f) φ =2.0, 3.0 MPa.

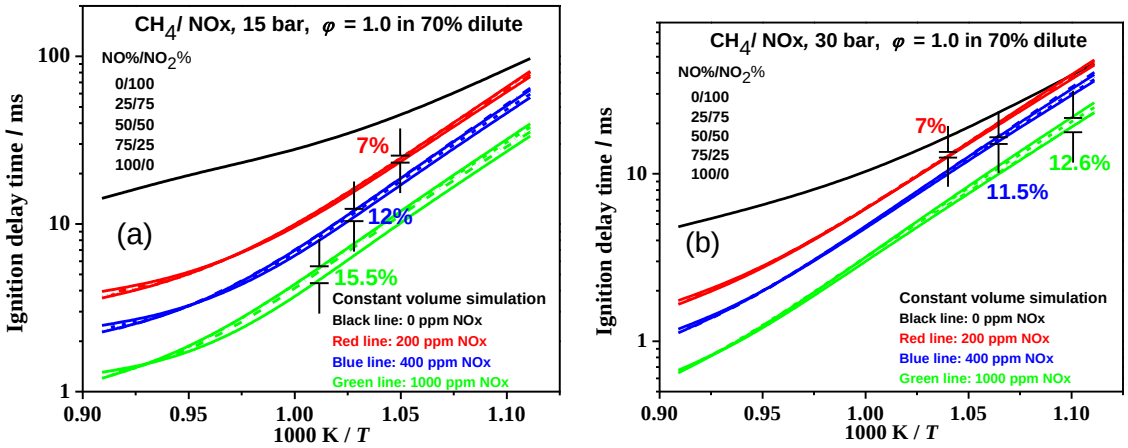

Figure BS9. constant volume simulation at stoichiometric condition and (a)1.5 MPa and (b) 3.0 MPa for five NO/NO_2 fractions for 200, 400, 1000 ppm NOx.

Effect of updates on IDT predictions of $CH_4/O_2/N_2/Ar/NO_2$ mixtures

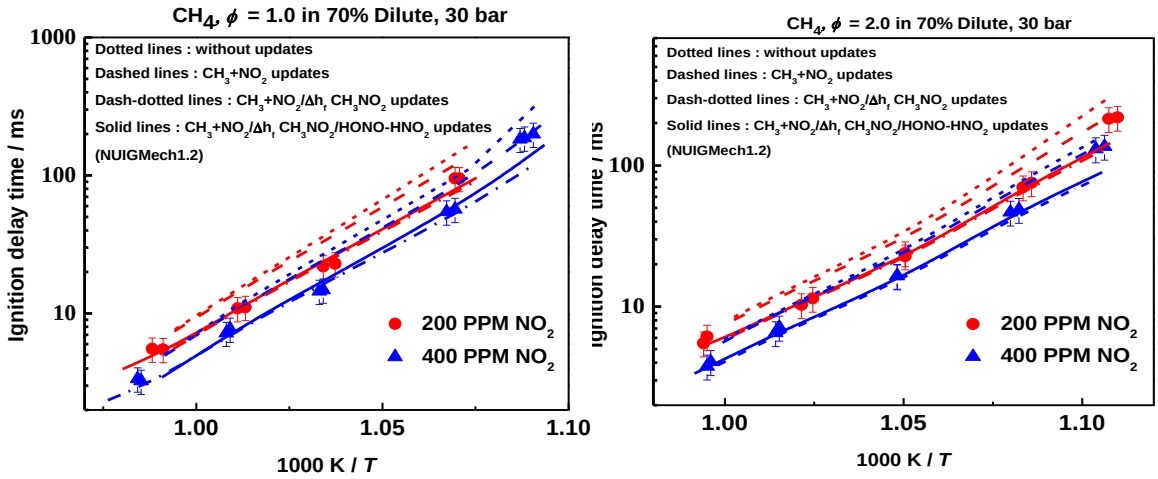

Figure BS10. Comparison of effect of mechanism updates on IDT predictions using NUIGMech1.2.

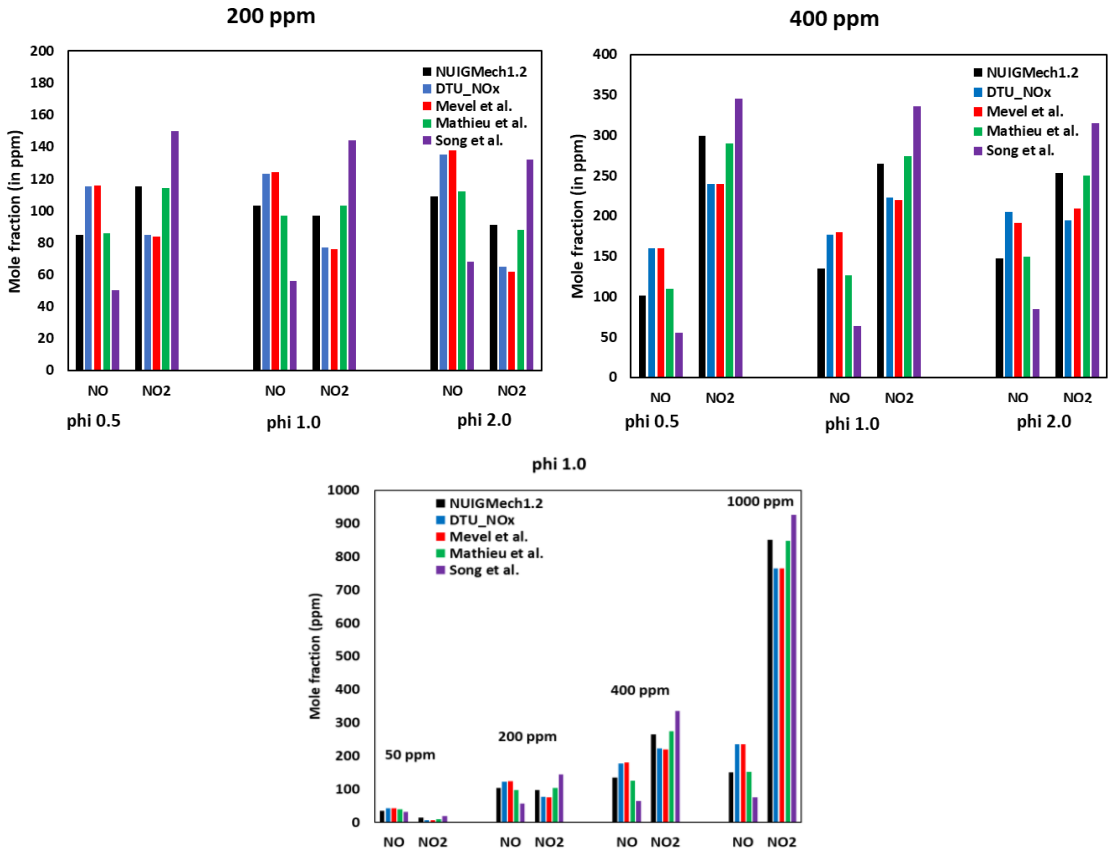

Figure BS11. Comparison of NO to NO_2 oxidation in $CH_4/O_2/N_2/Ar/NO$ mixtures during mixing period of 6 mins at $p = 0.3$ MPa using different mechanisms.

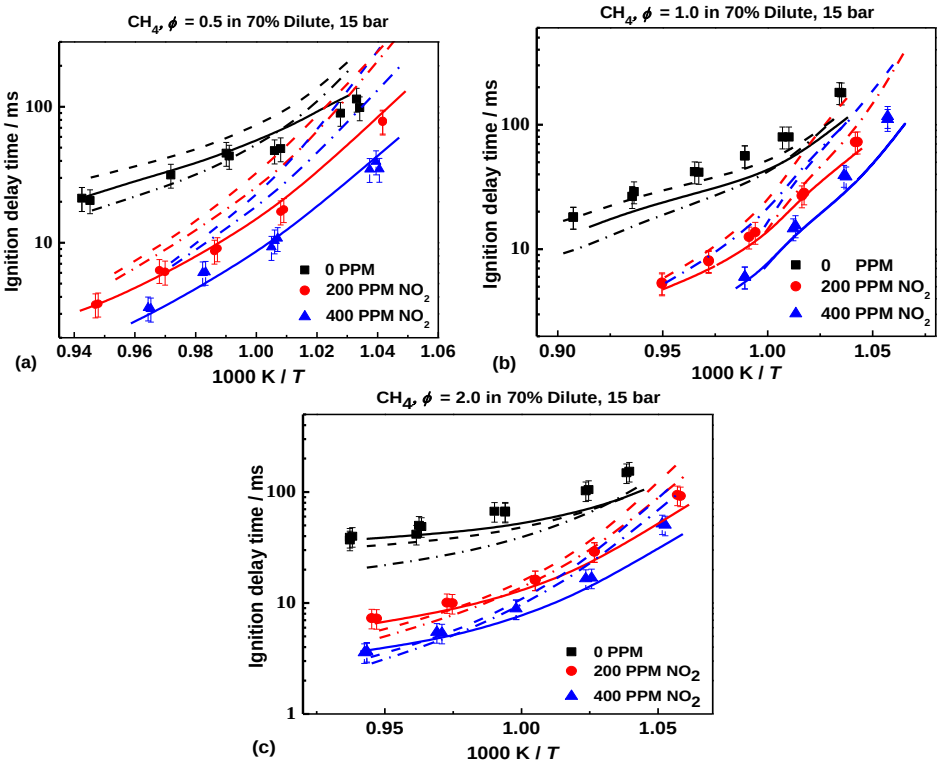

Figure BS12. Effect of NO_2 addition on methane IDT (symbols: experiments, solid line: NUIGMech1.2, dashed lines: Mathieu et al. mech, dash-dotted lines: Mevel mech) at 1.5 MPa for φ = (a) 0.5, (b) 1.0, and (c) 2.0.

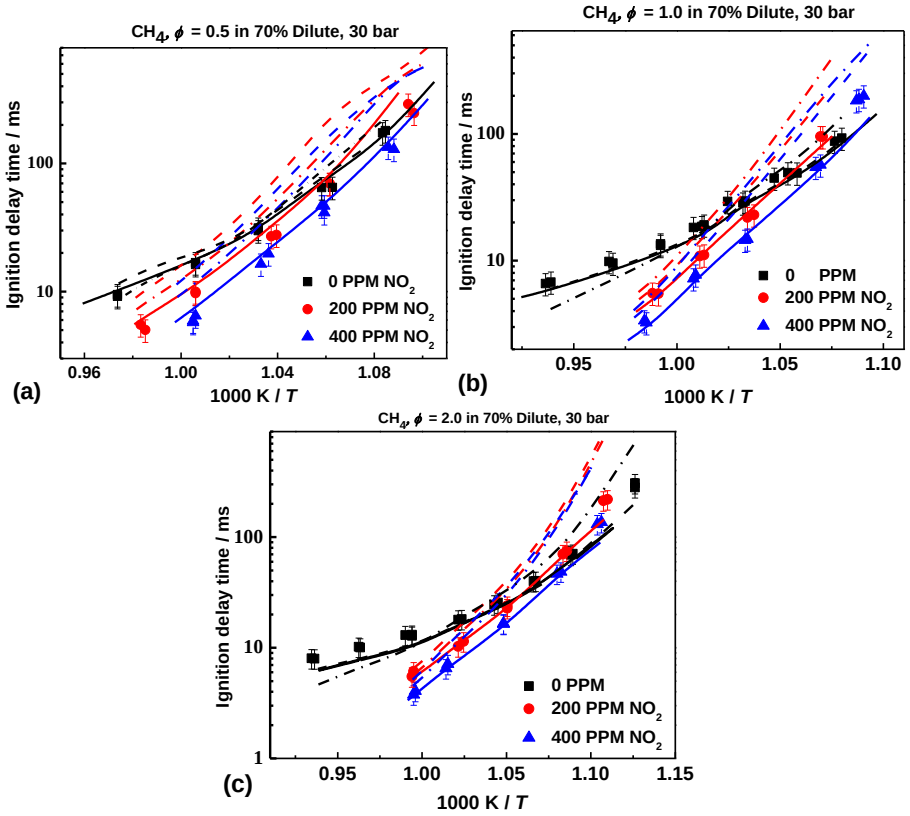

Figure BS13. Effect of NO_2 addition on methane IDT (symbols: experiments, solid line: NUIGMech1.2, dashed lines: Mathieu et al. mech, dash-dotted lines: Mevel mech) at 3.0 MPa for φ = (a) 0.5, (b) 1.0, and (c) 2.0.

Mechanism Validation

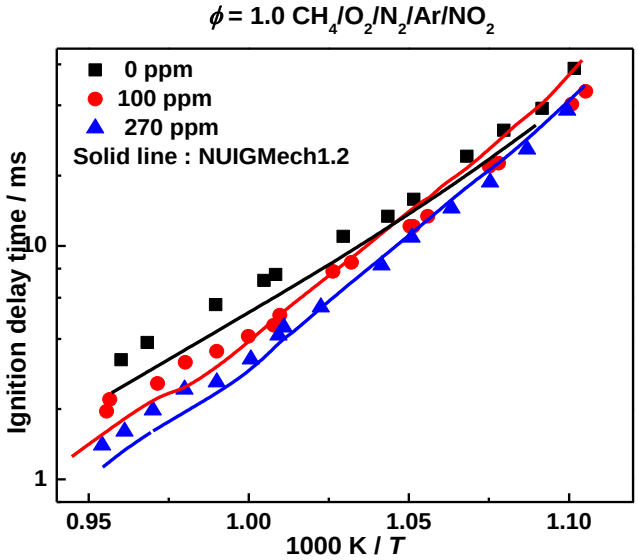

Figure BS14. Comparison of NUIGMech1.2 model predictions (solid lines) with measurements (symbols) [1] for methane ignition with and without NO_2 addition at p_C = 4.0 MPa.

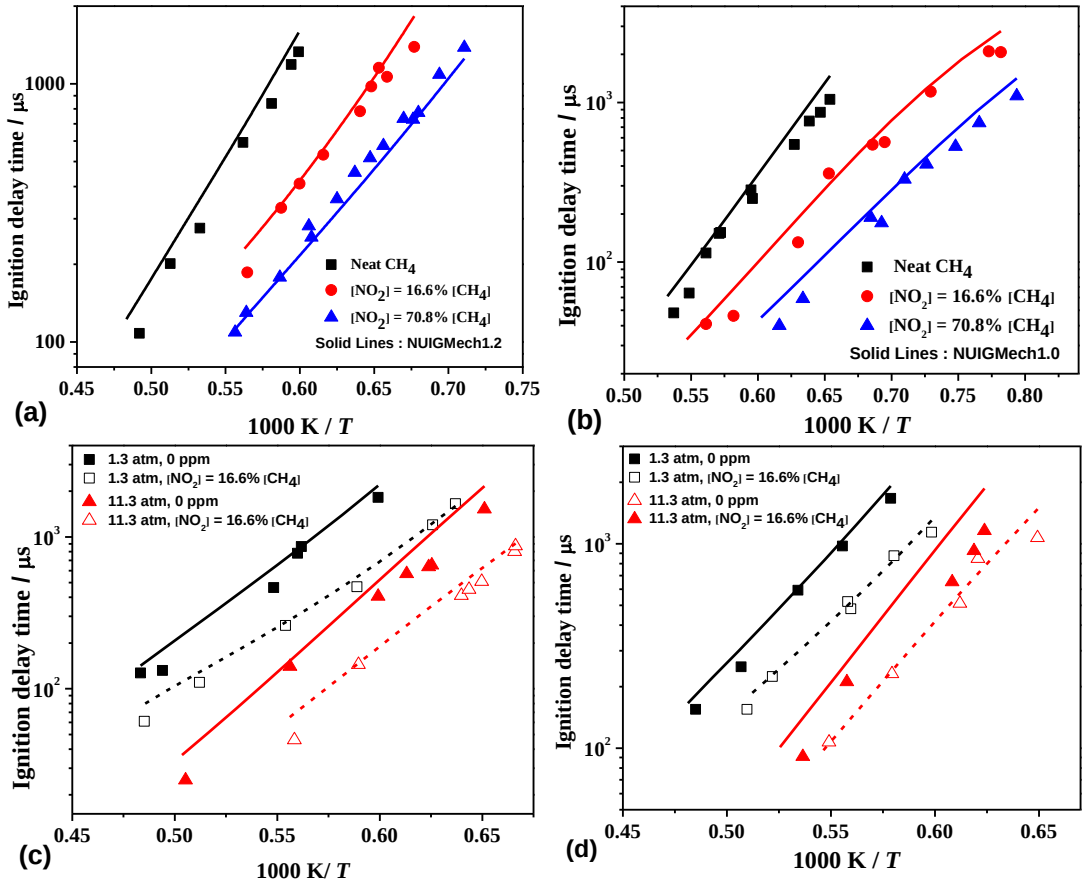

Figure BS15. Comparison of NUIGMech1.2 (lines) model predictions with shock tube measurements (symbols) [2] for methane ignition with and without NO_2 addition (a) φ = 0.5, p_C = 1.3 atm, (b) φ = 0.5, p_C = 11.3 atm, (c) φ = 1.0, (d)) φ = 2.0.

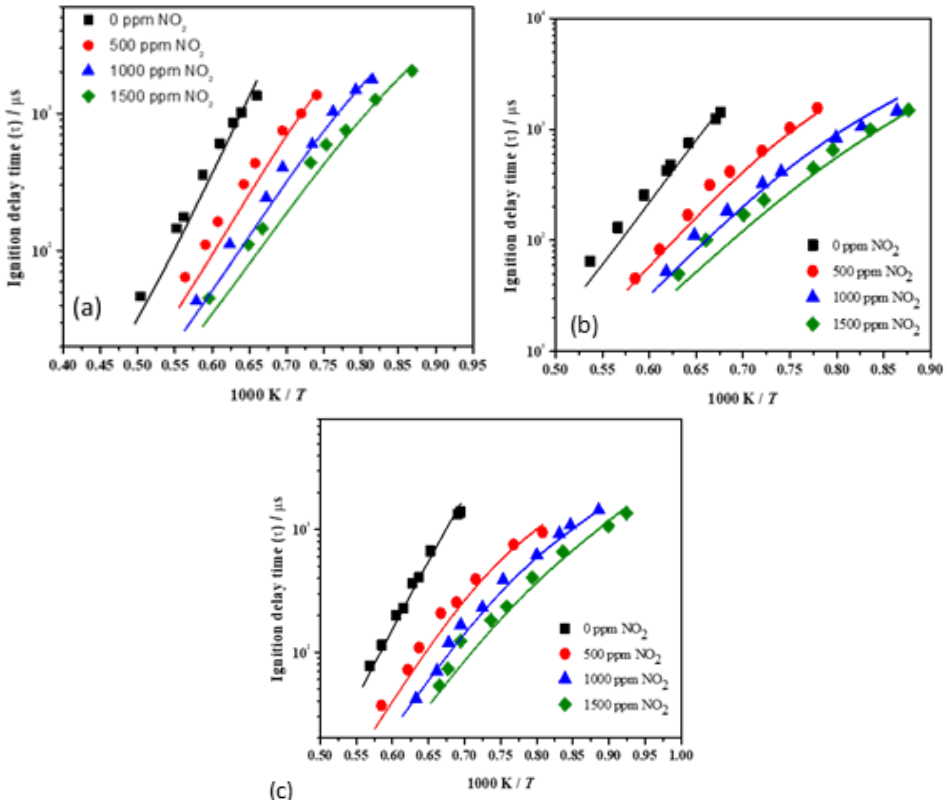

Figure BS16. Comparison of NUIGMech1.2 (lines) model predictions with shock tube measurements (symbols) [3] for methane ignition with and without NO_2 addition (a) φ = 0.5, (b) φ = 1.0, (c) φ = 2.0.

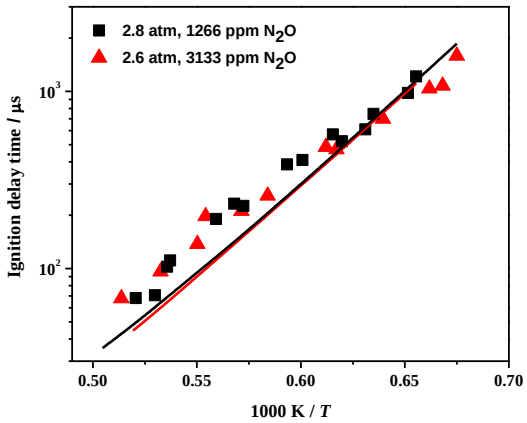

Figure BS17. Comparison of NUIGMech1.2 (solid lines) model predictions with IDT measurements (symbols) [4] for methane ignition N_2O addition. Mix 1 (red): CH_4: 0.00867, N_2O: 0.03133; Mix 2 (black): CH_4: 0.01066, O_2: 0.01666, N_2O: 0.01266.

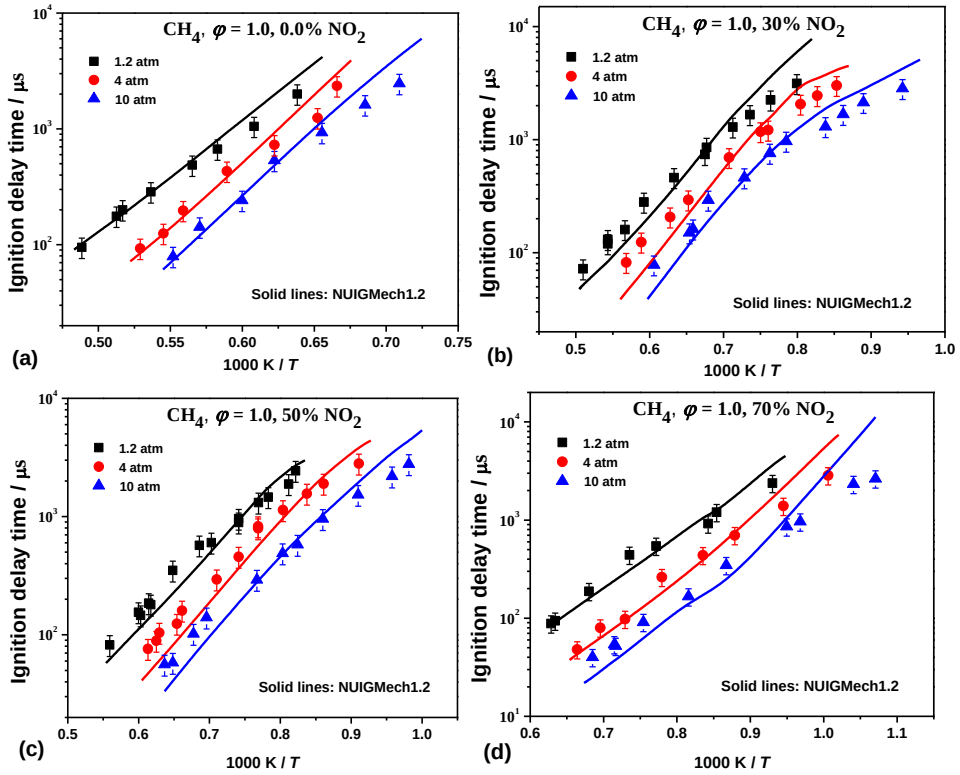

Figure BS18. Comparison of NUIGMech1.2 model predictions (solid lines) with measurements (symbols) [5] for methane ignition with and without NO_2 addition at φ = 1.0 and p = 1.2, 4, and 10 atm.

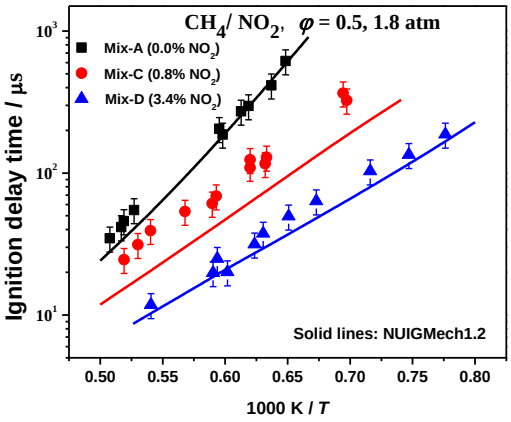

Figure BS19. Comparison of NUIGMech1.2 model predictions (solid lines) with measurements (symbols) [6] for methane ignition with NO_2 addition at φ = 0.5 and p = 1.2, 4, and 10 atm.

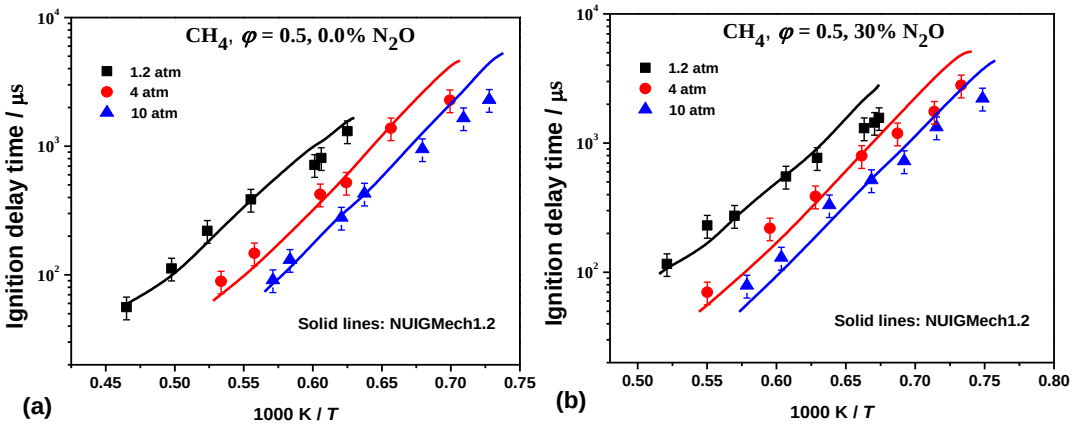

Figure BS20. Comparison of NUIGMech1.2 model predictions (solid lines) with measurements (symbols) [7] for methane ignition with and without N_2O addition at φ = 0.5 and p = 1.2, 4, and 16 atm.

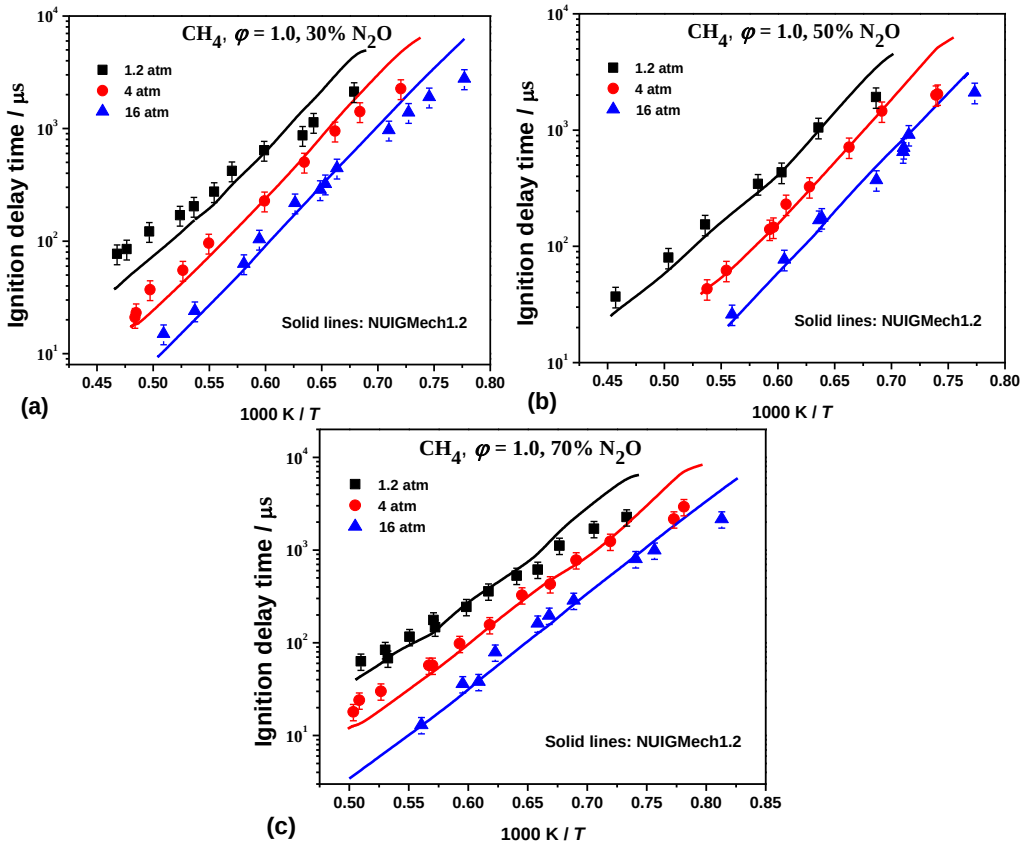

Figure BS21. Comparison of NUIGMech1.2 model predictions (solid lines) with measurements (symbols) [7] for methane ignition with N_2O addition at φ = 1.0 and p = 1.2, 4, and 16 atm.

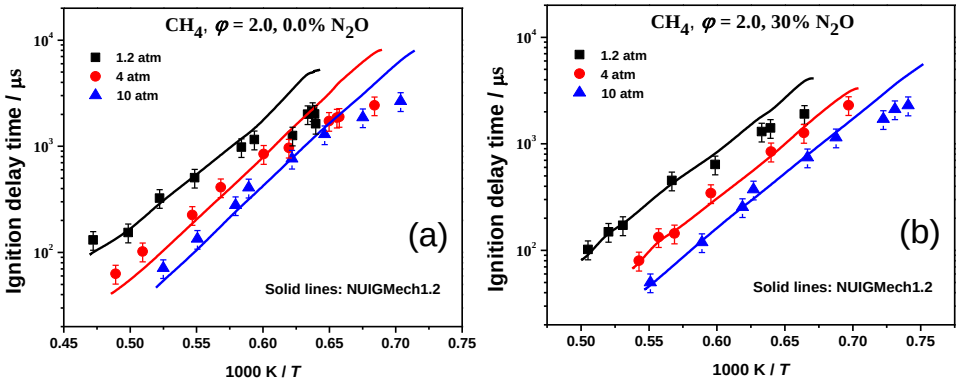

Figure BS22. Comparison of NUIGMech1.2 model predictions (solid lines) with measurements (symbols) [7] for methane ignition with and without N_2O addition at φ = 2.0 and p = 1.2, 4, and 16 atm.

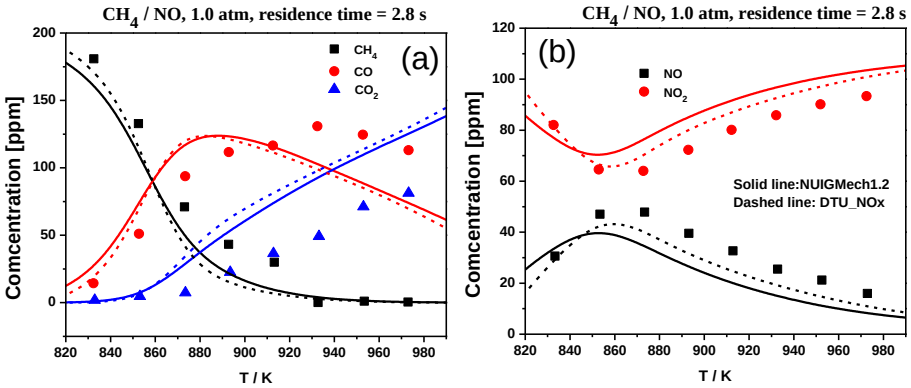

Figure BS23. Comparison of NUIGMech1.2 model predictions (solid lines) with measurements (symbols) [8] for methane oxidation with NO addition at p = 1.0 atm.

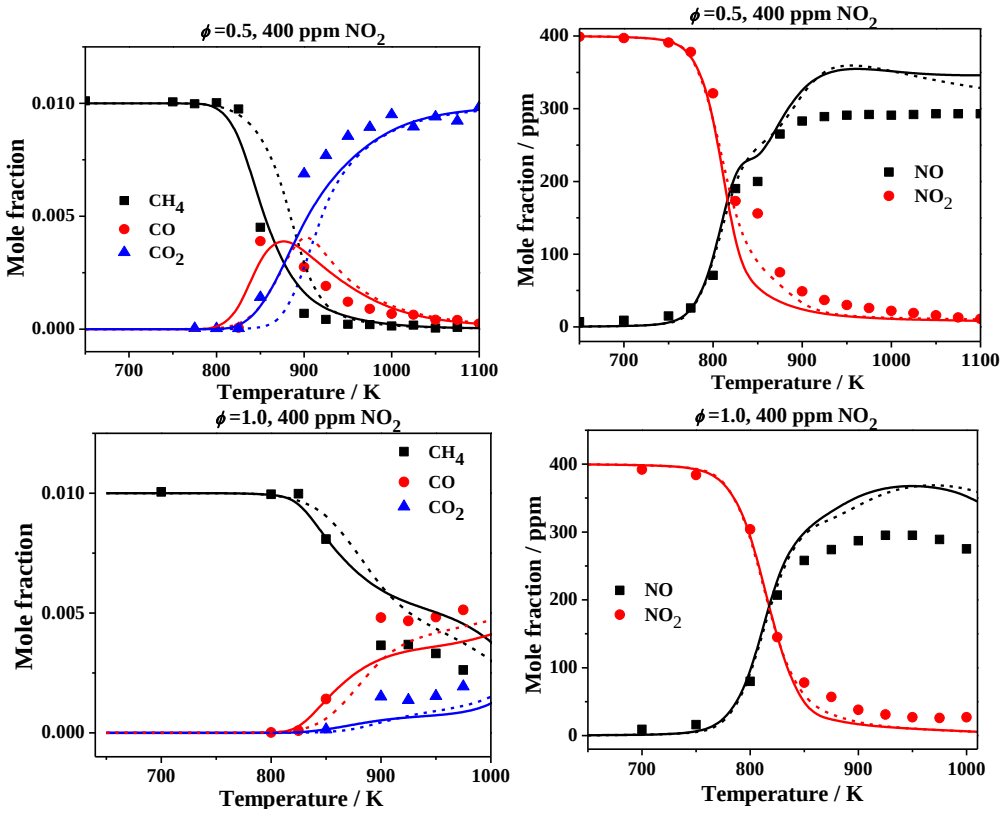

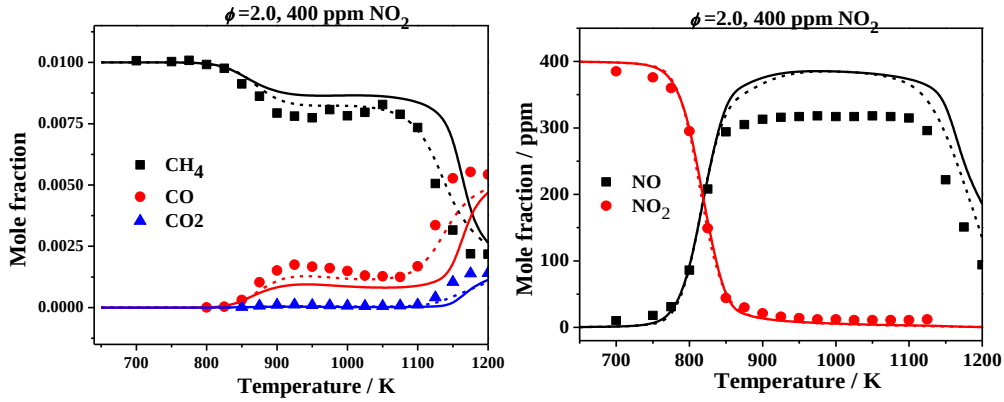

Figure BS24. Comparison of NUIGMech1.2 (solid lines) and Song et al. (dashed lines) model predictions with species measurements from JSR experiments (symbols) [9] for methane oxidation with NO_2 addition (a) φ = 0.5, (b) φ = 1.0, (c) φ = 2.0.

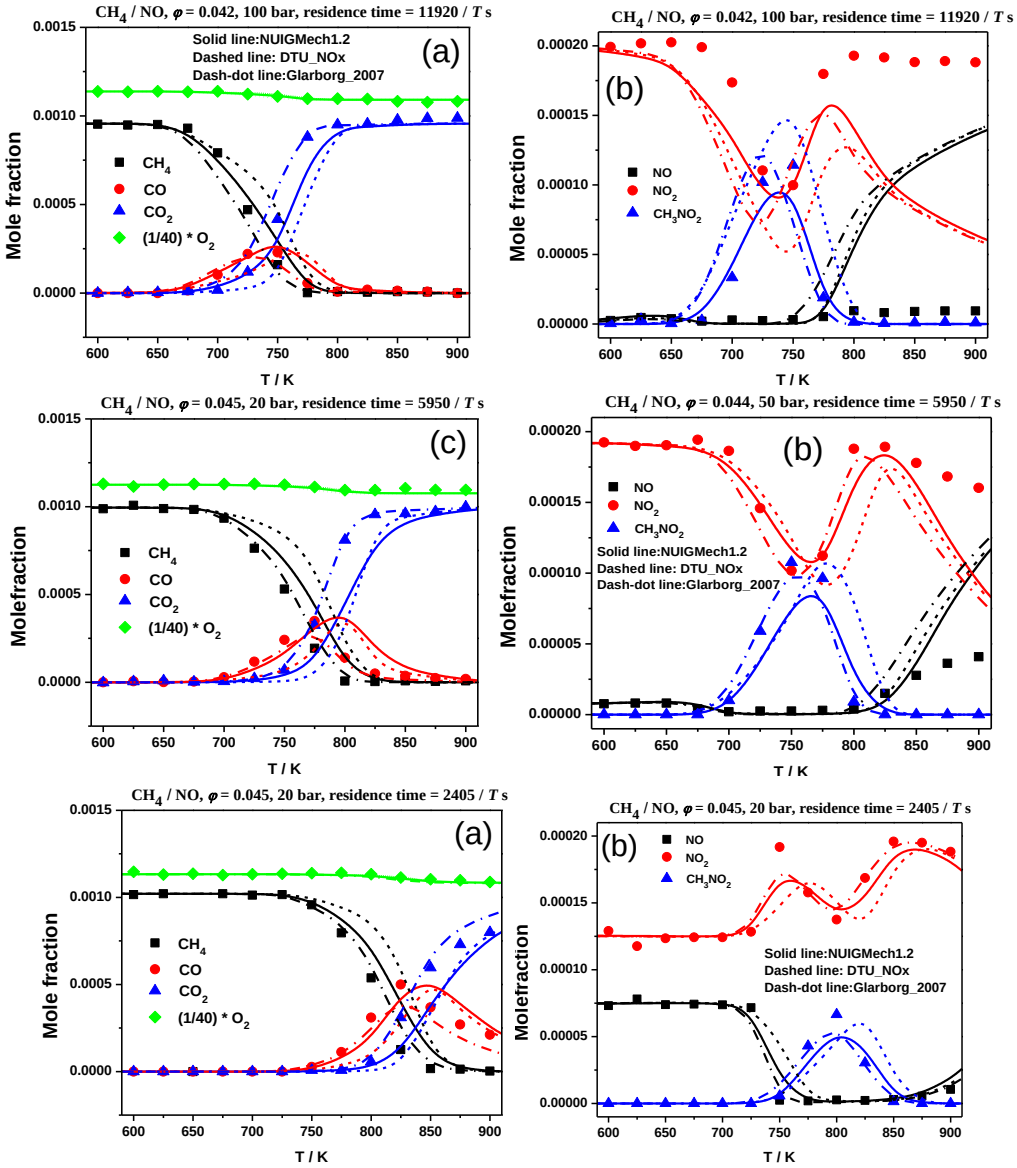

Figure BS25. Comparison of model predictions NUIGMech1.2 (solid lines), Glarborg_model (dash-dot lines), DTU_NOx model (dashed lines) with measurements (symbols) [10] for methane oxidation with NO addition at lean condition and p = 2.0 – 10.0 MPa.

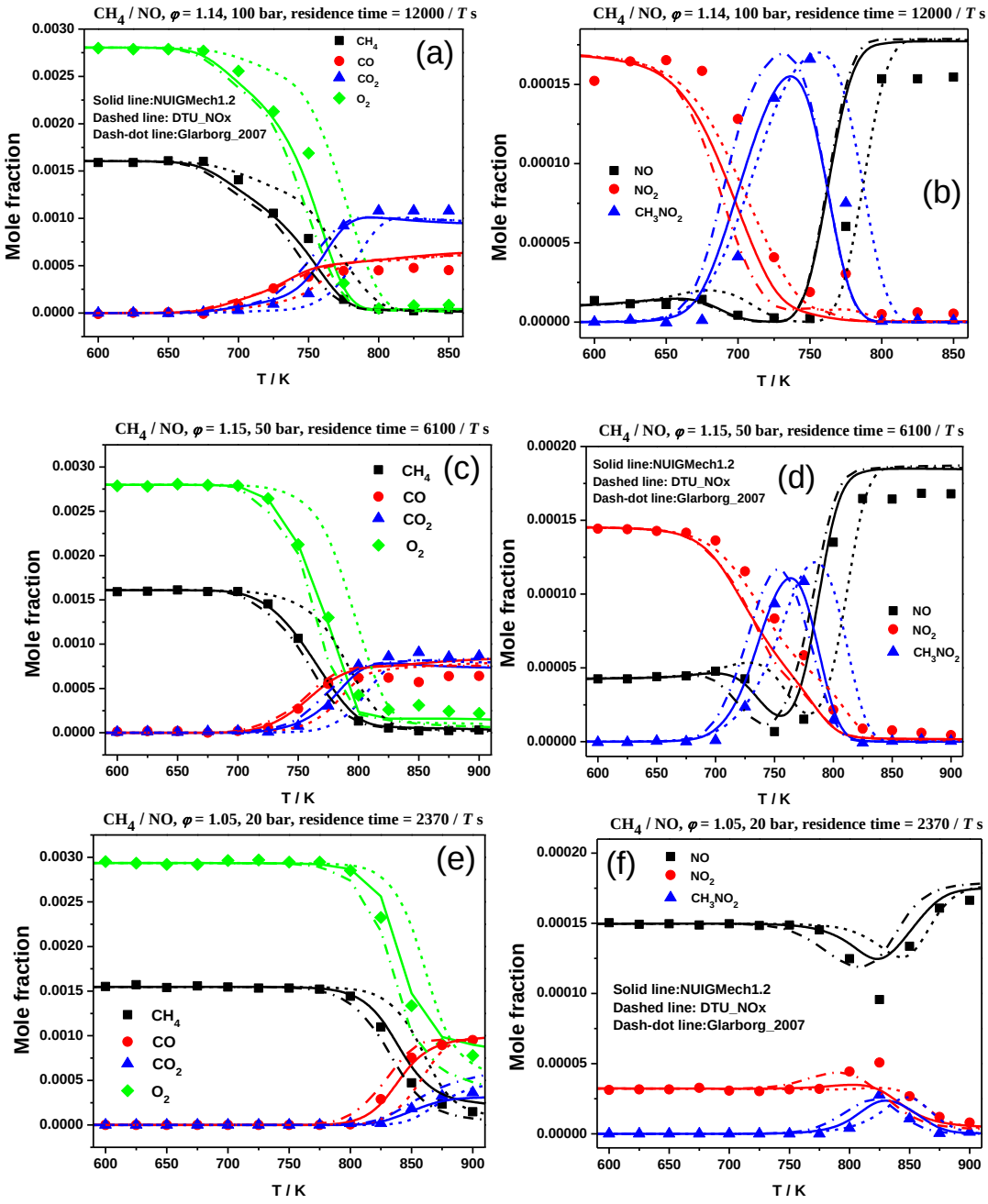

Figure BS26. Comparison of model predictions NUIGMech1.2 (solid lines), Glarborg_model (dash-dot lines), DTU_NOx model (dashed lines) with measurements (symbols) [10] for methane oxidation with NO addition at stoichiometric condition and p = 2.0 – 10.0 MPa.

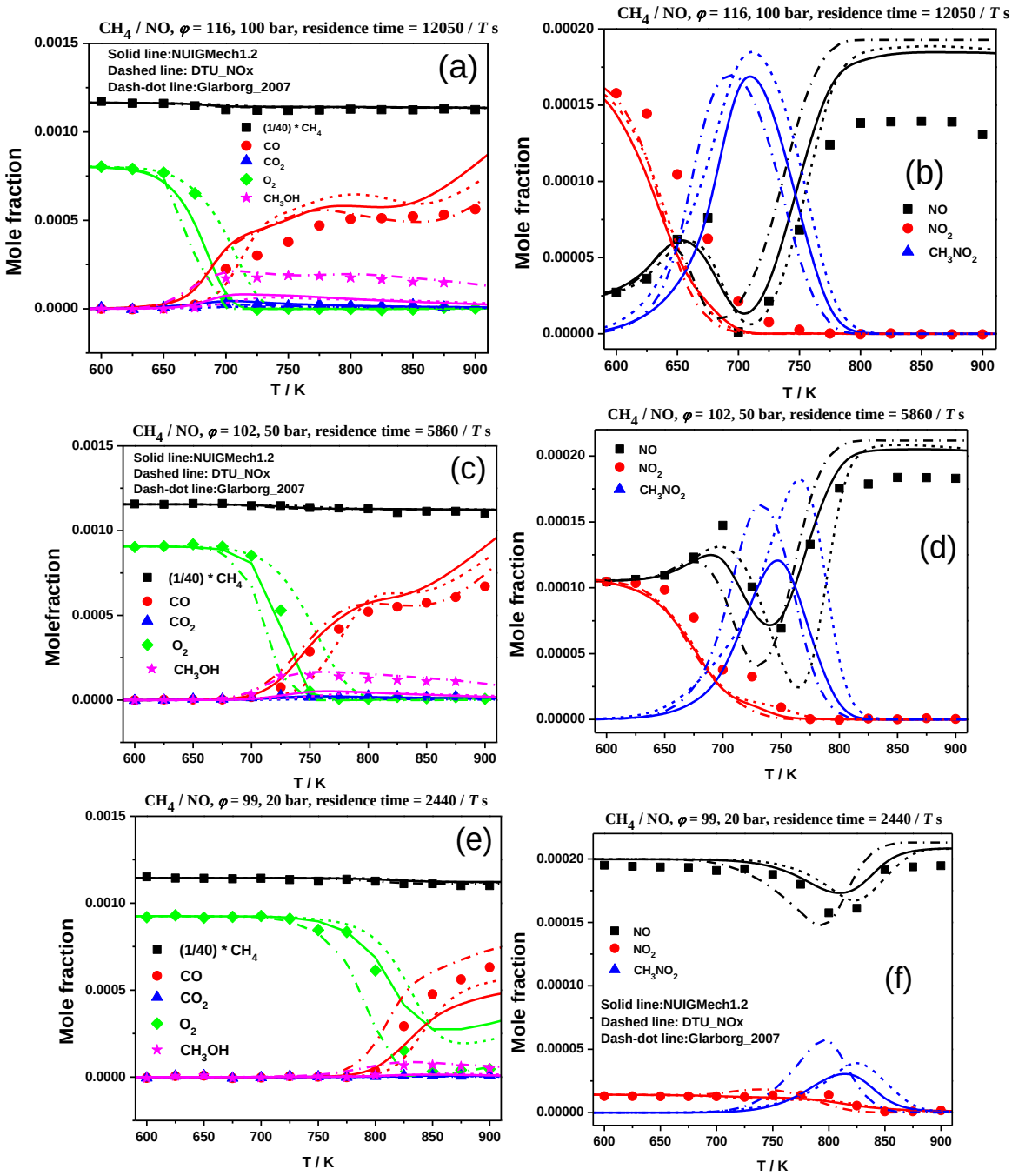

Figure BS27. Comparison of model predictions NUIGMech1.2 (solid lines), Glarborg_model (dash-dot lines), DTU_NOx model (dashed lines) with measurements (symbols) [10] for methane ignition with and without NO_2 addition at rich condition and p = 2.0 – 10.0 MPa.

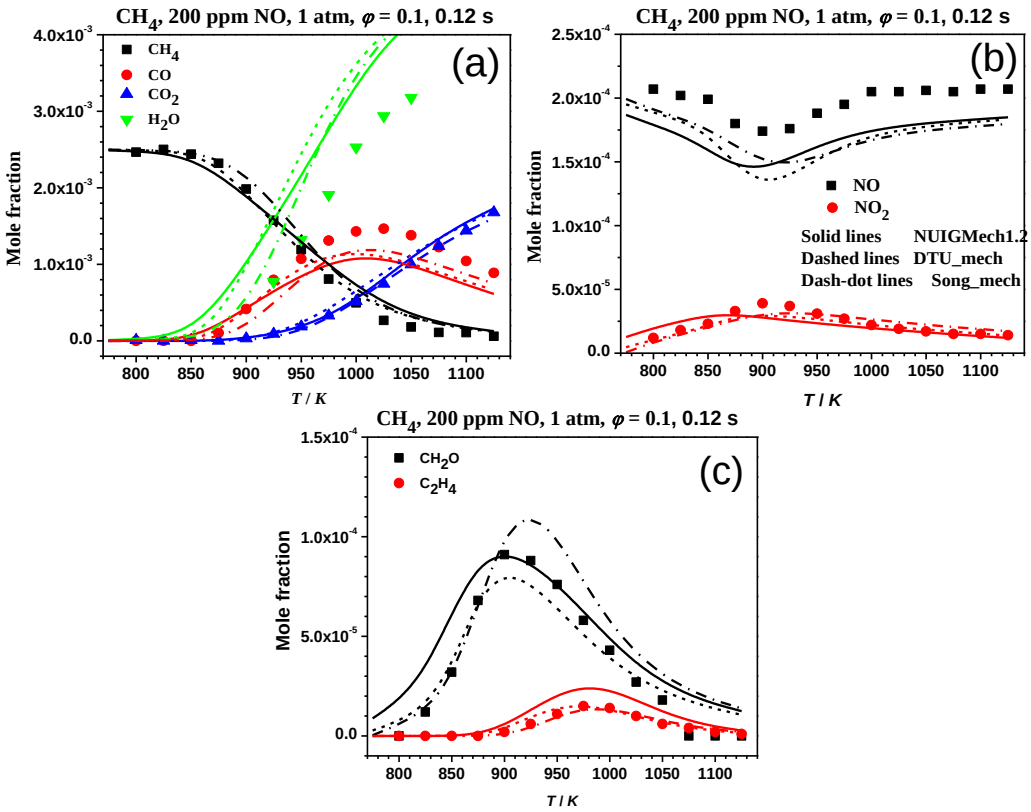

Figure BS28. Comparison of model predictions NUIGMech1.2 (solid lines), Song_model (dash-dot lines), DTU_NOx model (dashed lines) with measurements (symbols) [11] for methane ignition with NO addition at lean condition (φ = 0.1), τ = 0.12 s, and p = 1 atm.

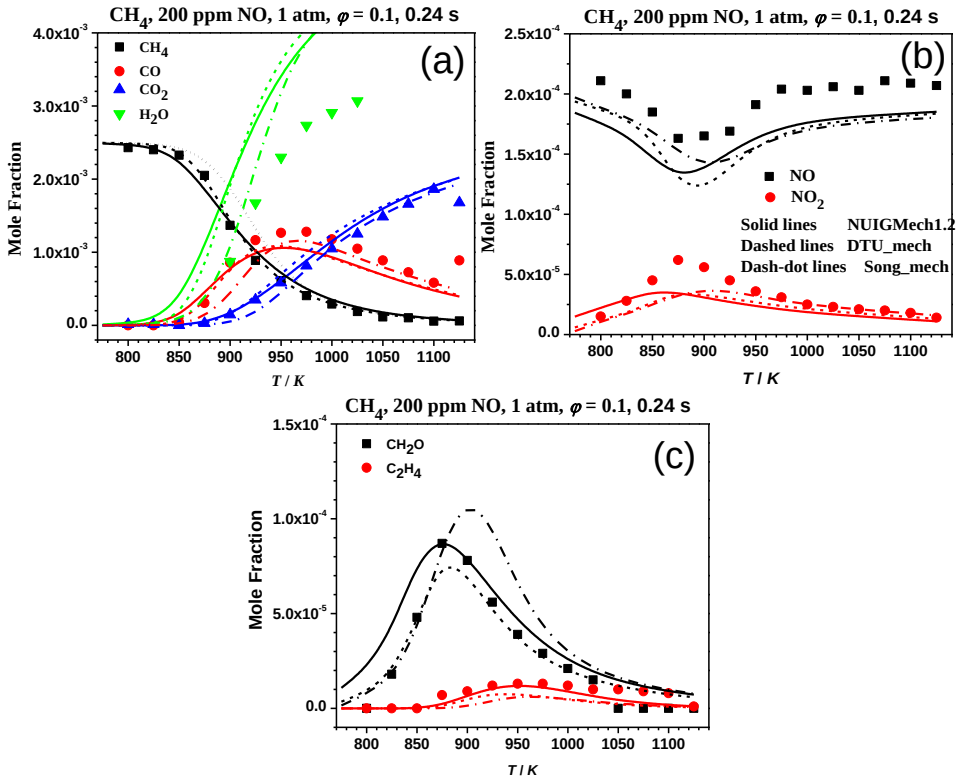

Figure BS29. Comparison of model predictions NUIGMech1.2 (solid lines), Song_model (dash-dot lines), DTU_NOx model (dashed lines) with measurements (symbols) [11] for methane ignition with NO addition at lean condition (φ = 0.1), τ = 0.24 s, and p = 1 atm.

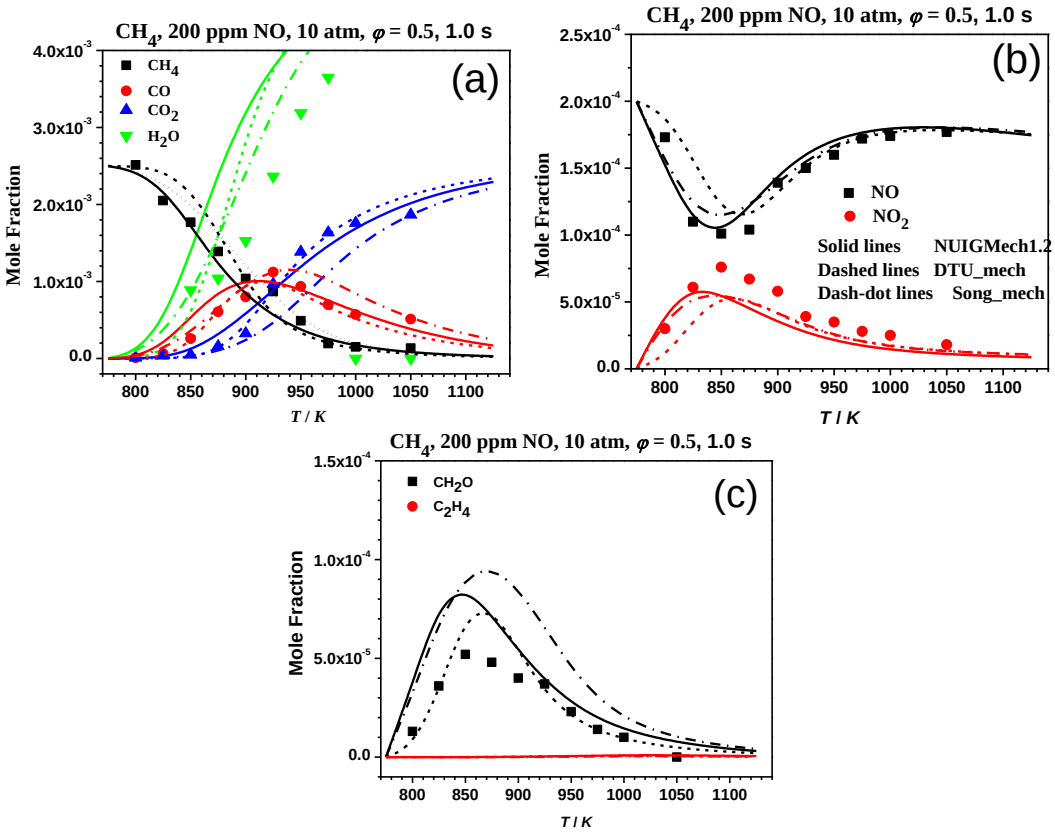

Figure BS30. Comparison of model predictions NUIGMech1.2 (solid lines), Song_model (dash-dot lines), DTU_NOx model (dashed lines) with measurements (symbols) [11] for methane ignition with NO addition at lean condition (φ = 0.5), τ = 1.0 s, and p = 10 atm.

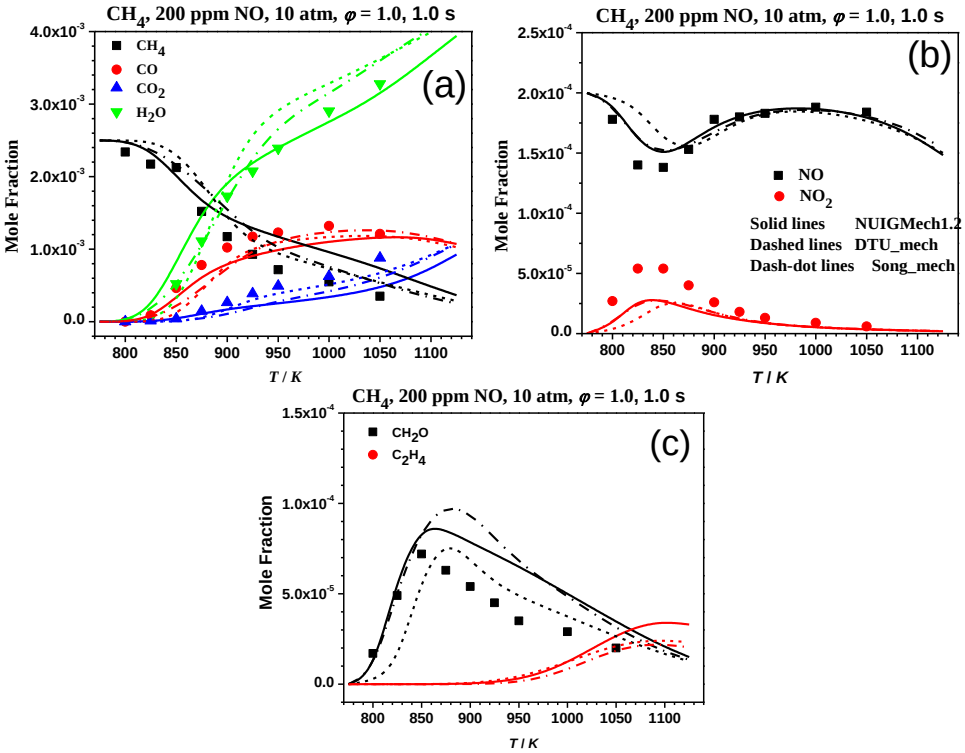

Figure BS31 Comparison of model predictions NUIGMech1.2 (solid lines), Song_model (dash-dot lines), DTU_NOx model (dashed lines) with measurements (symbols) [11] for methane ignition with NO addition at stochiometric condition (φ = 1.0), τ = 1.0 s, and p = 10 atm.

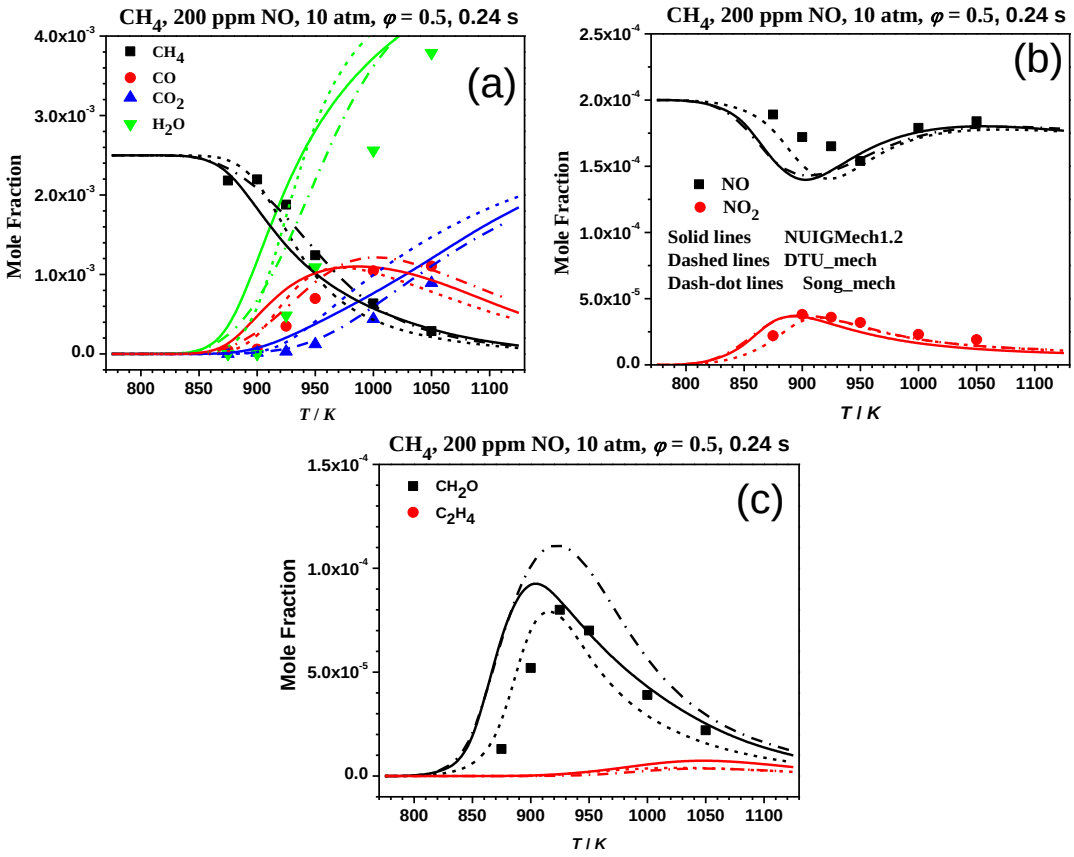

Figure BS32. Comparison of model predictions NUIGMech1.2 (solid lines), Song_model (dash-dot lines), DTU_NOx model (dashed lines) with measurements (symbols) [11] for methane ignition with NO addition at lean condition (φ = 0.5), t = 0.24 s, and p = 10 atm.

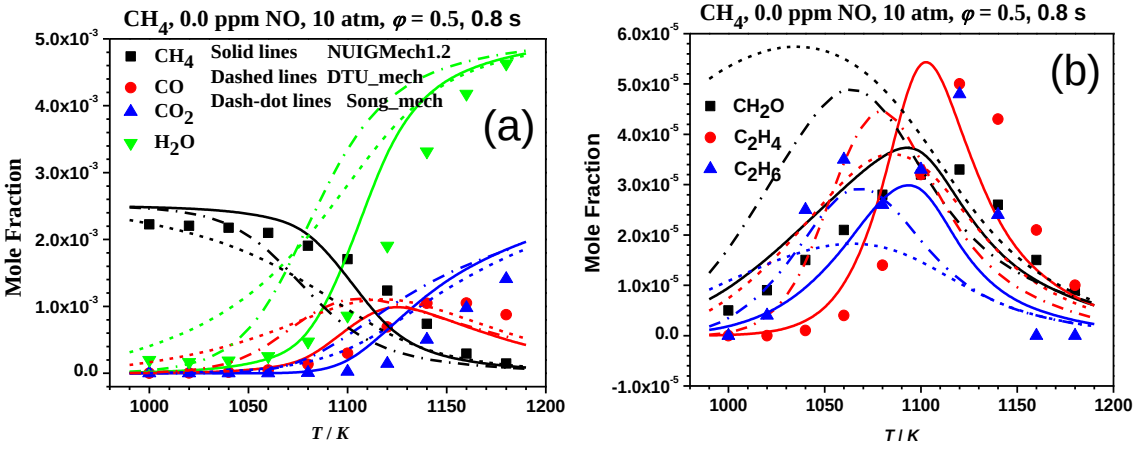

Figure BS33. Comparison of model predictions NUIGMech1.2 (solid lines), Song_model (dash-dot lines), DTU_NOx model (dashed lines) with measurements (symbols) [12] for methane ignition without NO addition at lean condition (φ = 0.5), τ = 0.8 s, and p = 10 atm.

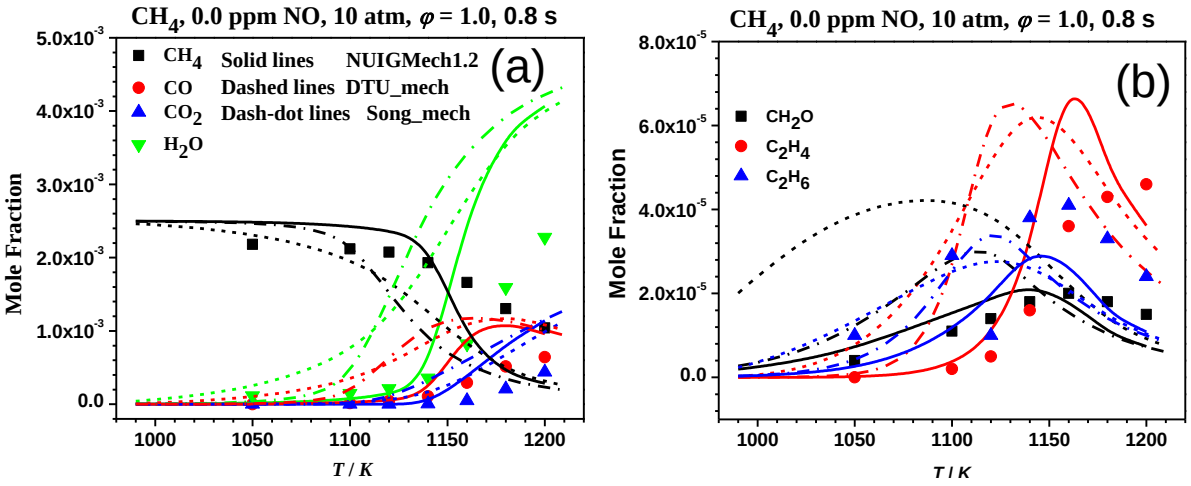

Figure BS34. Comparison of model predictions NUIGMech1.2 (solid lines), Song_model (dash-dot lines), DTU_NOx model (dashed lines) with measurements (symbols) [12] for methane ignition without NO addition at stochiometric condition (φ = 1.0), τ = 0.8 s, and p = 10 atm.

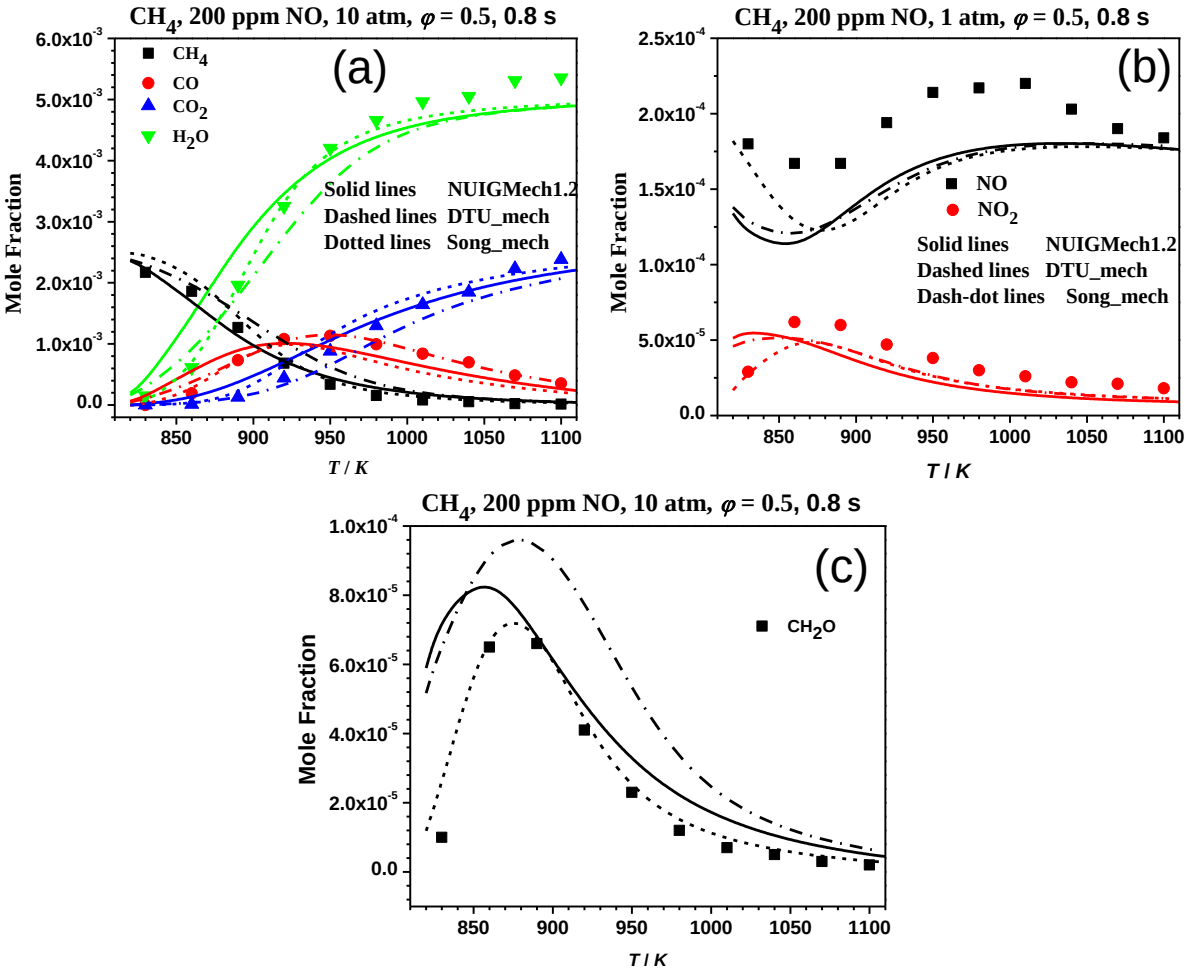

Figure BS35. Comparison of model predictions NUIGMech1.2 (solid lines), Song_model (dash-dot lines), DTU_NOx model (dashed lines) with measurements (symbols) [12] for methane ignition with NO addition at lean condition (φ = 0.5), τ = 0.8 s, and p = 10 atm.

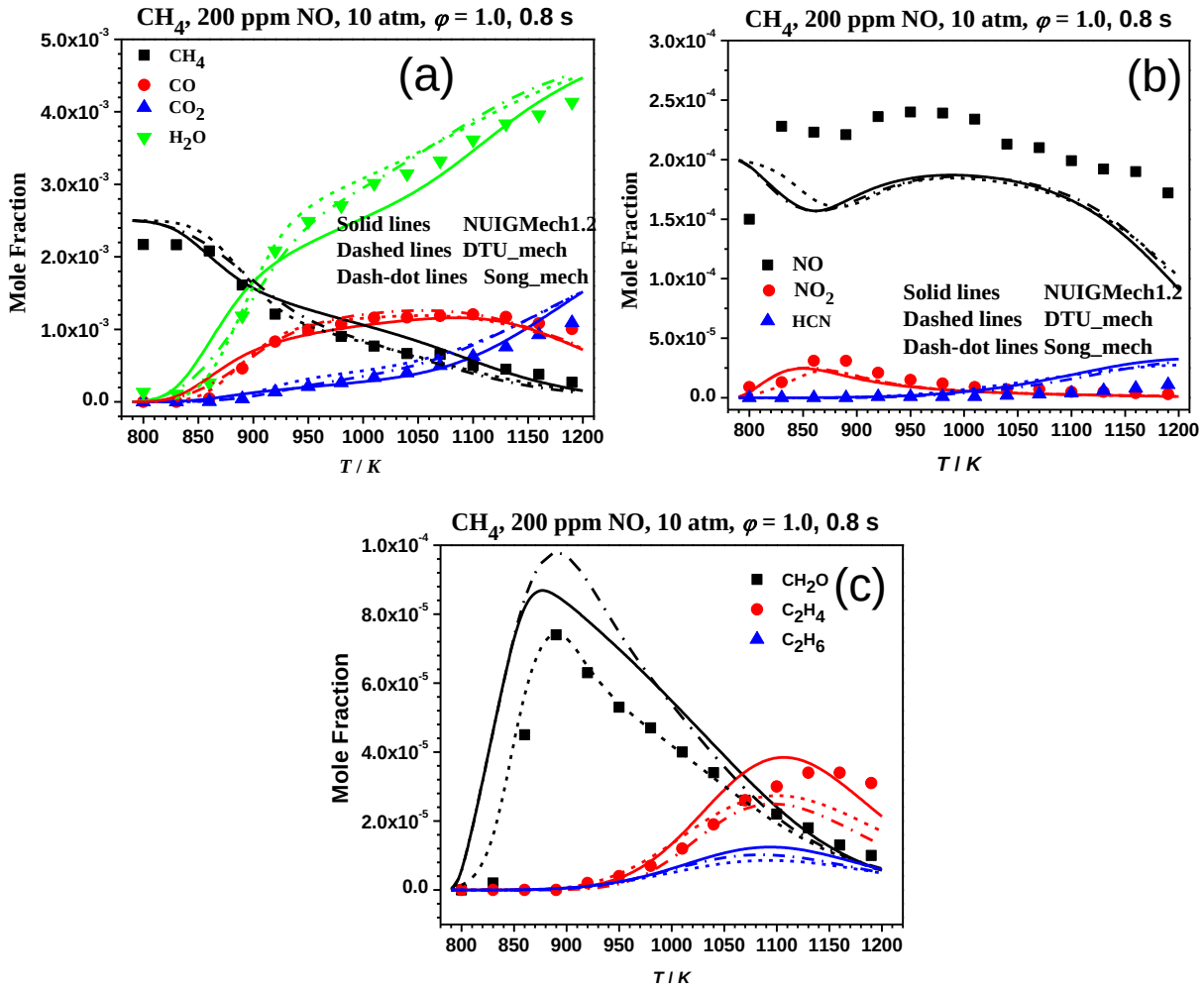

Figure BS36. Comparison of model predictions NUIGMech1.2 (solid lines), Song_model (dash-dot lines), DTU_NOx model (dashed lines) with measurements (symbols) [12] for methane ignition with NO addition at stochiometric condition (φ = 1.0), τ = 0.8 s, and p = 10 atm.

Appendix B

Tables of Experiments conditions and IDTs for CH_4/NO_X considered in the current study

Pure CH_4 data

Table BS1. IDTs and Experiments conditions for CH_4, φ = 0.5 at '70% dilution'.

T_i_K	p_i _bar	T_C_K	p_C_bar	IDT_ms	N_2/Ar
343.31	0.523	972	15	254	21.43/78.57
343.33	0.523	973	15.03	200.3	21.43/78.57
343.43	0.523	974	15.07	189.1	21.43/78.57
348.31	0.527	985	15.13	92.86	21.43/78.57
348.11	0.527	984	15.09	106.9	21.43/78.57
348.15	0.527	986	15.23	109.1	21.43/78.57
353.17	0.528	996	15.11	77.17	21.43/78.57
353.21	0.528	994	15.01	72.27	21.43/78.57
353.17	0.528	996	15.11	68.47	21.43/78.57
363.15	0.532	1022	15.34	45.88	21.43/78.57
363.11	0.532	1020	15.21	46.67	21.43/78.57
363.15	0.532	1020	15.24	45.77	21.43/78.57
373.15	0.533	1041	15.07	33.04	21.43/78.57
373.17	0.533	1040	15.02	33.44	21.43/78.57
383.15	0.536	1062	15.04	23.78	21.43/78.57
383.13	0.536	1064	15.12	22.6	21.43/78.57
319.19	1.002	923	29.88	173.4	21.43/78.57
319.31	1.002	922	29.77	180.3	21.43/78.57
329.39	1.018	943	29.8	77.67	21.43/78.57
329.25	1.018	945	30.01	64.73	21.43/78.57
329.19	1.018	940	29.53	60.92	21.43/78.57
329.23	1.018	941	29.6	65.08	21.43/78.57
342.31	1.026	969	29.38	31.27	21.43/78.57
342.27	1.026	969	29.4	29.83	21.43/78.57
353.13	1.047	994	29.8	16.24	21.43/78.57
353.13	1.047	994	29.75	16.79	21.43/78.57
368.15	1.065	1027	29.96	9.45	21.43/78.57
368.17	1.065	1027	29.95	9.16	21.43/78.57

Table BS2. IDTs and Experiments conditions for CH_4, φ = 1.0 at '70% dilution'.

T_i_K	p_i _bar	T_C_K	p_C_bar	IDT_ms	N_2/Ar
333.11	0.519	967	14.79	181.4	0/100
333.09	0.519	966	14.74	180.3	0/100
343.33	0.531	993	15.18	79.78	0/100
343.31	0.531	990	15.04	79.78	0/100
353.07	0.538	1011	15.08	56.38	0/100
353.07	0.538	1011	15.12	56.23	0/100
363.15	0.542	1036	15.24	41.89	0/100
363.13	0.542	1034	15.14	41.57	0/100
378.23	0.545	1068	15.15	28.95	0/100

378.15	0.545	1069	15.19	26.55	0/100
393.17	0.547	1102	15.17	18.03	0/100
393.17	0.547	1102	15.15	18.16	0/100
313.37	0.969	934	29.27	87.61	0/100
313.29	0.969	929	28.74	87.42	0/100
313.35	0.969	926	28.51	92.48	0/100
322.95	1.017	955	30.37	44.74	0/100
323.19	1.017	949	29.62	49.4	0/100
323.31	1.017	945	29.25	49.14	0/100
332.97	1.019	976	30.02	29.33	0/100
333.05	1.019	969	29.28	28.52	0/100
333.11	1.019	968	29.17	29.47	0/100
343.15	1.031	992	29.4	18.29	0/100
343.11	1.031	988	29.03	18.6	0/100
343.15	1.031	987	28.93	19.1	0/100
353.11	1.059	1008	29.45	13.2	0/100
353.15	1.059	1008	29.37	13.56	0/100
363.13	1.075	1032	29.87	9.55	0/100
363.13	1.075	1034	30.08	9.84	0/100
378.13	1.082	1068	30.05	6.59	0/100
378.15	1.082	1065	29.78	6.78	0/100

Table BS3. IDTs and Experiments conditions for CH_4, φ = 2.0 at '70% dilution'.

T_i_K	p_i _bar	T_C_K	p_C_bar	IDT_ms	N_2/Ar
348.11	0.543	963	15.23	148.9	0/100
348.09	0.543	962	15.13	153.7	0/100
358.11	0.547	977	14.86	102.6	0/100
358.17	0.547	976	14.78	105.04	0/100
373.11	0.561	1006	15.01	65.96	0/100
373.15	0.561	1010	15.26	66.97	0/100
373.19	0.561	1006	15.03	67.19	0/100
388.11	0.565	1040	15.25	41.61	0/100
388.05	0.565	1038	15.14	48.87	0/100
388.15	0.565	1039	15.19	50.05	0/100
403.11	0.567	1067	15	36.94	0/100
403.15	0.567	1067	14.99	39.12	0/100
403.21	0.567	1066	14.93	39.85	0/100
313.85	1.034	888	29.3	307.3	0/100
313.75	1.034	888	29.36	281.7	0/100
328.05	1.056	919	29.74	69.1	0/100
327.99	1.056	918	29.61	70.84	0/100
337.99	1.066	937	29.51	40.25	0/100
338.17	1.066	938	29.58	39.93	0/100
348.09	1.087	957	29.79	25.6	0/100
348.09	1.087	959	30.05	24.58	0/100
358.05	1.096	979	30.07	17.97	0/100
358.07	1.096	977	29.75	18.14	0/100

373.09	1.104	1010	30	13	0/100
373.05	1.104	1006	29.6	12.8	0/100
373.09	1.104	1006	29.6	13.12	0/100
388.17	1.12	1039	30	10.2	0/100
388.19	1.12	1038	29.95	10.03	0/100
403.25	1.13	1070	30.11	8.03	0/100
403.17	1.13	1068	30	7.98	0/100

CH_4/N_2O data

Table BS4. IDTs and Experiments conditions for CH_4/400 PPM N_2O, φ = 1.0 at '70% dilution'.

T_i_K	p_i _bar	T_C_K	p_C_bar	IDT_ms	N_2/Ar
328.27	0.512	964	14.95	225	0/100
328.25	0.512	966	15.09	211	0/100
344.15	0.518	1001	15.02	79.45	0/100
344.15	0.518	1003	15.17	75.1	0/100
371.17	0.528	1057	14.87	33.29	0/100
371.15	0.528	1060	15.02	33.1	0/100
391.19	0.54	1104	15.19	16.76	0/100
391.15	0.54	1105	15.24	17.29	0/100
305.29	0.944	926	29.73	149.5	0/100
305.29	0.944	923	29.33	166.2	0/100
313.33	0.981	934	29.51	96.92	0/100
313.29	0.981	935	29.55	95.45	0/100
328.21	1.003	969	29.92	34.46	0/100
328.27	1.003	968	29.77	35.2	0/100
344.13	1.015	1001	29.47	17.37	0/100
344.13	1.015	1003	29.67	17.5	0/100
371.09	1.041	1061	29.66	7.53	0/100
371.13	1.041	1058	29.38	7.75	0/100

Table BS5. IDTs and Experiments conditions for CH_4/1000 PPM N_2O, φ = 1.0 at '70% dilution'.

T_i_K	p_i _bar	T_C_K	p_C_bar	IDT_ms	N_2/Ar
313.25	0.981	939	29.77	89.55	0/100
313.29	0.981	939	29.75	86.27	0/100
313.37	0.981	939	29.76	85.54	0/100
328.11	1.003	973	30.13	30.98	0/100
328.21	1.003	974	30.18	31.89	0/100
328.23	1.003	974	30.13	31.79	0/100
344.11	1.015	1008	29.97	15.08	0/100
344.17	1.015	1007	29.88	15.89	0/100
371.15	1.041	1065	29.82	7.38	0/100
371.05	1.041	1067	30.02	7.4	0/100

Appendix B

CH_4/NO_2 data

Table BS6. IDTs and Experiments conditions for CH_4/200 PPM NO_2, φ = 0.5 at '70% dilution'.

T_i_K	p_i _bar	T_C_K	p_C_bar	IDT_ms	N_2/Ar
336.25	0.522	960	15.15	77.5	21.43/78.57
336.25	0.522	960	15.15	78.78	21.43/78.57
350.13	0.527	992	15.16	16.91	21.43/78.57
350.15	0.527	991	15.12	17.58	21.43/78.57
360.19	0.537	1013	15.26	9.06	21.43/78.57
360.15	0.537	1014	15.34	8.7	21.43/78.57
369.29	0.542	1033	15.3	6.27	21.43/78.57
369.27	0.542	1031	15.19	6.1	21.43/78.57
380.29	0.545	1056	15.22	3.5	21.43/78.57
380.19	0.545	1055	15.15	3.55	21.43/78.57
318.27	1.003	914	28.96	290.3	21.43/78.57
318.29	1.003	912	28.81	247.6	21.43/78.57
329.17	1.036	942	30.06	69.75	21.43/78.57
329.15	1.036	942	30.04	69.76	21.43/78.57
336.27	1.003	964	29.48	26.94	21.43/78.57
336.25	1.003	962	29.36	27.63	21.43/78.57
350.13	1.036	994	29.98	9.97	21.43/78.57
350.15	1.036	994	30.04	9.72	21.43/78.57
360.15	1.054	1017	30.38	5.5	21.43/78.57
360.13	1.054	1015	30.16	5.01	21.43/78.57

Table BS7. IDTs and Experiments conditions for CH_4/200 PPM NO_2, φ = 1.0 at '70% dilution'.

T_i_K	p_i _bar	T_C_K	p_C_bar	IDT_ms	N_2/Ar
328.37	0.513	959	14.7	72.83	0/100
328.31	0.513	960	14.81	72.41	0/100
339.33	0.522	984	14.89	26.87	0/100
339.23	0.522	983	14.83	28.37	0/100
349.15	0.518	1009	14.84	12.57	0/100
349.15	0.518	1006	14.66	13.72	0/100
359.05	0.534	1029	15.09	8.13	0/100
359.07	0.534	1029	15.06	8	0/100
369.27	0.536	1053	15.14	5.28	0/100
369.35	0.536	1053	15.12	5.39	0/100
313.63	1	935	30.11	95.37	0/100
313.65	1	934	29.95	95.15	0/100
328.21	1.012	964	29.66	22.95	0/100
328.21	1.012	967	29.91	21.9	0/100
339.15	1.027	989	29.93	10.88	0/100
339.27	1.027	987	29.68	11.09	0/100
349.11	1.029	1009	29.48	5.49	0/100
349.11	1.029	1012	29.85	5.54	0/100

Appendix B

Table BS8. IDTs and Experiments conditions for CH_4/200 PPM NO_2, φ = 2.0 at '70% dilution'.

T_i_K	p_i _bar	T_C_K	p_C_bar	IDT_ms	N_2/Ar
343.13	0.539	946	14.64	94.1	0/100
343.17	0.539	945	14.61	92.24	0/100
357.15	0.55	974	14.78	29.18	0/100
357.17	0.55	974	14.81	28.93	0/100
368.13	0.558	995	14.86	16.11	0/100
368.09	0.558	995	14.86	16.19	0/100
383.17	0.562	1028	14.95	10.06	0/100
383.15	0.562	1026	14.86	9.95	0/100
398.35	0.573	1058	15.11	7.31	0/100
398.35	0.573	1056	15.02	7.26	0/100
318.21	1.044	901	29.76	219.2	0/100
318.21	1.044	903	29.99	214.1	0/100
328.29	1.049	921	29.48	75.27	0/100
328.25	1.049	923	29.73	70.24	0/100
343.13	1.065	952	29.66	22.76	0/100
343.15	1.065	952	29.6	23.96	0/100
357.13	1.087	979	29.79	10.27	0/100
357.15	1.087	976	29.44	11.41	0/100
368.25	1.096	1006	30.37	5.5	0/100
368.15	1.096	1005	30.2	6.13	0/100

Table BS9. IDTs and Experiments conditions for CH_4/400 PPM NO_2, φ = 0.5 at '70% dilution'.

T_i_K	p_i _bar	T_C_K	p_C_bar	IDT_ms	N_2/Ar
336.27	0.522	964	15.24	34.71	21.43/78.57
336.27	0.522	962	15.17	39.49	21.43/78.57
350.13	0.527	993	15.14	10.76	21.43/78.57
350.19	0.527	995	15.2	9.27	21.43/78.57
350.19	0.527	994	15.15	10.35	21.43/78.57
360.15	0.537	1017	15.39	6.07	21.43/78.57
360.15	0.537	1018	15.43	6.01	21.43/78.57
369.29	0.542	1036	15.35	3.26	21.43/78.57
369.27	0.542	1037	15.38	3.32	21.43/78.57
318.63	1	921	29.38	134	21.43/78.57
318.37	1.003	919	29.33	129.1	21.43/78.57
329.25	1.036	945	30.15	46.64	21.43/78.57
329.05	1.036	944	30.09	46.62	21.43/78.57
329.13	1.036	944	30.07	41.25	21.43/78.57
336.39	0.997	968	29.53	16.38	21.43/78.57
336.27	0.997	965	29.2	19.72	21.43/78.57
350.05	1.036	994	29.86	6.46	21.43/78.57
350.13	1.036	995	29.93	5.73	21.43/78.57
350.19	1.036	995	29.88	5.89	21.43/78.57

Appendix B

Table BS10. IDTs and Experiments conditions for CH_4/400 PPM NO_2, φ = 1.0 in '70% dilute'.

T_i_K	p_i _bar	T_C_K	p_C_bar	IDT_ms	N_2/Ar
328.29	0.513	964	14.87	38.13	0/100
328.27	0.513	965	14.96	39.23	0/100
339.11	0.522	988	15.02	14.63	0/100
339.23	0.522	987	14.94	15.47	0/100
318.49	0.511	946	15.2	110.4	0/100
318.39	0.511	946	15.19	116.8	0/100
349.05	0.518	1011	14.85	5.97	0/100
349.17	0.518	1011	14.84	6.02	0/100
313.55	1	937	30.11	54.51	0/100
313.49	1	935	29.88	56.84	0/100
328.31	1.012	967	29.67	14.82	0/100
328.33	1.012	968	29.85	14.5	0/100
339.19	1.027	991	29.9	7.71	0/100
339.25	1.027	992	29.95	7.2	0/100
305.09	0.976	917	29.51	199.4	0/100
305.25	0.976	919	29.68	187.2	0/100
305.19	0.976	920	29.8	182.8	0/100
349.11	1.029	1015	29.9	3.24	0/100
349.19	1.029	1016	29.99	3.36	0/100

Table BS11. IDTs and Experiments conditions for CH_4/400 PPM NO_2, φ = 2.0 in '70% dilute'.

T_i_K	p_i _bar	T_C_K	p_C_bar	IDT_ms	N_2/Ar
343.15	0.539	950	14.76	50.43	0/100
343.15	0.539	951	14.94	51.59	0/100
357.15	0.55	977	14.84	16.57	0/100
357.13	0.55	975	14.75	16.82	0/100
368.17	0.558	1002	15.09	8.85	0/100
368.15	0.558	1002	15.09	8.88	0/100
383.05	0.562	1032	15.05	5.44	0/100
383.15	0.562	1030	14.96	5.36	0/100
398.05	0.573	1060	15.12	3.67	0/100
398.05	0.573	1061	15.16	3.57	0/100
398.05	0.573	1060	15.15	3.61	0/100
318.33	1.044	904	29.81	136.3	0/100
318.29	1.044	906	30.14	130.8	0/100
328.45	1.049	924	29.65	48.7	0/100
328.45	1.049	926	29.85	46.6	0/100
343.33	1.065	954	29.62	16.43	0/100
343.29	1.065	954	29.64	16.58	0/100
357.17	1.087	986	30.31	6.51	0/100
357.17	1.087	985	30.29	7.12	0/100
368.15	1.096	1004	29.85	4.06	0/100

368.15	1.096	1005	30.04	3.77	0/100

Table BS12. ST IDT measurments for CH_4, φ = 1.0 in '70% dilute'.

T_1 (K)	p_1 (bar)	T_5 (K)	p_5 (bar)	V_{Shock} (ms)	IDT_{total} (µs)
313.15	0.262	1286.6	14.678	1096.8	1156 (PI)
313.15	0.290	1204	14.089	1050.8	1644 (PI)
313.15	0.226	1408.6	15.187	1168.8	423.4
313.15	0.196	1497	14.939	1219.1	206.5
313.15	0.173	1578	14.616	1264.5	105.9
313.15	0.621	1188	29.354	1036.3	1234 (PI)
313.15	0.621	1205.6	30.290	1047.3	1022 (PI)
313.15	0.551	1263.8	29.685	1083	820.2
313.15	0.486	1335.1	29.318	1125.8	515.8
313.15	0.426	1403.8	28.500	1166	293.5
313.15	0.364	1494.1	27.550	1217.5	129.8
313.15	0.364	1516.4	28.370	1230	102

Table BS13. ST IDT measurments for CH_4/200 PPM NO_2, φ = 1.0 in '70% dilute'.

T_1 (K)	p_1 (bar)	T_5 (K)	p_5 (bar)	V_{Shock} (ms)	IDT_{total} (µs)
313.15	0.343	1153	15.135	1012.9	1565 (PI)
313.15	0.343	1162.6	15.404	1018.9	1198 (PI)
313.15	0.287	1262.2	15.345	1080.23	1184
313.15	0.287	1291.1	16.080	1097.6	906 (HP)
313.15	0.287	1332.8	17.167	1122.31	632(HP)
313.15	0.245	1340.6	14.814	1126.9	711.8
313.15	0.212	1452.1	15.060	1191.1	280.6
313.15	0.186	1546.9	14.947	1243.8	123.1
313.15	0.165	1619.9	14.474	1283.3	65
313.15	0.795	1054.8	28.870	949.68	2002 (PI)
313.15	0.795	1081.1	30.640	950	1593 (PI)
313.15	0.686	1130.7	29.020	998.77	1270 (PI)
313.15	0.604	1226	30.395	1058.24	776
313.15	0.513	1278.2	28.540	1095.3	585
313.15	0.513	1306.2	29.417	1106.6	514
313.15	0.455	1383	29.311	1151.6	282.6
313.15	0.396	1478	29.160	1205.6	124.2
313.15	0.367	1535	29.075	1237.2	81.6

CH_4/NO data

Table BS14. IDTs and Experiments conditions for CH_4/200 PPM NO, φ = 0.5 in '70% dilute'.

T_i_K	p_i _bar	T_C_K	p_C_bar	IDT_ms	N_2/Ar
343.11	0.527	975	15.24	40.45	21.43/78.57
343.13	0.527	973	15.13	34.2	21.43/78.57
343.11	0.527	975	15.25	39.52	21.43/78.57
343.13	0.527	973	15.14	33.56	21.43/78.57
363.15	0.533	1014	14.88	7.47	21.43/78.57
363.25	0.533	1010	14.67	7	21.43/78.57
373.15	0.542	1040	15.24	4.27	21.43/78.57
373.13	0.542	1039	15.19	4.4	21.43/78.57
353.35	0.532	987	14.69	18.5	21.43/78.57
353.09	0.532	986	14.64	18.7	21.43/78.57
383.17	0.552	1058	15.19	2.34	21.43/78.57
383.05	0.552	1059	15.29	2.48	21.43/78.57
323.31	1.005	927	29.18	105.6	21.43/78.57
323.25	1.005	926	29.06	105	21.43/78.57
333.31	1.024	950	29.56	35.27	21.43/78.57
333.27	1.024	947	29.23	33.46	21.43/78.57
343.05	1.048	968	29.57	14.78	21.43/78.57
343.05	1.048	972	30.05	13.98	21.43/78.57
353.19	1.057	993	29.8	7.38	21.43/78.57
353.17	1.057	996	30.2	6.85	21.43/78.57
363.11	1.065	1021	30.43	3.74	21.43/78.57
363.15	1.065	1013	29.59	3.6	21.43/78.57
363.15	1.065	1017	30.03	3.78	21.43/78.57

Table BS15. IDTs and Experiments conditions for CH_4/400 PPM NO, φ = 0.5 in '70% dilute'.

T_i_K	p_i _bar	T_C_K	p_C_bar	IDT_ms	N_2/Ar
343.15	0.527	971	14.98	21.72	21.43/78.57
343.13	0.527	973	15.07	20.38	21.43/78.57
363.15	0.533	1016	14.91	4.52	21.43/78.57
363.15	0.533	1013	14.76	4.38	21.43/78.57
373.13	0.542	1034	14.87	2.21	21.43/78.57
373.15	0.542	1036	14.95	2.26	21.43/78.57
333.15	0.524	943	14.67	101	21.43/78.57
333.25	0.524	941	14.58	92	21.43/78.57
353.13	0.532	988	14.7	10.72	21.43/78.57
353.17	0.532	986	14.62	11.6	21.43/78.57
323.33	1.005	926	28.94	57.34	21.43/78.57
323.29	1.005	926	28.95	56.45	21.43/78.57
343.13	1.048	972	29.92	10.52	21.43/78.57
333.27	1.024	948	29.22	21.5	21.43/78.57

333.33	1.024	947	29.12	20.96	21.43/78.57
343.05	1.048	975	30.25	10.13	21.43/78.57
353.15	1.057	997	30.14	5.104	21.43/78.57
353.17	1.057	994	29.87	4.812	21.43/78.57
363.09	1.065	1014	29.66	2.18	21.43/78.57
363.15	1.065	1018	30.06	2.4	21.43/78.57

Table BS16. IDTs and Experiments conditions for CH_4/50 PPM NO, φ = 1.0 in '70% dilute'.

T_i_K	p_i _bar	T_C_K	p_C_bar	IDT_ms	N_2/Ar
313.25	0.997	926	29.27	120.8	0/100
313.25	0.997	927	29.35	120.2	0/100
323.41	1.023	947	29.5	45.38	0/100
323.45	1.023	947	29.56	42.07	0/100
333.31	1.045	969	29.93	20.44	0/100
333.35	1.045	969	29.87	19.94	0/100
343.29	1.056	991	30.01	11.42	0/100
343.23	1.056	991	30.03	11.46	0/100
353.29	1.062	1010	29.64	6.68	0/100
353.27	1.062	1010	29.64	6.86	0/100

Table BS17. IDTs and Experiments conditions for CH_4/100 PPM NO, φ = 1.0 in '70% dilute'

T_i_K	p_i _bar	T_C_K	p_C_bar	IDT_ms	N_2/Ar
313.25	0.997	930	29.63	100.1	0/100
313.15	0.997	928	29.4	103.9	0/100
323.37	1.023	948	29.59	39.88	0/100
323.35	1.023	948	29.63	38.77	0/100
333.21	1.045	968	29.79	17.76	0/100
333.23	1.045	968	29.82	17.33	0/100
343.41	1.056	994	30.22	8.31	0/100
343.37	1.056	994	30.26	8.58	0/100
353.27	1.062	1014	29.96	4.85	0/100
353.33	1.062	1016	30.2	5.04	0/100

Table BS18. IDTs and Experiments conditions for CH_4/200 PPM NO, φ = 1.0 in '70% dilute'.

T_i_K	p_i _bar	T_C_K	p_C_bar	IDT_ms	N_2/Ar
323.15	0.513	946	14.77	152.2	0/100
323.15	0.513	945	14.67	162	0/100
333.15	0.519	963	14.54	43.59	0/100
333.17	0.519	964	14.59	47.35	0/100
343.15	0.536	984	14.85	18.07	0/100
343.13	0.536	987	15	17.74	0/100
353.15	0.517	1026	15.23	6.96	0/100
353.15	0.517	1023	15.08	7.15	0/100
353.17	0.517	1026	15.19	6.35	0/100
313.43	1.002	925	29.13	102.9	0/100
313.45	1.002	923	28.9	104.6	0/100

323.13	1.023	945	29.32	37.26	0/100
323.13	1.023	945	29.35	34.45	0/100
333.15	1.053	963	29.46	16.81	0/100
333.13	1.053	963	29.43	16.92	0/100
343.15	1.074	986	29.93	7.6	0/100
343.15	1.074	987	30.05	7.82	0/100
353.13	1.013	1027	29.94	3.32	0/100
353.15	1.013	1027	29.89	3.39	0/100

Table BS19. IDTs and Experiments conditions for CH_4/400 PPM NO, φ = 1.0 in '70% dilute'.

T_i_K	p_i _bar	T_C_K	p_C_bar	IDT_ms	N_2/Ar
323.25	0.513	944	14.6	73.26	0/100
323.29	0.513	943	14.51	79	0/100
333.23	0.519	965	14.56	23.37	0/100
333.19	0.519	965	14.57	24.34	0/100
343.05	0.536	985	14.88	10.02	0/100
343.07	0.536	986	14.89	10.17	0/100
353.13	0.517	1024	15.05	3.39	0/100
353.15	0.517	1026	15.16	3.52	0/100
353.17	0.517	1026	15.18	3.57	0/100
303.25	0.967	905	28.64	189.5	0/100
303.31	0.967	905	28.63	192.9	0/100
313.37	1.002	924	29.03	55.2	0/100
313.39	1.002	924	28.95	60	0/100
313.33	1.002	924	28.94	59.89	0/100
323.15	1.023	942	28.89	24.64	0/100
323.17	1.023	940	28.7	25.25	0/100
333.17	1.053	965	29.57	10.57	0/100
333.15	1.053	965	29.58	10.79	0/100
343.05	1.074	987	29.95	4.84	0/100
343.15	1.074	987	29.97	4.84	0/100
353.13	1.013	1029	30.05	1.72	0/100
353.15	1.013	1029	30.02	1.96	0/100

Table BS20. IDTs and Experiments conditions for CH_4/1000 PPM NO, φ = 1.0 in '70% dilute'

T_i_K	p_i _bar	T_C_K	p_C_bar	IDT_ms	N_2/Ar
303.27	0.955	915	29.14	66.58	0/100
303.33	0.955	914	28.96	64.59	0/100
313.41	0.997	929	29.08	20.68	0/100
313.39	0.997	929	29.08	21.09	0/100
323.33	1.023	954	29.92	6.99	0/100
323.49	1.023	953	29.74	7.47	0/100
333.31	1.045	976	30.22	3.39	0/100
333.19	1.045	974	30.03	3.46	0/100

Appendix B

Table BS21. IDTs and Experiments conditions for CH_4/200 PPM NO, φ = 2.0 in '70% dilute'.

T_i_K	p_i _bar	T_C_K	p_C_bar	IDT_ms	N_2/Ar
373.15	0.561	1009	15.16	9.12	0/100
373.17	0.561	1009	15.12	9.24	0/100
388.19	0.565	1037	14.99	6.31	0/100
388.23	0.565	1036	14.96	6.24	0/100
338.15	0.54	936	14.79	147.9	0/100
338.13	0.54	938	14.94	141	0/100
348.17	0.543	957	14.81	50.52	0/100
348.15	0.543	959	14.94	48.96	0/100
358.17	0.547	979	14.93	22.63	0/100
358.13	0.547	977	14.8	25.46	0/100
358.13	0.547	977	14.83	25.32	0/100
313.35	1.034	889	29.4	388	0/100
328.15	1.056	919	29.59	64.51	0/100
328.15	1.056	920	29.7	62.72	0/100
348.13	1.087	966	30.65	13.5	0/100
348.21	1.087	963	30.29	13.49	0/100
358.15	1.096	984	30.44	8.74	0/100
358.19	1.096	983	30.32	8.63	0/100
373.13	1.104	1009	29.79	3.9	0/100
373.11	1.104	1008	29.73	3.86	0/100
338.11	1.066	934	29.07	39.25	0/100
338.13	1.066	938	29.42	38.6	0/100

Table BS21. IDTs and Experiments conditions for CH_4/400 PPM NO, φ = 2.0 in '70% dilute'.

T_i_K	p_i _bar	T_C_K	p_C_bar	IDT_ms	N_2/Ar
373.19	0.561	1012	15.27	5.19	0/100
373.19	0.561	1010	15.12	5.17	0/100
388.05	0.565	1043	15.28	3.39	0/100
388.05	0.565	1039	15.08	3.31	0/100
388.09	0.565	1038	15.03	3.25	0/100
338.13	0.54	936	14.78	68.37	0/100
338.13	0.54	935	14.73	70.37	0/100
348.07	0.543	962	15.03	28.76	0/100
348.15	0.543	958	14.83	31.2	0/100
348.15	0.543	959	14.85	30.55	0/100
358.05	0.547	985	15.19	13.6	0/100
358.11	0.547	981	15.01	14.62	0/100
358.17	0.547	982	15.01	14.71	0/100
313.45	1.034	891	29.57	161.3	0/100
313.39	1.034	891	29.56	163.1	0/100
328.19	1.056	920	29.62	41.3	0/100

328.09	1.056	918	29.39	43.62	0/100
348.05	1.087	963	30.29	9.93	0/100
348.05	1.087	963	30.3	9.7	0/100
358.05	1.096	986	30.65	5.36	0/100
358.15	1.096	983	30.25	5.25	0/100
373.11	1.104	1016	30.46	2.39	0/100
373.17	1.104	1014	30.24	2.28	0/100
338.29	1.066	943	29.86	22.37	0/100
338.09	1.066	939	29.48	26.44	0/100

Appendix B

References

[1] S. Gersen, A. V Mokhov, J.H. Darmeveil, H.B. Levinsky, P. Glarborg, Ignition-promoting effect of NO_2 on methane, ethane and methane/ethane mixtures in a rapid compression machine, Proc. Combust. Inst., 33 (2011) 433–440.

[2] O. Mathieu, J.M. Pemelton, G. Bourque, E.L. Petersen, Shock-induced ignition of methane sensitized by NO2 and N2O, Combust. Flame, 162 (2015) 3053–3070.

[3] X. Zhang, W. Ye, J.C. Shi, X.J. Wu, R.T. Zhang, S.N. Luo, Shock-Induced Ignition of Methane, Ethane, and Methane/Ethane Mixtures Sensitized by NO_2, Energy Fuels, 31 (2017) 12780–12790.

[4] R. Mével, J.E. Shepherd, Ignition delay-time behind reflected shock waves of small hydrocarbons–nitrous oxide(–oxygen) mixtures, Shock Waves, 25 (2015) 217–229.

[5] F. Deng, F. Yang, P. Zhang, Y. Pan, J. Bugler, H.J. Curran, Y. Zhang, Z. Huang, Towards a kinetic understanding of the NOx promoting-effect on ignition of coalbed methane: A case study of methane/nitrogen dioxide mixtures, Fuel, 181 (2016) 188–198.

[6] M.W. Slack, A.R. Grillo, Shock tube investigation of methane-oxygen ignition sensitized by NO2, Combust. Flame, 40 (1981) 155–172.

[7] F. Deng, F. Yang, P. Zhang, Y. Pan, Y. Zhang, Z. Huang, Ignition Delay Time and Chemical Kinetic Study of Methane and Nitrous Oxide Mixtures at High Temperatures, Energy Fuels, 30 (2016) 1415–1427.

[8] J.H. Bromly, F.J. Barnes, S. Muris, X. You, B.S. Haynes, Kinetic and Thermodynamic Sensitivity Analysis of the NO-Sensitised Oxidation of Methane, Combust. Sci. Technol., 115 (1996) 259–296.

[9] Y. Song, L. Marrodán, N. Vin, O. Herbinet, E. Assaf, C. Fittschen, A. Stagni, T. Faravelli, M.U. Alzueta, F. Battin-Leclerc, The sensitizing effects of NO_2 and NO on methane low temperature oxidation in a jet stirred reactor, Proc. Combust. Inst., 37(1) (2019) 667–675.

[10] C.L. Rasmussen, A.E. Rasmussen, P. Glarborg, Sensitizing effects of NOx on CH4 oxidation at high pressure, Combust. Flame, 154 (2008) 529–545.

[11] P. Dagaut, A. Nicolle, Experimental study and detailed kinetic modeling of the effect of exhaust gas on fuel combustion: mutual sensitization of the oxidation of nitric oxide and methane over extended temperature and pressure ranges, Combust. Flame, 140 (2005) 161–171.

[12] R. Sivaramakrishnan, K. Brezinsky, G. Dayma, P. Dagaut, High pressure effects on the mutual sensitization of the oxidation of NO and CH_4–C_2H_6 blends, Phys. Chem. Chem. Phys., 9 (2007) 4230–4244.

Appendix C

(Supplementary information of chapter 6)

The effect of the addition of nitrogen oxides on the oxidation of ethane: an experimental and modeling study

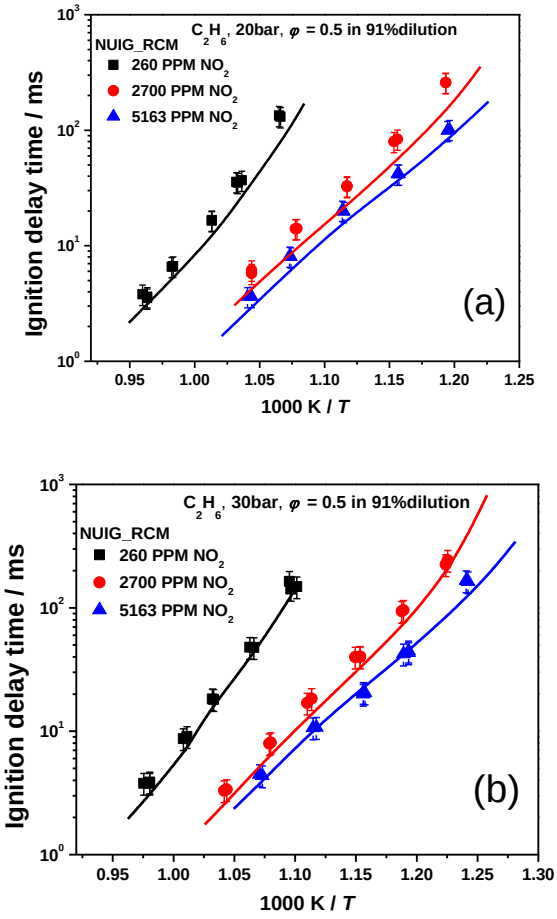

Figure CS1. Comparison of RCM IDT measurements from (symbols, current study) and NUIGMech1.2 IDT prediction (solid lines) of C_2H_6/ (260, 2700, and 5163 ppm) NO_2 at φ = 0.5 in 91% dilution, (a) 20 bar; and (b) 30 bar.

Appendix C

Comparison of current IDT measurements with the available C2/NOx models

1. RCM IDT measurements

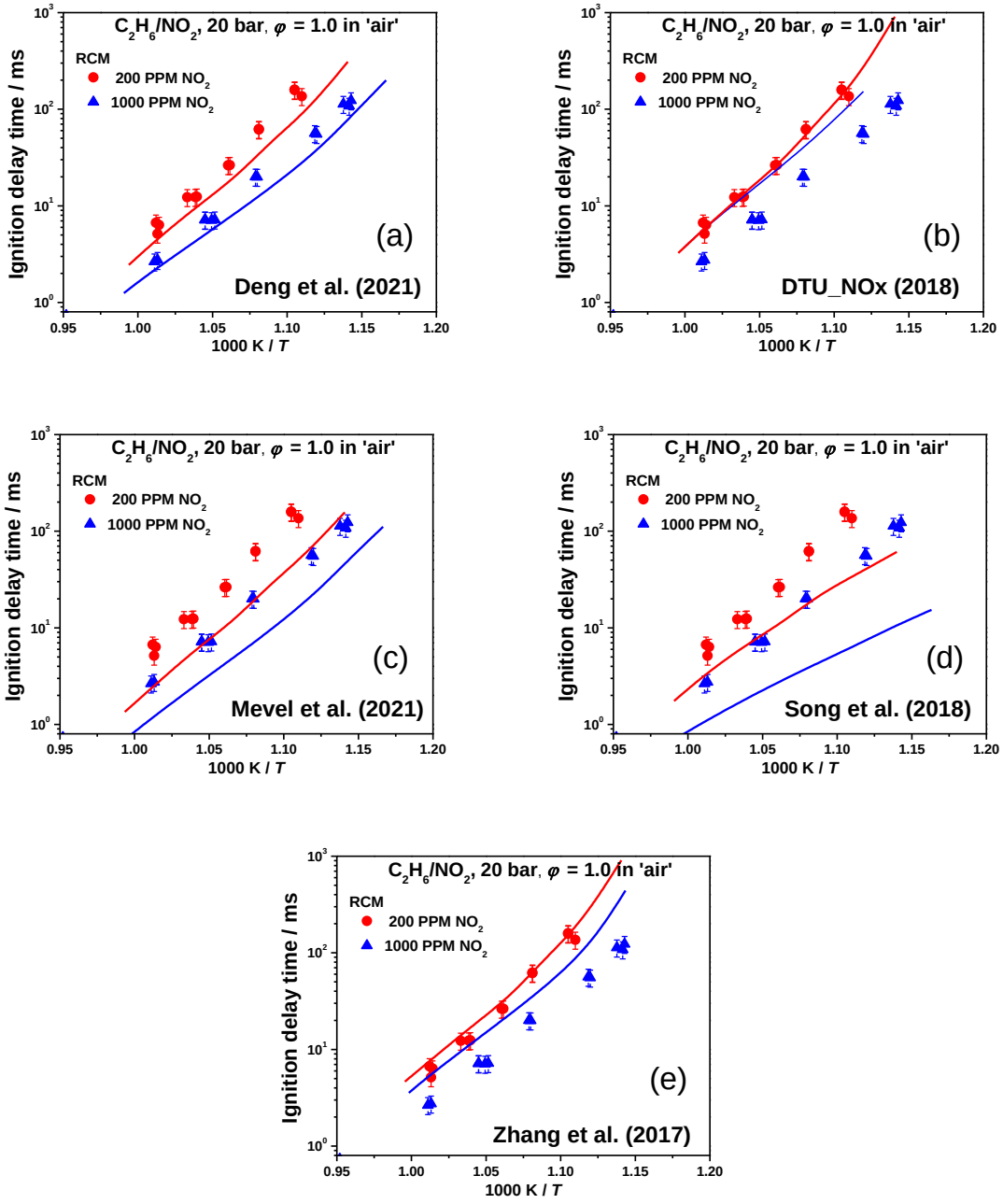

Figure CS2. Comparison of current RCM IDT measurements from (symbols, current study) and five models' predictions (solid lines) of C_2H_6/ (200 and 1000 ppm) NO_2 at φ = 1.0 in 'air' and p_C = 20 bar.

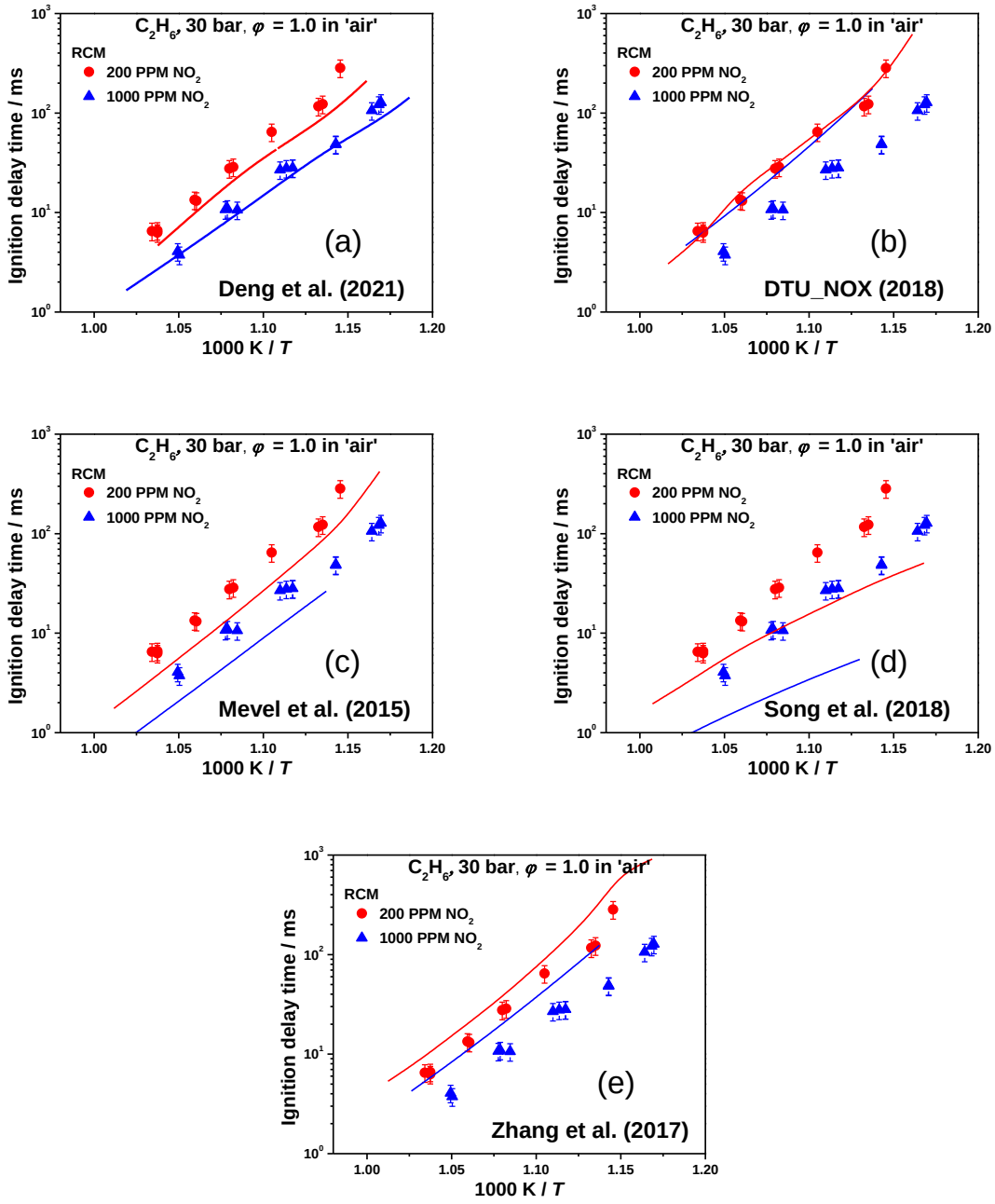

Figure CS3. Comparison of current RCM IDT measurements from (symbols, current study) and five models' predictions (solid lines) of C_2H_6/ (200 and 1000 ppm) NO_2 at φ = 1.0 in 'air' and p_C = 30 bar.

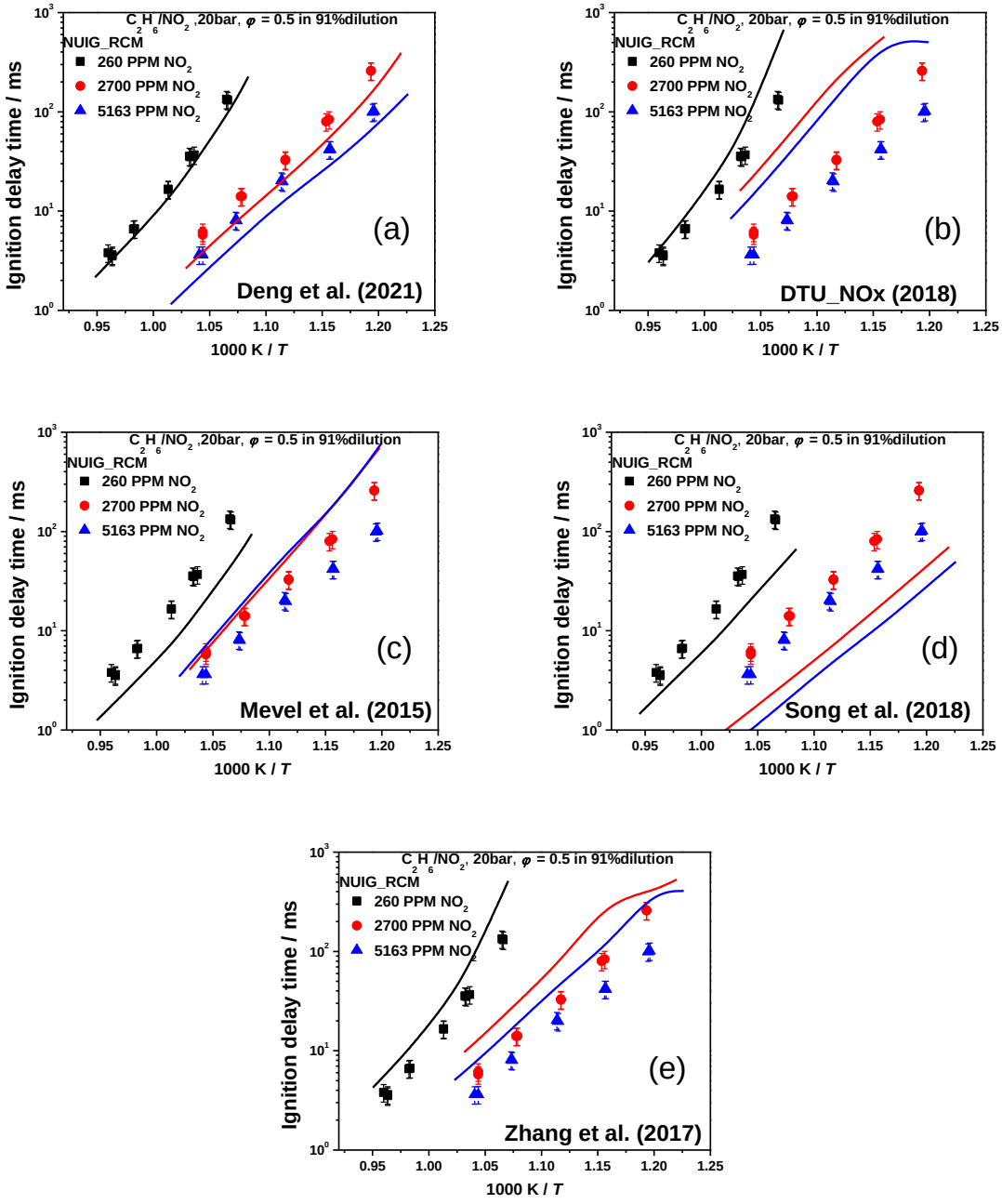

Figure CS4. Comparison of current RCM IDT measurements from (symbols, current study) and five models' predictions (solid lines) of C_2H_6/ (200 and 1000 ppm) NO_2 at φ = 1.0 in 'air' and p_C = 30 bar.

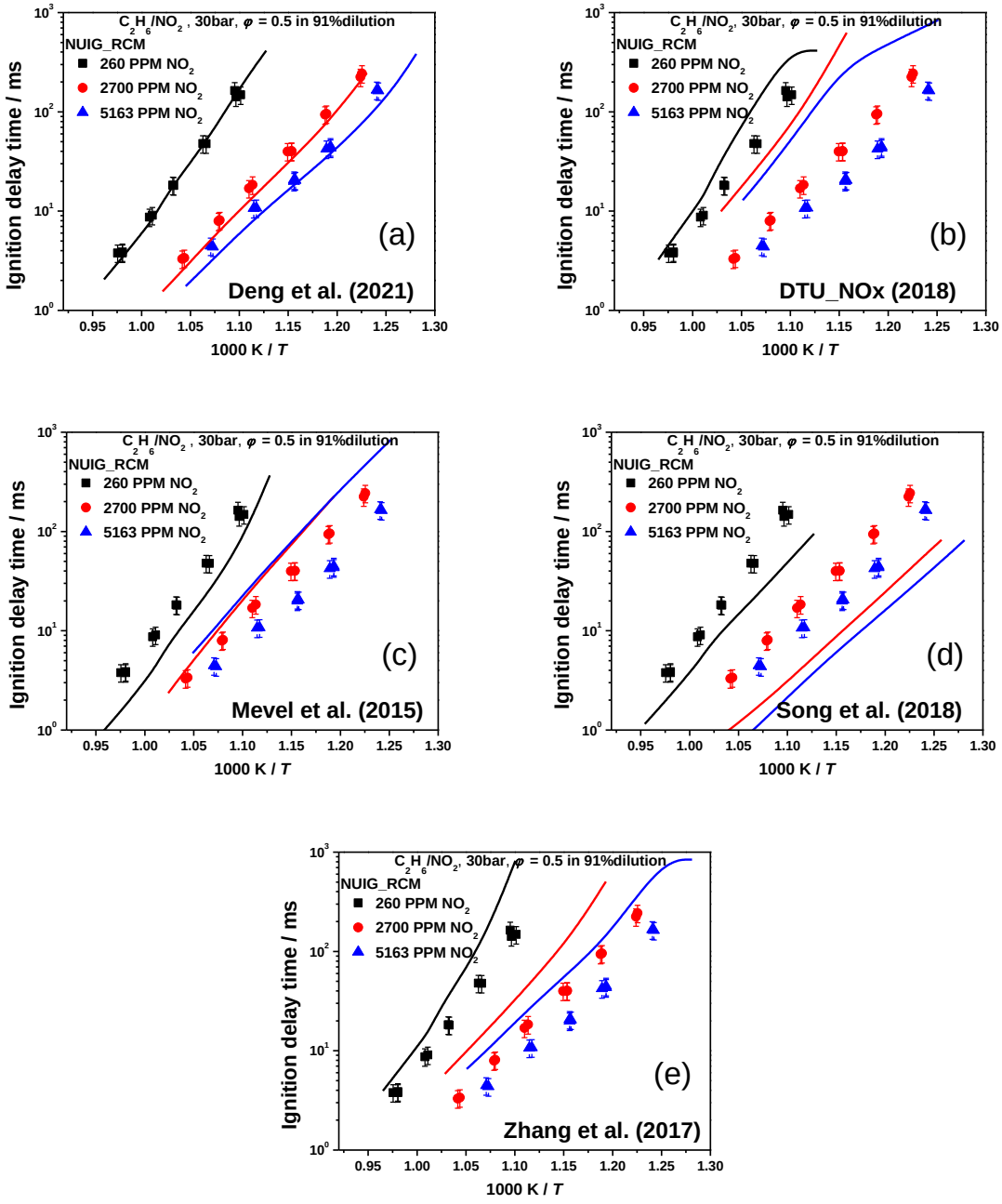

Figure CS5. Comparison of current RCM IDT measurements from (symbols, current study) and five models' predictions (solid lines) of C_2H_6/ (200 and 1000 ppm) NO_2 at φ = 1.0 in 'air' and p_C = 30 bar.

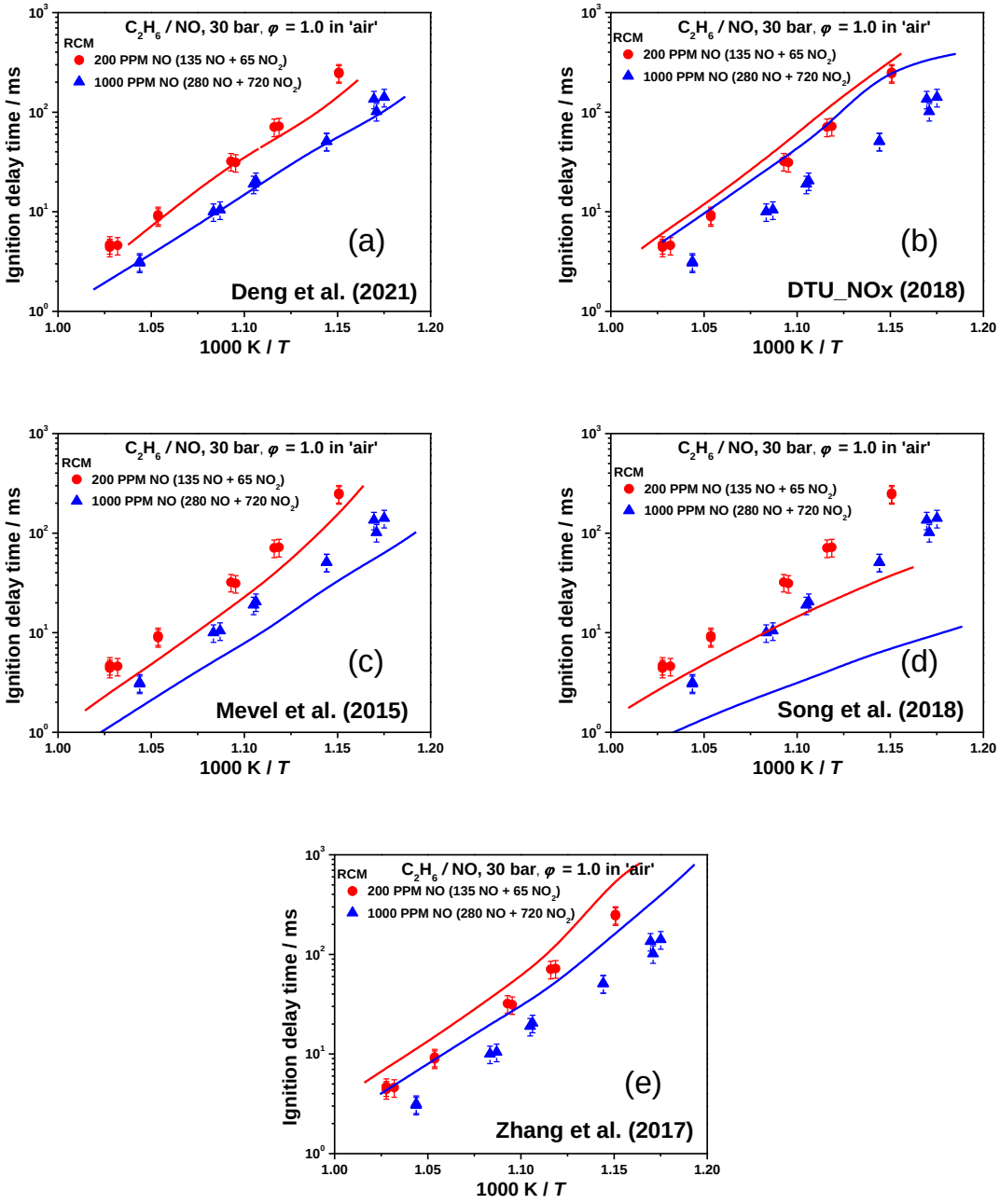

Figure CS6. Comparison of current RCM IDT measurements from (symbols, current study) and five models' predictions (solid lines) of C_2H_6/ (200 and 1000 ppm) NO at φ = 1.0 in 'air' and p_C = 30 bar.

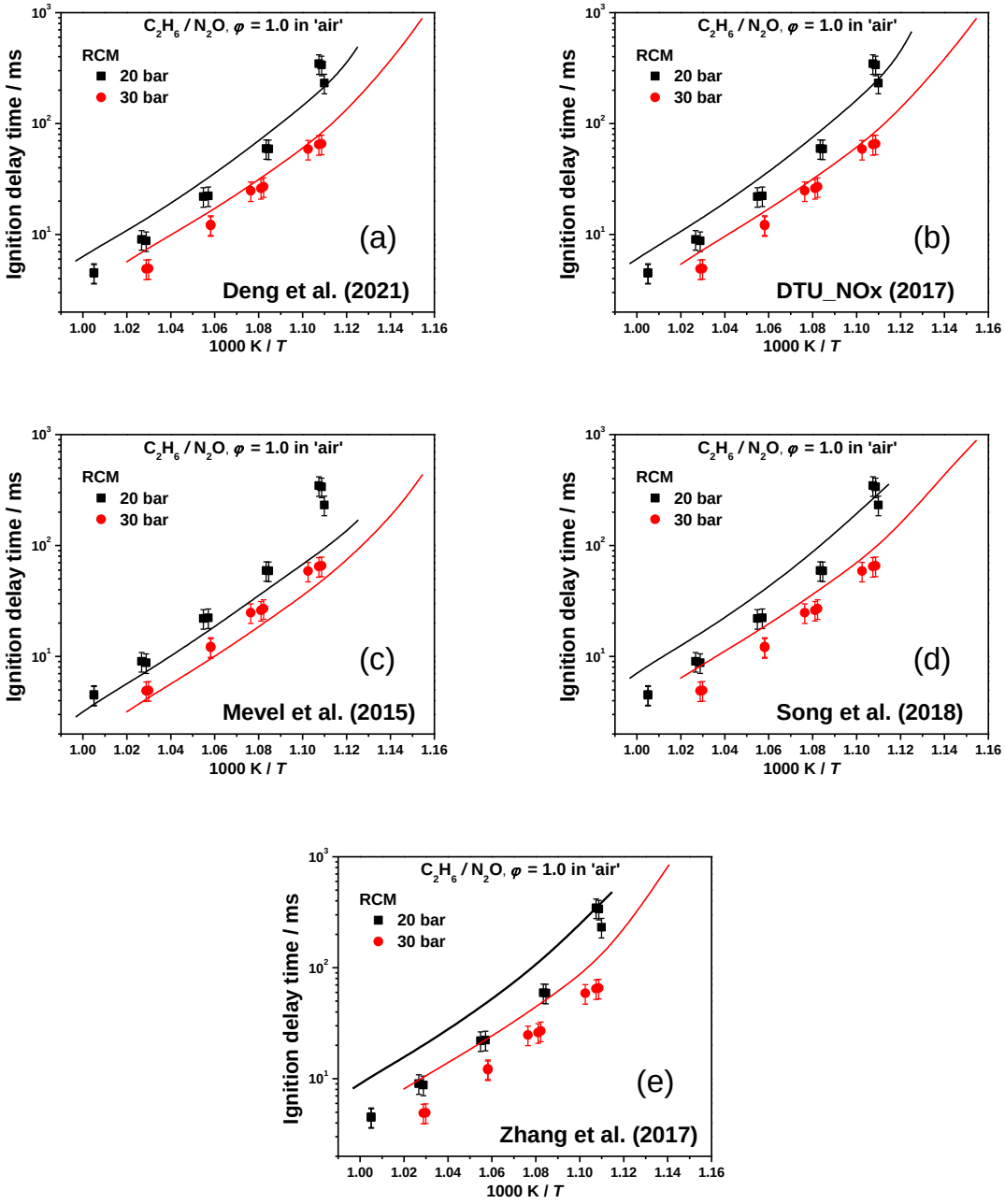

Figure CS7. Comparison of current RCM IDT measurements from (symbols, current study) and five models' predictions (solid lines) of C_2H_6/ 1000 ppm N_2O at φ = 1.0 in 'air' and p_C =20 and 30 bar.

2. ST IDT measurements

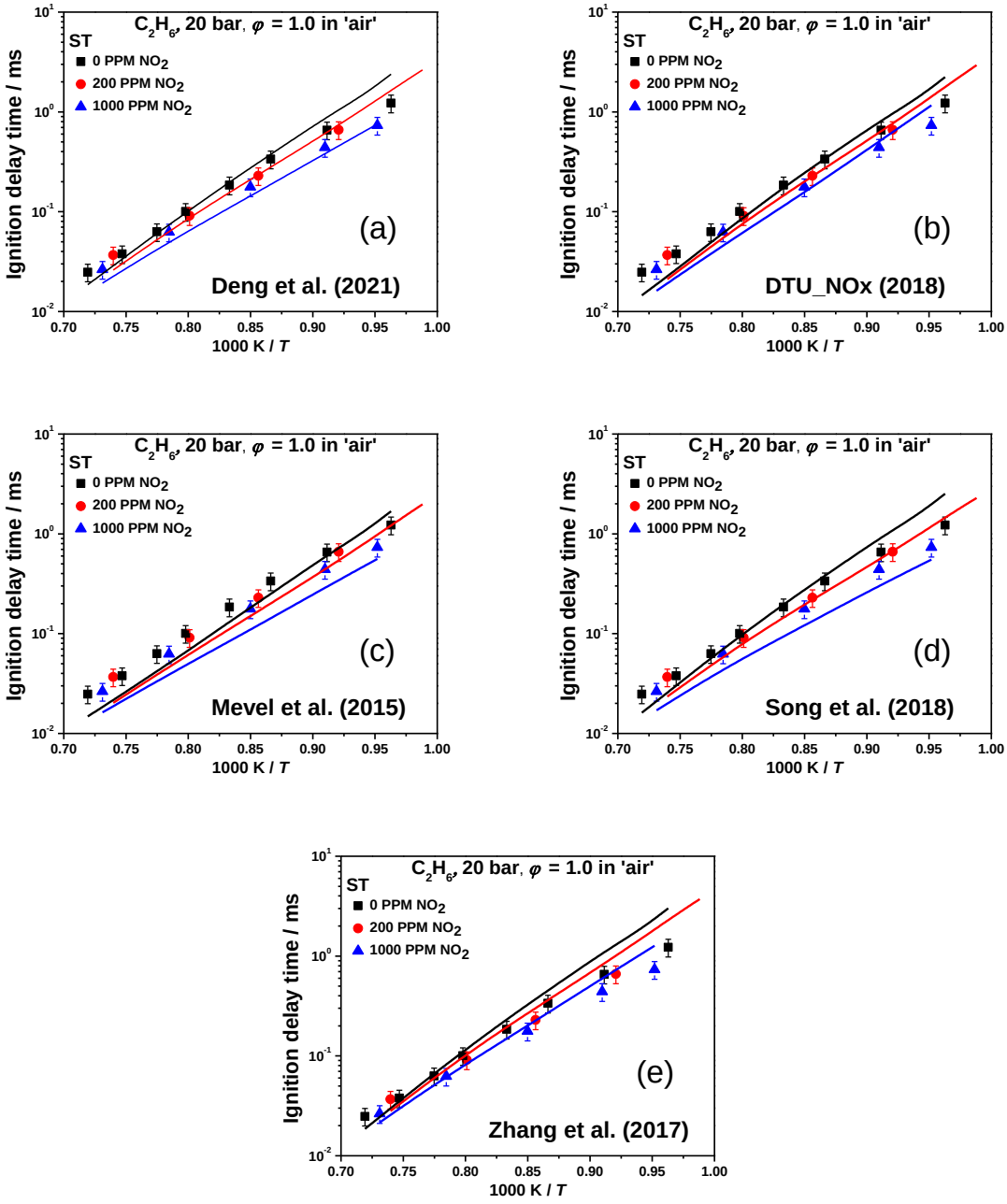

Figure CS8. Comparison of current ST IDT measurements from (symbols, current study) and five models' predictions (solid lines) of C_2H_6/ (200 and 1000 ppm) NO_2 at φ = 1.0 in 'air' and p_5 = 20 bar.

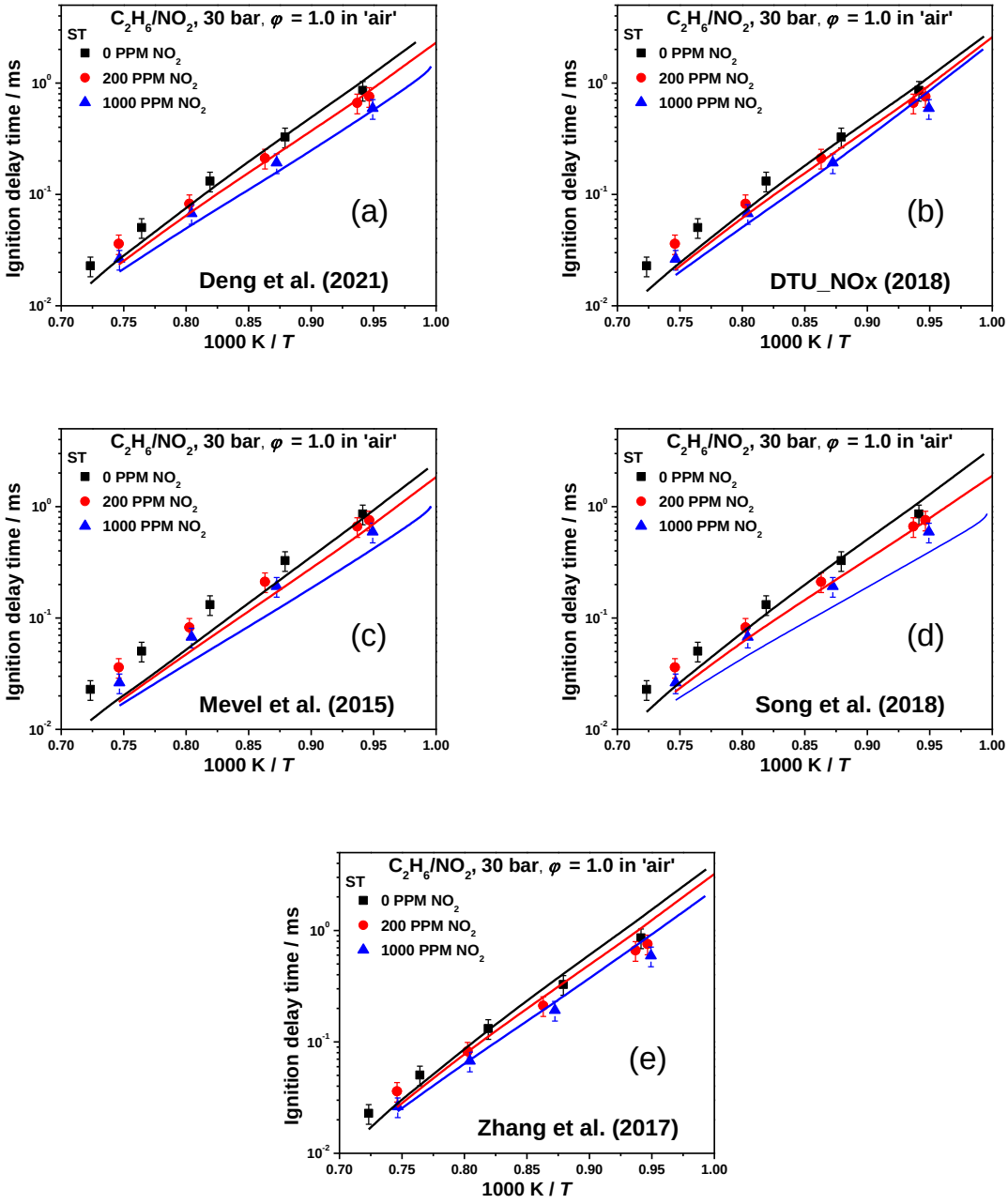

Figure CS9. Comparison of current ST IDT measurements from (symbols, current study) and five models' predictions (solid lines) of C_2H_6/ (200 and 1000 ppm) NO_2 at φ = 1.0 in 'air' and p_5 = 30 bar.

Appendix C

NUIGMech1.2 validation

1. IDT validation

1.1. RCM measurements

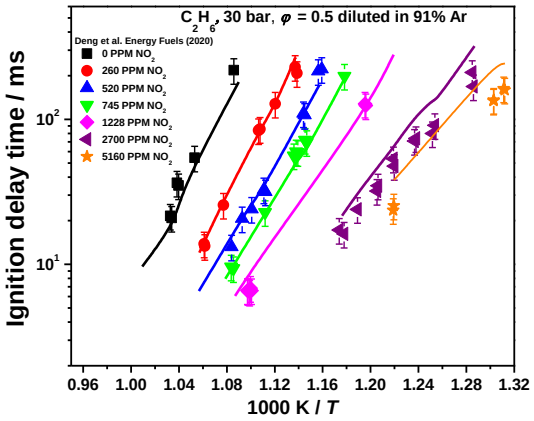

Figure CS10. Comparison of IDT measurements from Deng et al. [1] (symbols) and NUIGMech1.2 IDT prediction (solid lines) at φ = 0.5, and 30 bar.

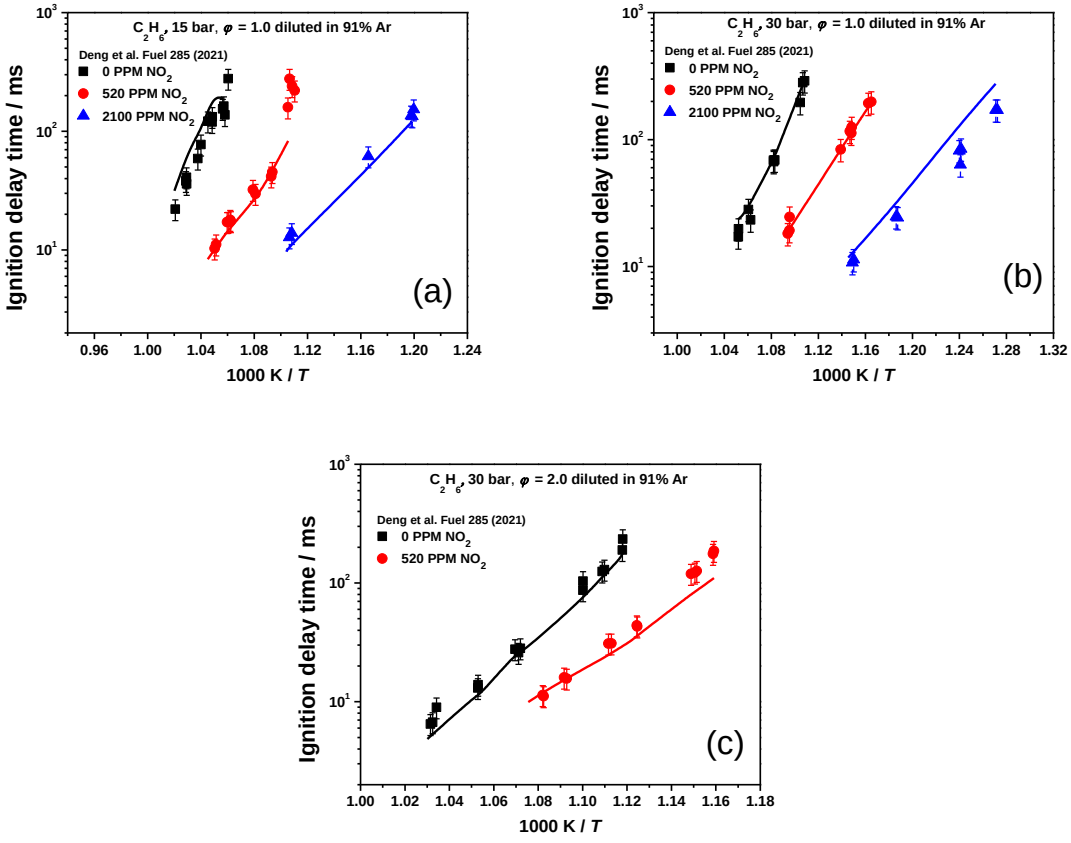

Figure CS11. Comparison of IDT measurements from Deng et al. [2] (symbols) and NUIGMech1.2 IDT prediction (solid lines); (a) φ = 1.0, 15 bar; (b) φ = 1.0, 30 bar; and (c) φ = 2.0, 30 bar, at 91% dilution.

1.2. Shock tube measurements

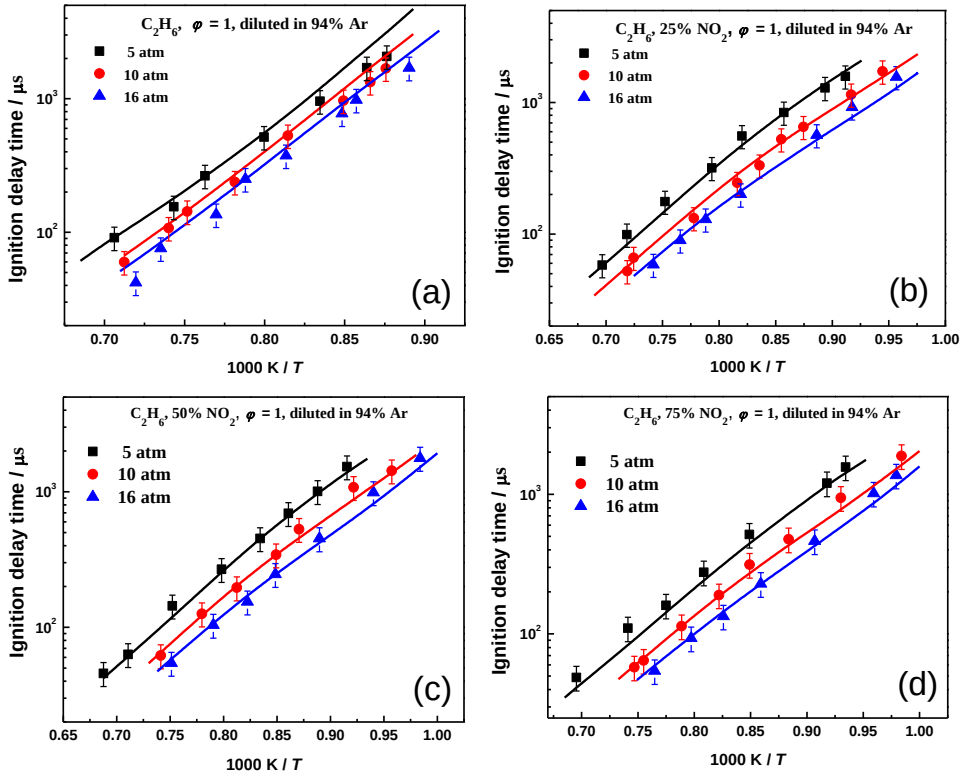

Figure CS12. Comparison of NUIGMech1.2 IDT predictions verses ST IDT measurements of ethane/NO_2 at 5, 10, and 16 atm at 94% Ar dilution [3].

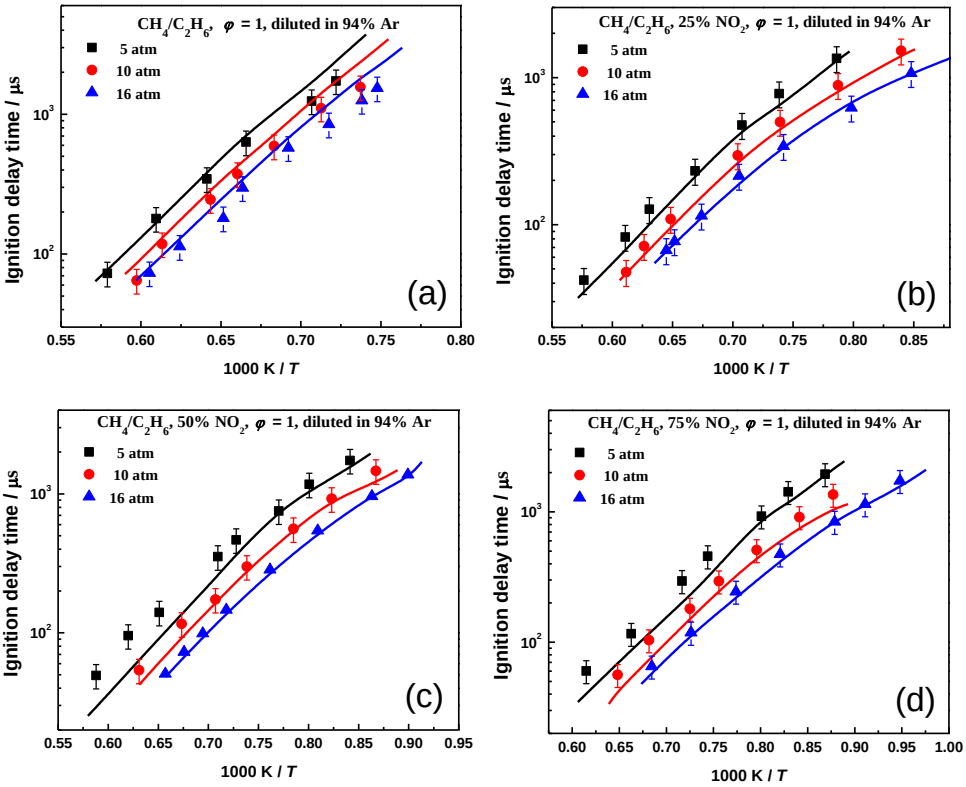

Figure CS13. Comparison of NUIGMech1.2 IDT predictions verses ST IDT measurements of methane/ethane/NO_2 at 5, 10, and 16 atm at 94% Ar dilution [3].

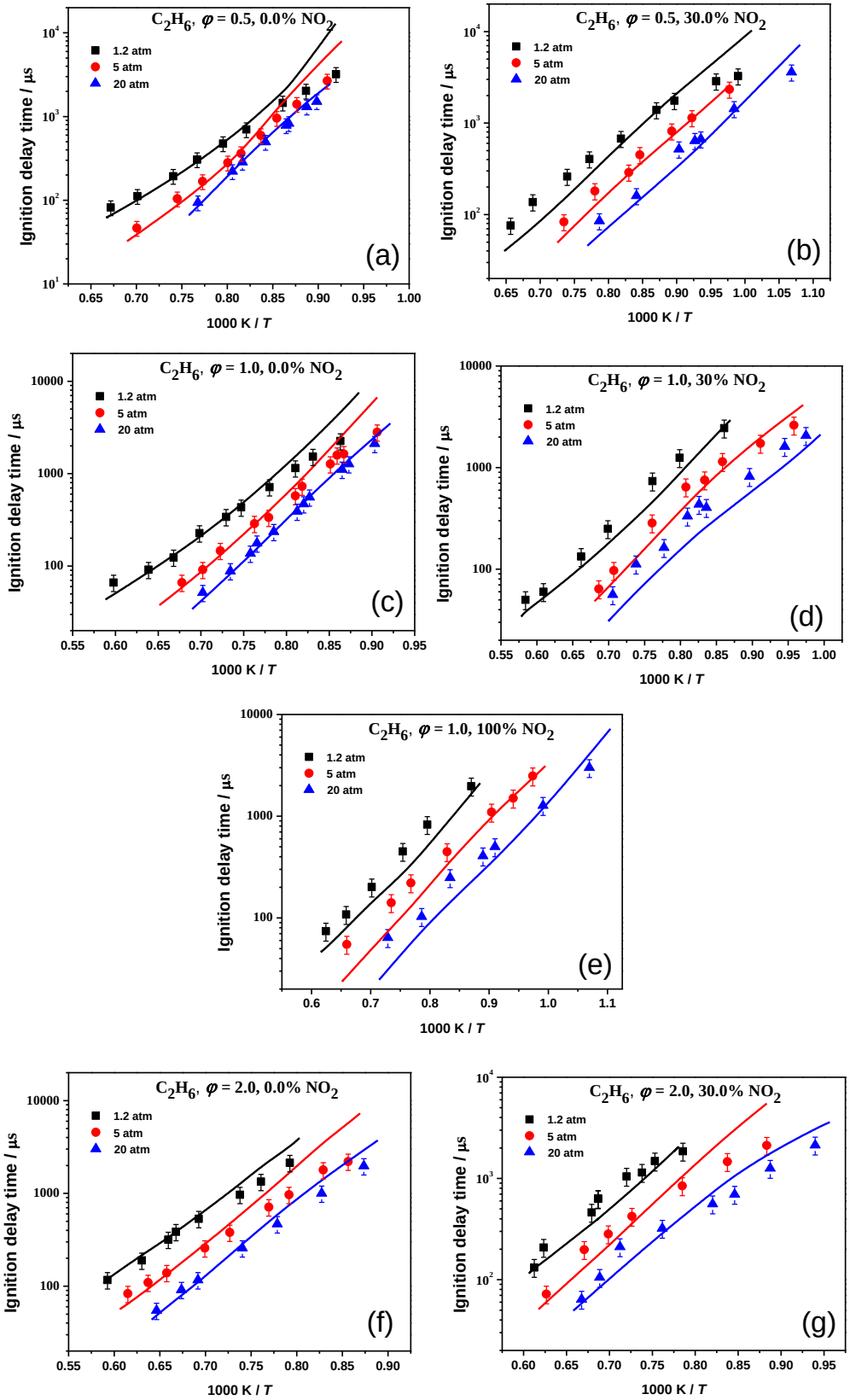

Figure CS14. Comparison of NUIGMech1.2 IDT predictions verses ST IDT measurements of ethane/NO_2 at 1.2, 5, and 20 atm at 94% Ar dilution [4,5].

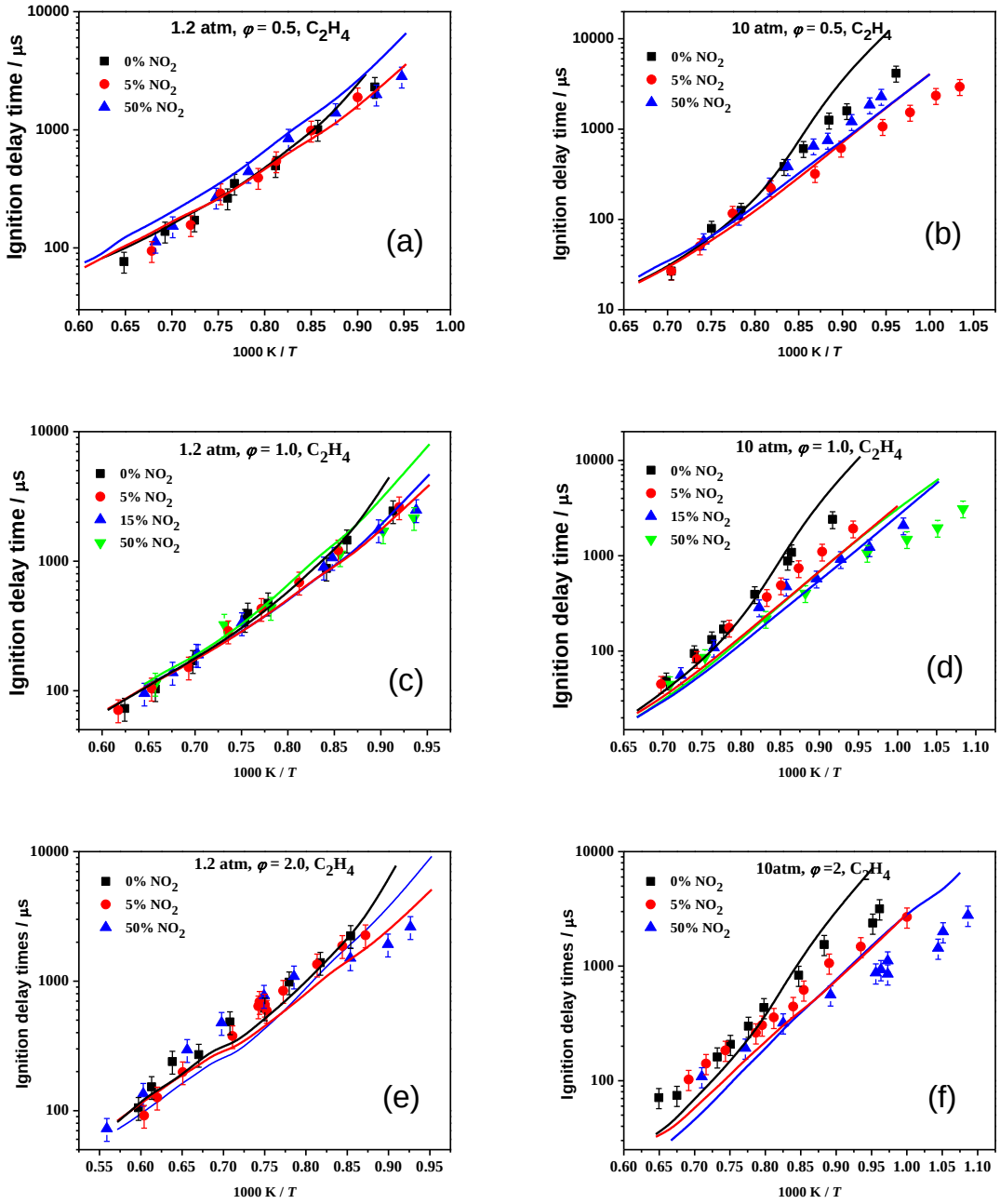

Figure CS15. Comparison of NUIGMech1.2 IDT predictions verses ST IDT measurements of ethylene/NO_2 at 1.2, and 10 atm at 94% Ar dilution [6].

2. Speciation validation

2.1. Jet-stirred reactor

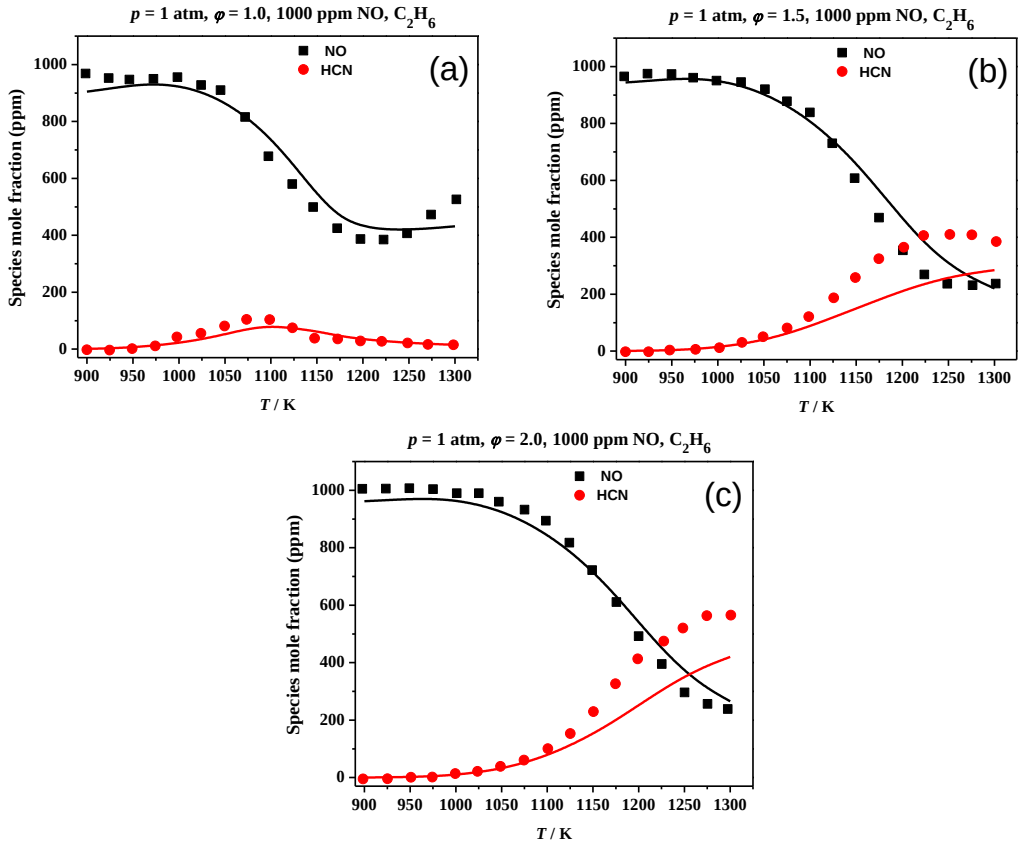

Figure CS16. Comparison of NUIGMech1.2 IDT predictions verses JSR measurements of ethane/NO at 1.0 atm [7].

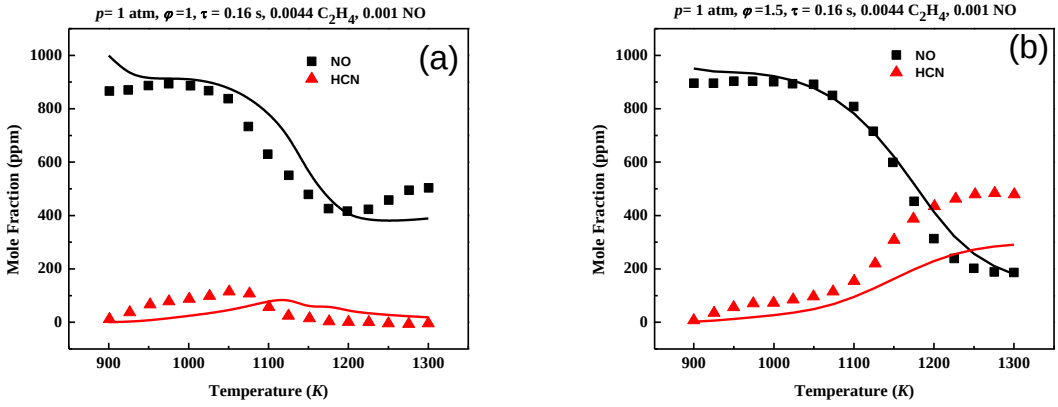

Figure CS17. Comparison of NUIGMech1.2 IDT predictions verses JSR measurements of ethane/NO at 1.0 atm [8]

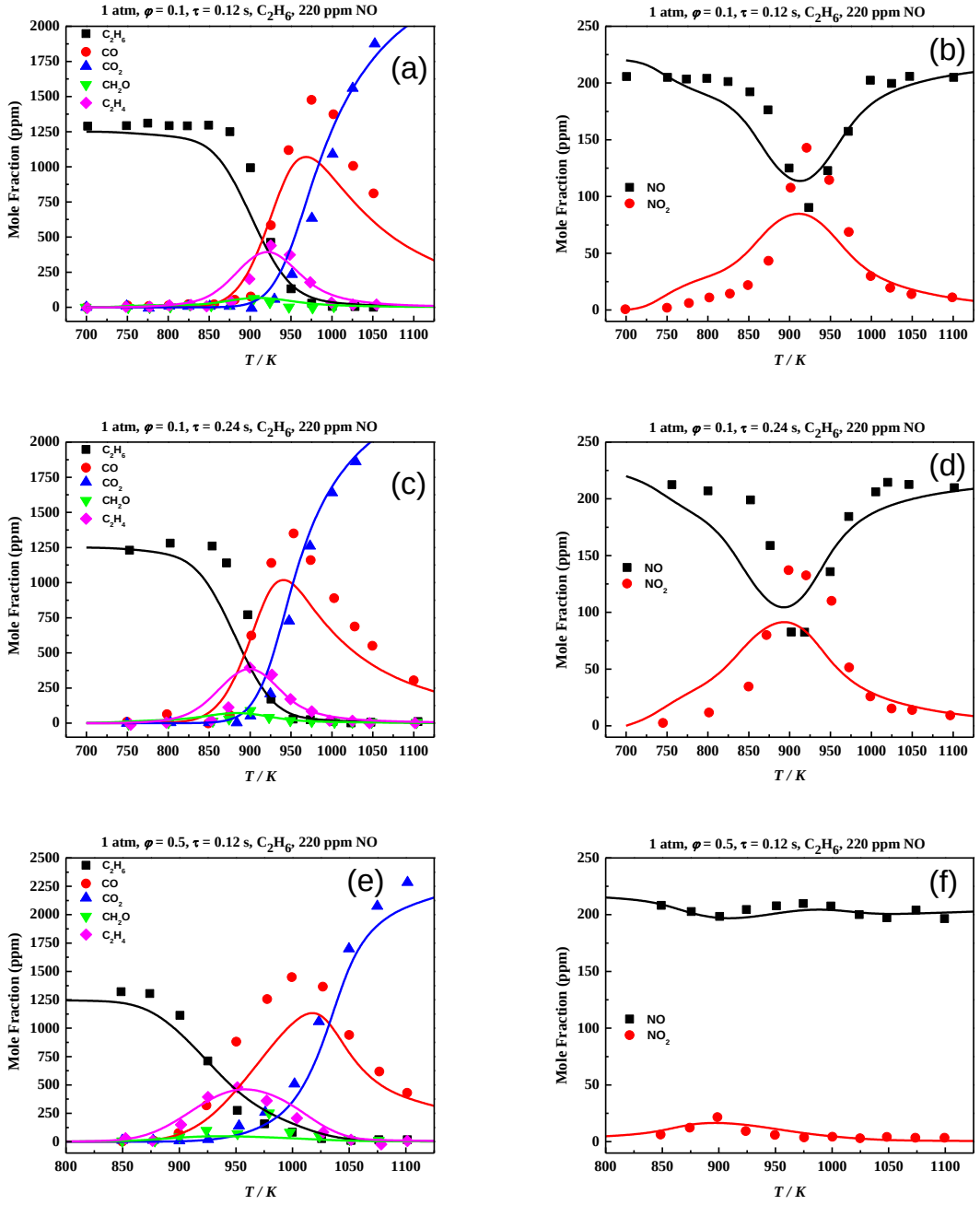

Figure CS18. Comparison of NUIGMech1.2 IDT predictions verses JSR measurements of ethane/NO at 1.0 atm [9].

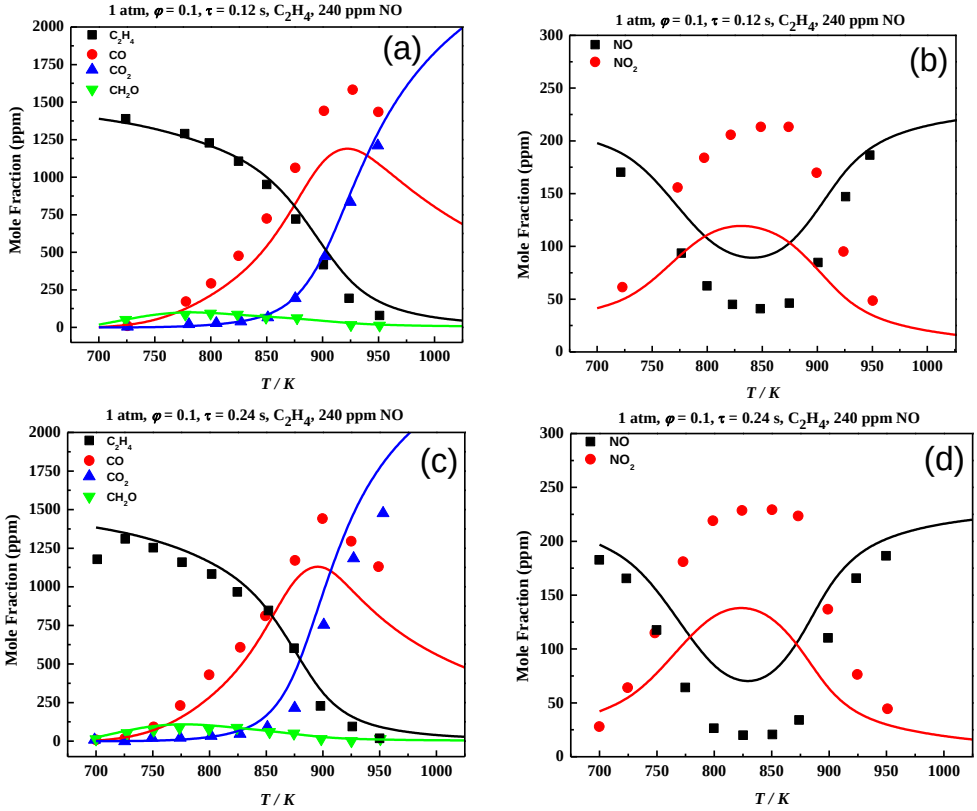

Figure CS19. Comparison of NUIGMech1.2 IDT predictions verses JSR measurements of ethylene/NO at 1.0 atm [9].

2.2. Flow reactor

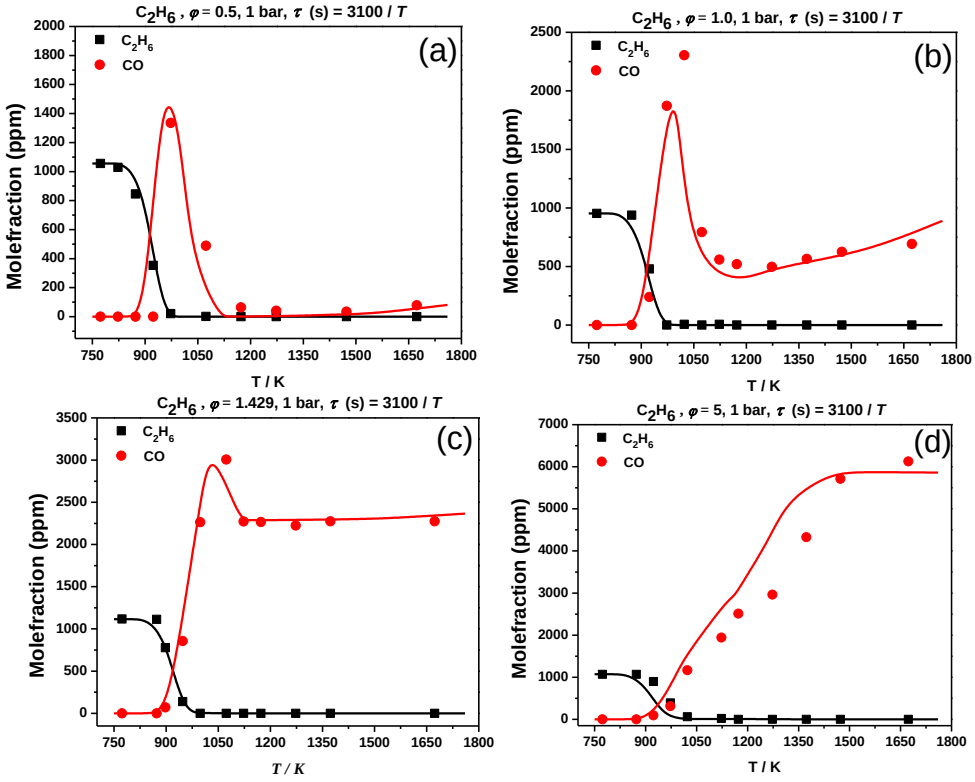

Figure CS20. Comparison of NUIGMech1.2 IDT predictions verses FR measurements of ethane [10].

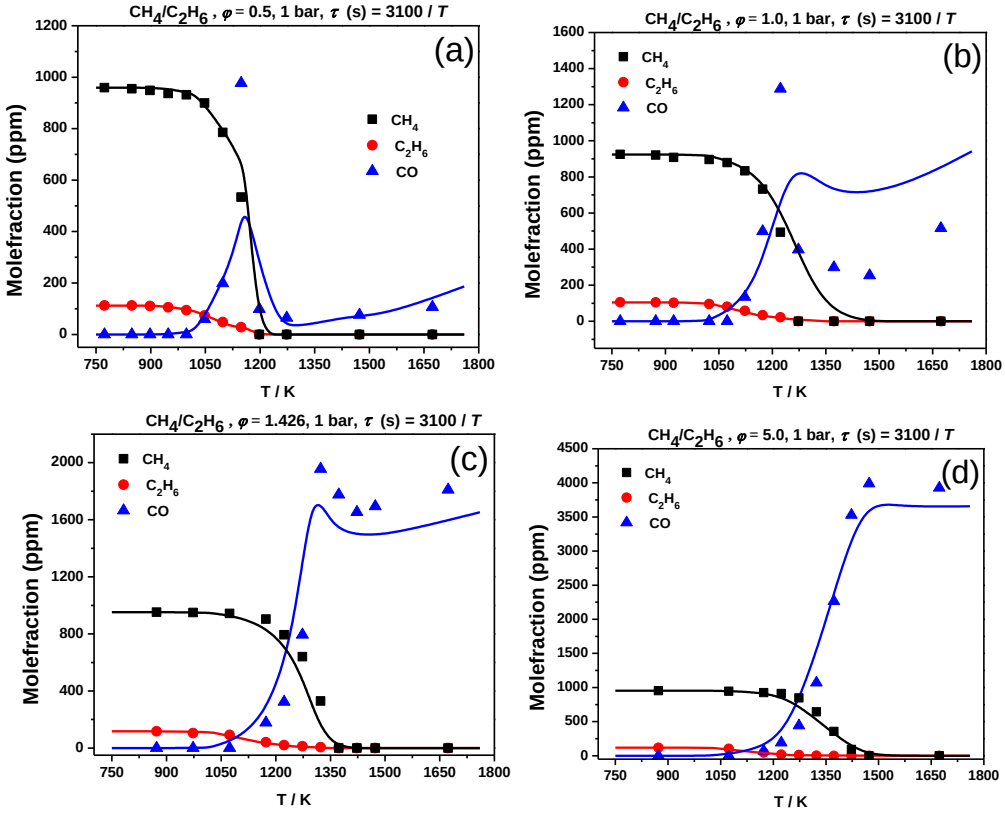

Figure CS21. Comparison of NUIGMech1.2 IDT predictions verses FR measurements of NG (methane/ethane)[10].

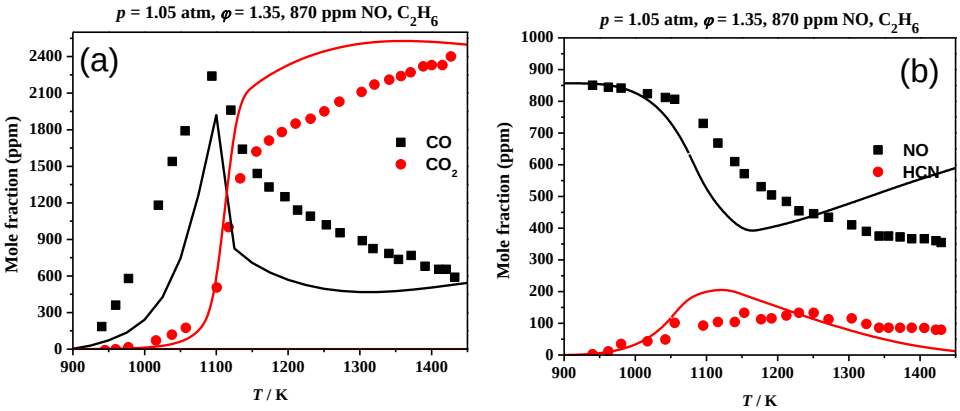

Figure CS22. Comparison of NUIGMech1.2 IDT predictions verses FR measurements of ethane/NO [11].

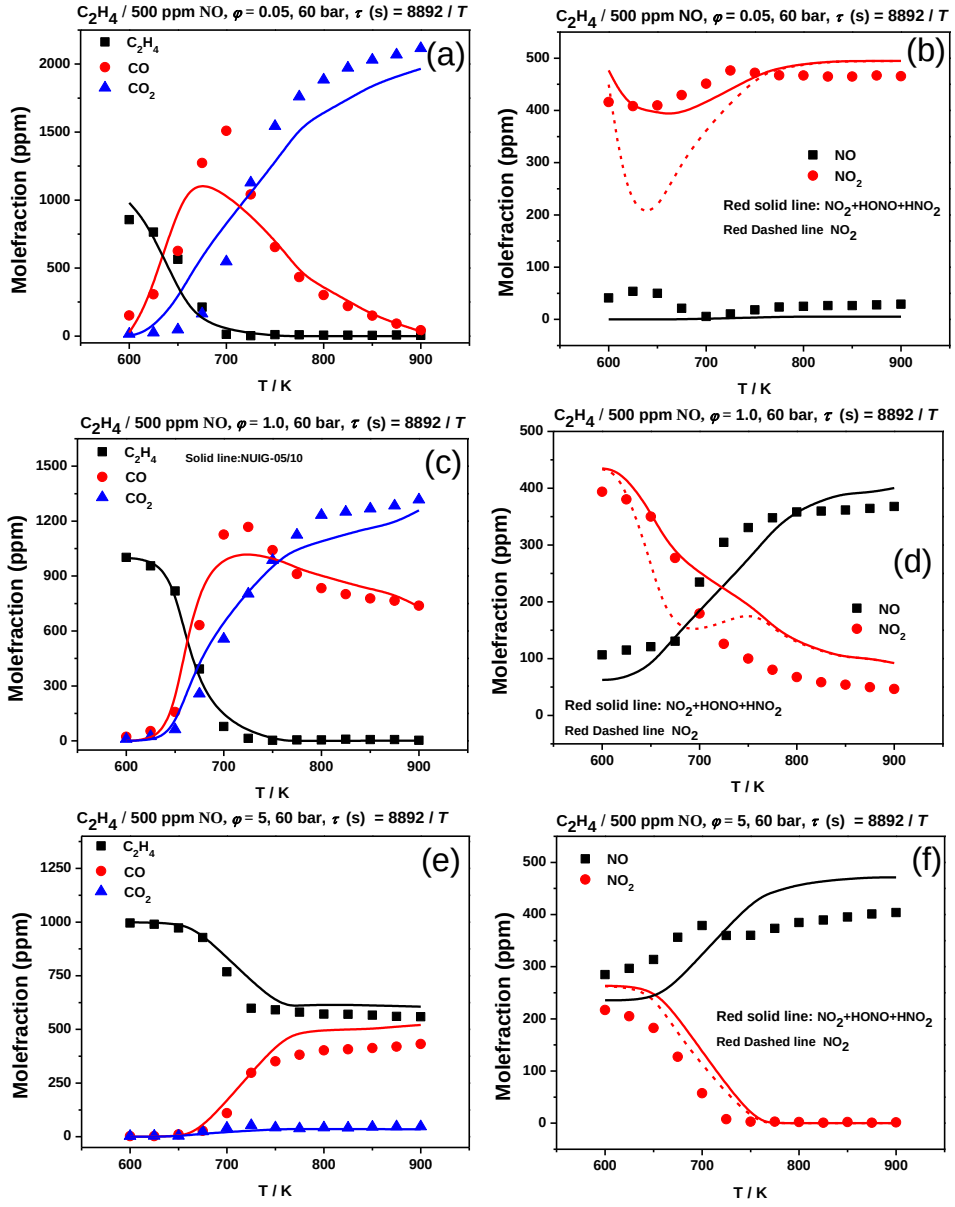

Figure CS23. Comparison of NUIGMech1.2 IDT predictions verses FR measurements of ethylene/NO [12].

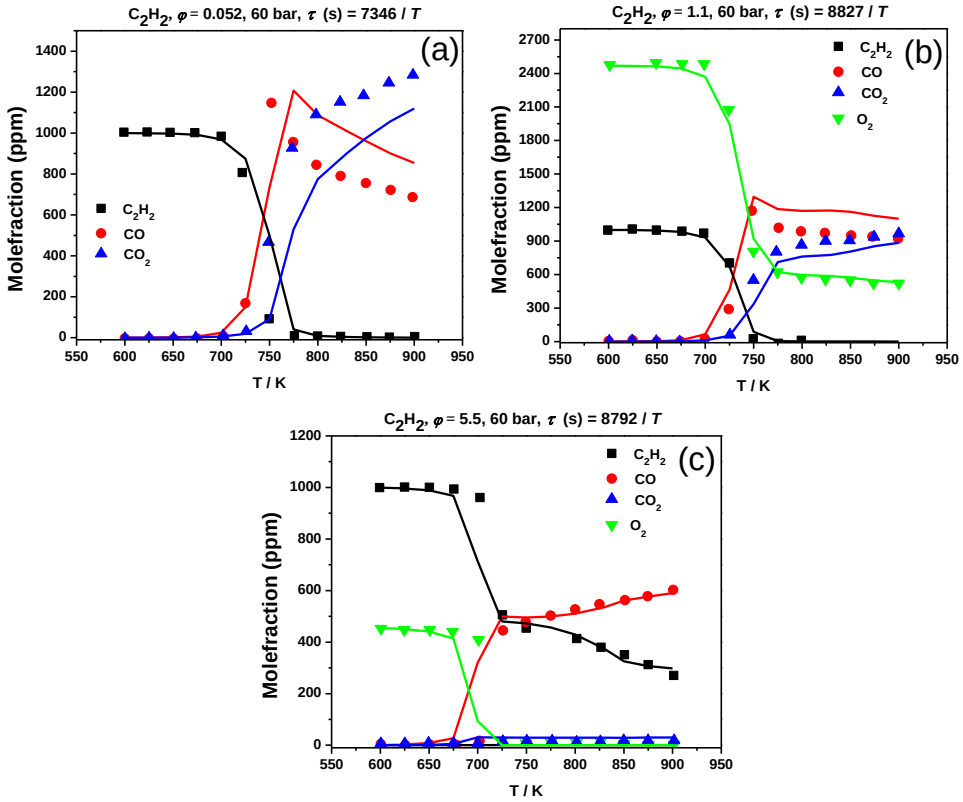

Figure S24. Comparison of NUIGMech1.2 IDT predictions verses FR measurements of acetylene [13].

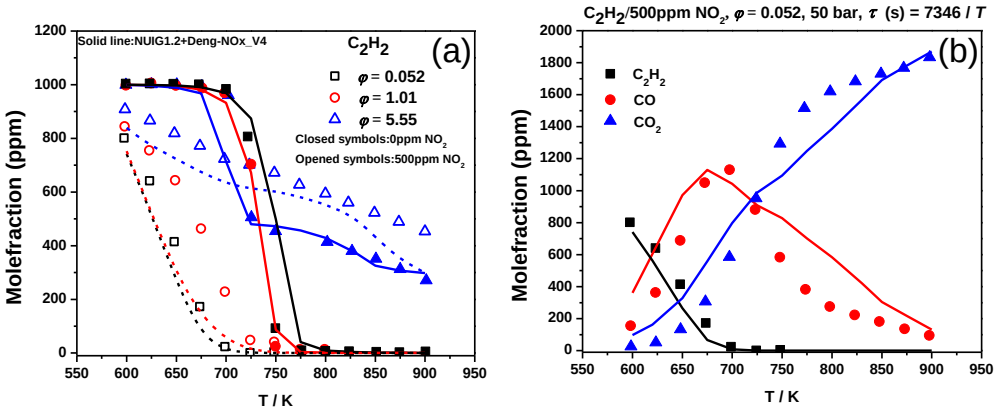

Figure CS25. Comparison of NUIGMech1.2 IDT predictions verses FR measurements of acetylene/NO[14].

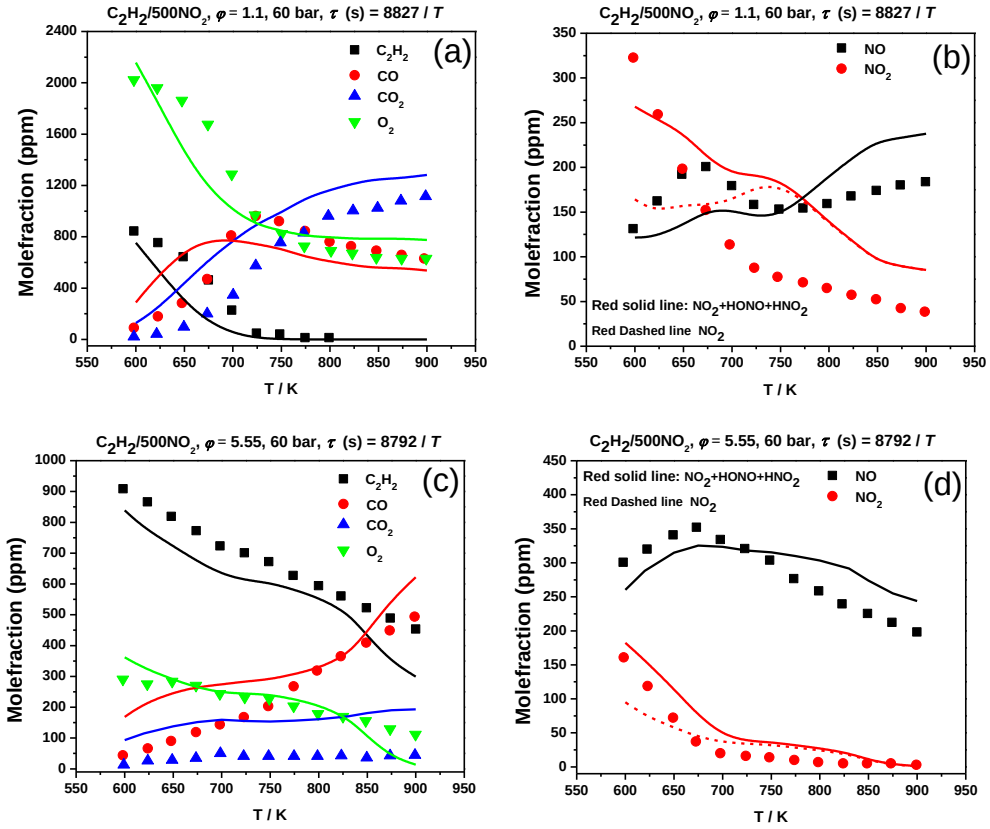

Figure CS26. Comparison of NUIGMech1.2 IDT predictions verses FR measurements of acetylene/NO [14].

Appendix C

Experimental conditions and IDT measurements

Table CS1. RCM IDT measurments for C_2H_6 at φ = 1.0 in 'air' and p_C = 20, 30 bar.

T_i (K)	p_i (bar)	T_C (K)	p_C (bar)	IDT_{total} (ms)	Diluent
353.15	0.768	925.0	19.97	56.62	20% N_2/80% Ar
353.05	0.768	927.0	20.17	57.16	20% N_2/80% Ar
373.15	0.767	969.0	19.92	11.96	20% N_2/80% Ar
373.15	0.767	967.0	19.82	13.06	20% N_2/80% Ar
333.15	1.129	885.0	29.93	121.3	20% N_2/80% Ar
333.13	1.129	881.0	29.49	137.6	20% N_2/80% Ar
343.15	1.14	904.0	29.77	62.35	20% N_2/80% Ar
343.15	1.14	907.0	30.16	58.08	20% N_2/80% Ar
353.15	1.161	929.0	30.66	22.88	20% N_2/80% Ar
353.15	1.161	926.0	30.26	23.87	20% N_2/80% Ar
363.15	1.153	945.0	29.7	11.45	20% N_2/80% Ar
363.15	1.153	950.0	30.35	12.04	20% N_2/80% Ar
363.15	1.153	948.0	30.05	12.68	20% N_2/80% Ar
373.15	1.158	969.0	30.12	5.94	20% N_2/80% Ar
373.23	1.158	965.0	29.6	5.74	20% N_2/80% Ar
373.15	1.158	970.0	30.27	5.95	20% N_2/80% Ar

Table CS2. ST IDT measurments for C_2H_6 at φ = 1.0 in 'air' and p_C = 20, 30 bar.

T_1 (K)	P_1 (bar)	T_5 (K)	p_5 (bar)	V_{Shock} (ms)	IDT_{total} (µs)
303.15	0.49184	1063	20.54	950.44	958.7
303.15	0.33898	1244.7	19.562	1063.89	110.6
303.15	0.82271	1006.7	30.45	913.43	1240 (PI)
303.15	0.82271	952.5	26.84	876.9	2347 (Lp_c)
303.15	0.73776	1062.3	30.67	948.93	859.8
303.15	0.73776	1063.5	30.85	950.8	670.2 (PI)
303.15	0.617	1137.5	29.85	997.98	327.6
303.15	0.51698	1221	29.034	1049.4	131.8
303.15	0.45141	1308.4	29.235	1101.7	50.4
303.15	0.40429	1343.6	27.625	1122.2	35
303.15	0.40429	1382.5	29.251	1144.6	22.81

Table CS3. RCM IDT measurments for C_2H_6 + 200 PPM NO_2 at φ = 1.0 in 'air' and p_C = 20, 30 bar.

T_i (K)	p_i (bar)	T_C (K)	p_C (bar)	IDT_{total} (ms)	Diluent
341.33	0.77	901.0	20.07	136.3	20% N_2/80% Ar
341.39	0.77	905.0	20.39	157.9	20% N_2/80% Ar
341.25	0.77	905.0	20.38	159.4	20% N_2/80% Ar
351.31	0.772	925.0	20.24	62.38	20% N_2/80% Ar
351.35	0.772	925.0	20.22	61.61	20% N_2/80% Ar
362.17	0.779	943.0	19.95	26.32	20% N_2/80% Ar
362.15	0.779	942.0	19.87	26.37	20% N_2/80% Ar
372.25	0.782	968.0	20.26	12.29	20% N_2/80% Ar
372.31	0.782	963.0	19.84	12.34	20% N_2/80% Ar
372.25	0.782	962.0	19.8	12.45	20% N_2/80% Ar
382.45	0.791	987.0	20.25	5.13	20% N_2/80% Ar
382.55	0.791	986.0	20.16	6.33	20% N_2/80% Ar
382.1	0.791	988.0	20.37	6.68	20% N_2/80% Ar
325.75	1.089	873.0	29.14	283.9	20% N_2/80% Ar
331.09	1.128	883.0	29.95	116.9	20% N_2/80% Ar
331.09	1.128	881.0	29.73	123.1	20% N_2/80% Ar
341.37	1.135	905.0	30.09	64.6	20% N_2/80% Ar

341.41	1.135	904.0	29.96	65.7	20% N_2/80% Ar
351.39	1.144	926.0	30.05	27.7	20% N_2/80% Ar
351.35	1.144	924.0	29.93	28.68	20% N_2/80% Ar
362.11	1.15	943.0	29.44	13.15	20% N_2/80% Ar
362.21	1.15	944.0	29.57	13.39	20% N_2/80% Ar
372.27	1.186	964.0	30.19	6.27	20% N_2/80% Ar
372.15	1.186	967.0	30.62	6.51	20% N_2/80% Ar
372.25	1.186	964.0	30.28	6.6	20% N_2/80% Ar

Table CS4. ST IDT measurments for C_2H_6 + 200 PPM NO_2 at φ = 1.0 in 'air' and p_C = 20, 30 bar.

T_1 (K)	P_1 (bar)	T_5 (K)	p_5 (bar)	V_{Shock} (ms)	IDT_{total} (µs)
303.15	0.51725	997.2	18.6	903.85	1867.4 (PI)
303.15	0.51725	1011.9	19.22	913.56	1633 (PI)
303.15	0.49565	1028.3	19.113	924.28	1302 (PI)
303.15	0.47551	1086	20.652	961.7	661.7
303.15	0.40696	1167.8	20.66	1013.1	229
303.15	0.34458	1248.4	20.12	1062.2	91.2
303.15	0.29442	1351.8	20.199	1122.6	36.78
303.15	0.829	944.2	26.312	868.13	3083 (PI)
303.15	0.829	992.1	29.455	900.43	1437 (PI)
303.15	0.728	1056.5	29.780	942.76	756.6
303.15	0.728	1067.3	30.510	949.72	662.4
303.15	0.599	1158.6	29.907	1007.3	211.4
303.15	0.504	1245.9	29.304	1060.5	82.4
303.15	0.438	1340.5	29.572	1116.1	36

Table CS5. RCM IDT measurments for C_2H_6 + 1000 PPM NO_2 at φ = 1.0 in 'air' and p_C = 20, 30 bar.

T_i (K)	p_i (bar)	T_C (K)	p_C (bar)	IDT_{total} (ms)	Diluent
323.15	0.7458	876	20.10	108.1	20% N_2/80% Ar
323.15	0.7458	879	20.38	113.2	20% N_2/80% Ar
323.15	0.7458	875	20.02	123	20% N_2/80% Ar
333.15	0.7549	893	19.91	55.14	20% N_2/80% Ar
333.15	0.7549	894	19.97	56.38	20% N_2/80% Ar
346.15	0.7569	927	20.30	19.98	20% N_2/80% Ar
346.15	0.7569	926	20.22	19.88	20% N_2/80% Ar
360.15	0.7640	951	19.86	7.18	20% N_2/80% Ar
360.15	0.7640	957	20.32	7.2	20% N_2/80% Ar
360.15	0.7640	953	20.04	7.08	20% N_2/80% Ar
360.15	0.7640	957	20.32	7.14	20% N_2/80% Ar
373.15	0.7660	989	20.58	2.64	20% N_2/80% Ar
373.15	0.7660	987	20.48	2.74	20% N_2/80% Ar
313.15	1.01850	859	28.98	105.9	20% N_2/80% Ar
313.15	1.08316	856	29.62	121.4	20% N_2/80% Ar
313.15	1.08316	855	29.53	127.3	20% N_2/80% Ar
323.15	1.11457	875	30.01	48.83	20% N_2/80% Ar
323.15	1.11457	875	29.94	48.2	20% N_2/80% Ar
333.15	1.12572	901	30.59	26.86	20% N_2/80% Ar
333.15	1.12572	898	30.31	27.73	20% N_2/80% Ar
333.15	1.12572	895	29.88	28.12	20% N_2/80% Ar
333.15	1.12572	895	29.87	28.08	20% N_2/80% Ar
346.15	1.14193	922	30.05	10.6	20% N_2/80% Ar
346.00	1.14193	927	30.68	10.95	20% N_2/80% Ar
346.09	1.14193	928	30.72	10.7	20% N_2/80% Ar
360.15	1.12673	952	29.48	3.74	20% N_2/80% Ar

360.15	1.12673	953	29.50	4.06	20% N_2/80% Ar

Table CS6. ST IDT measurments for C_2H_6 + 1000 PPM NO_2 at φ = 1.0 in 'air' and p_C = 20, 30 bar.

T_1 (K)	P_1 (bar)	T_5 (K)	p_5 (bar)	V_{Shock} (ms)	IDT_{total} (µs)
303.15	0.511	995.3	17.760	889	1515 (Low *p*c&dp/dt)
303.15	0.511	1050.5	20.032	925.09	732.8
303.15	0.453	1099.2	19.586	955.83	440
303.15	0.420	1176.6	20.989	1003.22	177.1
303.15	0.353	1274.5	20.811	1061.09	62.51
303.15	0.302	1367.9	20.533	1114.3	26.39
303.15	0.751	1004.1	26.614	895.3	1111(Low *p*c&dp/dt)
303.15	0.855	1007.4	30.503	897.42	1011
303.15	0.751	1053.4	29.608	926.93	591.7 (PI)
303.15	0.630	1146.3	29.798	984.85	192.2
303.15	0.530	1243.3	29.671	1042.87	67.35
303.15	0.453	1339.3	29.527	1098.2	26.18

Table CS7. RCM IDT measurments for C_2H_6 + 260 PPM NO_2 at φ = 0.5 in 91% dilute and p_C = 20, 30 bar.

T_i (K)	p_i (bar)	T_C (K)	p_C (bar)	IDT_{total} (ms)	Diluent
340.15	0.7042	938	19.85	130.8	59% N_2/41% Ar
340.15	0.7042	939	19.92	134	59% N_2/41% Ar
353.15	0.7194	965	19.83	36.84	59% N_2/41% Ar
353.15	0.7194	969	20.15	35.78	59% N_2/41% Ar
353.15	0.7194	968	20.06	35.22	59% N_2/41% Ar
363.15	0.7316	987	20.00	16.66	59% N_2/41% Ar
363.15	0.7316	987	19.99	16.46	59% N_2/41% Ar
376.15	0.7397	1018	20.16	6.59	59% N_2/41% Ar
376.15	0.7397	1017	20.10	6.66	59% N_2/41% Ar
385.15	0.7447	1042	20.43	3.8	59% N_2/41% Ar
385.15	0.7447	1038	20.19	3.62	59% N_2/41% Ar
385.15	0.7447	1038	20.19	3.52	59% N_2/41% Ar
328.15	1.04973	913	30.09	163.8	59% N_2/41% Ar
328.15	1.04973	908	29.60	148.2	59% N_2/41% Ar
328.15	1.04973	912	30.02	141.4	59% N_2/41% Ar
340.15	1.05479	938	29.72	47.75	59% N_2/41% Ar
340.15	1.05479	941	30.06	47.91	59% N_2/41% Ar
353.15	1.06695	968	29.75	18.12	59% N_2/41% Ar
353.15	1.06695	969	29.85	18.27	59% N_2/41% Ar
363.15	1.08215	992	30.13	8.71	59% N_2/41% Ar
363.15	1.08215	989	29.79	9.07	59% N_2/41% Ar
376.15	1.09938	1025	30.74	3.79	59% N_2/41% Ar
376.15	1.09938	1020	30.19	3.88	59% N_2/41% Ar
376.15	1.09938	1020	30.16	3.79	59% N_2/41% Ar

Table CS8. RCM IDT measurments for C_2H_6 + 2704 PPM NO_2 at φ = 0.5 in 91% dilute and p_C = 20, 30 bar.

T_i (K)	p_i (bar)	T_C (K)	p_C (bar)	IDT_{total} (ms)	Diluent
335.15	0.767	838	19.72	258.1	86% N_2/14% Ar
335.15	0.767	838	19.72	259.6	86% N_2/14% Ar
348.15	0.781	867	20.03	79.79	86% N_2/14% Ar
348.15	0.781	865	19.88	83.7	86% N_2/14% Ar
363.15	0.792	895	19.83	33	86% N_2/14% Ar
363.15	0.792	895	19.83	32.45	86% N_2/14% Ar
378.15	0.808	928	20.25	14.02	86% N_2/14% Ar

378.15	0.808	927	20.17	14.09	86% N_2/14% Ar
393.15	0.810	958	20.03	6.16	86% N_2/14% Ar
393.15	0.810	958	20.02	5.75	86% N_2/14% Ar
323.15	1.137	817	30.07	224.1	86% N_2/14% Ar
323.15	1.137	816	29.97	243.3	86% N_2/14% Ar
335.15	1.144	842	29.95	93.77	86% N_2/14% Ar
335.15	1.144	841	29.84	95.47	86% N_2/14% Ar
348.15	1.167	867	29.84	40.39	86% N_2/14% Ar
348.15	1.167	870	30.39	39.94	86% N_2/14% Ar
348.15	1.167	867	29.93	40.04	86% N_2/14% Ar
363.15	1.187	901	30.46	16.93	86% N_2/14% Ar
363.15	1.187	898	30.06	18.41	86% N_2/14% Ar
378.15	1.204	927	30.03	7.93	86% N_2/14% Ar
378.15	1.204	926	29.91	8.09	86% N_2/14% Ar
393.15	1.214	960	30.25	3.3	86% N_2/14% Ar
393.15	1.214	958	30.11	3.37	86% N_2/14% Ar

Table CS9. RCM IDT measurments for C_2H_6 + 5163 PPM NO_2 at φ = 0.5 in 91% dilute and p_C = 20, 30 bar.

T_i (K)	p_i (bar)	T_C (K)	p_C (bar)	IDT_{total} (ms)	Diluent
318.15	0.744	837	20.04	99.27	72% N_2/28% Ar
318.15	0.744	836	19.90	101.20	72% N_2/28% Ar
330.15	0.747	864	19.98	41.68	72% N_2/28% Ar
330.15	0.747	865	20.00	41.64	72% N_2/28% Ar
344.15	0.754	897	20.09	19.75	72% N_2/28% Ar
344.15	0.754	898	20.20	20.26	72% N_2/28% Ar
360.15	0.757	931	19.93	8.00	72% N_2/28% Ar
360.15	0.757	932	19.98	8.13	72% N_2/28% Ar
373.15	0.762	958	19.80	3.63	72% N_2/28% Ar
373.15	0.762	961	20.04	3.62	72% N_2/28% Ar
303.07	1.0872	806	29.92	165.9	72% N_2/28% Ar
303.09	1.0872	805	29.76	162.8	72% N_2/28% Ar
318.15	1.1115	841	30.40	42.33	72% N_2/28% Ar
318.15	1.1115	838	30.04	43.3	72% N_2/28% Ar
318.15	1.1115	838	30.00	44.72	72% N_2/28% Ar
330.15	1.1176	865	29.98	19.95	72% N_2/28% Ar
330.15	1.1176	864	29.85	20.44	72% N_2/28% Ar
330.15	1.1176	865	30.04	20.69	72% N_2/28% Ar
344.15	1.1267	897	30.06	10.67	72% N_2/28% Ar
344.15	1.1267	895	29.89	10.75	72% N_2/28% Ar
360.15	1.1318	932	29.89	4.36	72% N_2/28% Ar
360.15	1.1318	934	30.18	4.46	72% N_2/28% Ar

Table CS10. RCM IDT measurments for C_2H_6 + 200 PPM NO at φ = 1.0 in 'air' and p_C = 30 bar.

T_i (K)	p_i (bar)	T_C (K)	p_C (bar)	IDT_{total} (ms)	Diluent
324.15	1.11964	869	30.17	250.8	20% N_2/80% Ar
324.15	1.11964	869	30.07	244.3	20% N_2/80% Ar
338.15	1.12471	896	29.66	71	20% N_2/80% Ar
338.15	1.12471	894	29.49	72.13	20% N_2/80% Ar
348.15	1.13687	913	29.40	31.25	20% N_2/80% Ar
347.95	1.13687	915	29.66	32.1	20% N_2/80% Ar
365.15	1.16524	949	29.85	9.28	20% N_2/80% Ar
365.15	1.16524	949	29.86	8.93	20% N_2/80% Ar
375.15	1.18044	973	30.52	4.41	20% N_2/80% Ar
375.15	1.18044	969	30.01	4.6	20% N_2/80% Ar

375.15	1.18044	973	30.47	4.69	20% N_2/80% Ar

Table S11. RCM IDT measurments for C_2H_6 + 1000 PPM NO at φ = 1.0 in 'air' and p_C = 30 bar.

T_i (K)	p_i (bar)	T_C (K)	p_C (bar)	IDT_{total} (ms)	Diluent
313.15	1.06189	854	29.41	101.6	20% N2/80% Ar
313.15	1.06189	855	29.47	135	20% N2/80% Ar
313.15	1.06189	851	28.98	141.2	20% N2/80% Ar
324.15	1.10647	874	29.98	50.94	20% N2/80% Ar
324.15	1.10647	874	29.98	51.1	20% N2/80% Ar
338.15	1.11609	905	30.08	18.96	20% N2/80% Ar
338.15	1.11609	904	29.99	20.45	20% N2/80% Ar
348.15	1.12268	922	29.56	10	20% N2/80% Ar
348.15	1.12268	919	29.22	10.46	20% N2/80% Ar
365.15	1.15510	958	30.20	3.16	20% N2/80% Ar
365.15	1.15510	958	30.19	3.06	20% N2/80% Ar

Table CS12. RCM IDT measurments for C_2H_6 + 1000 PPM N_2O at φ = 1.0 in 'air' and p_C = 20, 30 bar.

T_i (K)	p_i (bar)	T_C (K)	p_C (bar)	IDT_{total} (ms)	Diluent
343.15	0.7691	901	19.89	232.1	20% N_2/80% Ar
343.15	0.7691	903	20.09	347	20% N_2/80% Ar
343.15	0.7691	902	19.98	337.7	20% N_2/80% Ar
354.15	0.7782	923	19.97	59.47	20% N_2/80% Ar
354.15	0.7782	922	19.91	59.15	20% N_2/80% Ar
365.15	0.7853	948	20.19	22	20% N_2/80% Ar
365.15	0.7853	946	20.06	22.31	20% N_2/80% Ar
378.15	0.7964	974	20.29	9.03	20% N_2/80% Ar
378.15	0.7964	972	20.14	8.79	20% N_2/80% Ar
388.15	0.7974	995	20.30	4.47	20% N_2/80% Ar
388.15	0.7974	995	20.27	4.54	20% N_2/80% Ar
343.15	1.13281	907	30.11	58.82	20% N_2/80% Ar
343.15	1.13281	903	29.53	64.77	20% N_2/80% Ar
343.15	1.13281	902	29.47	65.61	20% N_2/80% Ar
354.15	1.16321	929	30.61	24.8	20% N_2/80% Ar
354.15	1.16321	925	30.03	26.09	20% N_2/80% Ar
354.15	1.16321	924	29.99	27.01	20% N_2/80% Ar
365.15	1.17132	945	29.81	12.05	20% N_2/80% Ar
365.15	1.17132	945	29.85	12.28	20% N_2/80% Ar
378.15	1.18348	972	29.97	4.91	20% N_2/80% Ar
378.15	1.18348	971	29.80	4.94	20% N_2/80% Ar

Appendix C

References

[1] D. Fuquan, Z. Ningbo, W. Yingtao, Y. Jialong, T. Chenglong, L. Zhiming, Z. Hongtao, H. Zuohua, Experimental and Kinetic Study of the Promoting Effect of Nitrogen Dioxide on Ethane Autoignition in a Rapid Compression Machine, Energy Fuels, 34 (2020) 7509–7521.

[2] F. Deng, H. Xu, X. Liu, Y. Wu, H. Zheng, Z. Li, Effect of nitrogen dioxide addition on ethane auto-ignition at different pressures and equivalence ratios: Experiments and chemical kinetic modeling, Fuel, 285 (2021) 119042.

[3] X. Zhang, W. Ye, J.C. Shi, X.J. Wu, R.T. Zhang, S.N. Luo, Shock-Induced Ignition of Methane, Ethane, and Methane/Ethane Mixtures Sensitized by NO_2, Energy Fuels, 31 (2017) 12780–12790.

[4] F. Deng, Y. Pan, W. Sun, F. Yang, Y. Zhang, Z. Huang, An ignition delay time and chemical kinetic study of ethane sensitized by nitrogen dioxide, Fuel, 207 (2017) 389–401.

[5] E. Hu, Y. Chen, Z. Zhang, X. Li, Y. Cheng, Z. Huang, Experimental Study on Ethane Ignition Delay Times and Evaluation of Chemical Kinetic Models, Energy Fuels, 29 (2015) 4557–4566.

[6] F. Deng, Y. Zhang, W. Sun, W. Huang, Q. Zhao, X. Qin, F. Yang, Z. Huang, Towards a kinetic understanding of the NOx sensitization effect on unsaturation hydrocarbons: A case study of ethylene/nitrogen dioxide mixtures, Proc. Combust. Inst. 37(1) (2019) 719–726.

[7] F. Lecomte, P. Dagaut, S. Chevailler, M. Cathonnet, NO-Reduction by Ethane in a JSR at Atmospheric Pressure: Experimental and Kinetic Modeling, Combust. Sci. Technol., 150 (2000) 181–203.

[8] P. Dagaut, F. Lecomte, S. Chevailler, M. Cathonnet, The reduction of NO by ethylene in a jet-stirred reactor at 1 atm: experimental and kinetic modelling, Combust. Flame, 119 (1999) 494–504.

[9] P. Dagaut, O. Mathieu, A. Nicolle, G. Dayma, Experimental study and detailed kinetic modeling of the mutual sensitization of the oxidation of nitric oxide, ethylene, and ethane, Combust. Sci. Technol., 177 (2005) 1767–1791.

[10] J. Giménez-López, A. Millera, R. Bilbao, M.U. Alzueta, Experimental and kinetic modeling study of the oxy-fuel oxidation of natural gas, CH_4 and C_2H_6, Fuel, 160 (2015) 404–412.

[11] P. Glarborg, M.U. Alzueta, K. Dam-Johansen, J.A. Miller, Kinetic Modeling of Hydrocarbon/Nitric Oxide Interactions in a Flow Reactor, Combust. Flame, 115 (1998) 1–27.

[12] J. Giménez-López, M.U. Alzueta, C.T. Rasmussen, P. Marshall, P. Glarborg, High pressure oxidation of C_2H_4/NO mixtures, Proc. Combust. Inst., 33 (2011) 449–457.

[13] J. Gimenez-Lopez, C.T. Rasmussen, H. Hashemi, M.U. Alzueta, Y. Gao, P. Marshall, C.F. Goldsmith, P. Glarborg, Experimental and Kinetic Modeling Study of C_2H_2 Oxidation at High Pressure, Int. J. Chem. Kinet., 48 (2016) 724–738.

[14] P. Marshall, C. Leung, J. Gimenez-Lopez, C.T. Rasmussen, H. Hashemi, P. Glarborg, M. Abian, M.U. Alzueta, The $C_2H_2 + NO_2$ reaction: Implications for high pressure oxidation of C_2H_2/NOx mixtures, Proc. Combust. Inst., 37 (2019) 469–476.

[15] M. Baigmohammadi, V. Patel, S. Martinez, S. Panigrahy, A. Ramalingam, U. Burke, K.P. Somers, K.A. Heufer, A. Pekalski, H.J. Curran, A Comprehensive Experimental and Simulation Study of Ignition Delay Time Characteristics of Single Fuel C_1–C_2

Hydrocarbons over a Wide Range of Temperatures, Pressures, Equivalence Ratios, and Dilutions, Energy Fuels, 34 (2020) 3755–3771.

Appendix D

(Supplementary material for Chapter 7)

A Comprehensive Experimental and Simulation Study of the Ignition Delay Time Characteristics of Binary Blended Methane, Ethane, and Ethylene Over a Wide Range of Temperature, Pressure, Equivalence ratio, and Dilution

1. Design of experiments

The applied approach for designing the experiments has been already discussed in details by Baigmohammadi et al [1]. As seen in Table DS1, there are four factors (e.g. fuel composition; A, dilution level; B, equivalence ratio; C, and pressure; D) and 3 levels for each parameter (e.g. three pressure levels, 1.0, 20.0, and 40.0 bar) L_9 orthogonal array could be still employed for designing the required experiments.

Table DS1. Applied factors/variables and levels for designing the current experiments using the Taguchi method.

Factors / *Levels*	*Fuel composition (A)*	*Dilution (B)*	*Equivalence ratio (C)*	*Pressure (bar) (D)*
1	50% C_2H_4 + 50% C_2H_6	75%	0.5	1.0
2	30% C_2H_4 + 70% C_2H_6	85%	1.0	20.0
3	10% C_2H_4 + 90% C_2H_6	90%	2.0	40.0

2. Applied gases for making the mixtures

As mentioned in Section 7.2 of the manuscript, in the current study, the ignition delay time characteristics of methane + ethylene (CH_4 + C_2H_4), methane + ethane (CH_4 + C_2H_6), and ethane + ethylene (C_2H_6 + C_2H_4) have been investigated individually over a wide range of temperature, pressure, ethylene concentration, equivalence ratio, and dilution conditions. For those experiments performed at the combustion chemistry centre (C^3) of National University of Ireland, the studied alkane/alkene fuels with purity of 99.5% (Grade: 2.5) have been supplied through high pressure bottles which were provided from Air liquide UK. The other applied gases such as oxygen, argon, nitrogen, and helium in the experiments have been provided by BOC Ireland with purities of O_2 (99.99%), N_2 (99.99%), Ar (99.99%), and He (99.96%). However, for those experiments performed at the Physico-Chemical Fundamentals of Combustion (PCFC) of

RWTH Aachen University, the studied C_2H_4 + C_2H_6 with purity of 99.95% (Grade: 3.5) were provided by Westfalen AG. Also, the other applied gases such as oxygen, argon, and nitrogen, in the experiments have been provided by Westfalen AG and Praxair with purities of O_2 ((≥99.995%), N_2 ((≥99.95%), and Ar (≥99.996%).

3. Low–pressure shock tube

As known, shock-tube is a robust facility for getting the ignition delay time data under low and high pressures and high temperature (≥ 1000 K) regime and IDTs ≤ 2 ms. Thus, the NUIG–LPST has been used for getting the IDT data under 1 bar operating condition. The applied NUIG-LPST has been previously documented and explained in details [2,3]. Here, only general information of the facility is presented in Table DS2. In the current study, helium was used as the primary driver gas for doing the experiments unless there was a need to reduce the incident shock velocity through adding nitrogen to helium for the tailored cases.

Table DS2. Specifications of the applied low–pressure shock tube.

Total length	6.33 m	
Section	Length (m)	Diameter (mm)
Driver	0.53	520
Driven	5.8	102.4
Material	Stainless steel	
Controlling system	Sharp edges arrow	
Diaphragm's material	Polycarbonate/Polyester	
Diaphragm's thickness	105–120 μm (nominal)	

Further, as presented in Table DS3, the incident shock velocity has been measured using five piezoelectric pressure transducers located on the driven section of the LPST and then the shock velocity at the end-wall was extrapolated through a fitted line to the collected shock velocities over these pressure transducers. All conditions such as the compressed gas temperature (T_5) and pressure (p_5) behind the reflected shock were calculated using the shock velocity at the end-wall using "Gaseq" software [4]. Also, the ignition delay times of the studied mixtures were measured using photomultiplier (PMT) systems equipped with CH^* filter (CWL: 430 nm ± 10 FWHM; Thorlabs) installed on the side wall of the shock tube's endcap due to very weak pressure signals. Also, it is demonstrated in Figure DS1 that the ignition delay time is defined as a maximum gradient in pressure ($\left(\frac{dP}{dt}\right|_{max}$) or CH^* ($\left(\frac{dCH^*}{dt}\right|_{max}$) behind the reflected shock. Further, for increasing the accuracy of experiments and reducing the scattered points, all measured pressures behind the reflected shocks have been forced to be restricted to ±0.05 bar of the target pressure of 1 bar. In this regard, all pressure versus time data including oscilloscope files

(software is accessible through https://www.tiepie.com/en/oscilloscope-software) and the experimentalist spreadsheets related to the current studied conditions in NUIG–LPST are provided as Supplementary data files with the online version of the paper.

Table DS3. Number of installed PCB sensors on the driven section of LPST shock tube and their distances from the end-wall.

Sensors	Distance from the end wall (cm)
PCB#1	3.0
PCB#2	23.7
PCB#3	36.6
PCB#4	49.5
PCB#5	189.0

4. High–pressure shock–tube

The NUIG–HPST has been used for getting the IDT data for 20 and 40 bar operating conditions. As already mentioned, the applied NUIG-HPST has been previously documented and explained in details [5] and ,here, only general information of the facility is presented in Table DS4 Table. In the current study, helium was used as the primary driver gas for doing the experiments unless there was a need to reduce the incident shock velocity through adding nitrogen to helium for the tailored cases.

Table DS4. Specifications of the applied high-pressure shock tube.

Total length	9.1 m	
Section	Length (m)	Diameter (mm)
Driver	3.0	63.5
Middle	0.04	63.5
Driven	5.7	63.5
Material	Stainless-steel (1.4571/316Ti and 1.4462/F51)	
Controlling system	Double-diaphragm type	
Diaphragm's material	Aluminium (1050 H14)	
Diaphragm's thickness	0.8~2 mm; according to target pressure	
Pre-scoring the diaphragms	0.2~1.1 mm; according to target pressure and the diaphragms' thickness	

Further, as presented in Table DS5, the incident shock velocity has been measured using six piezoelectric pressure transducers located on the driven section of the HPST and then the shock velocity at the end-wall was extrapolated through a fitted line to the collected shock velocities over these pressure transducers. All conditions such as the compressed gas temperature (T_5) and pressure (p_5) behind the reflected shock were calculated using the shock velocity at the end-wall through "Gaseq" software [4]. Also, the ignition delay times of the studied normal mixtures (pressure-time profiles) with diluent concentration of ≤ 85% were recorded using a Kistler 603B transducer mounted on the end–wall, while for the mixtures with 90% dilution, the ignition delay

times were measured using photodiode array detector (PDA) or photomultiplier (PMT) systems equipped with CH^* filter (CWL: 430 nm ± 10 FWHM; Thorlabs) installed on the side wall of the shock tube's endcap due to very weak signals of the Kistler pressure transducer. For increasing the accuracy of experiments and reducing the scattered points, all measured pressures behind the reflected shocks have been forced to be restricted to ±0.5 bar of the target pressures (20 and 40 bar). Moreover, all of the experimental results have been divided into two main categories of the acceptable and the affected by facility, so that the affected results have been marked using "☒" symbol. Thus, these data wouldn't be reliable to be applied for evaluating the performance of a chemical mechanism. In this regard, all of the pressure versus time data including oscilloscope files (software is accessible through https://www.tiepie.com/en/oscilloscope-software) and the experimentalist spreadsheets related to the current studied conditions in NUIG–HPST are provided as Supplementary data files with the online version of the paper.

Table DS5. Number of installed PCB sensors on the driven section of the shock-tube and their distances from the end-wall.

Sensors	Distance from the end wall (cm)
PCB#1	1.0
PCB#2	15.0
PCB#3	29.0
PCB#4	57.0
PCB#5	85.0
PCB#6	116.50

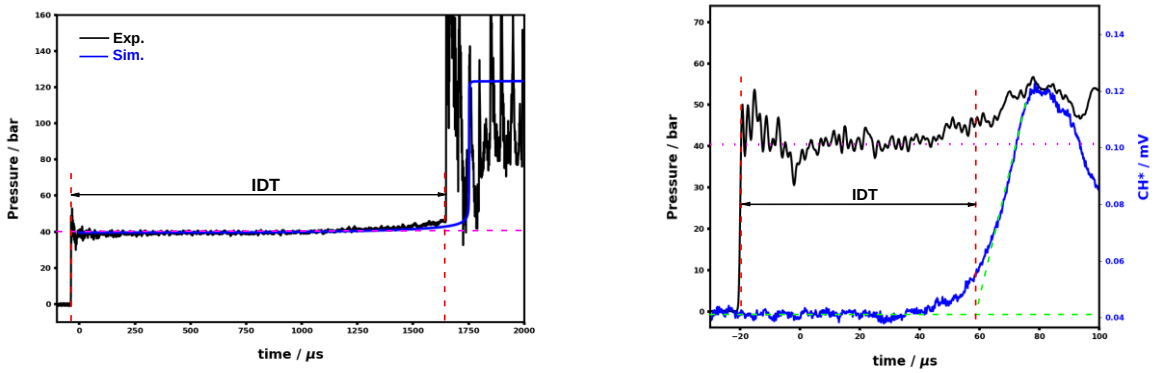

(a) **(b)**

Figure DS1. Applied definition for measuring IDT in the NUIG-shock tube: (a) using Kistler pressure trace mounted on the end–wall of the endcap; (b) using PDA–CH^* trace mounted on the side wall of the end-cap.

5. Rapid compression machine

The rapid compression machine is a common facility for getting the ignition delay time data under high pressure and low-to-moderate temperature regime (< 1000 K). In the current study,

the experiments have been taken using NUIG– and PCFC–RCMs. According to the previous studies [6,7], the experimental IDTs have been modelled using the adiabatic core assumption in which the non-adiabatic condition can be compensated by imposing the volume–time profiles of the same non–reactive mixtures to calculations. Thus, general information about each facility have been presented in the following subsections.

5.1.NUIG-RCM

The general specifications of NUIG–RCM have been presented in Table DS6. The details of the facility has been already documented and explained in details [5,6,8–11]. In this facility, the ignition delay time of the normal studied mixtures (diluent concentration = 75%) and the pressure-time histories of their relevant non-reactive mixtures were recorded using a Kistler 6045A transducer mounted on the reaction chamber. However, the ignition delay times of the mixtures with 85% and 90% dilution percent and the post–compression pressures of 20 and 40 bar, were reordered using both the Kistler and photomultiplier (PMT) equipped with CH^* filter (CWL: 430 nm ± 10 FWHM; Thorlabs) due to vague signal of the Kistler pressure transducer under these conditions. Also, as shown in Figure DS2, the ignition delay time is defined as a maximum gradient in pressure ($\left(\frac{dP}{dt}\right|_{max}$) or CH^* ($\left(\frac{dCH^*}{dt}\right|_{max}$) after compressing the studied mixtures. Subsequently, the post compression temperatures (T_C) were calculated by assuming isentropic compression condition using Gaseq software [4]. Similar to the applied procedure in NUIG–HPST, all measured post compression pressures (p_C) have been forced to be restricted to ±0.5 bar of the target pressures due to increasing the accuracy of experiments and also reducing the scattered points. Moreover, unlike the standard operating procedure in NUIG–HPST, all the experimental results have been repeated at least three times and the repeatability of all reported IDTs was ≥ 90%. In this regard, all pressure versus time data including pressure/volume profiles and the experimentalist spreadsheets related to the studied conditions in NUIG–RCM have been provided as the Supplementary files with the online version of the paper.

Table DS6. Specifications of NUIG–RCM.

Parameter	Value
Bore size of the reaction chamber (cm)	3.820
Volume of the reaction chamber (cm^3)	33.191
Piston's velocity (U_p) (cm/s)	934.0 ~ 1294.0
Pistons' stroke length (cm)	16.817
Piston's type	Flat head with the crevice
Type	Twin-counter pistons

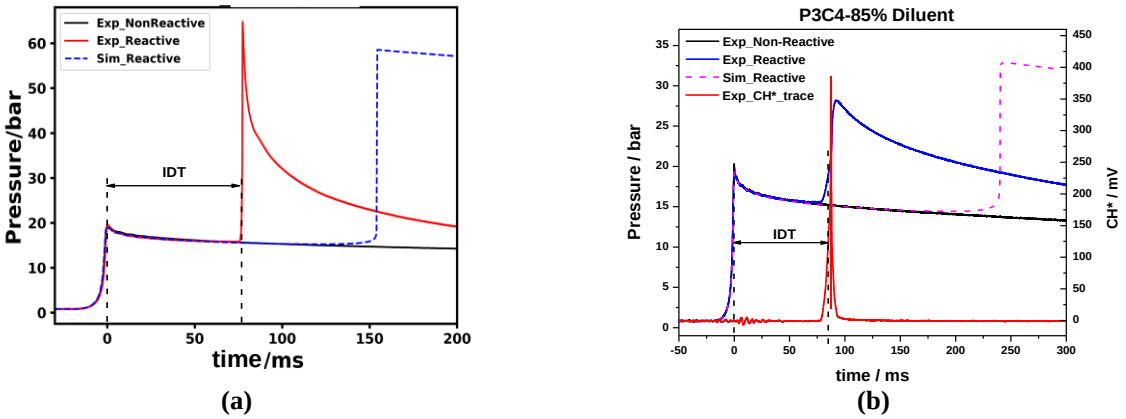

Figure DS2. Applied definition for measuring IDT in the NUIG–RCM: (a) using Kistler pressure trace; (b) using both pressure and PMT–CH* trace mounted on the side wall of the reaction chamber.

5.2.PCFC–RCM

The PCFC–RCM is a well-known facility which has been already introduced properly in literature. As presented in Table DS7, this facility is constructed from a single–piston mechanism which is driven pneumatically and stopped hydraulically at the end of compression. Similar to the applied piston in NUIG–RCM, the crevice piston design has been applied in the PCFC–RCM. In the facility, the pressure–time profile during the compression and the post–compression processes and the initial temperature in the reaction chamber were monitored and controlled using a Kistler 6125C pressure transducer and type 'T' thermocouple, respectively. In this regard, the detail information about the construction, measurement procedure, and the applied sensors in the study have been already presented in [12]. As the same process explained in section 7.2.1, the compressed mixture's temperature (T_5) was calculated using the isentropic compression formulation of Gaseq software [4]. According to the procedure explained by Ramalingam et al. [7], the reproducibility of evaluated IDTs and also the experimental uncertainty of the compressed mixture's temperature for the measured conditions in the study were within 15% and ±5 K, respectively. In this regard, the related experimental data to PCFC–RCM facility and the volume-time profiles are reported in the Supplementary files.

Table DS7. Specifications of PCFC–RCM.

Parameter	Value
Bore size of the reaction chamber (cm)	5.0
Volume of the reaction chamber (cm^3)	506.0 – 551.0
Piston's velocity (U_p) (cm/s)	1667.0
Pistons' stroke length (cm)	25.0
Piston's type	Flat head with the crevice
Type	Single piston

Appendix D

6. Data acquisition system

As shown in Table DS8, in the current study, many sensors have been used in the four applied facilities at C^3–NUIG and PCFC–RWTH Aachen University to measure the required parameters. In this regard, all installed sensors in NUIG–L/HPST which had been used for measuring the incident shock velocities and the ignition delay times, were synchronized and connected to two TiePie Handyscope HS4 oscilloscopes [13]. Also, all generated signals from the installed sensors on NUIG–RCM including the Kistler pressure transducer, the position sensors, and the photomultiplier were synchronized and collected using a PicoScope 5443B [14].

Table DS8. Applied sensors and detectors for measuring during the current study (NUIG-HPST/RCM and PCFC–RCM).

Sensor	Company	Model	Accuracy	Resolution
Pressure sensor transducer	Kistler	603B	≤±1.0 % FSO; linearity	NA
Pressure sensor transducer	Kistler	6045A	≤±0.4 % /FSO; linearity	NA
Pressure sensor transducer	Kistler	6125C	≤±0.4 % /FSO; linearity	NA
Piezoelectric pressure sensor	PCB	113B24	≤±1.0 % FS; Non-linearity	±0.035 KPa
Digital Absolut pressure transmitter	Kurt J Lesker	ACG & HCG	0.25% of FS	±0.01 Torr
Digital Absolut pressure transmitter	Edwards	600 Barocel	0.15% of reading	±0.01 of FS
Digital Absolut pressure transmitter	MKS	Baratron 121AA-0100D	0.5% of reading	±0.01 Torr
Digital Absolut pressure transmitter	MKS	Baratron 121AA-01000D	0.5% of reading	±0.1 Torr
Digital Absolut pressure transmitter	MKS	Baratron 121AA-05000B	0.5% of reading	±0.5 Torr
Analog vacuum pressure gauge	Edwards	Pirani-PRE10K	NA	±2 of reading scale
Thermocouples and Controller	Radionics	T-type	±1.0 ˚C	±0.1 ˚C
Photodetector	Thorlabs	PDA36A/PDA55	NA	NA
Photomultiplier	EMI Electronics	9924P	NA	NA

7. Uncertainty analysis

For getting a detailed understanding about the uncertainty of the experimental tests of the current study, the following subsections have been presented. In fact, these subsections try to analytically explain the effect of some important factors including pressure, temperature, and equivalence ratio on the total uncertainty of the experimental results. It seems that the output of the section could provide a good clue for better analysing and evaluating the quality of the experimental data.

7.1.Equivalence ratio

In the following lines, it is tried to somehow evaluate probable uncertainties which may be included in equivalence ratios of the applied mixtures of the current study.

Appendix D

Making a mixture:

Fuel: $F = P_F = \sum_{i=1}^{n} P_i \rightarrow \sigma_F = \sqrt{\sum_{i=1}^{n} {\sigma_i}^2}$ (DS-1)

where, P_i and σ_i are absolute pressure of i–th component in the fuel mixture and uncertainty of each absolute pressure of i–th component in the fuel mixture, respectively. Because, in the current study, binary–fuel mixtures have been studied, thus:

Fuel: F = (p_{F1}±σF1) + (p_{F2}±σF2) and Oxygen: O = p_{O2}±σO2.

Equivalence ratio: $\varphi = \frac{\left(\frac{F}{O}\right)_{real}}{\left(\frac{F}{O}\right)_{Stoi}} \rightarrow \left(\frac{O}{F}\right)_{Stoi} = Cte \rightarrow \varphi = Cte\left(\frac{F_1+F_2}{O}\right)_{real} \rightarrow \sigma_\varphi = \left(\frac{\partial\varphi}{\partial F_1}\right)\sigma_{F_1} + \left(\frac{\partial\varphi}{\partial F_2}\right)\sigma_{F_2} + \left(\frac{\partial\varphi}{\partial O}\right)\sigma_O$ (DS-2)

$$\varphi = Cte\left(\frac{\sum_{i=1}^{n} p_{Fi}}{p_{O_2}}\right)_{real} \rightarrow \frac{\partial\varphi}{\partial p_{F_n}} = \frac{1}{O} \rightarrow \frac{\partial\varphi}{\partial p_{O_2}} = -\frac{\sum_{i=1}^{n} p_{F_i}}{\left(p_{O_2}\right)^2}$$

$$\sigma_\varphi = \frac{\partial\varphi}{\partial p_{F_1}} \cdot \sigma_{p_{F_1}} + \frac{\partial\varphi}{\partial p_{F_2}} \cdot \sigma_{p_{F_2}} + \frac{\partial\varphi}{\partial p_{F_3}} \cdot \sigma_{p_{F_3}} + \cdots + \frac{\partial\varphi}{\partial p_{F_n}} \cdot \sigma_{p_{F_n}} + \left(-\frac{\sum_{i=1}^{n} p_{F_i}}{\left(p_{O_2}\right)^2}\right)\sigma_{p_{O_2}}$$

If we assume that there is no correlation between measurements of $\sigma_i\sigma_j = 0$

$${\sigma_\varphi}^2 = \left(\frac{\partial\varphi}{\partial p_{F_1}} \cdot \sigma_{p_{F_1}}\right)^2 + \left(\frac{\partial\varphi}{\partial p_{F_2}} \cdot \sigma_{p_{F_2}}\right)^2 + \left(\frac{\partial\varphi}{\partial p_{F_3}} \cdot \sigma_{p_{F_3}}\right)^2 + \cdots + \left(\frac{\partial\varphi}{\partial p_{F_n}} \cdot \sigma_{p_{F_n}}\right)^2 + \left(\left(-\frac{\sum_{i=1}^{n} p_{F_i}}{\left(p_{O_2}\right)^2}\right)\sigma_{p_{O_2}}\right)^2$$

$$\sigma_\varphi = \sqrt{\left(\frac{1}{p_{O_2}} \cdot \sigma_{p_{F_1}}\right)^2 + \left(\frac{1}{p_{O_2}} \cdot \sigma_{p_{F_2}}\right)^2 + \left(\frac{1}{p_{O_2}} \cdot \sigma_{p_{F_3}}\right)^2 + \cdots + \left(\frac{1}{p_{O_2}} \cdot \sigma_{p_{F_n}}\right)^2 + \left(\left(-\frac{\sum_{i=1}^{n} p_{F_i}}{\left(p_{O_2}\right)^2}\right)\sigma_{p_{O_2}}\right)^2}$$

$$\sigma_\varphi = \sqrt{\left(\frac{\sum_{i=1}^{n} {\sigma_{F_i}}^2}{\left(p_{O_2}\right)^2}\right) + \left(\left(-\frac{\sum_{i=1}^{n} p_{F_i}}{\left(p_{O_2}\right)^2}\right)\sigma_{p_{O_2}}\right)^2} = \sqrt{\left(\frac{\sigma_{F_1}}{p_{O_2}}\right)^2 + \left(\frac{\sigma_{F_2}}{p_{O_2}}\right)^2 + \left(\left(-\frac{p_F}{{p_{O_2}}^2}\right)\sigma_{p_{O_2}}\right)^2} = \frac{Cte}{\left(p_{O_2}\right)^2}\sqrt{\left(p_{O_2}\right)^2\sigma_{F_1}^2 + \left(p_{O_2}\right)^2\sigma_{F_2}^2 + p_F^2{\sigma_{p_{O_2}}}^2}$$ (DS-3)

Based on the above analysis, the average uncertainty of the equivalence ratios is $\overline{\sigma_\varphi} = \pm 5 \times 10^{-3}$.

7.2.Diluent concentration

For determining the uncertainty of diluent concentration in the studied mixtures the following formulations are presented:

$$[D] = \frac{p_i}{RT_i}$$ (DS-4)

$$\sigma_{[D]} = \frac{\partial[D]}{\partial p_i}\sigma_{p_i}$$ (DS-5)

$$\frac{\partial[D]}{\partial p_i} = \frac{1}{RT_i}$$ (DS-6)

Appendix D

Because, in the study, all mixtures have been prepared under 303 K, so the Eq. (6) would be as follows:

$$\frac{\partial[D]}{\partial P_i} = 3.96961 \times 10^{-4}$$

Therefore, the worst uncertainty in diluent concentration in the studied mixtures is related to cases with 90% diluent in a mixture with total pressure of 4000 Torr which yields $\sigma_{[D]} = \pm 1.05848\ \frac{mol}{m^3} = \pm 1.05848 \times 10^{-5}\ \frac{mol}{10^5.m^3} \approx \pm 0.56\%\ [D]$

For calculating the uncertainty in concentration of each species under the compressed conditions, the following formulations are presented:

$$[D] = \frac{p_{c,[D]}}{RT_c} \tag{DS-7}$$

$$\sigma_{[D]} = \sqrt{\left(\frac{\partial[D]}{\partial p_{c,[D]}}\sigma_{p_{c,[D]}}\right)^2 + \left(\frac{\partial[D]}{\partial T_c}\sigma_{T_c}\right)^2} \tag{DS-8}$$

$$\sigma_{[D]} = \sqrt{\left(\frac{1}{RT_c}\sigma_{p_{c,[D]}}\right)^2 + \left(-\frac{p_{c,[D]}}{RT_c^2}\sigma_{T_c}\right)^2} = \frac{1}{8.314 \times T_c^2}\sqrt{\left(T_c\sigma_{p_{c,[D]}}\right)^2 + \left(p_{c,[D]}\sigma_{T_c}\right)^2} \tag{DS-9}$$

7.3.IDTs in Shock tube

If the following equations, for determining total uncertainty of the measured ignition delay times in NUIG–L/HPST, it is assumed:

$$p_c = p(p_1, V_s, \varphi, T_1);\ T_c = T(T_1, V_s, \varphi)$$

As shown by Petersen et al. [15], one could assume that:

$$T_C = \frac{T_1[2(\gamma_1 - 1)M^2 + (3 - \gamma_1)][(3\gamma_1 - 1)M^2 - 2(\gamma_1 - 1)]}{(\gamma_1 + 1)^2 M^2};\ M = \frac{V_s}{\sqrt{\gamma_1 R T_1}};\ V_s = \frac{\Delta z}{\Delta t} \tag{DS-10}$$

$$\sigma_{V_s} = \sqrt{\left(\frac{\partial V_s}{\partial(\Delta z)}\sigma_{\Delta z}\right)^2 + \left(\frac{\partial V_s}{\partial(\Delta t)}\sigma_{\Delta t}\right)^2} = \sqrt{\left(\frac{1}{\Delta t}\sigma_{\Delta z}\right)^2 + \left(-\frac{\Delta z}{(\Delta t)^2}\sigma_{\Delta t}\right)^2} \tag{DS-11}$$

$$\sigma_{T_c} = \sigma_T = \frac{\partial T_c}{\partial M}\sigma_M = \left(T_1\left[\left(\frac{4(3\gamma_1^2 - 4\gamma_1 + 1)}{(\gamma_1 + 1)^2}\right)M + \left(\frac{4(\gamma_1 - 1)(3 - \gamma_1)}{(\gamma_1 + 1)^2}\right)M^{-3}\right]\right)\frac{\sigma_{V_s}}{\sqrt{\gamma_1 R T_1}} \tag{DS-12}$$

$$p_c = \frac{P_1[2\gamma_1 M^2 - (\gamma_1 - 1)][(3\gamma_1 - 1)M^2 - 2(\gamma_1 - 1)]}{2(\gamma_1 + 1) + M^2(\gamma_1^2 - 1)};\ \sigma_{p_c} = \sigma_p = \frac{\partial p_c}{\partial M}\sigma_M$$
$$= \left(p_1\left[\frac{12M^5\gamma^4 - 4M^5\gamma^3 + 48M^3\gamma^3 + 32M^3\gamma^2 - 12M^5\gamma^2 + 4M^5\gamma - 16M^3\gamma - 20M\gamma^3 + 4M\gamma^2 + 20M\gamma - 4M\gamma^4}{(M^2\gamma^2 - M^2 + 2\gamma + 2)^2}\right]\right)\frac{\sigma_{V_s}}{\sqrt{\gamma_1 R T_1}} \tag{DS-13}$$

Here, it was supposed that the effect of changing in equivalence ratio on γ is negligible. Here, it is supposed that the maximum $\sigma_{\Delta t}$ which is related to TiePie Handyscope HS4 Oscilloscope is ±1

μs, and, $\sigma_{\Delta z}$ is ±0.001 m. Now, if it could be assumed the defined ignition delay time (IDT) could be correlated as follows, then:

$$\begin{aligned}\tau_{IDT} \cong A\cdot exp\left(\frac{B}{T}\right)p^m\varphi^n[D]^q \rightarrow \partial\tau = \frac{\partial\tau}{\partial T}\cdot\partial T + \frac{\partial\tau}{\partial p}\cdot\partial p + \frac{\partial\tau}{\partial\varphi}\cdot\partial\varphi + \frac{\partial\tau}{\partial[D]}\cdot\partial[D] \rightarrow (\sigma_\tau)^2 \\ = \left(\frac{\partial\tau}{\partial T}\cdot\partial T\right)^2 + \left(\frac{\partial\tau}{\partial p}\cdot\partial p\right)^2 + \left(\frac{\partial\tau}{\partial\varphi}\cdot\partial\varphi\right)^2 + \left(\frac{\partial\tau}{\partial[D]}\cdot\partial[D]\right)^2 + 2\left(\frac{\partial\tau}{\partial T}\cdot\frac{\partial\tau}{\partial p}\cdot\partial T\partial p\right) \\ + 2\left(\frac{\partial\tau}{\partial T}\cdot\frac{\partial\tau}{\partial\varphi}\cdot\partial T\partial\varphi\right) + 2\left(\frac{\partial\tau}{\partial\varphi}\cdot\frac{\partial\tau}{\partial p}\cdot\partial\varphi\partial p\right) + 2\left(\frac{\partial\tau}{\partial T}\cdot\frac{\partial\tau}{\partial[D]}\cdot\partial T\partial[D]\right) \\ + 2\left(\frac{\partial\tau}{\partial p}\cdot\frac{\partial\tau}{\partial[D]}\cdot\partial p\partial[D]\right) + 2\left(\frac{\partial\tau}{\partial\varphi}\cdot\frac{\partial\tau}{\partial[D]}\cdot\partial\varphi\partial[D]\right)\end{aligned} \quad \text{(DS-14)}$$

Now, one assumes that there is no correlation between measurements of (p, T, and φ), so the above equation would be followed by:

$$\begin{aligned}(\sigma_{\tau,i})^2 = \left(\frac{\partial\tau}{\partial T}\cdot\partial T\right)^2 + \left(\frac{\partial\tau}{\partial p}\cdot\partial p\right)^2 + \left(\frac{\partial\tau}{\partial\varphi}\cdot\partial\varphi\right)^2 + \left(\frac{\partial\tau}{\partial[D]}\cdot\partial[D]\right)^2 + 2\underbrace{\left(\frac{\partial\tau}{\partial T}\cdot\frac{\partial\tau}{\partial p}\cdot\partial T\partial p\right)}_{=0} + 2\underbrace{\left(\frac{\partial\tau}{\partial T}\cdot\frac{\partial\tau}{\partial\varphi}\cdot\partial T\partial\varphi\right)}_{=0} \\ + 2\underbrace{\left(\frac{\partial\tau}{\partial\varphi}\cdot\frac{\partial\tau}{\partial p}\cdot\partial\varphi\partial p\right)}_{=0} + 2\underbrace{\left(\frac{\partial\tau}{\partial T}\cdot\frac{\partial\tau}{\partial[D]}\cdot\partial T\partial[D]\right)}_{\neq 0} + 2\underbrace{\left(\frac{\partial\tau}{\partial p}\cdot\frac{\partial\tau}{\partial[D]}\cdot\partial p\partial[D]\right)}_{\neq 0} \\ + 2\underbrace{\left(\frac{\partial\tau}{\partial\varphi}\cdot\frac{\partial\tau}{\partial[D]}\cdot\partial\varphi\partial[D]\right)}_{=0}\end{aligned} \quad \text{(DS-15)}$$

One could re–write the above equation as follows:

$$(\sigma_{\tau,i})^2 = \left(\frac{\partial\tau}{\partial T}\cdot\sigma_T\right)^2 + \left(\frac{\partial\tau}{\partial p}\cdot\sigma_p\right)^2 + \left(\frac{\partial\tau}{\partial\varphi}\cdot\sigma_\varphi\right)^2 + \left(\frac{\partial\tau}{\partial[D]}\cdot\sigma_{[D]}\right)^2 + 2\left(\frac{\partial\tau}{\partial T}\cdot\frac{\partial\tau}{\partial[D]}\cdot\sigma_T\sigma_{[D]}\right) + 2\left(\frac{\partial\tau}{\partial p}\cdot\frac{\partial\tau}{\partial[D]}\cdot\sigma_p\sigma_{[D]}\right) \quad \text{(DS-16)}$$

$$\frac{\partial\tau}{\partial T} = A\cdot\left(-\frac{B}{T^2}\cdot\exp\left(\frac{B}{T}\right)p^m\varphi^n[D]^q\right) \quad \text{(DS-17)}$$

$$\frac{\partial\tau}{\partial P} = A\cdot\left(m\cdot\exp\left(\frac{B}{T}\right)p^{m-1}\varphi^n[D]^q\right) \quad \text{(DS-18)}$$

$$\frac{\partial\tau}{\partial\varphi} = A\cdot\left(n\cdot\exp\left(\frac{B}{T}\right)p^m\varphi^{n-1}[D]^q\right) \quad \text{(DS-19)}$$

$$\frac{\partial\tau}{\partial[D]} = A\cdot\left(q\cdot\exp\left(\frac{B}{T}\right)p^m\varphi^n[D]^{q-1}\right) \quad \text{(DS-20)}$$

$$\begin{aligned}(\sigma_{\tau,i})^2 = A^2\cdot\left(\left(-\frac{B}{T^2}\cdot\exp\left(\frac{B}{T}\right)p^m\varphi^n[D]^q\right)\cdot\sigma_T\right)^2 + A^2\cdot\left(\left(m\cdot\exp\left(\frac{B}{T}\right)p^{m-1}\varphi^n[D]^q\right)\cdot\sigma_p\right)^2 \\ + A^2\cdot\left(\left(n\cdot\exp\left(\frac{B}{T}\right)p^m\varphi^{n-1}[D]^q\right)\cdot\sigma_\varphi\right)^2 + A^2\cdot\left(\left(q\cdot\exp\left(\frac{B}{T}\right)p^m\varphi^n[D]^{q-1}\right)\cdot\sigma_{[D]}\right)^2 \\ - 2A^2\left(\frac{Bq}{T^2}\cdot\exp\left(\frac{2B}{T}\right)p^{2m}\varphi^{2n}[D]^{2q-1}\right)\cdot\rho_{T[D]}\sigma_T\sigma_{[D]} + 2A^2\left(qm\cdot exp\left(\frac{2B}{T}\right)p^{2m-1}\varphi^{2n}[D]^{2q-1}\right) \\ \cdot\rho_{p[D]}\sigma_p\sigma_{[D]}\end{aligned} \quad \text{(DS-21)}$$

$$\sigma_{\tau,i} \cong A\cdot\sqrt{\begin{array}{l}\left(\left(-\frac{B}{T^2}\cdot\exp\left(\frac{B}{T}\right)p^m\varphi^n[D]^q\right)\cdot\sigma_T\right)^2 + \left(\left(m\cdot\exp\left(\frac{B}{T}\right)p^{m-1}\varphi^n[D]^q\right)\cdot\sigma_p\right)^2 + \left(\left(n\cdot\exp\left(\frac{B}{T}\right)p^m\varphi^{n-1}[D]^q\right)\cdot\sigma_\varphi\right)^2 + \\ \left(\left(q\cdot\exp\left(\frac{B}{T}\right)p^m\varphi^n[D]^{q-1}\right)\cdot\sigma_{[D]}\right)^2 - 2\left(\frac{Bq}{T^2}\cdot exp\left(\frac{2B}{T}\right)p^{2m}\varphi^{2n}[D]^{2q-1}\right)\cdot\rho_{T[D]}\sigma_T\sigma_{[D]} + 2\left(qm\cdot exp\left(\frac{2B}{T}\right)p^{2m-1}\varphi^{2n}[D]^{2q-1}\right)\cdot\rho_{p[D]}\sigma_p\sigma_{[D]}\end{array}} \quad \text{(DS-22)}$$

$$\rho_{ij}\sigma_i\sigma_j = \sigma_{ij} = \sum_{ij} f(i,j)(x_i - \bar{x_i})(x_j - \bar{x_j}) \quad \text{(DS-23)}$$

The uncertainty of the measured ignition delay time in shock tube could be acceptably estimated using the above equation. As seen in the above expression, the uncertainty parameter is changing by changing in the compressed temperature and pressure, and equivalence ratio, so that it is not a constant parameter during the experimental tests. Thus, it should be calculated specifically for

each case. Therefore, regarding Eq. (DS-22) and Table DS9, specific uncertainty for each fuel according to its specific temperature, pressure, and equivalence ratio could be estimated.

Table DS9. Correlation variables of the studied experimental datasets for different fuels in shock tubes.

$\tau_{IDT} = 10^{A} \cdot exp\left(\frac{B}{T}\right) P^{m} \varphi^{n} [D]^{q}$								
Fuel		A	B	m	n	q	R^2	Adj R^2
$CH_4 + C_2H_4$	50% + 50%	-8.189	14359.44	-0.268	0.293	0.0	0.993	0.993
	70% + 30%	-13.96	-552.43	-13.16	1.371	12.77	0.996	0.995
	90% + 10%	-15.02	-5834.91	-16.69	1.625	16.36	0.997	0.997
$C_2H_6 + C_2H_4$	50% + 50%	-12.14	7982.58	-7.49	-0.177	6.88	0.971	0.968
	70% + 30%	-20.50	-11369.34	-21.85	3.283	22.48	0.992	0.992
	90% + 10%	-15.27	1437.05	-12.64	0.770	12.48	0.999	0.999

7.4.Rapid compression machine

As shown in the previous section, the uncertainty of each experimental point is changing by varying temperature, pressure, and mixture composition, so that it is not identical during IDT measurement experimental tests. Therefore, for doing the uncertainty analysis for the studied RCM regimes, the same procedure performed for shock–tube is followed and relevant correlations between parameters and IDTs have been evaluated as shown in Table DS10. As already mentioned by Weber et al. [16], using Monte Carlo analysis or independent parameters methodology doesn't led to significant change in the calculated uncertainties. Therefore, like the performed uncertainty analysis for NUIG–HPST, it is supposed that there is no correlation between p_C, T_C and φ which can affect measured ignition delay time in the rapid compression machine. However, the correlation between [D] and p_C, T_C is taken in to account according to Eq. (DS-23). In this regard, the effect of temperature on the measured ignition delay time has been correlated through fitting an exponential equation to the experimental IDT data, and then the individual effect of pressure on the measured ignition delay time has been estimated using the applied approach by Weber et al. [16]. Also, the effect of each individual parameter such as equivalence ratio (0.5-2.0) and dilution (75%-90%) on the simulated ignition delay times has been correlated using fitted equations to the experimentally measured ignition delay times. Therefore, the following formulations could be proposed to estimate available uncertainties in the measured independent parameters and consequently the measured ignition delay times:

$$\frac{\partial T_C}{\partial P_C} = \frac{W\left(\frac{b}{a} exp\left[\frac{bT_0}{a}\right] T_0 \left[\frac{P_C}{P_0}\right]^{\frac{1}{a}}\right)}{bP_C\left(W\left(\frac{b}{a} exp\left[\frac{bT_0}{a}\right] T_0 \left[\frac{P_C}{P_0}\right]^{\frac{1}{a}}\right) + 1\right)} \quad \text{(DS-24)}$$

where, W, T_0, and P_0 are Lambert's W function, initial temperature, and initial pressure in the reaction chamber, respectively. In Eq. (DS-24), "a", "b", and $\frac{\partial T_C}{\partial P_C}$ were calculated using a Python code developed by Weber et al. [16].

$$\frac{\partial \tau_{IDT}}{\partial P_C} = \frac{\partial \tau_{IDT}}{\partial T_C} \cdot \frac{\partial T_C}{\partial P_C} = \frac{\partial \tau_{IDT}}{\partial T_C}\ (from\ \text{Table10}) \cdot \frac{W\left(\frac{b}{a} exp\left[\frac{bT_0}{a}\right] T_0 \left[\frac{P_C}{P_0}\right]^{\frac{1}{a}}\right)}{bP_C\left(W\left(\frac{b}{a} exp\left[\frac{bT_0}{a}\right] T_0 \left[\frac{P_C}{P_0}\right]^{\frac{1}{a}}\right) + 1\right)} \quad \text{(DS-25)}$$

$$\left(\sigma_{\tau,i}\right)^2 = \left(\frac{\partial \tau}{\partial T} \cdot \sigma_T\right)^2 + \left(\frac{\partial \tau}{\partial p} \cdot \sigma_p\right)^2 + \left(\frac{\partial \tau}{\partial \varphi} \cdot \sigma_\varphi\right)^2 + \left(\frac{\partial \tau}{\partial [D]} \cdot \sigma_{[D]}\right)^2 + 2\left(\frac{\partial \tau}{\partial T} \cdot \frac{\partial \tau}{\partial [D]} \cdot \sigma_T \sigma_{[D]}\right) + 2\left(\frac{\partial \tau}{\partial p} \cdot \frac{\partial \tau}{\partial [D]} \cdot \sigma_p \sigma_{[D]}\right) \quad \text{(DS-26)}$$

$$\tau_{IDT} = f(T_C, p_C, \varphi, [D]) \rightarrow \sigma_{\tau_{IDT}} = \sqrt{\left(\frac{\partial \tau_{IDT}}{\partial T_C} \cdot \sigma_{T_C}\right)^2 + \left(\frac{\partial \tau_{IDT}}{\partial p_C} \cdot \sigma_{p_C}\right)^2 + \left(\frac{\partial \tau_{IDT}}{\partial \varphi} \cdot \sigma_\varphi\right)^2 + \left(\frac{\partial \tau_{IDT}}{\partial [D]} \cdot \sigma_{[D]}\right)^2 + 2\left(\frac{\partial \tau_{IDT}}{\partial T_C} \cdot \frac{\partial \tau_{IDT}}{\partial [D]} \cdot \sigma_{T_C} \sigma_{[D]}\right) + 2\left(\frac{\partial \tau_{IDT}}{\partial p_C} \cdot \frac{\partial \tau_{IDT}}{\partial [D]} \cdot \sigma_{p_C} \sigma_{[D]}\right)} \quad \text{(DS-27)}$$

By substituting correlations from Table DS10 and Eqs. (DS-23) and (DS-25) into Eq. (DS-27), the uncertainty of the measured ignition delay times in RCM regime would be calculated based on a Python code developed by Weber et al. [16].

Table DS10. Correlation variables of the studied experimental datasets for different fuels in RCMs.

$\tau_{IDT} = 10^A \cdot exp\left(\frac{B}{T}\right) \varphi^n [D]^q$							
Fuel		A	B	n	q	R^2	Adj R^2
$CH_4 + C_2H_4$	50% + 50%	-33.82	16398.20	-14.03	10.79	0.995	0.994
	70% + 30%	-5.88	31697.98	-3.11	-4.22	0.996	0.996
	90% + 10%	204.42	126728.67	-63.23	-107.3	0.997	0.997
$C_2H_6 + C_2H_4$	50% + 50%	14.92	42743.02	15.25	-15.40	0.998	0.998
	70% + 30%	-118.99	-8476.95	-20.06	49.20	0.991	0.990
	90% + 10%	186.68	131240.51	-60.44	-101.1	0.975	0.971

8. Pressure profiles of the applied rapid compression machines (RCMs)

The reactive and non–reactive pressure profiles of the applied rapid compression machines including NUIG–RCM and PCFC–RCM for the studied cases alongside the simulation profiles are shown in the following figures. Here, it should be noted that all the simulations were performed using NUIGMech1.0 mechanism, otherwise, it is mentioned in caption or legend of figures.

Appendix D

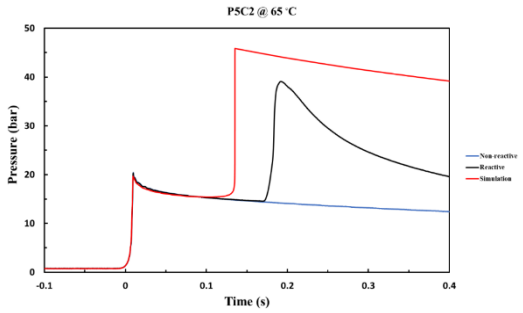

Figure DS3. Pressure history of tested reactive and non–reactive mixtures of P5C2 case alongside the simulation's profile for initial temperature of 338 K.

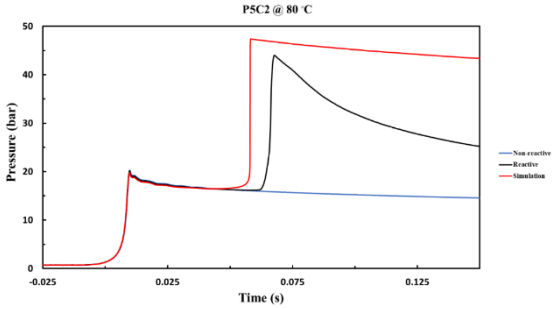

Figure DS4. Pressure history of tested reactive and non–reactive mixtures of P5C2 case alongside the simulation's profile for initial temperature of 353 K.

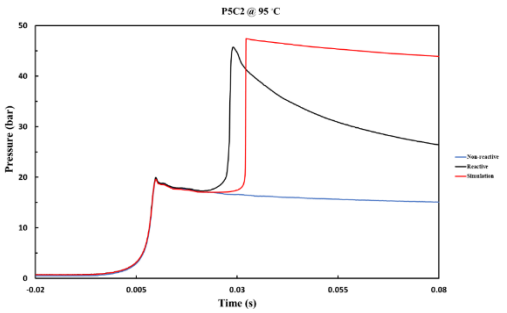

Figure DS5. Pressure history of tested reactive and non–reactive mixtures of P5C2 case alongside the simulation's profile for initial temperature of 368 K.

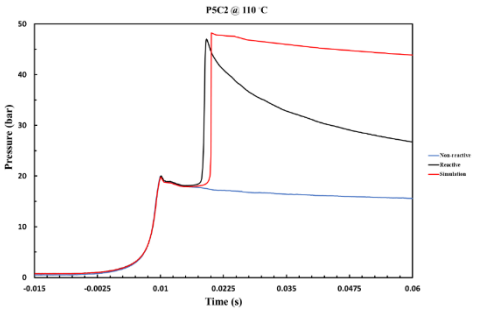

Figure DS6. Pressure history of tested reactive and non–reactive mixtures of P5C2 case alongside the simulation's profile for initial temperature of 383 K.

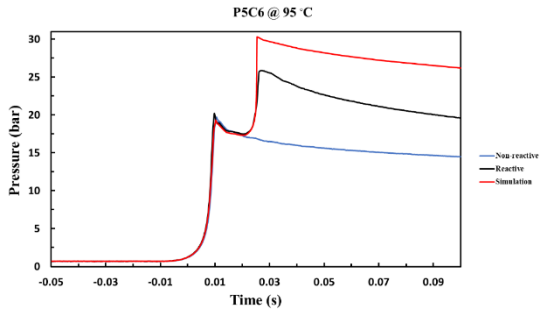

Figure DS7. Pressure history of tested reactive and non–reactive mixtures of P5C6 case alongside the simulation's profile for initial temperature of 368 K.

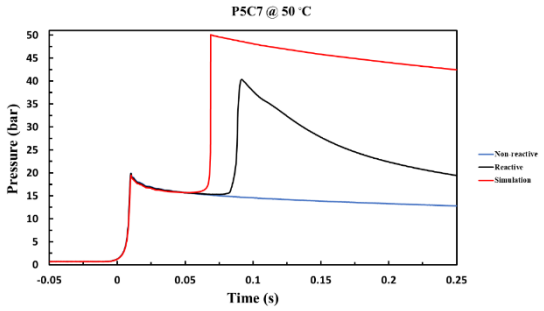

Figure DS8. Pressure history of tested reactive and non–reactive mixtures of P5C7 case alongside the simulation's profile for initial temperature of 323 K.

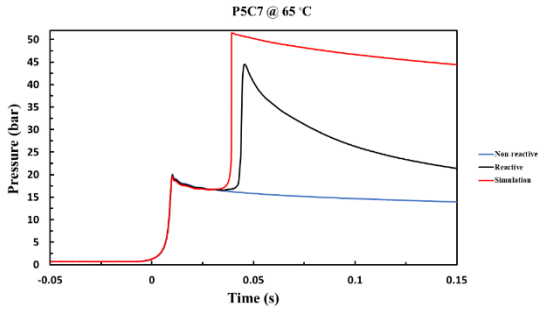

Figure DS9. Pressure history of tested reactive and non–reactive mixtures of P5C7 case alongside the simulation's profile for initial temperature of 338 K.

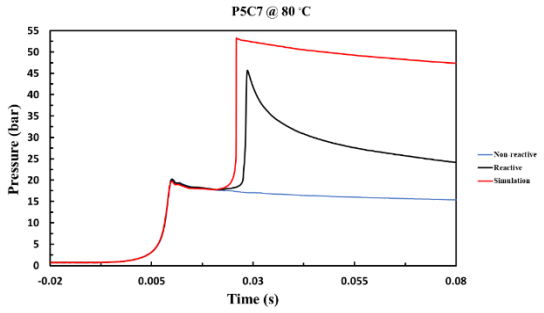

Figure DS10. Pressure history of tested reactive and non–reactive mixtures of P5C7 case alongside the simulation's profile for initial temperature of 353 K.

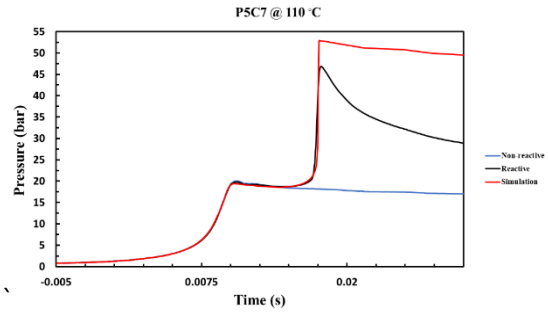

Figure DS11. Pressure history of tested reactive and non–reactive mixtures of P5C7 case alongside the simulation's profile for initial temperature of 383 K.

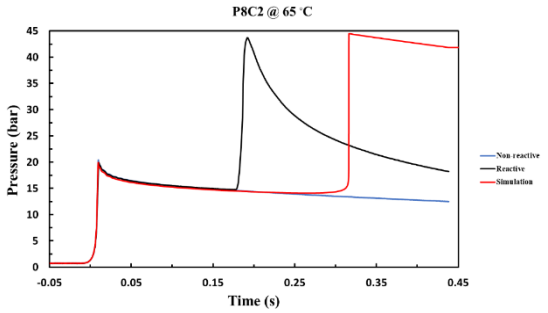

Figure DS12. Pressure history of tested reactive and non–reactive mixtures of P8C2 case alongside the simulation's profile for initial temperature of 338 K.

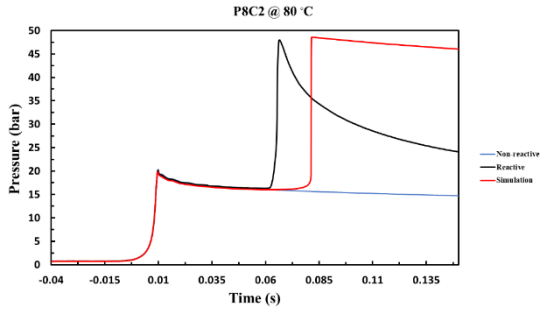

Figure DS13. Pressure history of tested reactive and non–reactive mixtures of P8C2 case alongside the simulation's profile for initial temperature of 353 K.

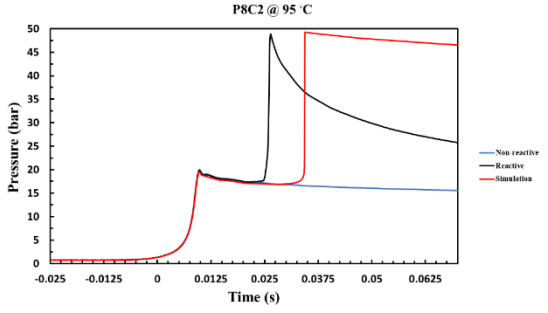

Figure DS14. Pressure history of tested reactive and non–reactive mixtures of P8C2 case alongside the simulation's profile for initial temperature of 368 K.

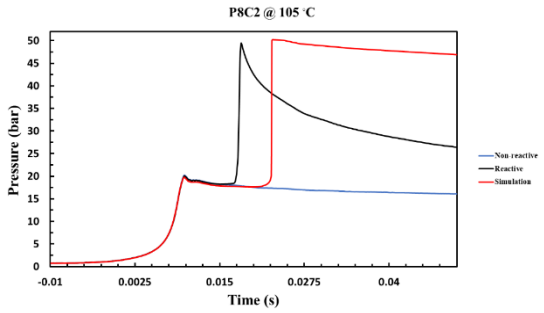

Figure DS15. Pressure history of tested reactive and non–reactive mixtures of P8C2 case alongside the simulation's profile for initial temperature of 378 K.

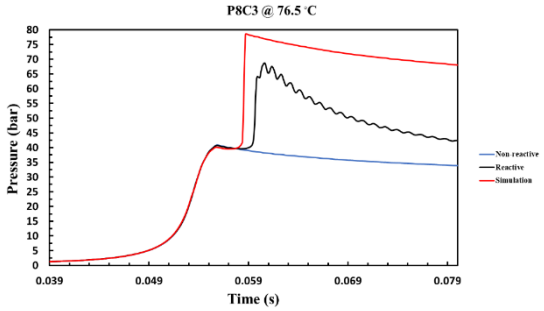

Figure DS16. Pressure history of tested reactive and non–reactive mixtures of P8C3 case alongside the simulation's profile for initial temperature of 349.5 K.

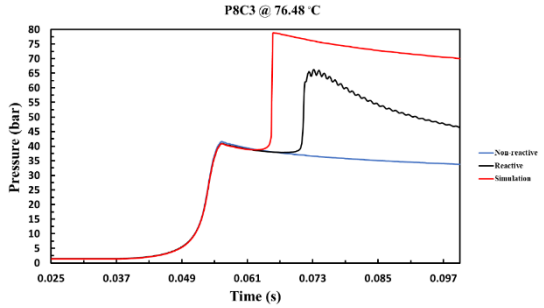

Figure DS17. Pressure history of tested reactive and non–reactive mixtures of P8C3 case alongside the simulation's profile for initial temperature of 349.6 K.

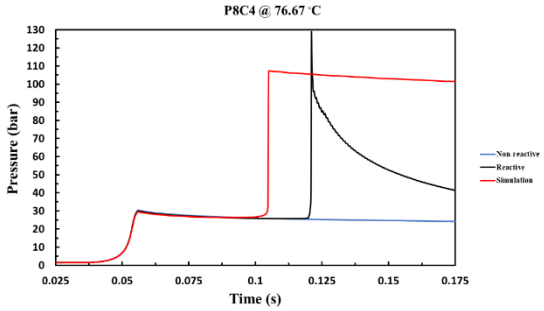

Figure DS18. Pressure history of tested reactive and non–reactive mixtures of P8C4 case alongside the simulation's profile for initial temperature of 349.8 K.

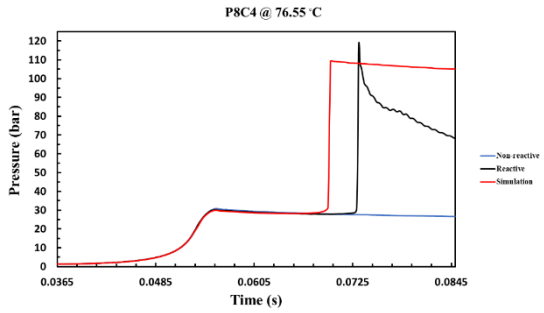

Figure DS19. Pressure history of tested reactive and non–reactive mixtures of P8C4 case alongside the simulation's profile for initial temperature of 349.7 K.

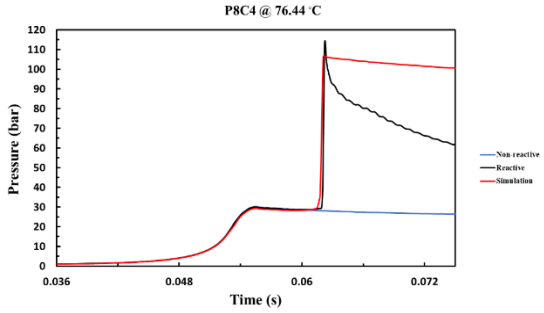

Figure DS20. Pressure history of tested reactive and non–reactive mixtures of P8C4 case alongside the simulation's profile for initial temperature of 349.6 K.

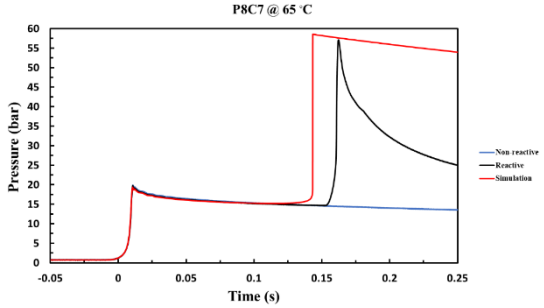

Figure DS21. Pressure history of tested reactive and non–reactive mixtures of P8C7 case alongside the simulation's profile for initial temperature of 338 K.

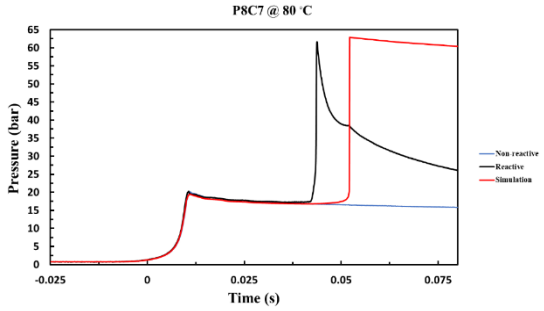

Figure DS22. Pressure history of tested reactive and non–reactive mixtures of P8C7 case alongside the simulation's profile for initial temperature of 353 K.

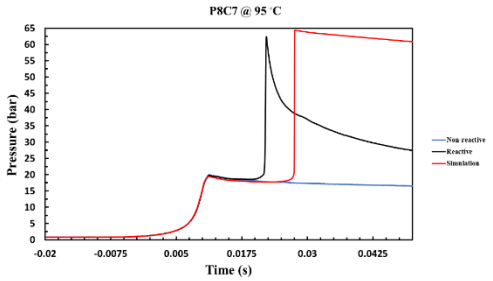

Figure DS23. Pressure history of tested reactive and non–reactive mixtures of P8C7 case alongside the simulation's profile for initial temperature of 368 K.

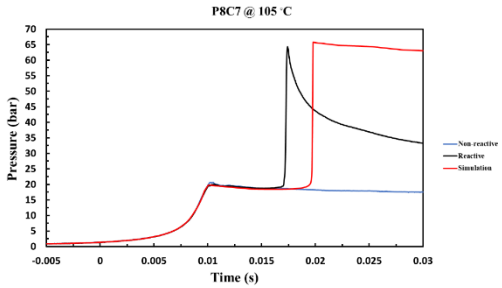

Figure DS24. Pressure history of tested reactive and non–reactive mixtures of P8C7 case alongside the simulation's profile for initial temperature of 378 K.

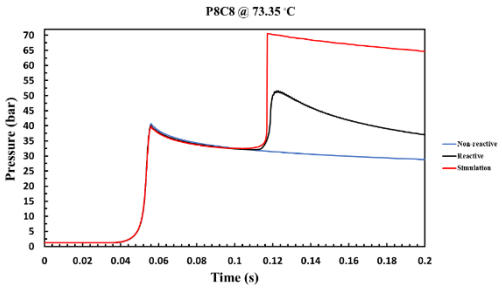

Figure DS25. Pressure history of tested reactive and non–reactive mixtures of P8C8 case alongside the simulation's profile for initial temperature of 346.5 K.

9. Comparing the performances of NUIGMech1.0 versus other available mechanisms

In this regard, the performances of chemical mechanisms presented in have been evaluated and compared over a wide range of conditions studied in the article.

Table DS11. Applied chemical mechanisms.

No	Mechanism	Number of reactions	Number of species	Comments
1	AramcoMech 3.0	3037	581	Released at 2018; [17]
2	AramcoMech 2.0	2716	493	Released at 2016; [10,18–23]
3	AramcoMech 1.3	1542	253	Released at 2013; [10]
4	DTU–C_3	142	1308	Released at 2019; [24]
5	CRECK	1941	114	Released at 2020; [25]
6	UCSD	268	57	Released at 2016; [26]
7	GRI 3.0	325	53	Released at 2000; [27]
8	JetSurF 2.0	348	2163	Released at 2010; [28]
9	FFCM-1	291	38	C_1-C_2; Low temperature reactions are not included; released at 2016; [29]

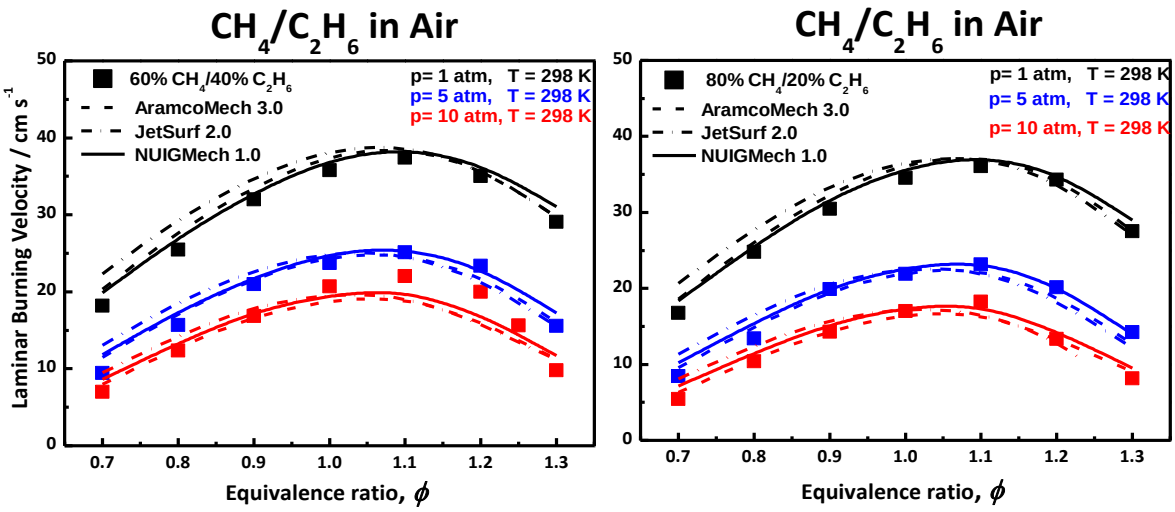

Figure DS26. Performance of NUIGMech1.0 for predicting LBVs in comparison to AramcoMech 3.0 and JetSurf II. [30].

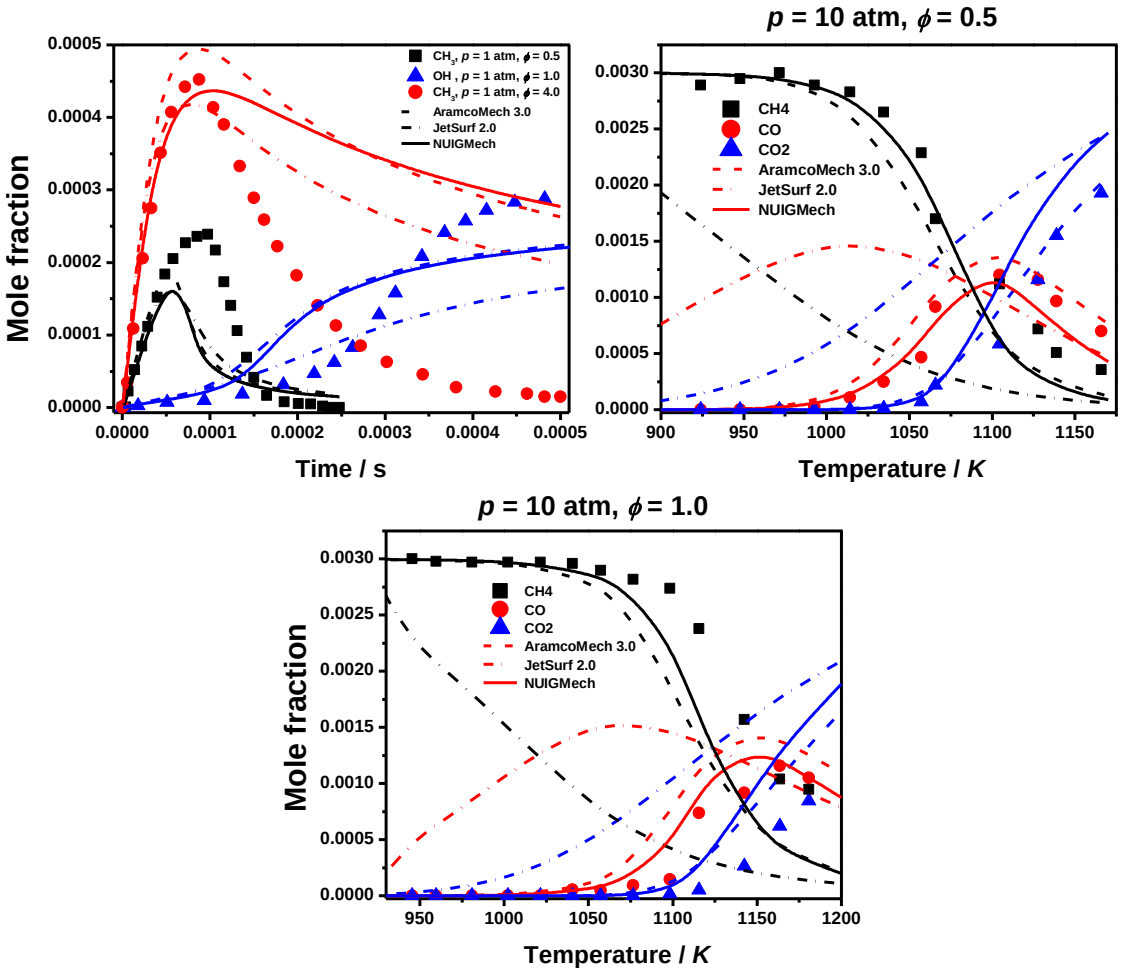

Figure DS27. Performance of NUIGMech1.0 for predicting methane's speciation in comparison to AramcoMech 3.0 and JetSurf II. [31,32].

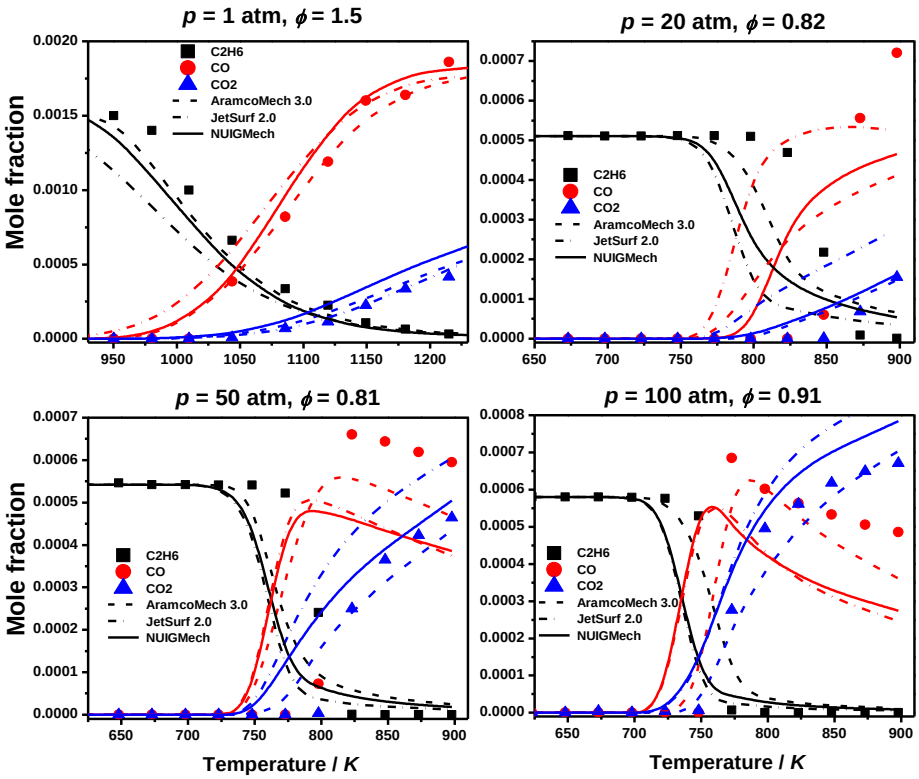

Figure DS28. Performance of NUIGMech1.0 for predicting ethane's speciation in comparison to AramcoMech 3.0 and JetSurf II. [33,34].

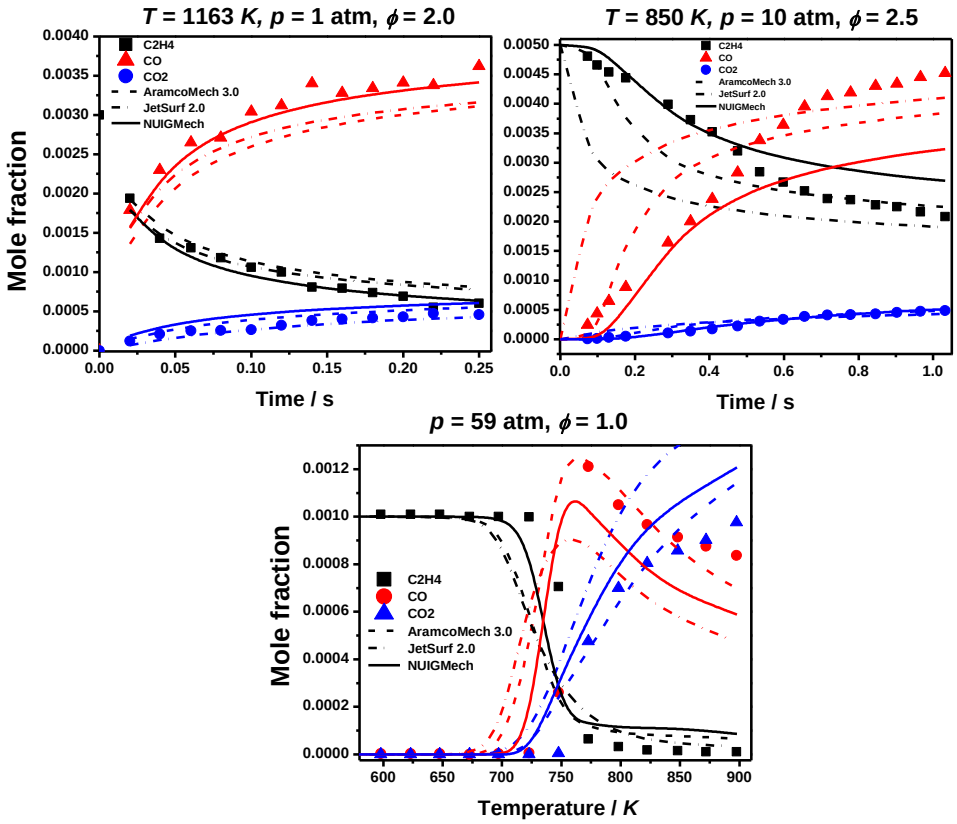

Figure DS29. Performance of NUIGMech1.0 for predicting ethylene's speciation in comparison to AramcoMech 3.0 and JetSurf II. [31,35,36].

Appendix D

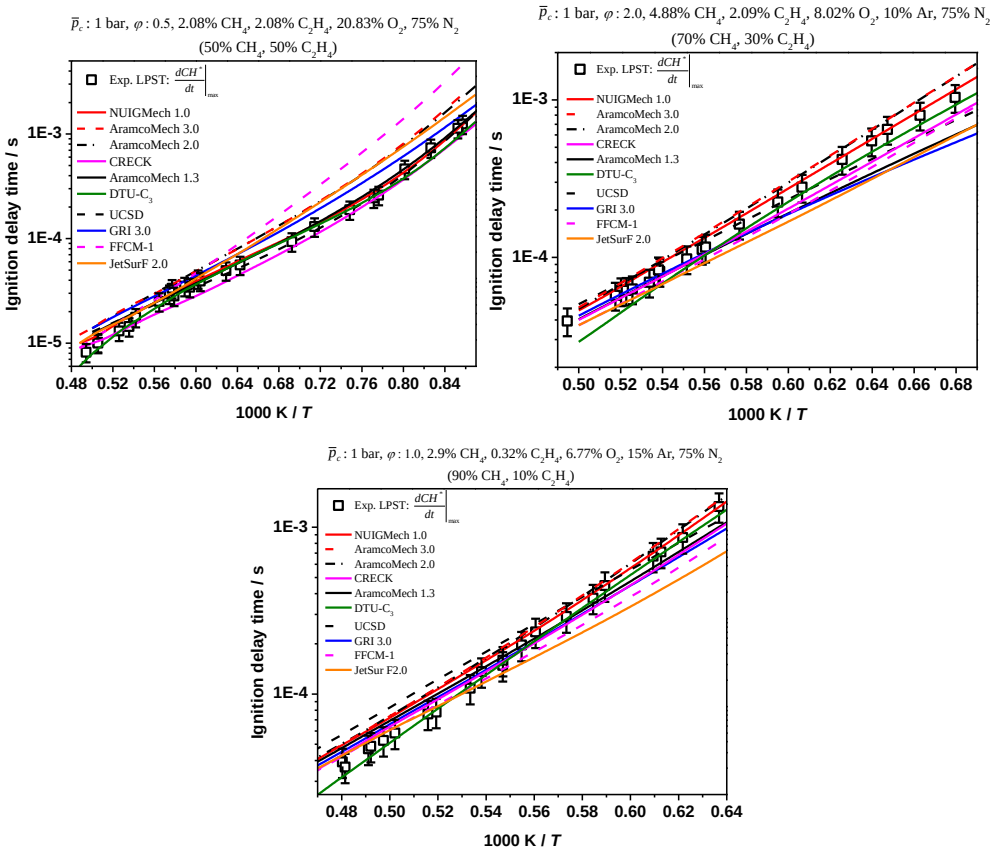

Figure DS30. Performance of NUIGMech1.0 for predicting methane + ethylene's IDTs at 1 bar in comparison to the other examined chemical mechanisms.

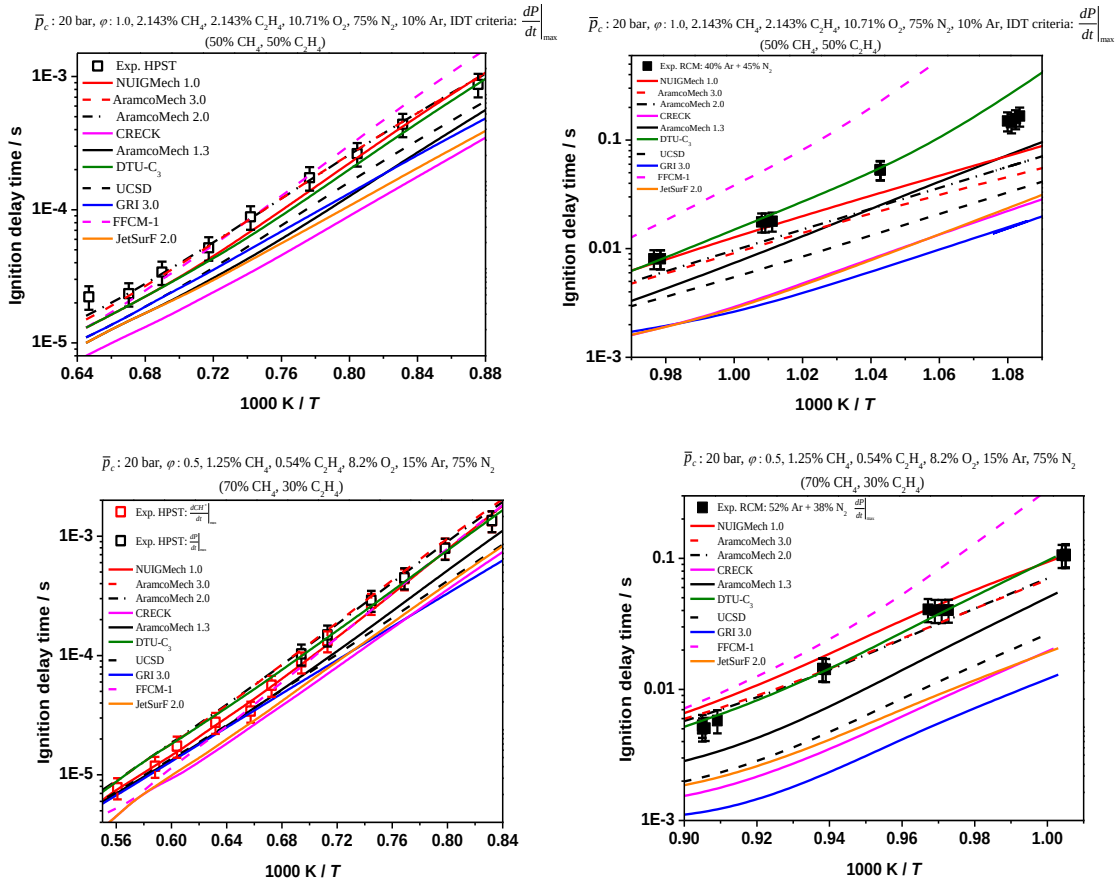

Appendix D

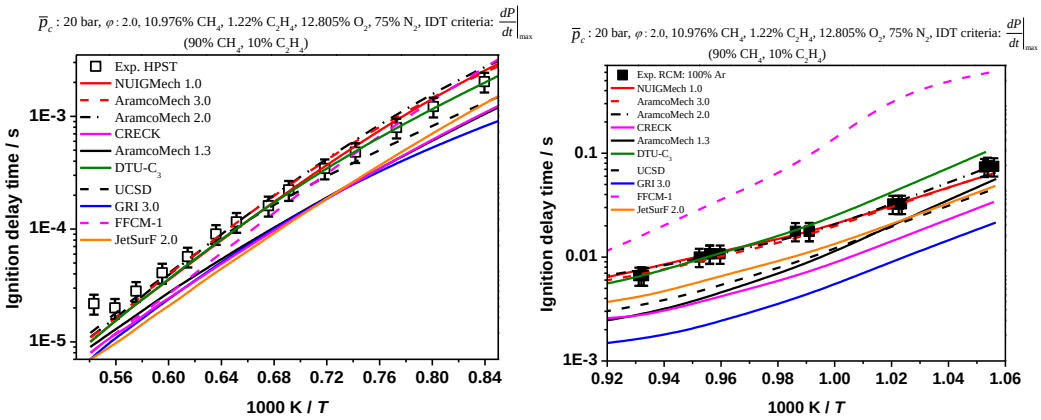

Figure DS31. Performance of NUIGMech1.0 for predicting methane + ethylene's IDTs at 20 bar in comparison to the other examined chemical mechanisms.

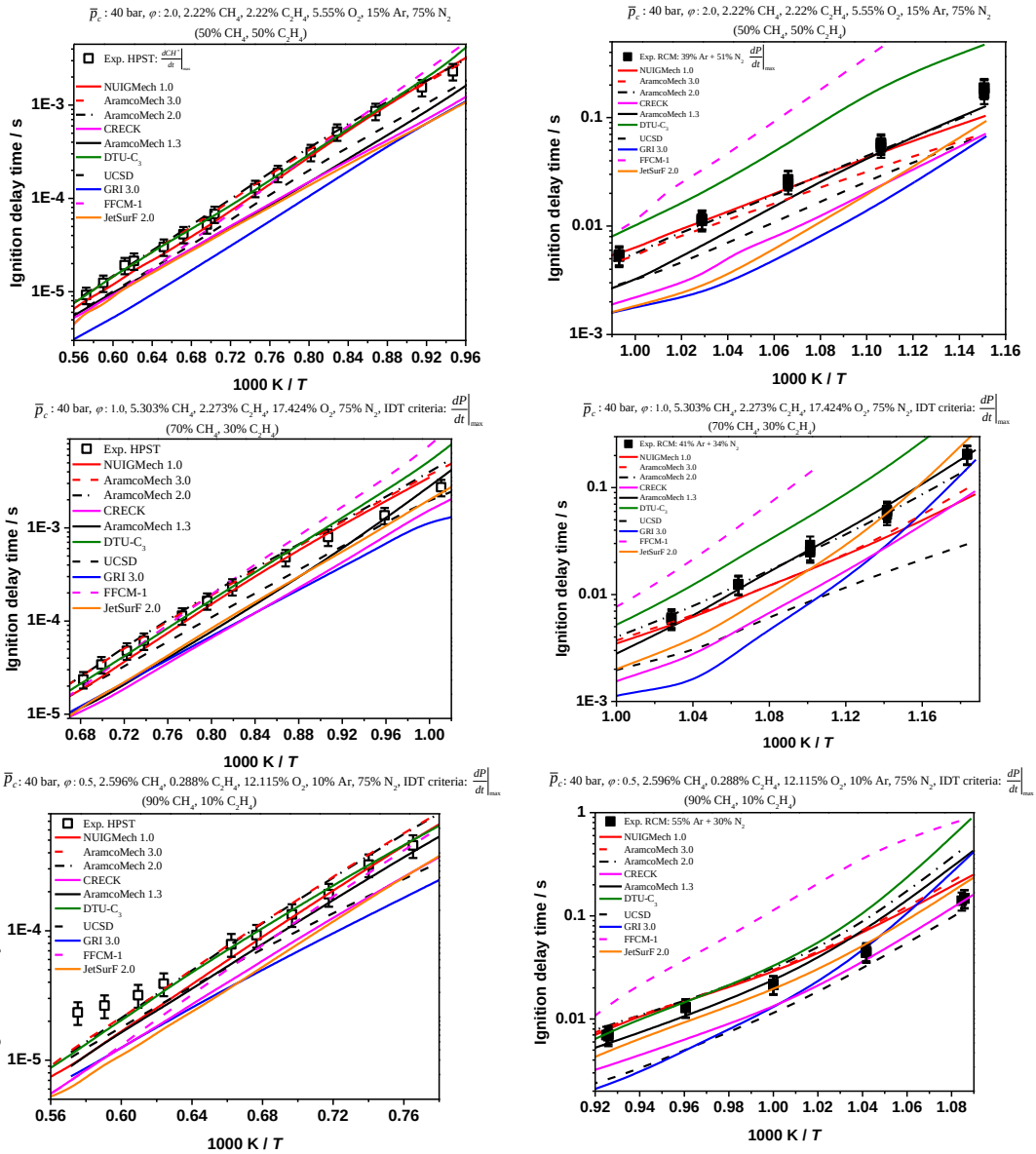

Figure DS32. Performance of NUIGMech1.0 for predicting methane + ethylene's IDTs at 40 bar in comparison to the other examined chemical mechanisms.

Appendix D

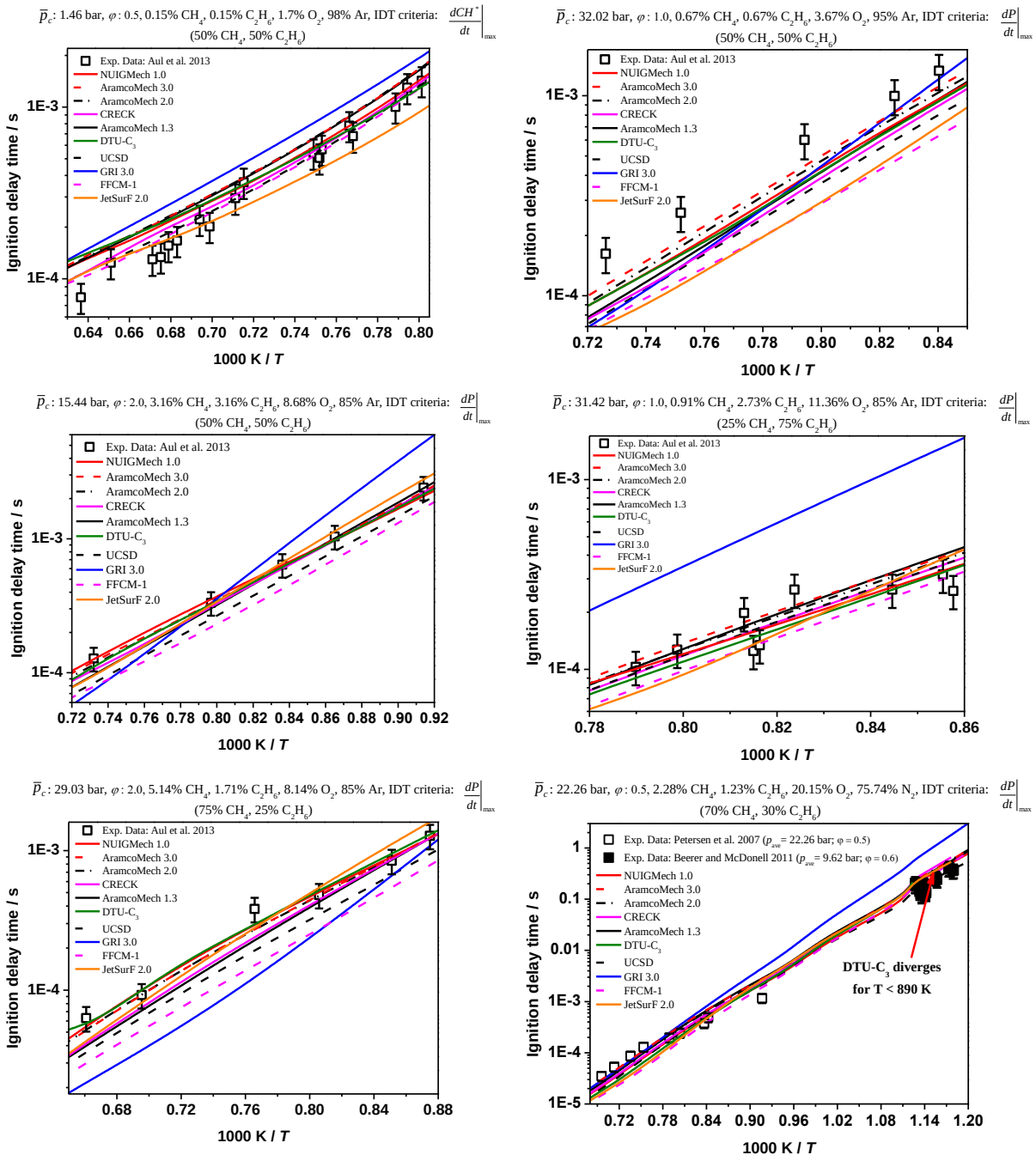

Figure DS33. Performance of NUIGMech1.0 for predicting methane + ethane's IDTs in comparison to the other examined chemical mechanisms.[37–39].

Appendix D

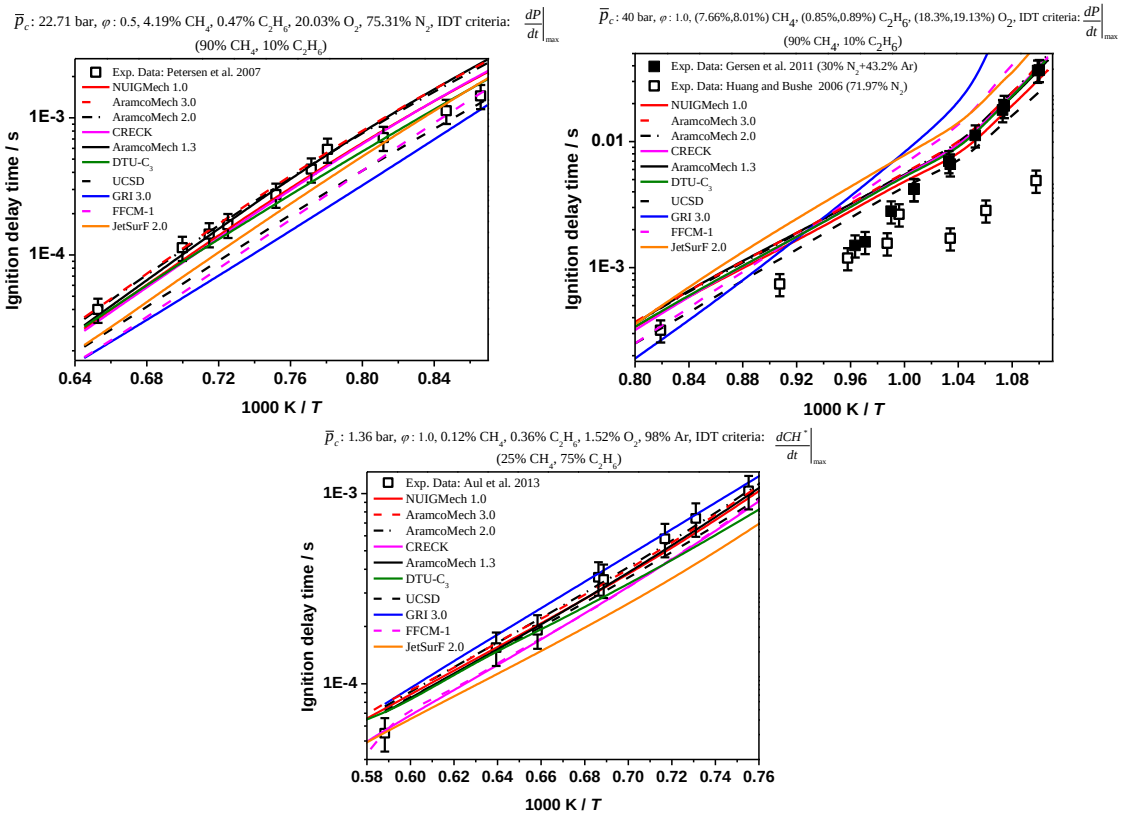

Figure DS34. Performance of NUIGMech1.0 for predicting methane + ethane's IDTs in comparison to the other examined chemical mechanisms. [37,39–41]

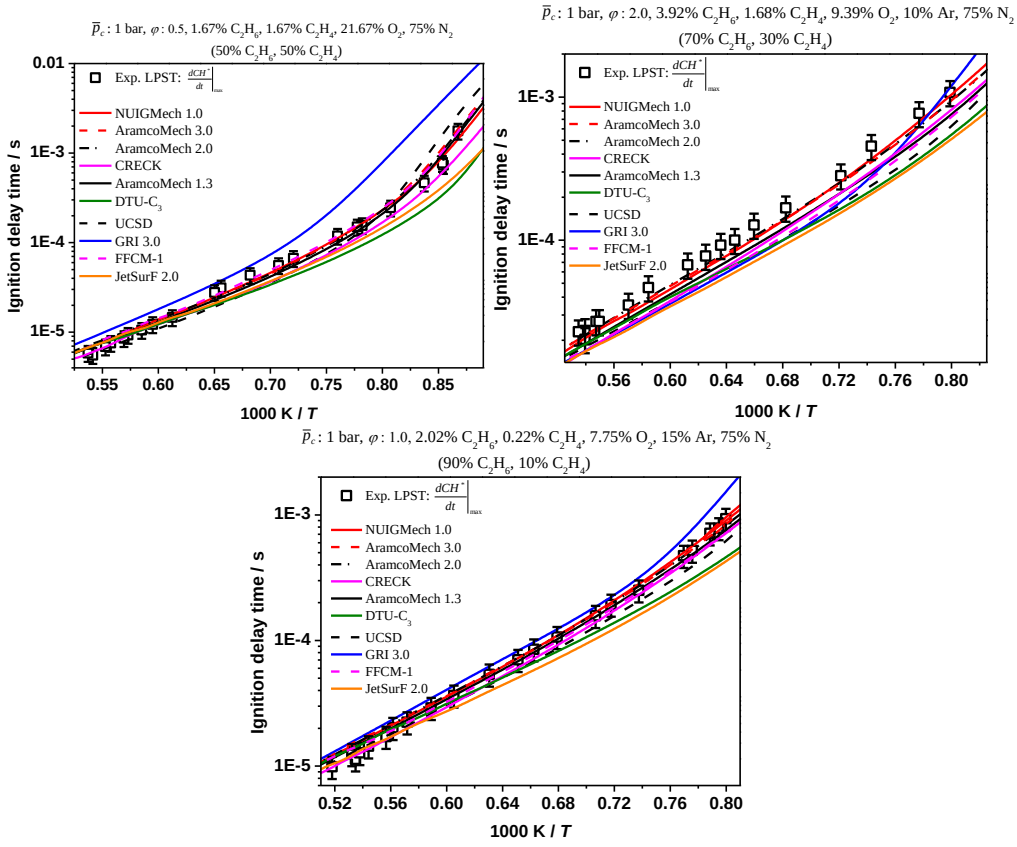

Figure DS35. Performance of NUIGMech1.0 for predicting ethane + ethylene's IDTs at 1 bar in comparison to the other examined chemical mechanisms.

Appendix D

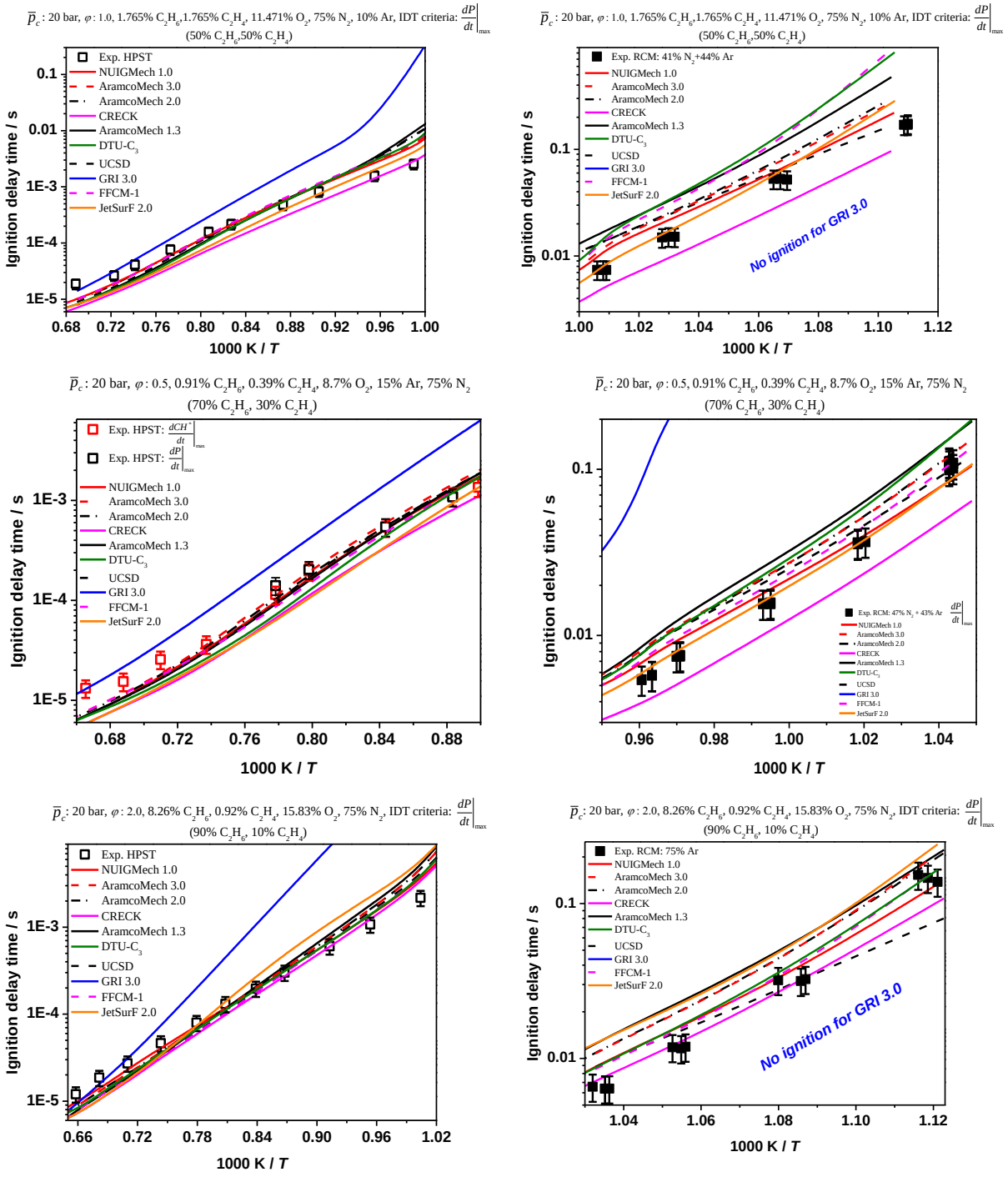

Figure DS36. Performance of NUIGMech1.0 for predicting ethane + ethylene's IDTs at 20 bar in comparison to the other examined chemical mechanisms.

Appendix D

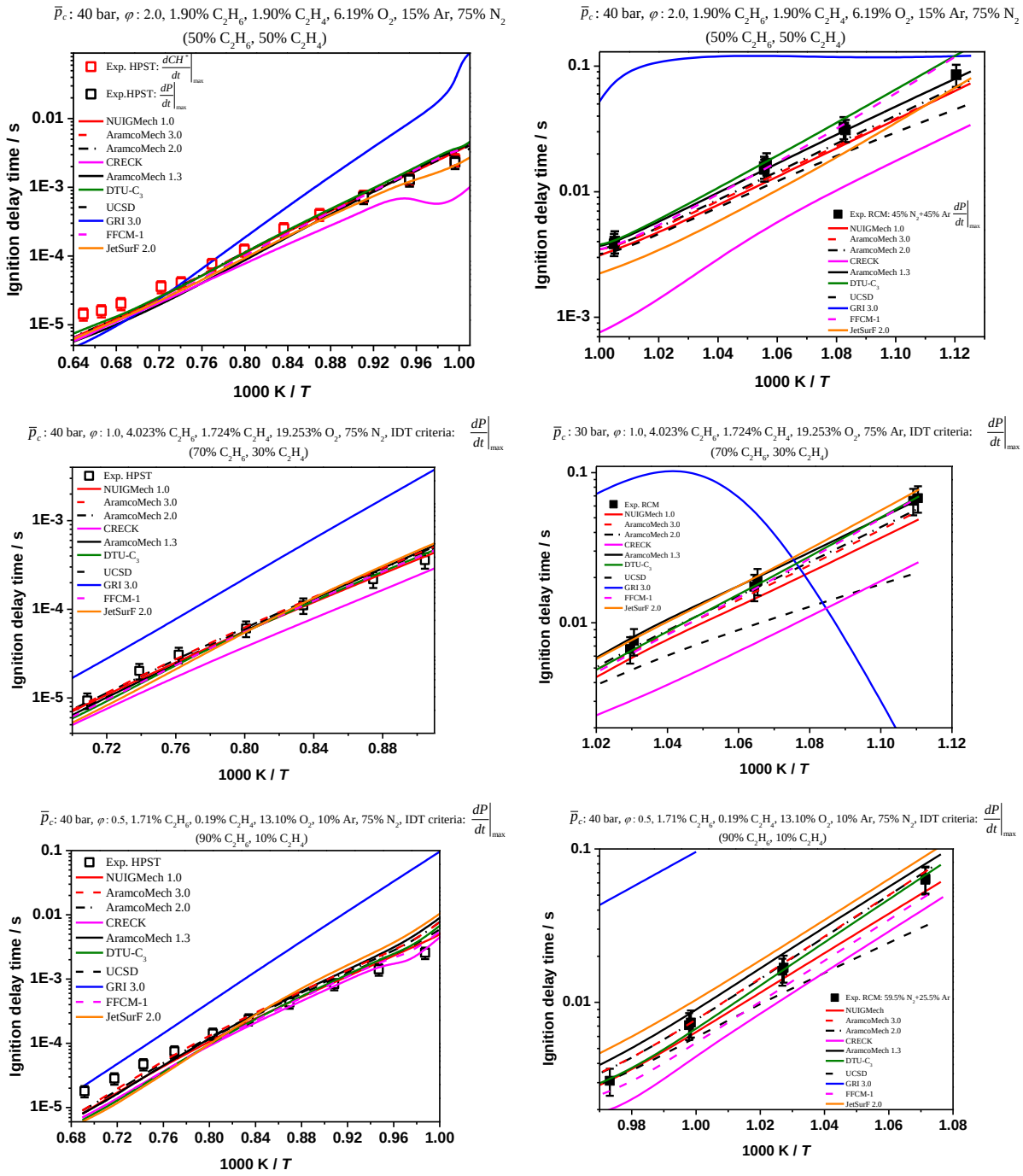

Figure DS37. Performance of NUIGMech1.0 for predicting ethane + ethylene's IDTs at 40 bar in comparison to the other examined chemical mechanisms.

10. Chemical kinetics development

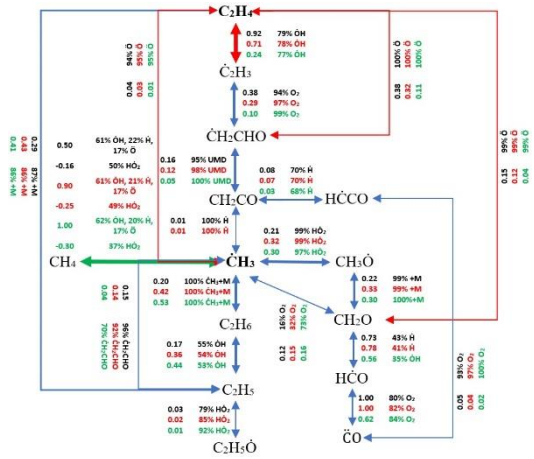

Figure DS38. Flux analysis of the ten prominent reactions at 1200 K in Figure 5(a) for the methane + ethylene blends at different methane/ethylene combinations; Black numbers: 50/50, Red numbers: 70/30, and Green numbers: 90/10.

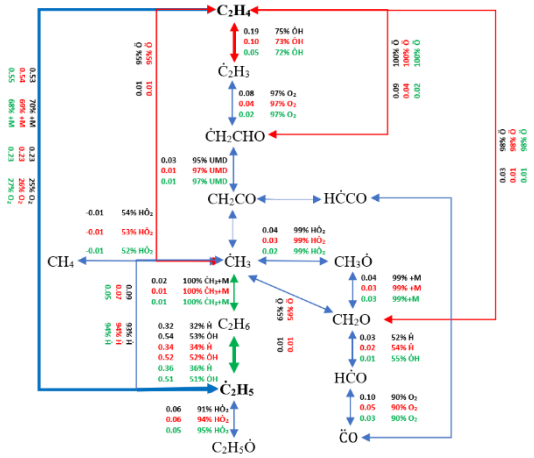

Figure DS39. Flux analysis of the ten prominent reactions at 1200 K in Figure 5(a) for the ethane + ethylene blends at different ethane/ethylene combinations; Black numbers: 50/50, Red numbers: 70/30, and Green numbers: 90/10.

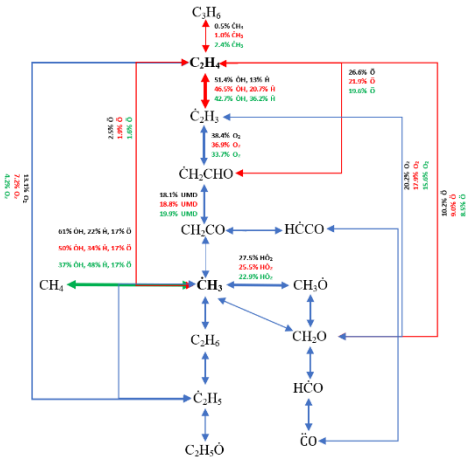

Figure DS40. Flux analysis of the ten prominent reactions at 1200 K in Figure 5(c) for the methane + ethylene blends at different equivalence ratios; Black numbers: 0.5, Red numbers: 1.0, and Green numbers: 2.0.

Appendix D

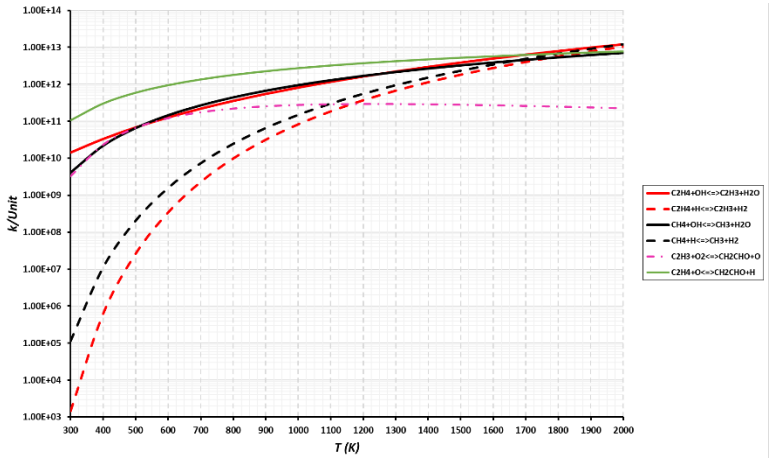

Figure DS41. Comparing the rates related to Ḣ–abstraction reactions from fuel by Ḣ atom or ȮH radical and also two important reactions for production of vinyloxy radical.

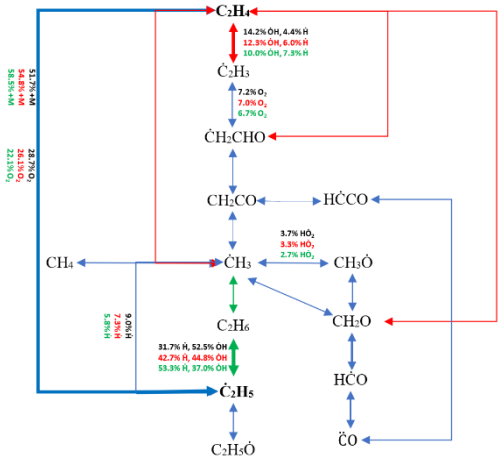

Figure DS42. Flux analysis of the ten prominent reactions at 1200 K in Figure 5(c) for the ethane + ethylene blends at different equivalence ratios; Black numbers: 0.5, Red numbers: 1.0, and Green numbers: 2.0.

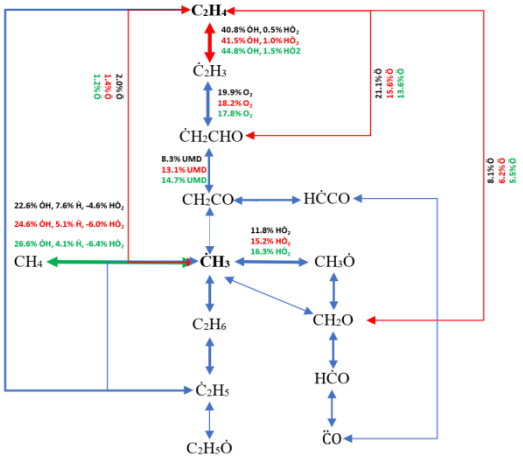

Figure DS43. Flux analysis of the ten prominent reactions at 1200 K in Figure 5(d) for the methane + ethylene blends at different pressures; Black numbers: 1 bar, Red numbers: 20 bar, and Green numbers: 40 bar.

Appendix D

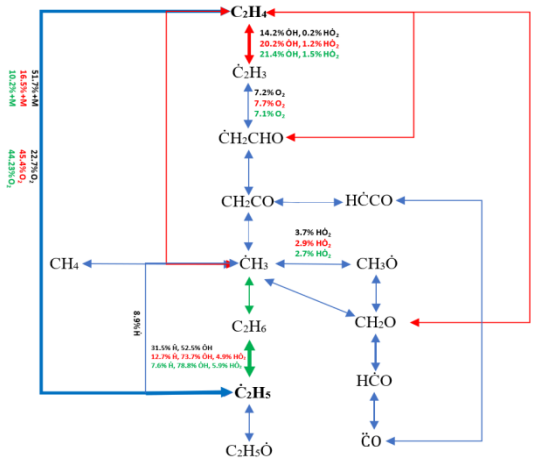

Figure DS44. Flux analysis of the ten prominent reactions at 1200 K in Figure 5(d) for the ethane + ethylene blends at different pressures; Black numbers: 1 bar, Red numbers: 20 bar, and Green numbers: 40 bar.

References

[1] M. Baigmohammadi, V. Patel, S. Martinez, S. Panigrahy, A. Ramalingam, U. Burke, K.P. Somers, K.A. Heufer, A. Pekalski, H.J. Curran, A Comprehensive Experimental and Simulation Study of Ignition Delay Time Characteristics of Single Fuel C_1–C_2 Hydrocarbons over a Wide Range of Temperatures, Pressures, Equivalence Ratios, and Dilutions, Energy Fuels, 34 (2020) 3755–3771.

[2] F.R. Gillespie, An experimental and modelling study of the combustion of oxygenated hydrocarbons, Natl. Univ. Irel. (2014).

[3] J. Würmel, M. McGuinness, J.M. Simmie, High-temperature oxidation of ethylene oxide in shock waves, J. Chem. Soc. Faraday Trans., 92 (1996) 715–721.

[4] C. Morley, Gaseq program, (n.d.). http://www.gaseq.co.uk (accessed September 29, 2017).

[5] H. Nakamura, D. Darcy, M. Mehl, C.J. Tobin, W.K. Metcalfe, W.J. Pitz, C.K. Westbrook, H.J. Curran, An experimental and modeling study of shock tube and rapid compression machine ignition of n-butylbenzene/air mixtures, Combust. Flame, 161 (2014) 49–64.

[6] U. Burke, K.P. Somers, P. O'Toole, C.M. Zinner, N. Marquet, G. Bourque, E.L. Petersen, W.K. Metcalfe, Z. Serinyel, H.J. Curran, An ignition delay and kinetic modeling study of methane, dimethyl ether, and their mixtures at high pressures, Combust. Flame, 162 (2015) 315–330.

[7] A. Ramalingam, K. Zhang, A. Dhongde, L. Virnich, H. Sankhla, H. Curran, A. Heufer, An RCM experimental and modeling study on CH_4 and CH_4/C_2H_6 oxidation at pressures up to 160 bar, Fuel, 206 (2017) 325–333.

[8] D. Healy, H.J. Curran, S. Dooley, J.M. Simmie, D.M. Kalitan, D.K. Petersen, G. Bourque, Methane/propane mixture oxidation at high pressures and at high, intermediate and low temperatures, Combust. Flame, 155 (2008) 451–461.

[9] D. Healy, H.J. Curran, J.M. Simmie, D.M. Kalitan, C.M. Zinner, A.B. Barrett, E.L. Petersen, G. Bourque, Methane/ethane/propane mixture oxidation at high pressures and at high, intermediate and low temperatures, Combust. Flame, 155 (2008) 441–448.

[10] W.K. Metcalfe, S.M. Burke, S.S. Ahmed, H.J. Curran, A Hierarchical and Comparative Kinetic Modeling Study of $C_1 - C_2$ Hydrocarbon and Oxygenated Fuels, Int. J. Chem.

Kinet., 45 (2013) 638–675.
[11] S. Yousefian, N.J. Quinlan, R.F.D. Monaghan, Simulation of turbulent flow in a rapid compression machine: Large Eddy Simulation and computationally efficient alternatives for the design of ignition delay time experiments, Fuel, 234 (2018) 30–47.
[12] C. Hemken, U. Burke, K.Y. Lam, D.F. Davidson, R.K. Hanson, K.A. Heufer, K. Kohse-Höinghaus, Toward a better understanding of 2-butanone oxidation: Detailed species measurements and kinetic modeling, Combust. Flame, 184 (2017) 195–207.
[13] TiePie engineering, No Title, (n.d.). https://www.tiepie.com/en/oscilloscope-software.
[14] P. Technology, No Title, (n.d.). https://www.picotech.com/downloads.
[15] E.L. Petersen, M.J.A. Rickard, M.W. Crofton, E.D. Abbey, M.J. Traum, D.M. Kalitan, A facility for gas- and condensed-phase measurements behind shock waves, Meas. Sci. Technol., 16 (2005) 1716–1729.
[16] B.W. Weber, C.J. Sung, M.W. Renfro, On the uncertainty of temperature estimation in a rapid compression machine, Combust. Flame. 162(6) (2015) 2518–2528.
[17] C.-W. Zhou, Y. Li, U. Burke, C. Banyon, K.P. Somers, S. Ding, S. Khan, J.W. Hargis, T. Sikes, O. Mathieu, E.L. Petersen, M. AlAbbad, A. Farooq, Y. Pan, Y. Zhang, Z. Huang, J. Lopez, Z. Loparo, S.S. Vasu, H.J. Curran, An experimental and chemical kinetic modeling study of 1,3-butadiene combustion: Ignition delay time and laminar flame speed measurements, Combust. Flame, 197 (2018) 423–438.
[18] S.M. Burke, W. Metcalfe, O. Herbinet, F. Battin-Leclerc, F.M. Haas, J. Santner, F.L. Dryer, H.J. Curran, An experimental and modeling study of propene oxidation. Part 1: Speciation measurements in jet-stirred and flow reactors, Combust. Flame, 161 (2014) 2765–2784.
[19] A. Kéromnès, W.K. Metcalfe, K.A. Heufer, N. Donohoe, A.K. Das, C.-J. Sung, J. Herzler, C. Naumann, P. Griebel, O. Mathieu, M.C. Krejci, E.L. Petersen, W.J. Pitz, H.J. Curran, An experimental and detailed chemical kinetic modeling study of hydrogen and syngas mixture oxidation at elevated pressures, Combust. Flame, 160 (2013) 995–1011.
[20] S.M. Burke, U. Burke, R. Mc Donagh, O. Mathieu, I. Osorio, C. Keesee, A. Morones, E.L. Petersen, W. Wang, T.A. DeVerter, M.A. Oehlschlaeger, B. Rhodes, R.K. Hanson, D.F. Davidson, B.W. Weber, C.J. Sung, J. Santner, Y. Ju, F.M. Haas, F.L. Dryer, E.N. Volkov, E.J.K. Nilsson, A.A. Konnov, M. Alrefae, F. Khaled, A. Farooq, P. Dirrenberger, P.A. Glaude, F. Battin-Leclerc, H.J. Curran, An experimental and modeling study of propene oxidation. Part 2: Ignition delay time and flame speed measurements, Combust. Flame, 162 (2015) 296–314.
[21] U. Burke, W.K. Metcalfe, S.M. Burke, K.A. Heufer, P. Dagaut, H.J. Curran, A detailed chemical kinetic modeling, ignition delay time and jet-stirred reactor study of methanol oxidation, Combust. Flame, 165 (2016) 125–136.
[22] C.W. Zhou, Y. Li, E. O'Connor, K.P. Somers, S. Thion, C. Keesee, O. Mathieu, E.L. Petersen, T.A. DeVerter, M.A. Oehlschlaeger, G. Kukkadapu, C.J. Sung, M. Alrefae, F. Khaled, A. Farooq, P. Dirrenberger, P.A. Glaude, F. Battin-Leclerc, J. Santner, Y. Ju, T. Held, F.M. Haas, F.L. Dryer, H.J. Curran, A comprehensive experimental and modeling study of isobutene oxidation, Combust. Flame, 167 (2016) 353–379.
[23] Y. Li, C.W. Zhou, K.P. Somers, K. Zhang, H.J. Curran, The oxidation of 2-butene: A high pressure ignition delay, kinetic modeling study and reactivity comparison with isobutene

and 1-butene, Proc. Combust. Inst., 36(1) (2017) 403–411.
[24] H. Hashemi, J.M. Christensen, L.B. Harding, S.J. Klippenstein, P. Glarborg, High-pressure oxidation of propane, Proc. Combust. Inst., 37(1) (2019) 461–468.
[25] G. Bagheri, E. Ranzi, M. Pelucchi, A. Parente, A. Frassoldati, T. Faravelli, Comprehensive kinetic study of combustion technologies for low environmental impact: MILD and OXY-fuel combustion of methane, Combust. Flame, 212 (2020) 142–155.
[26] Chemical-Kinetic Mechanisms for Combustion Applications, No Title, (n.d.). https://web.eng.ucsd.edu/mae/groups/combustion/mechanism.html.
[27] W. Gardiner, V. Lissianski, Z. Qin, G. Smith, D. Golden, M. Frenklach, B. Eiteneer, M. Goldenberg, N.W. Moriarty, C.T. Bowman, The gri-mechtm model for natural gas combustion and no formation and removal chemistry, in: 5th Int. Conf. Combust. Technol. a Clean Environ., 1999.
[28] H. Wang, E. Dames, B. Sirjean, D.A. Sheen, R. Tango, A. Violi, J.Y.W. Lai, F.N. Egolfopoulos, D.F. Davidson, R.K. Hanson, C.T. Bowman, C.K. Law, W. Tsang, N.P. Cernansky, D.L. Miller, R.P. Lindstedt, A high-temperature chemical kinetic model of n-alkane (up to n-dodecane), cyclohexane, and methyl-, ethyl-, n-propyl and n-butyl-cyclohexane oxidation at high temperatures, JetSurF Version 2.0, Sept. 19, 2010. (2010).
[29] G.P. Smith, Y. Tao, H. Wang, Foundational Fuel Chemistry Model Version 1.0 (FFCM-1), (n.d.). http://nanoenergy.stanford.edu/ffcm1, 2016.
[30] W. Lowry, J. de Vries, M. Krejci, E. Petersen, Z. Serinyel, W. Metcalfe, H. Curran, G. Bourque, Laminar Flame Speed Measurements and Modeling of Pure Alkanes and Alkane Blends at Elevated Pressures, J. Eng. Gas Turbines Power, 133(9) (2011) 091501 (9 pages).
[31] P. Dagaut, J.C. Boettner, M. Cathonnet, Methane oxidation: Experimental and kinetic modeling study, Combust. Sci. Technol., 77 (1991) 127–148.
[32] E.J. Chang, Shock tube experiments for the development and validation of models of hydrocarbon combustion, (1995).
[33] H. Hashemi, J.G. Jacobsen, C.T. Rasmussen, J.M. Christensen, P. Glarborg, S. Gersen, M. van Essen, H.B. Levinsky, S.J. Klippenstein, High-pressure oxidation of ethane, Combust. Flame, 182 (2017) 150–166.
[34] P. Dagaut, M. Cathonnet, J. Boettner, Kinetics of ethane oxidation, Int. J. Chem. Kinet., 23 (1991) 437–455.
[35] T. Carriere, P.R. Westmoreland, A. Kazakov, Y.S. Stein, F.L. Dryer, Modeling ethylene combustion from low to high pressure, Proc. Combust. Inst., 29 (2002) 1257–1266.
[36] J.G. Lopez, C.L. Rasmussen, M.U. Alzueta, Y. Gao, P. Marshall, P. Glarborg, Experimental and kinetic modeling study of C_2H_4 oxidation at high pressure, Proc. Combust. Inst., 32 (2009) 367–375.
[37] E.L. Petersen, J.M. Hall, S.D. Smith, J. de Vries, A.R. Amadio, M.W. Crofton, Ignition of Lean Methane-Based Fuel Blends at Gas Turbine Pressures, J. Eng. Gas Turbines Power, 129 (2007) 937–944.
[38] D.J. Beerer, V.G. McDonell, An experimental and kinetic study of alkane autoignition at high pressures and intermediate temperatures, Proc. Combust. Inst., 33 (2011) 301–307.
[39] C.J. Aul, W.K. Metcalfe, S.M. Burke, H.J. Curran, E.L. Petersen, Ignition and kinetic modeling of methane and ethane fuel blends with oxygen: A design of experiments

approach, Combust. Flame, 160 (2013) 1153–1167.

[40] S. Gersen, A. V Mokhov, J.H. Darmeveil, H.B. Levinsky, P. Glarborg, Ignition-promoting effect of NO_2 on methane, ethane and methane/ethane mixtures in a rapid compression machine, Proc. Combust. Inst., 33 (2011) 433–440.

[41] J. Huang, W.K. Bushe, Experimental and kinetic study of autoignition in methane/ethane/air and methane/propane/air mixtures under engine-relevant conditions, Combust. Flame, 144 (2006) 74–88.

Appendix E

(Supplementary material for Chapter 8)

An experimental and kinetic modeling study of the ignition delay characteristics of binary blends of ethane/propane and ethylene/propane in multiple shock tubes and rapid compression machines over a wide range of temperature, pressure, equivalence ratio, and dilution

1. Design of experiments

The method applied to design the matrix of experiments is a robust approach for experimental research with many parameters involved, and it has already been discussed by Baigmohammadi et al. [1, 2] for single and binary fuel blends. The variables and levels involved in designing the matrix of experiments for the current study are presented in Table ES1 and Table ES2, for C_2H_4/C_3H_8 and C_2H_6/C_3H_8 blends, respectively.

Table ES1. Variables and levels for designing of C_2H_4/C_3H_8 blend in the current experiments using the Taguchi[3] method.

Variables / *Levels*	*Fuel composition*	*Dilution*	*Equivalence ratio*	*Pressure (bar)*
1	50% C_2H_4 + 50% C_3H_8	75%	0.5	1.0
2	70% C_2H_4 + 30% C_3H_8	85%	1.0	20.0
3	90% C_2H_4 + 10% C_3H_8	90%	2.0	40.0

Table ES2. Variables and levels for designing of C_2H_6/C_3H_8 blend in the current experiments using the Taguchi[3] method.

Variable / *Levels*	*Fuel composition*	*Dilution*	*Equivalence ratio*	*Pressure (bar)*
1	50% C_2H_6 + 50% C_3H_8	75%	0.5	1.0
2	70% C_2H_6 + 30% C_3H_8	85%	1.0	20.0
3	90% C_2H_6 + 10% C_3H_8	90%	2.0	40.0

2. Facilities

All of the facilities used for the experiments performed in the current study, such as the low-pressure shock tube (LPST), high-pressure shock tube (HPST), and rapid compression machines

(RCM), were described in detail by Baigmohammadi et al. [1, 2, 4-12] and thus here we present a summary description, especially for those facilities located at NUIG. The measured IDTs in the HPST and RCMs, as discussed in Section 8.2, "design of experiments", are defined as the maximum gradient in pressure ($\frac{dP}{dt}$) behind the reflected shock, Figs. ES1 and ES3. However, for the LPST data and when the test mixture is highly diluted in the HPST, Figure ES2, the IDT is defined as the maximum gradient in CH*($\frac{dCH^*}{dt}$) behind the reflected shock.

2.1. Low-/High-pressure shock-tube

The ST is a facility that is most ideal to measure IDTs of ≤ 2 ms, for low- and high-pressure and high-temperature (≥ 1000 K) conditions. In this regard, for the current study, a LPST was used to record the IDT data at ~1 bar. Most of the experiments were carried out using helium as the primary driver gas, but some experiments were performed in which the incident shock velocity had to be reduced to reach the desired conditions, and so nitrogen was added to the helium driver gas to tailor the condition. The physical configuration of the five PCB sensors installed in the driven section is displayed in Table ES3, including the distance from the endwall. The properties behind the reflected shock, such as the reflected-shock temperature (T_5) and pressure (p_5), were calculated using the Gaseq software [13]. Additionally, for the highly diluted cases which have weak pressure signals, IDTs were determined from light emission profiles using a photomultiplier with a Thorlabs CH* filter, within CWL:430 nm ± 10 FWHM installed at the sidewall of the ST's endcap. Finally, to improve the accuracy of the experimental data collected, fluctuations allowed in pressure measurements were restricted to ± 0.05 bar of the target pressure of 1 bar.

The HPST was used to measure the IDTs for pressures ranging from 20 – 40 bar. Similar to the LPST, helium was used as the driver gas with a small number of tailored experiments performed in which nitrogen was added to helium for conditions where it was required to reduce the incident shock velocity. Six piezoelectric pressure transducers, located near the endwall of the

driven section, were used to extrapolate and calculate the incident shock velocity at the endwall. As mentioned before for the LPST, the Gaseq software [13] was used to calculate the conditions behind the reflected shock wave by considering the mixture composition, incident shock pressure, temperature, and shock velocity. In mixtures with dilution concentrations of ≤ 85%, a Kistler 603B transducer mounted at the endwall was used to record the IDTs. For mixtures with dilution concentrations of ≥ 90%, IDTs were measured using a photodiode array detector system with a Thorlabs CH* filter, within CWL:430 nm ± 10 FWHM installed on the sidewall of the ST's endcap.

Table ES3. Specifications of the applied LPST.

Total length	6.33 m	
Section	Length (m)	Diameter (mm)
Driver	0.53	520
Driven	5.8	102.4
Material	Stainless-steel	
Controlling system	Sharp edges arrow	
Diaphragm's material	Polycarbonate/Polyester	
Diaphragm's thickness	105–120 µm (nominal)	
Sensor PCB#1	0.03 m	
Sensor PCB#2	0.237 m	
Sensor PCB#3	0.366 m	
Sensor PCB#4	0.495 m	
Sensor PCB#5	1.89 m	

Table ES4. Specifications of the applied high-pressure shock tube

Total length	9.1 m	
Section	Length (m)	Diameter (mm)
Driver	3.0	63.5
Middle	0.04	63.5
Driven	5.7	63.5
Material	Stainless-steel (1.4571/316Ti and 1.4462/F51)	
Controlling system	Double-diaphragm type	
Diaphragm's material	Aluminium (1050 H14)	
Diaphragm's thickness	0.8~2 mm; according to target pressure	
Pre-scoring the diaphragms	0.2~1.1 mm; according to target pressure and the diaphragms' thickness	
Sensor PCB#1	0.01 m	
Sensor PCB#2	0.15 m	
Sensor PCB#3	0.29 m	
Sensor PCB#4	0.57 m	
Sensor PCB#5	0.85 m	
Sensor PCB#6	1.165 m	

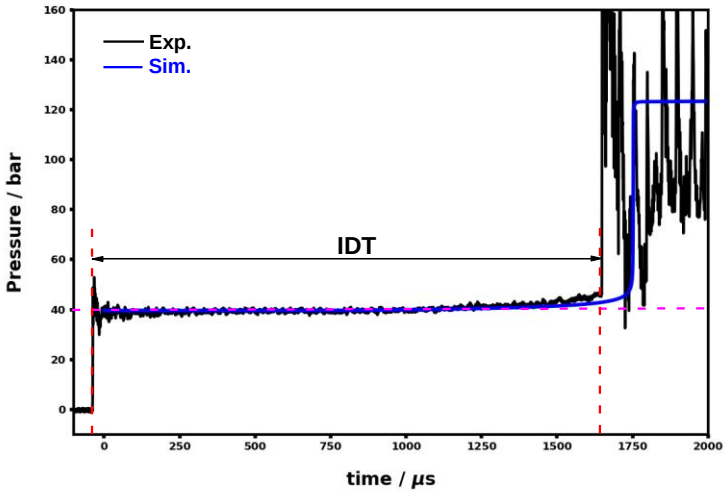

Figure ES1. IDT definition [1, 2] for the LPST and the HPST using the experimental pressure profile (solid black line) against the simulated profile (solid blue line).

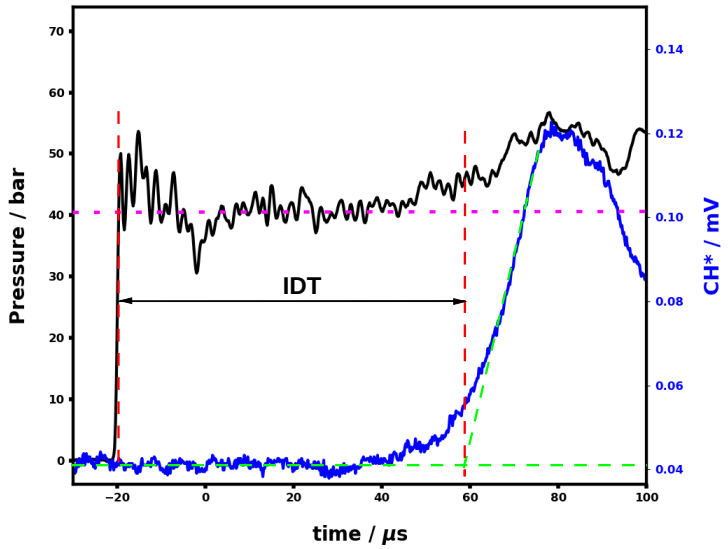

Figure ES2. Definition of IDT[1, 2] showing experimental pressure profile (solid black line) and experimental CH* history (solid blue line) for the LPST and the HPST.

2.2. NUIG/PCFC–RCM

The rapid compression machine (RCM) at NUIG is a facility designed to measure IDTs at high to moderate pressures (~10 – 40 bar), and at low temperatures $600 \leq T \leq 1000$ K. The adiabatic core assumption was used to simulate the IDT measurements with the imposition of volume profiles based on the non-reactive pressure profiles to compensate for the non-adiabatic conditions. The general facility's specifications are presented in Table ES5, along with the general parameters. For cases with dilution concentrations of 75% (close to fuel in air) the IDTs and the pressure-time profiles of the non-reactive mixtures were recorded using a Kistler 6045A

transducer installed on the sidewall of the reaction chamber. However, for mixtures with dilution concentrations of approximately 85% and 90% and the post-compression pressures of 20 and 40 bar, a Kistler transducer and a photomultiplier with a Thorlabs CH* filter, within CWL:430 nm ± 10 FWHM from Thorlabs, was used. Similar to the procedure used in the LPST and HPST experiments, the Gaseq software was used to calculate the post-compression temperature (T_C), assuming isentropic compression in the RCM. All post-compression pressures (p_C) were restricted to ± 0.5 bar of the target pressure to improve the measurement consistency.

Table ES5. Specifications of the NUIG–RCM.

Parameter	Value
Bore size of the reaction chamber (cm)	3.82
Volume of the reaction chamber (cm^3)	33.191
Piston's velocity (U_p) (cm/s)	934.0 ~ 1294.0
Piston's stroke length (cm)	16.817
Piston's type	Flat head with the crevice
Type	Twin–counter piston

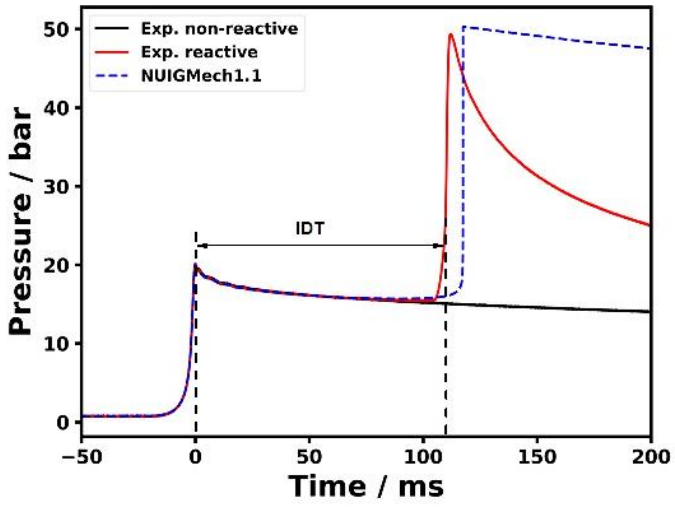

Figure ES3. IDT definition for NUIG–RCM showing pressure history profile of experimental non-reactive mixture (solid black line), experimental reactive mixture (solid red line), and mechanism simulated trace (blue dashed line).

Moreover, all of the experimental results have been divided into two categories, reliable or un-reliable. Some experiments exhibit pre-ignition, usually characterized by a noticeable pressure rise prior to the ignition event. When this occurs, we report the affected results using a symbol with an "x" through it, e,g, ☒. Thus, we also report all of these affected data in our Figures,

together with the simulation using NUIGMech1.1. These affected data are not reliable in evaluating the performance of the chemical mechanism. In this regard, all pressure versus time data, including the oscilloscope [14] files and the experimentalist spreadsheets for the conditions studied in the LPST, HPST, and RCM are provided as zip files with this Supplemental material.

The relatively high-pressure experiments in the RCM were performed at PCFC-RWTH Aachen University. The description of the facility is provided in (Lee et al. doi: 0.1524/zpch.2012.0185), and the detailed explanation of the experimental procedure along with the uncertainty analysis is provided in (Ramalingam et al. doi: https://doi.org/10.1016/j.fuel.2017.06.005).

3. NUIG/PCFC–RCM pressure vs. time traces

In this section a collection of NUIG/PCFC –RCM pressure vs. time traces are presented to demonstrate the reliability of experiments and simulations performed for the current study. The traces are plotted using the experimental non-reactive versus reactive pressure/time history profile. Moreover, the simulated pressure/time profile using NUIGMech1.1 is included for comparison. Thus, the next graphs present low-temperature conditions for 20–40 bar, φ = 0.5 – 2.0, dilution from 75 – 90% and different ratios for both of the blends, such as 50%/50%, 70%/30%, and 90%/10%.

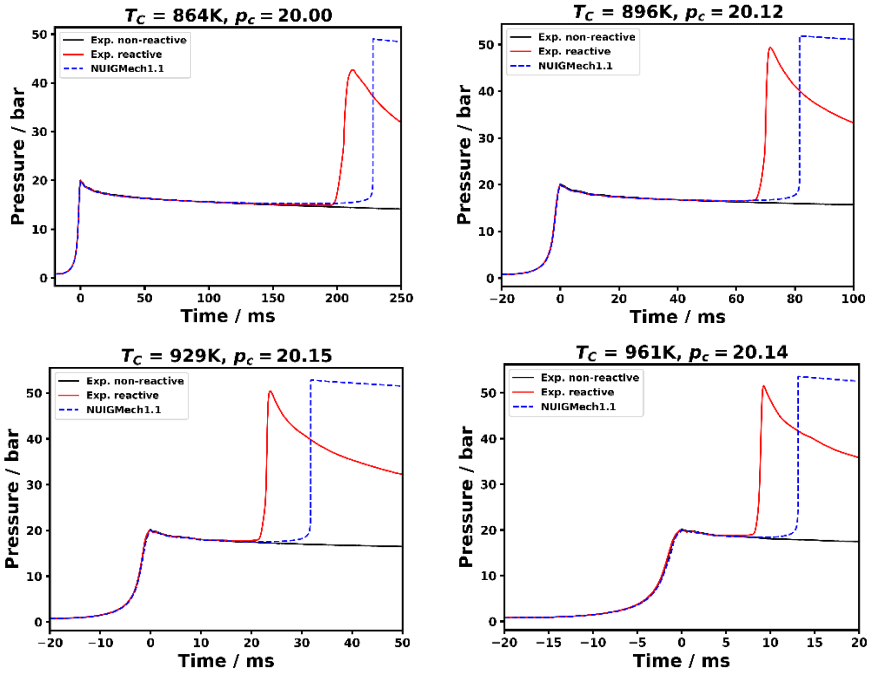

Figure ES4. NUIG–RCM experimental non-reactive (NR), reactive (R), and NUIGMech1.1 simulated pressure traces. For 50% C_2H_4 / 50% C_3H_8 blend with 75% N_2 + 10% Ar, at 20 bar and φ = 1.0.

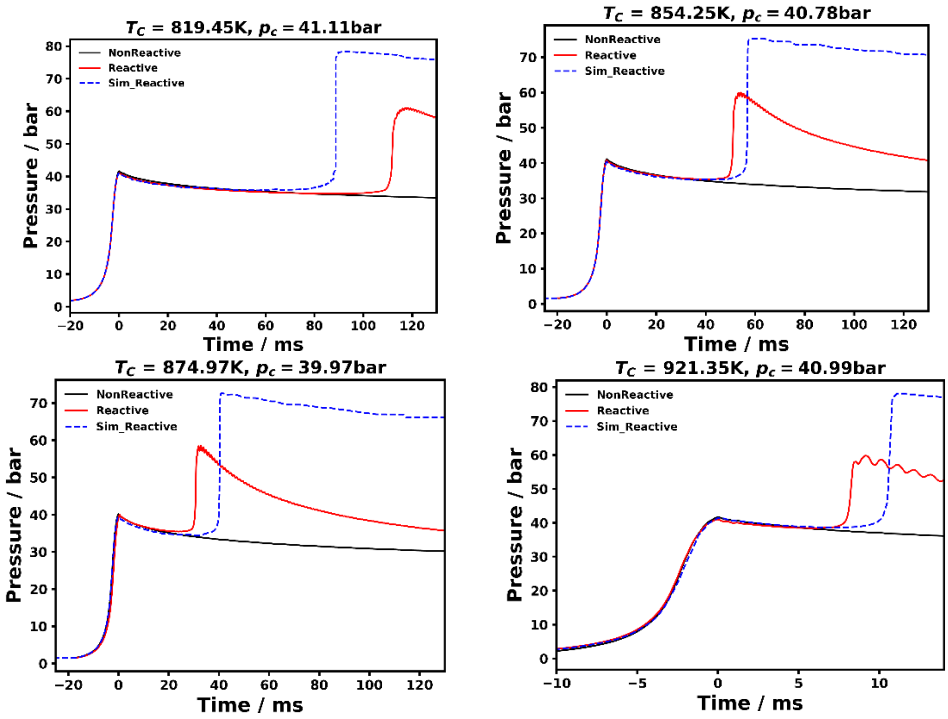

Figure ES5. PCFC–RCM experimental non-reactive (NR), reactive (R), and NUIGMech1.1 simulated pressure traces. For 50% C_2H_4 / 50% C_3H_8 blend with 75% N_2 + 15% Ar, at 40 bar and φ = 2.0.

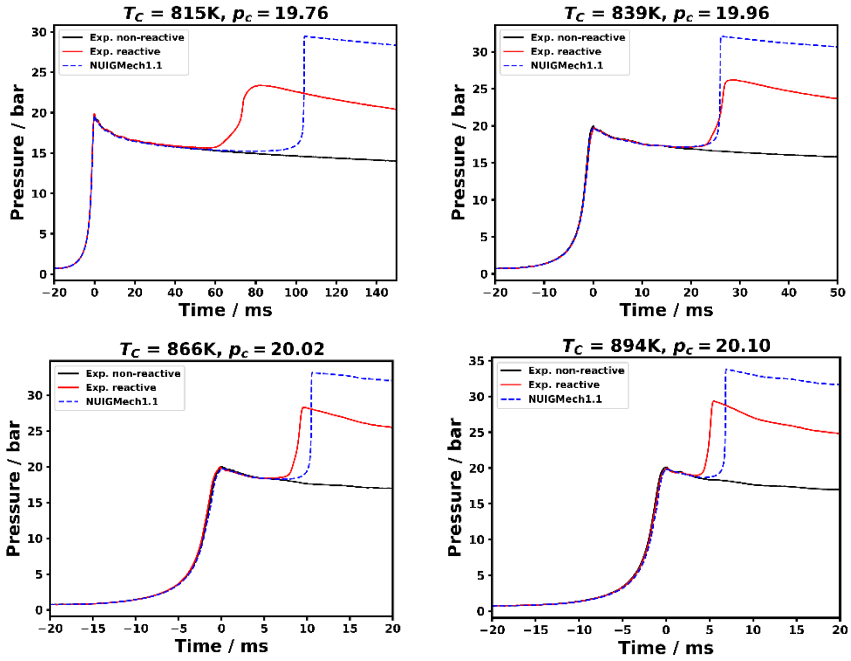

Figure ES6. NUIG–RCM experimental non-reactive (NR), reactive (R), and NUIGMech1.1 simulated pressure traces. For 70% C_2H_4 / 30% C_3H_8 blend with 75% N_2 + 15% Ar, at 20 bar and φ = 0.5.

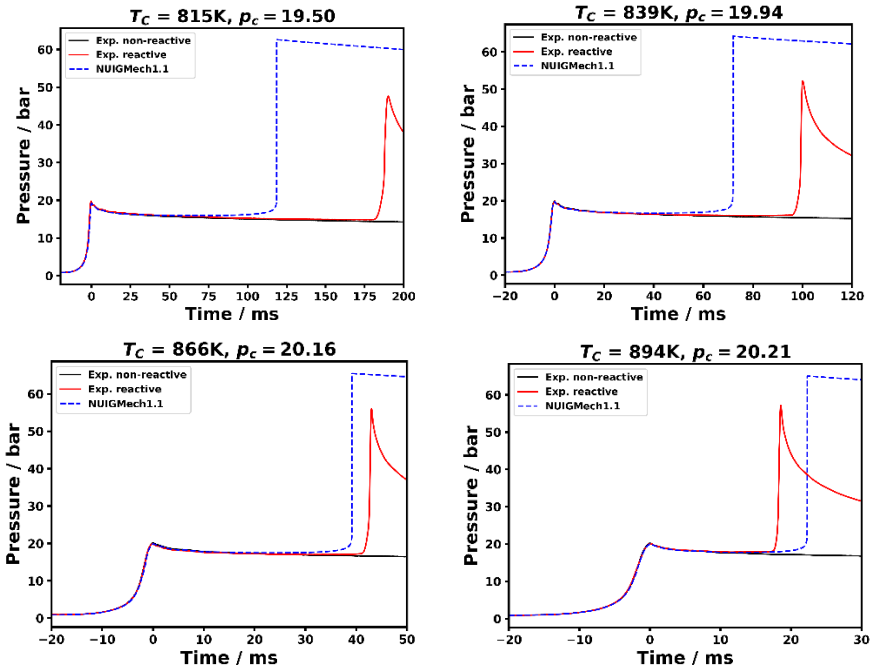

Figure ES7. NUIG–RCM experimental non-reactive (NR), reactive (R), and NUIGMech1.1 simulated pressure traces. For 90% C_2H_4 / 10% C_3H_8 blend with 75% N_2, at 20 bar and φ = 2.0.

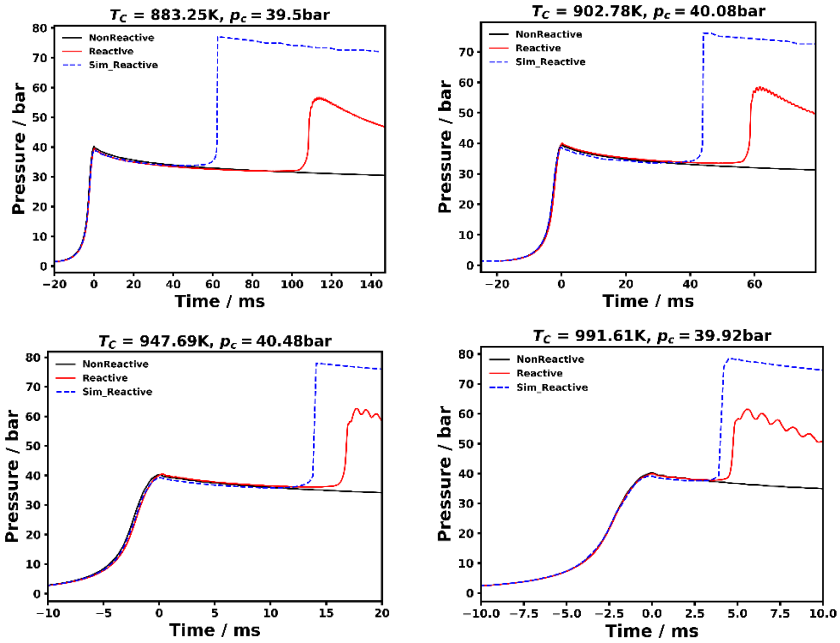

Figure ES8. PCFC–RCM experimental non-reactive (NR), reactive (R), and NUIGMech1.1 simulated pressure traces. For 90% C_2H_4 / 10% C_3H_8 blend with 75% N_2 + 10% Ar, at 40 bar and φ = 0.5.

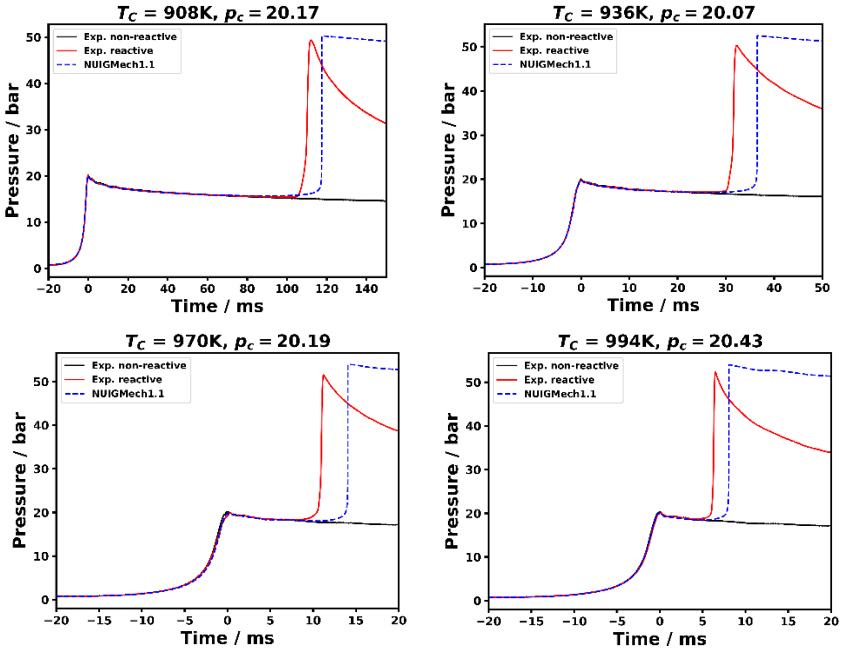

Figure S9. NUIG–RCM experimental non-reactive (NR), reactive (R), and NUIGMech1.1 simulated pressure traces. For 50% C_2H_6 / 50% C_3H_8 blend with 75% N_2 + 10% Ar, at 20 bar and φ = 1.0.

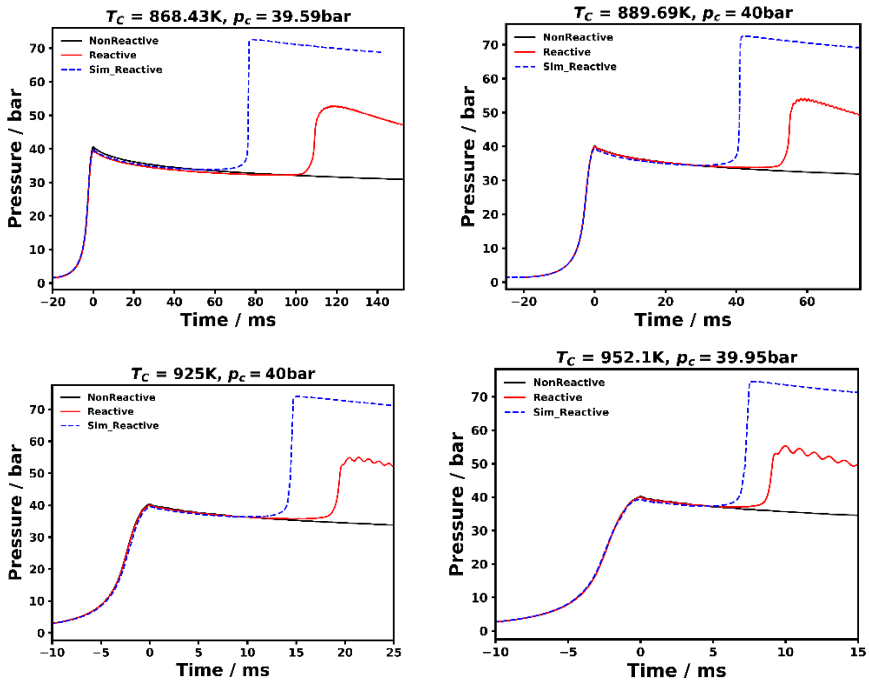

Figure ES10. PCFC–RCM experimental non-reactive (NR), reactive (R), and NUIGMech1.1 simulated pressure traces. For 50% C_2H_6 / 50% C_3H_8 blend with 75% N_2 + 15% Ar, at 40 bar and φ = 2.0.

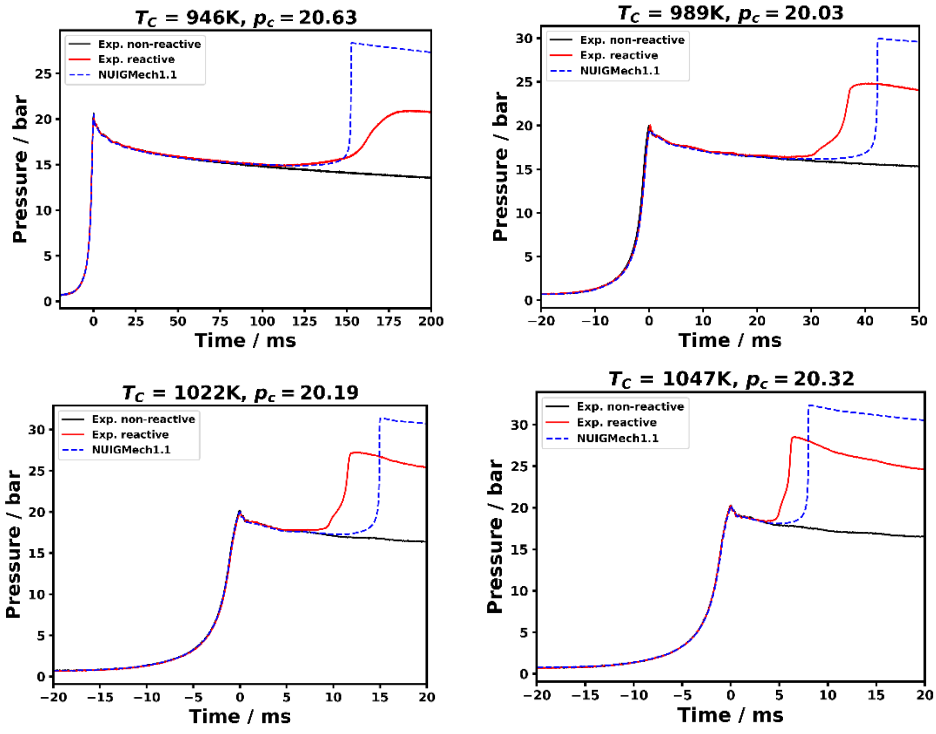

Figure ES11. NUIG–RCM experimental non-reactive (NR), reactive (R), and NUIGMech1.1 simulated pressure traces. For 70% C_2H_6 / 30% C_3H_8 blend with 75% N_2 + 15% Ar, at 20 bar and φ = 0.5.

Appendix E

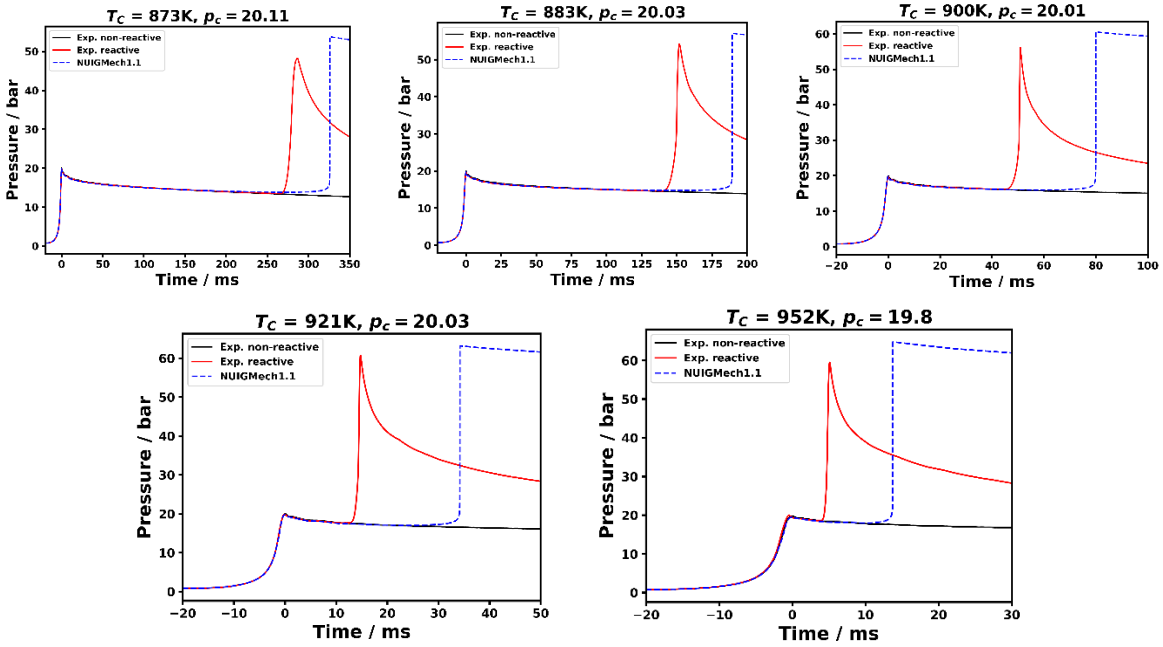

Figure ES12. NUIG–RCM experimental non-reactive (NR), reactive (R), and NUIGMech1.1 simulated pressure traces. For 90% C_2H_6 / 10% C_3H_8 blend with 75% N_2, at 20 bar and φ = 2.0.

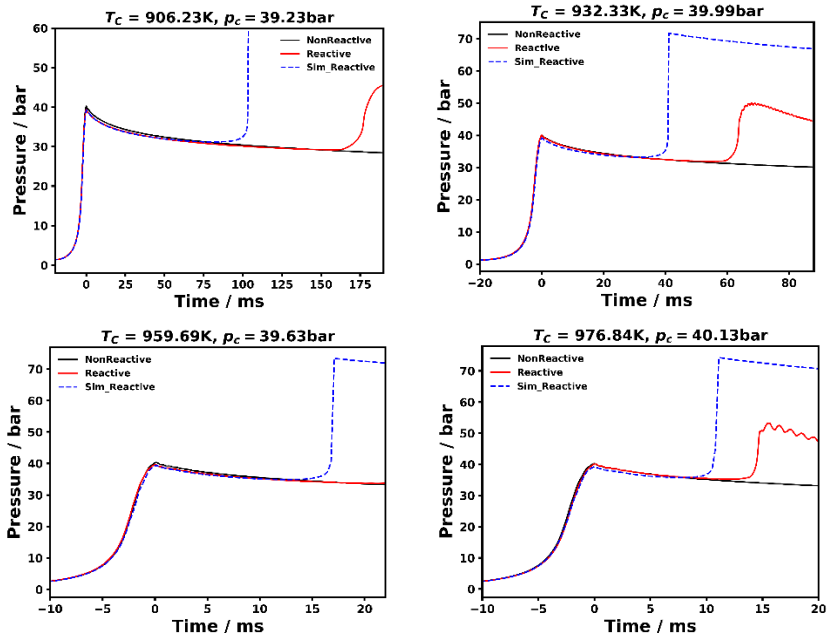

Figure ES13. PCFC–RCM experimental non-reactive (NR), reactive (R), and NUIGMech1.1 simulated pressure traces. For 90% C_2H_6 / 10% C_3H_8 blend with 75% N_2 +10% Ar, at 40 bar and φ = 0.5.

Appendix E

4. Correlation parameters

As mentioned in Section 8.4.6 of the manuscript, global correlations were generated using an extensive sample of ~17280 IDTs calculated by Cantera using constant volume (CV) simulations and NUIGMech1.1. The expression used for correlating the IDTs is presented as Equation ES-1,

$$\tau_{corr} = 10^{A} e^{\frac{B}{T_C}} [C_2H_4]^{C} [C_2H_6]^{D} [C_3H_8]^{E} [\text{Oxidizer}]^{F} [\text{Dilution}]^{G} \quad \text{(ES-1)}$$

where A, B, and C–G refer to the pre-exponential factor, the activation energy, and ethylene, ethane, propane, oxygen, and diluent concentrations, respectively. Table ES6 and ES7 present all of the coefficients, χ^2, R^2, and the ranges wherein the correlations are valid.

Table ES6. Correlation coefficients for the C_2H_4/C_3H_8 blend.

Coefficients	$1 \le p \le 20$ atm		$20 \le p \le 40$ atm		
	$800 \le T \le 1300$ K	$1300 \le T \le 2000$ K	$800 \le T \le 1100$ K	$1100 \le T \le 1500$ K	$1500 \le T \le 2000$ K
A	-9.22 ±0.029	-8.93 ±0.021	-7.22 ±0.030	-9.89 ±0.04	-10.34±0.028
B	18501.31 ±52.86	17848.85 ±72.58	14136.92 ±48.38	19220.37 ±94.22	21386.61 ±77.49
C[ethylene]	-0.504 ±0.002	-0.077 ±0.004	-0.440 ±0.003	-0.491±0.003	-0.502 ±0.003
D[ethane]	0	0	0	0	0
E[propane]	-0.141 ±0.002	0.527 ±0.004	-0.392 ±0.002	-0.056 ±0.003	0.463 ±0.003
F	-0.221 ±0.003	-1.32 ±0.007	-0.427±0.005	-0.447 ±0.006	-1.08 ±0.005
G	-0.272±0.005	0.1824 ±0.006	-0.017 ±0.008	0.149 ±0.009	0.355 ±0.008
χ^2	0.013	6.01E-12	5.14E-05	2.38E-09	1.06E-11
R^2	0.994	0.982	0.986	0.987	0.985

Table ES7. Correlation coefficients for the C_2H_6/C_3H_8 blend

Coefficients	$1 \le p \le 20$ atm		$20 \le p \le 40$ atm		
	$800 \le T \le 1300$ K	$1300 \le T \le 2000$ K	$800 \le T \le 1100$ K	$1100 \le T \le 1500$ K	$1500 \le T \le 2000$ K
A	-9.96 ±0.025	-8.61 ±0.053	-9.52 ±0.045	-9.79 ±0.029	-9.40 ±0.023
B	20110.92 ±44.80	18957.52±133.21	18630.75±78.03	19065.65 ±67.43	20465.02±68.93
C[ethylene]	0	0	0	0	0
D[ethane]	-0.248 ±0.001	0.336 ±0.005	-0.145 ±0.003	-0.408 ±0.002	0.113 ±0.003
E[propane]	-0.351 ±0.001	0.437 ±0.005	-0.555 ±0.003	-0.169±0.002	0.412 ±0.003
F	-0.112 ±0.003	-1.35 ±0.008	-0.186 ±0.005	-0.330 ±0.004	-1.34 ±0.005
G	-0.311 ±0.003	-0.108 ±0.008	-0.145 ±0.008	0.062 ±0.007	0.131 ±0.008
χ^2	0.017	3.70E-07	3.57E-04	2.30E-09	2.63E-13
R^2	0.998	0.965	0.992	0.989	0.988

Appendix E

Table ES8. Correlation coefficients for the C2H6/C3H8 blend

Coefficients	$90 \leq p \leq 135$ atm
	$800 \leq T \leq 1000$ K
A	-9.63 ±0.1
B	18232.41 ±152
C[ethylene]	0
D[ethane]	-0.18 ±0.01
E[propane]	-0.61 ±0.01
F	-0.16 ±0.01
G	-0.02 ±0.02
χ^2	2.92E-04
R^2	0.98768

5. Statistical analyses

As already mentioned in the results and discussion, Section 8.4 of the manuscript, all of the experimental IDTs, NUIGMech1.1, and AramcoMech3.0 predicted IDTs and correlated IDTs are reported in milliseconds (ms). For the experimental data presented in Figs. 8-2 and 8-3 of Section 8.4.1, a total of 328 IDTs were collected and simulated and were used to calculate the mean (μ), median, the standard deviation (σ), the mean absolute deviation (MAD), the mean square error (MSE), and the mean absolute percentage error (MAPE). Figs. S10(a) and (b) provide the RPE frequency distribution for NUIGMech1.1 and AramcoMech3.0 relative to the IDT experiments. The most extreme points beyond ~150% RPE can be considered outliers due to the relatively low frequency and distance from the rest of the population sample. Both histograms are right-skewed distributions, and consequently, their mean is always bigger than the median of the data. The standard deviation (σ) of the NUIGMech1.1 histogram in Figure S10(a) is ~35.4, while it is ~43.25 for AramcoMech3.0. This indicates that the values are more distributed around the mean for AramcoMech3.0 compared to NUIGMech1.1 predictions. Additionally, the MAD for the NUIGMech1.1 histogram was ~2.9, while it was ~5.0 using AramcoMech3.0, again highlighting that the discrepancies in predictions from measurements are more spread out for AramcoMech3.0 compared to those predicted using NUIGMech1.1.

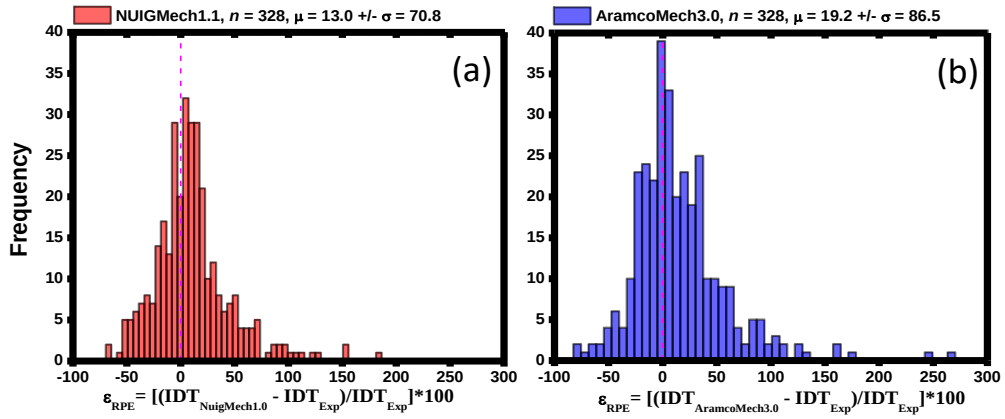

Figure ES13. Histograms presenting total sample size taken (n), mean of sample (μ), and the standard deviation (σ) for each mechanism. The occurrence of each specific % error is plotted as a function of individual relative percentage error (RPE) for; (a) NUIGMech1.1; and (b) AramcoMech3.0 predictions against the corresponding experimental IDTs.

Thereafter, all of the correlated IDTs used in the graphs presented in Sections 8.4.2 – 8.4.5 were used to determine the MAD, MSE, MAPE, and σ, for the correlations using 263 IDTs. The blending effects presented in Section 8.4.2 were correlated using 52 IDTs, and for the other effects such as pressure, equivalence ratio, and dilution, 78 IDTs were used. Table ES8 presents the detailed values for the statistical analyses of the overall performance of NUIGMech1.1, AramcoMech3.0 and the correlations against the and the correlated individual effects compared to NUIGMech1.1.

Table ES9. Overall statistical analyses values for the different mechanisms and correlations presented in the current study.

	Data source	n	μ	median	σ	MAD	MSE	MAPE
Figure ES11(a)	NUIGMech1.1 vs experiment	328	12.98	9.0	35.40	2.91	101.85	26.36%
Figure ES11 (b)	AramcoMech3.0 vs experiment	328	19.19	11.0	43.20	5.03	559.40	31.94%
Figure ES11 (c)	Correlation vs experiment	263	7.56	3.0	36.49	0.22	0.63	24.37%
Figure ES11 (d)	Correlation vs NUIGMech1.1	286	12.36	7.0	34.69	13627.71	2.1E+9	24.35%

Appendix E

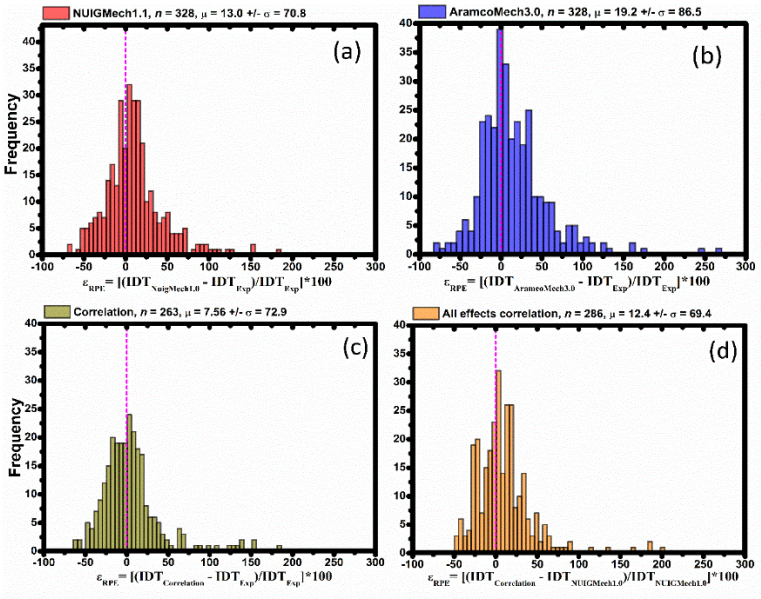

Figure ES14 Histograms presenting total sample size taken (n), mean of sample (μ) and the standard deviation (2σ) for each mechanism or correlation performance. On the *y*-axis, the occurrence of each specific % error against *x*-axis, that presents the individual relative percentage error (RPE). (a – c) All comparisons have been made versus the experimental data for; (a) NUIGMech1.1 (red bars); (b) AramcoMech3.0 (blue bars); (c) the derived correlations (green bars); and (d) the performance of the derived correlations versus NUIGMech1.1 (orange bars).

Individual effects of the studied parameters such as blending in Section 8.4.2, pressure in Section 8.4.3, equivalence ratio in Section 8.4.4, and dilution in Section 8.4.5 graphs, the Table ES9 shows that were correlated using 52 data points, and other effects such as pressure, equivalence ratio and dilution, used 78 data points, represented by n along with the detailed values for the statistical analyses done over all data sets.

Table ES10 Individual effects of the studied parameters on IDT, including statistical values for the derived correlations versus NUIGMech1.1.

	Data source	n	μ	median	σ	MAD	MSE	MAPE
Figure ES12 (a)	Blending effect correlation vs NUIGMech1.1	52	18.19	-1.0	58.61	5.644	640.525	35.401%
Figure ES12 (b)	Pressure effect correlation vs NUIGMech1.1	78	9.406	7.0	25.234	41.45	77954.098	20.399%
Figure ES12 (c)	ϕ effect correlation vs NUIGMech1.1	78	1.04	4.0	22.001	2.457	76.047	18.198%
Figure ES12 (d)	Dilution effect correlation vs NUIGMech1.1	78	22.68	19.0	27.114	2.299	50.2	27.085%

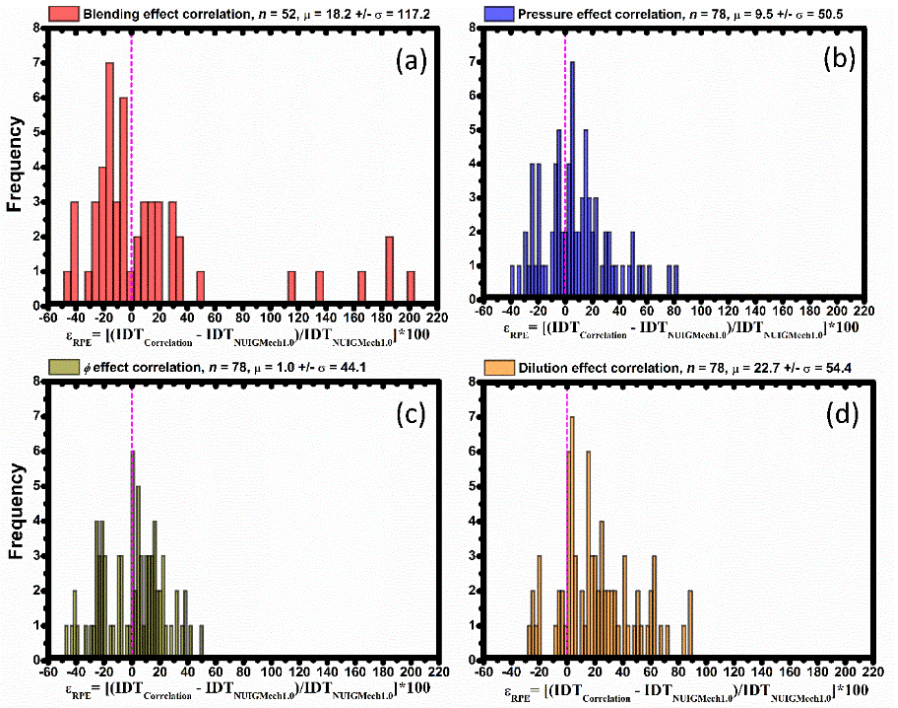

Figure ES15 Histograms presenting total sample size taken (n), mean of sample (μ) and the standard deviation (2xσ) for the effect of each studied parameter. On the *y*-axis, the occurrence of each specific % error against *x*-axis, that presents the individual relative percentage error (RPE). For all cases, the correlated IDTs against NUIGMech1.1's IDTs have been used; (a) for blending effect in red; (b) for pressure effect in blue; (c) for the equivalence ratio effect in green; and (d) for dilution effect in orange.

The blending effect correlated IDTs has already been discussed in Section 8.4.6 dedicated to the correlation performance, and Figure ES12 presents a histogram to illustrate the influence of each effect along with the statistical parameters provided in Table ES9.

In Figure 8-9 of Section 8.4.3 describing the effect of pressure on ignition, the derived correlations were included and represented as dotted lines for every pressure trend for each blend. For the binary blends, the coefficient values to calculate τ_{corr} were taken from Tables ES6 and ES7. In this regard, the correlation was compared using 78 correlated IDTs (τ_{corr}) compared to the simulated NUIGMech1.1 data, including a range of temperatures from 800 – 2000 K, at φ = 0.5 in air and at pressures ranging from 1 – 40 atm. The correlated IDT behaves as expected for trends based on the effect of pressure, hence as we decrease the pressure from 40 to 20 atm, the τ_{corr} increased by ~50%, whereas going from 20 atm to 1 atm, the τ_{corr} increased dramatically to ~200%. The statistical comparison of τ_{corr} against IDT collected using NUIGMech1.1 leads to an

overall performance of ~20.4% for the MAPE, a correlated MAD of 41.45 ms, and a standard deviation (σ) of ~25.2 ms that all details can be found in Table ES9.

As expected, such a behavior can be found in the correlated IDTs related to Figs. 8-12 and 8-13 of Sections 8.4.4 and 8.4.5, respectively. These correlations follow the simulated trends using NUIGMech1.1 for the effects of equivalence ratio and dilution. A total sample of 78 correlated IDTs compared to NUIGMech1.1's IDTs were used to calculate the statistical comparison of each effect, which leads to an overall performance of ~18.2% for the MAPE, a MAD of about 2.457 ms, and a standard deviation (σ) of ~22.0 ms for the equivalence ratio effect. The statistical comparison of τ_{corr} against IDT collected using NUIGMech1.1 for the dilution effect leads to an overall performance of ~27.0% of MAPE, a correlated MAD of about 2.3 ms, and a standard deviation (σ) of ~27.1 ms.

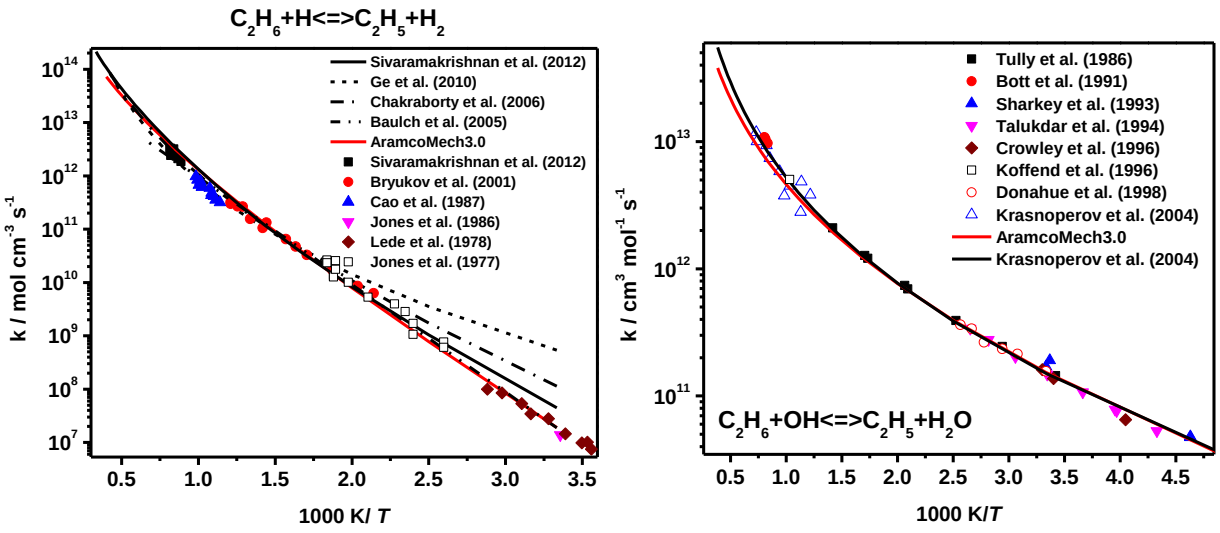

Figure ES16. Comparisons between experimental and theoretical data for the reaction rate constant of; (a) C_2H_6 + Ḣ [15-23]; and (b) C_2H_6 + ȮH [32-39].

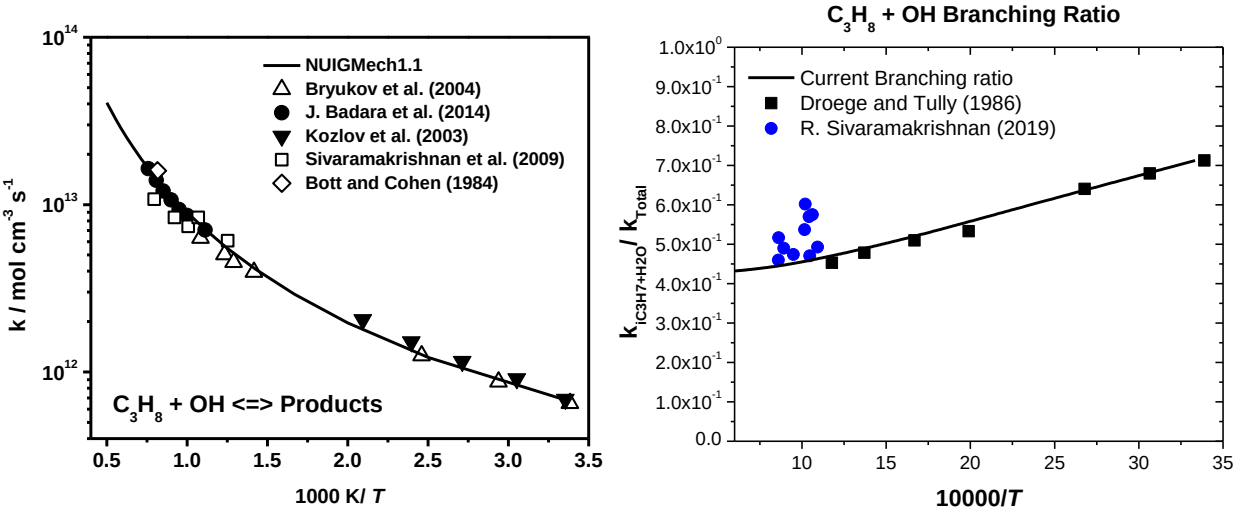

(a) (b)

Figure ES17. Comparisons between experimental and theoretical data for (a) C_3H_8 + $\dot{O}H$ [40-44] rate; and (b) branching product ratio for the reaction C_3H_8 + $\dot{O}H$ [24, 25]

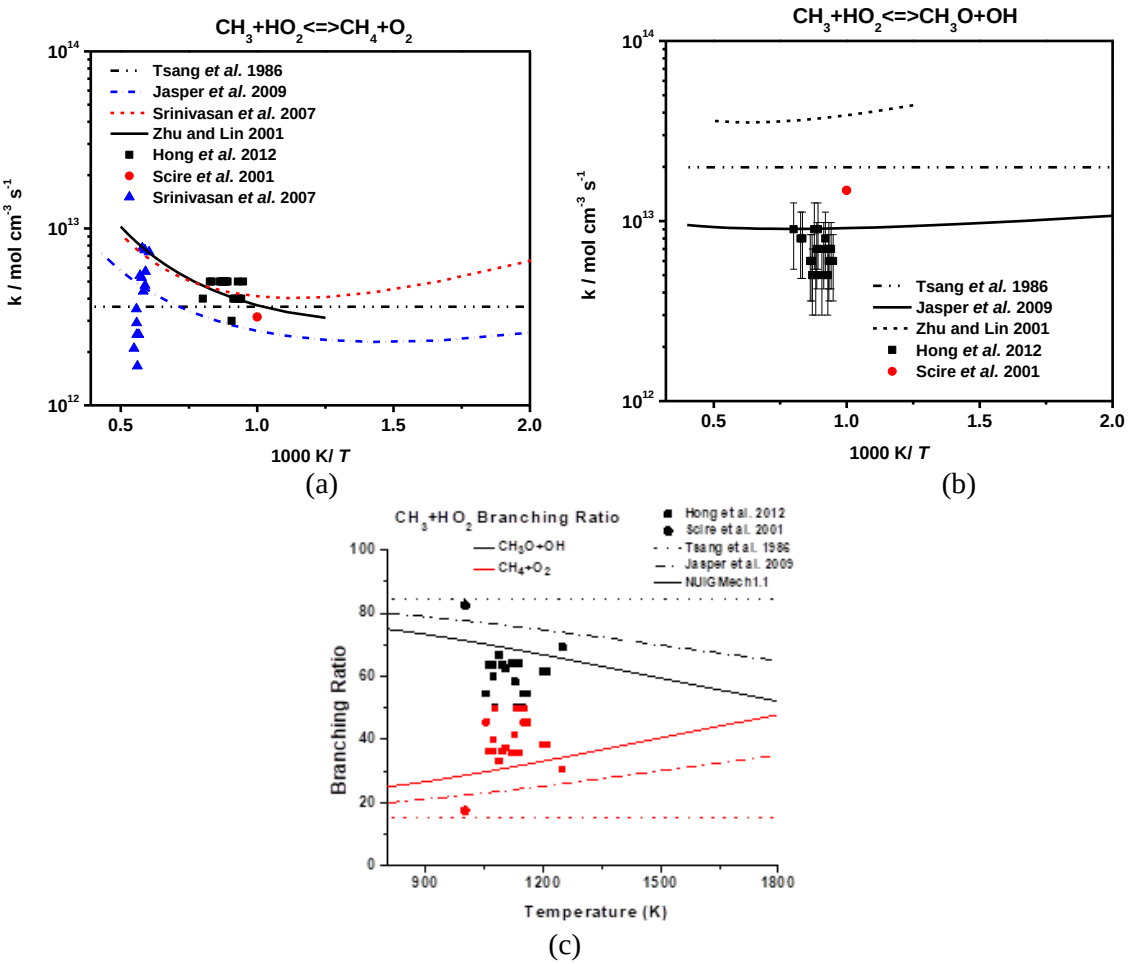

(a) (b)

(c)

Figure ES18. Comparisons between experimental and theoretical data for the total reaction rate constant of CH_3+$H\dot{O}_2$ system [26-31] and the branching ratio of the two channels in CH_3+HO_2. The reverse rate constant for CH_4+O_2 = CH_3+$H\dot{O}_2$ by Srinivasan et al. 2007 is obtained using the equilibrium constant based on NUIGMech1.1 thermodynamic property.

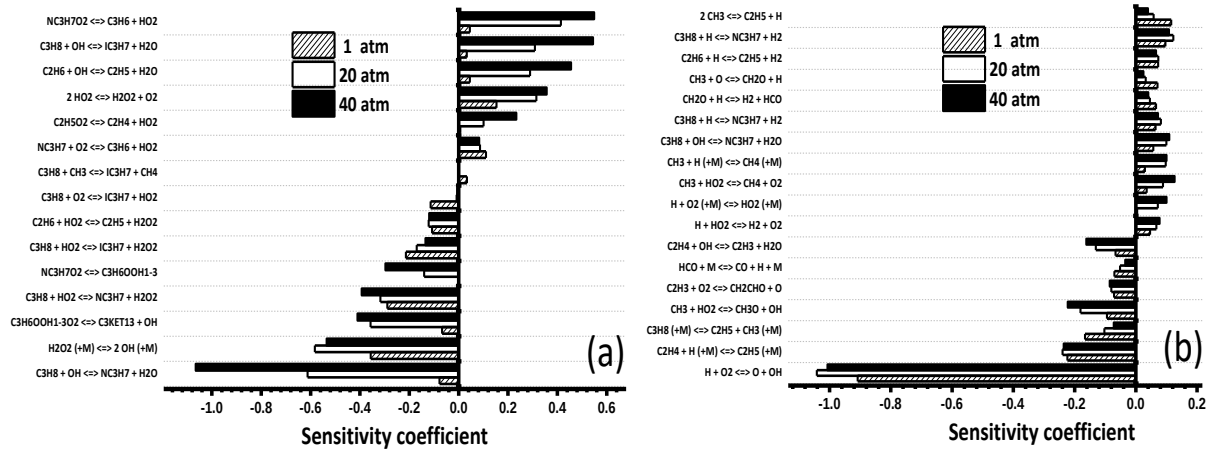

Figure ES19. Sensitivity analyses of IDT as a function of pressure at; (a) 800K; and (b) 1600 K, φ = 0.5, 50%/50% C_2H_6/C_3H_8 and 75% N_2 as diluent.

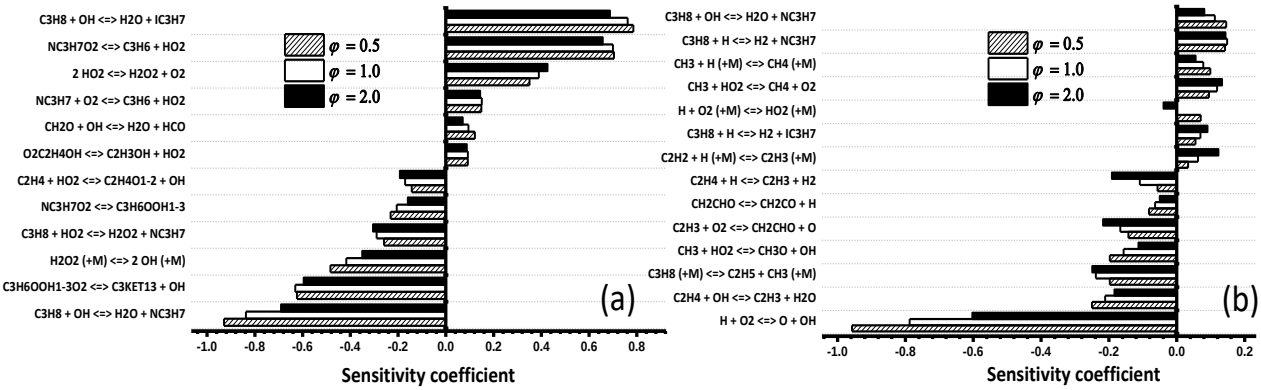

Figure ES20. Sensitivity analyses of IDT as function of equivalence ratio at; (a) 800K; and (b) 1600 K, 20 atm, 50% C_2H_4/50% C_3H_8 and 75% N_2 as diluent.

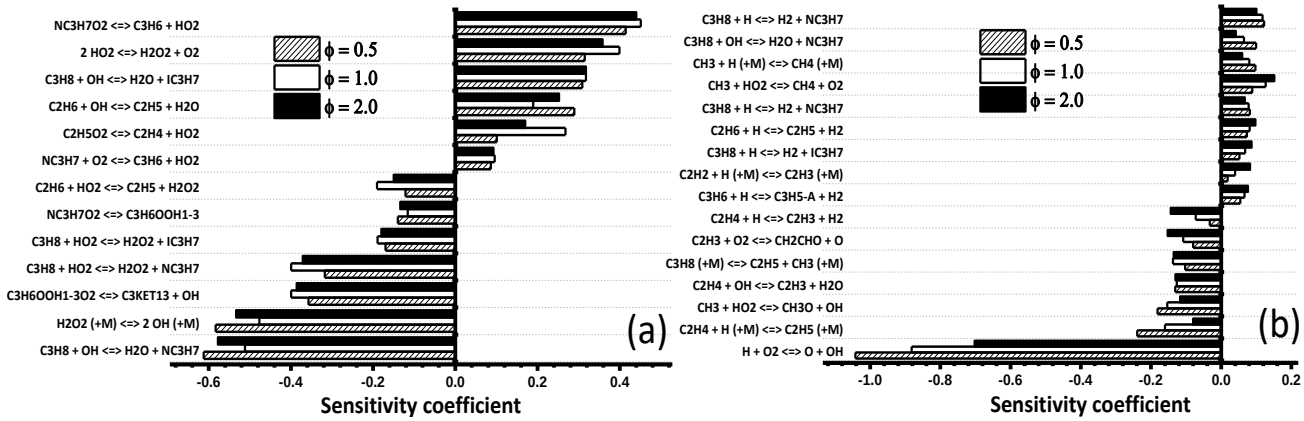

Figure ES21. Sensitivity analyses of IDT as a function of equivalence ratio for 50%/50% C_2H_6/C_3H_8 at 75% N_2 dilution at 20 atm and at; (a) 800K; and (b) 1600 K.

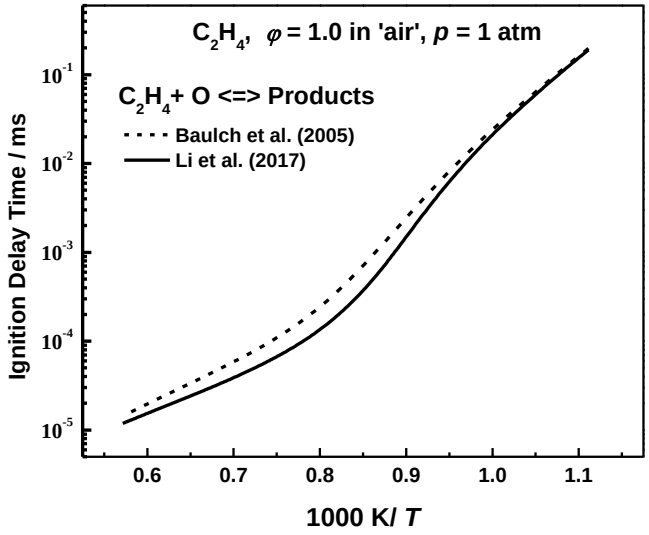

Figure ES22. Effect of updating the rate constant for C_2H_4 + Ö → products on IDT predictions for C_2H_4/air mixtures.

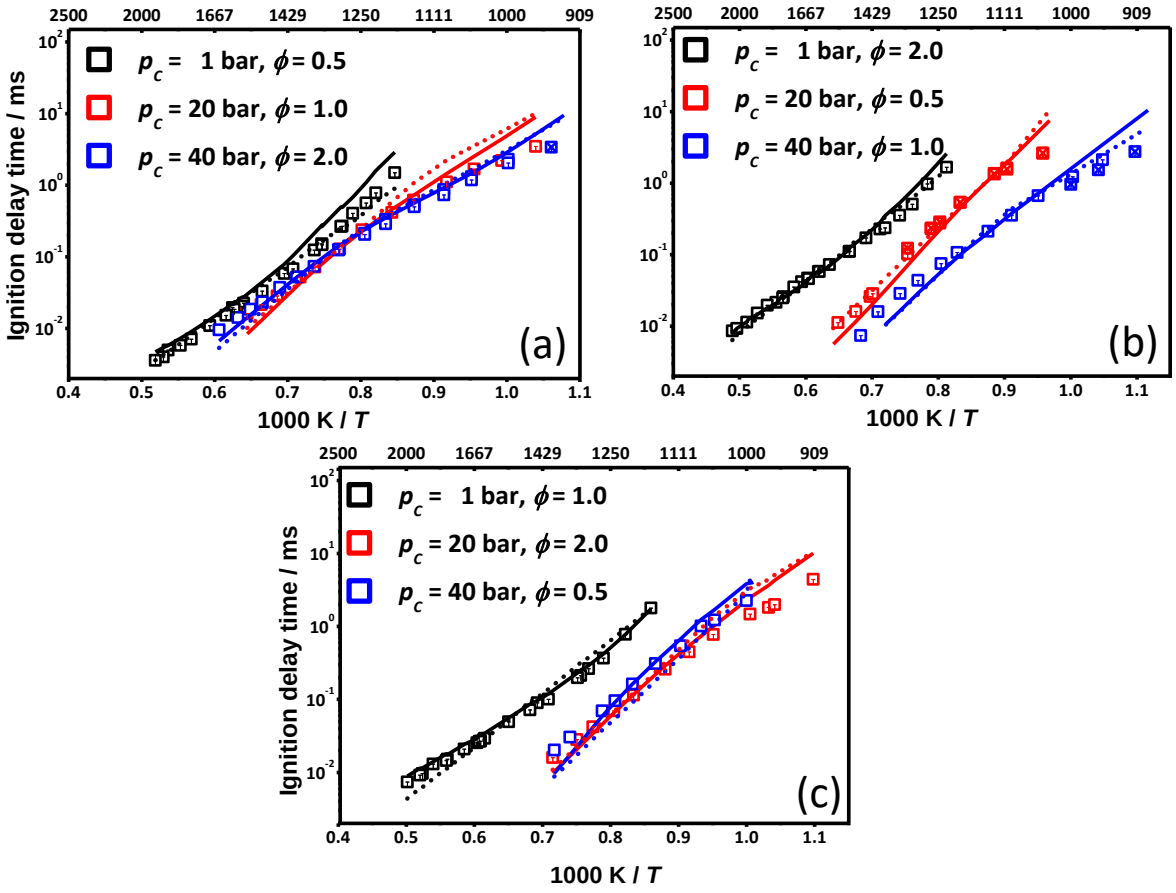

Figure ES23. Comparisons of experimental ST (□) data against model predictions by NUIGMech1.1 (solid lines) and correlation (dotted lines) for; (a) 50% C_2H_4/50% C_3H_8 blend at 75% N_2 (black symbols/lines), 75% N_2 + 10% Ar (red symbols/lines), and 75% N_2 + 15% Ar (blue symbols/lines); (b) 70% C_2H_4/30% C_3H_8 blend at 75% N_2 + 10% Ar (black symbols/lines), 75% N_2 + 15% Ar (red symbols/lines), and 75% N_2 (blue symbols/lines); and (c) 90% C_2H_4/10% C_3H_8 blend at 75% N_2 + 15% Ar (black symbols/lines), 75% N_2 (red symbols/lines), and 75% N_2 + 10% Ar (blue symbols/lines).

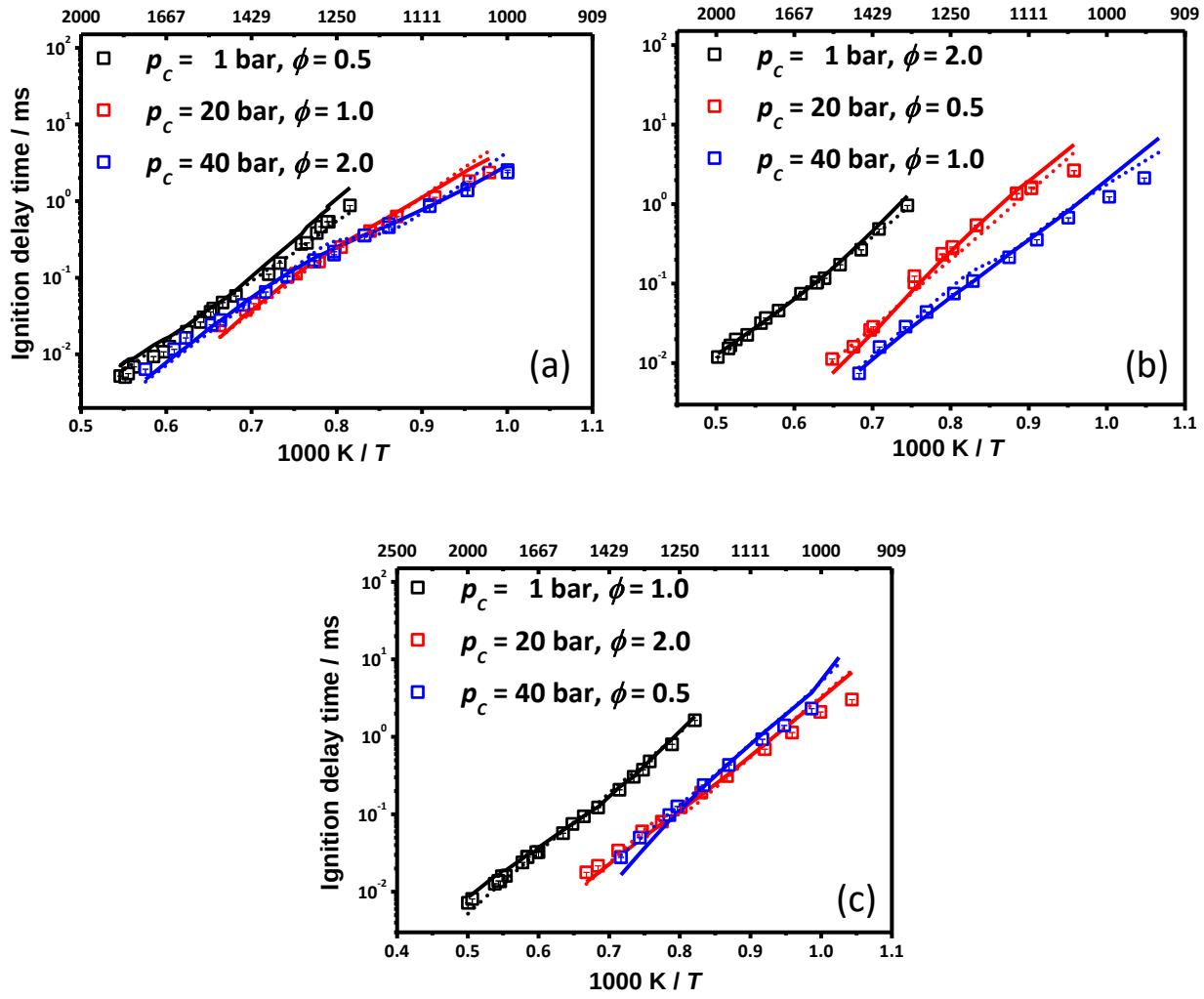

Figure ES24. Comparisons of experimental ST (□) data, against model prediction by NUIGMech1.1 (solid lines) and correlation (dotted lines), for; (a) 50% C_2H_6/50% C_3H_8 blend at 75% N_2 (black symbols/lines), 75% N_2 + 10% Ar (red symbols/lines), and 75% N_2 + 15% Ar (blue symbols/lines); (b) 70% C_2H_6/30% C_3H_8 blend at 75% N_2 + 10% Ar (black symbols/lines), 75% N_2 + 15% Ar (red symbols/lines), and 75% N_2 (blue symbols/lines); and (c) 90% C_2H_6/10% C_3H_8 blend at 75% N_2 + 15% Ar (black symbols/lines), 75% N_2 (red symbols/lines), and 75% N_2 + 10% Ar (blue symbols/lines)

Appendix E

References

[1] M. Baigmohammadi, V. Patel, S. Martinez, S. Panigrahy, A. Ramalingam, U. Burke, K. P. Somers, K. A. Heufer, A. Pekalski, H.J. Curran, A comprehensive experimental and simulation study of ignition delay time characteristics of single fuel C_1−C_2 hydrocarbons over a wide range of temperatures, pressures, equivalence ratios, and dilutions, Energy Fuels, 34 (3) (2020) 3755–3771.

[2] M. Baigmohammadi, V. Patel, S. Nagaraja, A. Ramalingam, S. Martinez, S. Panigrahy, A. A. E. Mohamed, K.P. Somers, U. Burke, K.A. Heufer, A. Pekalski, H.J. Curran, Comprehensive experimental and simulation study of the ignition delay time characteristics of binary blended methane, ethane, and ethylene over a wide range of temperature, pressure, equivalence ratio, and dilution, Energy Fuels, 34(7) (2020) 8808–8823.

[3] P.J. Ross, Taguchi Techniques for Quality Engineering, New York, 1988.

[4] F.R. Gillespie, An experimental and modelling study of the combustion of oxygenated hydrocarbons, (2014) 1–250.

[5] J Wurmel, M. McGuinness, J.M. Simmie, High-temperature oxidation of ethylene oxide in shock waves, J Chem Soc Faraday, 92 (1996) 715–721.

[6] S.S. Nagaraja, J. Liang, S. Dong, S. Panigrahy, A. Sahu, G. Kukkadapu, S.W. Wagnon, W.J. Pitz, H.J. Curran, A hierarchical single-pulse shock tube pyrolysis study of C_2–C_6 1-alkenes, Combust. Flame, 219 (2020) 456–466.

[7] S.M. Gallagher, H.J. Curran, W.K. Metcalfe, D. Healy, J.M. Simmie, G. Bourque, A rapid compression machine study of the oxidation of propane in the negative temperature coefficient regime, Combust. Flame, 153 (2008) 316–333.

[8] S.M. Burke, U. Burke, R. Mc Donagh, O. Mathieu, I. Osorio, C. Keesee, A. Morones, E.L. Petersen, W. Wang, T.A. DeVerter, M.A. Oehlschlaeger, B. Rhodes, R.K. Hanson, D.F. Davidson, B.W. Weber, C.-J. Sung, J. Santner, Y. Ju, F.M. Haas, F.L. Dryer, E.N. Volkov, E.J.K. Nilsson, A.A. Konnov, M. Alrefae, F. Khaled, A. Farooq, P. Dirrenberger, P.-A. Glaude, F. Battin-Leclerc, H.J. Curran, An experimental and modeling study of propene oxidation. Part 2: Ignition delay time and flame speed measurements, Combust. Flame, 162 (2015) 296–314.

[9] S.M. Burke, W. Metcalfe, O. Herbinet, F. Battin-Leclerc, F.M. Haas, J. Santner, F.L. Dryer, H.J. Curran, An experimental and modeling study of propene oxidation. Part 1: Speciation measurements in jet-stirred and flow reactors, Combust. Flame ,161 (2014) 2765–2784.

[10] D. Healy, H.J. Curran, S. Dooley, J.M. Simmie, D.M. Kalitan, E.L. Petersen, G. Bourque, Methane/propane mixture oxidation at high pressures and at high, intermediate and low temperatures, Combust. Flame, 155 (2008) 451–461.

[11] D. Healy, H.J. Curran, J.M. Simmie, D.M. Kalitan, C.M. Zinner, A.B. Barrett, E.L. Petersen, G. Bourque, Methane/ethane/propane mixture oxidation at high pressures and at high, intermediate and low temperatures, Combust. Flame, 155 (2008) 441–448.

[12] D. Healy, D.M. Kalitan, C.J. Aul, E.L. Petersen, G. Bourque, H.J. Curran, Oxidation of C_1−C_5 alkane quinternary natural gas mixtures at high pressures, Energy Fuels, 24 (2010) 1521–1528.

[13] C. Morley, http://www.gaseq.co.uk

[14] https://www.tiepie.com/en/oscilloscope-software.

[15] Y. Ge, M.S. Gordon, F. Battaglia, &, R.O. Fox, Theoretical study of the pyrolysis of methyltrichlorosilane in the gas phase. 3. Reaction rate constant calculations, J. Phys. Chem. A, 114(6) (2010) 2384–2392.

[16] A. Chakraborty, Y. Zhao, H. Lin, & , D.G. Truhlar, Combined valence bond-molecular mechanics potential-energy surface and direct dynamics study of rate constants and kinetic isotope effects for the H+ C_2H_6 reaction, J. Chem. Phys., 124(4) (2006) 044315.

[17] D.L. Baulch, C. Cobos, R.A. Cox, C. Esser, P. Frank, T. Just, & , J. Warnatz, Evaluated kinetic data for combustion modelling, J. Phys. Chem. Ref. Data, 21(3) (1992) 411–734.
[18] M.G. Bryukov, I.R. Slagle, V.D. Knyazev, Kinetics of reactions of H atoms with ethane and chlorinated ethanes, J. Phys. Chem. A, 105 (2001) 6900–6909.
[19] J.R. Cao, &, M.H. Back, Kinetics of the reaction $H+C_2H_6 \rightarrow H_2+ C_2H_5$ in the temperature region of 1000 K, Can. J. Chem., 62(1) (1984) 86–91.
[20] W.E. Jones, & , J.L. Ma, An electron spin resonance study of the reactions of hydrogen atoms with halocarbons, Can. J. Chem., 64(11) (1986) 2192–2195.
[21] J. Lede, & , J. Villermaux, Mesure de la constante de vitesse de réaction des atomes d'hydrogène sur l'éthane et le propane en réacteurs tubulaire et parfaitement agité ouverts, Can. J. Chem., 56(3) (1978) 392–401.
[22] D. Jones, P.A. Morgan, & , J.H. Purnell, Mass spectrometric study of the reaction of hydrogen atoms with ethane, J. Chem. Soc. Faraday Trans., 73 (1977) 1311–1318.
[23] R. Sivaramakrishnan, J.V. Michael, B. Ruscic, High-temperature rate constants for H/D+ C2H6 and C3H8, Int. J. Chem. Kinet., 44(3) (2012) 194–205.
[24] A.T. Droege, F.P. Tully, Hydrogen-atom abstraction from alkanes by hydroxyl. 3. Propane, J. Phys. Chem., 90 (1986) 1949–1954.
[25] R. Sivaramakrishnan, C.F. Goldsmith, S. Peukert, J.V. Michael, Direct measurements of channel specific rate constants in $OH + C_3H_8$ illuminates prompt dissociations of propyl radicals, Proc. Combust. Inst., 37 (2019) 231–238.
[26] A.W. Jasper, S.J. Klippenstein, L.B. Harding, Theoretical rate coefficients for the reaction of methyl radical with hydroperoxyl radical and for methylhydroperoxide decomposition, Proc Combust Inst., 32 (2009) 279–286.
[27] R. Zhu, C. Lin, The $CH_3 + HO_2$ Reaction: First-principles prediction of its rate constant and product branching probabilities, J. Phys. Chem. A, 105 (2001) 6243–6248.
[28] Z. Hong, D.F. Davidson, K.Y. Lam, R.K. Hanson, A shock tube study of the rate constants of HO_2 and CH_3 reactions, Combust. Flame, 159 (2012) 3007–3013.
[29] Jr. Scire, J. James.; Yetter, R.A. Yetter;, F.L. Dryer, Flow reactor studies of methyl radical oxidation reactions in methane-perturbed moist carbon monoxide oxidation at high pressure with model sensitivity analysis, Int. J. Chem. Kinet., 33 (2001) 75–100.
[30] N.K. Srinivasan, J.V. Michael, L.B. Harding, S.J. Klippenstein, Experimental and theoretical rate constants for $CH_4 + O_2 \rightarrow CH_3 + HO_2$, Combust Flame 149 (2007) 104–111.
[31] W. Tsang, R.F. Hampson, Chemical kinetic data base for combustion chemistry. Part I. Methane and related compounds, Int. J. Chem. Kinet., 15 (1986) 1087–1279.
[32] F.P. Tully, A.T. Droege, M.L. Koszykowski, C.F. Melius, Hydrogen-atom abstraction from alkanes by OH. 2. Ethane, J. Phys. Chem., 90 (1986) 691–698.
[33] J.F. Bott, N. Cohen, A shock tube study of the reaction of methyl radicals with hydroxyl radicals, Int. J. Chem. Kinet., 23 (1991) 1017–1033.
[34] P. Sharkey, I.W. Smith, Kinetics of elementary reactions at low temperatures : Rate, J. Chem. Soc., Faraday Trans., 89 (1993) 631–638.
[35] R.K. Talukdar, A. Mellouki, T. Gierczak, S. Barone, S.Y. Chiang, R. Ravishankara, Kinetics of the reactions of OH with alkanes, Int. J. Chem. Kinet., 26 (1994) 973–990.
[36] J.N. Crowley, P. Campuzano-Jost, G.K. Moortgat, Temperature dependent rate constants for the gas-phase reaction between OH and CH_3OCl, J. Phys. Chem., 100 (1996) 3601–3606.
[37] J.B. Koffend, N. Cohen, Shock tube study of OH reactions with linear hydrocarbons near 1100 K, Int. J. Chem. Kinet., 28 (1996) 79–87.
[38] N.M. Donahue, J.G. Anderson, K.L. Demerjian, New rate constants for ten OH alkane reactions from 300 to 400 K: An assessment of accuracy, J. Phys. Chem. A, 102 (1998) 3121–3126.

[39] L.N. Krasnoperov, J.V. Michael, Shock tube studies using a novel multipass absorption Cell: Rate constant results for OH + H_2 and OH + C_2H_6, J. Phys. Chem. A, 108 (2004) 5643–5648.
[40] M.G. Bryukov, V.D. Knyazev, S.M. Lomnicki, C.A. McFerrin, B. Dellinger, Temperature-dependent kinetics of the gas-phase reactions of OH with Cl_2, CH_4, and C_3H_8, J. Phys. Chem. A, 108 (2004) 10464–10472.
[41] J. Badra, E.F. Nasir, A. Farooq, Site-Specific Rate constant measurements for primary and secondary H- and D-abstraction by OH radicals: Propane and n-Butane, J. Phys. Chem. A, 118 (2014) 4652–4660.
[42] S.N. Kozlov, V.L. Orkin, R.E. Huie, M.J. Kurylo, OH reactivity and UV spectra of Propane, n-Propyl Bromide, and Isopropyl Bromide, J. Phys. Chem. A, 107 (2003) 1333–1338.
[43] R. Sivaramakrishnan, C.F. Goldsmith, S. Peukert, J.V. Michael, Direct measurements of channel specific rate constants in OH + C_3H_8 illuminates prompt dissociations of propyl radicals, Proc. Combust. Inst., 37 (2019) 231–238.
[44] J.F. Bott, N. Cohen, A shock tube study of the reaction of the hydroxyl radical with propane, Int. J. Chem. Kinet., 16 (1984) 1557–1566.